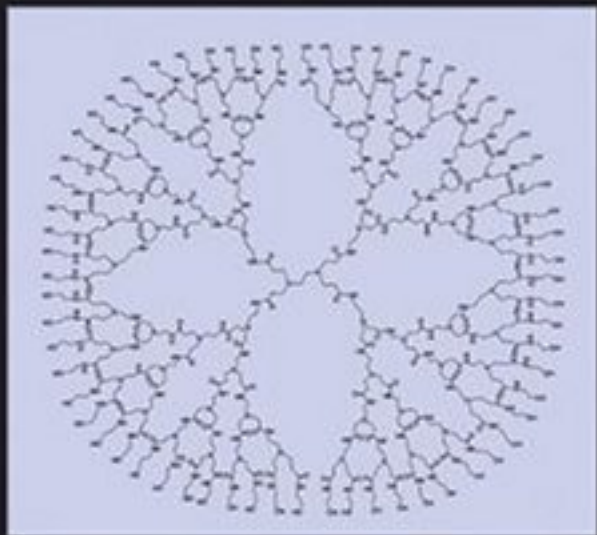




NANOSTRUCTURE SCIENCE AND TECHNOLOGY  
Series Editor: David J. Lockwood

# *Self-Organized Nanoscale Materials*



Motonari Adachi  
and David J. Lockwood

# Self-Organized Nanoscale Materials

# Nanostructure Science and Technology

Series Editor: David J. Lockwood, FRSC  
*National Research Council of Canada*  
*Ottawa, Ontario, Canada*

---

*Current volumes in this series:*

Alternative Lithography: Unleashing the Potentials of Nanotechnology  
*Edited by Clivia M. Sotomayor Torres*

Controlled Synthesis of Nanoparticles in Microheterogeneous Systems  
*Vincenzo Turco Liveri*

Interfacial Nanochemistry: Molecular Science and Engineering at Liquid-Liquid Interfaces  
*Edited by Hitoshi Watarai*

Introduction to Nanoscale Science and Technology, Vol. 6  
*Di Ventra, Massimiliano, Evoy Stephane, and James R. Helfin Jr.*

Nanoparticles: Building Blocks for Nanotechnology  
*Edited by Vincent Rotello*

Nanoscale Assembly—Chemical Techniques  
*Edited by Wilhelm T.S. Huck*

Nanostructured Catalysts  
*Edited by Susannah L. Scott, Cathleen M. Crudden, and Christopher W. Jones*

Nanotechnology in Catalysis, Volumes 1 and 2  
*Edited by Bing Zhou, Sophie Hermans, and Gabor A. Somorjai*

Ordered Porous Nanostructures and Applications  
*Edited by Ralf B. Wehrspohn*

Polyoxometalate Chemistry for Nano-Composite Design  
*Edited by Toshihiro Yamase and Michael T. Pope*

Self-Assembled Nanostructures  
*Jin Z. Zhang, Zhong-lin Wang, Jun Liu, Shaowei Chen, and Gang-yu Liu*

Self-Organized Nanoscale Materials  
*Edited by Motonari Adachi and David J. Lockwood*

Semiconductor Nanocrystals: From Basic Principles to Applications  
*Edited by Alexander L. Efros, David J. Lockwood, and Leonid Tsybeskov*

Surface Effects in Magnetic Nanoparticles  
*Dino Fiorani*

---

A Continuation Order Plan is available for this series. A continuation order will bring delivery of each new volume immediately upon publication. Volumes are billed only upon actual shipment. For further information please contact the publisher.

# Self-Organized Nanoscale Materials

Motonari Adachi and David J. Lockwood  
Editors

With 197 Figures

 Springer

Motonari Adachi  
International Innovation Center  
Kyoto University  
Uji, Kyoto 611-0011  
Japan  
adachi@iae.kyoto-u.ac.jp

David J. Lockwood  
Institute for Microstructural Sciences  
National Research Council of Canada  
Ottawa, Ontario K1A 0R6  
Canada  
david.lockwood@nrc-cnrc.gc.ca

Library of Congress Control Number: 2005931831

ISBN-10: 0-387-27975-X  
ISBN-13: 978-0387-27975-6

e-ISBN 0-387-27976-8

Printed on acid-free paper.

© 2006 Springer Science+Business Media, Inc.

All rights reserved. This work may not be translated or copied in whole or in part without the written permission of the publisher (Springer Science+Business Media, Inc., 233 Spring Street, New York, NY 10013, USA), except for brief excerpts in connection with reviews or scholarly analysis. Use in connection with any form of information storage and retrieval, electronic adaptation, computer software, or by similar or dissimilar methodology now known or hereafter developed is forbidden. The use in this publication of trade names, trademarks, service marks, and similar terms, even if they are not identified as such, is not to be taken as an expression of opinion as to whether or not they are subject to proprietary rights.

Printed in the United States of America. (TB/SBA)

9 8 7 6 5 4 3 2 1

springer.com

# Preface

Novel system performance through nanostructuring has been recognized in many branches of science in the latter half of the 20th century. In computer science, the computational efficiency has improved by nearly four orders of magnitude in 30 years, using energy consumed per operation as a metric. To achieve further advances will require the reduction in size of electronic devices to the scale of molecules; that is, a totally different type of computational machinery is required: molecular electronics. The requirement for inventing a new technology paradigm has created research opportunities for scientists in a very wide range of disciplines.

Nature uses molecular self-assemblies composed of surfactant molecules in biomineralization to construct nanostructures regulated at the atomic scale. Advances in synthetic molecular biology have resulted in highly efficient biological systems, which perform elegant energy and mass conversions using hierarchical assemblies of microstructures, again regulated at the atomic scale (e.g., the structure of the photosynthetic reaction center of a purple bacterium and the structure and reaction mechanism of enzymes).

In order to realize the tremendous potential of nanostructure science and technology, the extremely important challenges are how to exploit synthetic methods for structures regulated at the atomic scale and to construct materials across the hierarchy of length scales from the atomic to mesoscopic and/or to macroscopic scale.

This book comprises a survey of different approaches to the synthesis of nanoscale materials and the hierarchical assemblies produced from them, which have been prepared using self-organized mechanisms via chemical and bio-inspired methods. These methods have two principal advantages. First, nanoscale materials can be synthesized under mild conditions. For example, the layer-by-layer adsorption method in the liquid phase can accumulate different layers consecutively at room temperature just like the multilayer formation by molecular beam deposition at high temperature. The prime advantage of mild conditions such as room-temperature formation is essential for the utilization of biomaterials and is also recommended from an environmental point of view. Second, synthesis using self-organized mechanisms can make nanosize materials at the

scale of Avogadro's number. For comparison, it is very difficult to make nanosize materials at the scale of Avogadro's number by fabrication methods using an individual atom or molecule, such as manipulating atoms or molecules with the atomic force microscope (AFM) tip. Thermal, chemical, and structural stabilization of the nanostructured materials and removal of defects are other challenges still for the future.

The growth and properties of semiconductor quantum dots have been studied extensively in the last decade. These novel nanostructures offer interesting prospects for the development of new electronic or optoelectronic devices. In particular, if the size, shape, and positioning of those structures can be controlled, they become very attractive for applications in areas such as telecommunication wavelength integrated photodetectors, tunable light sources, and single-photon light sources. In Chapter 1, "Self-Assembled  $\text{Si}_{1-x}\text{Ge}_x$  Dots and Islands," Jean-Marc Baribeau, Nelson L. Rowell, and David J. Lockwood review progress in our understanding of  $\text{Si}_{1-x}\text{Ge}_x$  island growth on (001) Si. The evolution of the island morphology with  $\text{Si}_{1-x}\text{Ge}_x$  coverage is particularly complex and understanding it has led to a better knowledge of strained heterosystems. The chapter summarizes the effect of various growth parameters or postgrowth treatments on the shape of the  $\text{Si}_{1-x}\text{Ge}_x$  islands, their composition and strain distribution, their spatial distribution, and their vertical correlation in multilayer stacks. The vibrational properties of these  $\text{Si}_{1-x}\text{Ge}_x$  nanostructures are presented along with a detailed review of their optical properties, which are of key importance in device applications. The self-organization of the  $\text{Si}_{1-x}\text{Ge}_x$  islands is a feature of special significance if they are to become building blocks of novel devices. Various approaches that have been used to engineer  $\text{Si}_{1-x}\text{Ge}_x$  islands and, in particular, to control their size and spatial distribution are described. Recent progress in the use of  $\text{Si}_{1-x}\text{Ge}_x$  island superlattices as fast telecommunication infrared photodetectors is detailed.

One of the most active trends in modern materials chemistry is the development of synthetic methods to obtain size- and shape-controlled inorganic nanocrystals. The shape and size of inorganic nanocrystals determine their widely varying electrical and optical properties. As reported in Chapter 2, "Synthesis of Titania Nanocrystals: Application for Dye-Sensitized Solar Cells" by Motonari Adachi, Yusuke Murata, Fumin Wang, and Jinting Jiu, titania nanocrystals, which have a large surface area with controlled surface structure and high electron transport properties, are important for producing high-efficiency dye-sensitized solar cells (DSCs). DSCs have significant potential as a low-cost alternative to conventional *p-n* junction solar cells. Morphological control and high crystallinity are key properties needed in titanium oxide materials for such cells. A promising way to increase the efficiency of titanium oxide DSCs is to improve the properties of the semiconductor electrode using a network structure of single-crystalline anatase nanowires instead of a porous titania film composed of nanosize particles. In this chapter, the formation of a network structure of single-crystalline  $\text{TiO}_2$  nanowires by an "oriented attachment" mechanism is presented in detail. Methods are given for the morphological control of anatase nanocrystals using dodecanediamine as a surfactant, and the formation mechanism is discussed together with the synthesis

of nanosheets of quasi-anatase phase. Finally, the application of a  $\text{TiO}_2$  network of single-crystalline anatase nanowires in DSCs is considered.

Nanosized building blocks with low dimensionality such as nanowires, nanorods, nanotubes, and nanosheets have emerged as technically important systems, which provide fundamental scientific opportunities for investigating the influence of size and dimensionality on their optical, magnetic, and electronic properties as well as potential components for nanodevices. In Chapter 3, “Soft Synthesis of Inorganic Nanorods, Nanowires, and Nanotubes” by Shu-Hong Yu and Yi-Tai Qian, the latest developments on new mild soft-solution-based strategies for the fabrication of low-dimensional nanocrystals are reviewed. Examples of such approaches are the hydrothermal/solvothermal process, the solution–liquid–solid mechanism, capping agent/surfactant-assisted synthesis, the bio-inspired approach, and the oriented attachment growth mechanism. Current developments show that soft-solution synthesis provides alternative strategies for the rational synthesis of a variety of low-dimensional nanorods, nanowires, nanosheets, and nanotubes with a controllable size, shape, length scale, and structural complexity. This new growth mechanism could offer an additional tool to design advanced materials with anisotropic material properties and could be used for the synthesis of more complex crystalline three-dimensional structures.

Porous inorganic materials such as zeolites and zeolitelike crystalline molecular sieves are of great interest due to their range of commercial applications in traditional areas such as catalysis, adsorption/separation, and ion exchange and the more specialized fields of MRI contrast agents and blood-clotting agents. The term *zeolite* refers to the specific class of aluminosilicate molecular sieves, although the term is frequently used more loosely to describe compounds other than aluminosilicates that have frameworks similar to known zeolites. Here, in Chapter 4, “Assembly of Zeolites and Crystalline Molecular Sieves” by Jennifer L. Anthony and Mark E. Davis, various aspects of the assembly processes for synthesizing zeolites and other crystalline molecular sieves are overviewed. Topics covered include the thermodynamics and kinetics of the crystallization process, the possible self-assembly mechanisms in the crystallization, and the roles that the various components of the synthesis play in determining the ultimate structure that is formed. The importance of understanding how zeolites and zeolitelike molecular sieves are assembled from a molecular/atomic point of view is emphasized and the knowledge gained is applied to designing a chiral molecular sieve.

As discussed in Chapter 5, “Molecular Imprinting by the Surface Sol-Gel Process” by Seung-Woo Lee and Toyoki Kunitake, molecular imprinting is a fairly representative method of template synthesis and it has been recognized as a means for preparing specific binding sites for given molecules in appropriate matrices. In this approach, the shape and functionality of organic molecules as the template are transcribed onto microporous materials. The configuration of the functional groups in the template can be fixed within the matrix. In comparison with the more conventional sol-gel procedures, the characteristics of the surface sol-gel process, which was developed as a means for preparation of ultrathin metal oxide films, are presented. This process gives rise to oxide gel films of nanosize thickness, and



the individual metal oxide layers have a thickness close to 1 nm under carefully controlled conditions. Recent progress in molecular imprinting in metal oxide matrices is summarized together with the application of the surface sol-gel process to mixtures of organic carboxylic acids and titanium alkoxide, which provides ultrathin layers of titania gel. Many substances such as aromatic carboxylic acids, amino acid derivatives, peptides, saccharide monomers, phosphonic acid derivatives, mercaptans, and metal ions are examined as templates. Possible practical applications and unsolved problems of this technique are presented and discussed.

Nanotubes offer some important advantages for biotechnological and biomedical applications because of their tremendous versatility in terms of materials that can be used, sizes that can be obtained, and the chemistry and biochemistry that can be applied. The template method might prove to be a particularly advantageous approach for preparing nanotubes for such applications. However, this field of nanotube biotechnology is in its infancy, and there is much work still to be done before products based on this technology are brought to fruition. In Chapter 6, "Fabrication, Characterization, and Applications of Template-Synthesized Nanotubes and Nanotube Membranes," Punit Kohli and Charles R. Martin report on the synthesis, characterization, and applications of nanotubes and nanotube membranes synthesized using template synthesis. They discuss in detail the applications of nanotube and nanotube membranes in biosensing, bioseparation, and bioanalytical areas such as drug detoxification using functionalized nanotubes, enzyme- and antibody-immobilized nanotubes for biocatalysis and bioextractions, synthesis of nano test tubes, DNA-functionalized nanotube membranes with single-nucleotide mismatch selectivity, and the fabrication of an artificial ion channel using a single-conical nanotube membrane.

Metal nanoparticles have been intensively studied in the past from the points of view of scientific interest and practical applications. These nanoparticles, with their diameters of 1–10 nm, consist of several tens or thousands of metal atoms in each cluster. These nanoparticles can be considered as a new class of material in the nanotechnology field. Specific aspects of interest include their spectroscopic and magnetic properties, the synthesis and catalysis of polymer-stabilized or ligand-coated metal nanoparticles, and the nonlinear optical properties of metal nanoparticle-doped metal oxides. Thanks to the size limit of these nanoparticles, they are expected to show novel properties, which can be explained by a "nanoscopic effect." This size limit introduces quite a high population of surface atoms that control their properties. The synthesis of monodispersed nanoparticles is of prime importance because their properties vary strongly by their dimensions, and economical mass production of monodispersed metal nanoparticles is now a very important issue. One solution to improving the unique properties of metal nanoparticles is the addition of another element. This is especially so in the field of catalysis, where the addition of second and third elements to the principal monometallic nanoparticle is a common way to improve catalytic properties of selectivity and/or activity. Studies of bimetallic nanoparticles have been intensively carried out for more than a decade and many preparative methods have been proposed, such as the successive reduction of the corresponding two metal precursors. Thanks to improvements

in analytical methods and nanosize analyses, detailed characterizations of such complex material systems have been carried out. In Chapter 7, “Synthesis and Characterization of Core-Shell Structured Metals” Tetsu Yonezawa focuses on the synthesis and characterization of “core-shell”-type bimetallic nanoparticles, reporting especially on recent progress in this field.

The emergence of new methods and concepts for the organization of nanoparticles has induced great expectations in the field of magnetism. The organization of nanoscale ferromagnetic particles opens up a new field of technology through the controlled fabrication of mesoscopic materials with unique magnetic properties. In particular, these ferromagnetic nanoparticles are potential candidates for magnetic storage, where the idea is that each ferromagnetic particle corresponds to one bit of information. However, there are several problems to be solved before their application to magnetic storage media becomes feasible. Devices based on magnetic nanocrystals are limited by thermal fluctuations of the magnetization and by the dipolar magnetic interaction between nanocrystals ordered in arrays. A detailed understanding of the magnetic properties of assemblies of nanocrystals is, therefore, essential to the future development of magnetic recording technology. In Chapter 8, “Cobalt Nanocrystals Organized in Mesoscopic Scale,” Marie-Paule Pileni describes how cobalt nanocrystals can be organized into one-, two-, and three-dimensional superlattices forming mesostructures. The collective magnetic properties, due to dipolar interactions and nanocrystal organization, of such assembled magnetic nanocrystals are reported. In spite of the long-range length scale of dipolar interactions, structural and intrinsic properties due to the self-organization are observed to affect the magnetic behavior.

Anodic porous alumina, which is formed by the anodization of Al, is a typical self-organized material that is eminently suitable for the fabrication of several types of functional nanodevices. The geometrical structure of anodic porous alumina can be described as a closed-packed array of uniform-sized cylindrical units called cells, each of which has central straight pores perpendicular to the surface. Compared with other nanomaterials, anodic porous alumina has an important advantage: The geometrical structure, pore size, pore interval, and pore depth can be controlled easily by the anodizing conditions. Anodic porous alumina has been applied in a wide variety of fields for many years due to its unique nanostructural geometry. Chapter 9, “Synthesis and Applications of Highly Ordered Anodic Porous Alumina” by Hideki Masuda and Kazuyuki Nishio describes the synthesis of highly ordered anodic porous alumina and its application to the fabrication of functional nanodevices. Anodic porous alumina formed under appropriate anodizing conditions has a naturally occurring long-range order, and this, in combination with a pretexturing process before anodization, yields the ideally ordered perfect pore arrangement. This highly ordered anodic porous alumina is applicable as a template in several nanofabrication methods producing various kinds of ordered nanostructures (e.g., nanocomposites, nanocylinder arrays, nanodot arrays, and nanohole arrays).

In conclusion, it is apparent that this book covers many of the exciting and recent developments in the field of self-assembly of nanostructures from basic research to

applications. We expect it to attract a broad community of researchers in physics, chemistry, biology, engineering, and materials science and hope that established scientists and technologists as well as graduate students will find much relevant and interesting information contained between these covers. The extensive references appearing at the end of each chapter are also valuable resources in themselves. In the preparation of this book, we have had the opportunity to see how far this field has developed, but we are sure that much exciting work lies ahead of us still in this field!

Motonari Adachi

Kyoto, Japan

David J. Lockwood

Ottawa, Ontario, Canada

# Contents

<b>Preface</b>	<b>v</b>
<b>1 Self-Assembled <math>\text{Si}_{1-x}\text{Ge}_x</math> Dots and Islands</b>	<b>1</b>
<i>Jean-Marc Baribeau, Nelson L. Rowell, and David J. Lockwood</i>	
1.1 Introduction	1
1.2 $\text{Si}_{1-x}\text{Ge}_x$ Island Growth	2
1.2.1 Growth Modes in Heteroepitaxy	2
1.2.2 $\text{Si}_{1-x}\text{Ge}_x$ Island Growth and Shape Evolution	4
1.2.3 $\text{Si}_{1-x}\text{Ge}_x$ Island Composition and Strain Distribution	7
1.3 Stacked $\text{Si}_{1-x}\text{Ge}_x$ Islands	8
1.3.1 Development of Morphological Instabilities in Heteroepitaxy	9
1.3.2 Synthesis, Structure, and Vertical Correlation	9
1.3.3 Vibrational Properties	16
1.3.4 Optical Properties	25
1.4 Engineering of $\text{Si}_{1-x}\text{Ge}_x$ Islands	41
1.4.1 Influence of Surface Morphology	42
1.4.2 Influence of Adsorbed Species	44
1.5 Applications of $\text{Si}_{1-x}\text{Ge}_x$ Islands and Dots	46
1.5.1 Photodetectors	46
1.5.2 Other Applications	50
1.6 Summary and Future Prospects	51
References	52
<b>2 Synthesis of Titania Nanocrystals: Application for Dye-Sensitized Solar Cells</b>	<b>71</b>
<i>Motonari Adachi, Yusuke Murata, Fumin Wang, and Jinting Jiu</i>	
2.1 Formation of Titania Nanocrystals by Surfactant-Assisted Methods	71
2.1.1 Introduction: How to Control Morphology and Functionalize Ceramic Materials	71

2.1.2	Formation of Network Structure of Single Crystalline TiO <sub>2</sub> Nanowires by the “Oriented Attachment” Mechanism.....	73
2.1.3	Morphological Control of Anatase Nanocrystals Using Dodecanediamine as a Surfactant.....	79
2.2	Application of TiO <sub>2</sub> Network of Single-Crystalline Nanowires for Dye-Sensitized Solar Cells.....	87
2.2.1	Introduction.....	87
2.2.2	How to Make the Dye-Sensitized Solar Cells.....	88
2.2.3	Characterization of the Solar Cells Made of Network of Single-Crystalline Anatase Exposing Mainly the {101} Plane.....	89
2.3	Summary.....	94
	References.....	95
<b>3</b>	<b>Soft Synthesis of Inorganic Nanorods, Nanowires, and Nanotubes.....</b>	<b>101</b>
	<i>Shu-Hong Yu and Yi-Tai Qian</i>	
3.1	Introduction.....	101
3.2	An Overview: Emerging Synthetic Routes for the Synthesis of Low-Dimensional Nanocrystals.....	102
3.2.1	“Hard” Approaches.....	102
3.2.2	“Soft” Approaches.....	103
3.3	Soft Synthesis of Low-Dimensional Nanocrystals.....	109
3.3.1	Hydrothermal/Solvothermal Processes.....	109
3.3.2	Synthesis of Semiconductor Nanorods/Nanowires by Solution–Liquid–Solid Mechanism.....	125
3.3.3	Capping Agents/Surfactant-Assisted Soft Synthesis.....	126
3.3.4	Bio-Inspired Approach for Complex Superstructures.....	134
3.3.5	Oriented Attachment Growth Mechanism.....	140
3.4	Summary and Outlook.....	142
	References.....	143
<b>4</b>	<b>Assembly of Zeolites and Crystalline Molecular Sieves.....</b>	<b>159</b>
	<i>Jennifer L. Anthony and Mark E. Davis</i>	
4.1	Introduction.....	159
4.2	Thermodynamics of Synthesis Processes.....	160
4.3	Kinetics of Synthesis Processes.....	162
4.4	Assembly Processes.....	164
4.4.1	Proposed Mechanisms for Zeolite Assembly.....	165
4.4.2	Metal-Ion-Assisted Assembly Processes.....	168
4.5	Components of Synthesis.....	169
4.5.1	Organic Components.....	169
4.5.2	Inorganic Components.....	170

4.6	Chirality: Can a “Designer” Zeolite Be Synthesized?.....	176
4.7	Summary.....	178
	References.....	178
<b>5</b>	<b>Molecular Imprinting by the Surface Sol-Gel Process: Templated Nanoporous Metal Oxide Thin Films for Molecular Recognition.....</b>	<b>186</b>
	<i>Seung-Woo Lee and Toyoki Kunitake</i>	
5.1	Introduction.....	186
5.2	Surface Sol-Gel Process.....	189
5.2.1	Preparation of Amorphous Metal Oxide Thin Films.....	189
5.2.2	Rich Variety of Organic Components in Nanohybrid Layers.....	190
5.3	Molecular Imprinting in Amorphous Metal Oxide Films.....	194
5.3.1	Incorporation and Removal of Templates.....	194
5.3.2	Stability and Selectivity of Imprinted Sites.....	198
5.3.3	Nature of Imprinted Sites for Guest Binding.....	200
5.3.4	Multifunctional Nature of Imprinted Cavity.....	202
5.3.5	Varied Molecular Selectivity.....	205
5.4	Practical Potentials.....	206
5.4.1	Recognition of Biological Molecules.....	206
5.4.2	Contrivance for High Sensitivity.....	209
5.4.3	Recognition of Coordination Geometry.....	210
5.4.4	Nanoporous Thin Films with Ion-Exchange Sites.....	210
5.4.5	Direct Observation of Imprinted Cavity–Physical Cavity Versus Topological Cavity.....	212
5.5	Unsolved Problems and Future Prospects.....	215
	References.....	217
<b>6</b>	<b>Fabrication, Characterization, and Applications of Template-Synthesized Nanotubes and Nanotube Membranes.....</b>	<b>221</b>
	<i>Punit Kohli and Charles R. Martin</i>	
6.1	Introduction.....	221
6.2	Nomenclature.....	223
6.3	Template Synthesis of Nanotubes.....	223
6.4	Silica Nanotubes.....	224
6.4.1	Attaching Different Functional Groups to the Inside Versus Outside Surfaces.....	224
6.4.2	Nanotubes for Chemical and Bioextraction and Biocatalysis: Demonstration of Potential Drug Detoxification Using Nanotubes.....	226
6.5	Template Synthesis of Nano Test Tubes.....	229
6.6	Nanotube Membranes for Bioseparations.....	234

6.6.1	Antibody-Functionalized Nanotube Membranes for Selective Enantiomeric Separations .....	234
6.6.2	Functionalized Nanotube Membranes with “Hairpin”-DNA Transporter with Single-Base Mismatch Selectivity .....	236
6.7	Conical Nanotubes: Mimicking Artificial Ion Channel .....	241
6.8	Conclusions .....	245
	References .....	246
<b>7</b>	<b>Synthesis and Characterization of Core-Shell Structured Metals .....</b>	<b>251</b>
	<i>Tetsu Yonezawa</i>	
7.1	Introduction .....	251
7.2	Preparation of Core-Shell Bimetallic Nanoparticles .....	252
7.2.1	Preparation Procedures .....	252
7.2.2	Successive Reduction of the Corresponding Two Metal Ions .....	252
7.2.3	Simultaneous Reduction of the Corresponding Two Metal Ions .....	256
7.2.4	Other Systems .....	259
7.3	Characterization of Core-Shell Bimetallic Nanoparticles .....	260
7.3.1	X-ray Characterization .....	260
7.3.2	Electron Microscopic Observations .....	263
7.3.3	UV-vis Spectroscopy .....	264
7.3.4	IR Spectroscopy of Chemical Probes .....	265
7.4	Summary .....	266
	References .....	267
<b>8</b>	<b>Cobalt Nanocrystals Organized in Mesoscopic Scale .....</b>	<b>270</b>
	<i>Marie-Paule Pileni</i>	
8.1	Introduction .....	270
8.2	Self-Organization of Cobalt Nanocrystals .....	271
8.3	Collective Magnetic Properties of Mesostructures Made of Magnetic Nanocrystals .....	283
8.4	Conclusion .....	291
	References .....	291
<b>9</b>	<b>Synthesis and Applications of Highly Ordered Anodic Porous Alumina .....</b>	<b>296</b>
	<i>Hideki Masuda and Kazuyuki Nishio</i>	
9.1	Introduction .....	296
9.2	Synthesis of Highly Ordered Anodic Porous Alumina .....	296
9.2.1	Growth of Anodic Porous Alumina on Al .....	296
9.2.2	Synthesis of Highly Ordered Anodic Porous Alumina ....	297

9.2.3	Ideally Ordered Anodic Porous Alumina by the Pretexturing Process Using Molds.....	299
9.3	Ordered Nanostructures Based on Highly Ordered Anodic Porous Alumina .....	300
9.3.1	Nanocomposite Structures Using Highly Ordered Anodic Porous Alumina.....	300
9.3.2	Nanofabrication Using Anodic Porous Alumina Masks...	304
9.3.3	Two-Step Replication Process for Functional Nanohole Arrays.....	307
9.3.4	Ordered Array of Biomolecules Using Highly Ordered Anodic Porous Alumina.....	308
9.4	Conclusions .....	310
	References.....	311

<b>Index</b>	<b>313</b>
--------------	------------



# 1 Self-Assembled $\text{Si}_{1-x}\text{Ge}_x$ Dots and Islands

JEAN-MARC BARIBEAU,<sup>†</sup> NELSON L. ROWELL,<sup>‡</sup>  
AND DAVID J. LOCKWOOD<sup>†</sup>

<sup>†</sup> *Institute for Microstructural Sciences and* <sup>‡</sup> *Institute for National Measurements Standards,  
National Research Council Canada, Ottawa, Ontario K1A 0R6, Canada*

## 1.1. Introduction

The growth and properties of semiconductor quantum dots have been studied extensively in the last decade. These novel nanostructures offer interesting prospects for the development of new electronic or optoelectronic devices. In particular, if the size, shape, and positioning of those structures can be controlled, they become very attractive for applications such telecommunication wavelength-integrated photodetectors or tunable or single-photon light sources.

$\text{Si}_{1-x}\text{Ge}_x$  is a prototypical system of self-organization of nanostructures in semiconductor heteroepitaxy. Despite the 4.18% lattice mismatch between Si and Ge, it is possible to grow  $\text{Si}_{1-x}\text{Ge}_x$  alloys pseudomorphically on Si. This misfit causes the deformation of the alloy lattice to conform to the substrate lattice constant in the plane of growth. This leads to a tetragonal distortion in the deposited film that persists up to a critical thickness<sup>1-3</sup> beyond which deformation can no longer be elastically accommodated and relaxation of the lattice occurs through the generation of misfit dislocations. When deposited on (001) Si, Ge and  $\text{Si}_{1-x}\text{Ge}_x$  alloys can also undergo a transition from planar two-dimensional growth at small thickness to a three-dimensional island structure at higher coverage.<sup>4,5</sup> The development of a three-dimensional morphology is an alternative to the generation of dislocations as a means to minimize the energy of the heterosystem.<sup>6,7</sup>

In the last decade, considerable work has been done on the growth and characterization of  $\text{Si}_{1-x}\text{Ge}_x$  islands and dots.<sup>8-11</sup> In this chapter, we review progress in our understanding of  $\text{Si}_{1-x}\text{Ge}_x$  island growth on (001) Si. In particular, we discuss the evolution of the island morphology with  $\text{Si}_{1-x}\text{Ge}_x$  coverage, which is particularly complex and has led to a better understanding of strained heterosystems. We look at the effect of various growth parameters or postgrowth treatments on the shape of the islands. We also review recent progress in the determination of the composition and strain distribution of  $\text{Si}_{1-x}\text{Ge}_x$  islands. The spatial distribution of the islands and their vertical correlation in multilayer stacks is also described. We also discuss the vibrational properties of these  $\text{Si}_{1-x}\text{Ge}_x$  nanostructures and present a detailed review of their optical properties that are of key importance in device applications. The self-organization of the  $\text{Si}_{1-x}\text{Ge}_x$  islands is a feature of special

importance if they are to become building blocks of novel devices. We describe various approaches that have been examined to engineer  $\text{Si}_{1-x}\text{Ge}_x$  islands and, in particular, control their size and spatial distribution. Finally, we briefly review recent progress in the use of  $\text{Si}_{1-x}\text{Ge}_x$  island superlattices as fast telecommunication infrared photodetectors and for other applications.

## 1.2. $\text{Si}_{1-x}\text{Ge}_x$ Island Growth

### 1.2.1. *Growth Modes in Heteroepitaxy*

Based on considerations from thermodynamics, epitaxy of dissimilar materials can proceed according to three different growth modes.<sup>12</sup> The system will evolve into a specific morphology in order to minimize energy. Planar growth, commonly referred to as the Frank–van der Merwe mode,<sup>12</sup> is predicted if the sum of the surface free energy of the epitaxial film and the free energy of the epitaxial layer/substrate interface is smaller than the original substrate surface free energy. In other words, under those conditions the deposited film wets the substrate. The opposite case leads to three-dimensional growth or the Volmer–Weber mode, as it is energetically favorable that the original surface remains exposed, that is, the film does not wet the substrate. In an intermediate case, known as the Stranski–Krastanow mode,<sup>13</sup> growth initially proceeds layer by layer to wet the surface and then undergoes a transition to three-dimensional morphology as the surface free energy evolves. The different situations are illustrated in Figs. 1.1a–1.1c. Because epitaxy is most often carried out under nonequilibrium conditions, kinetics may dictate the exact growth morphology, and deviations from the simple thermodynamic description often arise.

A further complication in the description of heteroepitaxy arises if there exists a mismatch between the lattice constants of the substrate and the film. In general, epitaxy of dissimilar materials with a large lattice misfit will not be possible, because the deposited atoms are not in registry with the host lattice. However, if the mismatch is sufficiently small, defect-free growth can proceed through strained-layer epitaxy.<sup>15</sup> In this case, strain builds up in the film to accommodate the lattice mismatch with the substrate. Eventually, the associated stress in the crystal cannot be maintained and is relieved by the formation of interface or misfit dislocations. If growth is carried out close to equilibrium conditions (high temperature, low growth rate), morphological changes may be another pathway available for the relief of strain. It may be energetically favorable for the surface atoms of a planar film to diffuse sideways and form three-dimensional structures if this results in a reduction of the stress energy larger than the gain in surface free energy. This is illustrated schematically in Fig. 1.1d. Although the minimization of surface energy favors nucleation at sites that share the most atomic bonds (site 2), this results in increased strain energy as the lattice is distorted to conform both to the host lattice and the adjacent atom. It may then become energetically favorable for the incoming atoms to nucleate on isolated sites (site 1) or even on top of adsorbed atoms (site 3), which

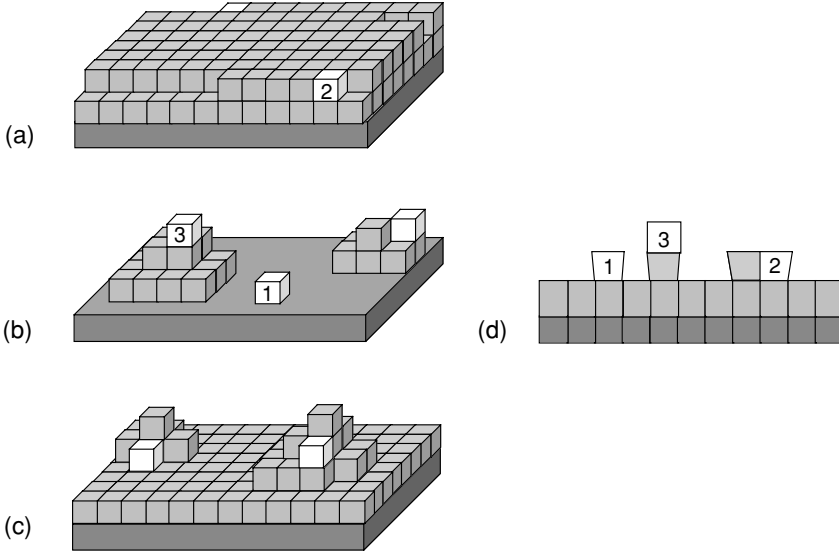


FIGURE 1.1. Schematic illustration of the three growth modes in heteroepitaxy: (a) Frank-van der Merwe, (b) Volmer-Weber, and (c) Stranski-Krastanow. Lighter blocks represent preferred nucleation sites in each case. (d) Schematic illustration of stress-driven morphological evolution. (After Ref. 14.)

while increasing the surface energy, reduce the strain energy. In such circumstance, the roughness of the surface will increase with continuous film growth, leading to the formation of three-dimensional islands. These strain-induced morphological instabilities may result in a complex evolution of three-dimensional islands on the surface with coverage, as their shape evolves to minimize energy.

The development of strained-layer epitaxy in the early 1980s<sup>16,17</sup> has revolutionized solid-state electronics by enabling band-gap engineering of semiconductors. The synthesis of defect-free semiconductor heterostructures and multiple quantum wells has led to the development of novel devices. Avoiding strain relaxation by limiting the thickness of heterostructures and maintaining two-dimensional morphology were key requirements in the fabrication of most devices. In the last decade, however, the morphological instabilities of strained systems that were first seen as undesirable (see Fig. 1.2) have attracted considerable interest. Heteroepitaxy in the regime of growth instability is an attractive way to synthesize novel structures at the nanometer scale without resorting to lithographic techniques. By optimizing growth parameters, it is also possible to fabricate semiconductor nanostructures with well-controlled physical properties. Furthermore, those nanostructures can exhibit high size uniformity or form ordered arrays on a substrate. This tendency for semiconductor islands to self-organize is very attractive for the conception of novel quantum devices. The  $\text{Si}_{1-x}\text{Ge}_x/(001)\text{Si}$  heterostructures are prototypical examples of such self-assembled islanding systems. In the following

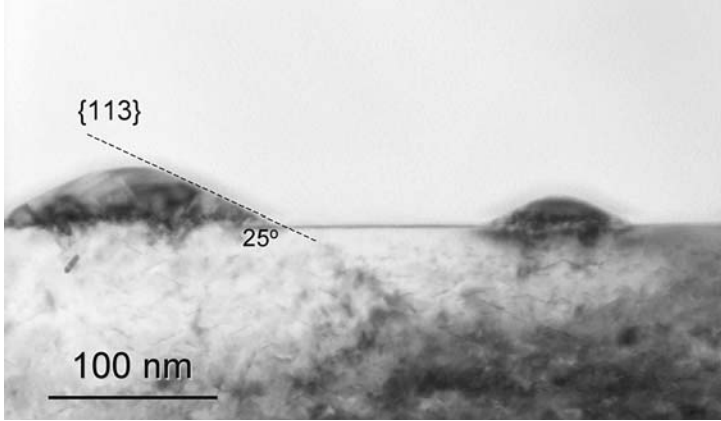


FIGURE 1.2. An early observation, in early 1987, of uncapped Ge islands grown on (001) Si. This result was obtained as part of an investigation aimed at optimizing the growth of pure Ge on Si for use as buffer layer for GaAs growth.<sup>18,19</sup> The three-dimensional growth morphology was obtained for growth at  $\sim 650^\circ\text{C}$ . Here, the larger island is heavily dislocated, whereas the smaller island appears strained, as suggested by the dark strain contrast in the substrate beneath the island. A light contrast at the base and edge of the strained island is also an indication of Si/Ge intermixing.

sections we discuss the formation and evolution of  $\text{Si}_{1-x}\text{Ge}_x$  islands and review some of their physical properties.

### 1.2.2. $\text{Si}_{1-x}\text{Ge}_x$ Island Growth and Shape Evolution

Since the early reports of growth of coherent Ge islands on (001) Si,<sup>18–21</sup> considerable work has been devoted to the growth of Ge islands and to the study of their properties. Ge and  $\text{Si}_{1-x}\text{Ge}_x$  island synthesis by epitaxial techniques such as molecular beam epitaxy (MBE),<sup>20,22</sup> gas-source MBE,<sup>23–26</sup> atmospheric, low-pressure,<sup>27</sup> and ultrahigh vacuum chemical vapor deposition (CVD),<sup>28–32</sup> and magnetron sputtering<sup>33</sup> has been reported. The evolution of  $\text{Si}_{1-x}\text{Ge}_x$  islands with coverage has been studied extensively, and although variations are seen among the various growth techniques, the following broad picture emerges. Growth proceeds via the Stranski–Krastanow mode and is characterized by the formation of a two-dimensional wetting layer (WL) about three monolayers (ML,  $1\text{ ML} = 6.3 \times 10^{14}\text{ atoms/cm}^2$ ) thick. As the coverage is increased, Ge atoms form small platelets or prepyramids<sup>34,35</sup> on the surface. Further deposition leads to the formation of well-defined square pyramids or elongated pyramids, or so-called hut clusters,<sup>21</sup> with side walls oriented along [105] crystallographic directions. As more Ge is deposited, those pyramids evolve discontinuously into larger dome-shaped islands with steeper facets such as {113} and {111} and {15 3 23}. These domes that are initially coherently strained evolve into strained-relaxed larger

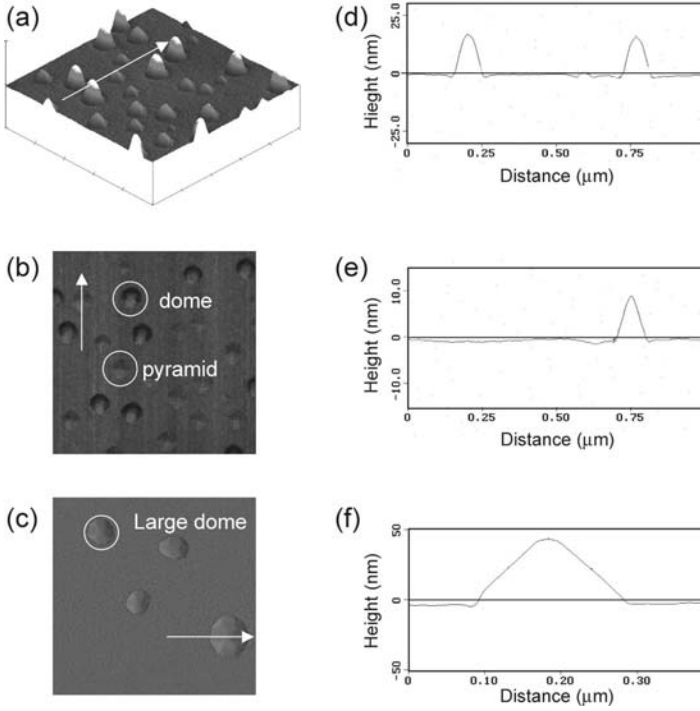


FIGURE 1.3. AFM images [all  $1\ \mu^2$ , vertical scale of  $40\ \text{nm}/\text{division}$  for (a)] of the surface topography of Ge islands on (001) Si. Images (a) and (b) are top and perspective views, respectively, of a sample that exhibits both pyramid and dome islands. The profile of the pyramid and dome is illustrated in line scan along [110] in (d) and (e), respectively. Image (c) is from a sample that exhibits large faceted domes whose [110] line profile is shown in (f). The directions of the various line scans are indicated by arrows.

domes (superdomes) as the coverage is increased. This later stage often exhibits a bimodal dome size distribution, reflecting the coexistence of smaller coherent domes and larger dislocated domes.

Figure 1.3 illustrates this shape evolution in a series of atomic force microscope (AFM) images of Ge islands at different stages of formation. The two structures shown in Figs. 1.3a and 1.3b and Fig. 1.3c were grown by MBE by depositing 6 ML of Ge at a temperature of  $650^\circ\text{C}$  and growth rate of  $0.05\ \text{nm/s}$ . The AFM images (a) and (b) show a surface on which pyramids and domes coexist. In this particular sample, the size distribution of both types of island is fairly narrow with the domes are about five times the volume of the pyramids. The line profile of the domes and pyramids along a [110] direction is displayed in Figs. 1.3d and 1.3e, respectively. On the pyramids, the sidewalls are at angle of about  $11^\circ$  with respect to the (001) plane, consistent with  $\{105\}$  facets, whereas this angle is about  $25^\circ$  for the domes, corresponding to a [113] orientation. On the sample shown in Fig. 1.3c, the Ge

dots are at a later stage of development and only large dome features are observed. In this particular sample, the dot formation was influenced by the deposition of a submonolayer of C prior to Ge deposition. This is discussed in more detail in a later section. Figure 1.3f is an AFM line scan of a large dome that shows that the side walls are predominately oriented along [113] with steeper  $\{111\}$  facets at the base.

A trench below the WL level is seen at the periphery of both types of island (see Figs. 1.3d and 1.3f). An anisotropy of the trenches, which are more pronounced along [110] directions, has also been reported<sup>36</sup> and attributed to the strain anisotropy of the Si crystal lattice at the base of the islands. Also, at higher temperatures, Si surface diffusion over long distances can cause a long-range Si depletion around an island (this is possibly seen here in Fig. 1.3e). The trench formation reported by several authors<sup>36–39</sup> is more pronounced at higher growth temperature and was first believed to result from strained-enhanced Si atom diffusion<sup>40</sup> in the vicinity of the strained islands. Microscopy imaging of the trenches<sup>41</sup> and recent modeling,<sup>42</sup> however, suggests that the driving force for this phenomenon is rather the reduction of the concentrated stress below the edges of the islands.

The results presented in Fig. 1.3 are, by and large, representative of the morphological evolution of Ge islands on (001) Si. At low coverage ( $\sim 4\text{--}6$  ML), the Ge island size is characterized by a bimodal distribution with coexisting small pyramids and larger domes. The formation of pyramids with  $\{105\}$  facets is a configuration that minimizes the surface free energy for islands under compressive stress.<sup>21</sup> The domes correspond to another geometry that minimizes the energy at higher Ge coverage. A thermodynamic model<sup>43</sup> has attributed the transformation from pyramids to domes to a phase transition in which pyramids and two-dimensional Ge islands floating on the WL combine to form larger dome islands in a thermally activated process. Real-time studies of the island evolution during growth or upon annealing have, however, revealed a far more complex transition from island to dome, involving different intermediate configurations.<sup>44</sup>

The driving force behind these shape transitions has not yet been fully elucidated, but all experimental results point to the importance of kinetics in the shape evolution. Conditions that favor mass transport at the surface (high temperature, low deposition rate) are generally conducive to three-dimensional growth, pointing to an interplay between strain-induced instabilities and growth kinetics. For example, anisotropy in the sticking and surface diffusion of adsorbates can lead to three-dimensional growth. A continuum description of the energetic and evolution of stepped surfaces in strain systems<sup>45</sup> also predicts surface faceting as a means to minimize surface energy. Differences observed in the island evolution on (111) and (001) Si points to an instability of the latter under compressive stress leading to  $\{105\}$  faceting.<sup>46</sup>

The size of the Ge islands grown by MBE increases with growth temperature<sup>37</sup> and the size distribution becomes narrower.<sup>22</sup> Coarsening of the islands is also observed upon postgrowth annealing, dominated by the Ge consumption of the WL at low temperature ( $450^\circ\text{C}$ ), Si/Ge interdiffusion at intermediate temperatures

(550°C), and Oswald ripening at high temperature (650°C).<sup>30,47</sup> Oswald ripening is the process by which larger particles (or, here, Ge dots) grow at the expense of smaller ones due to the higher detachment rate of the smaller dots and to atomic diffusion through the wetting layer.<sup>48</sup> Ge islands deposited at a lower rate will be larger and less dense than when deposited at a high rate.<sup>25</sup> Some island ordering has been reported in Ge films deposited at a fast rate, whereas dome formation was inhibited at small separation at low deposition rates due to the existence of a denuded zone around islands.<sup>49,50</sup> The effect of capping the Ge island with Si has also been examined. Depositing a Si cap at low temperature<sup>33</sup> (300°C) is a good means to preserve the shape of the islands. When capped at high temperature however, domes are flattened<sup>51</sup> or transform into large pyramids that evolve into stepped mounds.<sup>33</sup> These various results illustrate how some control on the structural properties of Ge islands can be achieved by optimizing growth parameters or performing postgrowth treatments. An alternative approach to tailor island formation and morphology is via the control of the host substrate through patterning or surface treatment. This is discussed in a later section.

### 1.2.3. $\text{Si}_{1-x}\text{Ge}_x$ Island Composition and Strain Distribution

Experimental observations such as the coarsening of Ge islands, shape transformation upon annealing<sup>52</sup> and Si depletion near islands<sup>53</sup> point to the importance of  $\text{Si}_{1-x}\text{Ge}_x$  interdiffusion phenomena in  $\text{Si}_{1-x}\text{Ge}_x$  island formation and evolution. The determination of composition and strain in Ge and  $\text{Si}_{1-x}\text{Ge}_x$  islands has been the subject of a number of investigations. Techniques such as X-ray diffraction and X-ray scattering,<sup>39,54–59</sup> X-ray absorption,<sup>27,60,61</sup> AFM,<sup>62</sup> transmission electron microscopy (TEM),<sup>23,24,63</sup> Raman scattering,<sup>64–66</sup> electron energy-loss spectroscopy (EELS),<sup>67</sup> selective etching,<sup>68</sup> and photoluminescence (PL)<sup>69</sup> have been used to probe the composition or strain of individual or ensemble of Ge islands and quantum dots.

Although a rate of volume increase of Ge dots superior to the Ge deposition rate,<sup>37,70–72</sup> and large Ge-Si coordination numbers<sup>61</sup> are evidence of  $\text{Si}_{1-x}\text{Ge}_x$  intermixing in Ge islands, determining the actual Si and Ge atom distribution within individual islands is quite challenging. X-ray diffraction and grazing incidence diffraction using reciprocal space mapping have provided insight on this question. Average strain and composition is obtained by modeling the intensity distribution of diffraction features arising from the presence of surface or buried islands.<sup>73–75</sup> This is most often done by measuring the diffracted intensity in the vicinity of a highly asymmetric Bragg reflection (such as (-1-13) or (-2-24) in the  $\text{Si}_{1-x}\text{Ge}_x$  system) in a glancing exit configuration. For uncapped Ge islands grown at 600°C, a Ge concentration gradient is observed with the Ge concentration decreasing from nearly 100% at the island apex to 50% at the base of the island.<sup>54</sup> For Si-capped islands grown at 700°C, a similar trend is seen with the Ge concentration reduced to 78% and 37% at the apex and base, respectively.<sup>39</sup> Anomalous X-ray scattering has revealed that the vertical decrease in the Ge concentration with height was

rather abrupt and occurring in the first 2 nm from the surface.<sup>55</sup> This technique also showed that in Ge dome islands, the Ge concentration does not vary uniformly with height but, rather, that the dome is made of a Si-rich core covered by a Ge-rich shell.<sup>76</sup> Note that the above measurements represent averages over a large number of islands. However, similar results were obtained in probing individual islands in EELS experiments.<sup>51,67</sup> EELS also suggests a fairly uniform lateral distribution of Ge atoms in the plane of growth, as was also observed in InAs/GaAs quantum dots.<sup>77</sup> As expected, interdiffusion is more pronounced in structures grown at high temperature and the average Ge composition of Ge islands falls linearly from 100% at 400°C to less than 40% at 700°C.<sup>67,71,78</sup> In the case of Ge islands stacked in multiple layer, a similar Ge increase is observed at the apex of the islands, whereas the average Ge concentration in the islands tends to decrease in upper layers.<sup>78,79</sup> The strain field above Ge island columns is expected to enhance diffusion and thus reduce the Ge composition in upper islands.

Strain plays a central role in the structural transition in lattice mismatch epitaxy. Strain in individual islands is best measured by microscopic techniques such as TEM. Strain contrast from TEM images of pyramid and dome islands reveals that the latter are heavily strained (about 2%) with respect to the substrate, whereas pyramids are almost commensurate (i.e., tetragonally distorted, with strain less than 0.5%) with the substrate.<sup>63</sup> This discontinuous strain evolution is mediated by formation of metastable domelike islands with intermediate strain. Stress calculations based on the linear elastic theory have shown that in addition to the reduction of the strain energy, islanding also causes a strain concentration at the edges of the island.<sup>80</sup> The stress at the island periphery contributes to the self-regulation of island size by introducing a kinetic barrier to diffusion of adsorbed atoms on to the island. Concentration of stress at the edge of Ge dome islands has been confirmed by Fourier transform mapping of high-resolution TEM images of Ge islands.<sup>81</sup> Molecular dynamics simulations of strain and stress distribution in Ge pyramids and domes<sup>82</sup> have reproduced these observations and shown that the Si lattice is significantly distorted below the edges of the Ge islands. As pointed out earlier, the strain gradient at the edge and underneath the island may enhanced Si–Ge interdiffusion and, thus, alloying constitutes an alternative strain relaxation pathway for large Ge islands, especially when grown at high temperature or upon postgrowth annealing.<sup>70</sup>

### 1.3. Stacked $\text{Si}_{1-x}\text{Ge}_x$ Islands

In order to be used in applications, it is advantageous to control the size, density, and position of  $\text{Si}_{1-x}\text{Ge}_x$  islands on a substrate. Inserting Si spacers between layers of islands to form a stacked superstructure is an attractive way to better control the island parameters and increase the volume of active material in a given structure. Furthermore, it has been found that stacking islands can promote their self-organization and improve their size uniformity. In this section, we discuss the growth and characterization of stacked  $\text{Si}_{1-x}\text{Ge}_x$  islands.



### 1.3.1. Development of Morphological Instabilities in Heteroepitaxy

Strain-induced roughening of a thin epitaxial film is generally described in terms of the Asaro-Tiller-Grinfeld instability.<sup>6,7</sup> For a Si<sub>1-x</sub>Ge<sub>x</sub> film on Si under compressive stress, undulation of the surface allows lattice planes to relax towards the ripple peaks. This lowers the elastic energy stored in the film, but increases the surface energy as compared to a planar surface. The balance between the reduced stress and increased surface energy defines a critical minimum wavelength  $\lambda_c$  for stable undulations given by<sup>83</sup>

$$\lambda_c = \frac{2\mu\pi\gamma}{(1-\nu)\sigma^2} = \frac{(1-\nu)\pi\gamma}{(1+\nu)^2\varepsilon^2}, \quad (1.1)$$

where  $\gamma$  is the surface energy density and  $\mu$  and  $\sigma$  are the misfit strain and stress, respectively,  $\mu$  is the shear modulus, and  $\nu$  is Poisson's ratio of the film. Surface undulations of wavelength larger than  $\lambda_c$  can form via surface diffusion to minimize the system energy. Conversely, for wavelengths smaller than  $\lambda_c$ , it is energetically favorable to fill surface troughs to reduce surface energy and smoothing is expected. In the case of a Si<sub>1-x</sub>Ge<sub>x</sub> film on Si, Ge atoms will migrate at the crest of the undulations, where the lattice constant is closer to that of bulk unstrained Si<sub>1-x</sub>Ge<sub>x</sub> material. Using the elastic constants of Si and Ge,<sup>84</sup> Eq. (1.1) yields  $\lambda_c$  of the order of 100 nm for a Si<sub>0.50</sub>Ge<sub>0.50</sub> alloy.

The above description has been confirmed experimentally in a number of systems, notably InAsP/GaInP on InP<sup>85,86</sup> and Si<sub>1-x</sub>Ge<sub>x</sub> on Si.<sup>87-89</sup> Factors such as kinetic limitations or a particular step structure can influence ripple formation. Although, Eq. (1.1) is not function of temperature, roughening may be inhibited at a low growth temperature because of reduced surface diffusion. The natural occurrence of surface steps is also key in determining the morphological evolution. In particular, if an energy barrier exists in the migration of atoms over down-steps, atoms nucleating on a terrace will preferentially attach to up-steps, causing step-bunching and increasing surface corrugation.<sup>90</sup> The phenomenon of step-bunching has recently been reviewed elsewhere.<sup>8</sup> The cooperative nucleation of surface islands and pits has also been shown to be a possible pathway to the formation of ripples.<sup>91</sup>

### 1.3.2. Synthesis, Structure, and Vertical Correlation

Growth of stacked Si<sub>1-x</sub>Ge<sub>x</sub> islands and undulated superlattices where identical layers of Si<sub>1-x</sub>Ge<sub>x</sub> islands are separated by thin Si spacers have been reported by a variety of nonequilibrium deposition methods.<sup>58,89,92-96</sup> As an illustration, we compare Si<sub>1-x</sub>Ge<sub>x</sub> structures that were prepared on (001) Si by MBE and by UHV-CVD. The details of the experiment have been described elsewhere.<sup>97</sup> The Si<sub>1-x</sub>Ge<sub>x</sub>/Si superlattices prepared by MBE<sup>98,99</sup> consist of 10, 15, or 20 periods of alternating Si and Si<sub>1-x</sub>Ge<sub>x</sub> layers. The Si layers in the structures have a nominal thickness of 1.3 nm, whereas the Si<sub>1-x</sub>Ge<sub>x</sub> layers have a nominal thickness ranging

from 3 to 5 nm and Ge composition  $x$  ranging from 0.3 to 0.55. Two growth temperatures were investigated, namely 675°C and 625°C. Most of the samples were terminated at the surface by a  $\text{Si}_{1-x}\text{Ge}_x$  alloy layer to enable the study of the alloy surface morphology. Some samples were also terminated with Si layer to investigate the effectiveness of a silicon cap in smoothing the surface. UHV-CVD  $\text{Si}_{0.5}\text{Ge}_{0.5}/\text{Si}$  superlattices were grown in a Leybold Sirius deposition system using a methodology described elsewhere.<sup>100,101</sup> A series of 10-period  $\text{Si}_{0.5}\text{Ge}_{0.5}/\text{Si}$  superlattices was prepared with nominal Si spacer layer 11 nm thick and different alloy layer thickness in the range 3–8 nm. These were grown at 525°C, with deposition rates of 1.2 nm/min for the Si spacer layers and of 4 nm/min for the  $\text{Si}_{0.5}\text{Ge}_{0.5}$  layers. All of the UHV-CVD-grown samples were terminated by a  $\text{Si}_{0.5}\text{Ge}_{0.5}$  layer at the surface.

A difference in the interface structure in superlattices grown by MBE and UHV-CVD is revealed by cross-section transmission electron microscopy (XTEM), as shown in Fig. 1.4. Both micrographs show the presence of pronounced interface undulations that extend from the bottom to the top of the superlattice structures. A number of interesting features can be observed. In both cases, the undulated morphology of a  $\text{Si}_{1-x}\text{Ge}_x$  alloy layer is replicated to the next alloy layer. The undulations are mostly vertically aligned (A in Fig. 1.4), but some oblique replication is also apparent (B in Fig. 1.4). The undulations are initially not uniformly distributed and some coarsening and self-organization of the waves, particularly apparent in the MBE case (C in Fig. 1.4), are observed in layers closer to the

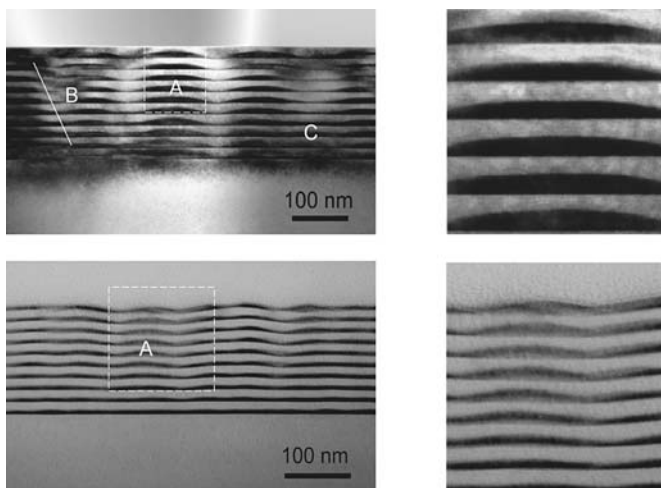


FIGURE 1.4. Transmission electron micrograph cross sections of island superlattices grown by MBE (top) ( $\text{Si}_{0.54}\text{Ge}_{0.46}/\text{Si}$  superlattice with 3.4-nm-thick alloy layers, grown at 625°C) and UHV-CVD (bottom) ( $\text{Si}_{0.50}\text{Ge}_{0.50}/\text{Si}$  superlattice on with 5-nm-thick alloy layers). The features marked by letters are discussed in the text. The panels to the right are magnified views of the square sections in the left micrographs. Further details are given elsewhere.<sup>97,102</sup>

surface. The lateral wavelength and amplitude of the oscillations is similar for both samples. There are also qualitative differences more apparent in the magnified views shown in Fig. 1.4. The MBE superlattice exhibits a strong asymmetry in the roughness between the Si on  $\text{Si}_{1-x}\text{Ge}_x$  and  $\text{Si}_{1-x}\text{Ge}_x$  on Si interfaces, the former being heavily undulated and the latter virtually flat, whereas in the UHV-CVD case, both types of interface show pronounced undulations. The deposition of a thin (10 nm) Si cap is sufficient to flatten the surface in MBE. In both cases, no dislocations can be seen, but the MBE sample is periodically strained, as evidenced by the periodic strain contrast in the TEM micrograph. The strain contrast is not as pronounced in the UHV-CVD-grown sample.

Figure 1.4 captures important characteristics of stacked  $\text{Si}_{1-x}\text{Ge}_x$  islands. The vertical alignment of the islands is explained by the partial relaxation of the  $\text{Si}_{1-x}\text{Ge}_x$  lattice at the apex of the island, which causes tensile strain in the Si lattice above the  $\text{Si}_{1-x}\text{Ge}_x$  island. This locally reduces the misfit strain and makes it an energetically favorable nucleation site for the Ge island atoms in the next alloy layer. The degree of vertical alignment depends on the thickness of the Si spacer layers. If these are made too thick, local strain will be reduced and alignment will be lost. This limiting thickness for the Si spacers depends on the growth methods and conditions, but, in general, strong vertical alignment is achieved for spacers less than 25 nm thick, whereas little alignment is preserved beyond 100 nm.<sup>103,104</sup> The critical Si spacer thickness for vertical self-alignment roughly scales with the island size and it may be as small as 12 nm for structures grown at lower temperatures.<sup>10</sup> The degree of vertical ordering has been correlated with a reduction of the thickness of the WL in stacked islands, which is also consistent with strain propagation in the Si spacers.<sup>94</sup> The oblique stacking of islands has been observed before and explained by the interplay of surface stress and the development of Si surface depressions in the vicinity of large islands.<sup>92</sup> Finally, the coarsening and coalescence of islands is another important observation.<sup>95</sup> This self-organization may be explained in the framework of a model based on the continuum elasticity theory.<sup>105</sup> In this model, the strain field overlap of two closely spaced small islands will induce the nucleation of a larger island in the next alloy layer rather than the replication of the small islands. On the other hand, for larger islands, the strain field will not expand beyond the lateral size of the islands. Nucleation of new islands is also expected in regions without buried islands. All of these phenomena contribute to the vertical self-alignment and size homogeneity of the islands. A number of ways have been devised to induce  $\text{Si}_{1-x}\text{Ge}_x$  island self-organization. For example, long-range ordered lines of Ge islands can be produced by pre patterning the substrate with surface grooves of dimensions comparable to  $\lambda_c$ .<sup>103</sup> Other approaches are discussed in a later section.

Cross-section TEM samples only a very small volume and cannot provide information on the long-range organization of islands. Figure 1.5 displays the surface morphology of alloy-terminated  $\text{Si}_{1-x}\text{Ge}_x$  island superlattices grown by MBE and CVD as obtained by AFM. The MBE-grown superlattice exhibits a rough surface morphology comprising pyramidal mounds with the base aligned predominantly along the [100] and [010] directions. Those pyramids form chainlike structures

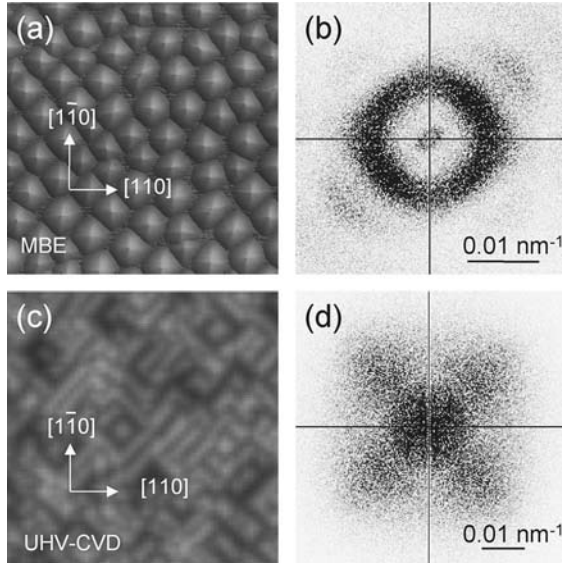


FIGURE 1.5. AFM images ( $1\ \mu\text{m}$  square) from (a) 10-period  $\text{Si}/\text{Si}_{0.54}\text{Ge}_{0.46}$  with  $\text{Si}_{1-x}\text{Ge}_x$  layers  $0.34\ \text{nm}$  thick grown by MBE at  $625^\circ\text{C}$  and corresponding Fourier transform (b) and from (c) 10-period  $\text{Si}/\text{Si}_{0.50}\text{Ge}_{0.50}$  with  $\text{Si}_{1-x}\text{Ge}_x$  layers  $0.30\ \text{nm}$  thick grown by CVD at  $525^\circ\text{C}$  and corresponding Fourier transform (d).

aligned predominantly along  $[100]$ -type directions. The sides of the pyramids have an angle of about  $11^\circ$  and thus probably originate from  $\{105\}$  faceting. The shape of these bumps is independent of the Ge composition in the range investigated, but their size decreases with increasing growth temperature. The surface root mean square (RMS) roughness of MBE-grown superlattices is typically  $4\ \text{nm}$ . The preferred size and orientation of the surface undulations are clearly seen in a Fourier transform of the surface topography (Fig. 1.5c). The well-defined size of the surface mounds is revealed in the Fourier image by the presence of a ring of constant reverse length. The fourfold symmetry of the Fourier image (higher intensity along  $\langle 001 \rangle$  directions) confirms the preferential orientation of the island facets along these crystallographic axes. The weak intensity in the center of the power spectrum density map indicates the absence of surface domains with  $[001]$  orientation.

Stacked island superlattices grown by UHV-CVD exhibit a different surface morphology. Elongated mounds meandering along  $[100]$  directions are observed on the surface (RMS roughness of  $2.5\ \text{nm}$ ). These mounds also exhibit atomic planes at an angle of  $\sim 10^\circ$  with respect to the  $(001)$  surface, consistent with  $\{105\}$  facets. This morphology is very similar to that reported on single layer  $\text{Si}_{1-x}\text{Ge}_x$  alloys grown by high-temperature low-pressure vapor deposition.<sup>89</sup> The Fourier transform of the AFM image exhibits an analogous fourfold symmetry with distinct lobes oriented along  $[100]$  directions. The alignment of the surface features is better

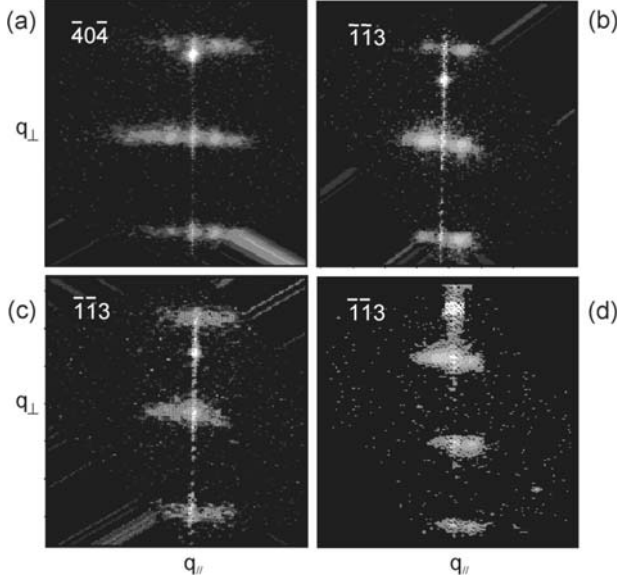


FIGURE 1.6. Reciprocal space maps from island superlattices: (a) and (b) 15-period  $\text{Si}/\text{Si}_{0.63}\text{Ge}_{0.37}$  ( $\text{Si}_{1-x}\text{Ge}_x$  layers 5 nm thick) grown by MBE at  $640^\circ\text{C}$ , measured at two different Bragg reflections; (c) 10-period  $\text{Si}/\text{Si}_{0.580}\text{Ge}_{0.42}$  grown by CVD at  $525^\circ\text{C}$  and (d) a 15-period  $\text{Si}/\text{Si}_{0.54}\text{Ge}_{0.46}$  ( $\text{Si}_{1-x}\text{Ge}_x$  3.6 nm thick) grown by MBE at  $625^\circ\text{C}$  and terminated by a 13-nm-thick Si layer. More details on the measurements are presented elsewhere.<sup>97</sup> Diagonal streaks are artifacts of the image processing.

defined here because no continuous ring is seen in the Fourier spectrum. Also, a strong signal at the center of the spectral power density map indicates the presence of region with  $[001]$  orientation on the surface between the islands.

Those two superlattices were also examined by high-resolution X-ray diffraction and grazing incidence X-ray reflectivity to further assess the interface roughness and correlation. Details on the X-ray measurements can be found elsewhere.<sup>106,107</sup> Figure 1.6 compares reciprocal space maps measured on representative samples. These maps were acquired using very asymmetric reflections in a low-exit-angle geometry to enhance diffraction effects due to undulations in the plane of growth.<sup>106</sup> The maps exhibit the usual satellite peaks in the vertical direction associated with the superperiodicity of the structures. The alignment of the satellite peaks in the same vertical line, as the substrate peak indicates that the structures have retained their strain. In addition, secondary features are seen in the horizontal direction beside the superlattice peaks. These side lobes are associated with the lateral undulation of the interfaces. Figures 1.6a and 1.6b compare maps recorded on the same samples, using  $(\bar{4}04)$  and  $(\bar{1}\bar{1}3)$  Bragg peaks corresponding to having the scattering plane along the  $[010]$  and  $[110]$  crystallographic directions, respectively. The larger spacing and stronger intensity of the side lobes and the presence

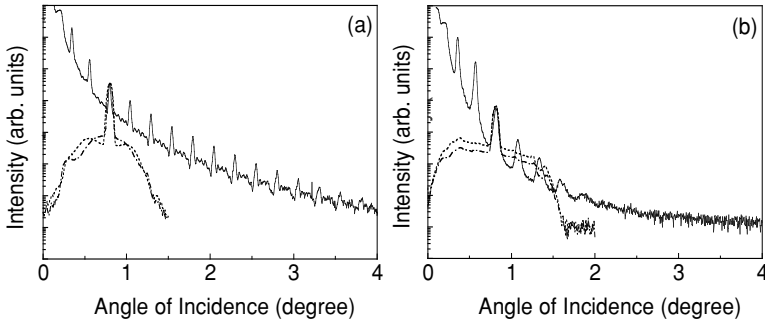


FIGURE 1.7. Specular X-ray reflectivity (full line) and angle of incidence rocking scans along [110] (dotted lines) and [010] (dash-dot lines) for (a) a 10-period wavy  $\text{Si}_{0.54}\text{Ge}_{0.4}/\text{Si}$  superlattice ( $\text{Si}_{1-x}\text{Ge}_x$  layers 3.6 nm thick) grown by MBE and (b) a 10-period  $\text{Si}_{0.50}\text{Ge}_{0.50}/\text{Si}$  superlattice ( $\text{Si}_{1-x}\text{Ge}_x$  layers 3.0 nm thick) grown by UHV-CVD.

of higher-order lobes in the measurement along the [010] azimuth are indications of a long-range preferential orientation of the interface undulations, in agreement with the AFM results for the surface found on a shorter range. The side lobes are also seen on the CVD-grown samples (Fig. 1.6c), although they are generally not as intense or well defined. They also become weaker in MBE samples, as the growth temperature is decreased (see Fig. 1.6d) and disappear below  $600^\circ\text{C}$ .

Interface structure can also be probed by grazing incidence X-ray scattering, a technique very sensitive to variations in the electron density in the direction perpendicular to the sample surface. Figure 1.7a shows the specular reflectivity (full line) measured on a typical island superlattice grown by MBE. Despite the pronounced wavy nature of the interfaces, the reflectivity curve exhibits sharp superlattice reflections. These remain visible and relatively sharp even at high angles of incidence. The observation of high-order satellites is explained by the fact that the Si on  $\text{Si}_{1-x}\text{Ge}_x$  interfaces remain abrupt throughout the structure (see Fig. 1.3) such that high Fourier components remain present. The undulated  $\text{Si}_{1-x}\text{Ge}_x$  on Si interfaces cause the intensity of successive satellites to decay monotonically rather than exhibit the usual intensity modulation seen in periodic bilayer systems.<sup>108</sup> Also displayed in Fig. 1.7a are angle of incidence rocking scans measured at the position of a strong satellite peak along both [110] and [010] azimuths. Off-specular diffuse scattering is weak and distributed in a narrow angular range centered on the specular direction. This is typical of interfaces with long ( $\sim 100$  nm) in-plane correlation.<sup>109</sup> The diffuse scattering is anisotropic and exhibits side lobes when the scattering is along the  $\langle 100 \rangle$  azimuth. The position of the side lobes can be associated with a length scale of  $\sim 1 \mu\text{m}$  on the surface, which is one order of magnitude larger than the wavelength of the surface undulations. Similar long-wavelength undulations have been observed before on MBE-grown multilayers and were related to the residual wafer misorientation with respect to the  $\langle 001 \rangle$  direction.<sup>108–111</sup>

In comparison, the satellite peaks on a CVD-grown island superlattice are broader and much weaker, as shown in Fig. 1.7b. The faster decay of specular intensity with angle of incidence is due to a large surface roughness of this sample, which does not have a Si cap. The broadening is explained by the wavy character of both types of interfaces, which makes the periodicity ill-defined, causing the damping of high Fourier components. The rocking scans (dotted lines) exhibit a strong and broad diffuse scattering spectrum extending further from the specular direction. This indicates a shorter in-plane correlation in UHV-CVD growth. Contrary to the MBE case, no strong anisotropy is observed as a function of azimuth direction and would indicate the absence of any long-range surface roughness correlation. This result is qualitatively similar to that obtained on longer-periodicity UHV-CVD-grown superlattices and seem to be typical of that growth technique.<sup>109</sup>

The intensity distribution about a strong satellite peak from an MBE- and an UHV-CVD-grown island superlattice is shown in Fig. 1.8. In both cases, the intensity is distributed on the Bragg sheet, indicating the good vertical correlation of the interface undulations. A broadening of the Bragg sheet at large  $q_{\parallel}$  indicates a relative stacking fault of islands in successive layers in multilayered islands.<sup>112</sup> In both cases, the half-width of the distribution intensity is close to that expected

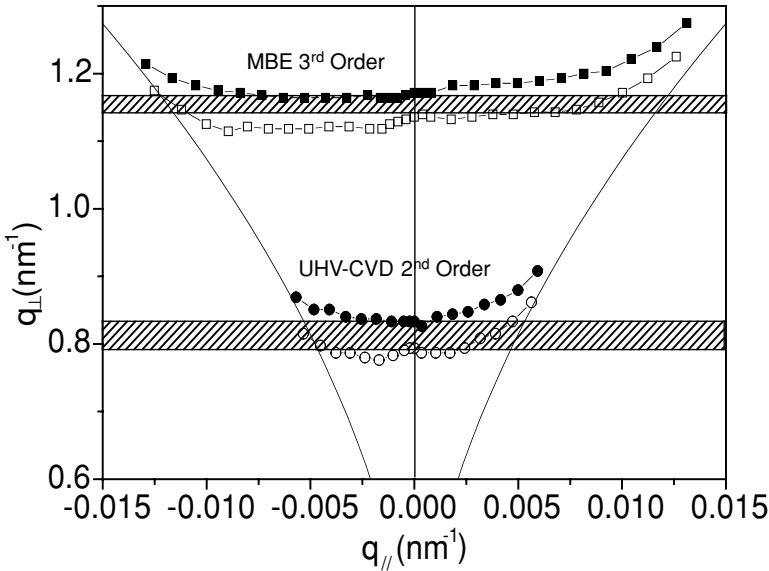


FIGURE 1.8. Intensity distribution in reciprocal space for two strong satellites from the samples of Fig. 1.7. The top two curves give the position of half-intensity for the third superlattice peak for the MBE sample, whereas the bottom two curves mark the half-intensity of the second-order satellite for the UHV-CVD sample. The cross-hatched regions indicate the theoretical width of the satellite reflections, taking into account the finite thickness of the superlattices.<sup>97</sup>

for interfaces correlated over the whole superlattice depth (cross-hatched regions in Fig. 1.8).<sup>104,112</sup>

### 1.3.3. Vibrational Properties

Raman spectroscopy entails the inelastic scattering of monochromatic light from some material.<sup>113</sup> The spectrum comprises a series of spectral features that are usually plotted as an energy shift (to lower absolute energy) from the exciting light in units of wave numbers. The spectral features are associated with elementary excitations of the medium such as atomic or lattice vibrations, spin waves or magnons, and electronic excited states. These excitations are unique to each material and thus serve as an identifying “fingerprint.”

In semiconductors, Raman spectroscopy can be used to provide information on the crystalline state and the presence of dopants and impurities.<sup>114</sup> In the case of semiconductor alloys, Raman scattering can be used to elucidate the alloy composition.<sup>115,116</sup> Raman scattering is particularly well suited to studying the electronic and vibrational properties of thin-layer semiconductor heterostructures and superlattices and has been widely applied to obtain information such as lattice strain and heterointerface sharpness and composition.<sup>117</sup> This is because the lattice vibrational energies, which are governed by short-range forces between atoms, are very sensitive to atomic bond lengths and angles and atomic masses. Because of the law of wave vector conservation, only excitations at very small wave vectors are probed in first-order Raman scattering.

The crystal structures of Si and Ge are the same as that of diamond and consist of two interpenetrating face-centered-cubic lattices. This structure yields one triply-degenerate optical mode of vibration at zero wave vector at a frequency of 1330, 520, and 300  $\text{cm}^{-1}$  in C (diamond structure), Si, and Ge, respectively, at room temperature. This mode is strongly Raman active, which makes these materials ideal for Raman characterization studies. Alloys of Si and Ge<sup>102</sup> and Si and C<sup>118</sup> are more complicated, however. They possess three clearly separated optic modes of vibration, which are termed the A-A, A-B, and B-B modes (where A is Si and B is Ge or C) by association with the dominant bond interaction that produces them. In the Raman spectrum of  $\text{Si}_{1-x}\text{Ge}_x$  these modes appear at approximately 505, 415, and 295  $\text{cm}^{-1}$ , as shown for example in Fig. 1.9. By measuring the peak frequencies of these modes as a function of the Ge concentration  $x$ , the results shown in Fig. 1.10 are obtained. Here, it can be seen that the Si–Si (Ge–Ge) mode frequency decreases (increases) linearly with  $x$ , whereas the Si–Ge mode behavior is best represented by a fourth-order polynomial.<sup>102</sup> All three mode frequencies are sensitive to the presence of strain.<sup>119,120</sup>

#### 1.3.3.1. Composition and Strain in $\text{Si}_{1-x}\text{Ge}_x$ Dots

Raman spectroscopy has been widely applied to characterizing the strain and composition of  $\text{Si}_{1-x}\text{Ge}_x$  dots grown on Si by a variety of growth methods ranging from MBE to CVD.<sup>26,97,102,125–153</sup> As a representative case study, we consider



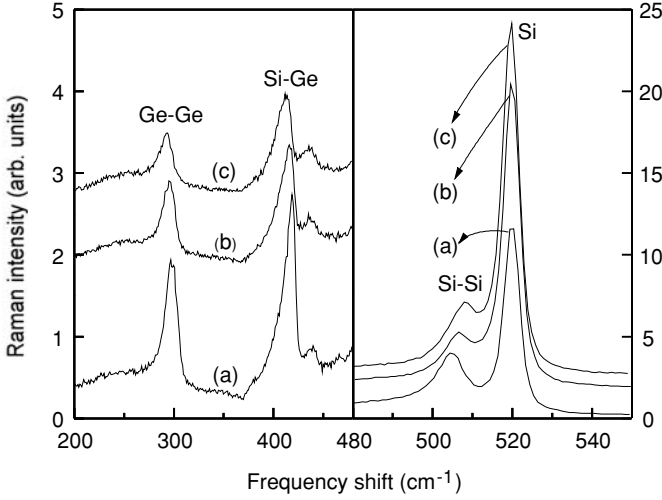


FIGURE 1.9. Room-temperature Raman spectrum showing the optic modes of (a) a  $\text{Si}_{1-x}\text{Ge}_x/\text{Si}$  planar superlattice for  $x = 0.52$ , (b) an island superlattice for  $x = 0.56$ , and (c) an island superlattice for  $x = 0.45$ .<sup>102</sup>

coherent-wave  $\text{Si}_{1-x}\text{Ge}_x$  superlattices with  $0.4 < x < 0.6$  and  $x = 1$  grown by MBE.<sup>102</sup> The  $\text{Si}_{1-x}\text{Ge}_x$  dots in these superlattices are in the form of vertically correlated flattened domes (see Fig. 1.4) of typical dimensions  $\sim 100$  nm by  $\sim 3.5$  nm with a vertical spacing of  $\sim 13$  nm. X-ray reflection measurements indicate that the island superlattices have atomically abrupt interfaces, as confirmed by the observation of folded acoustic modes by Raman spectroscopy.<sup>97</sup> Examples of folded acoustic modes are presented and discussed in Section 1.3.3.2. The X-ray diffraction study showed that a few of the thicker alloy layer superlattices had structurally relaxed, as the critical thickness for stability had been exceeded.

Figure 1.9 presents representative optic mode spectra of  $\text{Si}_{1-x}\text{Ge}_x/\text{Si}$  superlattices for three compositions  $x = 0.45$ ,  $0.52$ , and  $0.56$ , where the samples of  $x = 0.45$  and  $0.56$  are island superlattices and the sample of  $x = 0.52$  is a planar superlattice, which is shown for comparison purposes. The spectra show four main peaks corresponding to the Ge-Ge, Si-Ge and Si-Si vibrational modes of the alloy layers and the Si optic mode of the Si layers of the superlattice. Looking at the spectra in detail, the Si-Si, Si-Ge, and Ge-Ge mode frequencies of the planar superlattice  $x = 0.52$  (spectrum (a)) are at  $504.8$ ,  $418.6$ , and  $297.5$   $\text{cm}^{-1}$ , respectively. For the comparable  $x = 0.56$  island superlattice (spectrum (b)), the Si-Ge and Ge-Ge modes are at lower frequencies of  $416.6$   $\text{cm}^{-1}$  and  $296.1$   $\text{cm}^{-1}$ , respectively, and the Si-Si mode is at a higher frequency of  $507.0$   $\text{cm}^{-1}$ .

Strain derived from the lattice mismatch between the alloy and Si layers in a  $\text{Si}_{1-x}\text{Ge}_x/\text{Si}$  superlattice causes an upward shift of the Si-Si, Si-Ge, and Ge-Ge mode frequencies.<sup>119,120</sup> In Fig. 1.11, the frequencies of the three optic modes are displayed as a function of  $x$  for the strained planar superlattice (solid circles),<sup>120</sup>

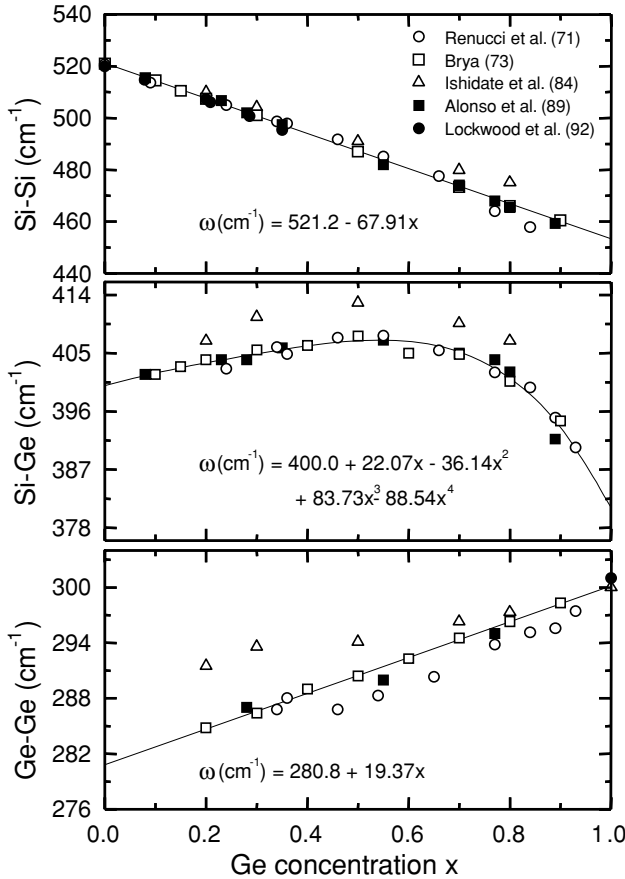


FIGURE 1.10. Dependence on composition  $x$  of the frequencies for the three optic modes in the unstrained  $\text{Si}_{1-x}\text{Ge}_x$  alloy system. The solid line is from fits of the data points to polynomial functions of  $x$ . All of the data points are taken from previous work<sup>119,121–124</sup> as noted in the figure by first author and year of publication.<sup>102</sup>

island superlattice (open circles), and unstrained alloy (solid lines, which are from the fits displayed in Fig. 1.10). The mode frequencies given in Fig. 1.11 in the case of overlapping Si and Si-Si lines were obtained by curve resolving. In addition, the frequencies of the Si mode from the Si layers in the island superlattices are represented by the open squares, and the dotted line indicates a bulk Si reference frequency of  $520\text{ cm}^{-1}$ . The island superlattice Si-mode data lie just below the bulk Si frequency of  $520\text{ cm}^{-1}$ , indicating the existence of a slight tensile strain in the alloy layers, as expected from the sample morphology. Note that the point at  $518.9\text{ cm}^{-1}$  for  $x = 0.48$  is from a partially relaxed island superlattice with an alloy layer thickness of  $5\text{ nm}$ . The short dashed lines in Fig. 1.11 are from fits of the planar superlattice mode frequencies to linear and quadratic functions of  $x$ . The

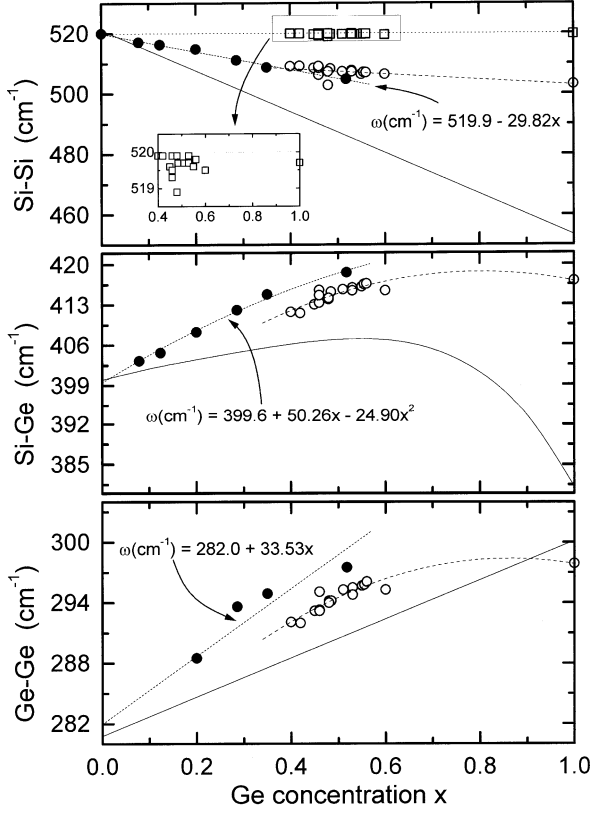


FIGURE 1.11. Frequencies of the three optic modes in  $\text{Si}_{1-x}\text{Ge}_x/\text{Si}$  island superlattices (open circles) and planar superlattices (solid circles) as a function of composition  $x$ . In addition, the Si mode frequency from the Si layers in  $\text{Si}_{1-x}\text{Ge}_x/\text{Si}$  island superlattices is given by the open squares in the graph for the Si-Si mode and are shown magnified in the inset. The solid lines are from the fits shown in Fig. 1.10. The short dashed line is from fits of the three alloy modes frequencies to polynomial functions of  $x$ , and the long dashed line is just a guide for the eye. For the Si mode, the dotted line indicates the bulk Si frequency of  $520 \text{ cm}^{-1}$ .<sup>102</sup>

results are  $519.9 - 29.82x$  for the Si-Si mode,  $399.6 + 50.26x - 24.90x^2$  for the Si-Ge mode and  $282.0 + 33.53x$  for the Ge-Ge mode. The overall dependence on composition  $x$  of the island superlattice mode frequencies is represented by the long dashed line, which is a guide for the eye. It shows that the three mode frequencies in the island superlattice behave as a function of  $x$  quite differently from those in both the unstrained bulk and planar superlattices. This indicates that other factors must be taken into account in analyzing the behaviors of the optic phonon mode frequencies in the island superlattice.

As was discussed in previous work on  $[\text{Si}_m\text{Ge}_n]_p$  planar atomic layer<sup>154</sup> and island<sup>129,130,134</sup> superlattices, where  $m$  and  $n$  are the numbers of Ge and Si

monolayers in each of the  $p$  periods, the effect of phonon confinement could play an important role in determining the vibrational frequency of phonon modes in a given superlattice layer. In order to observe a noticeable frequency shift due to the effect of confinement, calculations<sup>154</sup> have shown that the layer thickness of  $\text{Ge}_m\text{Si}_n$  superlattices should be restricted to ultrathin layers of  $m, n \leq 6$ . In this study, the  $\text{Si}_{1-x}\text{Ge}_x$  and Si layers typically are about 3.5 and 13.5 nm thick, respectively, corresponding to  $m \sim 104$  and  $n \sim 28$ , if the representation of the  $\text{Si}_{1-x}\text{Ge}_x/\text{Si}$  superlattice is converted to the form  $(\text{Si}_{1-x}\text{Ge}_x)_m\text{Si}_n$ . This indicates that the effect of phonon confinement can be neglected in this case. In Fig. 1.11, therefore, the  $x$  dependence of the deviations of the three mode frequencies in the planar and island superlattices from the frequencies of the three modes in the unstrained bulk alloy case have to be explained solely in terms of the strain and composition effects.

The optical phonon frequency shift  $\delta\omega$  due to the effect of strain can be described by the relationship<sup>119</sup>

$$\delta\omega = \omega - \omega_o = \frac{1}{\omega_o} \left[ \frac{pv}{v-1} + q \right] \varepsilon_{//} = b\varepsilon_{//}, \quad (1.2)$$

where  $p$  and  $q$  are phenomenological parameters and  $\varepsilon_{//} = (a_{\text{sub}} - a_{\text{epi}})/a_{\text{epi}}$  is the lattice mismatch between Si and  $\text{Si}_{1-x}\text{Ge}_x$ . Here,  $a_{\text{sub}}$  and  $a_{\text{epi}}$  are the bulk lattice constants of Si and  $\text{Si}_{1-x}\text{Ge}_x$ , respectively, and  $\omega_o$  is the phonon frequency for zero strain. For the Si-Si mode, results for the strain-shift coefficient  $b$  measured as a function of  $x$  were fitted to a linear function, and the best fit was obtained with<sup>119</sup>

$$b \text{ (cm}^{-1}\text{)} = -715 - 825x. \quad (1.3)$$

The lattice constant  $a_{\text{epi}}$  of  $\text{Si}_{1-x}\text{Ge}_x$  is well approximated by the quadratic equation<sup>155</sup>

$$a_{\text{epi}} \text{ (nm)} = 0.5431 + 0.02x + 0.0027x^2. \quad (1.4)$$

Combining Eqs. (1.2)–(1.4), we deduce a strain induced shift of  $\delta\omega = 22.9 \text{ cm}^{-1}$  for the Si-Si mode in the planar superlattice of  $x = 0.52$ . Experimentally, from the peak position of the Si-Si mode in the  $x = 0.52$  planar superlattice (spectrum (a) in Fig. 1.9) and the linear function for the Si-Si mode in the unstrained alloy given in Fig. 1.10, the frequency shift  $\delta\omega$  is estimated to be  $19.0 \text{ cm}^{-1}$ . This result is  $3.9 \text{ cm}^{-1}$  smaller than the predicted value. However, it should be noted that the linear function for  $b$  was deduced from a fit of data obtained for  $x \leq 0.35$  and some discrepancy could be expected at higher  $x$  values. Using the same procedure, one can calculate that  $\delta\omega = 25.5 \text{ cm}^{-1}$  for the Si-Si mode of the  $x = 0.56$  island superlattice, which compares favorably with the experimental value of  $\delta\omega = 23.8 \text{ cm}^{-1}$ . The difference between these two values is comparable to the result obtained from the same analysis in the planar superlattice case, indicating that the average strain in the alloy layer of the island superlattice determined from Raman scattering can be treated in the same way as the planar superlattice.

As can be seen in Fig. 1.11, the Ge–Ge and Si–Ge mode frequencies in the island superlattice are significantly less than those of the planar superlattice, indicating a reduction of average strain in the island superlattice compared with that in the planar superlattice. From the island superlattice Si–Ge mode at  $x = 0.56$ , the strain reduction is estimated to be about 25%, which is appreciable. On the other hand, the Si–Si mode shows a considerably different behavior in the strain shift from the other two modes: Aside from the relaxed sample of  $x = 0.48$ , the Si–Si mode frequency in the island superlattice is found to increase slightly compared with that in the planar superlattice. In general, the higher the proportion of Si there is in the Si<sub>1-x</sub>Ge<sub>x</sub> alloy, the shorter the Si–Si bond length,<sup>156</sup> so that the Si–Si mode frequency shifts up (see Fig. 1.11). Therefore, the origin of this inconsistency is related to the inhomogeneity in the Ge content of the alloy and Si layers, which is induced by the lateral diffusion of Ge into the Si layer valley during growth of the Si layer. There is clear evidence of Ge diffusion into the Si layer under these growth conditions in the limiting case of  $x = 1$  (i.e., the attempted growth of a pure Ge layer), where the Si–Si and Si–Ge modes can still be observed and the three mode frequencies are similar to their respective  $x \cong 0.55$  values, as can be seen in Fig. 1.11. The out diffusion of Ge results in Si-rich alloy regions in the valleys (between the Si<sub>1-x</sub>Ge<sub>x</sub> crests) that are under compression. Both effects will raise the Si–Si line frequency above expected values.

In summary, and as has been shown in a number of studies,<sup>131,132,134,137,140,143,148,150–152</sup> the Si–Ge and Ge–Ge mode frequencies as a function of  $x$  in the dome superlattice show a decrease with respect to those in the comparable fully strained planar superlattice, which means that the average strain in the dome superlattice is reduced from that in the planar superlattice. The strain reduction can be appreciable.<sup>151</sup> However, the situation is reversed for the Si–Si mode, which contradicts the case of the Si–Ge and Ge–Ge modes. The occurrence of such an apparent inconsistency is attributed to inhomogeneity in the alloy and Si layers, caused by the sideways diffusion of Ge into the Si layer valleys during the sample growth. The Si layer is thus under weak tensile strain above the domes and can be compressively strained between the domes,<sup>151</sup> because of the growth conditions. It is also possible that for high-Ge-content domes, the Ge atoms form nanometer-size clusters with a nearly pure Ge core surrounded by a Si<sub>1-x</sub>Ge<sub>x</sub> shell.<sup>143,146,152</sup> Interestingly, Raman measurements of pyramid-shaped Ge islands indicate that there can be no strain relaxation within the dots and, consequently, no strain transfer to the Si layers.<sup>131,142,151,157</sup> These differences in the strain distribution in the Si layers correlate with the degree of three-dimensional ordering in the superlattice.<sup>8</sup>

Finally, in this section, a cautionary tale. The Raman spectrum of Si contains weaker second-order features at 300 and 435 cm<sup>-1</sup><sup>114</sup> and, in some cases, these have led to their incorrect assignment as originating from the expected Ge–Ge and localized Si–Si modes in Ge dot nanostructures immersed in a Si matrix and grown on a Si substrate.<sup>133,135</sup> The errors have arisen when the Raman spectra of the dots are relatively weak. There is a very simple solution to this problem, which

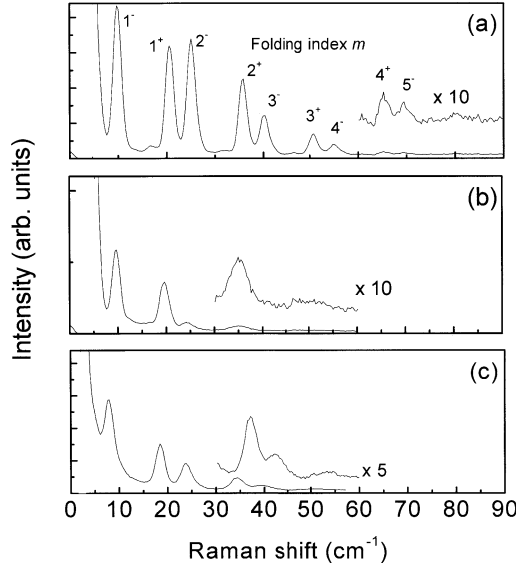


FIGURE 1.12. Low-frequency room-temperature Raman spectra showing the FLA modes of (a) a 10-period  $\text{Si}_{0.48}\text{Ge}_{0.52}/\text{Si}$  planar superlattice grown by MBE, (b) a 10-period  $\text{Si}_{0.515}\text{Ge}_{0.485}/\text{Si}$  island superlattice grown by MBE, and (c) a 10-period  $\text{Si}_{0.50}\text{Ge}_{0.50}/\text{Si}$  island superlattice grown by UHV-CVD. The alloy layer thickness ( $\sim 3.5$  nm) is comparable in all three superlattices. The pairs of modes are assigned according to their folding indices  $m^-$  and  $m^+$ .<sup>97</sup>

has successfully been applied in the cases of weak scattering from  $[\text{Si}_m\text{Ge}_n]_p$  superlattices<sup>158</sup> and  $\text{Si}_{1-x}\text{C}_x$  epitaxial layers.<sup>118</sup> The desired weak Raman features are revealed by a scaling (based on the strong Si line at  $520\text{ cm}^{-1}$ ) and subtraction process to remove the Si substrate and epitaxial layer contribution to the Raman spectrum.

### 1.3.3.2. Interfaces of $\text{Si}_{1-x}\text{Ge}_x/\text{Si}$ Superlattices

In the low-frequency Raman spectra of  $\text{Si}_{1-x}\text{Ge}_x/\text{Si}$  superlattices (see Fig. 1.12), folded longitudinal acoustic (FLA) modes are observed.<sup>159</sup> These modes arise essentially from the folding back of the acoustic phonon branches of the bulk material into the reduced Brillouin zone created by the new (artificial) periodicity in the superlattice growth direction. Such FLA modes are a sensitive indicator of the superlattice layer interface sharpness.<sup>159</sup> The FLA spectrum of the planar superlattice shows pairs of folded modes up to sixth order in the folding index  $m$ .<sup>159</sup> Even the  $m = 5$  modes are still very sharp (almost resolution limited), indicating excellent control of the superlattice periodicity and atomically abrupt  $\text{Si}/\text{Si}_{1-x}\text{Ge}_x$  interfaces. In the MBE-grown island superlattices, the FLA modes are still readily observed up to the order  $m = 3$ , although the overall FLA intensity is reduced compared with the planar sample, and there is a more rapid decrease in FLA peak

intensity with increasing  $m$  combined with a rapid increase in the FLA line width (see Fig. 1.12). These results show that the overall FLA intensity is derived mainly from the maintenance of atomic abruptness at the wavy-superlattice layer interfaces. The decrease in FLA peak intensity and increasing linewidth with increasing index  $m$  can be due to composition grading along the Si<sub>1-x</sub>Ge<sub>x</sub> / Si interface and/or a nonuniformity in the periodicity. As the FLA modes were observed to have similar characteristics in all the MBE-grown island superlattices, the compositional grading has to be the primary cause. It is indeed remarkable that FLA modes can be observed at all in these island superlattices given the strong interface undulation (see Fig. 1.4); their observation simply reflects the long-wavelength nature of acoustic modes compared with the undulation modulation. The FLA peaks in the various MBE-grown superlattices varied in frequency from sample to sample, consistent with the period variation, but they were not sensitive to strain variations. Similar FLA-mode Raman spectra were obtained from UHV-CVD-grown island superlattices (see Fig. 1.12), although the instrumental background due to stray light is higher because of their rougher surfaces. The FLA modes are also seen up to  $m = 3$ , indicating an interface atomic abruptness comparable to the MBE-grown superlattices despite the quite different growth modes (see Fig. 1.4). This confirms that the overall FLA intensity is governed primarily by interface sharpness. In UHV-CVD superlattices, where the composition was held at  $x = 0.5$  but the alloy layer thickness was varied, the overall FLA peak intensity increased with increasing alloy layer thickness, but the higher-order ( $m = 2$  and 3) FLA modes became more diffuse, indicating some variation in the superlattice period during growth. The FLA peak frequencies decreased with increasing alloy layer thickness, consistent with the increased superlattice periodicity.<sup>159</sup>

Similar FLA modes have been observed in smaller pyramidal dots (15–20 nm wide by 2 nm high)<sup>137,140,142,144,150,160</sup> and, in two cases,<sup>141,142</sup> the FLA-mode Raman peaks were superimposed on a broad continuum of acoustic phonons. The continuum, which was observed only under resonant Raman excitation conditions, has been explained as being due to the interaction of confined carriers and the acoustic phonons resulting in a breakdown in the wave vector conservation law for dots. A detailed theoretical analysis<sup>161</sup> of the FLA modes in a three-dimensional regimented array of Si<sub>1-x</sub>Ge<sub>x</sub> dots in Si has shown that the FLA modes can be used to distinguish confinement effects from alloying and strain-induced effects in the Raman spectrum.

### 1.3.3.3. Annealing Studies

Annealing an MBE-grown Si<sub>0.515</sub>Ge<sub>0.485</sub>/Si island superlattice for 100 s at temperatures ranging from 700°C to 850°C had no observable effect on the optic and acoustic mode Raman spectra (see Ref. 97). This indicates that the island superlattice structure is quite resistant to interface atomic interdiffusion and strain relaxation under these annealing conditions. However, this is not the case for Ge dot superlattices containing smaller pyramidal-shaped dots.<sup>134,136,143,150,160</sup> Here, annealing for 1 h at 650°C, 700°C, and 800°C resulted in a decrease in both the

overall intensity and number of FLA modes observed.<sup>150,160</sup> This indicates that there exists a significant Si/Ge intermixing during the annealing process. A shift to lower frequency of the Ge–Ge and Si–Ge optic modes on annealing together with an increase in frequency of the Si–Si mode confirms that Si/Ge interdiffusion is occurring.<sup>134,143,150</sup> The differences in the thermal stability of the wavy and pyramid superlattices is a reflection of the difference in their strain distributions, as discussed earlier. In the case of Ge pyramids, their high strain makes them susceptible to relaxation by Si/Ge diffusion at high temperatures, whereas this is not the case for  $\text{Si}_{1-x}\text{Ge}_x$  domes, where the strain distribution between the dots and the Si matrix is more equitable.

#### 1.3.3.4. Si/Ge/C Dots

As will be discussed later in Section 1.4.2, the use of C in the form of a fraction of a monolayer (ML) deposited on the Si substrate before the addition of Ge considerably modifies the Ge dot growth characteristics. Raman scattering has been used to examine the distribution and atomic bonding of C atoms in the case where the Ge content was fixed at 2 MLs and the C precoverage was varied from 0.1 to 0.3 ML.<sup>139</sup> Superlattice dot structures were grown with 8-nm-wide Si spacer layers. In addition to the usual Ge–Ge, Si–Ge, and Si–Si Raman features, a new Raman line was observed near  $605\text{ cm}^{-1}$ , which is associated with a localized Si–C mode of vibration<sup>118</sup> arising from C atoms surrounded by Si atoms. The localized Ge–C mode of C surrounded by Ge occurs at  $531\text{ cm}^{-1}$ ,<sup>162</sup> but this mode could not be observed due to interference from Si Raman features. The dot optical phonon frequencies indicate that the Ge dots are surrounded by a dilute  $\text{Si}_{1-x}\text{Ge}_x$  alloy.

The Si–C mode is lower in frequency by  $4\text{ cm}^{-1}$  compared with reference samples grown without Ge deposition due to strain effects, and its frequency together with that of the Si–Ge mode increases with C coverage. This frequency increase is correlated with effective local concentrations of Ge ( $\sim 8\%$ ) and C ( $\sim 2\%$ ) in the periphery of the Ge dots. These isolated substitutional C atoms are situated in the regions between Ge dots, in accordance with a natural repulsive interaction between C and Ge.<sup>163</sup> As more C is deposited, the substitutional C atoms are more spread out and, thus, are more likely to contact the Ge dots, which results in an increase in the local Ge concentration in the C neighborhood. At the same time, the strain contrast around the dot is increased.

The latter is evidenced from annealing studies. Just short (10 min) anneals at temperatures of  $650^\circ\text{C}$  and  $800^\circ\text{C}$  result in a decrease in both the Si–C and Si–Ge mode frequencies. The anneal at  $650^\circ\text{C}$  affects only the Si–Ge mode, whereas both mode frequencies shift on annealing at  $850^\circ\text{C}$ , with the Si–Ge mode affected most. This indicates that strain-induced interdiffusion of Ge is enhanced over that of C under these annealing conditions. From the frequency shifts of these two Raman lines, it is inferred that Ge tends to avoid C during the diffusion process and that adding more C during growth increases the Ge concentration in the vicinity of the dots.



### 1.3.4. Optical Properties

Efficient optical emission in indirect gap materials such as Si or Si<sub>1-x</sub>Ge<sub>x</sub> can be obtained by localizing the charge carriers in three dimensions (3D) (e.g., with lower band-gap islands or quantum dots).<sup>164–168</sup> Improving radiative properties is necessary because, in such bulk materials, photon emission requires phonon assistance for wave vector conservation and the strongest phonon [transverse optic (TO)] assisted photoluminescence (PL) in Si is 10<sup>4</sup>–10<sup>5</sup> times weaker than the no-phonon (NP) PL of direct-gap III-V materials. Although in Si the NP line is several orders of magnitude weaker than the TO replica, in Si<sub>1-x</sub>Ge<sub>x</sub> the two lines have roughly equal strength due to alloy scattering.<sup>169</sup> For reasonable optical performance, however, it is still necessary to greatly enhance the NP efficiency. Such an improvement occurs in small dots because carrier localization in real space requires wave function spreading in *k*-space.<sup>170,171</sup> Therefore, as in the case of small crystallites in porous silicon samples, indirect electron-hole recombination is greatly modified for small dots because a phonon is not required to complete the process. For holes, localization and carrier confinement energies larger than *kT*, where *k* is Boltzman's constant, at temperature *T* of 293 K, can be achieved with engineered<sup>172</sup> or self-organized structures<sup>173</sup> containing Ge-rich dots imbedded in Si<sub>1-x</sub>Ge<sub>x</sub>/Si. For electrons, localization is more problematic and has been improved, for example, by the introduction of carbon<sup>174</sup> in the silicon spacer layers to introduce tensile strain and thereby providing a conduction band offset and confinement. The optical properties of Si<sub>1-x</sub>Ge<sub>x</sub> self-organized islands were first studied to understand the fundamental properties of carriers in the regions with reduced dimensionality. More importantly, however, this type of material produced in a three-dimensional growth mode has provided an engineering pathway to novel and potentially efficient Si-based active optical components such as detectors and emitters. Light emission and detection in the optical communication band (1.3–1.55 μm) requires the use of Si<sub>1-x</sub>Ge<sub>x</sub> alloys with a Ge fraction of 0.5 or more, which greatly restricts the thickness of the Si<sub>1-x</sub>Ge<sub>x</sub> active layers, due to built-in strain. A small Si<sub>1-x</sub>Ge<sub>x</sub> layer thickness not only reduces the photocurrent response efficiency of the structure but also introduces a widening of the band gap that shifts the photocurrent response to shorter wavelengths due to quantum confinement. As discussed earlier, it is possible to adjust the growth conditions such that these Si<sub>1-x</sub>Ge<sub>x</sub>/Si multilayer interfaces become undulated rather than planar to minimize strain energy. This three-dimensional growth mode induces the diffusion of Ge to regions of maximum quantum well thickness and reduces the local quantum confinement at these thickness maxima. The combination of these two effects produces a significant increase in the photocurrent response of Ge islands and dots at longer wavelengths. This is further discussed in a later section.

#### 1.3.4.1. Photoluminescence

Phonon-resolved (PR), near-band-gap PL from strained Si<sub>1-x</sub>Ge<sub>x</sub> epitaxial layers, although now considered normal for device-grade material, was obtained only

after considerable effort in the early 1990s by Terashima et al.<sup>175</sup> and by Sturm et al.<sup>169</sup> for MBE- and CVD-grown layers, respectively. These PL spectra were similar to those from bulk  $\text{Si}_{1-x}\text{Ge}_x$ , except that transition energies were lower due to strain<sup>176</sup> and quantum confinement effects for very thin layers.<sup>177</sup> Accurate values for the strained band-gap energy versus  $x$  were obtained from PL from layers prepared by ultrahigh-vacuum vapor phase epitaxy and CVD.<sup>178,179</sup> A comprehensive study was published of the PL mechanisms in fully strained  $\text{Si}_{1-x}\text{Ge}_x/\text{Si}$  heterostructures grown by solid-source MBE.<sup>180</sup> Part of the MBE study<sup>180</sup> was the presentation of a model that defines the role of growth parameters that give rise to the broad intense PL band and PR luminescence. The unified treatment draws together many of the previous experimental observations and compares the relative strengths of broad PL bands and near-band-gap transitions as a function of  $\text{Si}_{1-x}\text{Ge}_x/\text{Si}$  heterostructure dimensions and growth temperature.

Emission from small regions with locally high Ge concentrations (e.g., hut clusters, domes, islands, quantum dots, undulations, etc.), in single  $\text{Si}_{1-x}\text{Ge}_x$  epitaxial layers and  $\text{Si}_{1-x}\text{Ge}_x/\text{Si}$  superlattices grown pseudomorphically on (001) Si has been reported by many authors.<sup>26,79,164,174,181–203</sup> In their pioneering work, Noël et al.<sup>164</sup> in 1990 reported very intense PL<sup>164,180</sup> and electroluminescence<sup>204</sup> from the NP recombination of electrons and holes in Ge-rich platelets,<sup>180,205</sup> which are essentially small, relatively isolated Ge-rich islands (see Fig. 15 of Ref. 180). Their luminescence spectra were similar to those reported more recently by many authors, including Denker et al.<sup>206</sup> and Schmidt et al.<sup>184</sup> for the initial stages of Ge island formation on (001) Si and by Boucaud et al.,<sup>207</sup> who calculated the spectral line shape from the heavy-hole density of states assuming lens-shaped Ge/Si dots. These spectra differed significantly from the normally observed PR PL in that they contained a broad, intense band that was consistently shifted below the alloy band gap by  $\sim 120$  meV for a wide range of alloy concentrations. Compositional inhomogeneity was implicated as causing the luminescence from the heteroepitaxial strained layers prepared by the solid-source MBE method of Noël et al.<sup>164,204</sup> The assignment of the luminescence to Ge-rich islands has been recently confirmed with Raman measurements<sup>208</sup> on the same samples studied earlier by PL and electroluminescence (EL). In the original work, the centers responsible for the broad PL band are shown to be Ge-rich lattice perturbations  $\sim 1.5$  nm in size, occurring in area densities up to  $\sim 7 \times 10^8 \text{ cm}^{-2}$  per quantum well. The nearly 20 samples, which contained small Ge-rich dots, were fully strained structures in the form of single quantum wells, epitaxial layers, or superlattices. When compared with the samples with PR spectra, the samples exhibiting dot luminescence had higher strain due to increasing either the Ge concentration, the  $\text{Si}_{1-x}\text{Ge}_x$  layer thickness, or the number of periods.

The physical phenomena responsible for the PL spectra observed by Rowell et al.<sup>180</sup> are illustrated in Fig. 1.13. On the left-hand side of this figure, we show a schematic cross section within a  $\text{Si}_{1-x}\text{Ge}_x$  layer in a direction perpendicular to the growth direction where a number of relatively Ge-rich dots are illustrated as valence band energy peaks with corresponding but much weak features in the conduction band (not, of course, to scale). In the PL experiment, the excitons

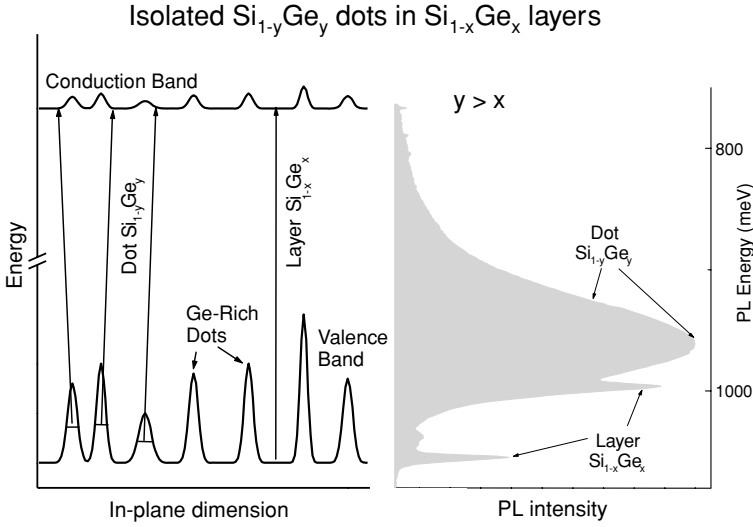


FIGURE 1.13. Schematic representation (left panel) of energy band variations due to clustering and dot formation in a  $\text{Si}_{1-x}\text{Ge}_x$  layer. Photoluminescence spectrum (right panel) containing dot related and layer recombination peaks.

created at low temperature are localized first in the  $\text{Si}_{1-x}\text{Ge}_x$  layers after diffusing vertically. Thereafter, the excitons diffuse laterally generally becoming trapped in the relatively Ge-rich  $\text{Si}_{1-y}\text{Ge}_y$  dots before the recombination of electrons and holes occurs. As the Ge concentration is locally high in the dots, the emitted photon energy is smaller than that for PL from the laterally adjacent  $\text{Si}_{1-x}\text{Ge}_x$ . However, the dot photon energy is not as small as the energy difference between the valence band at the dot's center and the conduction band because of a blue shift due to hole confinement in three dimensions. On the right-hand side of Fig. 1.13, we indicate how this further localization perpendicular to the growth direction is manifested in a real PL spectrum in which the relatively narrow  $\text{Si}_{1-x}\text{Ge}_x$  layer PL (consisting of two lines, the NP one and its phonon replica) is superimposed on the Ge-island PL to lower energy. This spectrum largely reflects the energy variations in a SiGe valence band, like that illustrated on the left-hand side of Fig. 1.13. The fact that the layer PL is observed along with the energetically favored island recombination indicates that the dots are relatively isolated because some excitons are being captured by the background-level dopant atoms in the SiGe layer before finding dots. Note that the island PL begins at an energy below the layer NP peak, as expected because the dots have higher a Ge concentration than the layers, which causes the recombination energy to have a significant net red shift (including confinement effects), the amount of which for a specific dot depends on the dot's characteristics, such as size and Ge concentration. Because there is a range of possible dot configurations, the spectrum for the sample's ensemble of

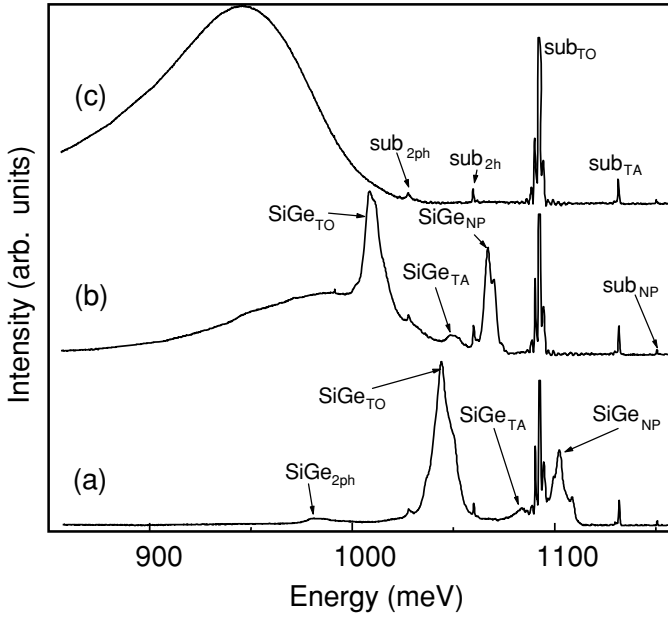


FIGURE 1.14. Evolution from PR to dot PL (2 K,  $0.5 \text{ W cm}^{-2}$  of 458-nm excitation light) for three superlattice structures of the same alloy composition but of different thicknesses: (a) 20 repeats of (2.7 nm  $\text{Si}_{0.85}\text{Ge}_{0.15}$  / 20 nm Si), (b) 20 repeats of (5.2 nm  $\text{Si}_{0.85}\text{Ge}_{0.15}$  / 20 nm Si), and (c) 15 repeats of (6.8 nm  $\text{Si}_{0.815}\text{Ge}_{0.19}$  / 30 nm Si).<sup>209</sup>

dots is necessarily much broader than the layer spectrum. We will now discuss various characteristics of Ge islands obtained using PL spectroscopy.

#### (a) 2D–3D Growth Transition with Accumulated Strain

In Fig. 1.14 we illustrate how the changeover from a 2D to a 3D growth mode influences the PL spectrum. The spectral change is quite remarkable ranging from PR (2D: lower trace) to dot (3D: upper trace) PL peaks for three superlattice structures grown by MBE at  $600^\circ\text{C}$ . In this example, the superlattice growth sequences differed only in the  $\text{Si}_{1-x}\text{Ge}_x$  alloy layer growth times, giving  $\text{Si}_{1-x}\text{Ge}_x$  layer thicknesses of 2.7, 5.2, and 6.8 nm for samples (a), (b), and (c), respectively. In sample (a), the NP peaks originate from excitons in the 2.7-nm-thick  $\text{Si}_{0.85}\text{Ge}_{0.15}$  layers of the superlattice structure. In sample (b), an increase in the  $\text{Si}_{0.85}\text{Ge}_{0.15}$  layer thickness to 5.2 nm reduces the confinement shift by 25 meV and a broad, dot-related PL peak is seen with its high-energy edge near the PR NP energy. For sample (c), comprising  $\text{Si}_{0.81}\text{Ge}_{0.19}$  layers 6.8 nm thick, PR PL is not observed and a more intense dot PL peak is seen shifted further down in energy. In the TEM diffraction contrast images of the three samples with PL spectra shown in Fig. 1.14, the density of Ge-rich dot islands increased markedly with  $\text{Si}_{0.85}\text{Ge}_{0.15}$

layer thickness, mirroring the change in PL characteristics. This correlation was decisive in the assignment of the broad PL peak to self-annihilation of excitons within the Ge islands.

The connection between strain density and the spectra of Fig. 1.14 is consistent with changes in growth morphology (interfacial roughening where the onset of 3D growth takes place) that acts to reduce the strain energy of the superlattice stack. Because the other variables have been maintained constant in this comparison, and only slight differences in Ge fraction exist between the superlattices, the strained layer thicknesses remain the only significant difference in the series. The buildup of strain energy results in metastable structures that become thermodynamically unstable with respect to relaxation during growth by several strain relief mechanisms. However, in these samples, no evidence by TEM for misfit dislocation, one important possible relaxation mechanism, was observed, even in the high-strain-energy density samples, where only Ge-dot PL was obtained. This indicates that strain accommodation occurs through morphological evolution and formation of Ge-rich regions. Because the buildup of strain-energy density during growth is proportional to the square of the Ge fraction, increases linearly with each strained  $\text{Si}_{1-x}\text{Ge}_x$  layer deposition, and remains constant during Si layer growth, there are significant differences among the three superlattices of Fig. 1.14 regarding accumulated strain. From these samples and many others comprising a wide range of  $\text{Si}_{1-x}\text{Ge}_x/\text{Si}$  multilayers,<sup>180</sup> the strain energy contours that separated regimes of different PL behavior (PR only, PR/dot, and dot) were fairly well established and indicated that the growth morphology transition occurred at a strain energy density near  $10^5 \text{ J m}^{-2}$ .

The strain variation with well position for a mixed PR/dot PL, three-well sample (6.8 nm wells) is illustrated in Fig. 1.15, which shows two PL spectra. The upper spectrum a) taken from an as-deposited sample displays both the PR and Ge-dot peaks. Spectrum b, from a sample of the same material after a 70-s dilute Schimmel etch [ $1 \text{ M CrO}_3\text{:HF}$ (49%), 1:2 volume ratio], had only one quantum well left. After etching, the dot PL peak was not present consistent with the formation of dots during epitaxy, where the effective stress was relatively high, farthest from the substrate. Etching removed the outer material, leaving only a low stress layer and no broad dot PL signal. The spectroscopic evidence from PL together with detailed TEM analysis<sup>180</sup> of strained  $\text{Si}_{1-x}\text{Ge}_x$  layers grown under various conditions corroborated that a transition in growth morphology occurred when the critical strain-energy density was exceeded. Strain-energy density contours separate the three regimes of luminescence behavior<sup>180</sup> and the increase in density of strain perturbations observed in TEM also correlated linearly with the increase in strain-energy density, indicating a strain-mediated change in growth mechanism from 2D to 3D modes.

#### (b) Mixed 2D–3D Structures: Dot Stability

Homogenization effects can be observed for some mixed PR/dot (2D/3D) PL samples upon annealing. Figure 1.16 shows two spectra, one (a) taken for the

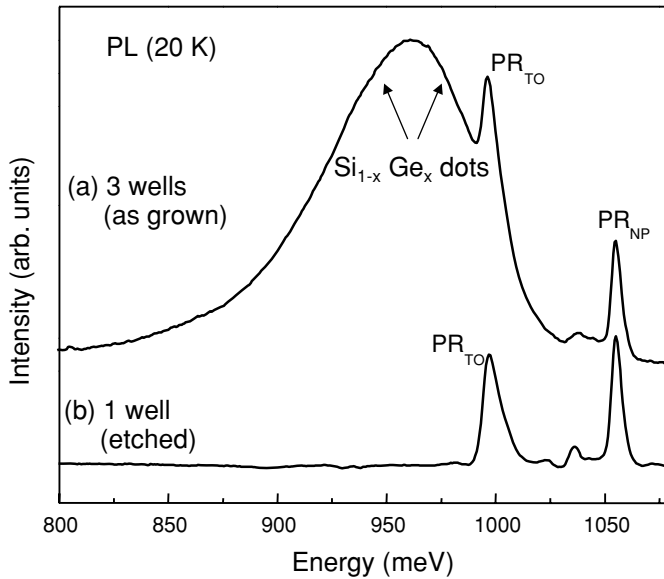


FIGURE 1.15. Variation in strain perturbation density (growth morphology) for a superlattice consisting of three repeats of (6.8 nm Si<sub>0.83</sub>Ge<sub>0.17</sub> / 20 nm Si) with decrease in the number of wells. Spectrum a, from an as-deposited sample, displays both the PR and Ge-dot PL peaks. Sample b, with one quantum well remaining after a Schimmel etch, has only the PR peaks.<sup>180</sup>

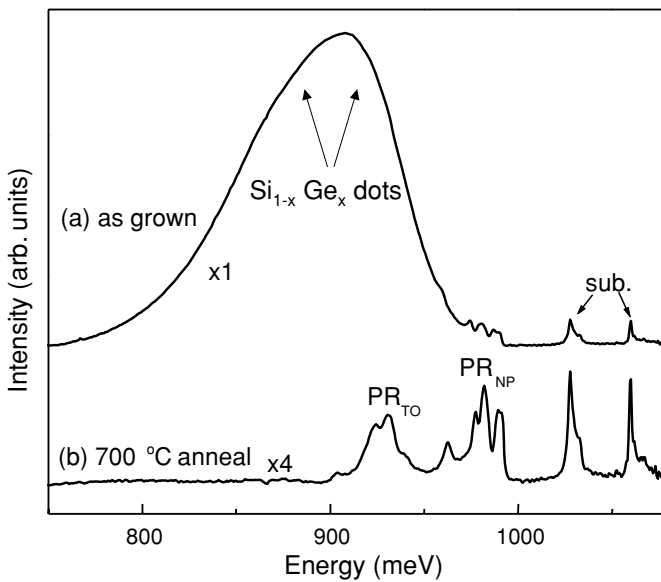


FIGURE 1.16. Variation of the PL spectrum with annealing for a superlattice consisting of 10 repeats of 4.2 nm Si<sub>0.73</sub>Ge<sub>0.27</sub>/20 nm Si exhibiting both Ge-dot and PR PL characteristics. The broad PL line disappears between trace a and trace b, obtained after a 700°C anneal.<sup>180</sup>

as-deposited material and the other (b) for a sample annealed at  $700^\circ\text{C}$  for 100 s. The most significant difference between these spectra is that the dot PL peak has completely disappeared upon annealing while the multiple PR peaks have remained unchanged. Effectively, the annealing removes the contribution of the Ge islands in the outer  $\text{Si}_{1-x}\text{Ge}_x$  wells from the PL spectrum. The growth conditions and structure for this sample indicate that the effective stress during growth was below the threshold for Ge-dot formation only for the first three or four quantum wells. It was also suspected that the area density of Ge dots in the upper wells was lower than necessary for overlap of the dot elastic fields, which extend out  $\sim 1\ \mu\text{m}$  from the dot. Thus, for this sample, annealing disturbs the dots sufficiently to homogenize their internal strain, in this way removing the broad PL line from the spectrum. In fact, this phenomenon appears to be quite general for the quantum well structures. When the elastic strain fields do not overlap, as seen in TEM and by the presence of PR peaks, annealing smoothes out the dots, and when the dot density is high enough, the elastic fields overlap and the dots are as stable to strain relaxation upon annealing as are quantum wells. The latter effect was also observed for the undulating samples. Many of the examples given here clearly illustrate how the evolution of the PL response is a direct indicator of the transition from 2D–3D growth in strained systems.<sup>182, 184, 185</sup> With techniques such as scanning tunneling and atomic force microscopy,<sup>210–212</sup> direct information can be obtained regarding the characteristic atomic disorder that lead to this morphological transition.

#### (c) 2D-3D Growth Transition Structures: Carrier Localization

The mixed 2D–3D samples allow us to use the PR PL to benchmark the strength of the dot luminescence. For example, by examining the PL temperature dependence for samples with both PR and dot PL, one obtains an insight into the improvement in thermal performance that carrier confinement gives in dots. Figure 1.17 shows the temperature dependence of the PL for a sample also shown in Fig. 1.15 taken with 100 mW of 458-nm exciting laser light. This sample consists of three wells of  $\text{Si}_{1-x}\text{Ge}_x$ , and in trace a, we see evidence for the NP PR peaks of the two layers nearest the substrate. As the temperature is increased from 2 to 20 K, there are two very noticeable changes in the spectra: (1) the bound exciton NP peaks changes to a single free exciton NP peak and (2) the dot PL peak becomes relatively stronger. As the temperature is increased further, the broad PL peak is stronger and persists to  $\sim 90\ \text{K}$ , consistent with the assignment of this line to Ge dots because the dots have greater localization potentials than the quantum well. Similarly, in the excitation density dependence, no threshold behavior was observed for the dot broad PL peak that was very efficient at low excitation density.<sup>213</sup> This peak, however, increased sublinearly in intensity with excitation density and shifted slightly to higher energy with increasing excitation power due to saturation effects.<sup>214</sup> Furthermore, at a higher excitation density, the PR PL intensity surpassed that of the dot PL.

Exciton diffusion and binding effects in mixed systems can be seen in the PL through both the temperature dependence (see Fig. 1.17) and excitation power

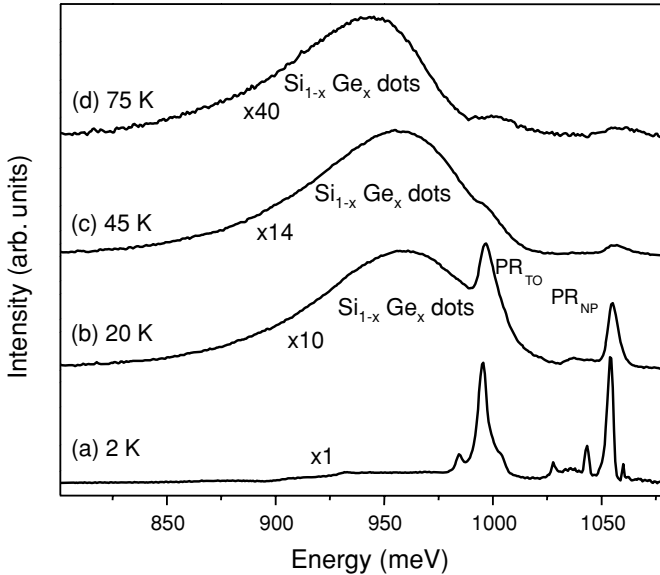


FIGURE 1.17. Temperature dependence of the PL (2 K,  $0.5 \text{ W cm}^{-2}$  of 458-nm excitation light) for a superlattice consisting of three repeats of 6.8 nm  $\text{Si}_{0.83}\text{Ge}_{0.17}/20 \text{ nm Si}$ . As the temperature increases, the bound exciton NP peak changes to a free exciton NP peak and the Ge-dot PL peak grows in intensity.<sup>180</sup>

variation. Although the dots themselves are small, their strain fields are relatively large, enhancing the capture of excitons.<sup>215</sup> Exciton diffusion in the volume between dots is important because dot elastic displacement fields are much larger ( $\sim 1 \mu\text{m}$ ) than the strain fields imaged in TEM; PR PL will not be observed if the regions between the elastic displacement fields are not large enough to include any shallow dopant atoms. Exciton diffusion effects are apparent in the variation with temperature of PL spectra like those shown in Fig. 1.17, where the PR PL disappears by 20 K while the broad PL intensity persists to  $\sim 70 \text{ K}$ . This behavior at higher temperatures occurs as shallow bound excitons become free excitons that diffuse within the  $\text{Si}_{1-x}\text{Ge}_x$  quantum wells and are captured by the Ge dots, where the decay time and radiative efficiency<sup>214</sup> are observed to be quite large in the absence of the usual competing nonradiative channels. Such persistence to high temperature of exciton-related PL is expected in quantum well systems, where exciton binding is increased, confirmed by a saturation behavior with excitation intensity. The variation of PL character in “transition samples” with incident power also provides indirect evidence for the presence of saturable exciton sinks, where the density per unit volume of dot centers is comparable with the exciton density. An increase in exciton density through increasing the power density produces PR luminescence from excess excitons free to migrate and self-annihilate at dopant atom sites.



## (d) PL of Isolated Quantum Dots

The PL phenomena noted in the early work on very small Ge-rich isolated  $\text{Si}_{1-x}\text{Ge}_x$  islands in  $\text{Si}_{1-x}\text{Ge}_x$  layers provide significant insight into the physical processes that come into play in Ge dots. These experiments and their conclusions will be discussed in the following paragraphs, including PL variation with (a)  $x$  for  $\text{Si}_{1-y}\text{Ge}_y$  low-concentration dots in  $\text{Si}_{1-x}\text{Ge}_x$  layers and self-organized islands (Figs. 1.13–1.15), (b) annealing (Figs. 1.16 and 1.24), (c) PL temperature (Figs. 1.18 and 1.22), (d) excitation density (Fig. 1.20), (e) excitation wavelength, (f) time after the excitation was removed (Fig. 1.24), (g)  $\text{Si}_{1-x}\text{Ge}_x$  layer thickness (Fig. 1.14), and (h) layer position in heterostructure (Fig. 1.15).

Originally, it was observed that the broad PL band from Ge dots followed the  $\text{Si}_{1-x}\text{Ge}_x$  strained band gap but was shifted downward in energy from it. The dependence on “background” Ge fraction of the dot-related broad PL peak is illustrated in Fig. 1.18, which contains three PL spectra from samples with Ge concentrations in the range 0.12–0.47. These particular epitaxial layers were grown by MBE methods<sup>213</sup> at relatively low growth temperatures ( $400 \pm 25^\circ\text{C}$ ) to avoid strain relaxation. Sample A contained a single  $\text{Si}_{0.868}\text{Ge}_{0.12}$  epitaxial layer 130 nm thick, sample B contained a 40-period superlattice with alternating  $\text{Si}_{0.75}\text{Ge}_{0.25}$  and

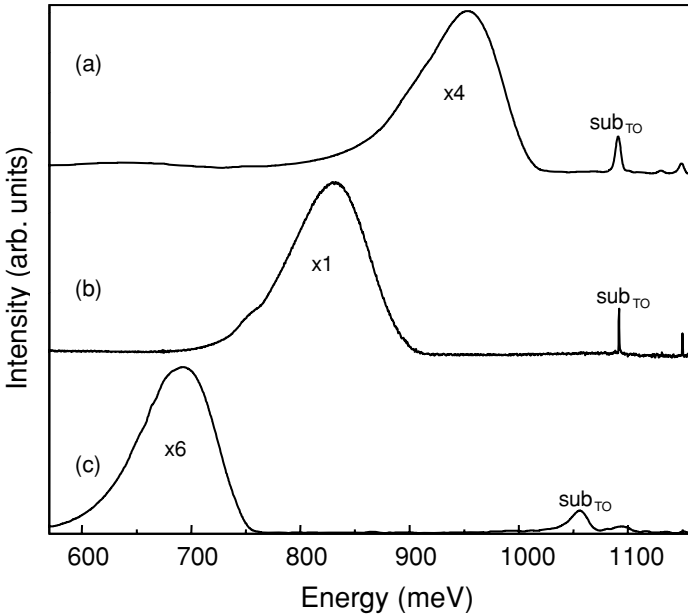


FIGURE 1.18. Low-temperature PL (4.2 K,  $1 \text{ W cm}^{-2}$  of 514-nm excitation light) spectra for three samples exhibiting dot PL characteristics with (a) a  $\text{Si}_{0.88}\text{Ge}_{0.12}$  epitaxial layer 130 nm thick (b) a 40-period superlattice of (7.3 nm  $\text{Si}_{0.75}\text{Ge}_{0.25}$  / 10.9 nm Si), and (c) a 15-period superlattice of (5 nm  $\text{Si}_{0.53}\text{Ge}_{0.47}$  / 20 nm Si).<sup>213</sup>

Si layers 7.3 and 10.9 nm thick, respectively, and sample C contained a 15-period superlattice with  $\text{Si}_{0.53}\text{Ge}_{0.47}$  and Si layers 5 and 20 nm thick, respectively. At energies above 1050 meV, only a substrate feature ( $\text{sub}_{\text{TO}}$ ) was observed. Below 1050 meV, the dot broad PL peak is seen corresponding to internal quantum efficiencies of the order of 1%. All of the dot-related broad PL peak widths are similar and the peak position shifts to lower energy with increasing Ge content. The dot-related broad PL features in all show the same degree of asymmetry in the low-energy sides of the peaks, and the most intense of these samples show a smaller peak overlapping the main peak, which is  $\sim 60$  meV higher in energy, close to the TO phonon energy in Si (58 meV), suggesting that the overall peak is from NP recombination. The NP transition is expected to be relatively strong for exciton localization in an alloy where the electron and holes locally see large potential fluctuations due to compositional disorder, as occurs near Ge-rich dots. Hence, in addition to the alloy effect in  $\text{Si}_{1-x}\text{Ge}_x$ , the NP intensity can be further greatly enhanced for small dots due to localization effects. The dot-related peak for sample A of Fig. 1.18 was confirmed<sup>180</sup> to have a NP characteristic with PL excitation (PLE) spectroscopy in which the excitation wavelength was varied while the PL intensity was monitored in the broad PL peak (855 meV). The onset of the PLE coincided with the high-energy edge of the dot PL peak, which could have occurred only if a NP process caused the broad peak PL.

Carrier localization, in principle, permits PL to be observed at higher temperatures from Ge-rich dots than in epitaxial layers. However, the confinement shift in small dots generally reduces the activation such that PL is quenched above 50 K, although for large self-organized dots, spatially indirect emission up to room temperature was observed.<sup>216,217</sup> For sample C of Fig. 1.18, the dot-related  $\text{Si}_{1-x}\text{Ge}_x$  broad peak persists to about 100 K, but weakens with increasing temperature as shown in Fig. 1.19.<sup>213</sup> The red-shift of this peak (49.5 meV between 10 and 80 K) reflects the thermal depopulation of energetically shallower dots with increasing temperature.

The samples of Fig. 1.18, which contained relatively small, weakly overlapped dots, exhibited a PL intensity first increasing with anneal temperature to about 600°C and then decreasing to zero at  $\sim 800^\circ\text{C}$  as shown for the epitaxial layer in Fig. 1.20. Compared with the as-deposited sample, the dot PL for a sample annealed at 575°C was  $\sim 16$  times stronger. When the anneal temperature was increased above 700°C, the dot PL peak disappeared. This behavior was correlated not with the appearance of PR peaks but with the rapid increase in the density of misfit dislocations originating at the  $\text{Si}_{1-x}\text{Ge}_x/\text{Si}$  interfaces. An Arrhenius analysis of the dot PL peak intensity versus annealing temperature  $T_{\text{an}}$  yielded (for  $T_{\text{an}} < 575^\circ\text{C}$ ) an activation energy of 352 meV corresponding to the annihilation of nonradiative traps that were grown-in at low temperature.<sup>218,219</sup>

#### (e) PL of Self-Organized Quantum Dots

Self-organized  $\text{Si}_{1-x}\text{Ge}_x$  island superlattice systems have PL properties similar to those for isolated quantum dots but with important differences, as will be

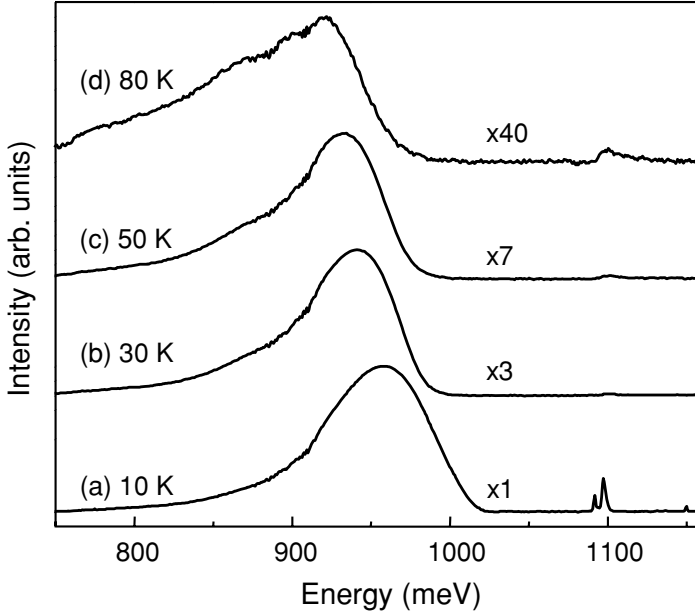


FIGURE 1.19. PL spectra ( $1 \text{ W cm}^{-2}$  of 514-nm excitation light) for an annealed epitaxial layer:  $\text{Si}_{0.88}\text{Ge}_{0.12}$  layer 130 nm thick for temperatures of (a) 10 K, (b) 30 K, (c) 50 K, and (d) 80 K. The Ge-dot PL peak persists to high temperatures but weakens.<sup>213</sup>

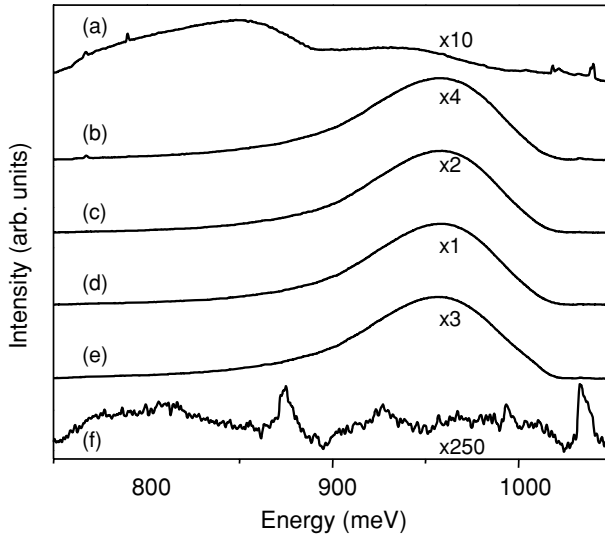


FIGURE 1.20. PL spectra (corrected for instrument response) at 10 K for a  $\text{Si}_{0.88}\text{Ge}_{0.12}$  epitaxial layer 130 nm thick (a) as-grown, (b) UHV annealed at 500°C, (c) at 555°C, (d) at 575°C, (e) at 625°C, and (f) at 700°C for 900 s.<sup>213</sup>

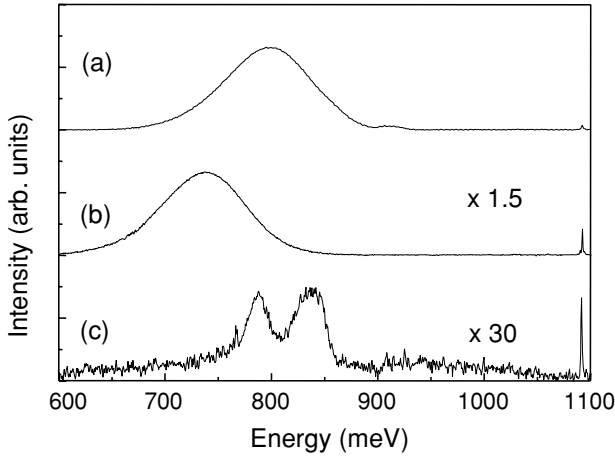


FIGURE 1.21. Low-temperature PL spectrum of (a) a 10-period  $\text{Si}_{0.45}\text{Ge}_{0.55}/\text{Si}$  island superlattice and (b) a 10-period  $\text{Si}_{0.47}\text{Ge}_{0.53}/\text{Si}$  island superlattice, both grown by MBE, and (c) a 10-period  $\text{Si}_{0.5}\text{Ge}_{0.5}/\text{Si}$  island superlattice grown by UHV-CVD. The samples have similar alloy layer and Si spacer layer thicknesses (0.33/0.35 and 0.30 nm, and 14 and 15 nm, for the MBE and UHV-CVD samples, respectively.). The PL spectra were recorded at 5 K with an excitation intensity of  $100 \text{ mW cm}^{-2}$ .<sup>97</sup>

discussed here. A comparison of the low-temperature PL spectrum for other MBE- and UHV-CVD-grown material in similar structures is shown in Fig. 1.21.<sup>97</sup> These structures were grown at higher temperatures and differ from those of Fig. 1.18 because of the self-organization, which occurred during growth, resulting in vertically aligned Ge-rich islands whose strain fields overlap to a high degree. These samples, similar to those displayed in Fig. 1.4, have undulating interfaces as opposed to the previous ones with planar interfaces. For both the MBE and CVD samples of Fig. 1.21, no defect-related PL emission lines are observed, confirming that these superlattices are strained and defect-free. The PL spectrum of the CVD sample shows a resolved TO-phonon replica and a NP peak corresponding to a band gap of 870 meV. This band gap is  $\sim 50$  meV lower than would be expected for a uniform planar quantum well with the same nominal growth parameters.<sup>220</sup> The low band gap can only be explained by a combination of reduced quantum confinement and an enhanced Ge concentration at the wave peaks. This Ge concentration gradient is the result of diffusion driven by the strain gradient between the wave troughs and peaks.<sup>87</sup> The PL spectra for the MBE-grown wafers show relatively strong single PL peaks at 730 and 790 meV, again at lower energies than expected given the nominal growth parameters. As in the case of UHV-CVD growth, this low energy is attributed to a combination of low quantum confinement and increased Ge concentration at the thickness maxima. In contrast to the CVD sample, the PL peak for the MBE material does not have a phonon replica and is both broader and more intense than the peak for the CVD wafer. Similar PL spectra have been observed previously for Ge islands grown on Si<sup>170,171</sup>

and from Ge-rich dots formed in  $\text{Si}_{1-x}\text{Ge}_x$  heterostructures<sup>209</sup> The strong PL is thought to arise from “phononless” transitions across the indirect gap, which are allowed when translational symmetry is broken by modulations in quantum well thickness, local strain, and Ge concentration.<sup>111</sup> Further discussion of the PR PL from undulating  $\text{Si}_{1-x}\text{Ge}_x$  island superlattices grown by CVD can be found elsewhere.<sup>220</sup>

The PL for the sample shown in Fig. 1.21a and other MBE samples is contained in a broad NP line with no resolved phonon replicas in a manner similar to the strong, phononless recombination described by Fukatsu et al.<sup>111</sup> for  $\text{Si}_{1-x}\text{Ge}_x$  dots. The shape of the PL spectra for these MBE samples is also similar to that for the samples of Fig. 1.18. The PL peak for the MBE samples shifts to lower energy with increasing Ge fraction, as can be observed between the top and middle traces of Fig. 1.15. The PL peaks shift to higher energy with increasing excitation density due to the fact that crests with highest Ge fraction, which give the lower-energy PL, have an exciton accommodation limit, which leads to PL saturation for these crests. At higher excitation densities, PL from lower Ge-fraction crests dominates. The spectra in the lower two traces were chosen such that the samples were fairly comparable in structure: one grown by MBE and the other by UHV-CVD ( $\text{Si}_{1-x}\text{Ge}_x$  alloy thickness of 3.5 nm and 3 nm;  $x = 0.53$  and 0.5 for the MBE and UHV-CVD samples, respectively). As is apparent, the spectra of these two samples differ greatly. First, the MBE PL is much too low in energy and is of much higher intensity. The occurrence at lower energy for the MBE material suggests a greater concentration of Ge at the wave crests and/or lower strain there, as suggested in Fig. 1.4. Furthermore, the peak energy shifts to lower energy compared to planar (parallel interface) layers because of lower confinement energy shifts obtained with undulated structures.<sup>220</sup> Second, the MBE PL comprises a relatively broad NP line, whereas the CVD PL exhibits PR lines with the NP and TO lines roughly equivalent in intensity. The PL peak position for various MBE-grown layers is displayed in Fig. 1.22. The peak shifts to lower energy with increasing Ge content. Furthermore, for a given composition, the shift is less pronounced in samples with thinner alloy layers, indicating, again, a confinement shift of the band gap. As we have already seen, the PL properties of the MBE and UHV-CVD undulating superlattices differ considerably. In MBE samples, the  $\text{Si}_{1-x}\text{Ge}_x$  islands are better defined and the PL signal arises from a phononless recombination mechanism. The PL peak position is also at energies below the band-gap energy for coherently strained  $\text{Si}_{1-x}\text{Ge}_x$  alloy layers of the same composition. This suggests a concentration of Ge greater in the islands than the nominal Ge concentration and is consistent with local relaxation of the strain in the alloy. Some quantum confinement shifts are also seen for undulating superlattices with small (<3 nm)  $\text{Si}_{1-x}\text{Ge}_x$  nominal layer thickness. The PL spectrum from UHV-CVD samples exhibits PR lines with the NP line appearing at a lower energy than a strained flat alloy layer of same composition, but at a higher energy than in an MBE sample of identical Ge concentration. This would suggest that less Ge migration and strain reduction occur at the  $\text{Si}_{1-x}\text{Ge}_x$  crests in UHV-CVD superlattices, again consistent with the morphology depicted in Fig. 1.4.

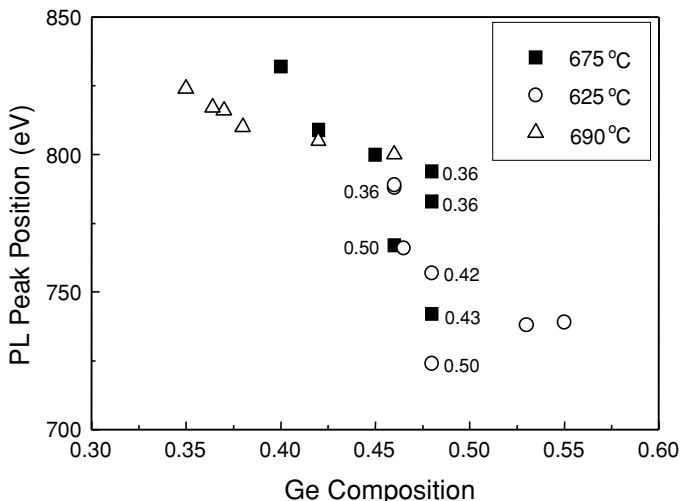


FIGURE 1.22. PL peak position as a function of composition for various island superlattices grown by MBE at the temperature indicated. The number next to some data points is the nominal thickness of the  $\text{Si}_{1-x}\text{Ge}_x$  layers in the structure.<sup>97</sup>

For self-organized island samples with undulating interfaces, there is good resistance to thermal treatment up to  $850^\circ\text{C}$ , presumably due to the inhomogeneous strain distribution. Undulating structures have been examined after heat treatment; for example, a MBE sample was annealed at various temperatures from  $700^\circ\text{C}$  to  $850^\circ\text{C}$  for a period of 100 s, as in Fig. 1.23. No significant shifting of the PL peak was observed even though the intensity decreased by 50% for the highest temperature. Nonetheless, from this result and those of Raman spectroscopy,<sup>97</sup> the structure was resistant to interface atomic interdiffusion and strain relaxation under annealing conditions where these structural degradations would probably have occurred for planar  $\text{Si}_{1-x}\text{Ge}_x$  strained layers with a Ge fraction above 0.3. This

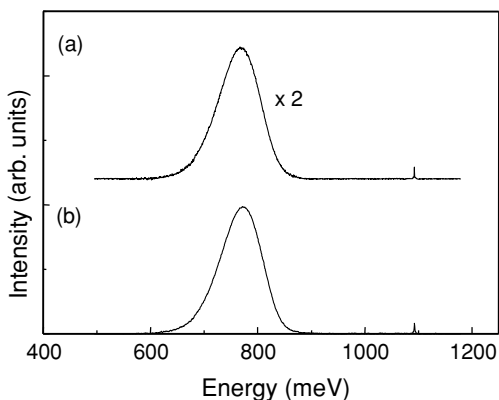


FIGURE 1.23. Low-temperature PL spectrum of a 10-period  $\text{Si}_{0.47}\text{Ge}_{0.53}/\text{Si}$  island superlattice annealed for 100 s at  $850^\circ\text{C}$  (a) compared to the as-grown sample (b). PL spectra were recorded at 5 K and at an excitation power density of  $100 \text{ mW cm}^{-2}$ .<sup>97</sup>

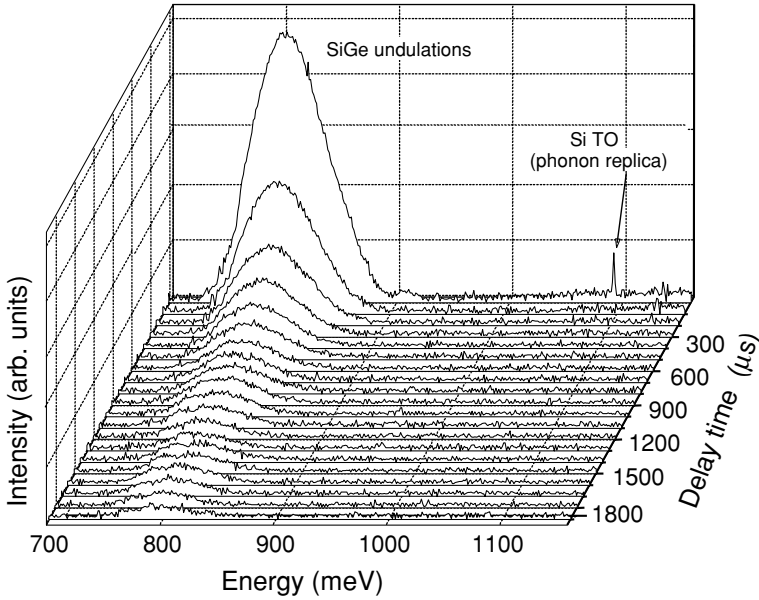


FIGURE 1.24. Time decay of the PL at 5 K for a 3.3-nm-thick  $\text{Si}_{0.55}\text{Ge}_{0.45}$  10-layer structure grown at  $675^\circ\text{C}$ . The spectra were obtained after the excitation was turned off. The PL from the  $\text{Si}_{1-x}\text{Ge}_x$  undulations decayed toward the lower photon energy within  $\sim 200\ \mu\text{s}$ , unlike the rapid substrate PL decay.

behavior with annealing is quite different than the relative instability of isolated dots under heat treatment.

The PL time-decay curves shown in Fig. 1.24 were obtained for the island-related band PL of a 3.3-nm-thick  $\text{Si}_{0.55}\text{Ge}_{0.45}$  10-layer structure grown at  $675^\circ\text{C}$  (the same sample as shown in the top trace of Fig. 1.21). The PL spectra shown were obtained at various times, beginning with the point when the exciting laser was turned off. The subsequent PL from the  $\text{Si}_{1-x}\text{Ge}_x$  undulations shown in Fig. 1.24 decay toward lower photon energy with approximately a  $200\text{-}\mu\text{s}$  time constant in contrast to the PL from the underlying Si substrate that decayed much more rapidly. The PL was contained in a broad NP line with no resolved phonon replicas. The  $\text{Si}_{1-x}\text{Ge}_x$  PL peak shifts to lower energy with increasing Ge fraction. The PL also moves to higher energy with increasing excitation density due to the fact that crests with highest Ge fraction (providing the lower-energy PL) have an exciton accommodation limit, which leads to PL saturation for these crests. Hence, the PL from lower-Ge-fraction crests predominates at higher excitation densities. At the same time, the PL from the higher-Ge-fraction crests has a longer lifetime due to the tighter confinement of excitons in these regions. This longer lifetime is observed as the PL peak shifts to lower energy with increasing decay time (see Fig. 1.24). The decays for the PR PL in the MBE material were found to be at least 100 times faster than for the dot PL. Although the result of Fig. 1.24 was obtained

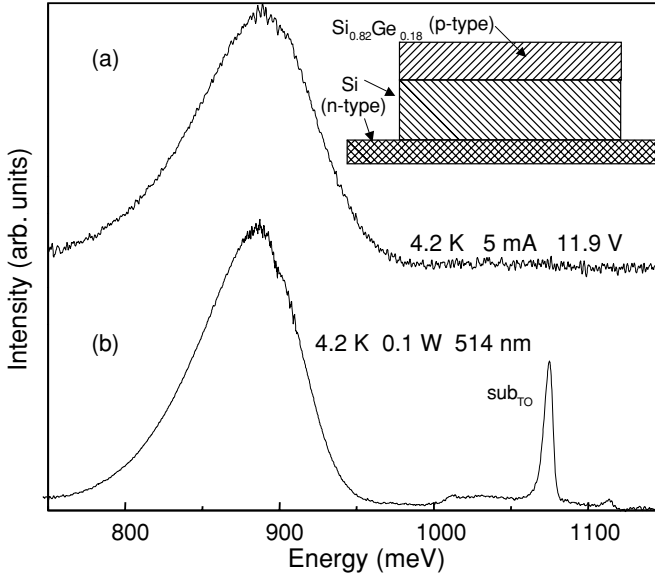


FIGURE 1.25. Electroluminescence (a) and PL (b) spectra at 4.2 K for the  $\text{Si}_{0.82}\text{Ge}_{0.18}$   $p$ - $n$  diode structure. Inset: Schematic of the heterostructure processed into light-emitting diodes.<sup>204</sup>

for self-organized island superlattices, similar decay lifetimes were observed for the isolated islands.

#### 1.3.4.2. Electroluminescence

There have been several recent reports of electroluminescence (EL) from Si/Ge dots and islands.<sup>221–223</sup> However, the first observation of EL from dots in  $\text{Si}_{1-x}\text{Ge}_x$  or, for that matter, from any Si-based, MBE-grown device was by Noël et al.<sup>204</sup> A schematic of their  $p$ - $n$   $\text{Si}_{1-x}\text{Ge}_x$  / Si heterostructure used to fabricate light-emitting diodes is given in the inset of Fig. 1.25. The structure was grown by MBE using conventional electron-beam evaporation and was doped *in situ* during growth with low-energy  $\text{As}^+$  ions<sup>224</sup> and B atoms from a  $\text{B}_2\text{O}_3$  source (the increase in incorporated O atoms was negligible for  $10^{17} \text{ cm}^{-3}$  doping).<sup>225</sup> To prevent strain relaxation,<sup>226</sup> a low growth temperature of  $\sim 400^\circ\text{C}$  was used during deposition of the  $\text{Si}_{0.82}\text{Ge}_{0.18}$  alloy layer. Dilute Schimmel etching revealed no misfit dislocations and around  $10^3\text{-cm}^{-2}$  particle-induced threading dislocations. Postgrowth annealing in the range  $550\text{--}700^\circ\text{C}$  was used to reduce the high point defect concentration typical of low growth temperatures.<sup>224</sup> Subsequent processing into mesa diodes with diameters of  $0.1\text{--}0.7 \text{ mm}$  was performed using conventional photore-sist, UV light exposure, and wet etching techniques. Aluminum contact rings were deposited onto the  $p$ -type alloy layer and the etch-exposed  $n^+$  substrate, followed by a contact anneal treatment at  $450^\circ\text{C}$  for 300 s. Electrical contact was made with



Au-wire ultrasonic bonding. The finished chip was mounted in a cryostat with the diode surfaces exposed to flowing He gas/liquid to prevent heating of the active layers during electrical excitation.

The diodes were observed to emit light with intensity proportional to the forward current density and a peak energy that varied with the Ge fraction in the alloy. A typical EL spectrum is shown in Fig. 1.25a, with the corresponding PL spectrum of a blanket sample (no mesas) given in Fig. 1.25b. The 1070-meV substrate peak is observed from the PL sample since, under optical excitation with 514-nm photons with an absorption distance of  $\sim 1 \mu\text{m}$ , there was substantial electron-hole production in the substrate. During electrical excitation, electrons and holes recombine only at the edges of, or within, the depletion region of the  $p$ - $n$  junction by one of several possible mechanisms (e.g., band-to-band, excitonic, and donor to acceptor). It is apparent from the EL spectrum that radiative recombination did not occur on the  $n$  (pure Si) side of the junction. Similar depletion effects, in which parts of the heterostructure were selectively excited, were observed in other EL samples.<sup>209</sup>

An estimate of the EL quantum efficiency (QE) was made by comparing the EL and PL intensities. In EL, the integrated intensity in the range 750–950 meV for a sample at 4.2 K and diode current of 5 mA was about one-sixtieth the corresponding PL intensity observed for 100 mW of incident 514.5-nm light on the blanket sample at 4.2 K. For EL, 5 mA corresponded to a current of  $3 \times 10^{16}$  charges/s, giving a maximum electron-hole (e-h) pair production rate of  $1.5 \times 10^{16} \text{ s}^{-1}$ . For PL, 100 mW of 514.5-nm light after surface reflection corresponds to  $\sim 2.6 \times 10^{17}$  photons/s, which, assuming an efficiency of 100% for the production of e-h pairs, gives an e-h pair rate  $\sim 17$  times that for EL. Therefore, the EL internal QE for the 890-meV band was  $\sim 0.25\%$ . The temperature dependencies for the PL and EL were similar and this suggests that the annihilation is excitonic. The similarities in spectral shape and peak energies between PL and EL point strongly to a common luminescence mechanism (i.e., recombination in dots). When the excitation (electrical or optical) was confined to the alloy region, the EL was similar in all respects to PL from material with the same Ge concentration [i.e., the same peak energies, persistence to  $\sim 80$  K, and comparable internal quantum efficiencies (estimated to be  $\sim 0.25$ – $0.75\%$ )]. As in previous PL studies on the same material,<sup>214</sup> the peak energy of the luminescence depended on the Ge concentration and was  $\sim 120$  meV lower than the previously published alloy band gap energy at any value of  $x$ .

## 1.4. Engineering of Si<sub>1-x</sub>Ge<sub>x</sub> Islands

In the previous sections we have seen that the shape, size, and distribution of Ge dots can, to a certain extent, be controlled by growth parameters such as temperature and deposition rate, or by postgrowth treatments. The formation and evolution of Ge dots is dictated by first principles and it is of great interest to devise ways to further control dot growth and self-organization. Development of dot engineering is of particular importance for the design of devices that rely critically on either

the position or size of the dots. The factors that can influence dot formation can be classified in two categories; those that modify the substrate surface morphology and those that alter the surface chemistry. In this section, some strategies to tailor Ge dots are reviewed.

### *1.4.1. Influence of Surface Morphology*

#### *1.4.1.1. Intrinsic Surface Morphology*

The presence of surface steps can influence the nucleation of Ge dots. For example, it has been observed that Ge dots preferentially align at surface steps when grown on a vicinal (001) Si surface miscut  $4^\circ$  along a  $[110]$  direction.<sup>227</sup> In that case, Si step-bunching during growth of a Si buffer layer results in the formation of Ge dots in a transition region between (100) terraces and  $\{11x\}$  facets, with  $x = 8-10$ . The lower coordination of Si atoms and concomitant partial lattice relaxation at steps both contribute to the preferential nucleation of Ge islands. Controlling accurately the miscut angle and orientation and devising ways to adjust the step height or terrace width may be a relatively easy way to control the placement of dots.

Surface undulations in  $\text{Si}_{1-x}\text{Ge}_x$  island superlattices may also represent a suitable template for the subsequent growth of ordered arrays of dots. A better approach to exploit wafer misorientation is to predeposit  $\text{Si}_{1-x}\text{Ge}_x$  prior to the Ge dots. In particular,  $\text{Si}_{1-x}\text{Ge}_x$  surface wires can be formed when an island superlattice is grown on a vicinal surface with a well-oriented regular step distribution.<sup>228</sup> The surface waves have a period comparable to the size of Ge dots and favor periodic arrangement of the dots. Ordered array of dots with surface symmetry governed by the direction of the substrate miscut have been achieved with this approach.<sup>229</sup> In addition to dot positioning, this technique can offer some control on the size and eliminate coalescence of dots.

Another approach to control the nucleation of 3D islands is to use the strain field of a misfit dislocation network in relaxed  $\text{Si}_{1-x}\text{Ge}_x$  material.<sup>230-234</sup> Here, the Ge islands are deposited on a planar  $\text{Si}_{1-x}\text{Ge}_x$  spacer layer of thickness exceeding the critical thickness for pseudomorphic growth. Such an epitaxial layer exhibits a network of misfit dislocations at the substrate interface, with dislocation lines running along  $[110]$  directions. The misfit strain associated with those dislocations extends into the epitaxial layer and induces a regular variation in the lattice constant at the surface. This residual strain, albeit small, is sufficient to cause preferential nucleation of the Ge dots at the intersection of perpendicular misfit dislocations. This technique can, in principle, be used to control dot placement, but it may not be practical for most applications. This is because, first, the intrinsic random fluctuations in dislocation line spacing in relaxed epitaxial layers will result in a distribution of Ge islands on an irregular square grid and thus have limited accuracy on the positioning. Second, misfit dislocations are terminated by threading dislocations that propagate into the epitaxial films and will, in most cases, adversely affect the optical and/or electrical properties of a device structure.

Other surface morphological features can promote dot nucleation. Surface pits, for example, may cause a high local surface step concentration or strain gradients suitable for dot formation. Pitted surfaces can be obtained in MBE by using a

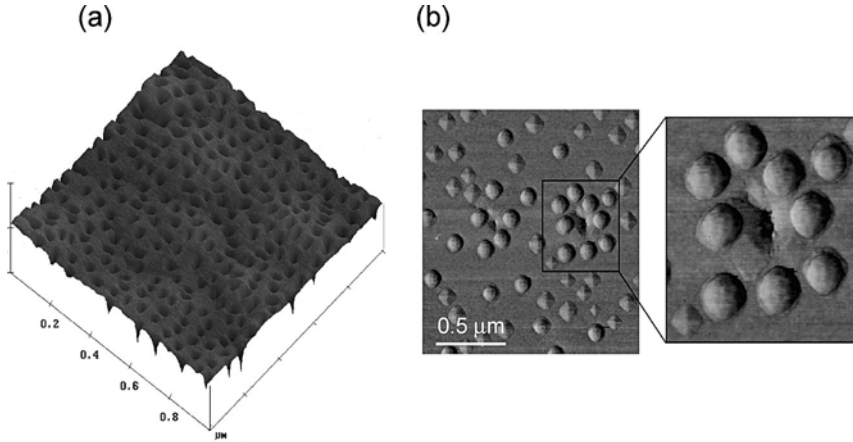


FIGURE 1.26. (a) AFM view of the morphology of (001) Si homoepitaxial layers deposited in conditions that favor surface pit formation. Here, the scanned area is  $1\ \mu\text{m}^2$  and the vertical scale is 20 nm/division. (b) AFM view ( $1\ \mu\text{m}^2$ ) of Ge dots formed on a similar Si pitted surface. The magnified view emphasizes the high concentration of dome islands in the vicinity of a surface pit. The depletion of the wetting layer in periphery of the domes is also apparent.

deposition temperature close to that of epitaxy breakdown.<sup>235–237</sup> Figure 1.26a illustrates a pitted morphology on a 2- $\mu\text{m}$ -thick homoepitaxial Si film on (001) Si grown at 435°C. The surface exhibits a dense network of pits of 50–100-nm depth and 400-nm diameter. When Ge dots are grown on such a pitted surface, it is observed that nucleation is enhanced in the vicinity of surface pits. This is illustrated in Fig. 1.26b, which displays an AFM image of Ge dots formed on a pitted Si surface. Here, the Ge dots were obtained by depositing 6 MLs of Ge at 650°C on a (001) Si surface where pits were formed by predeposition of 2  $\mu\text{m}$  of Si at a temperature of 420°C. It is clear that the surface concentration of Ge dome islands is larger near surface pits and that, conversely, no pyramid dot is seen by the pits. These observations are suggestive of preferential nucleation and enhanced mass transport in the vicinity of pits, consistent with the results obtained when other types of intrinsic morphological feature are present on the surface. This approach may be useful to control the relative number of pyramids and dome islands, but here, again, the randomness of the pit formation process makes it inadequate for accurate dot positioning.

#### 1.4.1.2. Extrinsic Surface Morphology

Surface patterning using standard lithographic techniques offers better possibilities for size control and exact placement of dots. This approach has been investigated by a number of authors.<sup>199,238–249</sup> The basic idea is to lithographically etch a nanotemplate suitable for the epitaxy of dots. Early attempts have exploited the high selectivity of CVD to grow Si on Si stripes etched through a SiO<sub>2</sub> layer along

the [100] direction.<sup>242</sup> This resulted in the formation of raised strips of epitaxial Si bounded by {011} side walls. Ge deposited on this template preferentially grows near the plateau edges, forming a linear array of dots. Analogous results were obtained on patterned Si with stripes along the [110] direction.<sup>238</sup> In this case, the anisotropy of the growth rate leads to the formation of mesas of trapezoidal cross section with {113} and {111} side-wall facets. Ge deposited on this surface results in self-aligned well-spaced 1D array of dots on the ridges of the mesas. Two-dimensional arrays of dots have also been obtained by growing on a surface patterned with square mesas. In particular, Si nanoimprinting at the 10–100-nm scale has also been shown to be a good means to position Ge dots at a length scale difficult to attain by conventional lithography.<sup>239</sup> In all cases, preferential nucleation of dots at the ridges of stripe mesas likely results from a number of factors: higher adatom diffusion on the inclined side walls, barrier to diffusion down the facets at the mesa edge, and reduced strain energy at the edges.

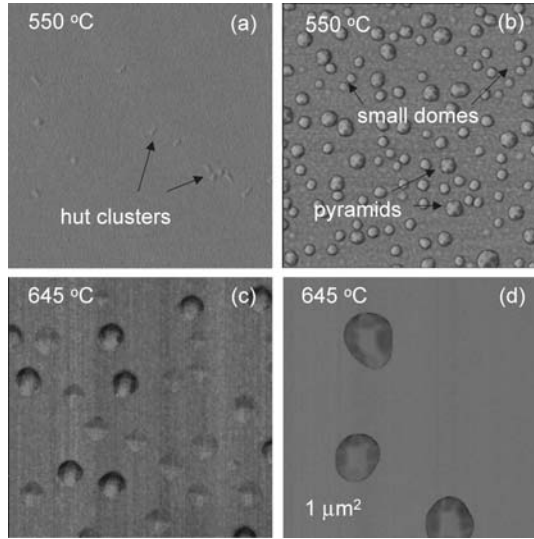
Similar results can be achieved by a nonselective growth technique such as MBE by depositing Si on a surface on which Si trenches have been etched.<sup>245,247,248,250–253</sup> Homoepitaxy then results in an undulated morphology analogous to that of Fig. 1.4a and offers preferred sites for dot nucleation.<sup>248</sup> In contrast with results obtained by CVD, the exact positioning of dots by MBE is more critically dependent on growth conditions and strain distribution. For example, on such an undulated surface, preferential nucleation of dots can occur at the side walls rather than on the top of the flat top terraces. Nucleation at the top of the ridges may be achieved, however, if the surface is strained by the insertion of a  $\text{Si}_{1-x}\text{Ge}_x$  buffer layer or if the growth temperature is increased.<sup>245,247</sup> The interplay among surface kinetics, strain energy, and surface free energy is clearly crucial in determining the precise morphology and, clearly, more work is needed to elucidate to unravel this problem.

### 1.4.2. Influence of Adsorbed Species

Although the presence of periodic morphological features on the surface greatly influences the placement and arrangement of Ge dots, it has relatively minor effects on their shape or physical dimensions. A modification of the surface chemistry through adsorption of foreign species, the presence of a surfactant, and dopant segregation may all impact on the intrinsic properties of the dots.

The effect of C pretreatment on the nucleation and evolution of Ge dots is, by far, the best studied example for the  $\text{Si}_{1-x}\text{Ge}_x$  semiconductor system. The predeposition of a fraction of a ML of C on (001) Si creates an inhomogeneous  $\text{Si}_{1-x}\text{Ge}_x$  layer that strongly influences dot formation.<sup>254–262</sup> This is illustrated in Fig. 1.27, which compares MBE-grown Ge dots formed with and without C predeposition at two different temperatures. At a low temperature of 550°C (Figs. 1.27a and 1.27b), a 5 ML Ge deposition without C leads to the formation of only a few hut clusters, whereas the dot formation is well established when C is predeposited. This is consistent with a significant thickness reduction or perhaps complete suppression

FIGURE 1.27. AFM images of the surface morphology of a series of 5 ML Ge epitaxial layers grown on Si at 550°C (a) without and (b) with a 0.2 ML C predeposition, and at 645°C (c) without and (d) with a 0.2 ML C predeposition. Here, the films were grown by MBE using an electron cyclotron resonance plasma source for the deposition of C.<sup>254,255</sup>



of the Ge wetting layer in the presence of C.<sup>263</sup> Moreover, the surface presents an unusual morphology characterized by the presence of classic pyramids and domelike dots of dimensions much less than those normally seen. The latter are very regular in size (about 25 nm in diameter) and probably result from heterogeneous nucleation at  $\text{Si}_{1-x}\text{Ge}_x$  clusters on the surface. At a higher temperature of 645°C (Figs. 1.27c and 1.27d), the C precovered surface exhibits large-dome islands rather than a mixed distribution of pyramids, indicating that the dot formation has reached a later stage, which is again consistent with a thinner wetting layer.

Other studies of C-induced Ge quantum dots have reached similar conclusions. Carbon pretreatment makes it possible to synthesize dome-shaped Ge dots at lower temperature (500°C) and their size and density can be tailored through optimization of the growth conditions.<sup>260</sup> In particular, Ge dots prepared this way exhibit enhanced photoluminescence.<sup>264</sup> The size reduction of the domes puts them in a regime where quantum size effects are more prominent and makes them attractive for the conception of quantum optoelectronic devices. The dot position is, however, strongly influenced by the distribution of surface carbon clusters and the vertical self-organization in stacked dot structures is lost in C-mediated growth of dots.

The actual physical mechanism that underlies the influence of C atoms on Ge dot formation is still a matter under debate. A study of nucleation of Ge quantum dots on a C-treated surface at low temperature (350°C) has suggested that strain effects associated with C-rich domains repel Ge adatoms, leading to the formation of larger dots with a smaller aspect ratio.<sup>263</sup> In another study<sup>265</sup> performed at higher temperature (500°C), C atoms on the surface were believed to induce the

nucleation of Ge islands, the size of the latter increasing with the C coverage. Clearly, additional experimental work and modeling is required to fully elucidate the effect of C on  $\text{Si}_{1-x}\text{Ge}_x$  dot formation.

Gas adsorption can influence dot formation. Atomic hydrogen acts as a surfactant in the Ge/Si system, increasing the thickness of the wetting layer.<sup>266,267</sup> The presence of H on the surface should have an opposing effect to C and retard the transition to 3D growth. Atomic hydrogen, by reducing Ge surface segregation and affecting surface diffusion, should also modify the structural properties of dots. Although the effect of atomic hydrogen on dot formation has not been studied in any detail, molecular hydrogen has been found in low-pressure chemical vapour deposition (LPCVD) growth to shift the bimodal distribution of pyramids and domes to smaller sizes.<sup>259</sup> The use of Sb as a surfactant has also been found to influence the size and density of Ge dots.<sup>268,269</sup>

The introduction of dopants during growth may also influence dot formation by modifying the surface energy, by atomic bulk and surface diffusion, or by blocking nucleation sites. For example, Sb-doped dome-shaped Ge islands have been observed to develop large  $\{100\}$  facets upon annealing, whereas In-doped Ge islands exhibited strong faceting upon annealing.<sup>270</sup> More recently,<sup>271</sup> P doping was found to have a stabilizing effect on dome islands and to inhibit coarsening upon annealing.

All of the above examples illustrate the broad possibilities that are offered to tailor dot fabrication. Because of its high level of control and reproducibility, growth on patterned substrates is certainly the most promising direction to achieve device compatible structures. Research on chemical treatment of surfaces should not be neglected however, because if used in conjunction with patterning techniques, it may lead to further optimization of tailored quantum dot structures.

## 1.5. Applications of $\text{Si}_{1-x}\text{Ge}_x$ Islands and Dots

In this section, we briefly review recent progress in the exploitation of  $\text{Si}_{1-x}\text{Ge}_x$  islands and dots in electronic and photonic devices. Additional information on this subject can be found in a recent book on silicon-based photonics.<sup>272</sup>

### 1.5.1. Photodetectors

Although  $\text{Si}_{1-x}\text{Ge}_x$  and Ge dots have been used to improve the performance of above-band-gap near-infrared,<sup>132,273–277</sup> intra-subband mid-infrared<sup>278–285</sup> and inter-subband mid- to far-infrared<sup>286–288</sup> photodetectors, we will confine the discussion here to near-infrared devices, which has been arguably one of the most active research directions so far for the exploitation of  $\text{Si}_{1-x}\text{Ge}_x$  islands and dots.<sup>97,273,289</sup>

The absorption edge of a  $\text{Si}_{1-x}\text{Ge}_x$  quantum well can be extended to the telecommunication wavelength range and beyond, but the lowest-lying transitions are still indirect. As a result, the optical absorption and, hence, the carrier generation

efficiency remains small relative to direct-gap materials. Planar Si<sub>1-x</sub>Ge<sub>x</sub> alloys or pure Ge layers on Si were first used to extend the spectral response of photodetectors beyond the Si band edge.<sup>290</sup> Although some progress has recently been reported,<sup>291</sup> it is inherently difficult in standard 2D Si<sub>1-x</sub>Ge<sub>x</sub> structures to reach telecommunication wavelengths because of the high Ge content needed to achieve the desired band-gap reductions. Nonetheless, the use of planar Si<sub>1-x</sub>Ge<sub>x</sub> alloys has proven effective in fabricating photodetectors with reasonable quantum efficiencies at 1300 nm<sup>292-294</sup>, but not at 1550 nm. In practice, Ge concentrations well over  $x = 0.5$  are required to obtain a significant photocurrent response at 1550 nm, and the corresponding critical thicknesses of the order of 10 nm or less are unsuitable for device fabrication.<sup>295,296</sup> In Si<sub>1-x</sub>Ge<sub>x</sub> dots, the relaxation of the momentum conservation condition as well as the 3D charge-carrier confinement in the islands are expected to significantly enhance the radiative recombination probability.<sup>167,297-299</sup> Vertical alignment in stacked layers of dots can also favour carrier transport through the structure and enhance radiative recombination. Electroluminescence, persisting to room temperature in some cases, has been reported in self-assembled stacked Si<sub>1-x</sub>Ge<sub>x</sub> islands diode structures.<sup>165,222,300-302</sup> The increasing importance of quantum confinement effects in such thin layers tends to push the absorption edge to shorter wavelengths, thus counteracting the effect of increasing the Ge concentration. One solution has been to grow the Si<sub>1-x</sub>Ge<sub>x</sub>/Si multilayers in a regime in which the interfaces are undulated rather than planar, with the waviness reducing the strain energy and allowing thicker layers. This 3D growth mode also increases the effective Ge concentrations where there are local maxima in the quantum well thickness, thus reducing the local quantum confinement at these locations. The 3D growth regime enables the growth of thermally robust and defect-free structures with high Ge content. Furthermore, the volume of active material may be increased through imbedding stacks of dot layers in thicker nonabsorbing Si spacers or using a waveguide configuration to increase the absorption length.<sup>303,304</sup>

Undulated Si<sub>1-x</sub>Ge<sub>x</sub> layers have been applied successfully in the fabrication of photodetectors operating at telecommunication wavelengths.<sup>97,273,275,282,305-307</sup> Si<sub>1-x</sub>Ge<sub>x</sub> self-assembled islands imbedded in Si forming the intrinsic layer of a normal incidence *p-i-n* photodetector have been shown to extend the photodetection range of these devices to 1.3 and 1.55  $\mu\text{m}$  radiation with a room-temperature responsivity of 0.2 and 0.003 A W<sup>-1</sup> at these respective wavelengths.<sup>305</sup> Enhanced responsivity may be obtained by increasing the active region of the device by coupling radiation through a surface ridge waveguide. An example of structure for such device is illustrated in Fig. 1.28.<sup>273</sup> It consists of stacked wavy Si<sub>0.5</sub>Ge<sub>0.5</sub> layers grown by UHV-CVD on a silicon-on-insulator (SOI) substrate.<sup>308</sup> Here, embedding Si<sub>1-x</sub>Ge<sub>x</sub> layers in an SOI structure yields a well-confined waveguide with the optical mode profiles mainly governed by the large index contrast between the Si and the oxide cladding. This wafer was fabricated into a waveguide metal–semiconductor–metal (MSM) photodetector; the geometry is described elsewhere.<sup>308</sup> By placing the Si<sub>1-x</sub>Ge<sub>x</sub> stack close to the surface and using interdigitated electrodes at the surface, a responsivity of 0.1 A W<sup>-1</sup> was demonstrated for

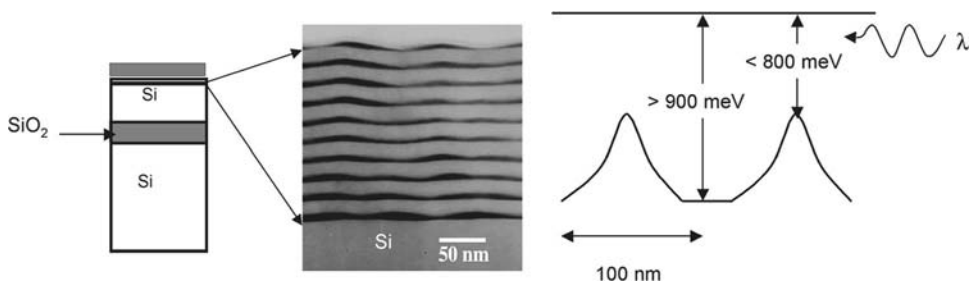


FIGURE 1.28. Schematic structure of an SOI-based  $\text{Si}_{1-x}\text{Ge}_x$  photodetector (left), XTEM image of the active  $\text{Si}_{1-x}\text{Ge}_x$  undulated layer stack (center), and schematic description of the lateral modulation of the transition energy caused by undulations and Ge accumulation at crests.

$\lambda = 1.52 \mu\text{m}$ .<sup>308</sup> As an alternative to the use of a SOI wafer, a thick dilute  $\text{Si}_{1-x}\text{Ge}_x$  sublayer has also been used to confine the optical modes in the active region of the detector.<sup>309</sup> This approach resulted in detectors of comparable responsivity at the telecommunication wavelengths as similar device structures grown on SOI wafers.

In addition to providing information on the room-temperature optical absorption, photocurrent spectroscopy is the most relevant measurement technique for the evaluation of  $\text{Si}/\text{Si}_{1-x}\text{Ge}_x$  island superlattice structures for photodetectors. As an illustration, Fig. 1.29 shows photocurrent spectra measured for two different samples.<sup>273,274</sup> The first sample consisted of a 10-period  $\text{Si}_{0.5}\text{Ge}_{0.5}/\text{Si}$  island superlattice grown by UHV-CVD on a conventional Si substrate with a thick Si cap layer to help planarize the surface. This wafer was fabricated into a waveguide MSM photodetector. The second sample was a MBE-grown  $\text{Si}_{0.5}\text{Ge}_{0.5}/\text{Si}$  undulated island superlattice, also grown on a conventional Si substrate. It was not possible to collect photocurrent spectra in the 1350–1480-nm range on these nonwaveguide samples, because the photocurrent noise floor was much larger due to the large

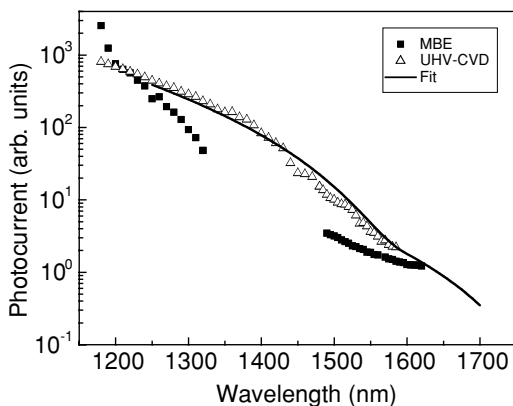


FIGURE 1.29. Photocurrent response measured at 2 V bias voltage for one MBE-grown island superlattice and one UHV-CVD island superlattice. The solid curve is a fit to the UHV-CVD sample photocurrent using Eq. (1.5).



dark current flowing in the Si substrate. This noise problem can be eliminated by growing the superlattice on an SOI wafer or incorporating it into a *p-i-n* diode geometry.

The photocurrent spectra near an absorption edge can be modeled using a simple polynomial expression of the form

$$I(E) = C(E - E_g)^x, \quad (1.5)$$

where  $E$  is the photon energy and  $E_g$  is the absorption edge energy.<sup>310,311</sup> A summation of such terms may be used if more than one optical band edge is involved. For indirect materials, the exponent  $x$  is expected to be 2, but values obtained for Si<sub>1-x</sub>Ge<sub>x</sub> superlattices vary between 2 and 4.<sup>310,311</sup> In any case, these thickness-modulated superlattices have a band edge that will vary from point to point, so the fitted value of  $x$  should be regarded as a purely empirical parameter. On the other hand, the transition energy  $E_g$  gives an unambiguous determination of the room-temperature absorption edge. In Fig. 1.29, the UHV-CVD data is fitted quite well by a sum of two expressions of the form given in Eq. (1.5), one with  $E_g = 0.785$  eV and a second much weaker contribution with an effective absorption edge at  $E_g = 0.68$  eV. This is consistent with previous PL measurements on these wafers,<sup>220</sup> which indicate a minimum band gap of 0.787 eV at 4.2 K. The photocurrent result establishes that these UHV-CVD samples have a room-temperature absorption edge well below 0.8 eV. The second transition energy may correspond to local areas of very high Ge concentration in the Si<sub>1-x</sub>Ge<sub>x</sub> islands or possibly defect-mediated photocurrent generation. However, no evidence of crystal defects appears in the TEM and PL characterization of this wafer.

The photocurrent spectrum from the MBE sample has a very different shape. A higher-energy absorption edge near 0.9 eV. ( $\sim 1380$  nm) is evident, followed by a strong absorption tail at wavelengths extending past 1600 nm. This is attributed to the fact that, unlike the CVD superlattices, this structure clearly exhibits the island/wetting layer geometry of the Stranski–Krastanow growth mode revealed by predominantly flat Si<sub>1-x</sub>Ge<sub>x</sub> on Si interfaces (see Fig. 1.4a). One interpretation of these data is that the low-energy tail corresponds to the high-Ge-concentration regions near the center of the Si<sub>1-x</sub>Ge<sub>x</sub> islands, whereas the 0.9-eV edge corresponds to absorption in the thinner wetting layer. By measuring the optical power coupled into the waveguide MSM photodetector, the absolute photocurrent quantum efficiency was determined. At 1550 nm, the measured responsivity for the 240-mm long-waveguide detector was approximately 0.05 A W<sup>-1</sup> at 1550 nm.<sup>273</sup>

Fast infrared Si<sub>1-x</sub>Ge<sub>x</sub> island superlattice detectors have also been realized in a vertical MSM configuration by growing the stacked Si<sub>1-x</sub>Ge<sub>x</sub> islands on an epitaxial buried cobalt silicide layer.<sup>284,307,312</sup> In that work, the stacked Si<sub>1-x</sub>Ge<sub>x</sub> islands were produced by MBE with the same apparatus and methodology described here and elsewhere.<sup>97</sup> The morphology of the superlattice presented in Fig. 1.30 in a TEM micrograph, obtained after mesa etching, is very similar to that shown in Fig. 1.4. The structure, however, exhibits threading dislocations formed

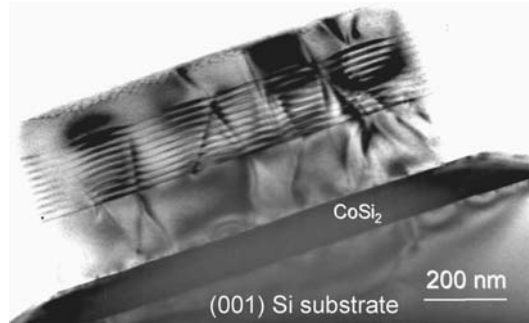


FIGURE 1.30. TEM cross-section view of a Si-Si<sub>0.61</sub>Ge<sub>0.39</sub> island superlattice grown on an epitaxial CoSi<sub>2</sub> layer on (011) Si. (TEM micrograph courtesy of Dr. C. Buchal.)

at the substrate/silicide and silicide/epitaxial interfaces. This constitutes a rather unique example of a device in which a Si<sub>1-x</sub>Ge<sub>x</sub> island superlattice is incorporated in a complex heteroepitaxial sequence involving wafer transfer between two growth apparatus. In this device, long-wavelength photons create e-h pairs in the small gap islands and the photocurrent is dominated by electrons drifting toward the silicide electrode. Detectors with a response time of 12 ps and a quantum efficiency of 5% and 1% at 1.32 and 1.55  $\mu\text{m}$ , respectively, were obtained with this approach.<sup>307</sup> Longer-wavelength photodetectors have also been realized by exploiting intra-valence-band transitions in self-assembled Ge dots.<sup>279,313</sup> Broad optical absorption in the wavelength range 2–6  $\mu\text{m}$  with responsivities of several  $\text{mA W}^{-1}$  for 20 K operation was achieved in these devices.

### 1.5.2. Other Applications

Relatively little work has been done on the application of Si<sub>1-x</sub>Ge<sub>x</sub> dots in microelectronics. Ge quantum dots may find application in the field of quantum computation where they could be used to localize carriers forming quantum memory units (qbits) or perhaps used as single-photon emitters. Considerable work needs to be done, however, to understand the electronic transport properties of Ge-dot structures. There have been several reports on hole charging and transport measurements in Ge-dot layers imbedded in Si.<sup>314–318</sup> For example, the Coulomb charging effect of quantum confined hole states in Ge dots embedded in Si barriers<sup>314</sup> and lateral tunneling of confined holes from Ge islands to the wetting layer<sup>316</sup> have been reported. Capacitance–voltage spectroscopy has shown that Ge-dome islands have a low, quasicontinuous, averaged density of states, due to the interplay of quantization and charging effects,<sup>315,317</sup> that may be exploited to tune the absorption wavelength in vertical gated structures.<sup>315</sup> Magnetotransport of thin Ge quantum wells that contain imbedded Ge hut clusters has shown that the latter may influence hole transport in a low-voltage regime, possibly through a carrier-trapping mechanism.<sup>318</sup> Finally, self-assembled Ge islands have been successfully

incorporated into Si-based interband tunneling diodes and record peak-to-valley ratio Si-based tunnel diodes were achieved.<sup>216,319</sup>

The luminescence properties of Si<sub>1-x</sub>Ge<sub>x</sub> islands in the near-infrared makes them attractive candidates for fabrication of emitters covering the 1.3–1.55- $\mu\text{m}$  spectral region in Si-based optoelectronics.<sup>272,298,320</sup> However, the indirect band gap of Si<sub>1-x</sub>Ge<sub>x</sub> results in low radiative combination rates and poor light emission properties. The optical emission, centered around 1.5  $\mu\text{m}$ , usually originates from the recombination of holes localized in Ge-rich islands with electrons localized in the surrounding strained Si. The luminescence is characterized by a broad spectrum that reflects the variations in the size and average composition of the dots. Improvements in quantum efficiency and spectral purity can be expected in the future and self-assembled Si<sub>1-x</sub>Ge<sub>x</sub> dots may become an interesting solution for on-chip optical interconnects or low-cost optical communications emitters integrated on Si.<sup>272</sup> Different ways of using self-assembled Ge dots as emitters at telecommunication wavelengths have been reviewed elsewhere.<sup>216</sup> The realization of a Si-based emitter incorporating Ge dots requires more research on the factors that influence dot size, shape, and density and the development of group IV semiconductor nanostructure deposition techniques for the selective growth of quantum dots. The latter is becoming the most active area of research in the physics of semiconductor quantum dots.

## 1.6. Summary and Future Prospects

In this chapter, we have reviewed recent developments in the physics and characterization of self-assembled islands and dots. We have attempted to give the reader a broad overview on the growth, shape evolution, structural, vibrational, and optical properties of a wide variety of such nanostructures. The principal points discussed may be summarized as follows:

- Island and dot formation in heteroepitaxy result from the interplay between the surface free energy and the built-in strain energy. Minimization of energy and kinetic barriers dictates the evolution of morphology of the epitaxial film.
- In the Si<sub>1-x</sub>Ge<sub>x</sub> system, the 3D growth mode evolves with coverage through a series of metastable island configurations.
- Stacked layers of dot or island superlattices are strongly correlated vertically. Island superlattices possess a characteristic modulation length that is a function of the strain and elastic properties of the material.
- The photoluminescence signature of Si<sub>1-x</sub>Ge<sub>x</sub> islands is a broad peak at about 800 meV. The exact energy, breadth, and intensity of the PL signal depend on the physical properties such as the dimension of the islands, their size distribution, average composition, and strain conditions.
- Si<sub>1-x</sub>Ge<sub>x</sub> dot growth can be engineered either through semiconductor surface treatment or surface patterning. Carbon predeposition can influence dot nucleation and growth.

- Dot engineering offers the possibility to tailor the properties of  $\text{Si}_{1-x}\text{Ge}_x$  semiconductor dots that may become building blocks for the next generation of devices.

It was not possible here to discuss in depth all of the topics covered in the chapter. For that reason, special care was taken to provide an extensive bibliography to guide any reader interested in learning more about the physics and applications of  $\text{Si}_{1-x}\text{Ge}_x$  nanostructures. Originally perceived as undesirable 3D features, self-assembled dots are now among the most studied semiconductor heteroepitaxial systems. Now that dot formation is better understood and the physical properties are becoming elucidated, the world of semiconductor quantum dots is becoming a fascinating playground for device physicists. One short-term challenge will be to devise ways to control the size, composition, and placement of those nanostructures in order to better tailor their properties. The next challenge will be the integration of dot structures in actual devices and circuits. The development of quantum computing is a daunting task and it is very likely that quantum dot structures may play a central role in this endeavor.

*Acknowledgments.* The authors express their thanks to all of the co-workers and collaborators whose contributions over the years have helped to further our understanding of self-assembled quantum dots and islands. We are particularly grateful to Dr. D.C. Houghton, J.-P. Noël, and Dr. H. Lafontaine for their involvement in the early stages of the development of  $\text{Si}_{1-x}\text{Ge}_x$  strained epitaxy and dot synthesis. The collaboration of Dr. D.D. Perovic, Dr. D.E. Jesson, Dr. R.L. Headrick, and Dr. H.K. Shin on structural aspects, Dr. L. Tsybeskov and Dr. B.V. Kamaney on the study of optical properties and Dr. S. Janz and D.-X. Xu on the development of photodetectors is acknowledged. We thank Dr. C. Buchal for providing the TEM micrograph of a SiGe/silicide photodetector structure. Finally, we thank H.J. Labbé, D. Elliot, S. Moisa, M. Beaulieu, Dr. J.P. McCaffrey, and J. Balle for their technical assistance.

## References

1. J. W. Matthews and E. A. Blakeslee, Defects in epitaxial materials: I. Misfit dislocations, *J. Cryst. Growth* **27**, 118–125 (1974).
2. R. People and J. C. Bean, Calculation of critical layer thickness versus lattice mismatch for  $\text{Si}_{1-x}\text{Ge}_x/\text{Si}$  strained-layer heterostructures, *Appl. Phys. Lett.* **47**, 322–342 (1985).
3. R. People and J. C. Bean, Erratum: Calculation of critical layer thickness versus lattice mismatch for  $\text{Si}_{1-x}\text{Ge}_x/\text{Si}$  strained-layer heterostructures [*Appl. Phys. Lett.* **47**, 322 (1985)], *Appl. Phys. Lett.* **49**, 229 (1986).
4. D. D. Perovic, B. Bahierathan, D. C. Houghton, H. Lafontaine, and J.-M. Baribeau, Strain relaxation at low misfits: Dislocation injection vs. surface roughening, in: *Evolution of Epitaxial Structure and Morphology*, edited by A. Zangwill, D. Jesson, D. Chambliss, and R. Clarke, Materials Research Society, Boston, 1995, Vol. 399, pp. 325–336.

5. H. Lafontaine, D. C. Houghton, B. Bahierathan, D. D. Perovic, and J.-M. Baribeau, Si<sub>1-x</sub>Ge<sub>x</sub> critical thickness for surface wave generation during UHV-CVD growth, in: *Evolution of Epitaxial Structure Morphology*, edited by D. J. A. Zangwill, D. Chambliss, and R. Clarke, Materials Research Society, Pittsburgh, PA, 1996, Vol. 399, pp. 413–418.
6. R. J. Asaro and W. A. Tiller, Interface morphology development during stress corrosion cracking. I. Via surface diffusion, *Metall. Trans. A* 1789–1796 (1972).
7. M. A. Grinfeld, Instability of the separation boundary between a non-hydrostatically stressed elastic body and a melt, *Dokl. Akad. Nauk SSSR* **290**, 1358–1363 (1986).
8. B. Teichert, Self-organization of nanostructures in semiconductor heteroepitaxy, *Phys. Rep.* **365**, 335–432 (2002).
9. Z. Zhang and M. G. Lagally, Morphological organization in epitaxial growth and removal, in: *Series on Directions in Condensed Matter Physics*, World Scientific, Singapore, 1998, Vol. 14, p. 498.
10. K. Brunner, Si/Ge nanostructures, *Rep. Prog. Phys.* **65**, 27–72 (2002).
11. B. Voigtländer, Fundamental processes in Si/Si and Ge/Si epitaxy studied by scanning tunneling microscopy during growth, *Surf. Sci. Rep.* **43**, 127–254 (2001).
12. E. Bauer, Phänomenologische theorie der kristallabscheidung an oberflächen, I/II, *Z. Kristallogr.* **110**, 372–394/395–431 (1958).
13. I. N. Stranski and L. Krastanow, Zur theorie der orientierten ausscheidung von ionenkristallen aufeinander, *Sitzungaber. Akad. Wien, Mat. Nat. Kl. IIb* **146**, 797–810 (1937).
14. M. A. Grinfeld and D. J. Srolovitz, Stress driven morphological instabilities and islanding of epitaxial films, in: *Properties of Strained and Relaxed Silicon Germanium*, edited by E. Kasper, INSPEC, London, 1995, Vol. 12, pp. 3–16.
15. J. C. Bean, L. C. Feldman, A. T. Fiory, S. Nakahara, and I. K. Robinson, Si<sub>1-x</sub>Ge<sub>x</sub>/Si strained-layer superlattice grown by molecular beam epitaxy, *J. Vac. Sci. Technol. A* **2**, 436–440 (1984).
16. M. L. Green, M. L. Baglin, G. Y. Chin, H. W. Deckman, W. Mayo, and D. Narasimham, *Si-Based Heterostructures: Interfacial Structure and Stability*, The Metallurgical Society, Warrendale, PA, 1986.
17. E. Rosencher, *Heterostructures on Si: One Step Further with Silicon*, Kluwer Academic Publishers, Dordrecht, 1988.
18. M. L. Swanson, N. R. Parikh, E. C. Frey, G. S. Sandhu, W. K. Chu, T. E. Jackman, J.-M. Baribeau, S. Kechang, and J. McCaffrey, RBS/channeling and TEM analysis of thin sandwiched epi-layers of germanium on silicon, in: *Characterization of the Structure and Chemistry of Defects in Materials*, edited by B. C. Larson, M. Rühle, and D. N. Seidman, Materials Research Society, Boston, 1989, Vol. 138.
19. J.-M. Baribeau, D. C. Houghton, T. E. Jackman, and J. P. McCaffrey, Molecular beam epitaxy growth of Ge on (100) Si, *J. Electrochem. Soc.* **136**, 1158–1162 (1989).
20. D. J. Eaglesham and M. Cerullo, Dislocation-free Stranski Krastanow growth of Ge on Si(100), *Phys. Rev. Lett.* **64**, 1943–1946 (1990).
21. Y.-W. Mo, D. E. Savage, B. S. Swartzentruber, and M. G. Lagally, Kinetic pathway in Stranski–Krastanov growth of Ge on Si(001), *Phys. Rev. Lett.* **65**, 1020–1023 (1990).
22. J. Drucker and S. Chapparo, Diffusional narrowing of Ge on Si(100) coherent island quantum dot size distributions, *Appl. Phys. Lett.* **71**, 614–616 (1997).
23. X. Z. Liao, J. Zou, D. J. H. Cockayne, Z. M. Jiang, and X. Wang, Extracting composition and alloying information of coherent Ge(Si)/Si(001) islands from [001] on-zone bright-field diffraction contrast images, *J. Appl. Phys.* **90**, 2725–2729 (2001).

24. X. Z. Liao, J. Zou, D. J. H. Cockayne, J. Wan, Z. M. Jiang, G. Jin, and K. L. Wang, Annealing effects on the microstructure of Ge/Si(001) quantum dots, *Appl. Phys. Lett.* **79**, 1258–1261 (2001).
25. B. Cho, T. Schwarz-Selinger, K. Ohmori, D. G. Cahill, and J. E. Greene, Effect of growth rate on the spatial distributions of dome-shaped Ge islands on Si(001), *Phys. Rev. B* **66**, 195,407 (2002).
26. M. M. Rzaev, T. M. Burbaev, V. A. Kurbatov, N. N. Melnik, M. Mühlberger, A. O. Pogosov, F. Schäffler, N. N. Sibeldin, V. A. Tsvetkov, P. Werner, N. D. Zakharov, and T. N. Zavaritskaya, Photoluminescence of self-assembled Ge islands grown by Si MBE at low temperatures, *Phys. Stat. Solid (c)* **4**, 1262–1266 (2003).
27. F. Boscherini, G. Capellini, L. Di Gaspare, M. De Seta, F. Rosei, A. Sgarlata, N. Motta, and S. Mobilio, Ge-Si intermixing in Ge quantum dots on Si, *Thin Solid Films* **380**, 173–175 (2000).
28. D. Dentel, L. Vescan, O. Chrétien, and B. Holländer, Influence of molecular hydrogen on Ge island nucleation on Si(001), *J. Appl. Phys.* **88**, 5113–5118 (2000).
29. T. I. Kamins, E. C. Carr, R. S. Williams, and S. J. Rosner, Deposition of three-dimensional Ge islands on Si(001) by chemical vapor deposition at atmospheric and reduced pressures, *J. Appl. Phys.* **81**, 211–219 (1997).
30. M. D. Seta, G. Capellini, F. Evangelisti, and C. Spinella, Intermixing-promoted scaling of Ge/Si(100) island sizes, *J. Appl. Phys.* **92**, 614–619 (2002).
31. W. T. Huang, N. Deng, P. Y. Chen, G. L. Luo, and P. X. Qian, Self-organized growth of Ge quantum dots by UHV-CVD, *Microelectron. Technol.* **41**, 17–22 (2004).
32. S. W. Lee, L. J. Chen, P. S. Chen, M.-J. Tsai, C. W. Liu, T. Y. Chien, and C. T. Chia, Self-assembled nanorings in Si-capped Ge quantum dots on (001) Si, *Appl. Phys. Lett.* **83**, 5283–5285 (2003).
33. A. Rastelli, M. Kummer, and H. V. Känel, Reversible shape evolution of Ge islands on Si(001), *Phys. Rev. Lett.* **87**, 256,101–256,101 (2001).
34. A. Vailionis, B. Cho, G. Glass, P. Desjardins, D. G. Cahill, and J. E. Greene, Pathway for the strain-driven two-dimensional to three-dimensional transition during growth of Ge on Si(001), *Phys. Rev. Lett.* **85**, 3672–3675 (2000).
35. A. Rastelli, H. V. Känel, B. J. Spencer, and J. Tersoff, Prepyramid-to-pyramid transition of SiGe islands on Si(001), *Phys. Rev. B* **68**, 115,301 (2003).
36. U. Denker, M. W. Dashiell, N. Y. Jin-Phillipp, and O. G. Schmidt, Trenches around and between self assembled silicon/germanium islands grown on silicon substrates investigated by atomic force microscopy, *Mater. Sci. Eng. B* **89**, 166–170 (2002).
37. S. A. Chaparro, Y. Zhang, J. Drucker, D. Chandrasekhar, and D. J. Smith, Evolution of Ge/Si(100) islands: Island size and temperature dependence, *J. Appl. Phys.* **87**, 245–248 (2000).
38. U. Denker, O. G. Schmidt, N.-Y. Jin-Phillipp, and K. Eberl, Trench formation around and between self-assembled Ge islands on Si, *Appl. Phys. Lett.* **78**, 3723–3725 (2001).
39. A. Hesse, J. Stangl, V. Holý, T. Roch, G. Bauer, O. G. Schmidt, U. Denker, and B. Struth, Effect of overgrowth on shape, composition and strain of SiGe islands on Si(001), *Phys. Rev. B* **66**, 085321 (2002).
40. J.-M. Baribeau, R. Pascual, and S. Saimoto, X-ray study of interdiffusion and strain relaxation in  $\text{Si}_m\text{Ge}_n$  superlattices, *Appl. Phys. Lett.* **57**, 1502–1504 (1990).
41. X. Z. Liao, J. Zou, D. J. H. Cockayne, J. Qin, Z. M. Jiang, X. Wang, and R. Leon, Strain relaxation by alloying effects in Ge islands grown on Si(001), *Phys. Rev. B* **60**, 15,605–15,608 (1999).
42. P. Sonnet and P. C. Kelires, Physical origin of trench formation in Ge/Si(100) islands, *Appl. Phys. Lett.* **85**, 203–205 (2004).

43. G. Medeiros-Ribeiro, M. Bratkovski, T. I. Kamins, D. A. A. Ohlberg, and R. S. Williams, Shape transition of germanium nanocrystals on silicon (001) surface from pyramids to domes, *Sci. Technol. Adv. Mater.* **279**, 353–355 (1998).
44. F. M. Ross, R. M. Tromp, and M. C. Reuter, Transition states between pyramids and domes during Ge/Si island growth, *Sci. Technol. Adv. Mater.* **286**, 1931–1934 (1999).
45. V. B. Shenoy and L. B. Freund, A continuum description of the energetics and evolution of stepped surfaces in strained nanostructures, *J. Mech. Phys. Solids* **50**, 1817–1841 (2002).
46. I. Berbezier, A. Ronda, F. Volpi, and A. Portavoce, Morphological evolution of SiGe layers, *Surf. Sci.* **531**, 231–243 (2003).
47. Y. Zhang and J. Drucker, Annealing-induced Ge/Si(100) island evolution, *J. Appl. Phys.* **93**, 9583–9590 (2003).
48. R. Kern, G. Le Lay, and J. J. Metois, Basic mechanisms in the early stages of epitaxy, in: *Current Topics in Materials Science*, edited by E. Kaldis, North-Holland, Amsterdam, 1979, Vol. 3.
49. G. Capellini, M. De Seta, and F. Evangelisti, Influence of the growth parameters on self-assembled Ge islands on Si(100), *Mater. Sci. Eng. B* **89**, 184–187 (2002).
50. G. Capellini, M. D. Seta, and F. Evangelisti, Ge/Si(100) islands: Growth dynamics versus growth rate, *J. Appl. Phys.* **93**, 291–295 (2003).
51. Rastelli, E. Müller, and H. V. Känel, Shape preservation of Ge/Si(001) islands during Si capping, *Appl. Phys. Lett.* **80**, 1438–1440 (2002).
52. T. I. Kamins, G. Medeiros-Ribeiro, D. A. A. Ohlberg, and R. S. Williams, Evolution of Ge islands on Si(001) during annealing, *J. Appl. Phys.* **85**, 1159–1171 (1999).
53. U. Denker, O. G. Schmidt, N.-Y. Jin-Philipp, and K. Eberl, Trench formation around and between self-assembled Ge islands on Si, *Appl. Phys. Lett.* **78**, 3723–3725 (2001).
54. J. Stangl, A. Daniel, V. Holý, T. Roch, G. Bauer, I. Kegel, T. H. Metzger, T. Wiebach, O. G. Schmidt, and K. Eberl, Strain and composition distribution in uncapped SiGe islands from x-ray diffraction, *Appl. Phys. Lett.* **79**, 1474–1476 (2001).
55. T. U. Schüllli, J. Stangl, Z. Zhong, R. T. Lechner, M. Sztucki, T. H. Metzger, and G. Bauer, Direct determination of strain and composition profiles in SiGe islands by anomalous x-ray diffraction at high momentum transfer, *Phys. Rev. Lett.* **90**, 066105 (2003).
56. J. Stangl, A. Hesse, V. Holý, Z. Zhong, G. Bauer, U. Denker, and O. G. Schmidt, Effect of overgrowth temperature on shape, strain, and composition of buried Ge islands deduced from x-ray diffraction, *Appl. Phys. Lett.* **82**, 2251–2253 (2003).
57. O. Kirfel, E. Müller, D. Grützmacher, K. Kern, A. Hesse, J. Stangl, V. Holý, and G. Bauer, Shape and composition change of Ge dots due to Si capping, *Appl. Surf. Sci.* **224**, 139–142 (2004).
58. A. A. Darhuber, V. Holý, P. Schittenhelm, J. Strangl, I. Kegel, Z. Kovats, T. H. Metzger, G. Bauer, G. Abstreiter, and G. Grubel, Structural characterization of self-assembled Ge dot multilayers by x-ray diffraction and reflectivity methods, *Physica E* **2**, 789–793 (1998).
59. R. Magalhaes-Paniago, G. Medeiros-Ribeiro, A. Malachias, S. Kycia, T. I. Kamins, and R. S. Williams, Direct evaluation of composition profile, strain relaxation, and elastic energy of Ge:Si(001) self-assembled islands by anomalous x-ray scattering, *Phys. Rev. B* **66**, 245,311 (2002).
60. F. Boscherini, X-ray absorption studies of atomic environments in semiconductor nanostructures, *Nucl. Instrum. Methods B* **199**, 169–173 (2003).

61. F. Boscherini, G. Capellin, L. D. Gaspare, F. Rosei, N. Motta, and S. Mobilio, Ge-Si intermixing in Ge quantum dots on Si(001) and Si(111), *Appl. Phys. Lett.* **76**, 682–684 (2000).
62. C. J. Huang, D. Z. Li, Z. Yu, B. W. Cheng, J. Z. Yu, and Q. M. Wang, Atomic-force-microscopy investigation of the formation and evolution of Ge islands on  $\text{Si}_{1-x}\text{Ge}_x$  strained layers, *Appl. Phys. Lett.* **77**, 391–393 (2000).
63. C. P. Liu, J. M. Gibson, D. G. Cahill, T. I. Kamins, D. P. Basile, and R. S. Williams, Strain evolution in coherent Ge/Si islands, *Phys. Rev. Lett.* **84**, 1958–1961 (2000).
64. M. Cazayous, J. Groenen, F. Demangeot, R. Sirvin, M. Caumont, T. Remmele, M. Albrecht, S. Christiansen, M. Becker, H. P. Strunk, and H. Wawra, Strain and composition in self-assembled SiGe islands by raman spectroscopy, *J. Appl. Phys.* **91**, 6772–6774 (2002).
65. V. O. Yukhymchuk, A. M. Yaremko, M. Y. Valakh, A. V. Novikov, E. V. Mozdor, P. M. Lytvyn, Z. F. Krasilnik, V. P. Klad'ko, V. M. Dzhanan, N. Mestres, and J. Pascual, Theoretical and experimental investigations of single- and multilayer structures with SiGe nanoislands, *Mater. Sci. Eng. C* **23**, 1027–1031 (2003).
66. V. Magidson, D. V. Regelman, R. Beserman, and K. Dettmer, Evidence of Si presence in self-assembled Ge islands deposited on a Si(001) substrate, *Appl. Phys. Lett.* **73**, 1044–1046 (1998).
67. M. Floyd, Y. Zhang, K. P. Driver, J. Drucker, P. A. Crozier, and D. J. Smith, Nanometer-scale composition measurements of Ge/Si islands, *Appl. Phys. Lett.* **82**, 1473–1475 (2003).
68. U. Denker, M. Stoffel, and O. G. Schmidt, Probing the lateral composition profile of self-assembled islands, *Phys. Rev. Lett.* **90**, 196,102 (2003).
69. U. Denker, H. Sigg, and O. G. Schmidt, Composition of self assembled Ge hut clusters, *Mater. Sci. Eng. B* **101**, 89–94 (2003).
70. C. J. Huang, Y. H. Zuo, D. Z. Li, B. W. Cheng, L. P. Luo, J. Z. Yu, and Q. M. Wang, Shape evolution of Ge/Si(001) islands induced by strain-driven alloying, *Appl. Phys. Lett.* **78**, 3881–3883 (2001).
71. Y. Zhang, M. Floyd, K. P. Driver, J. Drucker, P. A. Crozier, and D. J. Smith, Evolution of Ge/Si(100) island morphology at high temperature, *Appl. Phys. Lett.* **80**, 3623–3625 (2002).
72. S. A. Chaparro, J. Drucker, Y. Zhang, D. Chandrasekhar, M. R. McCartney, and D. J. Smith, Strain-driven alloying in Ge/Si(100) coherent islands, *Phys. Rev. Lett.* **83**, 1199–1202 (1999).
73. S. K. Sinha, E. B. Sirote, S. Garoff, and H. B. Stanley, X-ray and neutron scattering from rough surfaces, *Phys. Rev. B* **38**, 2297–2311 (1988).
74. V. Holý, U. Pietsch, and T. Baumbach, *High Resolution X-Ray Scattering from Thin Films and Multilayers*, Springer-Verlag, Berlin, 1999.
75. I. Kegel, H. Metzger, A. Lorke, J. Peisl, A. Stangl, G. Bauer, and K. Nordlund, Determination of strain fields and composition of self-organized quantum dots using x-ray diffraction, *Phys. Rev. B* **63**, 035318 (2001).
76. A. Malachias, S. Kycia, G. Medeiros-Ribeiro, R. Magalhaes-Paniago, T. I. Kamins, and R. S. Williams, 3D composition of epitaxial nanocrystals by anomalous x-ray diffraction: Observation of a Si-rich core in Ge domes on Si(100), *Phys. Rev. Lett.* **91**, 176,101–17,6104 (2003).
77. I. Kegel, H. Metzger, A. Lorke, J. Peisl, A. Stangl, G. Bauer, J. M. Garcia, and P. M. Petroff, Nanometer-scale resolution of strain and interdiffusion in self-assembled InAs/GaAs quantum dots, *Phys. Rev. Lett.* **85**, 1694–1697 (2000).



78. O. G. Schmidt, U. Denker, S. Christiansen, and F. Ernst, Composition of self-assembled Ge/Si islands in single and multiple layers, *Appl. Phys. Lett.* **81**, 2614–2616 (2002).
79. O. G. Schmidt and K. Eberl, Multiple layers of self-assembled Ge/Si islands: Photoluminescence, strain fields, material interdiffusion, and island formation, *Phys. Rev. B* **61**, 13,721–13,729 (2000).
80. Y. Chen and J. Washburn, Structural transition in large-lattice-mismatch heteroepitaxy, *Phys. Rev. Lett.* **77**, 4046–4049 (1996).
81. T. Ide, A. Sakai, and K. Shimizu, Nanometer-scale imaging of strain in Ge island on Si(001) surface, *Thin Solid Films* **357**, 22–25 (1999).
82. P. Raiteri, L. Miglio, F. Valentinotti, and M. Celino, Strain maps at the atomic scale below Ge pyramids and domes on a Si substrate, *Appl. Phys. Lett.* **80**, 3736–3738 (2002).
83. H. Gao, Some general properties of stress-driven surface evolution in a heteroepitaxial thin film structure, *J. Mech. Phys. Solids* **42**, 741–772 (1994).
84. K.-N. Tu, J. W. Mayer, and L. C. Feldman, *Electronic Thin Film Science for Electrical Engineers and Materials Scientists. Appendix E*, Macmillan, New York, 1992.
85. A. Ponchet, A. Rocher, J.-Y. Emery, C. Starck, and L. Goldstein, Lateral modulations in zero-net-strained GaInAsP multilayers grown by gas source molecular-beam epitaxy, *J. Appl. Phys.* **74**, 3778–3782 (1993).
86. T. Marschner, S. Lutgen, M. Volk, W. Stolz, E. O. Göbel, N. Y. Jin-Phillipp, and F. Phillipp, Strain-induced changes in epitaxial layer morphology of highly-strained III/V semiconductor heterostructures, *Superlattices Microstruct.* **15**, 183–186 (1994).
87. T. Walther, C. J. Humphreys, A. G. Cullis, and D. J. Robbins, A correlation between compositional fluctuations and surfaces undulations in strained layer epitaxy, in: *Proceedings of the 18<sup>th</sup> International Conference on Defects in Semiconductors*, Trans Tech Publications, Sendai, Japan, 1995, Vol. 196–201, pp. 505–510.
88. T. Spila, P. Desjardins, A. Vaionis, H. Kim, N. Taylor, D. G. Cahill, J. E. Greene, S. Guillon, and R. A. Masut, Hydrogen-mediated quenching of strain-induced surface roughening during gas-source molecular beam epitaxy of fully-coherent Si<sub>0.7</sub>Ge<sub>0.3</sub> layers on Si(001), *J. Appl. Phys.* **91**, 3579–3588 (2002).
89. A. G. Cullis, D. J. Robbins, S. J. Barnett, and A. J. Pidduck, Growth ripples upon strained SiGe epitaxial layers on Si and misfit dislocation interactions, *J. Vac. Sci. Technol. A* **12**, 1924–1931 (1994).
90. J. Tersoff, Y. H. Phang, Z. Zhang, and M. G. Lagally, Step-bunching instability of vicinal substrates under stress, *Phys. Rev. Lett.* **75**, 2730–2733 (1995).
91. D. E. Jesson, S. J. Pennycook, J.-M. Baribeau, and D. C. Houghton, Direct imaging of surface cusp evolution during strain-layer epitaxy and implications for strained relaxation, *Phys. Rev. Lett.* **71**, 1744–1747 (1993).
92. E. Sutter, P. Sutter, and L. Vescan, Organization of self-assembled quantum dots in SiGe/Si multilayers: Effect of strain and substrate curvature, *Mater. Sci. Eng. B* **89**, 196–200 (2002).
93. E. Mateeva, P. Sutter, and M. G. Lagally, Spontaneous self-embedding of three-dimensional SiGe islands, *Appl. Phys. Lett.* **74**, 567–569 (1999).
94. V. Le Thanh and V. Yam, Superlattices of self-assembled Ge/Si(001) quantum dots, *Appl. Surf. Sci.* **212–213**, 296–304 (2003).
95. E. Mateeva, P. Sutter, J. C. Bean, and M. G. Lagally, Mechanism of organization of three-dimensional islands in SiGe/Si multilayers, *Appl. Phys. Lett.* **71**, 3233–3235 (1997).

96. B. Teichert, M. G. Lagally, L. J. Peticolas, J. C. Bean, and J. Tersoff, Stress-induced self-organization of nanoscale structures in SiGe/Si multilayer films, *Phys. Rev. B* **53**, 16,334–16,337 (1996).
97. J.-M. Baribeau, A. Del  ge, S. Janz, H. Lafontaine, D. J. Lockwood, J. P. McCaffrey, S. Moisa, N. L. Rowell, and D.-X. Xu, Wavy SiGe/Si superlattices: Structural and optical properties and application to near infrared light detection, in: *Advanced Luminescent Materials and Quantum Confinement*, edited by M. Cahay, S. Bandyopadhyay, D. J. Lockwood, J.P. Leburton, N. Koshida, M. Meyyappan, and T. Sakamoto, The Electrochemical Society, Pennington, NJ (USA), 1999, Vol. PV 99-22, pp. 45–61.
98. J.-M. Baribeau, D. J. Lockwood, M. W. C. Dharma-wardana, N. L. Rowell, and J. P. McCaffrey, Growth and characterization of Si-Ge atomic layer superlattices, *Thin Solid Films* **183**, 17–24 (1989).
99. J.-M. Baribeau, T. E. Jackman, D. C. Houghton, P. Maign  , and M. W. Denhoff, Growth and characterization of Si/Ge<sub>x</sub>Si<sub>1-x</sub> and Ge epilayers on (100) Si, *J. Appl. Phys.* **63**, 5738–5740 (1988).
100. H. Lafontaine, D. C. Houghton, B. Bahierathan, D. D. Perovic, and J.-M. Baribeau, Si<sub>1-x</sub>Ge<sub>x</sub> critical thickness for surface wave generation during UHV-CVD growth at 525 degrees C, in: *Evolution of Epitaxial Structure and Morphology*, edited by A. Zangwill, D. Jesson, D. Chambliss, and R. Clarke, Material Research Society, Philadelphia, 1996, Vol. 399, pp. 413–418.
101. H. Lafontaine, D. C. Houghton, D. Elliott, N. L. Rowell, J.-M. Baribeau, S. Laframboise, G. I. Sproule, and S. J. Rolfe, Characterization of Si<sub>1-x</sub>Ge<sub>x</sub> epi-layers grown using a commercially available UHV-CVD reactor, *J. Vac. Sci. Technol. B* **14**, 1675–1681 (1996).
102. H. K. Shin, D. J. Lockwood, and J.-M. Baribeau, Strain in coherent-wave SiGe/Si superlattices, *Solid State Commun.* **114**, 505–510 (2000).
103. O. G. Schmidt, N. Y. Jin-Phillipp, C. Lange, U. Denker, K. Eberl, R. Schreiner, H. Grabelding, and H. Schweizer, Long-range ordered lines of self-assembled Ge islands on a flat Si(001) surface, *Appl. Phys. Lett.* **77**, 4139–4141 (2000).
104. J. Stangl, T. Roch, G. Bauer, I. Kegel, T. H. Metzger, O. G. Schmidt, K. Eberl, O. Kienzle, and F. Ernst, Vertical correlation of SiGe islands in SiGe/Si superlattices: X-ray diffraction versus transmission electron microscopy, *Appl. Phys. Lett.* **77**, 3953–3955 (2000).
105. J. Tersoff, C. Teichert, and M. G. Lagally, Self-organization in growth of quantum dot superlattices, *Phys. Rev. Lett.* **76**, 1675–1678 (1996).
106. J.-M. Baribeau, Interface morphology and relaxation in high temperature grown Si<sub>1-x</sub>Ge<sub>x</sub>/Si superlattices, *J. Cryst. Growth* **157**, 52–56 (1995).
107. J.-M. Baribeau, X-ray double-crystal characterization of molecular beam epitaxially grown Si/Si<sub>1-x</sub>Ge<sub>x</sub> strained-layer superlattices, *Appl. Phys. Lett.* **52**, 105–107 (1988).
108. J.-M. Baribeau, D. J. Lockwood, and R. W. G. Syme, Interfaces in Si/Ge atomic layer superlattices on (001) Si: Effect of growth temperature and wafer misorientation, *J. Appl. Phys.* **80**, 1450–1459 (1996).
109. J.-M. Baribeau, X-ray scattering analysis of interface roughness and diffusion, *J. Vac. Sci. Technol. B* **16**, 1568–1574 (1998).
110. Y. H. Phang, C. Teichert, M. G. Lagally, L. J. Peticolas, J. C. Bean, and E. Kasper, Correlated-interfacial-roughness anisotropy in Si<sub>1-x</sub>Ge<sub>x</sub>/Si superlattices, *Phys. Rev. B* **50**, 14,435–14,445 (1994).
111. S. Fukatsu, H. Sunamura, Y. Shiraki, and S. Komiyama, Phononless radiative recombination of indirect excitons in a Si/Ge type-II quantum dot, *Appl. Phys. Lett.* **71**, 258–260 (1997).

112. I. Kegel, H. Metzger, J. Peisl, J. Stangl, G. Bauer, and D. Smilgies, Vertical alignment of multilayers quantum dots studied by x-ray grazing-incidence diffraction, *Phys. Rev. B* **60**, 2516–2521 (1999).
113. W. Hayes and R. Loudon, *Light Scattering in Solids*, Wiley, New York, 1978.
114. J. Menéndez, Characterization of bulk semiconductors using Raman spectroscopy, in: *Raman Scattering in Materials Science*, edited by W. H. Weber and R. Merlin, Springer-Verlag, Berlin, 2000, pp. 55–103.
115. Z. R. Wasilewski, M. M. Dion, D. J. Lockwood, P. Poole, R. W. Streater, and A. J. SpringThorpe, Composition of AlGaAs, *J. Appl. Phys.* **81**, 1883–1694 (1997).
116. D. J. Lockwood, R. Radomski, and Z. R. Wasilewski, Raman study of phonons in Ga<sub>1-x</sub>Al<sub>x</sub>As, *J. Raman Spectrosc.* **33**, 202–206 (2002).
117. T. Ruf, *Phonon Raman Scattering in Semiconductors, Quantum Wells and Superlattices*, Springer-Verlag, Berlin, 1998.
118. D. J. Lockwood, H. X. Xu, and J.-M. Baribeau, Lattice vibrations of Si<sub>1-x</sub>C<sub>x</sub> epilayers on Si(100), *Phys. Rev. B* **68**, 115,308 (2003).
119. D. J. Lockwood and J.-M. Baribeau, Strain shift coefficients for phonons in Si<sub>1-x</sub>Ge<sub>x</sub> epilayers, *Phys. Rev. B* **45**, 8565–8571 (1992).
120. J.-M. Baribeau and D. J. Lockwood, Strain shift coefficients for phonons in Si-Ge heterostructures, in: *Thin Films, Stresses and Mechanical Properties III*, edited by W. D. Nix, J. C. Bravman, E. Artz, and L. B. Freund, Materials Research Society, Boston, 1992, Vol. 239, pp. 449–454.
121. M. A. Renucci, J. B. Renucci, and M. Cardona, in: *Light Scattering in Solids*, edited by M. Balkanski, Flammarion, Paris, 1971, pp. 326–329.
122. W. J. Brya, Raman scattering in GeSi alloys, *Solid State Commun.* **12**, 253–257 (1973).
123. T. Ishidate, S. Katagiri, K. Inoue, M. Shibuya, K. Tsuji, and S. Minomura, Lattice vibrational properties of crystalline Si-Ge alloys, *J. Phys. Soc. Jpn.* **53**, 2584–2591 (1984).
124. M. I. Alonso and K. Winer, Raman spectra of C-Si<sub>1-x</sub>Ge<sub>x</sub> alloys, *Phys. Rev. B* **39**, 10,056–10,062 (1989).
125. Y. S. Tang, C. M. Sotomayer Torres, B. Dietrich, W. Kessinger, T. E. Whall, and E. H. C. Parker, Raman spectroscopy of dry etched Si-Si<sub>1-x</sub>Ge<sub>x</sub> quantum dots, *Solid State Commun.* **94**, 369–372 (1995).
126. A. B. Talochkin, V. A. Markov, S. P. Suprun, and A. I. Nikiforov, Raman scattering of light by optical phonons in Si-Ge-Si structures with quantum dots, *JETP Lett.* **64**, 219–224 (1996).
127. X. Wang, Z.-M. Jiang, H. J. Zhu, D. Huang, X. Liu, C. W. Hu, Y. Chen, Z. Zhu, and T. Yao, Germanium dots with high uniform size distribution grown on Si(100) substrate by molecular beam epitaxy, *Appl. Phys. Lett.* **71**, 3543–3545 (1997).
128. A. A. Darhuber, T. Grill, A. Stangl, G. Bauer, D. J. Lockwood, J.-P. Noël, P. D. Wang, and C. M. Sotomayer Torres, Elastic relaxation of dry-etched Si/SiGe quantum dots, *Phys. Rev. B* **58**, 4825–4831 (1998).
129. S. H. Kwok, P. Y. Yu, C. H. Tung, Y. H. Zhang, M. F. Li, C. S. Peng, and J. M. Zhou, Confinement and electron–phonon interactions of the e<sub>1</sub> exciton in self-organized Ge quantum dots, *Phys. Rev. B* **59**, 4980–4984 (1999).
130. J. L. Liu, Y. S. Tang, K. L. Wang, T. Radetic, and R. Gronsky, Raman scattering from a self-organized Ge dot superlattice, *Appl. Phys. Lett.* **74**, 1863–1865 (1999).
131. A. B. Talochkin, V. A. Markov, A. I. Nikiforov, and S. A. Tiis, Optical phonon spectrum of germanium quantum dots, *JETP Lett.* **70**, 288–293 (1999).
132. J. H. Zhu, C. Meisner, K. Brunner, and G. Abstreiter, Strain relaxation of faceted Ge islands on Si (113), *Appl. Phys. Lett.* **75**, 2395–2397 (1999).

133. A. V. Kolobov and K. Tanaka, Comment on "Raman scattering from a self-organized Ge dot superlattice" [*Appl. Phys. Lett.* **74**, 1863 (1999)], *Appl. Phys. Lett.* **75**, 3572–3573 (1999).
134. J. L. Liu, G. Jin, Y. S. Tang, Y. H. Luo, K. L. Wang, and D. P. Yu, Optical and acoustic phonon modes in self-organized Ge quantum dot superlattices, *Appl. Phys. Lett.* **76**, 586–588 (2000).
135. A. V. Kolobov, Raman scattering from ge nanostructures grown on Si substrates: Power and limitations, *J. Appl. Phys.* **87**, 2926–2930 (2000).
136. J. L. Liu, G. Jin, Y. S. Tang, Y. H. Luo, K. L. Wang, and D. P. Yu, Study of phonons in self-organized multiple Ge quantum dots, *J. Electron. Mater.* **29**, 554–556 (2000).
137. A. Milekhin, N. P. Stepina, A. I. Yakimov, S. Schulze, and D. R. T. Zahn, Raman scattering of ge dot superlattices, *Eur. Phys. J. B* **16**, 355–359 (2000).
138. P. Y. Yu, Comment on "Optical and acoustic phonon modes in self-organized Ge quantum dot superlattices" [*Appl. Phys. Lett.* **76**, 586 (2000)], *Appl. Phys. Lett.* **78**, 1160–1161 (2001).
139. C. Guedj, A. Beyer, E. Müller, and D. Grützmacher, Raman spectroscopy of carbon-induced germanium dots, *Appl. Phys. Lett.* **78**, 1742–1744 (2001).
140. A. Milekhin, N. P. Stepina, A. I. Yakimov, A. I. Nikiforov, S. Schulze, and D. R. T. Zahn, Raman scattering study of Ge dot superlattices, *Appl. Surf. Sci.* **175–176**, 629–635 (2001).
141. M. Cazayous, J. Groenen, J. R. Huntzinger, A. Mlayah, and O. G. Schmidt, Spatial correlations and Raman scattering interferences in self-assembled quantum dot multilayers, *Phys. Rev. B* **64**, 033306 (2001).
142. A. G. Milekhin, A. I. Nikiforov, O. P. Pchelyakov, S. Schulze, and D. R. T. Zahn, Phonons in Ge/Si superlattices with Ge quantum dots, *JETP Lett.* **73**, 461–464 (2001).
143. J. Wan, Y. H. Luo, Z. M. Jiang, G. Jin, J. L. Liu, X. Z. Liao, K. L. Wang, and J. Zou, Ge/Si interdiffusion in GeSi dots and wetting layers, *J. Appl. Phys.* **90**, 4290–4292 (2001).
144. A. G. Milekhin, A. I. Nikiforov, O. P. Pchelyakov, S. Schulze, and D. R. T. Zahn, Phonons in self-assembled Ge/Si structures, *Physica E* **13**, 982–985 (2002).
145. A. V. Kolobov, H. Oyanagi, K. Brunner, G. Abstreiter, Y. Maeda, A. A. Shklyae, S. Yamasaki, M. Ichikawa, and K. Tanaka, Effect of the interface on the local structure of Ge-Si nanostructures, *J. Vac. Sci. Technol. A* **20**, 1116–1119 (2002).
146. A. V. Kolobov, K. Morita, K. M. Itoh, and E. E. Haller, A raman scattering study of self-assembled pure isotope Ge/Si(100) quantum dots, *Appl. Phys. Lett.* **81**, 3855–3857 (2002).
147. S.-F. Ren and W. Cheng, Calculations of surface effects on phonon modes and Raman intensities of Ge quantum dots, *Phys. Rev. B* **66**, 205,328 (2002).
148. J. L. Liu, J. Wan, Z. M. Jiang, A. Khitun, K. L. Wang, and D. P. Yu, Optical phonons in self-assembled Ge quantum dot superlattices: Strain relaxation effects, *J. Appl. Phys.* **92**, 6804–6808 (2002).
149. Y. Darma, H. Murakami, and S. Miyazaki, Formation of nanometer silicon dots with germanium core by highly-selective pressure chemical vapor deposition, *Jpn. J. Appl. Phys.* **42**, 4129–4133 (2003).
150. P. H. Tan, K. Brunner, D. Bougeard, and G. Abstreiter, Raman characterization of strain and composition in small self-assembled Si/Ge dots, *Phys. Rev. B* **68**, 125,302 (2003).

151. B. V. Kamenev, H. Grebel, L. Tsybeskov, T. I. Kamins, R. S. Williams, J. M. Baribeau, and D. J. Lockwood, Polarized Raman scattering and localized embedded strain in self-organized Si/Ge nanostructures, *Appl. Phys. Lett.* **83**, 5035–5037 (2003).
152. B. V. Kamenev, L. Tsybeskov, J.-M. Baribeau, and D. J. Lockwood, Photoluminescence and Raman scattering in three-dimensional Si/Si<sub>1-x</sub>Ge<sub>x</sub> nanostructures, *Appl. Phys. Lett.* **84**, 1293–1295 (2004).
153. Z. Yang, Y. Shi, B. Yan, Z. X. Huang, L. Pu, Y. D. Zheng, and K. L. Wang, Strain and phonon confinement in self-assembled Ge quantum dot superlattices, *Chin. Phys. Lett.* **20**, 2001–2003 (2003).
154. M. W. C. Dharma-wardana, G. C. Aers, D. J. Lockwood, and J.-M. Baribeau, Interpretation of raman spectra of GeSi ultrathin superlattices, *Phys. Rev. B* **41**, 5319–5331 (1990).
155. J. P. Dismukes, L. Ekstrom, and R. J. Paff, Lattice parameter and density in germanium–silicon alloys, *J. Phys. Chem.* **68**, 3021–3027 (1964).
156. H. D. Fuchs, C. H. Grein, M. I. Alonso, and M. Cardona, High-resolution Raman spectroscopy of Ge-rich C-Ge<sub>1-x</sub>Si<sub>x</sub> alloys: Features of the Ge-Ge vibrational modes, *Phys. Rev. B* **44**, 13,120–13,123 (1991).
157. A. B. Talochkin and S. A. Teys, Optical phonons in Ge quantum dots obtained on Si (111), *JETP Lett.* **75**, 264–267 (2002).
158. D. J. Lockwood, J.-M. Baribeau, T. E. Jackman, P. Aebi, T. Tylliszczak, A. P. Hitchcock, and R. L. Headrick, Influence of annealing on the interface structure and strain relief in Si/Ge heterostructures on (100) Si, *Scanning Microsc.*, 457–471 (1993).
159. D. J. Lockwood, M. W. C. Dharma-wardana, J.-M. Baribeau, and D. C. Houghton, Folded acoustic phonons in Si/Ge<sub>x</sub>Si<sub>1-x</sub> strained-layer superlattices, *Phys. Rev. B* **35**, 3243–3251 (1987).
160. P. H. Tan, D. Bougeard, G. Abstreiter, and K. Brunner, Raman scattering of folded acoustic phonons in self-assembled Si/Ge dot superlattices, *Appl. Phys. Lett.* **84**, 2632–2634 (2004).
161. O. L. Lazarenkova and A. A. Balandin, Raman scattering from three-dimensionally regimented quantum dot superlattices, *Superlattices Microstruct.* **33**, 95–101 (2003).
162. L. Hoffman, J. C. Bach, B. B. Nielsen, P. Leary, R. Jones, and S. Oberg, Substitutional carbon in germanium, *Phys. Rev. B* **55**, 11,167–11,173 (1997).
163. C. Guedj, J. Kolodzey, and A. Hairie, Structure and lattice dynamics of Ge<sub>1-x</sub>C<sub>y</sub> alloys using anharmonic Keating modeling, *Phys. Rev. B* **60**, 15,150–15,153 (1999).
164. J.-P. Noël, N. L. Rowell, D. C. Houghton, and D. D. Perovic, Intense photoluminescence between 1.3 and 1.8 mm from strained Si<sub>1-x</sub>Ge<sub>x</sub> alloys, *Appl. Phys. Lett.* **57**, 1037–1039 (1990).
165. R. Apetz, L. Vescan, A. Hartmann, C. Dieker, and H. Luth, Photoluminescence and electroluminescence of SiGe dots fabricated by island growth, *Appl. Phys. Lett.* **66**, 445–447 (1995).
166. Y. S. Tang, C. M. S. Torres, B. Dietrich, W. Kissinger, T. E. Whall, and E. H. C. Parker, Photoluminescence and raman spectroscopy of Si/Si<sub>1-x</sub>Ge<sub>x</sub> quantum dots, *J. Cryst. Growth* **157**, 280–284 (1995).
167. Y. S. Tang, W.-X. Ni, C. M. Sotomayor Torres, and G. V. Hansson, Fabrication and characterisation of Si-Si<sub>0.7</sub>Ge<sub>0.3</sub> quantum dot light emitting diodes, *Electron. Lett.* **31**, 1385–1386 (1995).
168. Y. S. Tang, C. M. Sotomayor Torres, W. X. Ni, and G. V. Hansson, Room temperature electroluminescence of nanofabricated Si-Si<sub>1-x</sub>Ge<sub>x</sub> quantum dot diodes, *Superlattices Microstruct.* **20**, 505–511 (1996).

169. J. C. Sturm, H. Manoharan, L. C. Lenchyshyn, M. L. W. Thewalt, N. L. Rowell, J.-P. Noël, and D. C. Houghton, Well-resolved band-edge photoluminescence of excitons confined in strained  $\text{Si}_{1-x}\text{Ge}_x$  quantum wells, *Phys. Rev. Lett.* **66**, 1362–1365 (1991).
170. H. Sunamura, Y. Shiraki, and S. Fukatsu, Growth mode transition and photoluminescence properties of  $\text{Si}_{1-x}\text{Ge}_x/\text{Si}$  quantum well structures with high Ge composition, *Appl. Phys. Lett.* **66**, 953–955 (1995).
171. H. Sunamura, N. Usami, Y. Shiraki, and S. Fukatsu, Island formation during growth of Ge on Si(100): A study using photoluminescence spectroscopy, *Appl. Phys. Lett.* **66**, 3024–3026 (1995).
172. Y. S. Tang, S. E. Hicks, W. X. Ni, C. M. Sotomayor Torres, G. V. Hansson, and C. D. W. Wilkinson, Controlling the strain and light emission from  $\text{Si-Si}_{1-x}\text{Ge}_x$  quantum dots, *Thin Solid Films* **294**, 304–307 (1997).
173. O. G. Schmidt, U. Denker, K. Eberl, O. Kienzle, and F. Ernst, Effect of overgrowth temperature on the photoluminescence of Ge/Si islands, *Appl. Phys. Lett.* **77**, 2509–2511 (2000).
174. O. G. Schmidt, C. Lange, K. Eberl, O. Kienzle, and F. Ernst, Formation of carbon-induced germanium dots, *Appl. Phys. Lett.* **71**, 2340–2342 (1997).
175. K. Terashima, M. Tajima, and T. Tatsumi, Near-band-gap photoluminescence of  $\text{Si}_{1-x}\text{Ge}_x$  alloys grown on Si(100) by molecular beam epitaxy, *Appl. Phys. Lett.* **57**, 1925–1927 (1990).
176. D. V. Lang, R. People, J. C. Bean, and A. M. Sergent, Measurement of the band gap of  $\text{Ge}_x\text{Si}_{1-x}/\text{Si}$  strained-layer heterostructures, *Appl. Phys. Lett.* **47**, 1333–1335 (1985).
177. X. Xiao, C. W. Liu, J. C. Sturm, L. C. Lenchyshyn, M. L. W. Thewalt, R. B. Gregory, and P. Fejes, Quantum confinement effects in strained silicon-germanium alloy quantum wells, *Appl. Phys. Lett.* **60**, 2135–2137 (1992).
178. D. J. Robbins, L. T. Canham, S. J. Barnett, A. D. Pitt, and P. Calcott, Near-band-gap photoluminescence from pseudomorphic  $\text{Si}_{1-x}\text{Ge}_x$  single layers on Silicon, *J. Appl. Phys.* **71**, 1407–1414 (1992).
179. D. Dutartre, G. Brémond, A. Souifi, and T. Benyattou, Excitonic photoluminescence from Si-capped strained  $\text{Si}_{1-x}\text{Ge}_x$  layers, *Phys. Rev. B* **44**, 11,525–11,527 (1991).
180. N. L. Rowell, J.-P. Noël, D. C. Houghton, A. Wang, L. C. Lenchyshyn, M. L. W. Thewalt, and D. D. Perovic, Exciton luminescence in  $\text{Si}_{1-x}\text{Ge}_x/\text{Si}$  heterostructures grown by molecular beam epitaxy, *J. Appl. Phys.* **74**, 2790–2805 (1993).
181. S. Fukatsu, H. Sunamura, Y. Shiraki, and S. Komiyama, Suppression of phonon replica in the radiative recombination of an MBE-grown type-II Ge/Si quantum dot, *Thin Solid Films* **321**, 65–69 (1998).
182. P. Boucaud, V. L. Thanh, S. Sauvage, D. Debarre, D. Bouchier, and J.-M. Lourtioz, Photoluminescence of self-assembled Ge dots grown by ultra-high-vacuum chemical vapor deposition, *Thin Solid Films* **336**, 240–243 (1998).
183. M. Goryll, L. Vescan, and H. Luth, Morphology and photoluminescence of Ge islands grown on Si(001), *Thin Solid Films* **336**, 244–247 (1998).
184. O. G. Schmidt, C. Lange, and K. Eberl, Photoluminescence study of the 2D–3D growth mode changeover for different Ge/Si island phases, *Phys. Stat. Solidi (b)* **215**, 319–324 (1999).
185. O. G. Schmidt, C. Lange, and K. Eberl, Photoluminescence study of the initial stages of island formation for Ge pyramids/domes and hut clusters on Si(001), *Appl. Phys. Lett.* **75**, 1905–1907 (1999).
186. A. Beyer, E. Müller, H. Sigg, S. Stutz, D. Grützmacher, O. Leifeld, and K. Ensslin, Size control of carbon-induced Ge quantum dots, *Appl. Phys. Lett.* **77**, 3218–3220 (2000).

187. O. G. Schmidt, K. Eberl, and Y. Rau, Strain and band-edge alignment in single and multiple layers of self-assembled Ge/Si and GeSi/Si islands, *Phys. Rev. B* **62**, 16,715–16,720 (2000).
188. N. Usami and Y. Shiraki, Optical investigation of modified Stranski-Krastanov growth mode in the stacking of self-assembled Ge islands, *Thin Solid Films* **369**, 108–111 (2000).
189. F. Gao, C. J. Huang, D. D. Huang, J. P. Li, D. Z. Sun, M. Y. Kong, Y. P. Zeng, J. M. Li, and L. Y. Lin, Changing the size and shape of Ge island by chemical etching, *J. Cryst. Growth* **231**, 17–21 (2001).
190. L. Vescan, Ge nanostructures grown by self-assembly; influence of substrate orientation, *J. Phys.: Condens. Matter* **14**, 8235–8252 (2002).
191. G. E. Cirlin, V. G. Talalaev, N. D. Zakharov, V. A. Erorov, and P. Werner, Room temperature superlinear power dependence of photoluminescence from defect-free Si/Ge quantum dot multilayer structures, *Phys. Stat. Solidi (b)* **232** R1–R3 (2002).
192. I. Berbezier, A. Ronda, and A. Portavoce, SiGe nanostructures: New insights into growth processes, *J. Phys. C* **14**, 8283–8331 (2002).
193. L. Vescan, T. Stoica, B. Holländer, A. Nassiopoulou, A. Olzierski, I. Raptis, and E. Sutter, Self-assembling of Ge on finite Si(001) areas comparable with the island size, *Appl. Phys. Lett.* **82**, 3517–3519 (2003).
194. M. Larsson, A. Elfving, P.-O. Holtz, G. V. Hansson, and W.-X. Ni, Luminescence study of Si/Ge quantum dots, *Physica E* **16**, 476–480 (2003).
195. A. G. Makarov, N. N. Ledentsov, A. F. Tsatsal'nikov, G. E. Cirlin, V. A. Egorov, V. M. Usinov, N. D. Zakharov, and P. Werner, Optical properties of structures with ultradense arrays of Ge QD's in a Si matrix, *Semiconductors* **37**, 210–214 (2003).
196. A. V. Novikov, D. N. Lobanov, A. N. Yablonsky, Y. N. Drozdov, N. V. Vostokov, and Z. F. Krasilnik, Photoluminescence of Ge(Si)/Si(001) self-assembled islands in the near infra-red wavelength range, *Physica E* **16**, 467–472 (2003).
197. F. Volpi, A. R. Peaker, I. D. Hawkins, M. P. Halsall, P. B. Kenway, A. Portavoce, A. Ronda, and I. Berbezier, Hole trapping in self-assembled SiGe quantum nanostructures, *Mater. Sci. Eng. B* **101**, 338–344 (2003).
198. U. Denker, H. Sigg, and O. G. Schmidt, Intermixing in Ge hut cluster islands, *Appl. Surf. Sci.* **224**, 127–133 (2004).
199. L. H. Nguyen, V. LeThanh, D. Debarre, V. Yam, M. Halbwax, M. El Kurdi, D. Bouchier, P. Rosner, M. Becker, M. Benamara, and H. P. Strunk, Selective epitaxial growth of ge quantum dots on patterned SiO<sub>2</sub>/Si(001) surfaces, *Appl. Surf. Sci.* **224**, 134–138 (2004).
200. V. Yam, V. Le Thanh, D. Debarre, Y. Zheng, and D. Bouchier, Kinetics of Si capping process of Ge/Si(001) quantum dots, *Appl. Surf. Sci.* **224**, 143–147 (2004).
201. W.-Y. Chen, W.-H. Chang, A.-T. Chou, T.-M. Hsu, P.-S. Chen, Z. Pei, and L.-S. Lai, Optical properties of stacked Ge/Si quantum dots with different spacer thickness grown by chemical vapor deposition, *Appl. Surf. Sci.* **224**, 148–151 (2004).
202. L. H. Nguyen, V. Le Thanh, D. Debarre, V. Yam, and D. Bouchier, Selective growth of ge quantum dots on chemically prepared SiO<sub>2</sub>/Si(001) surfaces, *Mater. Sci. Eng. B* **101**, 199–203 (2003).
203. L. H. Nguyen, T. K. Nguyen-Duc, V. Le Thanh, F. A. d'Avitaya, and J. Derrien, Growth and optical properties of Ge/Si quantum dots formed on patterned SiO<sub>2</sub>/Si(001) substrates, *Physica E* **23**, 471–475 (2004).
204. N. L. Rowell, J.-P. Noël, D. C. Houghton, and M. Buchanan, Electroluminescence and photoluminescence from Si<sub>1-x</sub>Ge<sub>x</sub> alloys, *Appl. Phys. Lett.* **58**, 957–958 (1991).

205. J.-P. Noël, N. L. Rowell, D. C. Houghton, A. Wang, and D. D. Perovic, Luminescence origins in molecular beam epitaxial  $\text{Si}_{1-x}\text{Ge}_x$ , *Appl. Phys. Lett.* **61**, 690–692 (1992).
206. U. Denker, M. Stoffel, O. G. Schmidt, and H. Sigg, Ge hut cluster luminescence below bulk Ge band gap, *Appl. Phys. Lett.* **82**, 454–456 (2003).
207. P. Boucaud, S. Sauvage, M. El Kurdi, E. Mercier, T. Brunhes, V. L. Thanh, D. Bouchier, O. Kermarrec, Y. Campidelli, and D. Bensahel, Optical recombination from excited states in Ge/Si self-assembled quantum dots, *Phys. Rev. B* **64**, 155,310–155,316 (2001).
208. B. V. Kamanev, J.-M. Baribeau, D. J. Lockwood, and L. Tsybeskov, Optical properties of Stranski-Krastanov grown three-dimensional  $\text{Si}/\text{Si}_{1-x}\text{Ge}_x$  nanostructures, *Physica E* **26**, 174–179 (2005).
209. J.-P. Noël, N. L. Rowell, D. C. Houghton, A. Wang, and D. D. Perovic, Luminescence origins in molecular beam epitaxial  $\text{Si}_{1-x}\text{Ge}_x$ , *Appl. Phys. Lett.* **61**, 690–692 (1992).
210. O. Leifeld, E. Müller, D. Grützmacher, B. Müller, and K. Kern, In situ scanning tunneling microscopy study of C-induced Ge quantum dot formation on  $\text{Si}(100)$ , *Appl. Phys. Lett.* **74**, 994–996 (1999).
211. F. Ratto, F. Rosei, A. Locatelli, S. Cherifi, S. Fontana, S. Heun, P.-D. Szkutnik, A. Sgarlata, M. D. Crescenzi, and N. Motta, Composition of Ge(Si) islands in the growth of Ge on  $\text{Si}(111)$ , *Appl. Phys. Lett.* **84**, 4526–4528 (2004).
212. A. Sgarlata, P. D. Szkutnik, A. Balzarotti, N. Motta, and F. Rosei, Self-ordering of Ge islands on step-bunched  $\text{Si}(111)$  surfaces, *Appl. Phys. Lett.* **83**, 4002–4004 (2003).
213. J.-P. Noël, N. L. Rowell, D. C. Houghton, and D. D. Perovic, Intense photoluminescence between 1.3 and 1.8  $\mu\text{m}$  from strained  $\text{Si}_{1-x}\text{Ge}_x$  alloys, *Appl. Phys. Lett.* **57**, 1037–1039 (1990).
214. L. C. Lenchyshyn, M. L. W. Thewalt, J. C. Sturm, P. V. Schwartz, E. J. Prinz, N. L. Rowell, J.-P. Noël, and D. C. Houghton, High quantum efficiency photoluminescence from localized excitons in  $\text{Si}_{1-x}\text{Ge}_x$ , *Appl. Phys. Lett.* **60**, 3174–3176 (1992).
215. P. L. Gourley and J. P. Wolfe, Thermodynamics of excitonic molecules in silicon, *Phys. Rev. B* **20**, 3319–3327 (1979).
216. K. Eberl, O. G. Schmidt, R. Duschl, O. Kienzle, E. Ernst, and Y. Rau, Self-assembling SiGe and SiGeC nanostructures for light emitters and tunneling diodes, *Thin Solid Films* **369**, 33–38 (2000).
217. K. Eberl, O. G. Schmidt, O. Kienzle, and F. Ernst, Preparation and optical properties of Ge and C-induced Ge quantum dots on Si, *Thin Solid Films* **373**, 164–169 (2000).
218. J.-P. Noël, J. E. Greene, N. L. Rowell, and D. C. Houghton, Photoluminescence studies of  $\text{Si}(100)$  doped with low-energy (100–1000 eV)  $\text{B}^+$  ions during molecular beam epitaxy, *Appl. Phys. Lett.* **56**, 265–267 (1990).
219. J.-P. Noël, J. E. Greene, N. L. Rowell, S. Kechang, and D. C. Houghton, Photoluminescence studies of  $\text{Si}(100)$  doped with low-energy ( $\leq 1000$  eV)  $\text{As}^+$  ions during molecular beam epitaxy, *Appl. Phys. Lett.* **55**, 1525–1527 (1989).
220. H. Lafontaine, N. L. Rowell, and S. Janz, Phonon-resolved photoluminescence at  $\lambda = 1.55 \mu\text{m}$  from undulating  $\text{Si}_{0.5}\text{Ge}_{0.5}$  epitaxial layers, *Appl. Phys. Lett.* **72**, 2430–2432 (1998).
221. O. Chrétien, T. Stoica, D. Dentel, E. Mateeva, and L. Vescan, Influence of the mesa size on Ge island electroluminescence properties, *Semicond. Sci. Technol.* **15**, 920–925 (2000).
222. L. Vescan, O. Chrétien, T. Stoica, E. Mateeva, and A. Muck, Room-temperature light-emitting diodes with Ge islands, *Mater. Sci. Semicond. Process.* **3**, 383–387 (2000).
223. Z. Pei, P. S. Chen, S. W. Lee, L. S. Lai, S. C. Lu, M.-J. Tsai, W. H. Chang, W. Y. Chen, A. T. Chou, and T. M. Hsu, Room temperature 1.3 and 1.5  $\mu\text{m}$  electroluminescence



- from Si/Ge quantum dots (QDs)/Si multi-layers, *Appl. Surf. Sci.* **224**, 165–169 (2004).
224. J.-P. Noël, J. E. Greene, N. L. Rowell, S. Kechang, and D. C. Houghton, Photoluminescence studies of Si(100) doped with low-energy ( $\leq 1000$  eV) As<sup>+</sup> ions during molecular beam epitaxy, *Appl. Phys. Lett.* **55**, 1525–1527 (1989).
  225. J.-P. Noël, J. E. Greene, N. L. Rowell, and D. C. Houghton, Photoluminescence studies of Si(100) doped with low-energy (100–1000 eV) B<sup>+</sup> ions during molecular beam epitaxy, *Appl. Phys. Lett.* **56**, 265–267 (1990).
  226. D. C. Houghton, Misfit dislocation dynamics in Si<sub>1-x</sub>Ge<sub>x</sub>/(100) Si: Uncapped alloy layers, buried strained layers, and multiple quantum wells, *Appl. Phys. Lett.* **57**, 1434–1436 (1990).
  227. K. Sakamoto, H. Matsuhata, M. O. Tanner, D. Wang, and K. L. Wang, Alignment of Ge three-dimensional islands on faceted Si(001) surfaces, *Thin Solid Films* **321**, 55–59 (1998).
  228. F. Liu, J. Tersoff, and M. G. Lagally, Self-organization of steps in growth of strained films on vicinal substrates, *Phys. Rev. Lett.* **80**, 1268–1271 (1998).
  229. J.-H. Zhu, K. Brunner, and G. Abstreiter, Two-dimensional ordering of self-assembled Ge islands on vicinal Si(001) surfaces with regular ripples, *Appl. Phys. Lett.* **73**, 620–622 (1998).
  230. Y. H. Xie, S. B. Samavedam, M. Bulsara, T. A. Langdo, and E. A. Fitzgerald, Relaxed template for fabricating regularly distributed quantum dot arrays, *Appl. Phys. Lett.* **71**, 3567–3568 (1997).
  231. C. Teichert, C. Hofer, K. Lyutovich, M. Bauer, and E. Kasper, Interplay of dislocation network and island arrangement in SiGe films grown on Si(001), *Thin Solid Films* **380**, 25–28 (2000).
  232. F. Leroy, J. Eymery, P. Gentile, and F. Fournel, Ordering of Ge quantum dots with buried Si dislocation networks, *Appl. Phys. Lett.* **80**, 3078–3080 (2002).
  233. S. Y. Shiryayev, E. V. Pedersen, F. Jensen, J. W. Petersen, J. L. Hansen, and A. N. Larsen, Dislocation patterning: A new tool for spatial manipulation of Ge islands, *Thin Solid Films* **294**, 311–314 (1997).
  234. B. Voigtländer and N. Theuerkauf, Ordered growth of Ge islands above a misfit dislocation network in a Ge layer on Si (111), *Surf. Sci.* **461**, L575–L580 (2000).
  235. D. D. Perovic, G. C. Weatherly, P. J. Simpson, P. J. Schultz, T. E. Jackman, G. C. Aers, J. P. Noël, and D. C. Houghton, Microvoid formation in low-temperature molecular-beam-epitaxy-grown silicon, *Phys. Rev. B* **43**, 14,257–14,260 (1991).
  236. T. E. Jackman, G. C. Aers, J. P. McCaffrey, D. Britton, P. Willtzki, P. J. Schultz, P. J. Simpson, and P. Mascher, Depth profiling of defects in low-temperature MBE-grown silicon, in: *Positron annihilation: Proceedings of the 9th International Conference on Positron Annihilation*, edited by Z. Kajcsos and C. Szeles, Trans Tech Publications Inc., Zurich, 1992, Vol. 105–110, pp. 301–308.
  237. J.-M. Baribeau, X. Wu, D. J. Lockwood, L. Tay, and G. I. Sproule, Low temperature Si growth on Si(001): Impurity incorporation and limiting thickness for epitaxy, *J. Vac. Sci. Technol. B* **22**, 1479–1483 (2004).
  238. G. Jin, J. L. Liu, S. G. Thomas, Y. H. Luo, K. L. Wang, and B.-Y. Nguyen, Controlled arrangement of self-organized Ge islands on patterned Si(001) substrates, *Appl. Phys. Lett.* **75**, 2752–2754 (1999).
  239. T. I. Kamins, D. A. A. Ohlberg, R. S. Williams, W. Zhang, and S. Y. Chou, Positioning of self-assembled, single-crystal, germanium islands by silicon nanoimprinting, *Appl. Phys. Lett.* **74**, 1773–1775 (1999).

240. G. Jin, Cooperative arrangement of self-assembled Ge dots on pre-grown Si mesas, *Thin Solid Films* **380**, 169–172 (2000).
241. G. Jin, Uniform and ordered self-assembled Ge dots on patterned Si substrates with selectively epitaxial growth technique, *J. Cryst. Growth* **227–228**, 1100–1105 (2001).
242. T. I. Kamins and R. S. Williams, Lithographic positioning of self-assembled Ge islands on Si(001), *Appl. Phys. Lett.* **71**, 1201–1203 (1997).
243. G. Jin, J. L. Liu, and K. L. Wang, Regimented placement of self-assembled Ge dots on selectively grown Si mesas, *Appl. Phys. Lett.* **76**, 3591–3593 (2000).
244. A. R. Woll, P. Rugheimer, and M. G. Lagally, Strain engineering, self-assembly, and nanoarchitectures in thin SiGe films on Si, *Mater. Sci. Eng. B* **96**, 94–101 (2002).
245. T. Kitajima, B. Liu, and S. R. Leone, Two-dimensional periodic alignment of self-assembled Ge islands on patterned Si(001) surfaces, *Appl. Phys. Lett.* **80**, 497–499 (2002).
246. K. L. Wang, Self-assembled Ge quantum dots on Si and their applications, *J. Cryst. Growth* **237–239**, 1892–1897 (2002).
247. Z. Zhong, A. Halilovic, M. Mühlberger, F. Schäffler, and G. Bauer, Positioning of self-assembled Ge islands on stripe-patterned Si(001) substrates, *J. Appl. Phys.* **93**, 6258–6264 (2003).
248. Z. Zhong, A. Halilovic, M. Mühlberger, F. Schäffler, and G. Bauer, Ge island formation on stripe-patterned Si(001) substrates, *Appl. Phys. Lett.* **82**, 445–447 (2003).
249. N. Deng, P. Chen, and Z. Li, Self-assembled SiGe islands with uniform shape and size by controlling Si concentration in islands, *J. Cryst. Growth* **263**, 21–24 (2004).
250. Z. Zhong, A. Halilovic, T. Fromherz, F. Schäffler, and G. Bauer, Two-dimensional periodic positioning of self-assembled Ge islands on prepatterned Si(001) substrates, *Appl. Phys. Lett.* **82**, 4779–4781 (2003).
251. Z. Zhong, A. Halilovic, M. Mühlberger, F. Schäffler, and G. Bauer, Positioning of self-assembled Ge islands on stripe-patterned Si(001) substrates, *J. Appl. Phys.* **93**, 6258–6264 (2003).
252. Z. Zhong, G. Chen, J. Stangl, T. Fromherz, F. Schäffler, and G. Bauer, Two-dimensional lateral ordering of self-assembled Ge islands on patterned substrates, *Physica E* **21**, 315–320 (2004).
253. Z. Zhong, A. Halilovic, H. Lichtenberger, F. Schäffler, and G. Bauer, Growth of Ge islands on prepatterned Si(001) substrates, *Physica E* **23**, 243–247 (2004).
254. J.-M. Baribeau, D. J. Lockwood, J. Balle, S. J. Rolfe, and G. I. Sproule,  $\text{Si}_{1-x-y}\text{Ge}_x\text{C}_y$  alloy growth by electron cyclotron resonance plasma-assisted Si molecular beam epitaxy, *Mater. Sci. Eng. B* **89**, 296–302 (2002).
255. J.-M. Baribeau, D. J. Lockwood, J. Balle, S. J. Rolfe, G. I. Sproule, and S. Moisa, Molecular beam epitaxy synthesis of  $\text{Si}_{1-y}\text{C}_y$  and  $\text{Si}_{1-x-y}\text{Ge}_x\text{C}_y$  alloys and Ge islands using an electron cyclotron resonance argon/methane plasma, *Thin Solid Films* **410**, 61–71 (2002).
256. O. G. Schmidt, C. Lange, K. Eberl, O. Kienzle, and F. Ernst, Formation of carbon-induced germanium dots, *Appl. Phys. Lett.* **71**, 2340–2342 (1997).
257. O. G. Schmidt, S. Schieker, K. Eberl, O. Kienzle, and F. Ernst, Carbon-induced germanium dots: Kinetically-limited islanding process prevents coherent vertical alignment, *Appl. Phys. Lett.* **73**, 59–61 (1998).
258. O. G. Schmidt, C. Lange, K. Eberl, and O. K. F. Ernst, C-induced Ge dots: A versatile tool to fabricate ultra-small Ge nanostructures, *Thin Solid Films* **336**, 248–251 (1998).

259. D. Dentel, L. Vescan, O. Chretien, and B. Holländer, Influence of molecular hydrogen on Ge island nucleation on Si(001), *J. Appl. Phys.* **88**, 5113–5118 (2000).
260. Y. Wakayama, L. V. Sokolov, N. Zakharov, P. Werner, and U. Gosele, Precise control of size and density of self-assembled Ge dot on Si(100) by carbon-induced strain-engineering, *Appl. Surf. Sci.* **216**, 419–423 (2003).
261. X. Shao, R. Jonczyk, M. Dashiell, D. Hits, B. A. Orner, A.-S. Khan, K. Roe, J. Kolodzey, P. R. Berger, M. Kaba, M. A. Barteau, and K. M. Unruh, Strain modification in thin Si<sub>1-x-y</sub>Ge<sub>x</sub>C<sub>y</sub> alloys on (100) Si for formation of high density uniformly sized quantum dots, *J. Appl. Phys.* **85**, 578–582 (1999).
262. D. Dentel, J. L. Bischoff, L. Kubler, M. Stoffel, and G. Castelein, Influence of a pre-deposited carbon submonolayer on the Ge island nucleation on Si(001), *J. Appl. Phys.* **93**, 5069–5074 (2003).
263. O. Leifeld, A. Beyer, E. Müller, D. Grützmacher, and K. Kern, Nucleation of Ge quantum dots on the C-alloyed Si(001) surface, *Thin Solid Films* **380**, 176–179 (2000).
264. K. Eberl, O. G. Schmidt, S. Schieker, N. Y. Jin-Phillipp, and F. Phillipp, Formation and optical properties of carbon-induced Ge dots, *Solid-State Electron.* **42**, 1593–1597 (1998).
265. J. Y. Kim, S. H. Ihm, J. H. Seok, C. H. Lee, Y. H. Lee, E.-K. Suh, and H. J. Lee, Growth temperature dependence on the formation of carbon-induced Ge quantum dots, *Thin Solid Films* **369**, 96–99 (2000).
266. A. Sakai and T. Tatsumi, Ge growth on Si using atomic hydrogen as a surfactant, *Appl. Phys. Lett.* **64**, 52–54 (1994).
267. J.-M. Baribeau, D. J. Lockwood, R. W. G. Syme, H.-J. Labbé, and S. J. Rolfe, Proc. Mat. Res. Soc. Symp. **448**, 113–118 (1997). Atomic hydrogen assisted growth of Si-Ge heterostructures on (001) Si, in: *Control of Semiconductor Surfaces and Interfaces*, edited by S. M. Prokes, O. J. Glembocki, S. K. Brierley, J. M. Gibson, and J. M. Woodall, Materials Research Society, Pittsburgh, PA.
268. A. Portavoce, A. Ronda, and I. Berbezier, Sb-surfactant mediated growth of Ge nanostructures, *Mater. Sci. Eng. B* **89**, 205–210 (2002).
269. A. Portavoce, F. Volpi, A. Ronda, P. Gas, and I. Berbezier, Sb segregation in Si and SiGe: Effect on the growth of self-organised Ge dots, *Thin Solid Films* **380**, 164–168 (2000).
270. D. J. Eaglesham, F. C. Unterwald, and D. C. Jacobson, Growth morphology and the equilibrium shape; the role of “surfactants” in Ge/Si island formation, *Phys. Rev. Lett.* **70**, 966–968 (1993).
271. T. I. Kamins, G. Medeiros-Ribeiro, D. A. A. Ohlberg, and R. S. Williams, Annealing of phosphorus-doped Ge islands on Si(001), *J. Appl. Phys.* **95**, 1562–1567 (2004).
272. L. Pavesi and D. J. Lockwood, *Silicon Photonics*, Springer, Heidelberg, 2004.
273. H. Lafontaine, N. L. Rowell, S. Janz, and D.-X. Xu, Growth of undulating Si<sub>0.5</sub>Ge<sub>0.5</sub> layers for photodetectors at  $\lambda = 1.55 \mu\text{m}$ , *J. Appl. Phys.* **86**, 1287–1291 (1999).
274. S. Janz, J.-M. Baribeau, D. J. Lockwood, J. P. McCaffrey, S. Moisa, N. L. Rowell, D.-X. Xu, H. Lafontaine, and M. R. T. Pearson, Si/Si<sub>1-x</sub>Ge<sub>x</sub> photodetectors using three-dimensional growth modes to enhance photoresponse at  $\lambda = 1550 \text{ nm}$ , *J. Vac. Sci. Technol. A* **18**, 588–592 (2000).
275. S. Tong, J. L. Liu, J. Wan, and K. L. Wang, Normal-incidence Ge quantum-dot photodetectors at 1.5  $\mu\text{m}$  based on Si substrate, *Appl. Phys. Lett.* **80**, 1189–1191 (2002).
276. B.-C. Hsu, S. T. Chang, T.-C. Chen, P.-S. Kuo, P. S. Chen, Z. Pei, and C. W. Liu, A high efficient 820 nm MOS Ge quantum dot photodetector, *IEEE Electron. Devices Lett.* **24**, 318–320 (2003).

277. A. Elfving, G. V. Hansson, and W.-X. Ni, SiGe (Ge-dot) heterojunction phototransistors for efficient light detection at 1.3–1.55  $\mu\text{m}$ , *Physica E* **16**, 528–532 (2003).
278. P. Boucaud, V. L. Thanh, S. Sauvage, D. Debarre, and D. Bouchier, Intraband absorption in Ge/Si self-assembled quantum dots, *Appl. Phys. Lett.* **74**, 401–403 (1999).
279. C. Miesner, O. Rothig, K. Brunner, and G. Abstreiter, Intra-valence band photocurrent spectroscopy of self-assembled Ge dots in Si, *Appl. Phys. Lett.* **76**, 1027–1029 (2000).
280. V. Le Thanh, V. Yam, P. Boucaud, Y. Zheng, and D. Bouchier, Strain-driven modification of the Ge/Si growth mode in stacked layers: A way to produce Ge islands having equal size in all layers, *Thin Solid Films* **369**, 43–48 (2000).
281. A. I. Yakimov, A. V. Dvurechenskii, A. I. Nikiforov, and Y. Y. Proskuryakov, Interlevel Ge/Si quantum dot infrared photodetector, *J. Appl. Phys.* **89**, 5676–5681 (2001).
282. J. Konle, H. Presting, H. Kibbel, K. Thonke, and R. Sauer, Enhanced performance of silicon based photodetectors using silicon/germanium nanostructures, *Solid-State Electron.* **45**, 1921–1925 (2001).
283. N. Rappaport, E. Finkman, P. Boucaud, S. Sauvage, T. Brunhes, V. Le Thanh, D. Bouchier, and S. E. Schacham, Photoconductivity of Ge/Si quantum dot photodetectors, *Infrared Phys. Technol.* **44**, 513–516 (2003).
284. D. Buca, S. Winnerl, S. Lenk, C. Buchal, and D.-X. Xu, Fast time response from Si-SiGe undulating layer superlattices, *Appl. Phys. Lett.* **80**, 4172–4174 (2002).
285. T. Fromherz, W. Mac, A. Hesse, G. Bauer, C. Miesner, K. Brunner, and G. Abstreiter, Intraband absorption and photocurrent spectroscopy of self-assembled p-type Si/SiGe quantum dots, *Appl. Phys. Lett.* **80**, 2093–2095 (2002).
286. J. L. Liu, W. G. Wu, A. Balandin, G. L. Jin, and K. L. Wang, Intersubband absorption in boron-doped multiple Ge quantum dots, *Appl. Phys. Lett.* **74**, 185–187 (1999).
287. A. I. Yakimov, A. V. Dvurechenskii, N. P. Stepina, and A. I. Nikiforov, Interlevel optical transitions and many-body effects in a dense array of Ge/Si quantum dots, *Thin Solid Films* **380**, 82–85 (2000).
288. M. S. Kagan, I. V. Altukhov, V. P. Sinis, S. G. Thomas, K. L. Wang, K. A. Chao, and I. N. Yassievich, Terahertz emission of SiGe/Si quantum wells, *Thin Solid Films* **380**, 237–239 (2000).
289. R. A. Soref, Silicon-based optoelectronics, *Proc. IEEE* **81**, 1687–1706 (1993).
290. S. Luryi, A. Kastalsky, and J. C. Bean, New infrared detector on a silicon chip, *IEEE Trans. Electron Devices* **31**, 1135–1139 (1984).
291. S. Fama, L. Colace, G. Masini, and G. Assanto, High performance germanium-on-silicon detectors for optical communications, *Appl. Phys. Lett.* **81**, 586–588 (2002).
292. H. Temkin, T. P. Pearsall, J. C. Bean, R. A. Logan, and S. Luryi, Ge<sub>x</sub>Si<sub>1-x</sub> strained-layer superlattice waveguide photodetectors operating near 1.3  $\mu\text{m}$ , *Appl. Phys. Lett.* **48**, 963–965 (1986).
293. A. Splett, T. Zinke, K. Petermann, E. Kasper, H. Kibbel, H.-J. Herzog, and H. Presting, Integration of waveguides and photodetectors in SiGe for 1.3  $\mu\text{m}$  operation, *Photonics Technol. Lett. IEEE* **6**, 59–61 (1994).
294. S. B. Samavedam, M. T. Currie, T. A. Langdo, and E. A. Fitzgerald, High-quality germanium photodiodes integrated on silicon substrates using optimized relaxed graded buffers, *Appl. Phys. Lett.* **73**, 2125–2127 (1998).
295. D. C. Houghton, Strain relaxation kinetics in Si<sub>1-x</sub>Ge<sub>x</sub>/Si heterostructures, *J. Appl. Phys.* **70**, 2136–2151 (1991).
296. H. Lafontaine, D. C. Houghton, B. Bahierathan, D. D. Perovic, and J.-M. Baribeau, Si<sub>1-x</sub>Ge<sub>x</sub> critical thickness for surface wave generation during UHV-CVD growth at 525°C, in: *Evolution of Exptial Structure and Morphology*, edited by A. Zangwill,

- D. Jesson, D. Chambliss, and R. Clarke, Materials Research Society, Pittsburgh, PA, 1999, Vol. 399, pp. 413–418.
297. L. Tsybeskov and D. J. Lockwood, Quantum confinement in nanocrystalline silicon superlattices, *Asian J. Phys.* **9**, 745–757 (2000).
  298. D. J. Lockwood, Light emission in silicon, in: *Silicon-Based Materials and Devices*, edited by H. S. Nalwa, Academic, New York, 2001, Vol. 2, pp. 225–246.
  299. L. Tsybeskov, K. D. Hirschman, S. P. Duttagupta, M. Zacharias, P. M. Fauchet, J. P. McCaffrey, and D. J. Lockwood, Nanocrystalline-silicon superlattice produced by controlled recrystallization, *Appl. Phys. Lett.* **72**, 43–45 (1998).
  300. T. Brunhes, P. Boucaud, S. Sauvage, F. Aniel, J.-M. Lourtioz, C. Hernandez, Y. Campidelli, O. Kermarrec, D. Bensahel, G. Faini, and I. Sagnes, Electroluminescence of Ge/Si self-assembled quantum dots grown by chemical vapor deposition, *Appl. Phys. Lett.* **77**, 1822–1824 (2000).
  301. M. Stoffel, U. Denker, and O. G. Schmidt, Electroluminescence of self-assembled Ge hut clusters, *Appl. Phys. Lett.* **82**, 3236–3238 (2003).
  302. A. Alguno, N. Usami, T. Ujihara, K. Fujiwara, G. Sazaki, K. Nakajima, and Y. Shiraki, Enhanced quantum efficiency of solar cells with self-assembled Ge dots stacked in multilayer structure, *Appl. Phys. Lett.* **83**, 1258–1260 (2003).
  303. L. Naval, B. Jalali, L. Gomelsky, and J. M. Liu, Optimization of Si<sub>1-x</sub>Ge<sub>x</sub>/Si waveguide photodetectors operating at  $\lambda = 1.3 \mu\text{m}$ , *J. Lightwave Technol.* **14**, 787–797 (1996).
  304. B. Jalali, L. Naval, and A. F. J. Levi, Si-based receivers for optical data links, *J. Lightwave Technol.* **12**, 1930–1934 (1994).
  305. M. El Kurdi, P. Boucaud, S. Sauvage, O. Kermarrec, Y. Campidelli, D. Bensahel, G. Saint-Girons, and I. Sagnes, Near-infrared waveguide photodetector with Ge/Si self-assembled quantum dots, *Appl. Phys. Lett.* **80**, 509–511 (2002).
  306. M. El Kurdi, P. Boucaud, S. Sauvage, G. Fishman, Y. C. O. Kermarrec, D. Bensahel, G. Saint-Girons, G. Patriarche, and I. Sagnes, Silicon-on-insulator and SiGe waveguide photodetectors with Ge/Si self-assembled islands, *Physica E* **16**, 523–527 (2003).
  307. S. Winnerl, D. Buca, S. Lenk, C. Buchal, S. Mantl, and D.-X. Xu, Fast IR Si/SiGe superlattice MSM photodetectors with buried CoSi<sub>2</sub> contacts, *Microelectron. Eng.* **64**, 205–209 (2002).
  308. D.-X. Xu, S. Janz, H. Lafontaine, and M. R. T. Pearson, Photodetectors for 1.3 mm and 1.55 mm wavelengths using SiGe undulating MQW's on SOI substrates, in: *Proceedings of the SPIE Silicon-Based Optoelectronics*, edited by D. C. Houghton and E. A. Fitzgerald, SPIE, San Jose, CA, 1999, Vol. 3630, pp. 50–57.
  309. M. El Kurdi, P. Boucaud, S. Sauvage, G. Fishman, O. Kermarrec, Y. Campidelli, D. Bensahel, G. Saint-Girons, G. Patriarche, and I. Sagnes, Silicon-on-insulator and SiGe waveguide photodetectors with Ge/Si self-assembled islands, *Physica E* **16**, 523–527 (2003).
  310. T. P. Pearsall, L. Colace, A. DiVergilio, W. Jäger, D. Stenkamp, G. Theodorou, H. Presting, E. Kasper, and K. Thonke, Spectroscopy of band-to-band optical transitions in Si-Ge alloys and superlattices, *Phys. Rev. B* **57**, 9128–9140 (1998).
  311. L. Colace, A. DiVergilio, S. Vaidyanathan, T. P. Pearsall, H. Presting, and E. Kasper, Photocurrent spectroscopy measurements of Si-Ge alloys and superlattices, *Appl. Surf. Sci.* **102**, 272–278 (1996).
  312. S. Winnerl, D. Buca, S. Lenk, C. Buchal, S. Mantl, and D.-X. Xu, MBE grown Si/SiGe undulating layer superlattices for infrared light detection, *Mater. Sci. Eng. B* **89**, 73–76 (2002).

- 313. C. Miesner, K. Brunner, and G. Abstreiter, Lateral photodetectors with Ge quantum dots in Si, *Infrared Phys. Technol.* **42**, 461–465 (2001).
- 314. S. K. Zhang, H. J. Zhu, F. Lu, Z. M. Jiang, and X. Wang, Coulomb charging effect in self-assembled Ge quantum dots studied by admittance spectroscopy, *Phys. Rev. Lett.* **80**, 3340–3343 (1998).
- 315. C. Miesner, T. Asperger, K. Brunner, and G. Abstreiter, Capacitance–voltage and admittance spectroscopy of self-assembled Ge islands in Si, *Appl. Phys. Lett.* **77**, 2704–2706 (2000).
- 316. K. Schmalz, I. N. Yassievich, P. Schittenhelm, and G. Abstreiter, Space-charge spectroscopy of self-assembled Ge-rich dots on Si grown by mbe, *Phys. Rev. B* **60**, 1792–1798 (1999).
- 317. C. M. A. Kapteyn, M. Lion, R. Heitz, D. Bimberg, C. Miesner, T. Asperger, K. Brunner, and G. Abstreiter, Many-particle effects in Ge quantum dots investigated by time-resolved capacitance spectroscopy, *Appl. Phys. Lett.* **77**, 4169–4171 (2000).
- 318. K.-M. Haendel, C. Lenz, U. Denker, O. G. Schmidt, K. Eberl, and R. J. Haug, Transport measurements of valence band holes in p-type SiGe quantum well structure containing Ge quantum dots, *Physica E* **13**, 757–760 (2002).
- 319. M. W. Dashiell, C. Müller, N. Y. Jin-Phillipp, U. Denker, O. G. Schmidt, and K. Eberl, Low temperature epitaxial growth of germanium islands in active regions of silicon interband tunneling diodes, *Mater. Sci. Eng. B* **89**, 106–110 (2002).
- 320. D. J. Lockwood, *Light Emission in Silicon*, Academic, New York, 1998.

## 2

# Synthesis of Titania Nanocrystals: Application for Dye-Sensitized Solar Cells

MOTONARI ADACHI, YUSUKE MURATA, FUMIN WANG, AND JINTING JIU  
*Institute of Advanced Energy, Kyoto University, Uji, Kyoto 611-0011, Japan*

## 2.1. Formation of Titania Nanocrystals by Surfactant-Assisted Methods

### *2.1.1. Introduction: How to Control Morphology and Functionalize Ceramic Materials*

Titania nanocrystals, which have a large surface area with controlled surface structure and high electron transport properties, are essentially important for high-efficiency dye-sensitized solar cells. Morphological control and high crystallinity are the key properties needed in titanium oxide materials for dye-sensitized solar cells. In this section, we first review morphological control and functionalization of nanosize ceramic materials from a wide point of view.

One of the most active trends in modern materials chemistry is the development of synthetic methods to obtain size- and shape-controlled inorganic nanocrystals.<sup>1–3</sup> The shape and size of inorganic nanocrystals determine their widely varying electrical and optical properties.<sup>4,5</sup> For example, quantum dots exhibit strongly size-dependent optical and electrical properties. Magnetic studies of nanocrystals show that the blocking temperature, saturation, and remnant magnetization of nanocrystals are solely determined by the size, regardless of the shape. However, the shape of the nanocrystals is the dominant factor in their coercivity.<sup>6</sup>

Morphological control of nanosize materials is essential for their functionalization, as shown by the above examples. Investigators have recently shown keen interest in controlling the morphology of nanomaterials and clarifying the correlations between a material's properties and its morphology.<sup>1,6–20</sup> Until now, a number of methods have been developed to control the shape of nanocrystals.

In the case of CdSe, the shape of the nanocrystals is controlled by a mixture of surfactants that differently bind to the crystallographic faces, utilizing the interaction between the surfactant and the nanocrystal surface.<sup>1,21,22</sup> The organic surfactants cannot coat one face of the nanocrystals, which raises the energy of this face relative to others, allowing it to grow quickly and form a rod shape. In the formation of CdSe nanocrystals, the monomer concentration in the growth solution is also a determining factor in shape control and shape evolution.<sup>7</sup> If the remaining

monomer concentration in the growth solution is extremely high, the solution can supply a sufficient amount of monomers for each seed to fully grow arms on the four (111) facets of the zinc-blende structure of the tetrahedral seeds, yielding tetrapoles. A moderately high monomer concentration can only support the growth of a single arm in its one-dimensional (1D) growth stage, generating rod-shaped nanocrystals. At low monomer concentrations, these elongated nanocrystals are not compatible with the low chemical potential environment. Consequently, the system can only generate dots. On the other hand, ligand influence on the monomer is also important.<sup>8</sup> In general, a relatively small number of nuclei are desired for the growth of elongated nanocrystals because the change of the monomer concentration in the solution caused by the nucleation process and the subsequent growth process should be relatively small. This should result in a relatively stable monomer concentration in the solution, suitable for the growth of a given shape.<sup>7,8</sup>

How to control the growth rate of the nanocrystal is another method for shape control. In the formation of the  $\text{CoFe}_2\text{O}_4$  nanocrystal, the growth rate of the nanocrystal is the key in shape control. A slow heating rate kept a low concentration of available metal cations from the decomposition of precursors, which, combined with the low growth temperature, gave a slow rate of crystal growth. The growth of cubic  $\text{CoFe}_2\text{O}_4$  nanocrystals was terminated at  $\{100\}$  planes, which were predicted to have the lowest surface energy. When a much faster heating rate was employed, a high concentration of metal cations was present. A faster growth rate at a high temperature with abundant metal cations available resulted in crystal growth with much less selectivity in direction and, hence, produced spherical  $\text{CoFe}_2\text{O}_4$  nanocrystals.<sup>6</sup>

The biological route is a developing and attractive method for the shape control of nanocrystals. Metal alloy ferromagnetic nanostructures FePt were successfully synthesized by biological methods.<sup>9</sup> A phage display methodology was adopted to identify peptide sequences that both specifically bind to the ferromagnetic  $\text{L1}_0$  phase of FePt and control the crystallization of FePt nanoparticles using a modified arrested precipitation technique. Transmission electron microscopy (TEM), electron diffraction, scanning transmission electron microscopy (STEM), and X-ray diffraction all indicated that these nanoparticles were composed of an FePt alloy with some degree of chemical ordering, and super quantum interface device (SQUID) analysis showed that these nanostructures are ferromagnetic at room temperature, possessing coercivities up to 1000 Oe.

Controlled removal of the stabilizing organic molecules from the surface of nanoparticles induces fusion of nanoparticles, which produces a simple method to synthesize 1D nanocrystals using self-assembly. Nanoparticles of CdTe were found to spontaneously reorganize into crystalline nanowires upon controlled removal of the protective shell of an organic stabilizer, thioglycolic acid.<sup>12,13</sup> In an early stage of the nanowire formation, “pearl necklace” agglomerates composed of nanoparticles were observed in the TEM image. The “pearl-neck-lace” shape of fused gold metal was successfully synthesized by controlling the concentration of the capping reagent.<sup>23</sup>

A template approach is an effective way to make nanorods and nanotubes. To date, the oxide nanotubes and nanorods such as  $\text{TiO}_2$ ,  $\text{MnO}_2$ ,  $\text{Co}_3\text{O}_4$ ,  $\text{WO}_3$ , and



ZnO have been formed by using anodic alumina membrane as templates.<sup>24–26</sup> The desired materials are then synthesized within the pore of anodic alumina. Recently, a  $\text{Eu}_2\text{O}_3$  nanotube array was successfully prepared by an improved sol-gel method combined with an anodic alumina template.<sup>12</sup>

Various ideas for the morphological control were introduced to each case, as mentioned earlier. Recently, an interesting phenomenon has been found to occur only for tiny nanosize particles. Penn and Banfield<sup>27,28</sup> showed that a long chain of highly ordered titania could be formed from a solution of primary titania nanoparticles. Until this finding, it seemed that aggregation of nanocrystals would always lead to a disordered solid. They referred to this as oriented attachment. ZnO and  $\text{SnO}_2$  nanorods were also formed from nanoparticles in the same mechanism.<sup>13,14</sup>

These findings encourage us to attempt to synthesize nanocrystals with a desired morphology by developing and exploring new methods. In the present chapter, new findings in our laboratory in the control morphology and functionalization of materials are presented. Section 2.1.2 describes in detail how the network structure of single-crystalline  $\text{TiO}_2$  anatase nanowires can be formed by an "oriented attachment" mechanism for application to dye-sensitized solar cells.<sup>29</sup> Section 2.1.3 shows that various morphologies of crystalline anatase  $\text{TiO}_2$  can be formed using dodecanediamine as a shape controller.<sup>30–31</sup>

For the application of these functional nanosize materials for devices, assembling such devices by self-organization of functional elements that take the proper position and shape and establish connections with the other components is an essentially important issue.<sup>17,18</sup> However, the details are not described here, as this issue is outside the topic of this chapter.

## 2.1.2. Formation of Network Structure of Single Crystalline $\text{TiO}_2$ Nanowires by the "Oriented Attachment" Mechanism

### 2.1.2.1. Introduction

Nanosize semiconductor ceramics are useful materials for photoactive systems such as dye-sensitized solar cells (DSCs), as shown by Grätzel in 1991.<sup>32</sup> A porous thin film composed of titania nanosize particles accumulated on a transparent conducting glass has been used as an electrode to achieve a high specific surface area for adsorption of a large number of dye molecules. However, the electron diffusion coefficients determined by laser flash-induced transient photocurrent measurement<sup>33–35</sup> and intensity modulated photocurrent spectroscopy<sup>36–37</sup> were more than two orders of magnitude smaller than the value for bulk anatase crystal. These small diffusion coefficients can be roughly understood by the hypothesis of electron traps in the porous  $\text{TiO}_2$  with a very broad distribution of release rate. Defects in the porous  $\text{TiO}_2$  may act as electron traps and exist in grain boundaries at the contacts between nanosize particles. Thus, the use of a single-crystalline network structure of  $\text{TiO}_2$  nanowires instead of  $\text{TiO}_2$  nanoparticles is expected to result in a great improvement in rapid electron transfer and, thus, higher efficiency.

In this section, we present the preparation of a  $\text{TiO}_2$  single-crystalline network structure of nanowires by an “oriented attachment” mechanism<sup>38–41</sup> using surfactant-assisted processes at low temperature (353 K).<sup>29</sup> We applied this anatase single-crystalline titania network structure, exposing the  $\{101\}$  plane as a semiconductor thin-film electrode in DSCs and attained a high light-to-electricity conversion yield of 9.3%.

#### 2.1.2.2. How to Make $\text{TiO}_2$ Network Structure of Anatase Nanowires

In a typical synthesis process, laurylamine hydrochloride (LAHC) was dissolved in distilled water and tetraisopropylorthotitanate (TIPT) was mixed with acetylacetone (ACA) in order to decrease the hydrolysis and condensation rates of TIPT. When TIPT was mixed with the same molar ratio of ACA, ACA coordinated to the titanium atom, with one isopropoxyl group unbound. The coordination number of the titanium atom changed from 4 to 5, resulting in a color change from colorless to yellow.<sup>42</sup> This yellow TIPT solution was added to 0.1 M LAHC aqueous solution (pH 4–4.5). The molar ratio of TIPT to LAHC was 4. When the two solutions were mixed, precipitation occurred immediately. The precipitates were dissolved completely by stirring the solution for several days at 313 K, and the solution became transparent, indicating that the precipitates were finely divided (i.e., the size became smaller than the wavelength of light), and surfactant molecules interacted well with the titania compounds. The temperature was then changed to 353 K. After 3 h at 353 K, the solution became a hard gel. After 5 h, the gel became weak and shrank with the proceeding condensation reaction, releasing isopropyl alcohol and ACA. After 3 days, the solution became a white gel with a thin yellow liquid layer. The titania products were separated by centrifugation. After washing with 2-propanol and successive centrifugation, the titania powders were dried in a vacuum.

Characterization of the produced materials was accomplished by X-ray diffraction (XRD) (Rigaku Goniometer PMG-A2, CN2155D2), transmission electron microscopy (TEM) (JEOL 200 CX), fast Fourier transform (FFT), selected-area electron diffraction (SAED), and isotherm of nitrogen adsorption (BEL SORP 18 PLUS).

#### 2.1.2.3. Formation of Network Structure of Single-Crystalline $\text{TiO}_2$ Nanowires

In general, morphological control of nanosize materials is attained by using a mixture of surfactants that bind differently to the crystallographic faces.<sup>21,22</sup> These organic molecules also act as surface ligands and have the ability to control the shape and size of the growing particles.<sup>43</sup> On the other hand, monomer concentrations also play an important role in shape control.<sup>7,8</sup> It also is worth noting that an “oriented attachment” mechanism was found to be able to control the formation of rather complicated structures using selective attachment between the specific crystallographic planes, especially for titania nanoparticles.<sup>27,28</sup> The results suggested that the morphology of the nanocrystal could be controlled by suitable modification of reaction conditions in the formation processes, as shown recently by Banfield et al.<sup>43</sup>

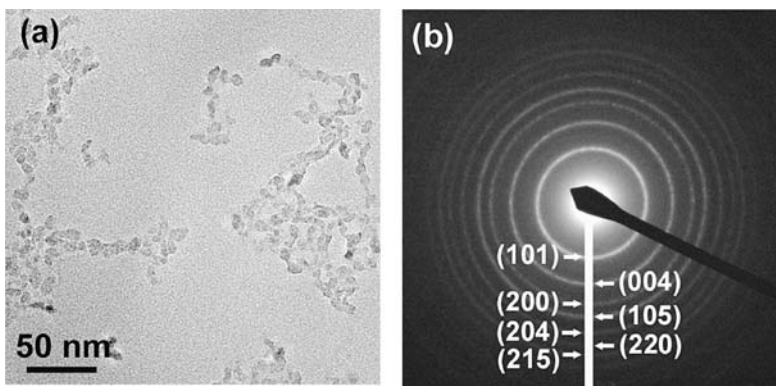


FIGURE 2.1. TEM image of vacuum-dried sample prepared at 353 K for 1 day. (a) Titania of wires and network structure were observed. (b) SAED pattern of titania nanowires.

We present the formation of single-crystalline titania nanowires made of crystalline spherical titania nanoparticles in aqueous solution based on oriented attachment.<sup>29</sup> Figure 2.1a shows a TEM image of the vacuum-dried titania powders heated at 353 K for 1 day. We can see the titania nanonetwork consisting of nanowires 5–15 nm in diameter. The titania nanowires have a very high crystallinity, as can be seen on SAED patterns (Fig. 2.1b) in a wide area, showing the Debye–Scherrer rings of {101}, (004), (200), (105), (204), (220), and (215) diffractions of the anatase phase.

An high resolution TEM (HRTEM) image of nanowires and nanonetworks with a single anatase crystal structure is shown in Figure 2.2. Most of the aggregated particles form a wire shape with a single-crystalline structure. There were almost no

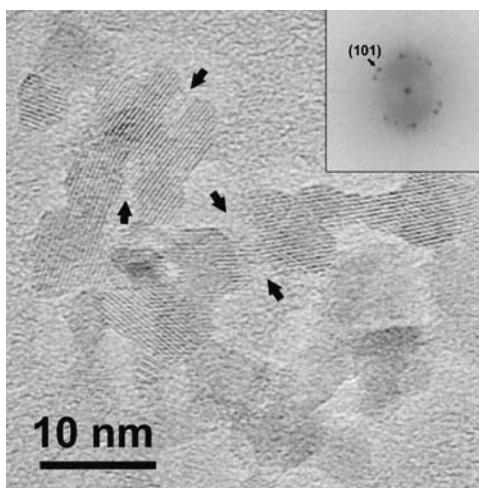


FIGURE 2.2. HRTEM image of several titania nanowires with a single anatase structure formed by oriented attachment. Arrows in the HRTEM image indicate the indentations. Inset: FFT pattern obtained from HRTEM. The spacing of the lattice was calculated as 3.51 Å by FFT analysis, corresponding to {101} spacing of the anatase phase of titania.

isolated particles observed. Lattice images were clearly observed, indicating that these nanowires, composed of fused nanoparticles with a diameter of 2–5 nm, had high crystallinity in spite of their small size. Because the lattice images aligned perfectly, the orientations of crystals of fused nanoparticles were completely aligned. This feature shows that nanowires were made by an oriented attachment mechanism. A lattice spacing of 3.51 Å was determined by a FFT pattern (inset of Fig. 2.2) and corresponded to the lattice spacing of the {101} plane of the anatase phase.

The lattice images in Fig. 2.2 may be directly related to the crystal growth of nanowires. Two arrows indicate the bond between two particles. These indentations are a feature of crystal growth by the oriented attachment mechanism. This suggested that the oriented attachment occurred in the [010] or  $\langle 101 \rangle$  direction and made a network structure. In this case, the {101} plane is mainly exposed. The network of nanowires formed by oriented attachment had an irregular shape, as shown in Fig. 2.2 because of the bonding process, as mentioned earlier. The lattice planes always aligned with each other in all observed cases of fusion of nanoparticles. Oriented attachment seemed to always occur when nanoparticles fused with each other under our experimental conditions. This finding was very interesting, because crystal growth by the oriented attachment mechanism was observed below 373 K. Usually a much higher temperature is needed, e.g., 433–523 K.<sup>27,28</sup> This observation confirmed a remarkable characteristic of our surfactant-assisted synthesis method using ACA.

The particle size distribution in the system can be modified by the oriented attachment of primary particles, leading to the formation of wire-shaped structures. There is certainly a strong thermodynamic driving force for oriented attachment, because the surface energy is reduced substantially when the interface is eliminated.<sup>39,40</sup> The driving force for the assembly process is thus the reduction of surface energy, and this mechanism has been reported already for a variety of metal oxide systems.<sup>13,14,44</sup>

In the titania system under hydrothermal conditions (433–523 K, 15–40 bars),<sup>27,28</sup> crystal growth was reported to occur along [001]. Oriented attachment in common titania systems occurs occasionally on [001] and rarely on  $\langle 101 \rangle$ . This mechanism effectively serves to reduce the overall surface energy by eliminating the surfaces at which the crystallites join. We speculated that organic molecules such as surfactants might hinder or modify oriented attachment. Organic molecules adsorbed on a crystallographically specific surface can modify the oriented attachment mechanism by changing the surface energy and also preventing contact between the faces on which adsorption has selectively occurred. In our surfactant-assisted system, the observed attached planes in the image are not [001] with high surface energy but  $\langle 101 \rangle$  with low energy. We supposed that the surface energy was decreased by the surfactants adsorbed to the (001) planes. It has been reported that the surface density of sixfold-coordinated Ti atoms with hydroxyl of the (001) surface structure is high compared to that with the {101} surface. The numbers of hydroxyl groups are 7.0 nm<sup>-2</sup> for (001) surfaces and 5.1 nm<sup>-2</sup> for {101} surfaces, respectively.<sup>45</sup> The (001) plane thus adsorbed much more surfactants than the

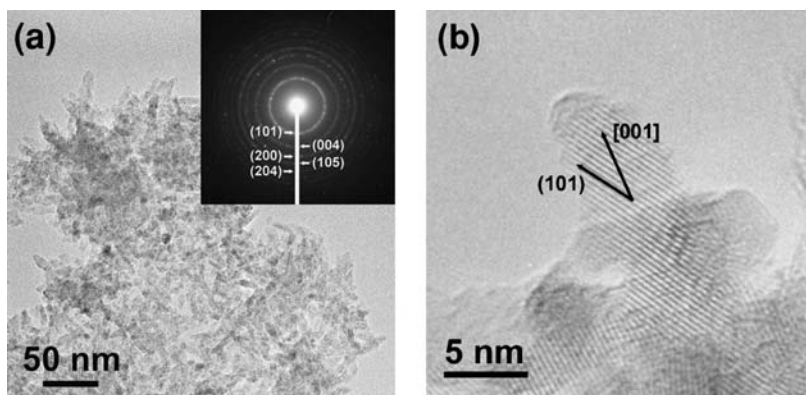


FIGURE 2.3. TEM (a) and HRTEM (b) images of titania nanorods prepared with ACA/Ti = 0.2 at 353 K for 1 day.

{101} plane and hindered the contact between (001) planes, resulting in oriented attachment occurring on the {101} plane.

We carried out the experiment repeatedly while varying the reaction rate to investigate the relationship between the adsorption of the surfactants and crystal growth.

The mole ratio of ACA to TIPT was changed to 0.2 from 1 and the reaction behavior drastically changed. When LAHC solution was added to TIPT-ACA solution at a mole ratio of 0.2, a white colloidal suspension was formed immediately. A transparent supernatant was formed after the precipitation. Although the temperature was changed to 353 K, gelation did not occur, indicating that surfactant molecules did not affect the formation process of  $\text{TiO}_2$ . The structure of the product heated at 353 K for 1 day was examined on TEM and HRTEM images. A rodlike morphology with average diameter of  $5 \pm 2$  nm and average length of  $20 \pm 10$  nm (aspect ratio  $\cong 5$ ) was observed as shown in Fig. 2.3a. The diameter of nanorods was not constant throughout their length. The SAED pattern of this sample indicated Debye–Sherrer rings corresponding to lattice planes of the anatase phase. The lattice configuration of the nanorods is clearly shown in HRTEM images of Fig. 2.3b, and the lattice spacing was found to be  $3.52 \text{ \AA}$ , in agreement with lattice spacing of {101} planes of the anatase phase. As shown in Fig. 2.3b, it was observed that the direction of crystal growth was not the {101} but the [001] direction. This result suggested that the attachment occurs mostly in the (001) plane.

The XRD pattern of titania nanorods prepared in the same way was measured under the conditions of 35 kV and 20 mA and is shown in Fig. 2.4, indicating the formation of the anatase phase. Comparing the intensity of the (004) peak of this sample to that of the standard  $\text{TiO}_2$  sample shown in Joint Committee on Powder Diffraction Standards (JCPDS), it was found that the relative intensity of (004) had increased 2.5 times from 20% to 50%. This implied that crystal growth of the titania nanorod occurs along the [001] direction, consistent with the HRTEM images in Fig. 2.3b.

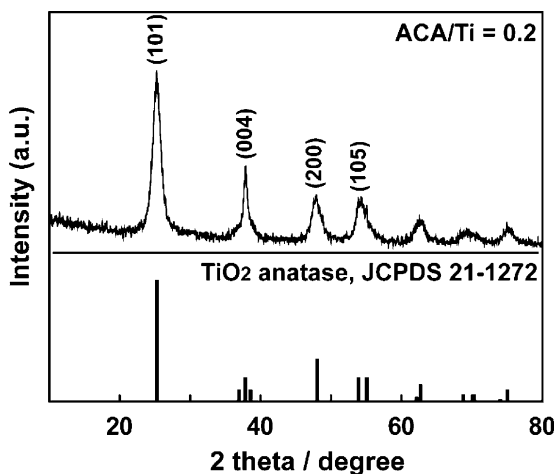


FIGURE 2.4. XRD pattern of titania nanorods prepared with ACA/Ti = 0.2.

Figure 2.5 clearly shows the crystal growth along the [001] direction under ACA/Ti = 0.2. The lattice spacings in Fig. 2.5a were determined to be 4.75 Å–3.52 Å and 2.38 Å, corresponding to the (002), {101}, and (004) planes of the anatase phase, respectively. The HRTEM image without the lattice image of the {101} plane in Fig. 2.5a was obtained by masking the {101} plane by the inverse FFT method, as shown in Fig. 2.5b. These results show that the surface energy of crystal growth differs with the reaction conditions. Because the condensation reaction speed was much faster under ACA/Ti = 0.2, it is predicted that the crystal growth occurred before the surfactant molecules were adsorbed on the titania

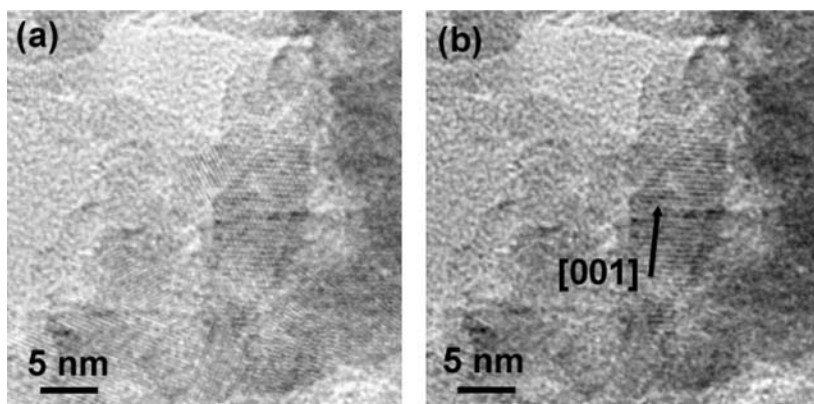


FIGURE 2.5. (a) HRTEM image of the aggregated titania nanorods prepared with ACA/Ti = 0.2 at 353 K for 1 day. (b) HRTEM image masked {101} plane in (a) by the inverse FFT method.

nanoparticles. Therefore, the crystal growth occurred along the [001] direction, which is common for oriented growth in titania systems. The results were also consistent with the findings of Banfield and Penn in the absence of ACA.<sup>27,28</sup>

Thus, it can be concluded that the direction of crystal growth by oriented attachment can be controlled by regulating adsorption of surfactant molecules via control of the reaction rate. By choosing a suitable condition, we can make single-crystalline anatase, exposing mainly the {101} plane by the surfactant-assisted oriented attachment mechanism at a low temperature (353 K).

### *2.1.3. Morphological Control of Anatase Nanocrystals Using Dodecanediamine as a Surfactant*<sup>30–31</sup>

#### 2.1.3.1. Introduction

Morphological control of TiO<sub>2</sub> nanocrystals with high crystallinity is a big challenge. Synthesis using the pore of an anodic aluminum oxide<sup>24,25</sup> template is the most common method.<sup>26,46–53</sup> Nanotubes and nanowires synthesized by this method give highly ordered arrays and, in some cases, show photoluminescence.<sup>52</sup> However, these materials usually have a polycrystalline phase, and the diameter is over 50 nm; that is, the surface area is not very large. Recently, a couple of methods have been developed to form a single-crystalline anatase phase by the sol-gel method<sup>52</sup> and electrochemically induced sol-gel preparation.<sup>53</sup> On the other hand, the simple hydrothermal method also has been used to synthesize nanotubes and nanowires as 1D TiO<sub>2</sub> nanocrystals.<sup>54–60</sup> Needle-shaped TiO<sub>2</sub> crystals with a diameter of 8 nm and a length of 100 nm were obtained by this method, indicating that TiO<sub>2</sub> nanotubes with a small diameter and very large surface area were obtained.<sup>54,55</sup> Unfortunately, these nanotubes did not show a clear anatase phase by XRD and were expected to be a layered titanate H<sub>2</sub>Ti<sub>3</sub>O<sub>7</sub>.<sup>59,61,62</sup> By improvement of the reaction conditions, recently single-crystalline anatase nanowires have been obtained with this method.<sup>58</sup> Surfactant-mediated synthesis was also reported.<sup>63</sup>

For the morphological control of nanocrystalline TiO<sub>2</sub>, the method of hydrolysis and polycondensation of titanium alkoxide using tetramethylammonium hydroxide (Me<sub>4</sub>NOH) as a catalyst has been developed and has demonstrated control over crystal structure, size, shape, and organization of TiO<sub>2</sub> nanocrystals by adjusting the relative concentrations of titanium alkoxide and Me<sub>4</sub>NOH, the reaction time, and pressure.<sup>64</sup> In some conditions, anatase clusters self-assemble into superlattices. This process can make highly structured titanium films, although the size is very small.<sup>64</sup>

In another article<sup>65</sup>, we described how uniform anatase-type TiO<sub>2</sub> nanocrystals with different shapes were formed by the phase transformation of a Ti(OH)<sub>4</sub> gel matrix in the presence of shape controllers [i.e., triethanolamine (TEOA), diethylenetriamine, ethylenediamine, trimethylenediamine]. The shape control can be explained in terms of the specific adsorption of TEOA onto the crystal plane parallel to the *c* axis at pH 11.5 and by the pH dependence of the adsorption onto ellipsoidal particles.

From the results of the shape control experiments mentioned earlier, amine compounds were found to play an important role. We introduced the hydrophobicity [i.e., dodecanediamine (DDA)] to the shape-controlling system<sup>65</sup> and succeeded in the formation of nanoparticles, nanowires, nanotubes, and even a flowerlike shape of the anatase phase and a nanosheet of the Lepidocrocite phase by controlling pH, the relative concentrations of titanium alkoxide and DDA, the reaction temperature, and time.

#### 2.1.3.2. How to make Shape-Controlled TiO<sub>2</sub> Nanocrystals

Tetraisopropylorthotitanate was mixed with TEOA at a molar ratio of [TIPT]/[TEOA] = 1/2 to form a compound of Ti(IV) (quadrivalent titanium compound), which is stable against the hydrolysis of Ti(IV) at room temperature<sup>65</sup> and distilled water was then added to make a homogeneous stock solution. The DDA solution was added into the above stock solution of Ti(IV), and the pH of the solution was adjusted by adding HClO<sub>4</sub> or NaOH solution to the reaction solution (initial pH). The mixed solution was stirred vigorously for 1 h, put into a Teflon reactor sealed with a stainless-steel vessel and aged at 373 K for 24 h and then kept at the desired temperature (413–453 K) for a desired period (72–96 h) to nucleate and grow the titania particles. The resulting white solid products were centrifuged and washed with distilled water and ethanol, followed by drying at 353 K in air.

The obtained samples were characterized by XRD using a Rigaku Goniometer (PMG-A2, CN2155D2) X-ray diffractometer with Cu-K $\alpha$  radiation ( $\lambda$  = 0.15417 nm). The morphology and crystalline structure were observed by TEM (JEOL 200CX) with an acceleration voltage of 200 kV, SAED, and scanning electron microscopy (SEM) (JEOL JSM-5510) images.

#### 2.1.3.3. Formation of Shape-Controlled Nanocrystals: Nanoparticles, Nanorods, and Nanotubes of Anatase Phase

From an application point of view, TiO<sub>2</sub> nanocrystals are important in photocatalysis, ceramic materials, fillers, coatings, pigments, and cosmetics and have been attracting attention in both fundamental research and practical studies. The electrical and optical properties of titania are greatly dependent on its size and shape, so the performance of titania in such applications can be optimized by control over the morphology of materials, control that depends on our understanding of the fundamental details of the nucleation and growth of titania. Among the different shapes of TiO<sub>2</sub>, 1D nanostructures, including nanowires, nanorods, and nanotubes, have attracted substantial research interest not only because of their specific quantum confinement effects but also because of their ability to conduct electrons, which makes them especially promising for future application in nanoelectronics and photovoltaic cells.

Figure 2.6 shows the SEM and TEM images of the samples obtained after 72 h of hydrothermal reactions at 413 K under different initial pH conditions. The other reaction conditions are [TIPT] = 0.25 M, [TEOA]/[TIPT] = 2, and [TIPT]/[DDA] = 5.



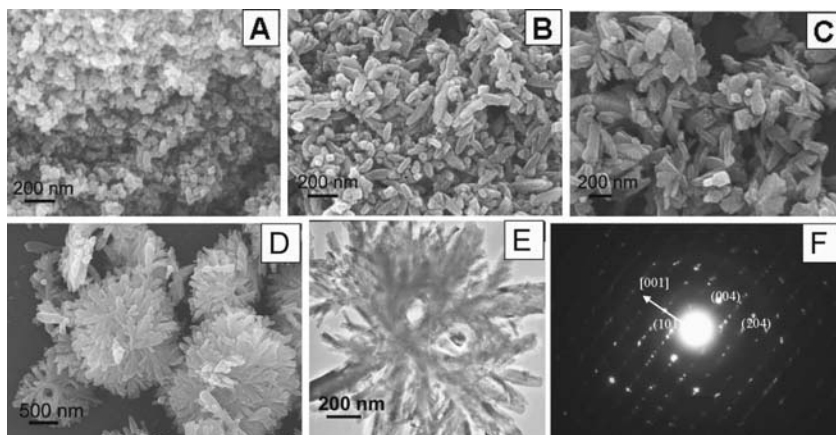


FIGURE 2.6. SEM micrographs of samples formed under initial pH of (A) 5.6, (B) 10.4, (C) 10.7, and (D) 11.1, (E) TEM micrographs of samples formed under a pH of 11.1, and (F) SAED pattern of image E.

Obviously, with an increase in the initial pH of the solution, the shape of the prepared sample changed from nanoparticles, ellipsoids, and nanorods to a flowerlike shape, which showed that the pH of the solution had a significant effect on the morphology of the titania and also showed that introduction of hydrophobicity by the addition of DDA made a new and interesting flowerlike shape of  $\text{TiO}_2$  with diameter of 1–2  $\mu\text{m}$ , as shown in Figs. 2.6D and 2.6E. SAED (Fig. 2.6F) showed many spots of anatase crystal. The TEM image and SAED indicated that the flowerlike  $\text{TiO}_2$  was composed of single-crystalline anatase nanorods with homocentric growth.

The XRD pattern shown in Fig. 2.7 revealed that all sharp peaks could be indexed as anatase  $\text{TiO}_2$ . No characteristic peaks of other impurities were observed. These

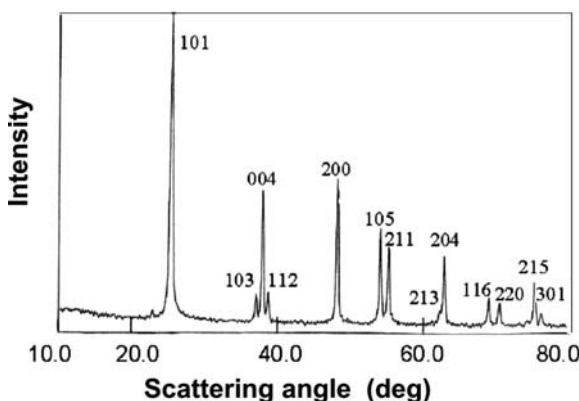


FIGURE 2.7. XRD patterns of  $\text{TiO}_2$  formed under initial pH of 11.1.

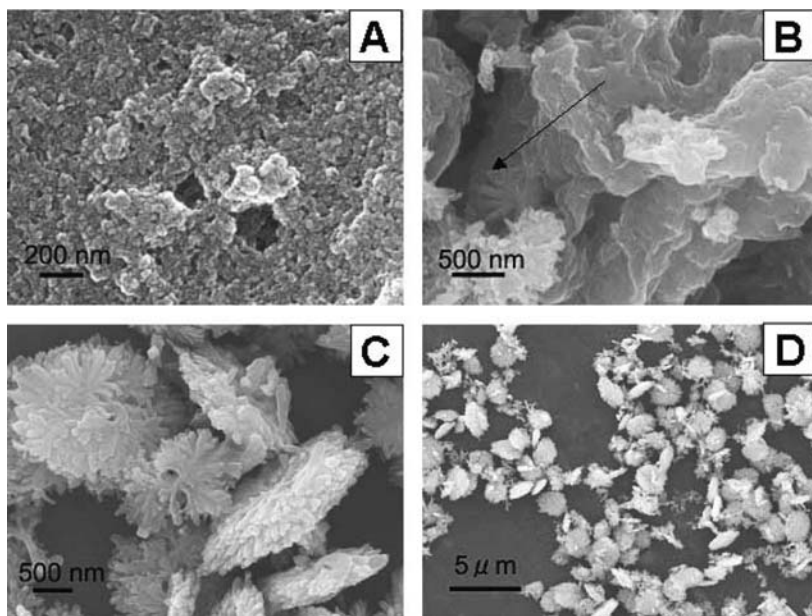


FIGURE 2.8. SEM micrographs of samples formed under pH of 11.1 at different hydrothermal times of (A) 1 h, (B) 30 h, and (C) 72 h; (D) low magnification image of (C).

results indicated that the products had high crystallinity and purity. Similar XRD results were obtained for all other samples shown in Fig. 2.7.

In order to elucidate the formation mechanism of the beautiful flower-shaped nanostructure, the shape evolution of titania formed during the preparation was measured (Fig. 2.8). From the SEM image shown in Fig. 2.8A, the first shape formed was a nanodisklike structure with a size of 10–30 nm. A sheet structure with a thickness of 10–30 nm was observed next, as shown in Fig. 2.8B. The sheets did not exist in an isolated state, but showed a multilayered structure similar to the lamellar phase of the surfactant. In Fig. 2.8B, some sheets on the outer surface have rolled into nanorods, as indicated by an arrow. Figure 2.8C shows flower-shaped aggregates composed of an orderly alignment of rods. In the low-magnification SEM image (Fig. 2.8D), almost all  $\text{TiO}_2$  show the same flowerlike shape with standing or flat orientation, which showed the very high yield of this shape. The reproducibility of the preparation of this structure was also confirmed.

As mentioned earlier, the pH value of the solution is very important for the shape control of  $\text{TiO}_2$ . This important effect of pH was explained by the variation in the charged state of DDA by pH. The charged state of DDA changes with pH value, as shown in Fig. 2.9:  $\text{H}_3^+\text{N}(\text{CH}_2)_{12}\text{NH}_3^+$  under pH lower than 8,  $\text{H}_2\text{N}(\text{CH}_2)_{12}\text{NH}_3^+$  under pH between 8 and 11, and  $\text{H}_2\text{N}(\text{CH}_2)_{12}\text{NH}_2$  under pH higher than 11.

Double-charged DDA under pH lower than 8 is expected to be hydrophilic. Therefore, only nanoparticles of  $\text{TiO}_2$  can be formed under this condition, because

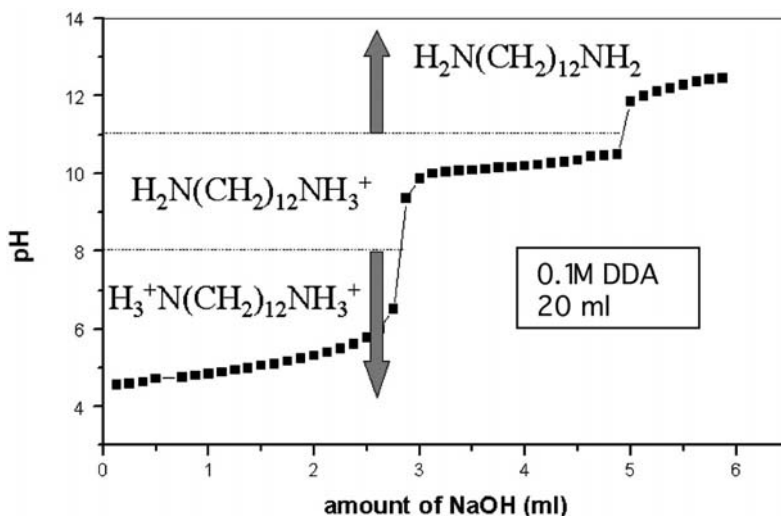


FIGURE 2.9. Titration curve of DDA solution.

the lamellar structure of the surfactant cannot be formed, and there is very little adsorption of DDA on the  $\text{TiO}_2$  crystal surface as well.<sup>61</sup> Monocharged DDA under a pH value between 8 and 11 is expected to become amphiphilic and make a lamellar phase.  $\text{NH}_2$  at one end of DDA is predicted to interact and be adsorbed on the  $\text{TiO}_2$  surface, but  $\text{NH}_3^+$  at the other end of DDA is hydrophilic, and little adsorption of DDA on the  $\text{TiO}_2$  surface is expected. Thus, the lamellar structure in this range was inferred to be a loose structure. Hydrolysis reaction of TIPT produces a molecule of isopropylalcohol four times larger than TIPT. Isopropyl alcohol penetrates and intercalates easily into the lamellar structure formed under this condition and removes DDA, resulting in rolling of the  $\text{TiO}_2$  nanosheets, breaking down of the lamellar structure, and making mainly nanorods of  $\text{TiO}_2$ . We confirmed this prediction by an experiment under pH 10.7. Under this condition, nanosheets were observed during the reaction. SEM and TEM images are shown in Figs. 2.10A and 2.10B. Rolling of nanosheets was observed everywhere in the sample (Fig. 2.10A), and a nanorodlike structure was formed (Fig. 2.10B).

When the pH value was adjusted higher than 11, DDA took a nonionic state, which was hydrophobic and strongly adsorbed on the  $\text{TiO}_2$  surface. In this state, the most stable inorganic/organic hybrid of titanium oxide–DDA lamellar structure was formed, as will be shown in Fig. 2.12 C. Both  $\text{NH}_2$  groups of DDA attached to the adjacent layer of  $\text{TiO}_2$  by a strong interaction with the  $\text{TiO}_2$  surface. The lamellar structure formed under this condition was very stable. We inferred that alcohol molecules have difficulty in penetrating or intercalating between the two layers. Thus, only the surface layer is exposed to isopropyl alcohol. When alcohol molecules remove the DDA of the first layer, the first layer of  $\text{TiO}_2$  starts rolling into nanorods. The second layer is then exposed to alcohol, resulting in removal of

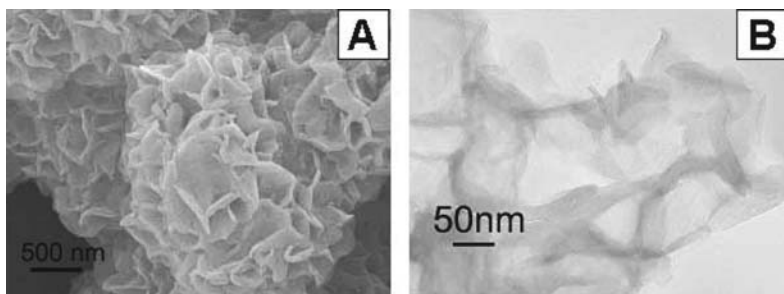


FIGURE 2.10. (A) SEM micrograph and (B) TEM micrograph of the sample prepared under pH of 10.7 with a hydrothermal time of 30 h.

DDA of the second layer and rolling into nanorods. Repetition of this process leads to the formation of flowerlike-shaped  $\text{TiO}_2$  with nanorods aligned in a homocentric shape.

When the pH was adjusted to 12.8, flowerlike-shaped particles composed of nanotubes were observed, as shown in Fig. 2.11. Low-magnification SEM image (Fig. 2.11A) shows a very high yield of the flowerlike-shaped particles. From the high-magnification SEM image (Fig. 2.11C), clear nanotubes were observed. Under very high pH conditions, the reaction  $\text{Ti}-\text{OH} + \text{OH}^- \rightarrow \text{Ti}-\text{O}^- + \text{H}_2\text{O}$  occurs, and the  $\text{TiO}_2$  surface of the thin layer was covered by  $\text{Ti}-\text{O}^-$  anions. Thus,

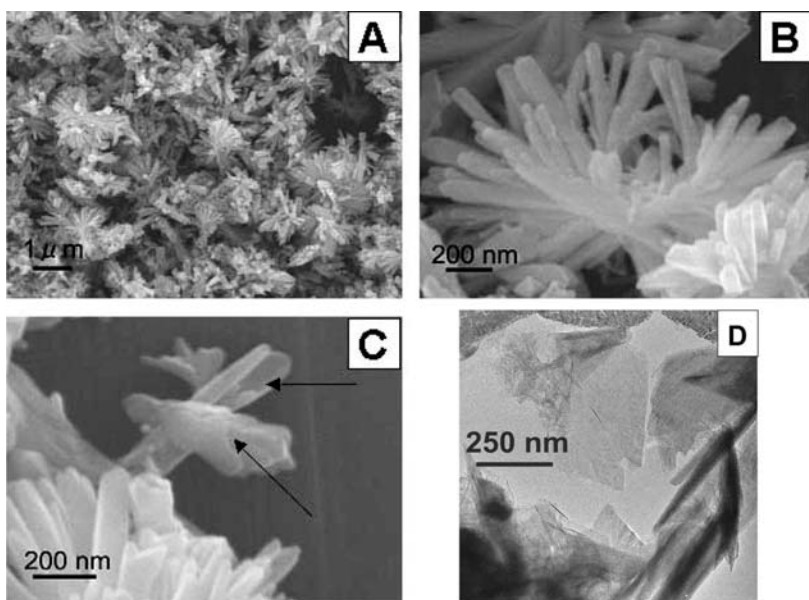


FIGURE 2.11. (A–C) SEM images of the sample prepared under pH 12.8. (D) TEM image in the middle of the formation processes under the same conditions.

the curvature of the rolling sheet becomes small because of the strong electrostatic repulsions, resulting in the formation of nanotubes. The TEM image shown in Fig. 2.11D clearly shows the formation processes of a nanotube from a nanosheet.

#### 2.1.3.4. Molecular Nanosheet Formation of Lepidocrocite Phase

Ceramic nanosheets can invite a range of applications, particularly in the field of nanoscience and nanomaterials. One of the outstanding challenges in this area is to devise synthetic methods that give a well-ordered monolayer and multilayer thin film from inorganic precursors with specific electronic, magnetic, catalytic, and other properties.<sup>66</sup> Toward this goal, it is important to provide a wide selection of desired nanosheet crystallites. These nanosheets have been provided by the exfoliation of functional materials<sup>67–72</sup> such as layered titania,<sup>67</sup> layered manganese oxides,<sup>68</sup> layered niobates,<sup>69</sup> and layered perovskite.<sup>70</sup> Preparation of these layered materials, however, requires calcinations at high temperature and a long time for acid treatment; that is, these materials are usually prepared by calcinations at from 1073 to 1573 K for 10–20 h, followed by acid treatment for 10 days.

In this subsection, we report a new process for fabrication of titania nanosheets. We modified the self-organizing method using DDA to synthesize anatase titanium oxide with various shapes, as described earlier. Until now, to the best of our knowledge, such a molecular nanosheet structure has not been synthesized via this route.

The formation of nanosheet titania is based on two points. One is that the highly hydrophobic property of the dodecanediamine under high pH condition results in the stable lamellar formation. The other is that a suitable molar ratio of DDA to TIPT provides lepidocrocite crystalline nanosheets.

Figure 2.12 shows TEM images of a sample prepared under the following reaction conditions:  $[\text{TIPT}] = 0.5\text{ M}$ ,  $[\text{DDA}]/[\text{TIPT}] = 0.4$ ,  $[\text{TEOA}]/[\text{TIPT}] = 2$ ,  $\text{pH} = 11.1$ , temperature = 413 K, and reaction time = 72 h. In the SEM image (Fig. 2.12A), a filmlike structure was observed.

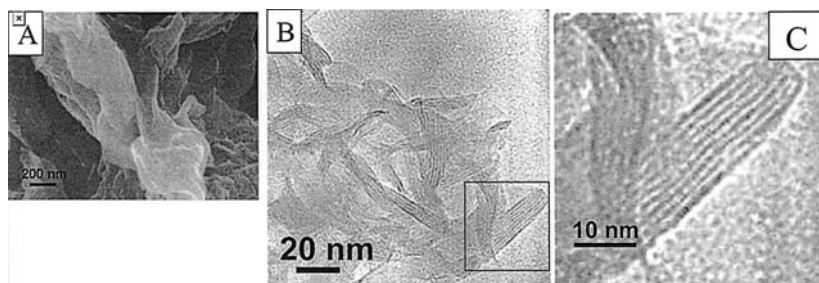


FIGURE 2.12. (A) SEM image of the sample prepared under the following reaction conditions:  $[\text{TIPT}] = 0.5\text{ M}$ ,  $[\text{DDA}]/[\text{TIPT}] = 0.4$ ,  $[\text{TEOA}]/[\text{TIPT}] = 2$ ,  $\text{pH} = 11.1$ , temperature = 413 K, and reaction time = 72 h. (B) TEM image of the same sample. (C) Magnified image of selected area indicated in (B).

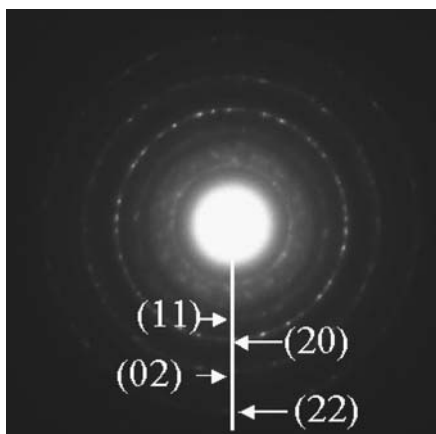


FIGURE 2.13. Electron diffraction pattern of the sample shown in Fig. 2.12.

A TEM image (Fig. 2.12B) showed the multilayer structure of the lamellar phase. A magnified image of the square area in (B) is shown in Fig. 2.12C. This figure clearly revealed the multilayered structure of  $\text{TiO}_2$  composed of a monosheet sandwiched by surfactant layers. This thickness was close to that of the monolayer crystallites of titanium oxide made by exfoliating layered titania.<sup>73–74</sup> The SAED results of the sample at a reaction time 96 h are shown in Fig. 2.13.

The observed Debye–Sherrer rings were indexed to two-dimensional lattices 11, 20, 02, and 22. The spacing was calculated as 0.235 nm for 11, 0.189 nm for 20, 0.151 nm for 02, and 0.120 nm for 22.

In Fig. 2.14, the atomic architecture of the monosheet crystallites of  $\text{TiO}_2$  is shown. These results revealed the formation of a two-dimensional unit cell (0.38 nm  $\times$  0.30 nm) of a single-crystalline nanosheet structure,<sup>73–74</sup> indicating that the multilayered structure was composed of a molecular nanosheet of titania (i.e., Lepidocrocite). In order to separate an individual molecular nanosheet from the multilayered structure, we need to remove DDA from the multilayer by alcohol and also to replace two amino groups of DDA with some cations, because cations cover

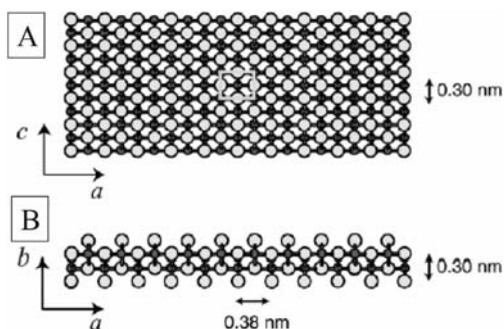


FIGURE 2.14. Atomic architecture of the monosheet crystallites of  $\text{TiO}_2$ : (A) top view and (B) side view. Red and blue circles represent Ti and O atoms, respectively. (After Sasaki et al.<sup>67,70,73,74</sup>)

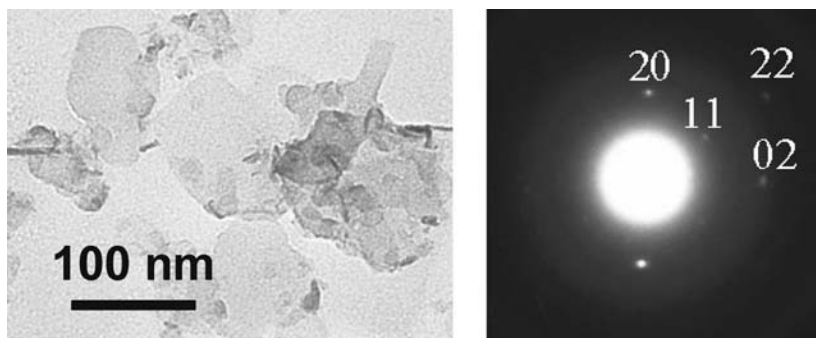


FIGURE 2.15. TEM image of delaminated monosheet (A) and electron diffraction pattern of the monosheet (B).

and stabilize the monosheet of TiO<sub>2</sub>. Tetrabutylammonium hydroxide (TBAOH) is the best candidate.<sup>67</sup> The transparent colloidal suspension was obtained immediately after we put the sample of multilayered structure in the mixture of isopropyl alcohol and TBAOH solution. A TEM image and SAED result are shown in Fig. 2.15. The observed very faint contrast showed the very thin thickness of the sample. The SAED pattern of this sample disclosed single-crystalline properties. The different spots in Fig. 2.15B displayed an orthogonal array of sharp spots, which indicated single-crystal quality as well as the high crystallinity of the nanosheets. The diffraction can be indexed as 11, 20, 02, and 22 reflections, respectively, indicating the formation of a two-dimensional lattice with unit cell 0.38 nm × 0.30 nm, as shown in Fig. 2.14.

## 2.2. Application of TiO<sub>2</sub> Network of Single-Crystalline Nanowires for Dye-Sensitized Solar Cells

### 2.2.1. Introduction

Solar energy is one of the most promising future energy resources. The dye-sensitized solar cell (DSC) appears to have significant potential as a low-cost alternative to conventional *p-n* junction solar cells. There are some excellent reviews of the dye-sensitized solar cells.<sup>75–79</sup> The operating principles of the DSC are given in Fig. 2.16.

A DSC consists of a nanocrystalline mesoporous network of a wide-band-gap semiconductor (usually TiO<sub>2</sub>), which is covered with a monolayer of dye molecules (usually a Ru dye). Photoexcitation of the dye results in the injection of an electron into the conduction band of the oxide. The original state of the dye is subsequently restored by electron donation from the electrolyte, usually an organic solvent containing a redox system, such as the iodide/triiodide couple. The regeneration of the sensitizer by iodide intercepts the recapture of the conduction band electron

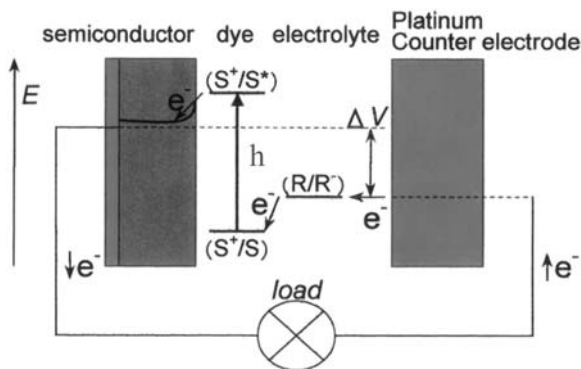


FIGURE 2.16. Principle of operation and energy-level scheme of the dye-sensitized solar cell.

by the oxidized dye. The iodide is regenerated in turn, by the reduction of triiodide at the counterelectrode (usually Pt). The circuit is completed via electron migration through the external load. Overall, the device generates electric power from light without suffering any permanent chemical transformation.

To increase the efficiency of a DSC, an improvement in short-circuit current, open-circuit voltage, and fill factor is essential. To accomplish this, a breakthrough in the preparation of a thin semiconductor film of titania is expected. Among many possible approaches, the use of a  $\{101\}$  exposure plane with a network structure of single-crystalline anatase nanowires is one of the most promising, because the intercrystalline titania contacts are greatly decreased by using a single-crystalline network structure in comparison with a porous titania thin film composed of accumulated nanosize particles. This might be useful for easier electron transfer through the titania layer and also high dye adsorption on the titania surface, as shown later in detail. We succeeded in the preparation of such a network of single-crystalline anatase nanowires, and successfully used it in a thin film for a DSC with high efficiency.

### 2.2.2. How to Make the Dye-Sensitized Solar Cells

Thin titania films were made by applying a titania sample on an electric conducting glass plate. Indium–tin oxide (ITO) and fluorine-doped tin oxide (FTO) were used as electric conducting glass plates. The ITO and FTO glass plates were kindly donated by Geomatec Co. Ltd. and by Asahi Glass Co., respectively. We used a gel with white color, which was obtained after reactions at 353 K for 3 days, as the starting titania sample. Because the titania gel contained surfactant molecules, they were removed from the gel by washing with isopropyl alcohol. We controlled the alcohol content and viscosity of the gel simultaneously by changing the centrifugation speed, causing the sample to be separated from the alcohol solution. Next, titania gel sample 1 was prepared by mixing the washed gel with polyethylene glycol (PEG: MW 20,000; Wako Chemicals) in the range from 5 wt%



to 10 wt%. Titania gel sample 2 was prepared by mixing the gel sample 1 with titania nanoparticle Degussa P-25 (P-25) in the range from 5 wt% to 10 wt%. These gel samples were applied repetitively to the conducting glass (ITO) as follows. The conducting glass was covered on two parallel edges with adhesive tape to control the thickness of the  $\text{TiO}_2$  film and to provide a noncoated area for electrical contact. Titania gel sample 1 was then applied to the free edges of the conducting glass and distributed with a glass rod sliding over the tape-covered edges. Gel sample 1 was coated several times (usually three times) with the coating film, as mentioned earlier. In several cases, gel sample 2 was then coated several times (mostly two times) with the coated gel sample 1. After every coating, the sample was calcined at 723 K for 30 min after drying. After the last time, the sample was calcined at 723 K for 60 min. Dye was introduced to the titania thin films by soaking the film for about 20 h in a  $3 \times 10^{-4} M$  solution of ruthenium dye in ethanol. *Cis*-di(thiocyanate)bis(2,2'-bipyridyl-4,4'-dicarboxylate)-ruthenium(II) (N3) and *cis*-di(thiocyanate)bis(2,2'-bipyridyl-4,4'-dicarboxylate)-ruthenium(II) bis-tetra-butylammonium (N719) (Solaronix SA and Kojima Chemical Reagents Inc.) produced by Grätzel's group<sup>80</sup> was used as the dye.

The DSC was composed of a titania thin-film electrode on a conducting glass plate and a platinum electrode made by sputtering on the conducting glass plus an electrolyte between the titania thin film and the platinum. We used two kinds of electrolyte: electrolyte 1: 0.1 M of LiI, 0.6 M of 1,2-dimethyl-3-*n*-propylimidazolium iodide (DMPII), 0.05 M of  $\text{I}_2$ , 1 M of 4-*tert*-butylpyridine (TBP) in methoxyacetonitrile; electrolyte 2: 0.03–0.05 M of  $\text{I}_2$ , 0.3–0.5 M of LiI in 3-methyl-2-oxazolidinone (NMO)/acetonitrile solution in some cases. The volume ratio of NMO to acetonitrile was 1/9. The photocurrent–voltage characteristics were measured using a potentiostat (Hokuto Denko HA-501G, HB-105) by irradiating with simulated solar light [i.e., AM1.5 100 mW  $\text{cm}^{-2}$  (ORIEL 1000W 91192)]. The cell size was 1  $\text{cm}^2$  or 0.25  $\text{cm}^2$ . Cells made of P-25 were also prepared according to the method reported by Grätzel<sup>80</sup> for comparison, and the photocurrent–voltage characteristics of P-25 cells were measured under the same conditions. The incident photon-to-current conversion efficiency (IPCE) was measured using the IPCE Evaluation System for Dye-Sensitized Solar Cell (Bunkoh-Keiki Co. Ltd., CEP-2000).

### 2.2.3. Characterization of the Solar Cells Made of Network of Single-Crystalline Anatase Exposing Mainly the {101} Plane

In order to compare a cell composed of a titania network of nanowires with one composed of standard titania particles (P-25), we measured the photocurrent–voltage characteristics of both cells under the conditions described in the experimental section using FTO glass as the electric conducting glass and electrolyte 2. Figure 2.17 shows the short-circuit current density obtained from the cells made of the titania network of nanowires, together with those of P-25, versus

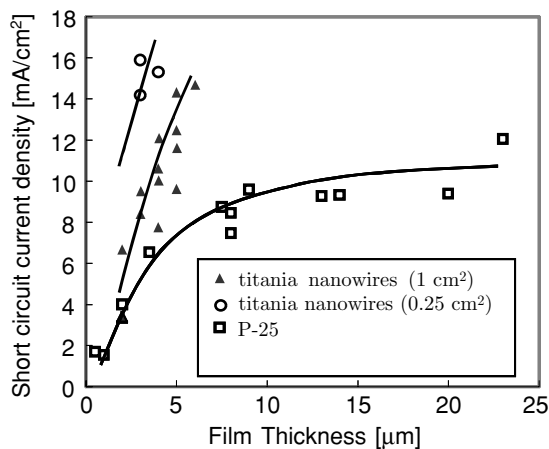


FIGURE 2.17. Relationship between the short-circuit current density and the film thickness of titania nanowires.

the film thickness. In the thin-film region, the current density of the cell made of a network of nanowires was more than two times higher than that of P-25. The high current density in the thin-film region might be attributable to both the high adsorption of dye due to the large surface area mainly exposing the  $\{101\}$  plane and the very high rate of electron transfer through the single-crystalline  $\text{TiO}_2$  nanonetwork, which is shown in Fig. 2.2 by HRTEM. The use of a  $\text{TiO}_2$  nanonetwork with single-crystal anatase nanowires instead of  $\text{TiO}_2$  nanoparticles also contributes to the decreased number of contacts between titania materials, which form grain boundaries and act as electron traps.

Figure 2.18 shows the short-circuit current density obtained for both cells against the amount of dye adsorbed on the titania thin film on the unit area of the conducting glass. In the range from 0 to  $6 \times 10^{-8} \text{ mol/cm}^2$ , both cells gave almost the same photocurrent density. In the higher dye amount range, the photocurrent density of the P-25 cell stopped increasing and became constant. On the other hand, the photocurrent density of the network cell gave a linear increase. This linear increase in the high dye concentration region shows the potential higher efficiency of this cell with the  $\text{TiO}_2$  network of nanowires. The film thickness of the cell with the  $\text{TiO}_2$  network of nanowires is significantly thinner in comparison with the cell made of P-25 for the same amount of dye adsorbed, especially in the high amount range. This might produce the above results.

In order to explain the amount of adsorbed dye on the film, the nitrogen adsorption measurement was applied to analyze the properties of titania samples. The nitrogen adsorption–desorption isotherm of the titania sample taken from a semiconductor layer in the DSC system calcined at 723 K for 30 min is shown in Fig. 2.19a, together with that of a bulk sample of vacuum-dried titania. The isotherm pattern for the calcined sample was IUPAC type IV, indicating that

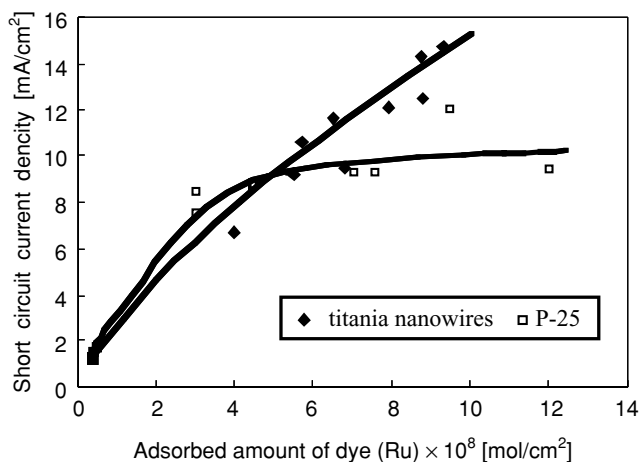


FIGURE 2.18. Relationship between the short-circuit photocurrent density and the dye amount of titania nanowires.

mesosize pores were formed, as in the bulk sample. However, the hysteresis loop for the calcined one was H1 type; that is, the loop was relatively narrow and the adsorption and desorption branches were nearly parallel. A hysteresis loop of this type is shown by adsorbents with a narrow distribution of uniform pores (e.g. open-ended tubular pores). The BET (Brunauer–Emmett–Teller)-specific surface area of the calcined powders was  $189 \text{ m}^2/\text{g}$ , and the peak pore size and the pore volume obtained by the Barrett–Joyner–Halenda method were  $5.04 \text{ nm}$  and  $0.420 \text{ cm}^3/\text{g}$ , respectively. (see Fig. 2.19b) Thus, the network structure of titania nanowires became more rigid by repeated calcinations and the pore size and the pore volume increased in comparison with the bulk sample of vacuum-dried titania, which had a BET-specific surface area of  $248 \text{ m}^2/\text{g}$ , pore size of  $3.48 \text{ nm}$ , and pore volume of  $0.267 \text{ cm}^3/\text{g}$ .

The relationship between the film thickness and the adsorbed N3 dye amount is shown in Fig. 2.20. The adsorbed N3 dye was dissolved completely from  $\text{TiO}_2$  to the sodium hydroxide aqueous solution, and the concentration of N3 was determined by the spectroscopic method. In the range  $0\text{--}10 \text{ }\mu\text{m}$ , the amount of dye adsorbed by the titania network of nanowires was about four to five times higher than that of P-25 film. The BET-specific surface area of the calcined titania network of nanowires and P-25 were  $189$  and  $55 \text{ m}^2/\text{g}$ , respectively. Thus, the titania network of nanowires adsorbed dyes more than the increase in the BET-specific surface area. This finding suggests the importance of control of the interaction of dye molecules at the interface with the titania nanosize materials.

The interaction of the dye with the nanocrystalline  $\text{TiO}_2$  electrode and the photophysical and electrochemical properties of the dye have been investigated.<sup>81–87</sup> Recently, the anchoring nature of the dye on a semiconductor surface was also investigated, mainly by Fourier transform infrared (FTIR).<sup>81</sup> A carboxylate group

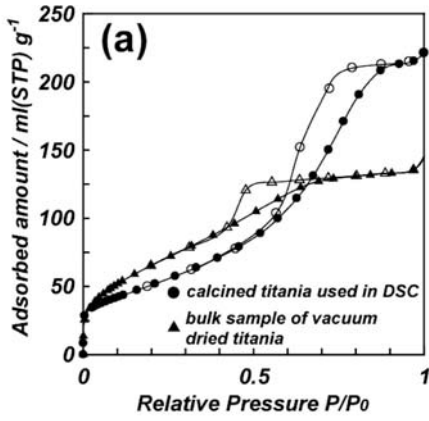


FIGURE 2.19. (a) Nitrogen adsorption-desorption isotherms of titania using dye-sensitized solar cells calcined at 723 K for 30 min and vacuum-dried titania nanowires. Filled and open symbols represent adsorption and desorption, respectively. (b) Pore size distribution obtained from (a).

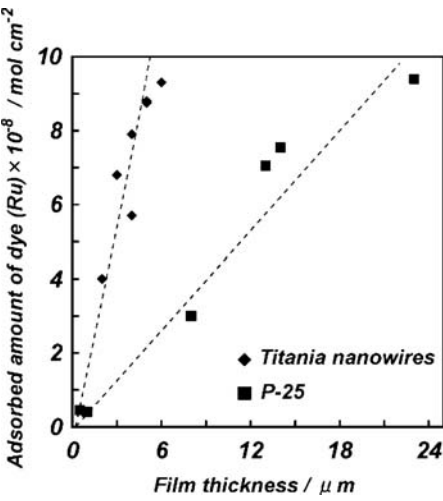
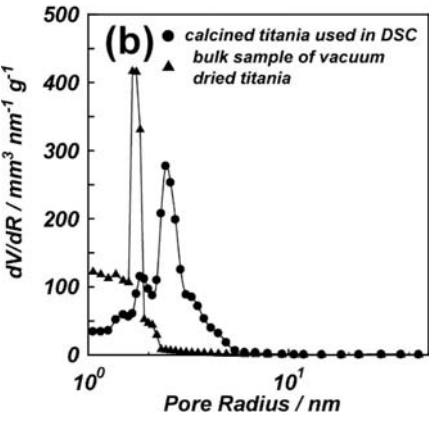


FIGURE 2.20. Relationship between the film thickness and the adsorbed dye amount for titania nanowires.

can coordinate to the  $\text{TiO}_2$  surface<sup>85</sup> in three main ways<sup>81,86</sup>: unidentate mode, chelating mode, and bridging bidentate mode. The possible anchoring models of the dye on the  $\text{TiO}_2$  were proposed by Shklover et al.<sup>81</sup> on the basis of the crystal structure of the N3 dye. For N719, the most stable anchoring on the  $\text{TiO}_2$  was determined as follows. The FTIR spectra of N719 showed the presence of mainly carboxylate groups, demonstrating that N719 was being adsorbed on the surface using the two carboxylic groups, which are trans to the sulfur cyanide SCN ligands. However, the presence of a small band (around 5%) at the carboxylic position indicated that around 5% of N719 was being adsorbed on the surface, employing one carboxylic acid and one carboxylate group. The distances between these two binding carboxylate groups and between one carboxylate and one carboxylic group agreed quite well with the distance between Ti atoms on the anatase (101) plane.<sup>81,84</sup> Thus, the anatase (101) plane is the best surface for adsorbing N3 or N719, indicating the reason why the  $\text{TiO}_2$  network of nanowires adsorbed much more dye than did P-25. The area occupied by the dye at the surface were determined to be  $1.6 \text{ nm}^2/\text{molecule}$ .<sup>81</sup>

Figure 2.21 shows the current-voltage characteristics obtained for the cell with a  $\text{TiO}_2$  thin film composed of a network structure of single-crystalline anatase nanowires. The titania thin film was prepared as follows. Titania gel sample 1 was first coated three times on ITO conductive glass. Gel sample 2 was then coated two times on top of coated gel sample 1. The sample was calcined after every coating at 723 K for the times described in the previous section. The cell size was  $0.25 \text{ cm}^2$ . After calcinations, N719 was introduced to the titania thin film. The photocurrent voltage characteristics were measured using electrolyte 1 by

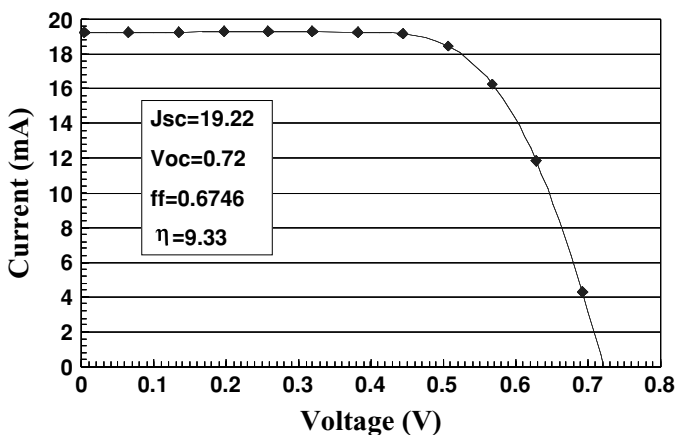


FIGURE 2.21. An illustration of the photocurrent–voltage characteristics of the cell with titania thin film composed of a  $\text{TiO}_2$  network structure of single anatase nanowires. A high light-to-electricity conversion efficiency of 9.3% was achieved with the cell, and the short-circuit photocurrent density, open-circuit voltage, and fill factor were obtained as  $19.2 \text{ mA cm}^{-2}$ , 0.72 V, and 0.675, respectively.

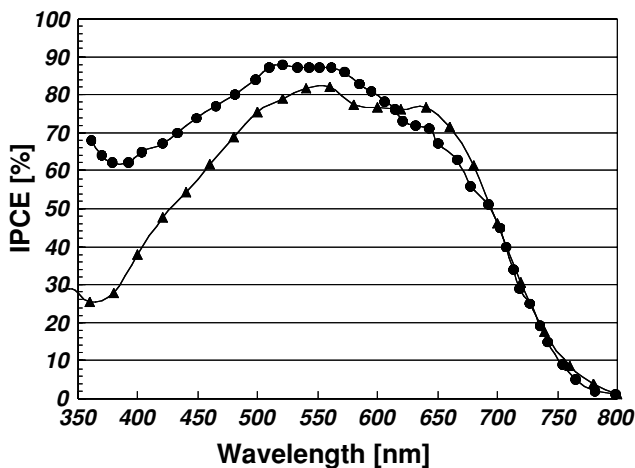


FIGURE 2.22. ▲: IPCE of the cell with a titania thin film composed of a  $\text{TiO}_2$  network structure of single-crystalline anatase nanowires. ●: Data from Grätzel et al., *J. Am. Chem. Soc.*, **115**, 6382–6390 (1993).

irradiating with simulated solar light [i.e., AM 1.5  $100 \text{ mW cm}^{-2}$  (ORIEL)]. A high light-to-electricity conversion rate of 9.3% was obtained for the cell with a  $\text{TiO}_2$  network of single-crystalline anatase nanowires. The short-circuit photocurrent density, open-circuit voltage, and fill factor were obtained as  $19.2 \text{ mA cm}^{-2}$ , 0.72 V, and 0.675, respectively. This high light-to-electricity conversion was attributed to the network structure of single-crystalline anatase nanowires shown in Fig. 2.2.

The IPCE result of this dye-sensitized solar cell is shown in Fig. 2.22, together with the result reported by Grätzel et al.<sup>80</sup> The obtained IPCE spectrum for our titania network structure gave almost the same efficiency as the curve reported by Grätzel et al., confirming the high light-to-electricity conversion yield of our cell composed of a  $\text{TiO}_2$  network structure of single-crystalline anatase nanowires.

## 2.3. Summary

In this chapter we have reviewed briefly the morphological control and functionalization of ceramic nanosize materials. We presented new findings from our laboratory. Section 2.1.2 described the formation of a network structure of single-crystalline  $\text{TiO}_2$  anatase nanowires by the “oriented attachment” mechanism. Section 2.1.3 showed that various morphologies of crystalline anatase  $\text{TiO}_2$  could be formed using dodecanediamine as a surfactant. Section 2.2 presented applications of the  $\text{TiO}_2$  network of single-crystalline nanowires for dye-sensitized solar cells. The principal points presented may be summarized as follows:

- Various ideas for morphological control were introduced: (1) using a mixture of surfactants that bind differently to the crystallographic faces for CdS, (2)

using monomer concentration and ligand effect for CdS, (3) using growth rate by controlling heating rate for  $\text{CoFe}_2\text{O}_4$ , (4) biological routes using peptide sequence for FePt, (5) using controlled removal of protecting organic stabilizer for CdTe, (6) using anodic alumina as a template, and (7) using the “oriented attachment” mechanism for nanoparticles.

- Synthesis of a network structure of single-crystalline anatase nanowires by the “oriented attachment” mechanism can be performed under suitable conditions, and the direction of the crystal growth by oriented attachment can be controlled.
- The morphology of anatase nanocrystals can be controlled by pH, reaction temperature, and time using dodecanediamine as a surfactant in a TIPT–triethanolamine–DDA system. The stability of the lamellar structure composed of  $\text{TiO}_2$  and DDA depends on the hydrophobicity of DDA and adsorption of DDA to the  $\text{TiO}_2$  surface, which depends strongly on pH. Variation in the stability of the lamellar structure is responsible for the different shapes.
- At a suitable molar ratio of DDA to TIPT, a multilayered structure composed of molecular lepidocrocite nanosheets and DDA is obtained. Individual molecular lepidocrocite nanosheets can be recovered in the colloidal solution.
- A  $\text{TiO}_2$  network of single anatase nanowires was successfully applied to titanium oxide electrodes of dye-sensitized solar cells, and a 9.3% light-to-electricity conversion efficiency was attained.

*Acknowledgments.* The authors wish to express their thanks to all the co-workers and collaborators whose contribution over the years have helped in our findings and understanding of morphological control of titania nanocrystals and their application in dye-sensitized solar cells. We are particularly grateful to Mr. Jun Takao for his DSC experiments and to Professor S. Isoda for TEM measurements.

## References

1. E. C. Scher, R. Soc, L. Manna, and A. P. Alivisatos, Shape control and application of nanocrystals, *Phil. Trans. R. Soc. Lond. A* **361**, 241–257 (2003).
2. M.P. Pileni, Colloidal self-assemblies used as templates to control size, shape and self-organization of nanoparticles, *Supramol. Sci.* **5**, 321–329 (1998).
3. T. S. Ahmadi, Z. L. Wang, T. C. Green, A. Henglein, and M. A. El-Sayed, Shape-controlled synthesis of colloid platinum nanoparticles, *Science* **272**, 1924–1925 (1996).
4. A. P. Alivisatos, Semiconductor clusters, nanocrystals, and quantum dots, *Science* **271**, 933–937 (1996).
5. C. M. Lieber, One-dimensional nanostructures: chemistry, physics & applications, *Solid State Commun.* **107**, 607–616 (1998).
6. Q. Song and Z. J. Zhang, Shape control and associated magnetic properties of spinel cobalt ferrite nanocrystals, *J. Am. Chem. Soc.* **126**, 6164–6168 (2004).
7. X. Peng, Mechanisms for the shape-control and shape-evolution of colloidal semiconductor nanocrystals, *Adv. Mater.* **15**, 459–463 (2003).
8. W. W. Yu, Y. A. Wang, and X. Peng, Formation and stability of size-, shape-, and structure-controlled CdTe nanocrystals: Ligand effects on monomers and nanocrystals, *Chem. Mater.* **15**, 4300–4308 (2003).

9. B. D. Reiss, C. Mao, D. J. Solis, K. S. Ryan, T. Thomson, and A. M. Belcher, Biological routes to metal alloy ferromagnetic nanostructures, *Nano Lett.* **4**, 1127–1132 (2004).
10. Z. Tang, B. Ozturk, Y. Wang, and N. A. Kotov, Simple preparation strategy and one-dimensional energy transfer in CdTe nanoparticle chains, *J. Phys. Chem. B* **108**, 6927–6931 (2004).
11. Z. Tang, N. A. Kotov, and M. Giersig, Spontaneous organization of single CdTe nanoparticles into luminescent nanowires, *Science* **297**, 237–240 (2002).
12. G. Wu, L. Zhang, B. Cheng, T. Xie, and X. Yuan, Synthesis of Eu<sub>2</sub>O<sub>3</sub> nanotube array through a facile sol-gel template approach, *J. Am. Chem. Soc.* **126**, 5976–5977 (2004).
13. C. Pacholski, A. Kornowski, and H. Weller, Self-assembly of ZnO: from nanodots to nanorods, *Angew. Chem. Int. Ed.* **41**, 1188–1191 (2002).
14. B. Cheng, J. M. Russell, W. Shi, L. Zhang, and E.T. Samulski, Large-scale, solution-phase growth of single-crystalline SnO<sub>2</sub> nanorods, *J. Am. Chem. Soc.* **126**, 5972–5973 (2004).
15. H. Zhang, J. Sun, D. Ma, X. Bao, A. Klein-Hoffmann, G. Weinberg, D. Su, and R. Schlogl, Unusual mesoporous SBA-15 with parallel channels running along the short axis, *J. Am. Chem. Soc.* **126**, 7440–7441 (2004).
16. Y. Cui, M. T. Bjork, J. A. Liddle, C. Sonnichsen, B. Boussert, and A. P. Alivisatos, Integration of colloidal nanocrystals into lithographically patterned devices, *Nano Lett.* **4**, 1093–1098 (2004).
17. R. Garcia, and M. Tello, Size and shape controlled growth of molecular nanostructures on silicon oxide templates, *Nano Lett.* **4**, 1115–1119 (2004).
18. D. Yang, R. Wang, J. Zhang, and Z. Liu, Synthesis of nickel hydroxide nanoribbons with a new phase: A solution chemistry approach, *J. Phys. Chem. B* **108**, 7531–7533 (2004).
19. Y. C. Cao, Synthesis of square gadolinium-oxide nanoplates, *J. Am. Chem. Soc.* **126**, 7456–7457 (2004).
20. C. Liu, X. Wu, T. Klemmer, N. Shukla, X. Yang, D. Weller, A. G. Roy, M. Tanase, and D. Laughlin, Polyol process synthesis of monodispersed FePt nanoparticles, *J. Phys. Chem. B* **108**, 6121–6123 (2004).
21. X. G. Peng, L. Manna, W. D. Yang, J. Wickham, E. Scher, A. Kadavanich, and A. P. Alivisatos, Shape control of CdSe nanocrystals, *Nature* **404**, 59–61 (2000).
22. V. F. Puentes, K. M. Krishnan, and A. P. Alivisatos, Colloidal nanocrystal shape and size control: The case of cobalt, *Science* **291**, 2115–2117 (2001).
23. L. Pei, K. Mori, and M. Adachi, The formation process of 2-D networked gold nanowires by citrate reduction of AuCl<sub>4</sub><sup>−</sup> and the shape stabilization, *Langmuir* **20**, 7837–7843 (2004).
24. H. Masuda and K. Fukuda, Ordered metal nanohole arrays made by a two-step replication of honeycomb structures of anodic alumina, *Science* **268**, 1466–1468 (1995).
25. H. Masuda, H. Yamada, M. Satoh, H. Asoh, M. Nakao, and T. Tamamura, Highly ordered nanochannel-array architecture in anodic alumina, *Appl. Phys. Lett.* **71**, 2770–2772 (1997).
26. B. B. Lakshmi, P. K. Dorhout, and C. R. Martin, Sol-gel template synthesis of semiconductor nanostructure, *Chem. Mater.* **9**, 857–862, (1997); B. B. Lakshmi, C. J. Patrissi, and C. R. Martin, Sol-Gel template synthesis of semiconductor oxide micro- and nanostructures, **9**, 2544–2550 (1997).
27. R. L. Penn and J. F. Banfield, Imperfect oriented attachment: dislocation generation in defect-free nanocrystals, *Science* **281**, 969–971 (1998).



28. J. F. Banfield, S. A. Welch, H. Zhang, T. T. Ebert, and R. L. Penn, Aggregation-based crystal growth and microstructure development in natural iron oxyhydroxide biomineralization products, *Science* **289**, 751–754.
29. M. Adachi, Y. Murata, J. Takao, J. Jiu, M. Sakamoto, and F. Wang, Highly efficient dye-sensitized solar cells with titania thin film electrode composed of network structure of single-crystal-like TiO<sub>2</sub> nanowires made by “oriented attachment” mechanism, *J. Am. Chem. Soc.* **126**, 14,943–14,949 (2004).
30. F. Wang, J. Jiu, and M. Adachi, Control of TiO<sub>2</sub> morphology via hydrothermal route, in: Proceedings of the 10th Asian Pacific Confederation of Chemical Engineering Congress, Kitakyushu, Japan. 2004.
31. F. Wang, J. Jiu, and M. Adachi, Hydrothermal synthesis of nanosheet quasi-TiO<sub>2</sub> by surfactant-assisted hydrolysis of titanium alkoxide, in: 2004 MRS Fall Meeting, Boston, 2004, abstract GG10.3; F. Wang, J. Jiu, L. Pei, K. Nakagawa, S. Isoda, and M. Adachi, hydrothermal synthesis of highly crystallized Lepidocrocite nanosheets of TiO<sub>2</sub> under low temperature, *Chem. Lett.* **34**, 418–419 (2005).
32. B. O'Regan and M. Grätzel, A low-cost, high-efficiency solar cell based on dye-sensitized colloidal TiO<sub>2</sub> films, *Nature (London)* **353**, 737–740 (1991).
33. Solbrand, H. Lindstrom, H. Rensmo, A. Hagfeldt, and S.-E. Lindquist, Electron transport in the nanostructured TiO<sub>2</sub>-electrolyte system studied with time-resolved photocurrents. *J. Phys. Chem.* **101**, 2514–2518 (1997).
34. S. Nakade, S. Kambe, T. Kitamura, Y. Wada, and S. Yanagida, Effect of lithium ion density on electron transport in nanoporous TiO<sub>2</sub> electrode, *J. Phys. Chem. B* **105**, 9150–9152 (2001).
35. S. Kambe, S. Nakade, T. Kitamura, Y. Wada, and S. Yanagida, Influence of the electrolytes on electron transport in mesoporous TiO<sub>2</sub>-electrolyte system, *J. Phys. Chem.* **106**, 2967–2972 (2002).
36. L. Dloczik, O. Ileperuma, I. Lauermann, L. M. Peter, E. A. Ponomarev, G. Redmond, N. J. Shaw, and I. Uhlendorf, Dynamic response of dye-sensitized nanocrystalline solar cells: Characterization by intensity-modulated photocurrent spectroscopy, *J. Phys. Chem.* **101**, 10,281–10,289 (1997).
37. A. C. Fisher, L. M. Peter, E. A. Ponomarev, A. B. Walker, and K. G. U. Wijayantha, Intensity dependence of the back reaction and transport of electrons in dye-sensitized nanocrystalline TiO<sub>2</sub> solar cells, *J. Phys. Chem. B* **104**, 949–958 (2000).
38. G. Oskam, A. Nellore, R. L. Penn, and P. C. Searson, The growth kinetics of TiO<sub>2</sub> nanoparticles from titanium(IV) alkoxide at high water/titanium ratio, *J. Phys. Chem. B* **107**, 1734–1738 (2003).
39. G. Oskam, Z. Hu, R. L. Penn, N. Pesika, and P. C. Searson, Coarsening of metal oxide nanoparticles, *Phys. Rev. E* **66**, 11,403 (2002).
40. A. P. Alivisatos, Naturally aligned nanocrystals, *Science* **289**, 736 (2000).
41. R. L. Penn and J. F. Banfield, Morphology dependent and crystal growth in nanocrystalline aggregates under hydrothermal conditions: insights from titania, *Geochim. Cosmochim. Acta* **63**, 1549–1557 (1999).
42. C. J. Brinker and G. W. Scherer, *Sol-Gel Science: The Physics and Chemistry of Sol-Gel Processing*, Academic Press, San Diego, CA, 1990, Chap. 3.
43. F. Huang, H. Zhang, and J. F. Banfield, Two-stage crystal-growth kinetics observed during hydrothermal coarsening of nanocrystalline ZnS, *Nano Lett.* **3**, 373–378 (2003).
44. D.-F. Zhang, L.-D. Sun, J.-L. Yin, and C.-H. Yan, Low-Temperature Fabrication of Highly Crystalline SnO<sub>2</sub> Nanorods, *Adv. Mater.* **15**, 1022–1025 (2003).

45. M. Lazzeri, A. Vittadini, and A. Selloni, Structure and energetics of stoichiometric TiO<sub>2</sub> anatase surfaces, *Phys. Rev. B* **63**, 155,409 (2001).
46. P. Hoyer, Semiconductor nanotube formation by a two-step template process, *Adv. Mater.* **8**, 857–859 (1996).
47. P. Hoyer, Formation of titanium dioxide nanotube array, *Langmuir* **12**, 1411–1413 (1996).
48. Y. Lei, L. D. Zhang, and J. C. Fan, Fabrication, characterization and Raman study of TiO<sub>2</sub> nanowire array prepared by anodic oxidative hydrolysis of TiCl<sub>3</sub>, *Chem. Phys. Lett.* **338**, 231–236 (2001).
49. A. Michailowski, D. AlMawlawi, G. Cheng, and M. Moskovits, Highly regular anatase nanotubule arrays fabricated in porous anodic templates, *Chem. Phys. Lett.* **349**, 1–5 (2001).
50. H. Imai, Y. Takei, K. Shimizu, M. Matsuda, and H. Hirashima, Direct preparation of anatase TiO<sub>2</sub> nanotubes in porous alumina membranes, *J. Mater. Chem.* **9**, 2971–2972 (1999).
51. M. Zhang, Y. Bando, and K. Wada, Sol-gel template preparation of TiO<sub>2</sub> nanotubes and nanorods, *J. Mater. Sci. Lett.* **20**, 167–170 (2001).
52. Y. Lei, L. D. Zhang, G. W. Meng, G. H. Li, X. Y. Zhang, C. H. Liang, and S. X. Wang, Preparation and photoluminescence of highly ordered TiO<sub>2</sub> nanowire arrays, *Appl. Phys. Lett.* **78**, 1125–1127 (2001).
53. Z. Miao, D. Xu, J. Ouyang, G. Guo, X. Zhao, and Y. Tang, Electrochemically induced sol-gel preparation of single-crystalline TiO<sub>2</sub> nanowires, *Nano Lett.* **2**, 717–720 (2002).
54. T. Kasuga, M. Hiramatsu, A. Hoson, T. Sekino, and K. Niihara, Formation of titanium oxide nanotube, *Langmuir* **14**, 3160–3163 (1998).
55. T. Kasuga, M. Hiramatsu, A. Hoson, T. Sekino, and K. Niihara, Titania nanotubes prepared by chemical processing, *Adv. Mater.* **11**, 1307–1311 (1999).
56. Z. Shunli, Z. Jingfang, Z. Zhijun, D. Zuliaqng, A. V. Vorontsov, and J. Zhensheng, Morphological structure and physical properties of nanotube TiO<sub>2</sub>, *Chin. Sci. Bull.* **45**, 1533–1536 (2000).
57. D.-S. Seo, J.-K. Lee, and H. Kim, Preparation of nanotube-shaped TiO<sub>2</sub> powder, *J. Crystal Growth* **229**, 428–432 (2001).
58. Y. X. Zhang, G. H. Li, Y. X. Jin, Y. Zhang, J. Zhang, and L. D. Zhang, Hydrothermal synthesis and photoluminescence of TiO<sub>2</sub> nanowires, *Chem. Phys. Lett.* **365**, 300–304 (2002).
59. G. H. Du, Q. Chen, R. C. Che, Z. Y. Yuan, and L.-M. Peng, Preparation and structure analysis of titanium oxide nanotubes, *Appl. Phys. Lett.* **79**, 3702–3704 (2001).
60. B. D. Yao, Y. F. Chan, X. Y. Zhang, W. F. Zhang, Z. Y. Yang, and N. Wang, Formation mechanism of TiO<sub>2</sub> nanotubes, *Appl. Phys. Lett.* **82**, 281–283 (2003).
61. G. R. Patzke, F. Krumeich, and R. Nesper, Oxidic nanotubes and nanorods: Anisotropic modules for a future nanotechnology, *Angew. Chem. Int. Ed.* **41**, 2446–2461 (2002).
62. R. Ma, Y. Bando, and T. Sasaki, Nanotubes of lepidocrocite titanates, *Chem. Phys. Lett.* **380**, 577–582 (2003).
63. T. Peng, A. Hasegawa, J. Qiu, and K. Hirao, Fabrication of titania with high surface area and well-developed mesostructural walls by surfactant-mediated templating method, *Chem. Mater.* **15**, 2011–2016 (2003).
64. A. Chemseddine and T. Moritz, Nanostructuring titania: Control over nanocrystal structure, size, shape, and organization, *Eur. J. Inorg. Chem.* 235–245 (1999).
65. T. Sugimoto, X. Zhou, and A. Muramatsu, Synthesis of uniform anatase TiO<sub>2</sub> nanoparticles by gel-sol method. 4. Shape control, *J. Colloid Interf. Sci.* **259**, 53–61 (2003).

66. R. E. Schaak and T. E. Mallouk, Self-assembly of tiled perovskite monolayer and multilayer thin films, *Chem. Mater.* **12**, 2513–2516 (2000).
67. T. Sasaki, M. Watanabe, H. Hashizume, H. Yamada, and H. Nakazawa, Macromolecule-like aspect for a colloidal suspension of an exfoliated titanate. Pairwise association of nanosheets and dynamic reassembling process initiated from it, *J. Am. Chem. Soc.* **118**, 8329–8335 (1996).
68. Y. Omomo, T. Sasaki, L. Wang, and M. Watanabe, Redoxable nanosheet crystallites of  $\text{MnO}_2$  derived via delamination of a layered manganese oxide, *J. Am. Chem. Soc.* **125**, 3568–3575 (2003).
69. R. E. Schaak and T. E. Mallouk, Prying apart Ruddlesden–Popper phase: Exfoliation into sheets and nanotubes for assembly of perovskite thin films, *Chem. Mater.* **12**, 3427–3434 (2000).
70. T. Tanaka, Y. Ebina, K. Takada, K. Kurashima, and T. Sasaki, Oversized titania nanosheet crystallites derived from flux-grown layered titanate single crystals, *Chem. Mater.* **15**, 3564–3568 (2003).
71. Q. Gao, O. Giraldo, W. Tong, and S. L. Suib, Preparation of nanometer-sized manganese oxides by intercalation of organic ammonium ions in synthetic Birnessite OL-1, *Chem. Mater.* **13**, 778–786 (2001).
72. L. Wang, Y. Omomo, N. Sakai, K. Fukuda, I. Nakai, Y. Ebina, K. Takada, M. Watanabe, and T. Sasaki, Fabrication and characterization of multilayer ultrathin films of exfoliated  $\text{MnO}_2$  nanosheets and polycations, *Chem. Mater.* **15**, 2873–2878 (2003).
73. T. Sasaki, Y. Ebina, Y. Kitami, and M. Watanabe, Two-dimensional diffraction of molecular nanosheet crystallites of titanium oxide, *J. Phys. Chem. B* **105**, 6116–6121 (2001).
74. T. Sasaki and M. Watanabe, Semiconductor nanosheet crystallites of quasi- $\text{TiO}_2$  and their optical properties, *J. Phys. Chem. B* **101**, 10,159–10,161 (1997).
75. A. Hagfeldt and M. Grätzel, Molecular photovoltaics, *Acc. Chem. Res.* **33**, 269–277 (2000).
76. M. Grätzel, Photoelectrochemical cells, *Nature* **414**, 338–344 (2001).
77. M. Grätzel, Dye-sensitized solar cells, *J. Photochem. Photobiol. C: Photochem. Rev.* **4**, 145–153 (2003).
78. J. Bisquert, D. Cahen, G. Hodes, S. Ruhle, and A. Zaban, Physical chemical principle of photovoltaic conversion with nanoparticulate, mesoporous dye-sensitized solar cells, *J. Phys. Chem.* **108**, 8106–8118 (2004).
79. M. Grätzel, Conversion of sunlight to electric power by nanocrystalline dye-sensitized solar cells, *J. Photochem. Photobiol. A: Chemistry* **164**, 3–14 (2004).
80. M. K. Nazeeruddin, A. Kay, I. Rodicio, B. R. Humphry, E. Mueller, P. Liska, N. Vlachopoulos, and M. Grätzel, Conversion of light to electricity by *cis*-X2bis(2,2'-bipyridyl-4,4'-dicarboxylate)ruthenium(II) charge-transfer sensitizers ( $\text{X} = \text{Cl}^-$ ,  $\text{Br}^-$ ,  $\text{I}^-$ ,  $\text{CN}^-$ , and  $\text{SCN}^-$ ) on nanocrystalline  $\text{TiO}_2$  electrodes, *J. Am. Chem. Soc.* **115**, 6382–6390 (1993).
81. V. Shklover, Yu. E. Ovchinnikov, L. S. Braginsky, S. M. Zakeeruddin, and M. Grätzel, Structure of organic/inorganic interface in assembled materials comprising molecular components. Crystal structure of sensitizer bis[(4,4'-carboxy-2,2'-bipyridine) (thiocyanate)]ruthenium(II), *Chem. Mater.* **10**, 2533–2541 (1998).
82. Md. K. Nazeeruddin, R. Humphry-Baker, P. Liska, and M. Grätzel, Investigation of sensitizer adsorption and the influence of protons on current and voltage of a dye-sensitized nanocrystalline  $\text{TiO}_2$  solar cell, *J. Phys. Chem. B* **107**, 8981–8987 (2003).

83. A. Fillinger and B. A. Parkinson, The adsorption behavior of a ruthenium-based sensitizing dye to nanocrystalline  $\text{TiO}_2$ . Coverage effect on the external and internal sensitization quantum yields, *J. Electrochem. Soc.* **146**, 4559–4564 (1999).
84. M. Grätzel, Molecular photovoltaics that mimic photosynthesis, *Pure Appl. Chem.* **73**, 459–467 (2001).
85. A. Vittadini, A. Selloni, F. P. Rotzinger, and M. Grätzel, Formic acid adsorption on dry and hydrated  $\text{TiO}_2$  anatase (101) surfaces by DFT calculations, *J. Phys. Chem. B* **104**, 1300–1306 (2000).
86. K. Finnie, J. R. Bartlett, and J. L. Woolfrey, Vibrational spectroscopic study of the coordination of (2,2'-bipyridyl-4,4'-dicarboxylic acid)ruthenium(II) complexes to the surface of nanocrystalline titania, *Langmuir* **14**, 2744–2749 (1998).
87. C. Bauer, G. Boschloo, E. Mukhtar, and A. Hagfeldt, Interfacial electron-transfer dynamics in  $\text{Ru}(\text{tcterpy})(\text{NCS})_3$ -sensitized  $\text{TiO}_2$  nanocrystalline solar cells, *J. Phys. Chem. B* **106**, 12,693–12,704 (2002).

# 3

## Soft Synthesis of Inorganic Nanorods, Nanowires, and Nanotubes

SHU-HONG YU<sup>†,‡</sup> AND YI-TAI QIAN<sup>†,‡</sup>

<sup>†</sup>*Division of Nanomaterials and Chemistry, Hefei National Laboratory for Physical Sciences at Microscale, University of Science and Technology of China, Hefei 230026, People's Republic of China* and <sup>‡</sup>*Departments of Chemistry, University of Science and Technology of China, Hefei 230026, People's Republic of China*

### 3.1. Introduction

In the past decades, synthesis of low-dimensional materials such as nanometer-size inorganic dots, wires, and tubes, which exhibit a wide range of electronic and optical properties that depend sensitively on both size and shape, has been of both fundamental and technological interest.<sup>1–4</sup> They are potentially ideal building blocks for nanoscale electronics and optoelectronics<sup>5</sup> because of their important nonlinear optical properties,<sup>6</sup> luminescent properties,<sup>7,8</sup> quantum size effects,<sup>9,10</sup> and other important physical and chemical properties.<sup>11</sup> The ability to control the shapes of semiconductor nanocrystals affords an opportunity to further test theories of quantum confinement and yields samples with desirable optical characteristics from the point of view of application.<sup>12,13</sup> One of the current hottest issues in nanotechnology and nanoscience is how to finely control the size, shape, and dimensionality of the nanocrystals because of their important applications in designing new materials and devices such as biological assays,<sup>14–16</sup> semiconductor nanodevices,<sup>17</sup> hybrid nanorods–polymer solar cells,<sup>18</sup> room-temperature ultraviolet (UV) lasing using ZnO nanowires arrays,<sup>19</sup> light-emitting diodes (LEDs),<sup>5</sup> and nanosensors for biological and chemical species.<sup>20,21</sup> Shape control has raised significant concern in the fabrication of semiconductor nanocrystals,<sup>13</sup> metal nanocrystals,<sup>22</sup> and other inorganic materials,<sup>23</sup> which may add alternative variables in tailoring the properties of nanomaterials and provide more possibilities in the fabrication of nanodevices. The ability of shape control over the crystals is still rather limited due to a lack in understanding the principles and mechanics about the formation of low-dimensional nanostructures. How to assemble individual atoms into one-dimensional (1D) nanostructures in an effective and controllable way remains a challenge.<sup>24</sup>

Several reviews have been published on the synthesis of various kinds of inorganic nanowire or nanorod,<sup>24–26</sup> oxide nanorod, and nanotube,<sup>27</sup> which already gave a general survey on the synthetic methodologies by mostly applied high-temperature approaches or hard template approaches.

In this chapter, we will give a general overview of the current state-of-the-art on the variety of different soft synthesis routes of low-dimensional nanocrystals with

focus on nanorods, nanowires, and nanotubes. Especially, we will introduce some promising new soft strategies for the synthesis of low-dimensional nanocrystals, as well as more complex structures. In Section 3.2, a general overview on the current status of the synthetic routes for the synthesis of various low-dimensional nanocrystals will be given. Then, we will focus on the emerging soft approaches for the synthesis of various important inorganic nanorods, nanowires, nanotubes, and other hierarchical nanostructures with complex structural features (Section 3.3). Finally, our own perspectives on this field will be given (Section 3.4).

## 3.2. An Overview: Emerging Synthetic Routes for the Synthesis of Low-Dimensional Nanocrystals

One obvious characteristic of low-dimensional nanostructures is that they are anisotropic nanocrystals with large aspect ratios (length/diameter). The strategies for growing such highly anisotropic solid nanostructures usually involve nucleation and growth stages as described previously for the crystallization of a solid from a vapor, a liquid, or a solid phase.<sup>28,29</sup> Based on the basic nucleation and crystal growth theories, the basic building units (atoms, ions, or molecules) of a solid will form nuclei or clusters if their concentrations are supersaturated; then they will start to self-assemble into larger clusters or nanocrystals by directional aggregation, accompanying the crystallization process and transformation process and, finally, form highly anisotropic nanocrystals.

Generally, the synthetic strategies of low-dimensional nanostructures can be classified into two types: the “hard” approaches and the “soft” approaches, according to the synthetic characteristics and reaction conditions.

### 3.2.1. “Hard” Approaches

Among the “hard” approaches, usually foreign hard templates or drastic reaction conditions are needed; for example, the reaction media was usually a gas phase while the high vacuum system and high temperature were applied. The main existing “hard” approaches for synthesis of 1D nanomaterials include four types:

- Template-directed growth method, in which the hard templates such as carbon nanotubes<sup>1,2,30,31</sup> and porous aluminum template are used.<sup>32–35</sup>
- Vapor–liquid–solid (VLS) mechanism, which was previously proposed by Wagner and Elhs in the 1960s.<sup>28</sup> This mechanism has been applied for the synthesis of various semiconductor nanowires.<sup>36–41</sup> A laser-ablation-based VLS catalytic growth process (LCG) allows one to synthesize semiconductor nanowires with many different compositions.<sup>42</sup>
- Vapor–solid (VS) mechanism,<sup>29</sup> in which the nanowires were generated directly from vapor condensation onto a substrate. Various metal oxides such as MgO, Al<sub>2</sub>O<sub>3</sub>, ZnO, and SnO<sub>2</sub> nanowires or nanobelts were grown by either a carbon-thermal reduction process<sup>43,44</sup> or direct thermal evaporation.<sup>45,46</sup>

- Oxide-assisted nanowires growth route,<sup>47–52</sup> which was reported by Lee’s group for growing GaAs, GaN nanowires, and Si nanowires with the advantage of using neither a metal catalyst nor a template.

### 3.2.2. “Soft” Approaches

Currently, a challenge in synthetic chemistry and materials science is how the traditional solid-state reaction can be conducted in round-bottom flasks in order to turn down the heat for the fabrication of crystals.<sup>53,54</sup> Recent development in soft solution processing may provide an alternative, convenient, lower-temperature, and environmentally friendly pathway for the fabrication of advanced ceramic materials with desirable shapes and sizes.<sup>55</sup> So-called “soft” approaches are based on solution chemistry and do not need a foreign hard template. It does not involve using drastic conditions (i.e., high temperature, high pressure, etc.), and the reaction is usually initiated under mild conditions or under natural conditions.

There are diverse soft routes for the synthesis of low dimensional nanocrystals; they are listed in Tables 3.1 and 3.2. Some intensive reviews on the synthesis

TABLE 3.1. Synthetic routes for oxide low-dimensional nanocrystals (published since 1995).

Nanomaterials	Synthetic method	Ref.
BaTiO <sub>3</sub> NRs and SrTiO <sub>3</sub> NRs	Solution-phase decomposition of bimetallic alkoxide precursors in the presence of coordinating ligands	82
BaSO <sub>4</sub> NWs and superstructures	Mineralization from aqueous solution in presence of polymers	67,83, 85
BaCrO <sub>4</sub> NWs and chain structures	Reversed micelle templating method	23,84
BaCrO <sub>4</sub> NWs and superstructures	Mineralization from aqueous solution in presence of polymers	84,86
BaCO <sub>3</sub> NWs	A reverse-micelle-based approach	69
CaCO <sub>3</sub> NWs	A reverse-micelle-based approach	87
BaWO <sub>4</sub> NRs	Reversed micelle templating method	70
BaWO <sub>4</sub> NWs	Catanionic reverse micelles	71
BaWO <sub>4</sub> NWs arrays	Langmuir–Blodgett assembly of 1D nanostructures	88,89
CaSO <sub>4</sub> NWs	A water-in-oil microemulsions route	90
CdWO <sub>4</sub> Nanosheets	Hydrothermal treatment in the presence of block copolymers	91
CdWO <sub>4</sub> NBs	Double jet reaction at room temperature	91
CdWO <sub>4</sub> NRs	Hydrothermal treatment of CdCl <sub>2</sub> and Na <sub>2</sub> WO <sub>4</sub>	92
MWO <sub>4</sub> NRs	Hydrothermal treatment of M <sup>2+</sup> and Na <sub>2</sub> WO <sub>4</sub> (M = Zn, Fe, Mn)	93
Bi <sub>2</sub> WO <sub>4</sub> NRs	Hydrothermal process	93
Ag <sub>2</sub> WO <sub>4</sub> NRs	Hydrothermal process	93
Ag <sub>2</sub> W <sub>2</sub> O <sub>7</sub> NRs	Hydrothermal process	93
Ag <sub>6</sub> Mo <sub>10</sub> O <sub>33</sub> NRs	Hydrothermal process	94
Co <sub>3</sub> O <sub>4</sub> NRs	Calcination of precursor powders prepared in a novel inverse microemulsion	95

(cont.)

TABLE 3.1. (Continued)

Nanomaterials	Synthetic method	Ref.
Eu <sub>2</sub> O <sub>3</sub> NRs	Sonication of an aqueous solution	96
Fe <sub>2</sub> O <sub>3</sub> NRs	Grown onto a polycrystalline (or single-crystalline) substrate from an aqueous solution of ferric salts	97
Fe <sub>3</sub> O <sub>4</sub> NRs	Sonication of aqueous iron(II) acetate in the presence of $\beta$ -cyclodextrin	98
Fe <sub>4</sub> [Fe(CN) <sub>6</sub> ] <sub>3</sub> · xH <sub>2</sub> O NWs	Electrodeposition with two-step anodizing anodic aluminum oxide films	99
TiO <sub>2</sub> NTs	Soft chemistry route	100
LnPO <sub>4</sub> NWs	Hydrothermal synthesis	101
LaPO <sub>4</sub> :Eu NWs	Hydrothermal synthesis	102
LaPO <sub>4</sub> :Ce NWs	Hydrothermal synthesis	102
Mg(OH) <sub>2</sub> NRs	Hydrothermal reaction of Mg, H <sub>2</sub> O, and ethylenediamine	103
MnO <sub>2</sub> NRs	Hydrothermal synthesis	104
Mg <sub>2.11</sub> Mn <sub>5.46</sub> O <sub>12</sub> · xH <sub>2</sub> O Nanoribbons	A combination of techniques consisting of a sol-gel process for tetraethylammonium manganese oxide layered material, an ion-exchange method to a thin-film Mg-buserite precursor, and a hydrothermal reaction to transform the Mg-buserite to nanoribbonlike Mg-todorokite material	105
MoO <sub>3</sub> NRs	Template-directed reaction of molybdic acid and subsequent leaching process	106
Ni(OH) <sub>2</sub> NRs	Hydrothermal Synthesis and deposition in a carbon-coated anodic alumina film	107
Sb <sub>2</sub> O <sub>3</sub> NRs	Microemulsion method for the system AOT–water–toluene	108
Sb <sub>2</sub> O <sub>3</sub> NRs	Microemulsion method for the system AOT–water–toluene	109
TiO <sub>2</sub> NWs	Electrochemically preparation using nanochannel alumina	110
TiO <sub>2</sub> NWs	Sol-gel template method employing alumina membranes	111
TiO <sub>2</sub> NWs	Electrochemically induced sol-gel preparation	112
TiO <sub>2</sub> NTs	Sol-gel-derived fine TiO <sub>2</sub> -based powders treated with NaOH aqueous solution	113
TiO <sub>2</sub> NTs	Solution growth method by hydrolyzing TiF <sub>4</sub> under acidic condition	114
TiO <sub>2</sub> NWs	Spontaneous self-organization	79
VO <sub>x</sub> NTs	Hydrothermal using long-chain amine as templates	115,116
V <sub>2</sub> O <sub>5</sub> NRs	Vanadium pentoxide gels	117
ZnO NWs arrays	Electrodeposited in the pores of anodic alumina membranes	118
ZnO NRs	Orientated attachment growth from ZnO nanoparticles from solution	80
ZnO helical NRs	Biomimetic controlled nucleation and growth on ZnO nanorods arrays	119
Dy(OH) <sub>3</sub> NTs	Hydrothermal synthesis	120
Dy <sub>2</sub> O <sub>3</sub> NTs	Hydrothermal synthesis	120
Ln(OH) <sub>3</sub> NWs (Ln = lanthanide)	Hydrothermal synthesis	121,122



TABLE 3.2. Synthetic routes for nonoxide low-dimensional nanocrystals (published since 1995)

Nanomaterials	Synthetic method	Ref.
Ag ultrathin NWs	Grow inside the pores of self-assembled organic nanotubes by electro-/photochemical redox reaction in an ambient aqueous phase	123
Ag NWs	Templated from the mesoporous silica	124,125
Ag NWs	Metal nanowires formation using $\text{Mo}_3\text{Se}_3^-$ as reducing and sacrificing templates	126
Ag NRs and dendrites	Ultraviolet photoreduction technique at room temperature using poly(vinyl-alcohol) (PVA) as protection agent	127
Ag NRs, NWs	Seed-mediated growth in a rodlike micellar media	128
Ag nanoprisms	A photoinduced method for converting large quantities of silver nanospheres into triangular nanoprisms	129
Ag NWs	Templated from AgBr nanocrystals	130
Ag nanoarrays	Formed inside micellar arrays of a template consisting of a (dendritic polysilane)/polyisocyanide block copolymer reduced under the TEM electron beam	131
Ag NWs	Solid-liquid phase arc discharge method	132
Ag truncated triangular nanoplates	A solution phase method in the presence of cetyltrimethylammonium bromide micelles	133
Ag nanodics	Mixing two reverse-micellar solutions	134
Ag nanoprisms	Boiling $\text{AgNO}_3$ in <i>N,N</i> -dimethyl formamide, in the presence of poly(vinylpyrrolidone)	135
Ag NWs	Solvothermal reaction using Pt nanoparticles as seeds in ethylene glycol at 160°C	136
Au NRs	Electrochemical oxidation/reduction within a simple two-electrode-type cell in the presence of cationic surfactant $\text{C}_{16}\text{TAB}$	137
Au NWs	Templated from the mesoporous silica	125
Au NWs	Metal nanowires formation using $\text{Mo}_3\text{Se}_3^-$ as reducing and sacrificing templates	126
Au NRs	A solution seeding growth approach in the presence of an aqueous micellar template CTAB	138,139
Au NRs	UV-irradiation of $\text{HAuCl}_4$ solutions with 253.7-nm light in the presence of rodlike micelles of hexadecyltrimethylammonium chloride	140
Au NWs	DNA-directed assembly of gold nanowires on complementary surfaces	141
2D Au NWs	Self-assembly of gold nanoparticles on water surfaces in the presence of surfactants	142
$\text{Au}_{\text{core}}\text{Ag}_{\text{shell}}$ NRs	Reducing $\text{AgCl}_4^{3-}$ (aq) with $\text{NH}_2\text{OH}$ selectively on the surface of gold NRs	143
Co NRs	The early stage of the thermal decomposition of $\text{Co}_2(\text{CO})_8$ in a mixture of oleic acid and TOPO	144
Cu NRs	Microemulsions and reverse micelles	145
Fe NRs	Thermal decomposition of organometallic precursor ( $\text{Fe}(\text{CO})_5$ ) in the presence of a stabilizing surfactant trioctylphosphine oxide (TOPO) at 340°C under argon atmosphere.	146
In NWs	Room-temperature organometallic route by using long-chain amines (hexadecylamine) as templates	147

(cont.)

TABLE 3.2. (Continued)

Nanomaterials	Synthetic method	Ref.
In <sub>3</sub> Sb NWs	Room-temperature organometallic route by using long-chain amines (hexadecylamine) as templates	147
Ni NRs	Surfactants hexadecylamine (HDA) or trioctylphosphineoxide (TOPO) as capping agents in THF	148
Pb NWs	The nanowires were embedded in tracked-etched polycarbonate membranes by electrodeposition	149
Pd tetrahedras and octahedras	Reduction of metal ions in sodium dodecyl sulfate (SDS)/poly(acrylamide) gel by UV irradiation	150
Pd dendrites	Ultrasonically assisted synthesis by using skeleton nickel as templates	151
Pt Tetrahedra	Tetrahedral, cubic, irregular-prismatic, icosahedral, and cube-octahedral particle shapes were prepared using sodium polyacrylate as capping agent	22
CoPt alloy NWs	Solvothermal reaction of platinum acetylacetonate and cobalt carbonyl compound in ethylenediamine solvent	152
Bi NWs	Decomposition of a precursor in the presence of a polymer	153
Bi NTs	Hydrothermal reduction reaction	154,155
Ge NWs	Liquid–solution synthesis, reduction of GeCl <sub>4</sub> and phenyl-GeCl <sub>3</sub> by sodium metal in an alkane solvent at elevated temperature and pressure.	62
Ge NWs	Nucleation and growth seeded by organic monolayer-coated Au nanocrystals	156
Si NWs	Supercritical fluid solution-phase growth, SLS	63
Si NWs arrays	Electrochemistry approach by etching Si wafer in HF solution containing AgNO <sub>3</sub>	157
Carbon-Sheathed Sn-Pb NWs	Electrolytic formation of carbon-sheathed mixed Sn-Pb nanowires,	158
C@Ag NWs	Hydrothermal carbonization of starch solution in the presence Ag <sup>+</sup>	159
Se NWs	Using cytochrome-c <sub>3</sub> to make selenium nanowires,	160
Se NWs	Solution phase process	161,162
Te NTs	Reflexing a solution of orthotelluric acid in ethylene glycol at ~197° C	163
Te nanobelts, NTs, Nanohelices	Controlled hydrothermal route by reaction of sodium tellurite (Na <sub>2</sub> TeO <sub>3</sub> ) in aqueous ammonia solution at 180° C.	164
C, NTs	Solvothermal reaction of hexachlorobenzene with potassium in the presence of Co/Ni catalyzer at 350° C	165
C, hollow vessels	Solvothermal reaction of NaNH <sub>2</sub> and Co/Ni alloy in CCl <sub>4</sub> at 190–230° C	166
BaF <sub>2</sub> NWs	Microemulsion-mediated hydrothermal synthesis	167
GaAs NWs	Solution–liquid–solid growth, SLS	54,61
GaP NRs	Solution–liquid–solid growth, SLS	54,60
GaP NRs	Thermal decomposition of Ga(PtBu <sub>2</sub> ) <sub>3</sub> in trioctylamine (TOA), which was injected into a mixture of TOA and hexadecylamine (HDA) at 330° C	168
Al <sub>x</sub> Ga <sub>1-x</sub> As NRs	Solution–liquid–solid growth, SLS	61
InAs NRs	Solution–liquid–solid growth, SLS	54
InP NRs	Solution–liquid–solid growth, SLS	54
FeP NWs	Solution route	169

TABLE 3.2. (Continued)

Nanomaterials	Synthetic method	Ref.
InN NWs	Solution state thermolysis of the dialkyl(azido)indane precursor	170
Si <sub>3</sub> N <sub>4</sub> NRs	Solvothermal reaction of SiCl <sub>4</sub> with NaN <sub>3</sub> at 670°C.	171
C <sub>3</sub> N <sub>4</sub> NTs	Solvothermal reaction of C <sub>3</sub> N <sub>3</sub> Cl <sub>3</sub> with NaN <sub>3</sub> in benzene at 220°C	172
SiC NWs	Solvothermal reaction	173
TiC NRs	Solvothermal reaction using C <sub>2</sub> Cl <sub>4</sub> , Ti and N-containing nucleophilic solvents	174
MMo <sub>3</sub> Se <sub>3</sub> NWs	Cation exchange in organic solution (M = Li <sup>+</sup> , Na <sup>+</sup> , Rb <sup>+</sup> , Cs <sup>+</sup> , NMe <sup>4+</sup> )	175
CdS NWs	Electrodeposit in porous anodic aluminum oxide templates	35,176
CdS NRs	Solvothermal reactions in ethylenediamine media	177,178
CdS NRs	Solvothermal reaction in <i>n</i> -butylamine	179
CdS NRs, Twinrod-, tetrapod-shaped	Solvothermal reaction in ethylenediamine media	180
CdS NWs	Polymer-controlled growth	181
Flat CdS Triangle	Using Cd(AOT) <sub>2</sub> /isooctane/H <sub>2</sub> O	182
CdS, CdSe NRs	Arrested precipitation from inorganic ions in a CTAB micellar solution	183
CdS, CdSe NRs	Controlled synthesis of multi-armed architectures using monosurfactant hexadecylamine (HAD)	184
CdSe NWs arrays	Electrodeposit in porous anodic aluminum oxide templates	185
CdSe NRs and other shape	Growth of the nanoparticles in a mixture of hexylphosphonic acid and trioctylphosphine oxide	13,64 186
CdSe NRs	Capping agent driven solution reaction using CdO as precursor	187
CdSe NRs	Solvothermal reaction in ethylenediamine	177,188
CdSe NRs	Solvothermal reaction in <i>n</i> -butylamine	179
CdSe NWs	PVA-assisted solvothermal synthesis	189
CdSe nanorods and dendrites	Hydrothermal method	190
CdS/ZnS Shells on CdSe NRs	Epitaxial growth of graded CdS/ZnS shells on colloidal CdSe NRs	191
CdTe NWs	Electrodeposition in alumina membrane	32
CdTe NRs	Capping agent driven solution reaction using CdO as precursor	187
CdTe NWs	Spontaneous oriented attachment from nanoparticles	81
CdTe NRs	Solvothermal reaction	177
CdTe NWs	PVA-assisted solvothermal synthesis	189
Cd <sub>x</sub> Se <sub>1-x</sub>	Solvothermal reaction	192
PbS NRs	Confined growth within the channels of mesoporous silica SBA-15	193
PbS NRs	Oriented growth in the presence of surfactant	194
Closed PbS NWs	Solvothermal reaction in the presence of poly[ <i>N</i> -(2-aminoethyl) acrylamide] in ethylenediamine/H <sub>2</sub> O (3:1, v/v) solvent.	195
PbS NRs	Solvothermal interface reaction route	196
PbSe NWs	Solution reaction at room temperature	197

(cont.)

TABLE 3.2. (Continued)

Nanomaterials	Synthetic method	Ref.
PbSe NWs arrays	Direct current electrodeposition within anodic alumina membrane	198
ZnS NWs	Synthesis in liquid crystal systems	199
ZnS NWs	Simultaneous formation in a liquid crystal template by gamma-irradiation	200
ZnS NWs	Micelle-template inducing synthesis	201
ZnS nanosheets	Templating from a sheet-like molecular precursor $\text{ZnS} \cdot (\text{NH}_2\text{CH}_2\text{CH}_2\text{NH}_2)_{0.5}$	202
ZnSe NRs	Solvothermal reaction in <i>n</i> -butylamine	179
ZnSe NWs	Solvothermal reaction in ethylenediamine	188
ZnSe NWs	Electrodeposition in a porous alumina film	203
ZnTe NRs	Thermal decomposition of a monomeric molecular precursor, [Zn(TePh) <sub>2</sub> ][TMEDA]	204
ZnTe NRs	Thermal decomposition of the precursor derived from a solvothermal reaction using Zn, Te, and $\text{N}_2\text{H}_4 \cdot \text{H}_2\text{O}$ as reactants	205
Bi <sub>2</sub> S <sub>3</sub> NWs	Solvothermal decomposition process	206,207
Bi <sub>2</sub> S <sub>3</sub> NRs	Hydrothermal ripening and crystallization	208
Bi <sub>2</sub> S <sub>3</sub> NWs arrays	Electrochemical deposition	209
Bi <sub>2</sub> Se <sub>3</sub> flakes	Solvothermal reaction	210
Bi(S, Se) NWs	Solvothermal reaction	211
Bi <sub>2</sub> Te <sub>3</sub> NWs arrays	Electrodeposition into porous alumina membrane	212,213
	Pulsed electrodeposition in anodic alumina membranes	214
Sb <sub>2</sub> S <sub>3</sub> NRs	Solvothermal decomposition process	215
Sb <sub>2</sub> S <sub>3</sub> NRs	Electrodeposition within a porous polycarbonate membrane	216
Sb <sub>2</sub> Se <sub>3</sub> NWs	Solvothermal reaction of SbCl <sub>3</sub> and Se with Na <sub>2</sub> SO <sub>3</sub> in ethylene glycol	217
Ag <sub>2</sub> S NRs	Room-temperature solution-growth method with AgNO <sub>3</sub> , thiourea, and NaOH as the reagents	218
Ag <sub>2</sub> Se NWs	Solution reaction using Se nanowires as templates	219,220
Cu <sub>2</sub> S NWs	Growth on copper surface at room temperature	221
Cu <sub>2</sub> S/Au core/sheath NWs	Redox deposition method	222
CuS NTs	Organic amine-assisted hydrothermal process	223
MnS NRs and Cd <sub>1-x</sub> Mn <sub>x</sub> S NRs	Thermal decomposition of Mn(S <sub>2</sub> CNEt <sub>2</sub> ) <sub>2</sub> or Cd(S <sub>2</sub> CNEt <sub>2</sub> ) <sub>2</sub> in the presence of hexadecylamine	224
MoS <sub>2</sub> NWs	Solvothermal reaction	225
SnS <sub>2</sub> nanoflakes	Thermal decomposition of (CH <sub>2</sub> CH <sub>2</sub> CH <sub>2</sub> CH <sub>3</sub> ) <sub>4</sub> Sn	226
CdIn <sub>2</sub> S <sub>4</sub> NRs	Converting CdS nanorods via the hydrothermal reaction	227
CuInS <sub>2</sub> NRs	Solvothermal reaction of In(S <sub>2</sub> CNEt <sub>3</sub> ) <sub>3</sub> and Cu(S <sub>2</sub> CNEt <sub>2</sub> ) <sub>2</sub> in ethylenediamine	228
AgInS <sub>2</sub> NRs	Solvothermal reaction of In(S <sub>2</sub> CNEt <sub>3</sub> ) <sub>3</sub> and Ag(S <sub>2</sub> CNEt <sub>2</sub> ) in ethylenediamine	228
AgBiS <sub>2</sub> NRs	Solvothermal process by using AgCl, BiCl <sub>3</sub> , and K <sub>2</sub> S in ethylenediamine	229
Ag <sub>3</sub> CuS <sub>2</sub> NRs	Hydrothermal reaction by using AgCl and CuCl and thiourea as reactants	230
Cu <sub>3</sub> SnS <sub>4</sub> NRs	Solvothermal reaction using CuCl <sub>2</sub> ·2H <sub>2</sub> O, SnCl <sub>4</sub> ·5H <sub>2</sub> O, CH <sub>3</sub> CSNH <sub>2</sub> as reactants in absolute ethanol	231
PbSnS <sub>3</sub> NRs	An iodine transport hydrothermal route	232

of semiconductor nanodots (0D) have been reviewed recently<sup>56,57</sup> however, we only focus on 1D and 2D nanomaterials such as nanowires (NWs), nanorods (NRs), nanobelts (NBs), nanoribbons, nanotubes (NTs), nanosheets (2D), and more complex structures in this review. Table 3.1 provides a general survey on various oxide nanorods, nanowires, nanotubes, and nanobelts or other novel/new nanostructures prepared by distinct soft strategies. Table 3.2 gives an intensive survey on the nonoxide inorganic nanomaterials such as metal, semiconductor, and carbide- or nitride-based nanomaterials (nanorods, nanowires, nanotubes, nanoribbons, nanobelts, etc.) based on soft approaches. We will only focus on the emerging main or general approaches developed in recent years:

- Hydrothermal/solvothermal process, which has been emerging as a versatile solution route for the synthesis of various semiconductor nanocrystals with different sizes and shapes.<sup>27,58</sup>
- Solution–liquid–solid (SLS) mechanism, which is used for growing III–V group nanofibers in hydrocarbon solvents at a relative low temperature.<sup>53,54,59–61</sup> Group IV Ge, Si nanowires can also be generated by a supercritical fluid solution-phase approach.<sup>62,63</sup>
- Capping agents/surfactants assisted synthesis of well-defined nanostructures and superstructures under either hot conditions or natural/mild conditions.<sup>13,23,64–71</sup>
- Bio-inspired approach for the synthesis of nanofibers and complex superstructures.<sup>65,72</sup> Soft templates such as polymers, organic additives, or supramolecular templates have been widely employed as crystal growth modifiers and templates. The selective adsorption of polymers on specific surfaces can break down the three-dimensional (3D) symmetry of the interaction between the nanosized building blocks into dimensional-specific communication, which results in the controlled 3D self-assembly.<sup>73</sup>
- Oriented attachment growth mechanism.<sup>74–77</sup> The spontaneous aggregation of smaller nanoparticles into well-defined nanostructures has been reported in the case of TiO<sub>2</sub>,<sup>74,78,79</sup> ZnO,<sup>80</sup> and CdTe.<sup>81</sup>

### 3.3. Soft Synthesis of Low-Dimensional Nanocrystals

#### 3.3.1. Hydrothermal/Solvothermal Processes

As one kind of solution-based chemical processes, the hydrothermal process has been widely used for the synthesis of a vast range of solid-state compounds such as oxides, sulfides, halides,<sup>233–236</sup> molecular, zeolites, and other microporous phases<sup>236</sup> since the pioneering work from the 1960s to 1980s. In recent years, this approach has been extended for the synthesis of various kinds of functional oxides<sup>27</sup> and nonoxide nanomaterials<sup>58</sup> with specific shape and size.

Hydrothermal synthesis can be defined as the use of water as a solvent in a sealed reaction container when the temperature is raised above 100°C. Under these conditions, autogeneous pressure (i.e., self-developing and not externally applied)

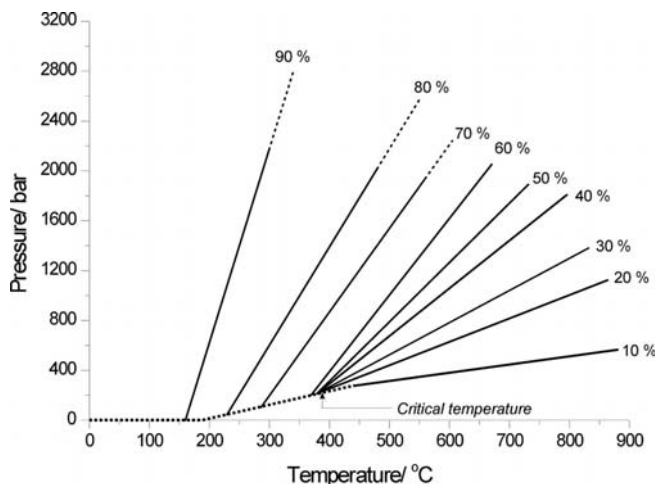


FIGURE 3.1. Pressure as a function of temperature and percentage fill of water in a sealed vessel.<sup>233,237</sup>

is developed. The pressure within the sealed reaction container is found to not only increase dramatically with temperature but also will depend on other experimental factors, such as the percentage fill of the vessel and any dissolved salts. Figure 3.1 shows these data and demonstrates, first, the dramatic rise in pressure when a high percentage fill of reaction vessel is used and, second, how the pressure inside the reaction container can be controlled by the choice of temperature and/or the volume of solvent used. Below the critical point of water, and even below 200°C, a high percentage fill allows access to pressures of hundreds of atmospheres.<sup>237</sup>

The use of hydrothermal conditions can exert significant effects on the reactivity of inorganic solids and the solubility of the compounds under conditions of elevated pressure and temperature. The chemical reactivity of usually insoluble reagents can be much enhanced and many sluggish solid-state reactions can be initiated under hydrothermal conditions. Usually, hydrothermal synthesis often applied higher temperatures (above 300°C) and often took place in the supercritical regime. However, even milder reaction conditions (temperature <250°C) can be applied not only to provide a convenient low-temperature route to materials with practical application but also in the exploratory synthesis of new solids.<sup>237,238</sup>

In recent years, the concepts embodied in the hydrothermal process have been extrapolated to a nonaqueous system; therefore, its counterpart, the so-called “solvothral process” emerges, in which an organic solvent is used as the reaction media instead of water at elevated temperatures near its boiling point. As the counterpart of the hydrothermal process, the solvothral process has emerged in recent years and has received great attention in synthetic chemistry and materials science.

The solvothral reaction is usually performed in a Teflon-lined stainless-steel autoclave, as shown in Fig. 3.2. The use of an autoclave is necessitated by the

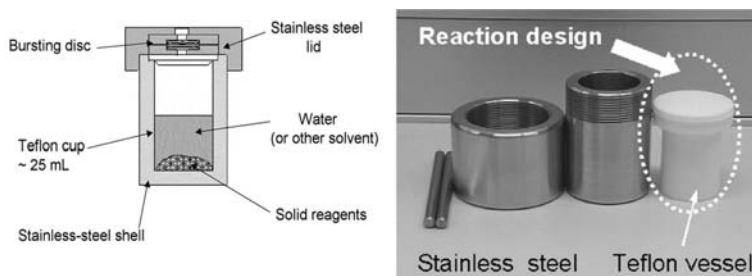


FIGURE 3.2. Left: Schematic of a Teflon-lined, stainless-steel autoclave typically used in the laboratory to perform subcritical solvothermal synthesis.<sup>237</sup> Right: A photograph of a set of the autoclave.

pressures developed in the solvothermal reactions, and the inert liner is used to protect the stainless-steel outer shell from the corrosive reagents and solvents typically used in synthesis. Such autoclaves can be used at up to 270°C, and depending on the engineering specification of the steel walls, pressures of ~150 bar can be withstood.<sup>237</sup> The synthetic procedure is simple; however, the rational design of the reaction requires multidisciplinary and interdisciplinary knowledge.

There are several obvious advantages of the solvothermal technique over the traditional solid-state reactions and hydrothermal process: First, many inorganic precursors can be solubilized in a suitable solvent, which is similar to reactants that were solubilized in the molten flux of the solid-state reaction at high temperatures.<sup>239</sup> Second, the solvothermal technique removes diffusion control by the use of a suitable solvent under mild conditions.<sup>239</sup> Third, the conventional hydrothermal method is confined under conditions that some reactants will decompose in the presence of water or the precursors are very sensitive to water, or some reactions will not happen while water exists, resulting in the failure in synthesis of the desired compounds. By substitution of nonaqueous solvents (both polar and apolar solvents) such as alcohols, C<sub>6</sub>H<sub>6</sub>, polyamines, NH<sub>2</sub>NH<sub>2</sub>, liquid NH<sub>3</sub> for water, the solvothermal process allows many possibilities for preparing various nanocrystalline compounds and for initiating some conventional solid-state reactions in organic media under mild conditions.<sup>58</sup> It can be even used to prepare carbonides, nitrides, phosphides, silicides, chalcogenides, and so on.

In the solvothermal process, one or several kinds of precursor are dissolved in nonaqueous solvents. The reactants are dispersed in solution and become more active. The reactions happen in the liquid phase or supercritical status. The solvothermal process is relatively simple and easy to control with several changeable parameters such as solvents, temperature, and reaction time. The sealed system can effectively prevent the contamination of the toxic and air-sensitive precursors. By the substitution of nonaqueous solvents such as polar and nonpolar solvents for water, the solvothermal process can be widely extended to prepare various kinds of nonoxide nanocrystalline material whose precursors are very sensitive to water.

In the past two decades, a trend to considerably mild conditions (100–200°C) has become increasing apparent for inorganic synthesis chemistry and materials synthesis. The potential of this technique for preparative solid-state chemistry has been intensively reviewed.<sup>237,239–241</sup> Various oxide ceramic ultrafine powders were prepared by the solvothermal process.

In recent years, exploration of rational solution routes to nanocrystals has been extensively conducted.<sup>27,58</sup> Various nonoxide compound nanocrystals such as metal chalcogenides, phosphides, and metal nitrides can be synthesized.<sup>242–244</sup> The results showed that the physicochemical properties of the solvents have strong effects on the reactivity, shapes, sizes, and phases of the particles, because solvent properties such as polarity, viscosity, and softness will strongly influence the solubility and transport behavior of the precursors under solvothermal conditions.

Various kinds of low-dimensional nanocrystals such as nanorods, nanowires, nanobelts, nanotubes, as well as other shaped nanocrystals can be synthesized by hydrothermal/solvothermal processes as listed in Tables 3.1 and 3.2. In the following subsections, the latest development of the fabrication of oxide and nonoxide low-dimensional nanocrystals with different shapes, sizes, and phases by mild solution routes will be overviewed with the focus on more general strategies. Specific examples will be given to illustrate the reaction activity, the principle, and key parameters, which dominated the synthesis process.

### 3.3.1.1. Hydrothermal/Solvothermal Synthesis of Low-Dimensional Oxide Nanostructures

#### 3.3.1.1.1. $\text{MoO}_3 \cdot \text{H}_2\text{O}$ and $\text{MoO}_3$ Nanorods

The solvothermal syntheses of  $\text{MoO}_3 \cdot \text{H}_2\text{O}$  nanorods were achieved by two steps (i.e., using amine as the intercalation agent to form a lamellar composite material and the leaching process to remove the amine from the intercalation compound).<sup>106</sup> The further dehydration at 400°C results in the formation of  $\text{MoO}_3$  nanorods. The synthetic procedure can be modified for the direct transformation of  $\text{MoO}_3 \cdot 2\text{H}_2\text{O}$  into  $\text{MoO}_3$  nanorods by hydrothermal treatment of the starting material with small amounts of diluted glacial acetic acid.<sup>27</sup>

#### 3.3.1.1.2. $\text{VO}_x$ Nanotubes

A new type of vanadium oxide nanotube ( $\text{VO}_x$ -NTs) with different layers was obtained by a hydrothermal approach using an amine with long alkyl chains as a structure-directing template (Fig. 3.3).<sup>115,116</sup> The nanotubes obtained using monoamines as templates can form thin tube walls with rather few layers (2–10), whereas diamines predominantly lead to tubes with a large number of layers (>10). The templates used include  $\text{C}_n\text{H}_{2n+1}\text{NH}_2$  with  $4 \leq n \leq 22$  or an  $\alpha,\omega$ -diaminoalkane ( $\text{H}_2\text{N}[\text{CH}_2]_n\text{NH}_2$  with  $4 \leq n \leq 22$ ). The precursors could even be  $\text{V}_2\text{O}_5$  and  $\text{VOCl}_3$ <sup>245</sup>; thus, it can reduce the production cost. The tube diameters can be tuned from a few nanometers in the conventional  $\text{VO}_x$ -NTs up to several hundred nanometers under controlled conditions.<sup>246</sup>



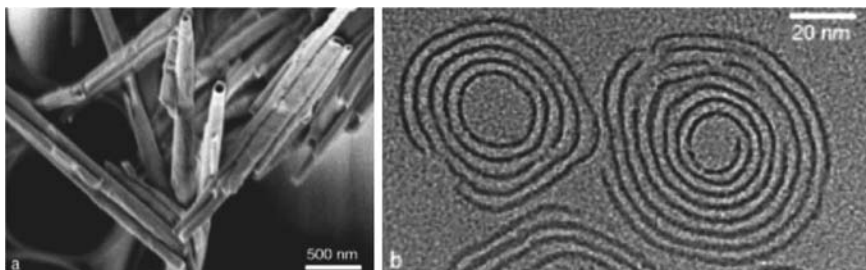


FIGURE 3.3. (a) Scanning electron microscopy image of vanadium oxide nanotubes, containing undecylamine as template ( $C_{11}$ -VO $_x$ -NTs). The tube tips are open. (b) Transmission electron microscopy image of the cross-sectional structure of  $C_{16}$ -VO $_x$ -NTs with different layers.<sup>27</sup>

#### 3.3.1.1.3. Lanthanide Hydroxide Nanowires, Nanorods, and Nanotubes

Recently, a family of lanthanide hydroxide nanowires and nanotubes has been synthesized by hydrothermal treatment of either commercial oxides<sup>120</sup> or the colloidal precipitated from a supersaturated solution.<sup>121,122</sup>

Hydrothermal treatment of Dy $_2$ O $_3$  powder in water under alkaline conditions leads to the formation of Dy(OH) $_3$  nanotubes, and they can be calcined to produce Dy $_2$ O $_3$  nanotubes (Fig. 3.4). A family of lanthanide hydroxide nanowires [La(OH) $_3$ , Pr(OH) $_3$ , Nd(OH) $_3$ , Sm(OH) $_3$ , Eu(OH) $_3$ , Gd(OH) $_3$ , Dy(OH) $_3$ , Tb(OH) $_3$ , Ho(OH) $_3$ , Tm(OH) $_3$ , and YbOOH] has been synthesized through a facile solution-based hydrothermal synthetic pathway, where colloidal Ln(OH) $_3$  obtained under alkaline condition by direct precipitation reaction at room temperature was used as the precursor and underwent subsequent hydrothermal treatment at (180°C).<sup>120,122</sup> In some case, rare earth hydroxide (from Y, La, to Yb) nanotubes can be obtained.<sup>121,122</sup>

#### 3.3.1.1.4. Tungstate/Molybdate Nanorods, Nanowires, and Nanobelts

General synthesis of a family of single-crystalline transition metal tungstate nanorods/nanowires in large scale has been realized recently by a facile hydrothermal crystallization technique under mild conditions using inexpensive and simple inorganic salts as precursors. Uniform tungstate single-crystalline nanorods/nanowires such as MWO $_4$  (M = Zn, Mn, Fe), Bi $_2$ WO $_6$ , Ag $_2$ WO $_4$ , and

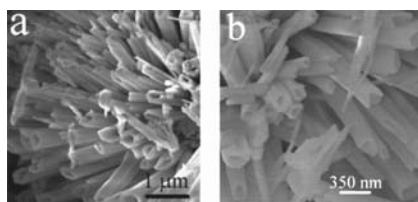


FIGURE 3.4. Scanning electron microscopy images of the obtained Dy(OH) $_3$  (a) and Dy $_2$ O $_3$  (b) nanotubes.<sup>120</sup>

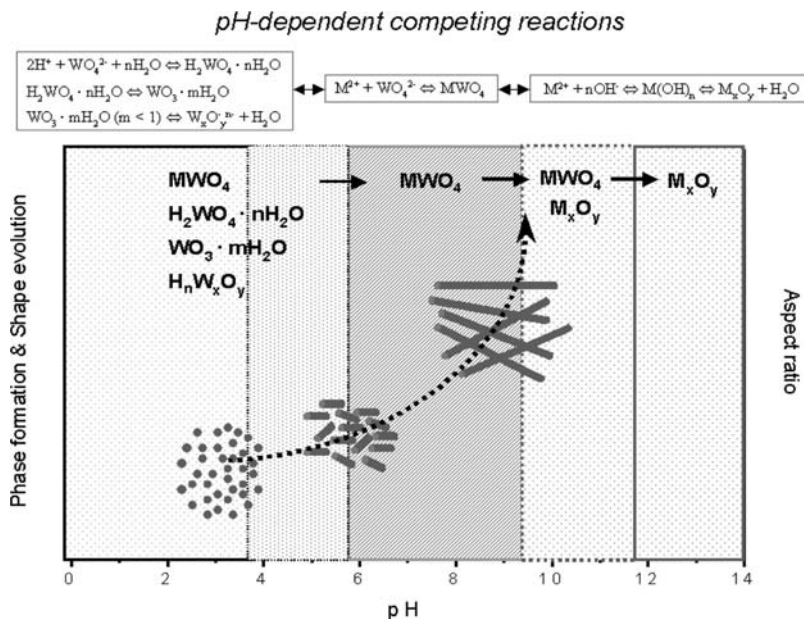


FIGURE 3.5. The map of shape and phase evolution for tungstate materials by the hydrothermal crystallization process.<sup>93</sup>

$\text{Ag}_2\text{W}_2\text{O}_7$  with diameters between 20 and 40 nm, lengths up to micrometers, and controlled aspect ratios can be readily obtained by hydrothermal transformation and recrystallization of amorphous particulates.<sup>93,94</sup>

The pH value of the precursor medium has a crucial effect on both the formation of the tungstate phase and its morphology in this system. In addition, the aspect ratio of  $\text{ZnWO}_4$ ,  $\text{FeWO}_4$ , and  $\text{MnWO}_4$  nanorods/nanowires strongly depends on the initial pH value of the amorphous nanoparticle dispersion. The phase formation zone and the shape evolution can be mapped as shown in Fig. 3.5 based on large amounts of experimental data obtained for various tungstate compounds by the variation of the pH and the compositions of the starting dispersions. Selective synthesis of uniform single-crystalline silver molybdate/tungstate nanorods/nanowires in large scale can be realized by a facile hydrothermal recrystallization technique.<sup>94</sup>

Recent work shows that this approach can be extended further for the general synthesis of various molybdates nanorods/nanowires, as well as rare earth molybdates with interesting shapes, phases, and nanostructures. Similar to the tungstate system, the synthesis is found to be strongly dependent on pH, temperature, and reaction time. Extremely long  $\text{Ag}_6\text{Mo}_{10}\text{O}_{33}$  single-crystal nanowires covered with many tiny nanoparticles can be obtained at pH 2, as shown in Fig. 3.6. Electron diffraction pattern taken along the [100] zone axis indicated that the nanowires are perfect single crystals.

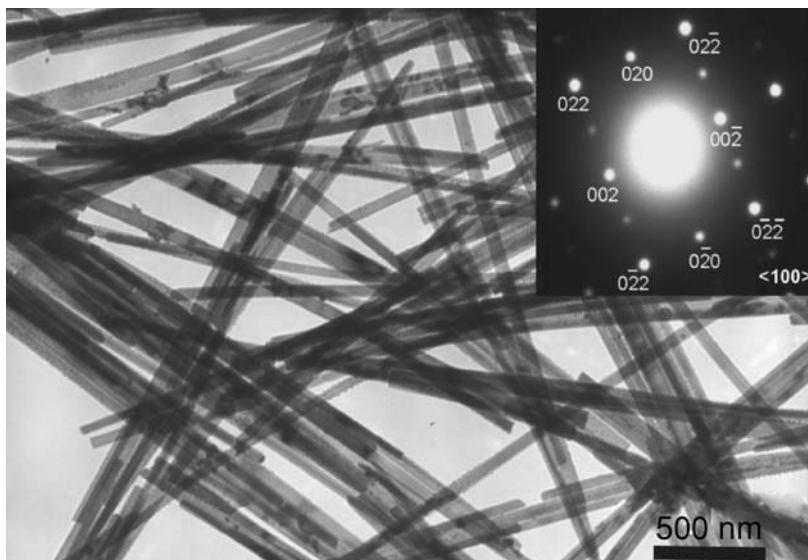


FIGURE 3.6. Transmission electronmicroscopy image and electron diffraction pattern of  $\text{Ag}_6\text{Mo}_{10}\text{O}_{33}$  nanowires.  $[\text{AgNO}_3] = 0.1 \text{ M}$ ,  $[(\text{NH}_4)_6\text{Mo}_7\text{O}_{24}] = 0.014 \text{ M}$ , pH 2,  $140^\circ\text{C}$ , 12 h. The electron diffraction pattern was taken along the  $[100]$  zone axis.<sup>94</sup>

#### 3.3.1.1.5. Lanthanide Orthophosphate Nanowires

A family of hexagonal-structured lanthanide orthophosphate  $\text{LnPO}_4$  ( $\text{Ln} = \text{La}, \text{Ce}, \text{Pr}, \text{Nd}, \text{Sm}, \text{Eu}, \text{Gd}, \text{Tb}, \text{and Dy}$ ) nanowires have been successfully synthesized by the hydrothermal approach. It has been found that pure  $\text{LnPO}_4$  compounds change structure with decreasing Ln ionic radius: that is, the orthophosphates from Ho to Lu as well as Y exist only in the tetragonal zircon (xenotime) structure, and only tetragonal  $\text{LnPO}_4$  ( $\text{Ln} = \text{Ho}, \text{Er}, \text{Tm}, \text{Yb}, \text{Lu}, \text{Y}$ ) nanoparticles can be obtained under the same hydrothermal conditions.<sup>101</sup> Hydrothermal treatment can also synthesize the doped lanthanide orthophosphate nanowires such as  $\text{LaPO}_4 : \text{Eu} (\text{Ce})$ .<sup>102</sup>

The access to various kinds of low-dimensional oxide nanowire, nanorod, and nanotube under mild conditions could open new opportunities for further investigating the novel properties of these materials due to their decreasing dimensionalities. The results demonstrated that it is possible to selectively synthesize other families of oxide nanowires/nanorods with controllable phases and structural specialty. The discovery of new families of oxide nanowires could lead to new applications of these materials. Furthermore, these new families of 1D nanoscale building blocks could further act as 1D nanoscale building blocks for the synthesis of other more complex oxide nanostructures, which would bring us a rich nanochemistry about hydroxides, tungstates, molybdates, orthophosphates, and their derivatives and thus could result in new opportunities for potential applications.

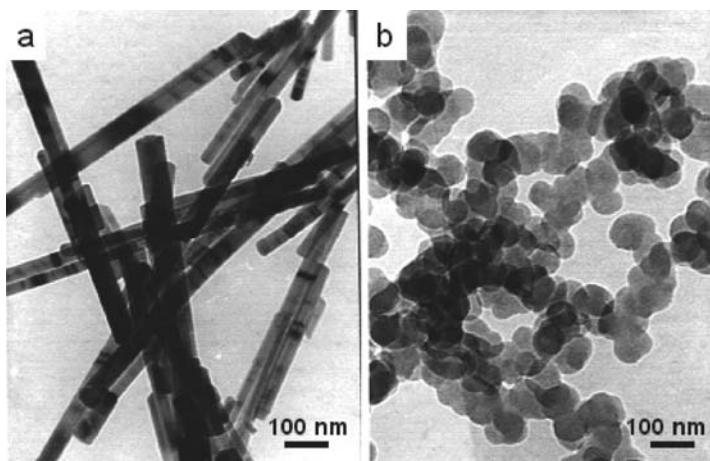


FIGURE 3.7. TEM images of the obtained CdS samples<sup>177</sup>: (a) CdS synthesized in en at 160°C for 12 h; (b) CdS nanoparticles synthesized in pyridine at 160°C for 12 h.

### 3.3.1.2. Hydrothermal/Solvothermal Synthesis of Low-Dimensional Nonoxide Nanocrystals

#### 3.3.1.2.1. Fabrication of II–VI Group Semiconductor Nanocrystals

The shape, particle size, and phase of II–VI group semiconductor nanoparticles can be controlled conveniently by a solvothermal process.<sup>177,179,202</sup> The CdS sample was synthesized in ethylenediamine (en) at 160°C for 12 h. The transmission electron microscopy (TEM) image in Fig. 3.7a shows that the CdS crystallites synthesized in ethylenediamine are uniform nanorods with diameters of 20–50 nm and lengths of 200–1300 nm. In addition, the CdS crystallites synthesized in other polyamines such as diethylene triamine (dien) and triethylene tetraamine (trien) under the same experimental conditions. Disklike particles with a size of 40 nm were produced in pyridine, as shown in Fig. 3.7b. The results indicate that the morphology of CdS, CdSe, and CdTe crystallites can be controlled by choosing different solvents.

The remarkable control of the shape, size, and phase of CdS can be readily realized by the choice of different solvents and reaction conditions using other modified solvothermal reactions. The widths and sizes of CdS nanorods can be varied by controlling the temperature and reaction time.<sup>247</sup> Rod-, twinrod- and tetrapod-shaped CdS nanocrystals have been successfully prepared from the starting spherical CdS nanocrystals via a highly oriented solvothermal recrystallization technique. The present technique could open a new doorway to one-dimensional nanosized semiconductors from the same kind of materials with irregular shape or larger size.<sup>180</sup>

A rational design of the solvothermal reaction makes it possible to control both the dimensionality (dots, rods, and sheets) of ZnS nanocrystals and the phase.<sup>202</sup>

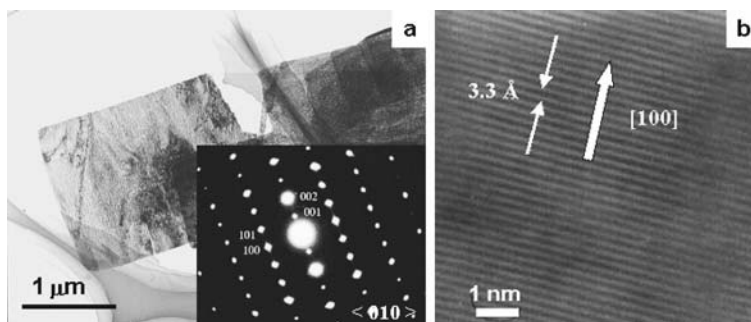


FIGURE 3.8. TEM images and SAED patterns for (a) wurtzite ZnS single-crystal nanosheets obtained by thermal decomposition of lamellar  $\text{ZnS} \cdot (\text{en})_{0.5}$  precursor at  $500^\circ\text{C}$  for 0.5 h in vacuum; inserted SEAD pattern recorded along the  $\langle 010 \rangle$  zone. (b) Well-resolved high-resolution TEM image of the wurtzite ZnS single-crystal nanosheet.<sup>202</sup>

The solvothermal reaction of zinc salts such as  $\text{Zn}(\text{CH}_3\text{COO})_2 \cdot 2\text{H}_2\text{O}$  or  $\text{ZnCl}_2$  and with thiourea in ethylenediamine (en) at  $120\text{--}180^\circ\text{C}$  for 6–12 h results in a white precipitate with the composition  $\text{ZnS} \cdot (\text{en})_{0.5}$ .<sup>202</sup> A new molecular precursor was obtained at  $180^\circ\text{C}$ . It has been confirmed that either a solvothermal reaction of  $\text{Zn}^{2+}$  with thiourea or a similar reaction between Zn (or  $\text{Zn}^{2+}$ ) and sulfur in an ethylenediamine medium at  $120\text{--}180^\circ\text{C}$  resulted in the same product. The TEM images in Fig. 3.8a show that ZnS nanoparticles are sheetlike with rectangle lateral dimensions in the range  $0.3\text{--}2\text{ }\mu\text{m}$ . The nanosheets are well-crystallized single crystals with the growth direction along the  $a$  and  $c$  axes, as indicated by the selected-area electron diffraction (SAED) pattern (Fig. 3.8a).

The synthetic method is both flexible and reproducible for controlling the phase, shape, and size of ZnS nanocrystals. By a similar solvothermal reaction at  $120^\circ\text{C}$  using ethanol instead of ethylenediamine as the solvent, sphalerite ZnS nanoparticles of size  $\sim 3\text{ nm}$  can be easily synthesized. Furthermore, wurtzite ZnS nanorods can also be synthesized by using  $n$ -butylamine, a monodentate amine, as the solvent. A typical TEM image is shown in Fig. 3.9. In addition, the nanorods could be aligned to form bundle structures or arrays under limited experimental conditions. The general synthetic strategies for ZnS nanocrystals with different phases and shapes and for ZnO dendrites are shown in Fig. 3.10.<sup>202</sup> The results show that both the shape and phase of the ZnS nanocrystals can be well controlled by choosing solvents.

These facile mild-solution-based methods shed light on the possibility of controlling the shape, dimensionality (0D, 1D, 2D), size, and phase. The unusual 1D, and 2D wurtzite ZnS single-crystal nanorods and nanosheets, flakelike ZnO dendrites, and ZnO nanorods can be easily generated based on the solvothermal reactions. This synthetic strategy implies that other semiconductor nanocrystals could also be synthesized along the same line by using a suitable “shape controller” under solvothermal conditions.

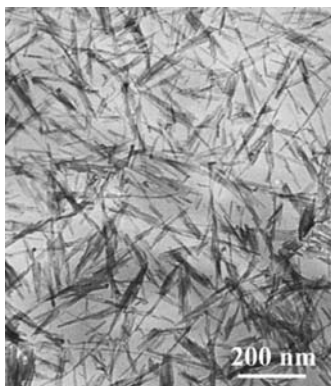


FIGURE 3.9. Wurtzite ZnS nanorods synthesized in *n*-butylamine at 250°C for 12 h.

There are different coordination modes between the metal ions with ethylenediamine, as shown in Fig. 3.11. The monodentate *n*-butylamine was chosen as a “shape controller” for the syntheses of other one-dimensional semiconductors. The coordination between *n*-butylamine and metal ions must be in a monodentate mode (Fig. 3.11c). The formation of rodlike CdS nanoparticles in *n*-butylamine indicates that one anchor atom in a ligand is necessary and adequate for the formation of nanorods even though more anchor atoms might be present in a ligand. The close interaction between anchor atoms in ligands (Lewis base) and metal ions on the surface (Lewis acid) is another prerequisite for the formation of nanorods.<sup>247</sup> CdSe, ZnSe, and PbSe nanorods can be synthesized in *n*-butylamine, indicating that a monodentate ligand can be used as a “shape controller” for the synthesis of a family of semiconductor nanorods (Figure 3.12).

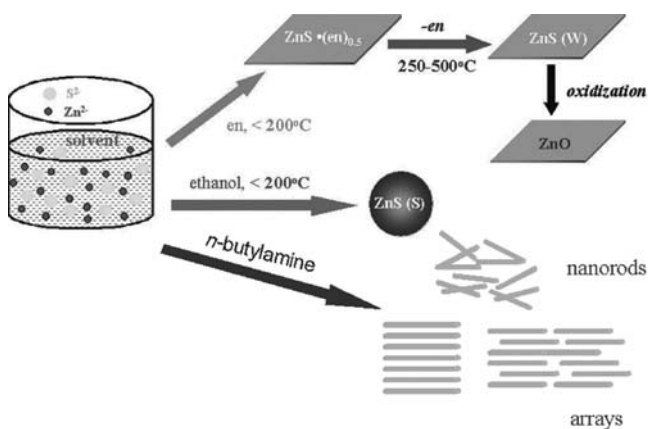


FIGURE 3.10. Illustration of controlled synthesis of ZnS nanocrystals with different dimensionalities and phases.<sup>202</sup>

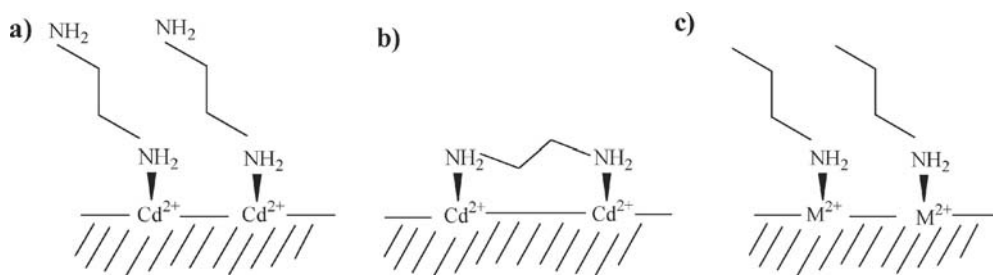


FIGURE 3.11. Illustration of the possible coordination mode on the surface: (a) monodentate mode of en molecules; (b) polydentate mode of en molecules; (c) monodentate mode of *n*-butylamine.<sup>179</sup>

A polymer-assisted solvothermal approach leads to the formation of CdS, CdSe, and CdTe nanowires with high aspect ratios.<sup>181,189</sup>

PbS closed nanowires with regular elliptic or parallelogrammic morphologies and nanorods were synthesized by a solvothermal approach in the presence of poly[*N*-(2-aminoethyl)acrylamide] in a mixed solvent of en/H<sub>2</sub>O (3 : 1, v/v) in the range 110–150°C (Figure 3.13).<sup>195</sup> The formation of such complex PbS structures is unusual and the detailed formation mechanism is still not clear.

This solvent-mediated controlling mechanism has been demonstrated to be successful in the synthesis of a variety of semiconductor nanorods/nanowires. In this mechanism, ligands control the shape of the nanocrystals through the interaction between ligands and metal ions on the surface of nuclei. One anchor atom in a ligand such as *n*-butylamine is necessary but sufficient for the formation of 1D nanocrystals, even though more anchor atoms might be present in a ligand. The close interaction between anchor atoms in ligands and metal ions on the surface is another important prerequisite for nanorod formation. Furthermore, this route provides not only a possible general route to other chalcogenide nanorods in large scale but also a guide for further rational design of 1D chalcogenides.

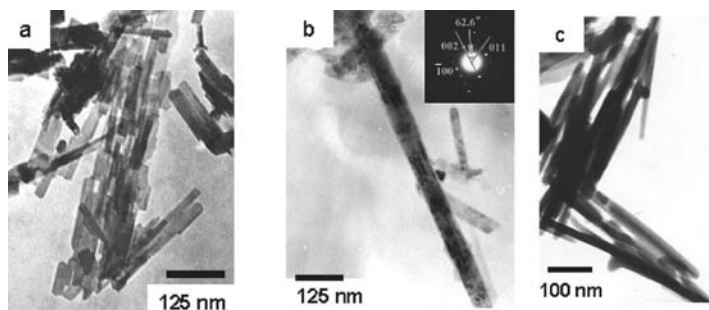


FIGURE 3.12. TEM images of (a) CdSe nanocrystals, 160°C, 12 h; (b) ZnSe nanocrystals, 220°C, 12 h; (c) PbSe nanocrystals, 80°C, 12 h.<sup>179</sup>

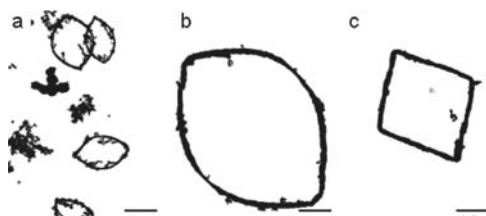


FIGURE 3.13. TEM images of the closed PbS NWs: (a) a general view; (b) a typical closed ellipse structure; (c) a typical parallelogrammic morphology.<sup>195</sup> All scale bars are 1.5  $\mu\text{m}$ .

### 3.3.1.2.2. Fabrication of V–VI Group Low-Dimensional Nanocrystals

Conventionally,  $\text{Bi}_2\text{S}_3$  and  $\text{Sb}_2\text{S}_3$  can be prepared by the direct reaction of element and sulfur vapor in a quartz vessel at high temperature.<sup>248,249</sup> The liquid-solution syntheses of  $\text{Bi}_2\text{S}_3$  and  $\text{Sb}_2\text{S}_3$  generally yield products that are mostly amorphous, poorly crystallized, or colloidal particles.<sup>250</sup> In order to avoid the hydrolysis of the bismuth and antimony salts in the presence of water, a so-called solvothermal decomposition process (SDP) was developed for the fabrication of  $\text{Bi}_2\text{S}_3$  and  $\text{Sb}_2\text{S}_3$  nanowires (or nanorods),<sup>206–208</sup> using  $\text{BiCl}_3$  or  $\text{SbCl}_3$  and thiourea (Tu) or thioacetamide as starting reactants in polar solvents.  $\text{Bi}_2\text{S}_3$  and  $\text{Sb}_2\text{S}_3$  nanorods/nanowires can be conveniently produced with a yield as high as 95% by this method. The particle sizes can be well controlled by choosing different solvents or using different processes. Pure  $\text{Bi}_2\text{S}_3$  can be easily obtained with high yield in several polar solvents such as ethanol, pyridine, ethylene glycol, water, tetrahydrofuran, ethylenediamine (en), and 1,2-dimethoxyethane. The results confirmed that the polar solvents are more favorable for the formation of  $\text{Bi}_2\text{S}_3$  nanowires. The controllable synthesis of  $\text{Bi}_2\text{S}_3$  nanocrystals is illustrated in Fig. 3.14.  $\text{Bi}_2\text{S}_3$  nanowires/nanorods with controllable sizes can be selectively synthesized conveniently by SDP and a hydrothermal process under suitable conditions. Because many metal ions can complex with thiourea or selenurea, the present technique is expected to synthesize other nanostructured metal chalcogenides.

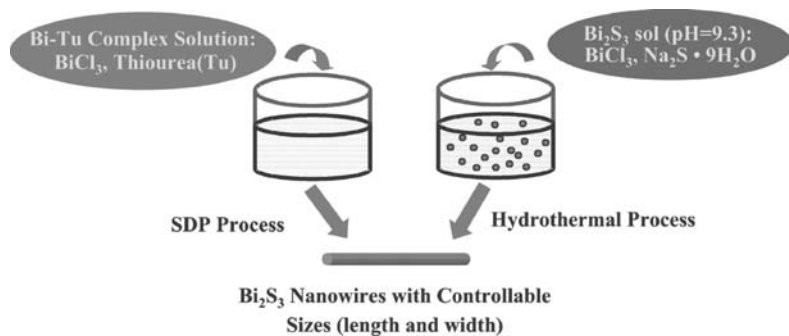
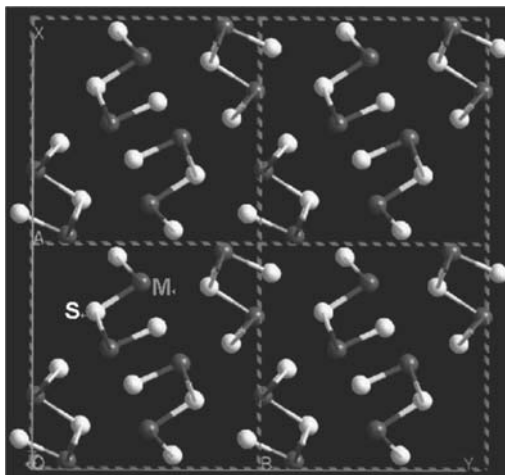


FIGURE 3.14. Schematic illustration for the preparation of  $\text{Bi}_2\text{S}_3$  nanowires with controllable sizes.<sup>58</sup>



FIGURE 3.15. The  $XY$  projection of the structure view of  $M_2S_3$  ( $M = \text{Bi, Sb}$ ), showing the infinite chain structure.



A recent work demonstrated that large-scale ultralong  $\text{Bi}_2\text{S}_3$  nanoribbons with lengths up to several millimeters can be synthesized by using  $\text{Bi}(\text{NO}_3)_3 \cdot 5\text{H}_2\text{O}$ ,  $\text{NaOH}$ , and  $\text{Na}_2\text{S}_2\text{O}_3$  as starting materials and glycerol/ $\text{H}_2\text{O}$  (v/v, 2 : 1) as the mixed solvent at  $160^\circ\text{C}$  for 20 h.<sup>251</sup> An intermediate,  $\text{NaBiS}_2$ , was found in the synthesis process and played a key role in the formation of such long nanoribbons.  $\text{Sb}_2\text{Se}_3$  nanowires with diameter 30 nm and length as long as 8  $\mu\text{m}$  can be synthesized in diethylene (DEG) media at  $120\text{--}140^\circ\text{C}$  by a solvothermal reaction using  $\text{SbCl}_3$ , ammonia,  $\text{NaSO}_3$ , and Se as reactants.<sup>217</sup>

The structure analysis shows that the infinite linear chains within the  $M_2S_3$  ( $M = \text{Sb, Bi}$ ) crystal structure will play a crucial role in the anisotropic growth characteristics, as shown in Fig. 3.15. In fact, the one-dimensional growth of nanocrystals actually is the outside embodiment of inside crystal structures. However, the autogenous pressure in the solvothermal/hydrothermal process was found to play a key role in the orientation growth of the nanocrystals, and the transformation from amorphous nanoparticles to crystallized nanorods is much faster in a closed system than that in an open system.<sup>215</sup>

The further optimization of the solvothermal reaction will make it possible to readily synthesize well-defined 1D III–IV nano-building blocks, which could be very useful for the synthesis of other 1D semiconductors based on sulfo salts of bismuth and related compounds and sulfoantimonates of bismuth (or antimony) and related compounds.

#### 3.3.1.2.3. Ternary Metal Chalcogenide Nanorods

Several ternary metal chalcogenide nanorods such as  $\text{CdIn}_2\text{S}_4$ ,<sup>227</sup>  $\text{Ag}_3\text{CuS}_2$ ,<sup>230</sup> and  $\text{PbSnS}_3$ <sup>232</sup> can be synthesized by the hydrothermal process.  $\text{CdIn}_2\text{S}_4$  nanorods were synthesized by the hydrothermal route, in which  $\text{CdS}$  nanorods were converted by reaction with  $\text{InCl}_3$  and thiourea in aqueous solution.<sup>227</sup> The hydrothermal reaction

of a starting solution containing  $\text{PbCl}_2$ ,  $\text{SnCl}_4 \cdot 5\text{H}_2\text{O}$ , thiourea, and a small amount of iodine leads to the formation of  $\text{PbSnS}_3$  nanorods.<sup>232</sup> In addition,  $\text{CuInS}_2$ ,  $\text{AgInS}_2$ ,<sup>228</sup>  $\text{AgBiS}_2$ ,<sup>229</sup> and  $\text{Cu}_3\text{SnS}_4$ <sup>231</sup> have been synthesized by solvothermal approaches under mild conditions.

#### 3.3.1.2.4. Metal Nanotubes, Alloy Nanowires, and Te Nanobelts/Helical Structures

Bismuth nanotubes can be synthesized by a hydrothermal reaction of bismuth nitrate and an excess amount of aqueous hydrazine solution in the pH range 12–12.5.<sup>154</sup> A solvothermal reaction of bismuth oxide in ethylene glycol leads to the formation of similar tubular structures as well as the sheetlike structures of metal Bi,<sup>155</sup> which shows the tendency of metallic Bi to form tubular structures. CoPt alloy nanowires were synthesized by direct decomposition of platinum acetylacetonate and cobalt carbonyl compound in ethylenediamine solvent through a solvothermal reaction.<sup>152</sup>

A very simple controlled hydrothermal route has been developed for synthesis of tellurium nanobelts, nanotubes, and nanohelices by the reaction of sodium tellurite ( $\text{Na}_2\text{TeO}_3$ ) in aqueous ammonia solution at  $180^\circ\text{C}$ .<sup>164</sup> The nanobelts have thicknesses of  $\sim 8$  nm, widths of 30–500 nm, and lengths up to several hundreds of micrometers, as shown in Fig. 3.16a. The nanobelts tend to twist and form helices, as shown in Fig. 3.16b. When the nanobelts were further twisted and rolled, the nanotubes formed. In addition, an interesting nanostructure so-called the “coaxed nanobelt-within-nanotube structure” was observed, as shown in Fig. 3.16c. The template-roll-growth mechanism and template-twist-joint-growth mechanism were proposed as explanations of the formation of such special nanostructures.<sup>164</sup>

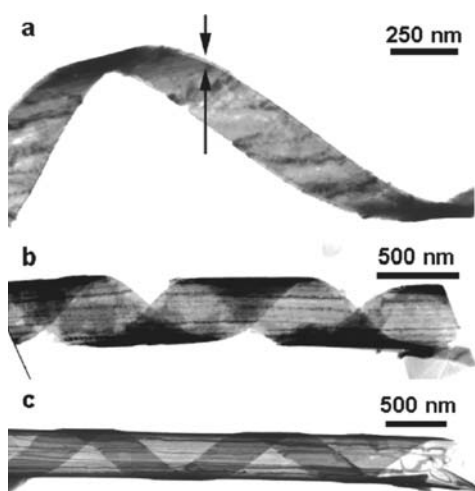
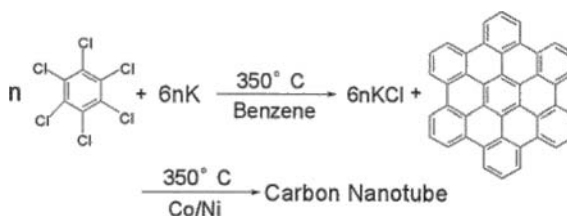


FIGURE 3.16. TEM images of (a) a typical tellurium nanobelt, (b) a helical nanobelt, and (c) a typical helical nanobelt within a nanobelt-roll nanotube.<sup>164</sup>

FIGURE 3.17. Illustration of the catalytic-assembly benzene-thermal route to multiwall carbon nanotube at a moderate temperature.<sup>165</sup>



The above novel chalcogen nanostructures can be used as templates for the synthesis of other 1D and 2D metal chalcogenide nanostructures with more speciality and complexity, which could find interesting applications. Even though the mechanism for the reaction and the formation of 1D nanorods is not well understood, solvothermal/hydrothermal processes have already shown powerful versatilities and capabilities in controlled solution synthesis of nonoxide 1D nanocrystals in contrast to previous high-temperature approaches.

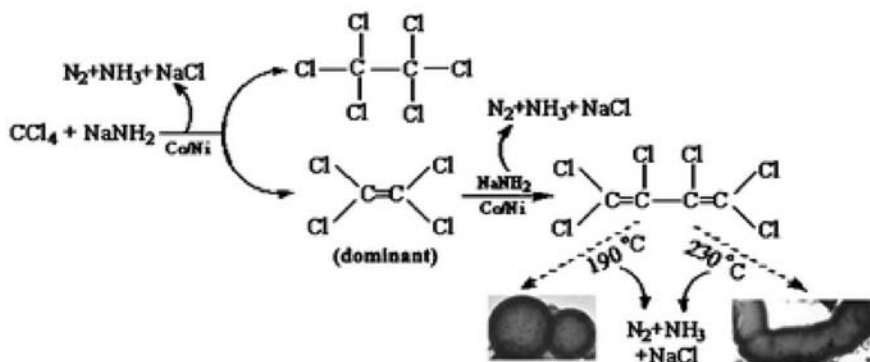
#### 3.3.1.2.5. Carbon Nanostructures

Hydrothermal synthesis of carbon nanofibers with a typical diameter of 50–200 nm has been demonstrated by the autoclave treatment of precursors in the C–H–O system at high temperatures (up to 800°C) and high pressures (up to 100 MPa) in the presence of a metal powder catalyst.<sup>252–254</sup> Recently, hydrothermal treatment of amorphous carbon at 800°C and 100 MPa in the absence of a metal catalyst leads to the formation of hollow carbon nanotubes with a multiwall graphitic layer.<sup>255</sup>

Solvothermal synthesis has been also used for the synthesis of carbon materials under mild conditions. A catalytic-assembly benzene-thermal route was used to synthesize carbon nanotubes.<sup>165</sup> Hexachlorobenzene was reduced by potassium in the presence of Co/Ni catalyzer at 350°C to form hexagonal carbon clusters (Fig. 3.17). The carbon clusters were then assembled into nanotubes and caused axial growth. Meanwhile, because the geometry structure of hexagonal carbon clusters is similar to that of a carbon nanotube wall built from a hexagonal lattice of  $sp^2$ -bonded carbons, the epitaxial growth of newly reduced hexagonal carbon clusters on the nanotube wall is favorable.

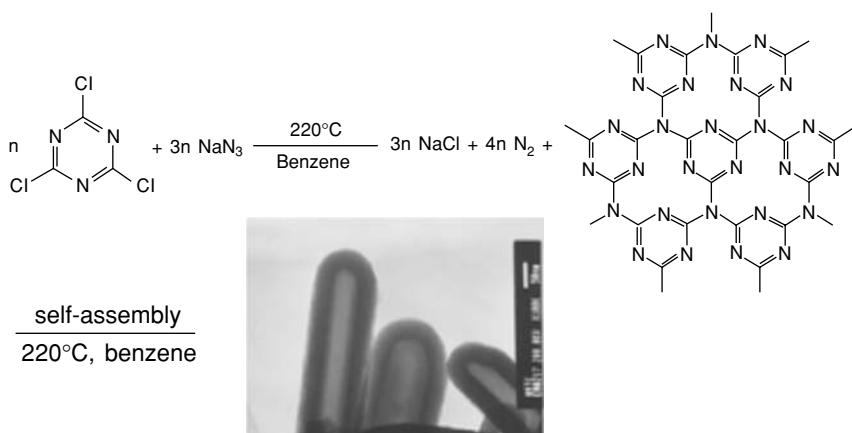
$\text{CCl}_4$  was also used as a carbon source for the formation of hollow carbon spheres and vessels by a solvothermal reaction of  $\text{NaNH}_2$  and  $\text{CCl}_4$  in the presence of Co/Ni alloy at 190–230°C.<sup>166</sup>  $\text{CCl}_2=\text{CCl}_2$  and  $\text{CCl}_2=\text{CCl}-\text{CCl}=\text{CCl}_2$  were found to be the residual intermediates in the dechlorination process catalyzed by Co/Ni alloys. Thus, it is proposed that  $\text{CCl}_2=\text{CCl}_2$  is most probably the reaction intermediate in the formation of  $sp^2$ -carbon nanostructures. Because the  $-\text{C}=\text{C}-\text{C}=\text{C}-$  conjugated products are more stable than the compounds with  $-\text{C}\equiv\text{C}-$  structures,  $\text{CCl}_2=\text{CCl}_2$  will couple to the former rather than the latter, resulting in the continuous dechlorination of  $-\text{C}=\text{C}-\text{C}=\text{C}-$  conjugated units and assembling into carbon nanostructures (Fig. 3.18).<sup>166</sup>

Recently, an efficient method has been successfully realized for the controlled synthesis of various metal/carbon nanoarchitectures, such as metal/carbon

FIGURE 3.18. Schematic formation path of carbon hollow spheres or vessels.<sup>166</sup>

nanocables, and nanochains by a facile and mild hydrothermal carbonization coreduction-process (HCCR), in which starch and noble metal salts are used as starting materials under mild conditions ( $\leq 200^\circ\text{C}$ ).<sup>159</sup>

Carbon nitride nanotubes with inner diameters of 50–100 nm and wall thicknesses of 20–50 nm with the  $\text{C}_3\text{N}_4$  stoichiometry on a high yield of 40% have been successfully synthesized via a simple benzene-thermal process involving the reaction of  $\text{C}_3\text{N}_3\text{Cl}_3$  with  $\text{NaN}_3$  at  $220^\circ\text{C}$  without using any catalyst or template (Fig. 3.19).<sup>172</sup> More importantly, these high-quality carbon nitride nanotubes, synthesized reproducibly in gram quantities under mild conditions, might provide researchers an opportunity to investigate the electrical and optical characteristics of these carbon nitride nanotubes in detail, which are expected as the future nanoscale devices.

FIGURE 3.19. Schematic formation path of  $\text{C}_3\text{N}_4$  nanotubes.<sup>172</sup>

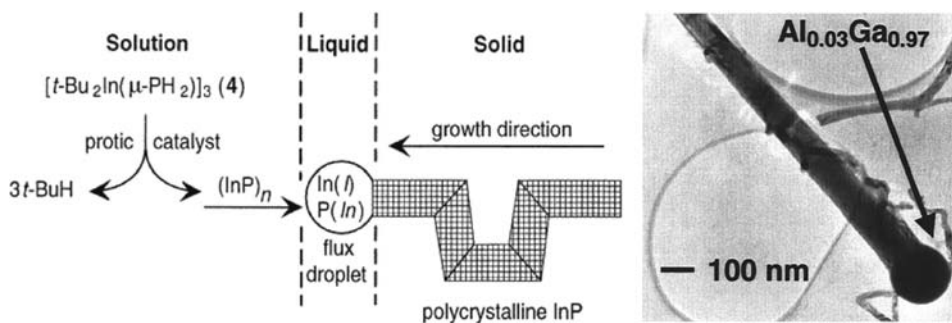


FIGURE 3.20. The SLS mechanism and a representative  $\text{Al}_{0.1}\text{Ga}_{0.9}\text{As}$  nanowhisker grown by the SLS mechanism.<sup>60,61</sup>

### 3.3.2. Synthesis of Semiconductor Nanorods/Nanowires by Solution–Liquid–Solid Mechanism

The solution–liquid–solid (SLS) growth mechanism, which is analogous to the well-known vapor–liquid–solid mechanism, was first discovered by Buhro et al.<sup>59</sup> This route is mainly for growing III–V group nanofibers (InP, InAs, GaAs,  $\text{Al}_x\text{Ga}_{1-x}\text{As}$ , and InN) in hydrocarbon solvents at relative low temperatures (less than or equal to  $203^\circ\text{C}$ ).<sup>54,59–61</sup> More features about this route have been summarized as shown in Fig. 3.20.<sup>54</sup>

The synthesis involved in the methanolysis of  $\{t\text{-Bu}_2\text{In}[\mu\text{-P}(\text{SiMe}_3)_2]\}_2$  in aromatic solvents to produce polycrystalline InP fibers (dimensions  $10\text{--}100\text{ nm} \times 50\text{--}1000\text{ nm}$ ) at  $111\text{--}203^\circ\text{C}$ .<sup>60</sup> The chemical pathway consists of a molecular component, in which precursor substituents are eliminated, and a nonmolecular component, in which the InP crystal lattices are assembled. The two components working in concert comprise the SLS mechanism. The molecular component proceeds through a sequence of isolated and fully characterized intermediates to form the  $[t\text{-Bu}_2\text{In}(\mu\text{-PH}_2)]_3$  complex. The complex, which is alternatively prepared from  $t\text{-Bu}_3\text{In}$  and  $\text{PH}_3$ , undergoes alkane elimination catalyzed by the protic reagent MeOH, PhSH,  $\text{Et}_2\text{NH}$ , or  $\text{PhCO}_2\text{H}$ . In the subsequent nonmolecular component of the pathway, the resulting  $(\text{InP})_n$  fragments dissolve into a dispersion of molten In droplets and recrystallize as the InP fibers.<sup>60</sup> This approach has been extended for the synthesis of InN nanowires by solution-state thermolysis of the dialkyl(azido)indane precursor.<sup>169</sup>

Group IV Si and Ge crystals can be generated by a supercritical fluid solution-phase approach.<sup>62</sup> Recently, Korgel et al. reported a supercritical fluid solution-phase self-assembly approach with a similar SLS mechanism for growing bulk quantities of defect-free Si nanowires with diameters of about  $4\text{--}5\text{ nm}$  and aspect ratios greater than 1000 by using alkanethiol-coated gold nanocrystals as uniform seeds to direct one-dimensional Si crystallization in supercritical hexane.<sup>63</sup> In this process, the sterically stabilized Au nanoparticles were dispersed in supercritical

hexane together with diphenylsilane, which underwent decomposition at 500°C and 270 bars. The phase diagram for Si and Au indicated that at temperatures above 363°C, Si and Au will form an alloy in equilibrium with pure solid Si when the Si concentration with respect to Au is greater than 18.6%. Under this condition, the Si atoms dissolve into the sterically stabilized Au nanocrystals until the supersaturation is reached, at which point they are expelled from the particles as a thin nanometer-scale wire. The supercritical fluid medium with a high temperature promotes Si crystallization. The Au nanocrystals will be maintained to seed the nanowires growth under supercritical conditions.

### 3.3.3. *Capping Agents/Surfactant-Assisted Soft Synthesis*

#### 3.3.3.1. Self-Assembly Under Hot Conditions

Capping agents/surfactant-assisted synthesis has been widely explored for fabrication of nanorods, nanotubes, and more complex nanostructures. Recently, Alivisatos's group synthesized the elongated CdSe nanocrystallites by injecting a solution of dimethylcadmium and selenium in tributylphosphine into a mixture of hexylphosphosphonic acid (HPA) and trioctylphosphine oxide (TOPO) at 340–360°C.<sup>13,64</sup> The surfactant molecules adsorb and desorb rapidly from the nanocrystal surface at the growth temperature, enabling the addition and removal of atoms from the crystallites, and aggregation is suppressed by the presence of (on average) one monolayer of surfactant at the crystallite surface. It is well known that the solubility of crystals increases as the size of the crystals decreases according to the Gibbs–Thompson law. This law plays an important role in determining the growth kinetics of the nanocrystals. Peng et al.<sup>13</sup> observed that if the monomer concentration in the solution is higher than the solubility of all existing nanocrystals, all nanocrystals in the solution grow and the size distribution narrows. The so-called “focusing of size distribution” can be exploited for the spontaneous formation of close to monodisperse colloidal nanocrystals and can form three-dimensional orientation.<sup>13</sup> The CdSe nanorods with variable aspect ratios can be well achieved by kinetic control growth of the nanoparticles (Fig. 3.21).

The diverse range of observed shapes can be understood as arising from three basic effects: The nanocrystals will eventually tend toward nearly spherical shapes at slow growth rates; rods form at high growth rates by unidirectional growth of one face; HPA accentuates the differences in the growth rates among various faces. A large injection volume or very high monomer concentration favors rod growth.

Peng and Peng proposed a diffusion-controlled crystal growth model based on their careful observation of the shape evolution of CdSe nanorods, as shown in Fig. 3.22.<sup>256</sup> They believed that a typical temporal shape evolution of CdSe quantum rods occurs in three distinguishable stages. The “1D-growth stage” was confirmed by a reaction whose monomer concentration was maintained in the corresponding 1D-growth range for a longer time through the addition of more monomers to the reaction system at certain time intervals. The long axis of the

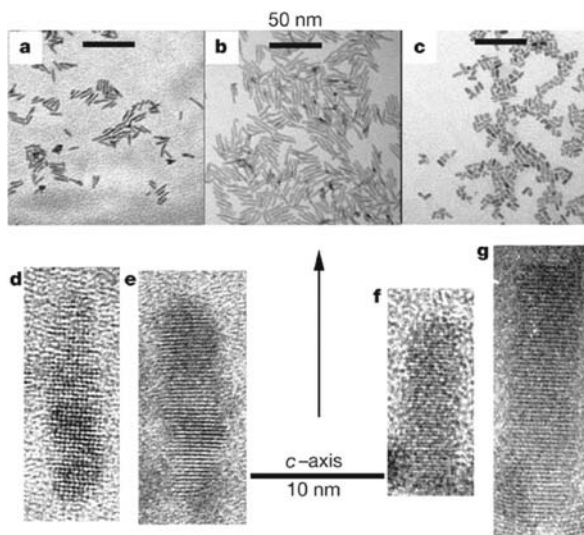


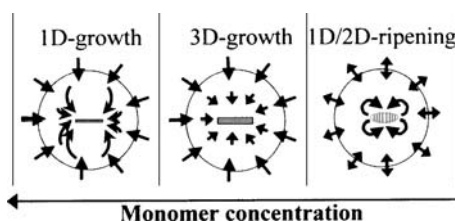
FIGURE 3.21. TEM images of different samples of quantum rods. (a–c) Low-resolution TEM images of three quantum-rod samples with different sizes and aspect ratios. (d–g) High-resolution TEM images of four representative quantum rods. (d) and (e) are from the sample shown in (a); (f) and (g) are from the sample shown in (c).<sup>13</sup>

quantum rods can be further extended from about 35 nm to over 100 nm by the secondary injections, but the short axis remains almost constant, about 3–4 nm.<sup>256</sup>

In this model, each crystal is surrounded by a diffusion sphere (Fig. 3.22).<sup>256</sup> The monomer concentration gradient between the bulk solution and the stagnant solution as well as the diffusion coefficient of the monomers determine the direction (out or into the diffusion sphere) and the diffusion flux. The monomer concentration in the stagnant solution maintains the solubility of a given facet by the rapid growth onto or dissolution from the facet.

The wurtzite structural characteristics were shown in Fig. 3.23, showing that all the atoms on both facets perpendicular to the *c* axis (unique facets) have only one dangling bond without surface reconstruction.<sup>256</sup> The facets terminated by negatively charged Se atoms and positively charged Cd atoms are the (001) facet

FIGURE 3.22. The proposed mechanisms of the three stages of the shape evolution. The circle in each stage is the interface between the bulk solution and the diffusion sphere. Arrows indicate the diffusion directions of the monomers. The double-headed arrows represent the diffusion equilibrium in the 1D-to-2D-ripening stage.<sup>256</sup>



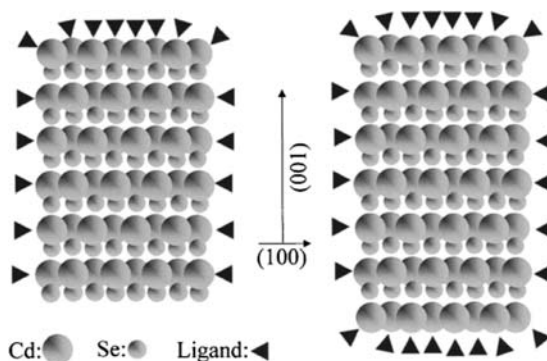


FIGURE 3.23. Schematic structure of CdSe quantum rods in growth.<sup>256</sup> The most stable form of a rod is shown on the left, its (001) facet terminated by Se atoms does not have any ligand on it. After growing a monolayer of Cd atoms on the (001) (right), this facet is still relatively active compared to the other facets, because each surface Cd atom on this facet has three dangling bonds.

and (001) facet, respectively. The negatively charged (001) facet is more or less uncoated, because the ligands in the solution are all electron-donating ligands and should bind exclusively to cationic species. Additionally, without surface reconstructions, any surface Cd atom grown on the (001) facet has to possess three dangling bonds, even if the surface Cd atoms reach a full monolayer. These unique structural features of the (001) facet and the dipole moment along the  $c$  axis significantly increase the chemical potential of the unique facets, especially the (001) facet, compared to the others.<sup>256</sup>

The above surfactant-driven shape-controlled synthesis strategy was further extended for synthesis of III–VI group semiconductor nanorods for the first time by Cheon's group.<sup>168</sup> Gallium phosphide semiconductor nanocrystals can be synthesized by using thermal decomposition of a single molecular precursor, *tris*(di-*tert*-butylphosphino)gallane [ $\text{Ga}(\text{PtBu}_2)_3$ ], in a hot mixture of amine stabilizers. Similarly to the case of CdSe, the shape of GaP nanocrystals can also be varied from nanospheres to rods with highly monodispersed size distributions by controlling the type and amount of stabilizing surfactants.

When only trioctylamine (TOA) was used as a stabilizer, spherical GaP nanoparticles with zinc-blende structure were formed. Increasing the stabilizer ratio of hexadecylamine (HAD) to TOA leads to the formation of nanorods. The addition of HDA into TOA leads to changes in the shape and crystalline phase of the GaP nanocrystals.<sup>168</sup> Wurtzite GaP nanorods with a diameter of 8 nm and a length of 45 nm were grown by thermal decomposition of the precursor in TOA solution (Fig. 3.24), which was injected into a mixture of TOA and HDA at 330°C. A low HAD-to-TOA ratio seems to favor the formation of zinc-blende nanospheres, but a high concentration of HDA leads to the formation of the wurtzite phase and also induces anisotropic growth of the nanocrystals.<sup>168</sup>



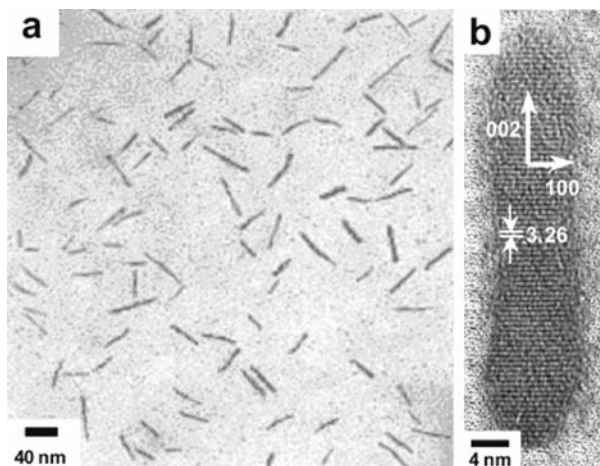


FIGURE 3.24. Large-area TEM image (a) and a HRTEM image (b) of GaP nanorods.<sup>168</sup>

The steric effects of the stabilizers during crystal growth are illustrated in Fig. 3.25.<sup>168</sup> The thermodynamically stable GaP zinc-blende structure is a staggered conformation with  $\langle 111 \rangle$  directions, and the kinetically stable wurtzite structure is an eclipsed conformation with  $\langle 002 \rangle$  directions (Fig. 3.25). Kinetic stability of the wurtzite structure is induced by strong dipole interaction of incoming GaP monomers with surface GaP lattice atoms. The conformation of crystal structures is highly affected by changing the stabilizer because stabilizers can dynamically bind to the crystal surfaces during the GaP crystal growth. When the highly bulky tertiary amines (e.g., TOA) are used as stabilizers, staggered

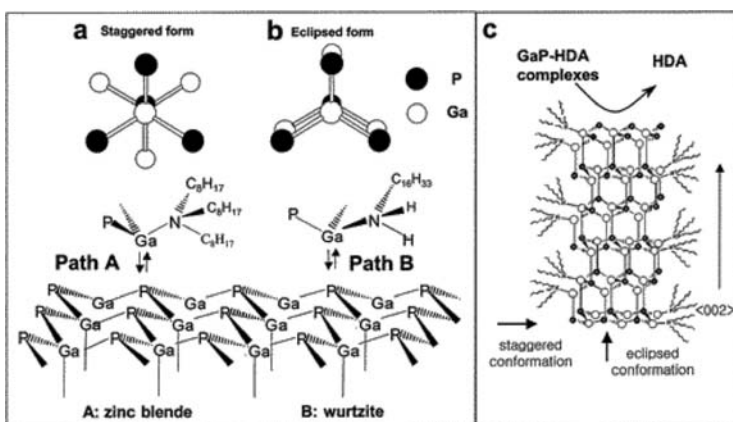


FIGURE 3.25. Proposed mechanism for surfactant-driven steric effects on the crystalline phases (a, b) and rod growth (c) of GaP nanocrystals.<sup>168</sup>

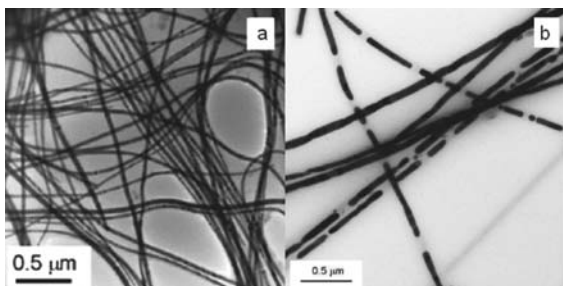


FIGURE 3.26. (a) TEM image of Te nanowires synthesized from  $\text{TeCl}_4$  and TOPO in polydecene at  $250^\circ\text{C}$ . (b) TEM image of dashed-line-like  $\text{Bi}_2\text{Te}_3$  nanowires obtained by reaction of  $\text{BiPh}_3$  and Te wires at  $200^\circ\text{C}$ .<sup>153</sup>

conformation is favoured, minimizing steric hindrance between these ligands and GaP lattices (Fig. 3.25, path A), and zinc-blende GaP is preferred rather than wurtzite. In contrast, when an excess amount of less sterically hindered HDA is added to TOA, the rotational barrier between GaP–HDA complexes and GaP lattices is reduced. Therefore, the formation of the kinetically stable wurtzite GaP is now facilitated (Fig. 3.25, path B) under the kinetic growth regime induced by a high monomer concentration.<sup>168</sup> The steric difference between these two stabilizers seems to induce the anisotropic growth of the wurtzite GaP. It is likely that when wurtzite seeds are formed, sterically bulky TOA selectively binds to the other faces (e.g., 100 and 110 faces) with staggered conformation rather than to 002 faces and blocks growth on these faces. On the other hand, GaP–HDA complexes continuously supply monomers on the 002 faces with high surface energy and, therefore, promote the growth along the  $c$  axis (Fig. 3.25c).

In addition, the thermolysis of a monomeric precursor  $[\text{Zn}(\text{TePh})_2][\text{TMEDA}]$  prepared from  $[\text{Zn}(\text{TePh})_2]$  and donor ligand TMEDA in a mixed-surfactant trioctylamine–dimethylhexylamine produced ZnTe nanorods,<sup>204</sup> which could be templated from the rodlike micelles formed in the mixed-solvent system. Currently, this approach has been successfully applied for the synthesis of transition metal nanorods such as Co,<sup>144</sup> Fe,<sup>146</sup> Ni,<sup>148</sup> Bi, Te,  $\text{Bi}_2\text{Te}_3$ ,<sup>153</sup>  $\text{BaTiO}_3$ , and  $\text{SrTiO}_3$ .<sup>82</sup>

When the high-temperature ( $250\text{--}300^\circ\text{C}$ ) decomposition of  $\text{TeCl}_4$  was conducted in polydecene, but in the presence of TOPO as a surfactant, uniform Te nanowires were formed (Fig. 3.26a).<sup>153</sup> Reactions of Te nanowires and  $\text{BiPh}_3$  conducted at the higher temperature of  $200^\circ\text{C}$  gave segmented wires consisting of  $\text{Bi}_2\text{Te}_3$  nanorods that seemed to be encased within a thin amorphous sheath, reminiscent of a sausage casing (Fig. 3.26b).<sup>153</sup> Some of the nanostructures were severely segmented and contained very short rods. Each rod seemed to be a single crystal, as confirmed by electron diffraction patterns. These patterns also established that each segment had the same [001] orientation as that of the low-temperature-synthesized, continuous  $\text{Bi}_2\text{Te}_3$  wires described earlier. The encased nanorod segments within the hollow sheaths gave the assemblies a dashed-line-like appearance.

More complex nanostructures of semiconductor nanocrystals can be synthesized by this approach in the case for  $\text{CdSe}$ <sup>64</sup> and  $\text{CdTe}$ ,<sup>257</sup> (Figure 3.27) based on the fact that the energy difference between the wurtzite and the zinc-blende structures,

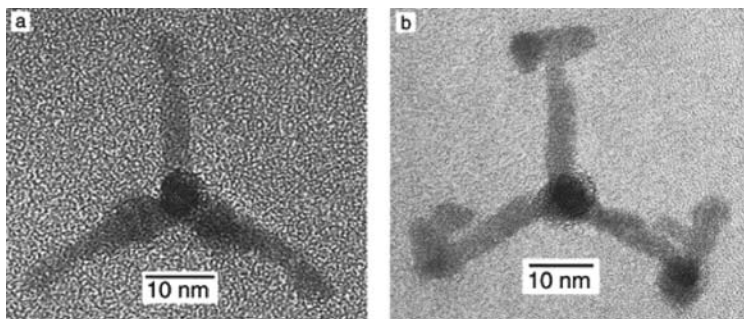


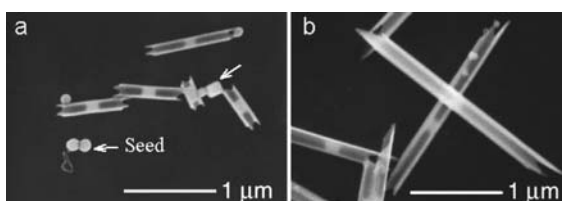
FIGURE 3.27. HRTEM image (a) of a typical tetrapod-shaped CdSe nanocrystal, looking down the [001] direction of one arm. Lattice spacings confirm that all four arms are of the wurtzite structure. In (b), it shows a tetrapod that has branches growing out of each arm. There are zinc-blende layers near the ends of the original arms, and the branches are wurtzite with some stacking faults.<sup>64</sup>

determining the temperature range in which one structure can be preferred during nucleation and the other during growth.<sup>257</sup>

In addition, tellurium nanotubes can be synthesized by a so-called “polyhol process” under refluxing conditions (Fig. 3.28).<sup>163</sup> The early stage shows that tubular structures grew from the cylindrical seeds (Fig. 3.28a). Trigonal selenium nanowires with well-defined sizes and aspect ratios have been synthesized by a solution-phase approach.<sup>161,162</sup> Aging amorphous  $\alpha$ -Se in an aqueous solution through the reduction of selenious acid with excess hydrazine by refluxing at 100°C at room temperature leads to the formation of a small amount of trigonal  $t$ -Se, which act as seeds for the formation of a large amount of trigonal Se nanowires by further aging the solution in dark place. Single-crystalline nanowires of  $\text{Ag}_2\text{Se}$  can be synthesized by being templated against these trigonal Se nanowires at room temperature.<sup>219,220</sup>

Recent advances demonstrated that it is possible to control the growth process of the nanocrystals and their nanoarchitectures with complex forms and different compositions (Fig. 3.29), which could be of great interest for futher nanotechnology.<sup>258</sup>

FIGURE 3.28. SEM images of the Te nanotubes synthesized by refluxing a solution of orthotelluric acid in ethylene glycol for (a) 4 and (b) 6 min, respectively. The white arrow indicated the presence of seeds.<sup>163</sup>



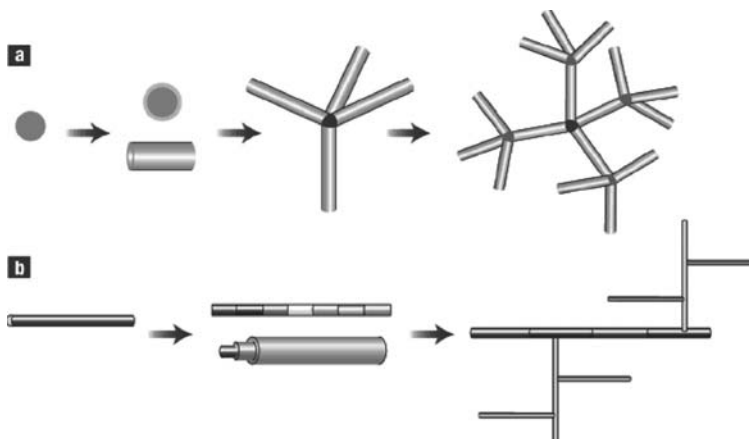


FIGURE 3.29. Emerging diversity in nanocrystal and nanowire building blocks. (a) Formation of complex and multibranched nanostructures from basic clusters, core-shell, and elongated nanostructure building blocks. (b) Multibranched materials constructed from nanowire structures, structures modulated in the axial and radial directions. Distinct colors indicate variations in material composition and/or doping.<sup>258</sup>

### 3.3.3.2. Self-Assembly Under Natural/Mild Conditions

In contrast to the above capping agents/surfactants-driven synthesis of semiconductor nanorods in hot solvent, self-assembly of nanofiber bundles, nanotubes, nanowires, and their structure modulation under natural/mild conditions has emerged recently.<sup>23,64–71</sup> The reverse micelle reaction media usually consisted of either the anionic surfactant AOT [sodium *bis*(2-ethylhexyl)sulfosuccinate)] or nonionic surfactants. Various kinds of 1D inorganic nanorods/nanowires such as  $\text{BaCrO}_4$ ,<sup>23,67</sup>  $\text{BaSO}_4$ ,<sup>66,67</sup>  $\text{BaCO}_3$ ,<sup>69</sup> and  $\text{BaWO}_4$ ,<sup>70</sup> and  $\text{CaSO}_4$ ,<sup>90</sup>  $\text{CaCO}_3$ ,<sup>87</sup>  $\text{BaF}_2$ ,<sup>167</sup>  $\text{CdS}$ ,<sup>183,259</sup> and  $\text{Cu}$  nanorods<sup>145</sup> have been synthesized in reverse micelle media or microemulsions. Other novel nanostructures such as  $\text{Ag}$  nanodisks,<sup>134</sup> flat  $\text{CdS}$  triangles,<sup>182</sup> and  $\text{CdS}$  and  $\text{CdSe}$  nanotubes/nanowires<sup>68</sup> can also be synthesized by this approach.

The strong binding interactions between surfactants and inorganic nuclei effectively inhibit the crystal growth and take the spontaneous structure reconstruction and self-organization of the primary nanoparticles under control. Micrometer-long twisted bundles of  $\text{BaSO}_4$  and  $\text{BaCrO}_4$  nanofilaments in water-in-oil microemulsions prepared from the anionic surfactant, sodium *bis*(2-ethylhexyl)sulfosuccinate (AOT),<sup>23</sup> The reaction occurs at room temperature in unstirred isooctane containing a mixture of  $\text{Ba}(\text{AOT})_2$  reverse micelles and  $\text{NaAOT}$  microemulsions with encapsulated sulfate (or chromate) anions.

The construction of higher-order structures from inorganic nanoparticle building blocks was successfully demonstrated by achieving sufficient informational content in the preformed inorganic surfaces to control long-range ordering through

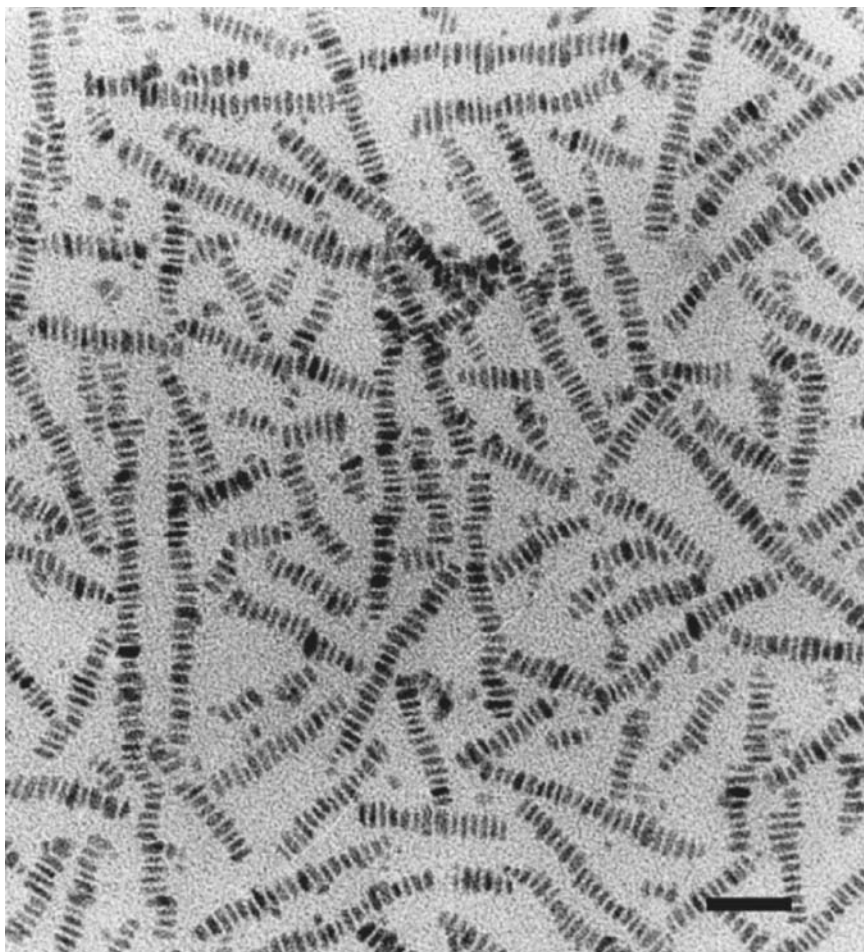


FIGURE 3.30. TEM image showing ordered chains of prismatic  $\text{BaSO}_4$  nanoparticles prepared in AOT microemulsions,<sup>23</sup>  $[\text{Ba}^{2+}] : [\text{SO}_4^{2-}]$  molar ratio = 1 and water content molar ratio  $w = [\text{H}_2\text{O}] : [\text{NaAOT}] = 10$ . Scale bar = 50 nm.

interactive self-assembly.<sup>23</sup> The nanorods have flat surfaces with low curvature so that the hydrophobic driving force for assembly can be strengthened through the intermolecular interaction, resulting in the formation of a bilayer between adjacent particles by the interdigitation of surfactant chains attached to nanoparticle surfaces. When the  $[\text{Ba}^{2+}] : [\text{SO}_4^{2-}]$  (or  $[\text{Ba}^{2+}] : [\text{CrO}_4^{2-}]$ ) molar ratio is equal to 1.0, remarkable linear chains of individual  $\text{BaSO}_4$  or  $\text{BaCrO}_4$  nanorods are formed (Fig. 3.30).

Semiconductor nanotubes and nanowires have been recently reported by employing nonionic surfactants such as *t*-octyl- $(\text{OCH}_2\text{CH}_2)_x\text{OH}$ ,  $x = 9, 10$  (Triton-X) and anionic surfactant AOT.<sup>68</sup> Nanowires of sulfides and selenides

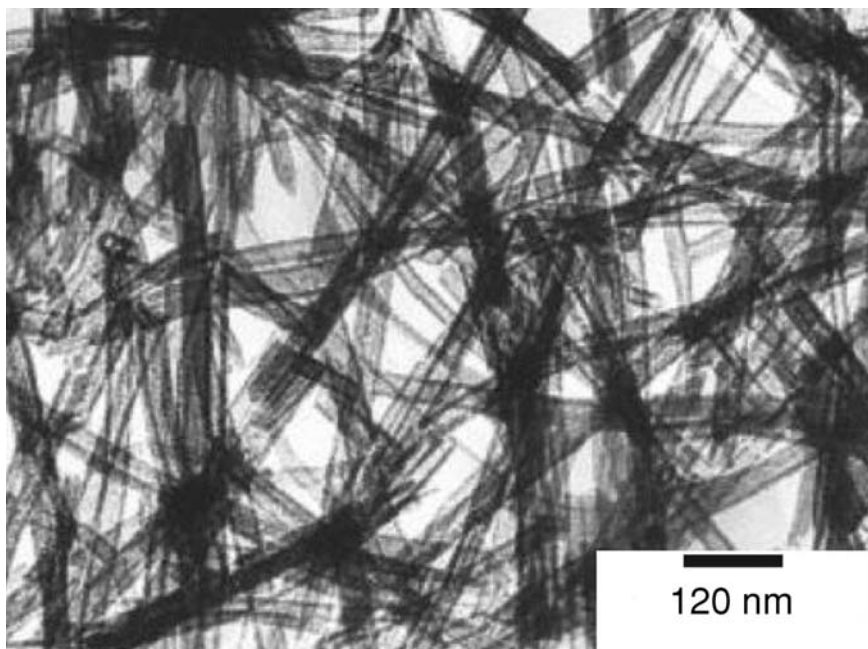


FIGURE 3.31. TEM image of CdSe nanotubes obtained by using Triton 100-X as the surfactant.<sup>68</sup>

of Cu, Zn, and Cd with high aspect ratios can be prepared by using Triton 100-X. The results show that it is possible to obtain both nanotubes and nanowires of CdSe and CdS by this surfactant-assisted synthesis. For the synthesis of CdSe nanotubes, a suspension of cadmium oxide (10 mmol) was prepared in 20 mL of Triton 100-X (~24 mmol). A solution of NaHSe ( $\text{NaBH}_4/\text{Se}$  in 40 mL water) was added dropwise under constant stirring to the suspension at 40°C in an argon atmosphere. The resulting mixture was refluxed for 12 h and left overnight. The nanotubes are generally long, with lengths up to 5  $\mu\text{m}$  and a wall thickness of 5 nm, as shown in Fig. 3.31. The formation mechanism of the nanotubes in the presence of surfactant is still not clear.

### 3.3.4. Bio-Inspired Approach for Complex Superstructures

#### 3.3.4.1. Polymer-Controlled Crystallization

The bio-inspired approach for synthesis of inorganic minerals has been a hot research subject.<sup>65,72</sup> Recently, it was shown that so-called double-hydrophilic block copolymers (DHBCs)<sup>72,260</sup> can exert a strong influence on the external morphology and/or crystalline structure of inorganic particles such as calcium carbonate,<sup>261,262</sup> calcium phosphate,<sup>263</sup> barium sulfate,<sup>83,264</sup> barium chromate,<sup>84,86</sup> cadmium tungstate,<sup>91</sup> and zinc oxide.<sup>265,266</sup>

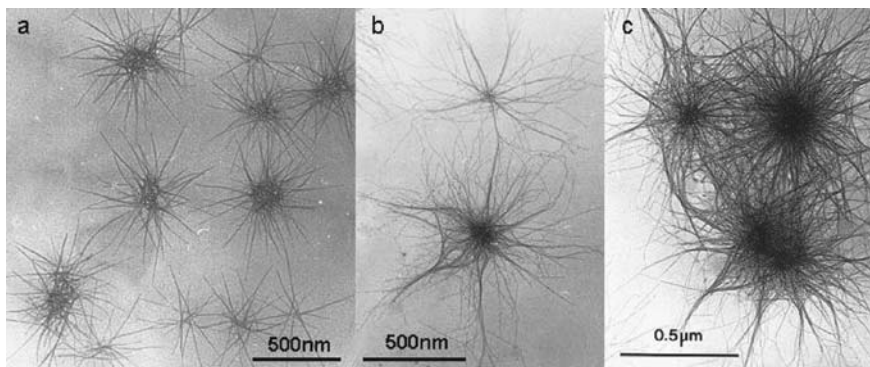


FIGURE 3.32. TEM images of calcium phosphate block copolymer nested colloids.<sup>263</sup> (a) Starlike form at early stage at pH 3.5; (b) later stage showing complex central core; (c) neuronlike tangles produced at pH 5.

Elegant nested calcium phosphate nanofibers were mineralized in the presence of double-hydrophilic block copolymer poly(ethylene oxide)-*b*-alkylated poly(methacrylic acid) (PEO-*b*-PMAA- $C_{12}$ ), which was synthesized from PEO-*b*-PMAA by partial alkylation with dodecylamine.<sup>263</sup> By controlling the pH of the  $Ca^{2+}$ -loaded polymer solution, a delicate mesoskeleton of interconnected calcium phosphate nanofibers with starlike, neuronlike, and more complex nested form can be obtained, as shown in Fig. 3.32.<sup>263</sup>

Very long  $BaSO_4$  and  $BaCrO_4$  nanofibers and fiber bundles with remarkable similarity have been successfully fabricated by a polymer-controlled crystallization process at room temperature. More complex morphologies of hashemite can be formed in the presence of partially the phosphonated block copolymer poly(ethylene glycol)-*block*-poly(methacrylic acid). Fibrous superstructures with sharp edges composed of densely packed, highly ordered, parallel nanofibers of  $BaCrO_4$  can be easily produced. The TEM micrograph with a higher resolution in Fig. 3.33a shows the self-organized nature of the superstructure. Whereas the majority of the fibers appear to be aligned in a parallel fashion, gaps between the single fibers can form, but are also closed again. An electron diffraction pattern taken from such an oriented planar bundle confirmed that the whole structure scatters as a well-crystallized single crystal, where scattering is along the [001] direction and the fibers are elongated along [210] (Fig. 3.33b). Based on above experimental observation and understanding, a self-limiting growth mechanism was proposed to explain the remarkable similarity of the superstructures.<sup>84</sup>

A very recent observation shows that low-molecular-weight polyacrylic acid sodium salt serves as a very simple structure-directing agent for the room-temperature, large-scale synthesis of highly ordered conelike crystals or very long, extended nanofibers made of  $BaCrO_4$  or  $BaSO_4$  with hierarchical and repetitive growth patterns, as shown in Fig. 3.34, where temperature and concentration variation allows for the control of the finer details of the architecture such as axial ratio,

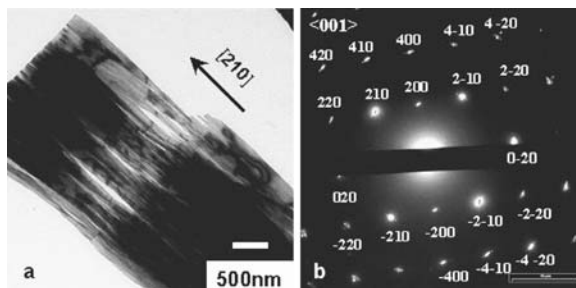


FIGURE 3.33. (a) TEM image of highly ordered  $\text{BaCrO}_4$  nanofibers obtained in the presence of  $\text{PEO-}b\text{-PMAA-PO}_3\text{H}_2$  (21%, phosphonation degree) ( $1 \text{ g L}^{-1}$ ) ( $[\text{BaCrO}_4] = 2 \text{ mM}$ ), pH 5. (b) Electron diffraction pattern taken along the  $\langle 001 \rangle$  zone, showing that the fiber bundles are well-crystallized single crystals and elongated along  $[210]$ .<sup>84</sup>

opening angle, and mutual packing.<sup>85</sup> The formation of interesting hierarchical and repetitive superstructures is worth being explored further for other mineral systems.

Interestingly, single uniform  $\text{BaCrO}_4$  nanofibers can be synthesized by the combination of the polymer-controlled crystallization process and controlled nucleation by colloidal species, producing locally a high supersaturation of both DHBCs and  $\text{Ba}^{2+}$ . The addition of a minor amount of a cationic colloidal structure such as PSS/PAH polyelectrolyte capsule [PSS/PAH: poly(styrene sulfonate, sodium salt)/polyallylamine hydrochloride] in the same reaction system can promote the independent growth of a number of fibers, thus leading to the dynamic discrimination of side nucleation and the resulting altered superstructures.<sup>86</sup>

In addition to the above formation of superstructures under the control of block copolymers, the DHBCs can also be used to fine-tune the nanostructure details of other inorganic crystals. Very thin 1D and 2D  $\text{CdWO}_4$  nanocrystals with controlled aspect ratios were conveniently fabricated at ambient temperature or by

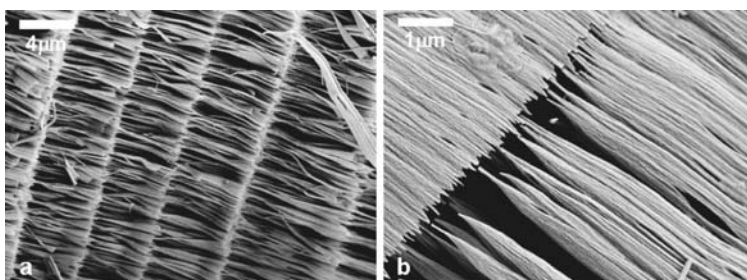


FIGURE 3.34. Complex forms of  $\text{BaSO}_4$  bundles and superstructures produced in the presence of  $0.11 \text{ mM}$  sodium polyacrylate ( $M_n = 5100$ ), at room temperature,  $[\text{BaSO}_4] = 2 \text{ mM}$ , pH = 5.3, for 4 days. (a) The detailed superstructures with repetitive patterns; (b) the well-aligned bundles.<sup>85</sup>



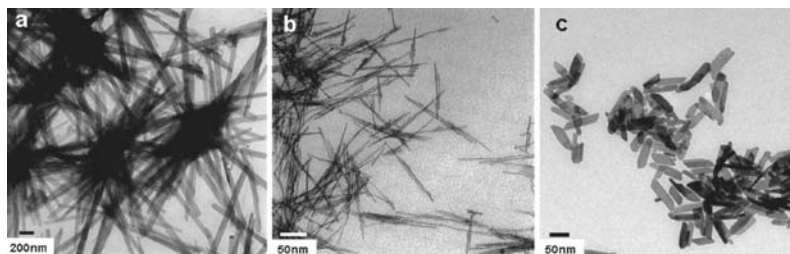


FIGURE 3.35. TEM images of the samples obtained under different conditions.<sup>91</sup> TEM images of the  $\text{CdWO}_4$  nanocrystals obtained under different conditions: (a) No additives, double jet, at room temperature; (b) in the presence of PEO-*b*-PMAA ( $1 \text{ g L}^{-1}$ ), 20 mL, double jet, then hydrothermal crystallization at  $80^\circ\text{C}$  for 6 h; (c) direct hydrothermal treatment of a 20-mL solution at  $130^\circ\text{C}$  for 6 h, in the presence of  $1 \text{ g L}^{-1}$  PEO-*b*-PMAA- $\text{PO}_3\text{H}_2$ ,  $\text{pH} = 5.3$ ,  $[\text{Cd}^{2+}]:[\text{WO}_4^{2-}] = 8.3 \times 10^{-3} M$  (final solution).

hydrothermal ripening under control of a double-hydrophilic block copolymer.<sup>91</sup> The TEM image in Fig. 3.35a shows very thin, uniform  $\text{CdWO}_4$  nanorods/nanobelts with lengths in the range  $1\text{--}2 \mu\text{m}$  and a uniform width of 70 nm along their entire length (aspect ratio of about 30). The thickness of the nanobelts is  $\sim 6\text{--}7 \text{ nm}$ . Very thin and uniform nanofibers with a diameter of 2.5 nm, a length of  $100\text{--}210 \text{ nm}$ , and an aspect ratio of 40–85, as shown in Fig. 3.35b, can be readily obtained when the double-hydrophilic block copolymer PEG-*b*-PMAA was added to the solvent reservoir before the double-jet crystallization process and the mixture was then hydrothermally ripened at  $80^\circ\text{C}$ . When the partly phosphonated hydrophilic block copolymer PEG-*b*-PMAA- $\text{PO}_3\text{H}_2$  (21%) ( $1 \text{ g L}^{-1}$ ) is added at an elevated temperature of  $130^\circ\text{C}$  even without using the double jets but at higher concentrations and coupled supersaturation, very thin plateletlike particles with a width of  $17\text{--}28 \text{ nm}$ , a length of  $55\text{--}110 \text{ nm}$ , and an aspect ratio of 2–4 are obtained by a direct hydrothermal process (Fig. 35c). The nanoparticles display an interesting shape-dependent evolution of the luminescent properties, which might be of interest for applications.

Polymer-controlled crystallization in water at ambient temperature provides an alternative and promising tool for morphogenesis of inorganic nanocrystals and superstructures, which could be extended to various inorganic systems.

#### 3.3.4.2. Supramolecular Self-Assembly

Supramolecular-directed self-assembly of inorganic and inorganic/organic hybrid nanostructures has been emerging as an active area of recent research. The recent advance shows the remarkable feasibility of mimicking a natural mineralization system by a designed artificial organic template.<sup>267</sup>

The supramolecular functional polymer can be directly employed for the mineralization template of novel inorganic nanoarchitectures. The CdS helices were successfully templated from supramolecular nanoribbons.<sup>268</sup> This novel inorganic

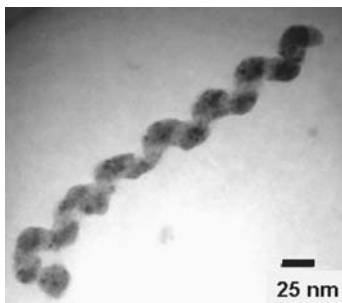


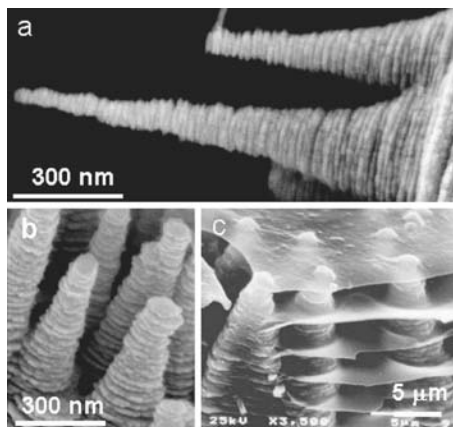
FIGURE 3.36. TEM micrograph of a typical CdS helix with a pitch of 40–50 nm precipitated in gels of the DRC in EHMA.<sup>268</sup>

nanostructure has a coiled morphology with a pitch of 40–60 nm, which can be rationalized in terms of the period of the twisted organic ribbons. A triblock architecture termed “dendron rodcoils” (DRC) can hydrogen-bond in head-to-head fashion through dendron segments and self-assemble into nanoribbons.<sup>268</sup> The mineralization of the helical structures was done in both 2-ethylhexyl methacrylate (EHMA) and ethyl methacrylate (EMA). Figure 3.36 shows a typical CdS helix with a zigzag pattern and a pitch of 40–50 nm, which was isolated from a 1 wt.% gel of the DRC in EHMA to which a solution of cadmium nitrate in THF had been added prior to exposure to hydrogen sulfide gas.<sup>268</sup> High-resolution TEM studies revealed that the polycrystalline zinc-blende CdS is made up of small domains with grain sizes of about 4–8 nm. The results suggest that it is possible to achieve good control over the morphology of the templated product by using extremely uniform, stable, nonaggregated supramolecular objects as templates.

A peptide-amphiphile (PA) molecule was designed for the mineralization of PA nanofibers and hydroxyapatite (HAp) nanofibers.<sup>269</sup> This amphiphile molecular can assemble in water into cylindrical micelles because of the amphiphile’s overall conical shape, resulting in that the alkyl tails are packed in the center of the micelle while the peptide segments are exposed to the aqueous environment.<sup>269</sup> The PA molecules were found to self-assemble at acidic pH but disassemble at neutral and basic pH. After self-assembling into nanofibers, the nanofibers were cross-linked by the oxidation of the cysteine thiol groups through treatment with 0.01 M I<sub>2</sub>. The cross-linked PA fibers contained intermolecular disulfide bonds, and intact fiber structures were still kept. These cross-linked fibers with negative-charged surfaces are able to direct mineralization of hydroxyapatite (HAp) to form a composite material in which the crystallographic *c* axes of hydroxyapatite are coaligned with the long axes of the fibers.<sup>269</sup>

In addition, the supramolecular self-assembly using organogelators as the template to transcribe inorganic nanostructures has been intensively studied.<sup>267</sup> Organogelators are low-molecular-weight compounds that can gelate organic fluids at low concentrations. The gelators can gelate in organic solvents to form unique superstructures, which can transcribe inorganic nanostructures.<sup>267</sup> Shinkai et al. first employed such a system to mineralize inorganic structures by transcribing the chiral gelator, fibers and other morphologies to form unique superstructures.<sup>270–279</sup>

FIGURE 3.37. Comparison of ZnO helical structures with nacre.<sup>119</sup> (a, b) High-magnification image of oriented ZnO helical columns. (c) Nacreous calcium carbonate columns and layers near the growth tip of a young abalone.



Sol-gel polymerization of gelled tetraethyl orthosilicate (TEOS) solutions produces silica with a novel hollow-fiber structure due to the template effect of the organogel fibers.<sup>270–276</sup> This approach can be extended for producing other metal oxide nanofibers or nanotubes with chiral structures such as TiO<sub>2</sub> fibers,<sup>277</sup> TiO<sub>2</sub> helical ribbons, and nanotubes.<sup>279</sup>

#### 3.3.4.3. Small Molecular Organic Species-Mediated Crystallization

In contrast to the above polymer-controlled crystallization and supramolecular template synthesis, some small molecular organic species can also exert significant influence on crystal orientation growth. A very recent report by Liu et al. showed unusual oriented and extended helical ZnO nanostructures grown by a synthetic ceramic method, which is surprisingly very similar to the growth morphology of nacreous calcium carbonate.<sup>119</sup>

The helical ZnO nanostructures were grown on the glass substrate containing the oriented ZnO nanorods arrays,<sup>280</sup> which was placed in a solution containing Zn(NO<sub>3</sub>)<sub>2</sub>, hexomethylenetetramine, and sodium citrate. Figure 3.37 shows the similarity of SEM images of the helical ZnO nanocolumns (Figs. 3.37a and 3.37b) and the growth tip of a young abalone shell containing oriented columns of aragonite nanoplates (Fig. 3.37c). The secondary growth on the helical nanorods, aligned and well-defined nanoplates, are formed, as in nacre. The side-width growth of the ZnO nanoplates leads to hexagonal ZnO plates that begin to overlap with one another.

The organic species were reported to act as simple physical compartments or act to control nucleation or to terminate crystal growth by surface poisoning in biomineralization of nacre.<sup>281,282</sup> The similar biomimetic structures of helical ZnO rods as the nacreous CaCO<sub>3</sub> indicated that helical growth might play some role in the formation of organized nacreous calcium carbonate. However, the organic species citrate ion still plays critical roles in the formation of such structures

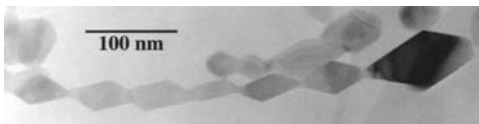


FIGURE 3.38. TEM micrograph of a single crystal of anatase that was hydrothermally coarsened in 0.001 *M* HCl, showing that the primary particles align, dock, and fuse to form oriented chain structures.<sup>74</sup>

because the citrate ion has a strong tendency to inhibit the growth of the (002) surfaces, possibly through the selective surface adsorption.

The above-discussed polymer-controlled crystallization and small molecular organic species-mediated mineralization could shed new light on morphology and orientation control of inorganic crystals.

### 3.3.5. *Oriented Attachment Growth Mechanism*

Recently, natural aggregation-based crystal-growth mechanisms and spontaneous self-organization of unstabilized nanoparticles in a surfactant/ligand-free solution system has been gradually recognized as an important strategy in designing inorganic crystals.

Traditionally, the crystal growth can be described as an Ostwald ripening process.<sup>283</sup> The formation of tiny crystalline nuclei in a supersaturated medium occurred at first and was then followed by crystal growth. The larger particles will grow at the cost of the small ones due to the difference between large particles and the smaller particles of a higher solubility. Penn and colleagues<sup>74–77</sup> confirmed that both anatase and iron oxide nanoparticles with sizes of a few nanometers can coalesce under hydrothermal conditions in a way called “oriented attachment” (Fig. 3.38). The crystal lattice planes might be almost perfectly aligned or dislocations at the contact areas between the adjacent particles will lead to defects in the finally formed bulk crystals. The so-called oriented attachment during crystal growth of TiO<sub>2</sub> was also proposed by other authors.<sup>78</sup>

A very recent report by Weller et al. provided some strong evidence that ZnO nanorods can be conveniently self-assembled from small ZnO quasi-spherical nanoparticles based on the oriented attachment mechanism by the evaporation and reflux of a solution containing 3–5-nm smaller nanoparticles.<sup>80</sup> Previously, self-assembly of nanoparticles capped by ligands is mainly driven by the interactions of the organic ligands rather than by the interaction of the particle cores.

ZnO sol with an average particle size of ~3 nm (Figure 3.39a) was easily prepared by adding a 0.03 *M* solution of KOH (65 mL) dropwise in methanol into a solution of zinc acetate dihydrate (0.01 *M*) in methanol (125 mL) under vigorous stirring at about 60°C. Refluxing of the concentrated solution leads to the formation of rodlike nanoparticles. Prolonging the heating time mainly leads to an increase of the elongation of the particle along the *c* axis. After refluxing for 1 day, single-crystalline nanorods with average lengths of 100 nm and widths of ~15 nm were formed (Fig. 3.39b). The authors argued that oxide nanoparticles are very

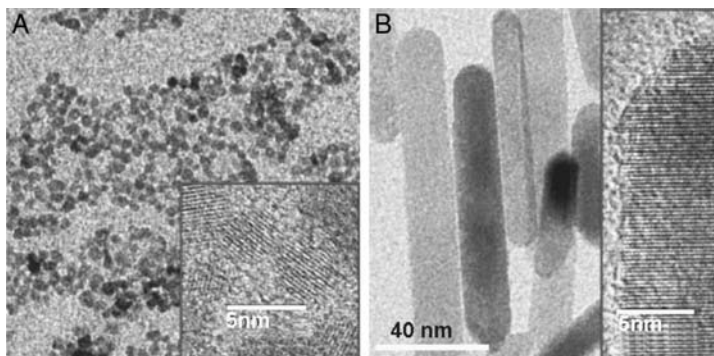


FIGURE 3.39. TEM images of ZnO: (A) starting sol; (B) after 1 day of reflux of the concentrated sol. The insets show high-resolution TEM images of individual nanoparticles.<sup>80</sup>

favorable for oriented attachment for two reasons: First, organic ligands, which prevent intimate contact of crystal planes, are usually not needed for stabilization and, second, crystalline fusion of correctly attached particles not only leads to a gain in lattice-free energy but also in free energy of polycondensation.<sup>80</sup>

The spontaneous aggregation and self-assembly of the small nanoparticles into much elongated nanorods/nanowires was again observed in the case of CdTe when the protective shell of the organic stabilizer on the surface of the initial CdTe nanoparticles was removed.<sup>81</sup> The presence of “pearl-necklace” agglomerates as intermediates of the nanoparticle–nanowire transition suggested that the growth mechanism should be related to a special interaction/attraction between the nanoparticles (Fig. 3.40). Recently, it has been found that pre-formed TiO<sub>2</sub> nanoparticles with a diameter of 5 nm functionalized by 2-amino-2(hydroxymethyl)-1,3-propanediol can be directed to self-assemble into highly anisotropic nanostructures.<sup>79</sup>

A dipole–dipole interaction was believed to be the driving force for such self-organization of the nanoparticles.<sup>81</sup> In addition, room-temperature crystallization

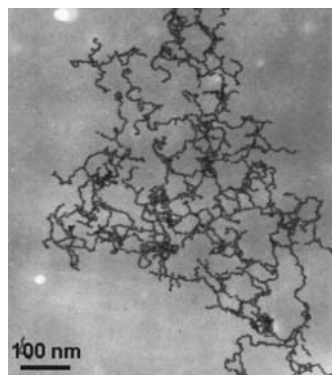


FIGURE 3.40. TEM image of the nanoparticle chain-like structures showing the intermediate state of a nanoparticle–nanowire transition. (Courtesy of Professor Nicholas A. Kotov of Oklahoma State University.)

and transformation of amorphous nanoparticles obtained from a fast double-jet reaction into highly anisotropic beltlike  $\text{CdWO}_4$  nanorods has also been achieved.<sup>91</sup> These results imply that the spontaneous self-organization with subsequent fusion into crystallographically aligned particles indeed could act in various inorganic systems.

Although there are only few reports on the self-organization of nanoparticles, this new growth mechanism could offer an additional tool for the design of advanced materials with anisotropic materials properties and could be used for the synthesis of more complex crystalline three-dimensional structures in which the branching sites could be added as individual nanoparticles, and can even lead to the highly perfect crystals.<sup>80, 284</sup>

### 3.4. Summary and Outlook

This chapter gives a general overview on soft synthesis of low-dimensional nanocrystals such as nanorods, nanowires, nanotubes, and more complex nanostructures. Recent advances demonstrated that the “soft” approaches are very promising alternative pathways for the synthesis of 1D nanocrystals under natural/mild conditions in contrast to traditional high-temperature approaches. The soft synthesis routes, such as solvothermal/hydrothermal processes, solution–liquid–solid mechanism, capping agents/surfactant-assisted synthesis, bio-inspired approaches, and oriented attachment growth mechanism, open alternative doorways to the low-dimensional nanocrystals and even more complex superstructures. Among these solution strategies, the solvothermal process shows the potential capabilities and versatilities for selective synthesis of various important semiconductor nanocrystals with controllable shape, size, phase, and dimensionalities under mild conditions.

In addition to the strategies by use of solvent-mediated shape and structure modulation, the “soft”–“hard” interface between polymers/surfactants (or organic species) and inorganic crystals is also an active area of great interest at present. It has to be emphasized that the nucleation, crystallization, self-assembly, and growth mechanism of the nanocrystals in these solution strategies are rather complicated and are still not well understood, and they are crucial for the rational synthesis of high-quality one-dimensional nanostructures. It is necessary that the various characterization techniques including *in situ* X-ray diffraction, Fourier transform infrared, nuclear magnetic resonance techniques, among others, be combined to get more detailed information in the reaction system, to follow the crystallization, structure evolution process, in order to get a through understanding on the reaction mechanics, shape evolution, and structure formation.

From the viewpoint of application, investigation of the relationship between the structural specialties (shape, sizes, phases, dimensionality, complexity, etc.) of the low-dimensional nanocrystals and their properties will result in discovering new applications of these novel building blocks in nanoscience and nanotechnology.

*Acknowledgments.* S. H. Yu acknowledges the special funding support by the Centurial Program of the Chinese Academy of Sciences and the Natural Science Foundation of China (NSFC) [the National Distinguished Youth Fund and the Distinguished Team Grant (Contract Nos. 20325104 and. 20321101) and NSFC Contract No. 50372065]. We are grateful for the financial support of the CAS and the NSFC.

## References

1. J. T. Hu, T. W. Odom, and C. M. Lieber, Chemistry and physics in one dimension: Synthesis and properties of nanowires and nanotubes, *Acc. Chem. Res.* **32**, 435–445 (1999).
2. C. M. Lieber, One-dimensional nanostructures: Chemistry, physics & applications, *Solid State Commun.* **107(11)**, 607–616 (1998).
3. R. Tenne, Inorganic Nanotubes and fullerene-Like Materials, *Chem. Eur. J.* **8(23)**, 5296–5304 (2002).
4. W. Tremel, Inorganic nanotubes, *Angew. Chem. Int. Ed.* **38(15)**, 2175–2179 (1999).
5. X. Duan, Y. Huang, Y. Cui, J. Wang, and C. M. Lieber, Indium phosphide nanowires as building blocks for nanoscale electronic and optoelectronic devices, *Nature* **409**, 66–69 (2001).
6. M. G. Bawendi, M. L. Steigerwald, and L. E. Brus, The quantum-mechanics of larger semiconductor clusters (quantum dots), *Annu. Rev. Phys. Chem.* **41**, 477–496 (1990).
7. M. G. Bawendi, W. L. Wilson, L. Rothberg, P. J. Carrol, T. M. Jedju, M. L. Steigerwald, and L. E. Brus, Electronic-structure and photoexcited-carrier dynamics in nanometer-size CdSe clusters, *Phys. Rev. Lett.* **65(13)**, 1623–1626 (1990).
8. W. Hoheisel, V. L. Colvin, C. S. Johnson, and A. P. Alivisatos, threshold for quasi-continuum absorption and reduced luminescence efficiency in CdSe nanocrystals, *J. Chem. Phys.* **101(10)**, 8455–8460 (1994).
9. A. P. Alivisatos, Semiconductor clusters, nanocrystals, and quantum dots, *Science* **271**, 933–937 (1996).
10. H. Weller, Colloidal semiconductor Q-particles-chemistry in the transition region between solid-state and molecules, *Angew. Chem. Int. Ed.* **32(1)**, 41–53 (1993).
11. S. Mann, Molecular recognition in biomineralization, *Nature* **322**, 119–124 (1988).
12. K. Leung, S. Pokrant, and K. B. Whaley, Exciton fine structure in CdSe nanoclusters *Phys. Rev. B* **57(19)**, 12291–12301 (1998).
13. X. G. Peng, L. Manna, W. D. Yang, J. Wickham, E. Scher, A. Kadavanich, and A. P. Alivisatos, Shape control of CdSe nanocrystals, *Nature* **404**, 59–61 (2000).
14. M. J. Bruchez, M. Maronne, P. Gin, S. Weiss, and A. P. Alivisatos, Semiconductor nanocrystals as fluorescent biological labels, *Science* **281**, 2013–2016 (1998).
15. W. C. W. Chan, and S. M. Nie, Quantum dot bioconjugates for ultrasensitive nonisotopic detection, *Science* **281**, 2016–2018 (1998).
16. M. Y. Han, X. H. Gao, J. Z. Su, and S. M. Nie, Quantum-dot-tagged microbeads for multiplexed optical coding of biomolecules, *Nature Biol.* **19(7)**, 631–635 (2001).
17. Y. Cui and C. M. Lieber, Functional nanoscale electronic devices assembled using silicon nanowire building blocks, *Science* **291**, 851–853 (2001).
18. W. U. Huynh, J. J. Dittmer, and A. P. Alivisatos, Hybrid nanorod–polymer solar cells, *Science* **295**, 2425–2427 (2002).

19. P. D. Yang, H. Q. Yan, S. Mao, R. Russo, J. Hohnson, R. Saykally, N. Morris, J. Pham, R. R. He, and H. J. Choi, Controlled growth of ZnO nanowires and their optical properties, *Adv. Funct. Mater.* **12**(5), 323–331 (2002).
20. Y. Cui, Q. Q. Wei, H. K. Park, and C. M. Lieber, Nanowire nanosensors for highly sensitive and selective detection of biological and chemical species, *Science* **293**, 1289–1292 (2001).
21. M. Law, H. Kind, B. Messer, F. Kim, and P. D. Yang, Photochemical sensing of NO<sub>2</sub> with SnO<sub>2</sub> nanoribbon nanosensors at room temperature, *Angew. Chem. Int. Ed.* **41**(13), 2405–2408 (2002).
22. T. S. Ahmadi, Z. L. Wang, T. C. Green, A. Henglein, and M. A. El-Sayed, Shape-controlled synthesis of colloidal platinum nanoparticles, *Science* **272**, 1924–1926 (1996).
23. M. Li, H. Schnablegger, and S. Mann, Coupled synthesis and self-assembly of nanoparticles to give structures with controlled organization, *Nature* **402**, 393–395 (1999).
24. P. D. Yang, Y. Y. Wu, and R. Fan, Inorganic semiconductor nanowires, *Int. J. Nanoscience.* **1**(1), 1–39 (2002).
25. Y. N. Xia, P. D. Yang, Y. G. Sun, Y. Y. Wu, B. Mayers, B. Gates, Y. D. Yin, F. Kim, and Y. Q. Yan, One-dimensional nanostructures: Synthesis, characterization, and applications, *Adv. Mater.* **15**, 353–389 (2003).
26. C. N. R. Rao, F. L. Deepak, G. Gundiah, and A. Govindaraj, Inorganic nanowires, *Prog. Solid State Chem.* **31**(1–2), 5–147 (2003).
27. G. R. Patzke, F. Krumeich, and R. Nesper, Oxidic nanotubes and nanorods: Anisotropic modules for a future nanotechnology, *Angew. Chem. Int. Ed.* **41**(14), 2447–2461 (2002).
28. R. S. Wagner and W. C. Elhs, Vapor–liquid–solid mechanism of single crystal growth, *Appl. Phys. Lett.* **4**(5), 89–90 (1964).
29. R. S. Wagner, In *Whisker Technology*, edited by A. P. Levitt, Wiley–Interscience, New York, 1970, pp. 47.
30. H. Dai, E. W. Wong, Y. Z. Lu, S. Fan, and C. Lieber, Synthesis and characterization of carbide nanorods, *Nature* **375**, 769–772 (1995).
31. W. Q. Han, S. S. Fan, Q. Q. Li, and Y. D. Hu, Synthesis of gallium nitride nanorods through a carbon nanotube-confined reaction, *Science* **277**, 1287–1289 (1997).
32. J. D. Klein, R. D. Herrick, D. Palmer, M. J. Sailor, C. J. Brumlik, C. R. Martin, Electrochemical fabrication of cadmium chalcogenide microdiode arrays, *Chem. Mater.* **5**(7), 902–904 (1993).
33. C. R. Martin, Nanomaterials: A membrane-based synthetic approach, *Science* **266**, 1961–1966 (1994).
34. D. Almwlawi, C. Z. Liu, and M. Moskovits, Nanowires formed in anodic oxide nanotemplates, *J. Mater. Res.* **9**(4), 1014–1018 (1994).
35. D. Routkevitch, T. Bigioni, M. Moskovits, and J. M. Xu, Electrochemical fabrication of CdS nanowire arrays in porous anodic aluminum oxide templates, *J. Phys. Chem.* **100**(33), 14037–14047 (1996).
36. M. Yazawa, M. Koguchi, A. Muto, M. Ozawa, and K. Hiruma, Effect of one monolayer of surface gold atoms on the epitaxial-growth of InAs nanowhiskers, *Appl. Phys. Lett.* **61**(17), 2051–2053 (1992).
37. J. Westwater, D. P. Gosain, S. Tomiya, S. Usui, and H. Ruda, Growth of silicon nanowires via gold/silane vapor–liquid–solid reaction, *J. Vac. Sci. Technol. B* **15**(3), 554–557 (1997).



38. A. M. Morales and C. M. Lieber, A laser ablation method for the synthesis of crystalline semiconductor nanowires, *Science* **279**, 208–211 (1998).
39. M. H. Huang, Y. Wu, H. Feick, E. Webber, and P. D. Yang, Catalytic growth of zinc oxide nanowires by vapor transport, *Adv. Mater.* **13**(2), 113–116 (2001).
40. M. Huang, S. Mao, H. Feick, H. Yan, Y. Wu, H. Kind, E. Weber, R. Russo, and P. D. Yang, Room-temperature ultraviolet nanowire nanolasers, *Science* **292**, 1897–1899 (2001).
41. Y. Y. Wu, H. Q. Yan, M. Huang, B. Messer, J.-H. Song, and P. D. Yang, Inorganic semiconductor nanowires: Rational growth, assembly, and novel properties, *Chem. Eur. J.* **8**(6), 1260–1268 (2002).
42. X. F. Duan and C. M. Lieber, General synthesis of compound semiconductor nanowires, *Adv. Mater.* **12**(4), 298–302 (2000).
43. P. D. Yang and C. M. Lieber, Nanostructured high-temperature superconductors: Creation of strong-pinning columnar defects in nanorod/superconductor composites, *J. Mater. Res.* **12**(11), 2981–2996 (1997).
44. P. Yang and C. M. Lieber, Nanorod-superconductor composites: A pathway to materials with high critical current densities, *Science* **273**, 1836–1840 (1996).
45. Z. W. Pan, Z. R. Dai, and Z. L. Wang, Nanobelts of semiconducting oxides, *Science* **291**, 1947–1949 (2001).
46. J. Y. Lao, J. G. Wen, and Z. F. Ren, Hierarchical ZnO nanostructures, *Nano Lett.* **2**(11), 1287–1291 (2002).
47. S. T. Lee, N. Wang, Y. F. Zhang, and Y. H. Tang, Oxide-assisted semiconductor nanowire growth, *MRS Bull.* **24**, 36–42 (1999).
48. S. T. Lee, N. Wang, and C. S. Lee, Semiconductor nanowires: Synthesis, structure and properties, *Mater. Sci. Eng. A* **286**, 16–23 (2000).
49. W. S. Shi, Y. F. Zheng, N. Wang, C. S. Lee, and S. T. Lee, A general synthetic route to III-V compound semiconductor nanowires, *Adv. Mater.* **13**(8), 591–594 (2001).
50. W. S. Shi, Y. F. Zheng, N. Wang, C. S. Lee, and S. T. Lee, Microstructures of gallium nitride nanowires synthesized by oxide-assisted method, *Chem. Phys. Lett.* **345**(5–6), 377–380 (2001).
51. C. C. Tang, S. S. Fan, H. Y. Dang, P. Li, and Y. M. Liu, Simple and high-yield method for synthesizing single-crystal GaN nanowires, *Appl. Phys. Lett.* **77**(13), 1961–1963 (2000).
52. W. S. Shi, H. Y. Peng, N. Wang, C. P. Li, L. Xu, C. S. Lee, R. Kalish, and S. T. Lee, Free-standing single crystal silicon nanoribbons, *J. Am. Chem. Soc.* **123**(44), 11,095–11,096 (2001).
53. A. Stein, S. W. Keller, and T. E. Mallouk, Turning down the heat: Design and mechanism in solid-state synthesis, *Science* **259**, 1558–1564 (1993).
54. W. E. Buhro, K. M. Hickman, and T. J. Trentler, Turning down the heat on semiconductor growth: Solution-chemical syntheses and the solution–liquid–solid mechanism, *Adv. Mater.* **8**(8), 685–688 (1996).
55. M. Yoshimura, W. Suchanek, and K. Byrappa, Soft solution processing: A strategy for one-step processing of advanced inorganic materials, *MRS Bull.* **25**(9), 17–25 (2000).
56. T. Trindade, P. O'Brien, and N. L. Pickett, Nanocrystalline semiconductors: Synthesis, properties, and perspectives, *Chem. Mater.* **13**(11), 3843–3858 (2001).
57. M. Green, Solution routes to III–V semiconductor quantum dots, *Curr. Opin. Solid State Mater. Sci.* **6**(4), 355–363 (2002).
58. S. H. Yu, Hydrothermal/solvothermal processing of advanced ceramic materials, *J. Ceram. Soc. Jpn.* **109**(5), S65–S75 (2001).

59. T. J. Trentler, K. M. Hickman, S. C. Goel, A. M. Viano, P. C. Gibbons, and W. E. Buhro, Solution-liquid growth of crystalline III-V semiconductors; An analogy to vapor-liquid-solid growth, *Science* **270**, 1791-1794 (1995).
60. T. J. Trentler, S. C. Goel, K. M. Hickman, A. M. Viano, M. Y. Chiang, A. M. Beatty, P. C. Gibbons, and W. E. Buhro, Solution-liquid-solid growth of indium phosphide fibers from organometallic precursors: Elucidation of molecular and nonmolecular components of the pathway, *J. Am. Chem. Soc.* **119**(9), 2172-2181 (1997).
61. P. D. Markowitz, M. P. Zach, P. C. Gibbons, R. M. Penner, and W. E. Buhro, Phase separation in  $\text{Al}_x\text{Ga}_{1-x}$  As nanowhiskers grown by the solution-liquid-solid mechanism, *J. Am. Chem. Soc.* **123**(19), 4502-4511 (2001).
62. J. R. Heath and F. K. LeGoues, A liquid solution synthesis of single-crystal germanium quantum wires, *Chem. Phys. Lett.* **208**(3-4), 263-268 (1993).
63. J. D. Holmes, K. P. Johnston, R. C. Doty, and B. A. Korgel, Control of thickness and orientation of solution-grown silicon nanowires, *Science* **287**, 1471-1473 (2000).
64. L. Manna, E. C. Scher, and A. P. Alivisatos, Synthesis of soluble and processable rod-, arrow-, teardrop-, and tetrapod-shaped CdSe nanocrystals, *J. Am. Chem. Soc.* **122**(51), 12,700-12,706 (2000).
65. S. Mann, The chemistry of form, *Angew. Chem. Int. Ed.* **39**(19), 3392-3406 (2000).
66. J. D. Hopwood and S. Mann, Synthesis of barium sulfate nanoparticles and nanofilaments in reverse micelles and microemulsions, *Chem. Mater.* **9**(8), 1819-1828 (1997).
67. M. Li and S. Mann, Emergence of morphological complexity in  $\text{BaSO}_4$  fibers synthesized in AOT microemulsions, *Langmuir* **16**(17), 7088-7094 (2000).
68. C. N. R. Rao, A. Govindaraj, F. L. Deepak, and N. A. Gunari, Surfactant-assisted synthesis of semiconductor nanotubes and nanowires, *Appl. Phys. Lett.* **78**(13), 1853-1855 (2001).
69. L. Qi, J. Ma, H. Cheng, and Z. Zhao, Reverse micelle based formation of  $\text{BaCO}_3$  nanowires, *J. Phys. Chem. B.* **101**(18), 3460-3463 (1997).
70. S. Kwan, F. Kim, J. Akana, and P. Yang, Synthesis and assembly of  $\text{BaWO}_4$  nanorods, *Chem. Commun.* 447-448 (2001).
71. H. T. Shi, L. M. Qi, J. M. Ma, and H. M. Cheng, Synthesis of single crystal  $\text{BaWO}_4$  nanowires in catanionic reverse micelles, *Chem. Commun.* 1704-1705 (2002).
72. S. H. Yu and H. Colfen, Bio-inspired crystal morphogenesis by hydrophilic polymers, *J. Mater. Chem.* **14**(14), 2123-2147 (2004).
73. M. Antonietti, Self-organization of functional polymers, *Nature Mater.* **2**(1), 9-10 (2003).
74. R. L. Penn and J. F. Banfield, Morphology development and crystal growth in nanocrystalline aggregates under hydrothermal conditions: Insights from titania, *Geochim. Cosmochim. Acta* **63**(10), 1549-1557 (1999).
75. R. L. Penn and J. F. Banfield, Imperfect oriented attachment: dislocation generation in defect-free nanocrystals, *Science* **281**, 969-971 (1998).
76. F. Banfield, S. A. Welch, H. Zhang, T. T. Ebert, and R. L. Penn, Aggregation-based crystal growth and microstructure development in natural iron oxyhydroxide biomineralization products, *Science* **289**, 751-754 (2000).
77. R. L. Penn, G. Oskam, T. J. Strathmann, P. C. Searson, A. T. Stone, and D. R. Veblen, Epitaxial assembly in aged colloids, *J. Phys. Chem. B* **105**(11), 2177-2182 (2001).
78. A. Chemseddine and T. Moritz, Nanostructuring titania: Control over nanocrystal structure, size, shape, and organization, *Eur. J. Inorg. Chem.* 235-245 (1999).

79. J. Polleux, N. Pinna, M. Antonietti, and M. Niederberger, Ligand-directed assembly of preformed titania nanocrystals into highly anisotropic nanostructures, *Adv. Mater.* **16**(5), 436–439 (2004).
80. C. Pacholski, A. Kornowski, and H. Weller, Self-assembly of ZnO: From nanodots to nanorods, *Angew. Chem. Int. Ed.* **41**, 1188–1191 (2002).
81. Z. Y. Tang, N. A. Kotov, and M. Giersig, Spontaneous organization of single CdTe nanoparticles into luminescent nanowires, *Science* **297**, 237–240 (2002).
82. J. J. Urban, W. S. Yun, Q. Gu, and H. Park, Synthesis of single-crystalline perovskite nanorods composed of barium titanate and strontium titanate, *J. Am. Chem. Soc.* **124**(7), 1186–1187 (2002).
83. L. M. Qi, H. Cölfen, M. Antonietti, M. Lei, J. D. Hopwood, A. J. Ashley, and S. Mann, Formation of BaSO<sub>4</sub> fibers with morphological complexity in aqueous polymer solutions, *Chem. Eur. J.* **7**(16), 3526–3532 (2001).
84. S. H. Yu, H. Cölfen, and M. Antonietti, Control of the morphogenesis of barium chromate by using double-hydrophilic block copolymers (DHBCs) as crystal growth modifiers, *Chem. Eur. J.* **8**(13), 2937–2345 (2002).
85. S. H. Yu, M. Antonietti, H. Cölfen, and J. Hartmann, Growth and self-assembly of BaCrO<sub>4</sub> and BaSO<sub>4</sub> nanofibers toward hierarchical and repetitive superstructures by polymer-controlled mineralization reactions, *Nano Lett.* **3**(3), 379–382 (2003).
86. S. H. Yu, H. Cölfen, and M. Antonietti, The combination of colloid-controlled heterogeneous nucleation and polymer-controlled crystallization: Facile synthesis of separated, uniform high-aspect-ratio single-crystalline BaCrO<sub>4</sub> nanofibers, *Adv. Mater.* **15**(2), 133–136 (2003).
87. D. Kuang, A. W. Xu, Y. P. Fang, H. D. Ou, and H. Q. Liu, Preparation of inorganic salts (CaCO<sub>3</sub>, BaCO<sub>3</sub>, CaSO<sub>4</sub>) nanowires in the Triton X-100/cyclohexane/water reverse micelles, *J. Crystal Growth* **244**, 379–383 (2002).
88. P. D. Yang and F. Kim, Langmuir–Blodgett assembly of one-dimensional nanostructures, *Chem. Phys. Chem.* **3**(6), 503–506 (2002).
89. F. Kim, S. Kwan, J. Akana, and P. D. Yang, Langmuir–Blodgett nanorod assembly, *J. Am. Chem. Soc.* **123**(18), 4360–4361 (2001).
90. G. D. Rees, R. Evans-Gowing, S. J. Hammond, and B. H. Robinson, Formation and morphology of calcium sulfate nanoparticles and nanowires in water-in-oil microemulsions, *Langmuir* **15**(6), 1993–2002 (1999).
91. S. H. Yu, M. Antonietti, H. Cölfen, and M. Giersig, Synthesis of very thin 1D and 2D CdWO<sub>4</sub> nanoparticles with improved fluorescence behavior by polymer control crystallization, *Angew. Chem. Int. Ed.* **41**(13), 2356–2360 (2002).
92. H.-W. Liao, Y.-F. Wang, X.-M. Liu, Y.-D. Li, and Y.-T. Qian, Hydrothermal preparation and characterization of luminescent CdWO<sub>4</sub> nanorods, *Chem. Mater.* **12**(10), 2819–2821 (2000).
93. S. H. Yu, B. Liu, M. S. Mo, J. H. Huang, X. M. Liu, and Y. T. Qian, General synthesis of single-crystal tungstate nanorods/nanowires: A facile, low-temperature solution approach, *Adv. Funct. Mater.* **13**(8), 639–647 (2003).
94. X. J. Cui, S. H. Yu, L. L. Li, L. Biao, H. B. Li, M. S. Mo, and X. M. Liu, Selective synthesis and characterization of single-crystal silver molybdate/tungstate nanowires by a hydrothermal process, *Chem. Eur. J.* **9**(1), 218–223 (2003).
95. Y. K. Liu, G. H. Wang, C. K. Xu, and W. Z. Wang, Fabrication of Co<sub>3</sub>O<sub>4</sub> nanorods by calcination of precursor powders prepared in a novel inverse microemulsion, *Chem. Commun.* 1486–1487 (2002).

96. V. G. Pol, O. Palchik, A. Gedanken, and I. Felner, Synthesis of europium oxide nanorods by ultrasound irradiation, *J. Phys. Chem. B* **106**(38), 9737–9743 (2002).
97. L. Vayssieres, N. Beermann, S.-E. Lindquist, and A. Hagfeldt, Controlled aqueous chemical growth of oriented three-dimensional crystalline nanorod arrays: Application to iron(III) oxides, *Chem. Mater.* **13**(12), 233–235 (2001).
98. R. V. Kumar, Y. Koltypin, X. N. Xu, Y. Yeshurun, A. Gedanken, and I. Felner, Fabrication of magnetite nanorods by ultrasound irradiation, *J. Appl. Phys.* **89**(11), 6324–6328 (2001).
99. P. Zhou, D. Xue, H. Luo, and X. Chen, Fabrication, structure, and magnetic properties of highly ordered Prussian blue nanowire arrays, *Nano Lett.* **2**(8), 845–847 (2002).
100. T. Kasuga, M. Hiramatsu, A. Hoson, T. Sekino, and K. Niihara, Titania nanotubes prepared by chemical processing, *Adv. Mater.* **11**(15), 1307–1311 (1999).
101. Y.-P. Fang, A.-W. Xu, R.-Q. Song, H.-X. Zhang, L.-P. You, J. C. Yu, and H.-Q. Liu, Systematic synthesis and characterization of single-crystal lanthanide orthophosphate nanowires, *J. Am. Chem. Soc.* **125**(51), 16,025–16,034 (2003).
102. H. Meyssamy, K. Riwozki, A. Kornowski, S. Naused, and M. Haase, Wet-chemical synthesis of doped colloidal nanomaterials: Particles and fibers of  $\text{LaPO}_4$ : Eu,  $\text{LaPO}_4$ : Ce, and  $\text{LaPO}_4$ : Ce,Tb, *Adv. Mater.* **11**(10), 840–844 (1999).
103. Y. Li, M. Sui, Y. Ding, G. Zhang, J. Zhuang, and C. Wang, Preparation of  $\text{Mg}(\text{OH})_2$  nanorods, *Adv. Mater.* **12**(11), 818–821 (2000).
104. X. Wang and Y. Li, Selected-control hydrothermal synthesis of  $\alpha$ - and  $\beta$ - $\text{MnO}_2$  single crystal nanowires, *J. Am. Chem. Soc.* **124**(12), 2880–2881 (2002).
105. J. Liu, J. Cai, Y. C. Son, Q. M. Gao, S. L. Suib, and M. Aindow, Magnesium manganese oxide nanoribbons: Synthesis, characterization, and catalytic application, *J. Phys. Chem. B* **106**(38), 9761–9768 (2002).
106. M. Niederberger, F. Krumeich, H.-J. Muhr, M. Müller, and R. Nesper, Synthesis and characterization of novel nanoscopic molybdenum oxide fibers, *J. Mater. Chem.* **11**(7), 1941–1945 (2001).
107. K. Matsui, T. Kyotani, and A. Tomita, Hydrothermal synthesis of single-crystal  $\text{Ni}(\text{OH})_2$  nanorods in a carbon-coated anodic alumina film, *Adv. Mater.* **14**(17), 1216–1219 (2002).
108. L. Guo, Z. Wu, T. Liu, W. Wang, and H. Zhu, Synthesis of novel  $\text{Sb}_2\text{O}_3$  and  $\text{Sb}_2\text{O}_5$  nanorods, *Chem. Phys. Lett.* **318**(1–3), 49–52 (2000).
109. S. Friedrichs, R. R. Meyer, J. Sloan, A. I. Kirkland, J. L. Hutchison, and M. L. H. Green, Complete characterisation of a  $\text{Sb}_2\text{O}_3$ /(21,-8)SWNT inclusion composite, *Chem. Commun.* 929–930 (2001).
110. X. Y. Zhang, L. D. Zhang, W. Chen, G. W. Meng, M. J. Zheng, and L. X. Zhao, Electrochemical fabrication of highly ordered semiconductor and metallic nanowire arrays, *Chem. Mater.* **13**(8), 2511–2515 (2001).
111. M. Zhang, Y. Bando, and K. Wada, Sol-gel template preparation of  $\text{TiO}_2$  nanotubes and nanorods, *J. Mater. Sci. Lett.* **20**(2), 167–170 (2001).
112. Z. Miao, D. Xu, J. Ouyang, G. Guo, X. Zhao, and Y. Tang, Electrochemically induced sol-gel preparation of single-crystalline  $\text{TiO}_2$  nanowires, *Nano Lett.* **2**(7), 717–720 (2002).
113. T. Kasuga, M. Hiramatsu, A. Hoson, T. Sekino, and K. Niihara, Formation of titanium oxide nanotube, *Langmuir* **14**(12), 3160–3163 (1998).
114. S. M. Liu, L. M. Gan, L. H. Liu, W. D. Zhang, and H. C. Zeng, Synthesis of single-crystalline  $\text{TiO}_2$  nanotubes, *Chem. Mater.* **14**(3), 1391–1397 (2002).

115. M. E. Spahr, P. Bitterli, R. Nesper, M. Müller, F. Krumeich, and H.-U. Nissen, Redox-active nanotubes of vanadium oxide, *Angew. Chem. Int. Ed.* **37**(9), 1263–1265 (1998).
116. F. Krumeich, H.-J. Muhr, M. Niederberger, F. Bieri, B. Schnyder, and R. Nesper, Morphology and topochemical reactions of novel vanadium oxide nanotubes, *J. Am. Chem. Soc.* **121**(36), 8324–8331 (1999).
117. J. Livage, Vanadium pentoxide gels, *Chem. Mater.* **3**(4), 578–593 (1991).
118. Y. Li, G. S. Cheng, and L. D. Zhang, Fabrication of highly ordered ZnO nanowire arrays in anodic alumina membranes, *J. Mater. Res.* **15**(11), 2305–2308 (2000).
119. Z. R. R. Tian, J. A. Voigt, J. Liu, B. McKenzie, and M. J. Mcdermott, Biomimetic arrays of oriented helical ZnO nanorods and columns, *J. Am. Chem. Soc.* **124**(44), 12954–12955 (2002).
120. A. W. Xu, Y. P. Fang, L. P. You, and H. Q. Liu, A simple method to synthesize Dy(OH)<sub>3</sub> and Dy<sub>2</sub>O<sub>3</sub> nanotubes, *J. Am. Chem. Soc.* **125**(6), 1494–1495 (2003).
121. X. Wang and Y. D. Li, Synthesis and characterization of lanthanide hydroxide single-crystal nanowires, *Angew. Chem. Int. Ed.* **41**(24), 4790–4793 (2002).
122. X. Wang and Y. D. Li, Rare-earth-compound nanowires, nanotubes, and fullerene-like nanoparticles: synthesis, characterization, and properties, *Chem. Eur. J.* **9**(22), 5627–5635 (2003).
123. B. H. Hong, S. C. Bae, C. W. Lee, S. Jeong, and K. S. Kim, Ultrathin single-crystalline silver nanowire arrays formed in an ambient solution phase, *Science* **294**, 348–351 (2001).
124. M. H. Huang, A. Choudrey, and P. D. Yang, Ag nanowire formation within mesoporous silica, *Chem. Commun.* 1063–1064 (2000).
125. Y.-J. Han, J. M. Kim, and G. D. Stucky, Preparation of noble metal nanowires using hexagonal mesoporous silica SBA-15, *Chem. Mater.* **12**(2), 2068–2069 (2000).
126. J. H. Song, Y. Wu, B. Messer, H. Kind, and P. D. Yang, Metal nanowire formation using Mo<sub>3</sub>Se<sup>3-</sup> as reducing and sacrificing templates, *J. Am. Chem. Soc.* **123**(42), 10397–10398 (2001).
127. Y. Zhou, S. H. Yu, C. Y. Wang, X. G. Li, Y. R. Zhu, and Z. Y. Chen, A novel ultraviolet irradiation photoreduction technique for the preparation of single-crystal Ag nanorods and Ag dendrites, *Adv. Mater.* **11**(10), 850–852 (1999).
128. N. R. Jana, L. Gearheart, and C. J. Murphy, Wet chemical synthesis of silver nanorods and nanowires of controllable aspect ratio, *Chem. Commun.* 617–618 (2001).
129. R. C. Jin, Y. W. Cao, C. A. Mirkin, K. L. Kelly, G. C. Schatz, and J. G. Zheng, Photoinduced conversion of silver nanospheres to nanoprisms, *Science* **294**, 1901–1903 (2001).
130. S. Liu, J. Yue, and A. Gedanken, Synthesis of long silver nanowires from AgBr nanocrystals, *Adv. Mater.* **13**(9), 656–658 (2001).
131. J. J. L. M. Cornelissen, R. van Heerbeek, P. C. J. Kamer, J. N. H. Reek, N. A. J. M. Sommerdijk, and R. J. M. Nolte, Silver nanoarrays templated by block copolymers of carbosilane dendrimers and polyisocyanopeptides, *Adv. Mater.* **14**(7), 489–492 (2002).
132. Y. Zhou, S. H. Yu, X. P. Cui, C. Y. Wang, and Z. Y. Chen, Formation of silver nanowires by a novel solid-liquid phase arc discharge method, *Chem. Mater.* **11**(3), 545–546 (1999).
133. S. H. Chen and D. L. Carroll, Synthesis and characterization of truncated triangular silver nanoplates, *Nano Lett.* **2**(9), 1003–1007 (2002).
134. M. Maillard, S. Giorgio, and M. P. Pileni, Silver nanodisks, *Adv. Mater.* **14**(15), 1084–1086 (2002).

135. I. Pastoriza-Santos and L. M. Liz-Marzan, Synthesis of silver nanoprisms in DMF, *Nano Lett.* **2**(8), 903–905 (2002).
136. Y. G. Sun, B. Gates, B. Mayers, and Y. Xia, Crystalline silver nanowires by soft solution processing, *Nano Lett.* **2**(2), 165–168 (2002).
137. Y. Yu, S. Chang, C. Lee, and C. R. C. Wang, Gold nanorods: Electrochemical synthesis and optical properties, *J. Phys. Chem. B* **101**(34), 6661–6664 (1997).
138. N. R. Jana, L. Gearheart, and C. J. Murphy, Wet chemical synthesis of high aspect ratio cylindrical gold nanorods, *J. Phys. Chem. B* **105**(19), 4065–4067 (2001).
139. C. J. Murphy and N. R. Jana, Controlling the aspect ratio of inorganic nanorods and nanowires, *Adv. Mater.* **14**(1), 80–82 (2002).
140. K. Esumi, K. Matsuhisa, and K. Torigoe, Preparation of rodlike gold particles by UV irradiation using cationic micelles as a template, *Langmuir* **11**(9), 3285–3287 (1995).
141. K. Soulantica, A. Maisonnat, F. Senocq, M.-C. Fromen, M.-J. Casanove, and B. Chaudret, Selective synthesis of novel in and In<sub>3</sub>Sn nanowires by an organometallic route at room temperature, *Angew. Chem. Int. Ed.* **40**(16), 2983–2986 (2001).
142. T. Hassenkam, K. Nørsgaard, L. Iversen, C. J. Kiely, M. Brust, and T. Bjørnholm, Fabrication of 2D gold nanowires by self-assembly of gold nanoparticles on water surfaces in the presence of surfactants, *Adv. Mater.* **14**(16), 1126–1130 (2002).
143. C. S. Ah, S. D. Hong, and D.-J. Jang, Preparation of Au coreAg shell nanorods and characterization of their surface plasmon resonances, *J. Phys. Chem. B* **105**(33), 7871–7873 (2001).
144. V. F. Puentes, K. M. Krishnan, and A. P. Alivisatos, Colloidal nanocrystal shape and size control: The case of cobalt, *Science* **291**, 2115–2117 (2001).
145. J. Tanori and M. P. Pileni, Control of the shape of copper metallic particles by using a colloidal system as template, *Langmuir* **13**(4), 639–646 (1997).
146. S. J. Park, S. Kim, S. Lee, Z. G. Khim, K. Char, and T. Hyeon, Synthesis and magnetic studies of uniform iron nanorods and nanospheres, *J. Am. Chem. Soc.* **122**(35), 8581–8582 (2000).
147. K. Soulantica, A. Maisonnat, F. Senocq, M.-C. Fromen, M.-J. Casanove, and B. Chaudret, Selective synthesis of novel in and In<sub>3</sub>Sn nanowires by an organometallic route at room temperature, *Angew. Chem. Int. Ed.* **40**(16), 2983–2986 (2001).
148. N. Cordente, M. Respaud, F. Senocq, M.-J. Casanove, C. Amiens, and B. Chaudret, Synthesis and magnetic properties of nickel nanorods, *Nano Lett.* **1**(10), 565–568 (2001).
149. G. Yi and W. Schwarzacher, Single crystal superconductor nanowires by electrodeposition, *Appl. Phys. Lett.* **74**(12), 1746–1748 (1999).
150. K. Torigoe and K. Esumi, Formation of nonspherical palladium nanocrystals in SDS polyacrylamide gel, *Langmuir* **11**(11), 4199–4201 (1995).
151. J. P. Xiao, Y. Xie, R. Tang, M. Chen, and X. B. Tian, Novel ultrasonically assisted templated synthesis of palladium and silver dendritic nanostructures, *Adv. Mater.* **13**(24), 1887–1891 (2001).
152. Z. D. Zhang, A. Blom, Z. Gai, J. R. Thompson, J. Shen, and S. Dai, High-yield solvothermal formation of magnetic CoPt alloy nanowires, *J. Am. Chem. Soc.* **125**(25), 7528–7529 (2003).
153. H. Yu, P. C. Gibbons, and W. E. Buhro, Bismuth, tellurium, and bismuth telluride nanowires, *J. Mater. Chem.* **14**(4), 595–602 (2004).
154. Y. D. Li, J. W. Wang, Z. X. Deng, Y. Y. Wu, X. M. Sun, D. P. Yu, and P. D. Yang, Bismuth nanotubes: A rational low-temperature synthetic route, *J. Am. Chem. Soc.* **123**(40), 9904–9905 (2001).

155. X. Y. Liu, J. H. Zeng, S. Y. Zhang, R. B. Zheng, X. M. Liu, and Y. T. Qian, Novel bismuth nanotube arrays synthesized by solvothermal method, *Chem. Phys. Lett.* **374**(3–4), 348–352 (2003).
156. T. Hanrath and B. A. Korgel, Nucleation and growth of germanium nanowires seeded by organic monolayer-coated gold nanocrystals, *J. Am. Chem. Soc.* **124**(7), 1424–1429 (2002).
157. K.-Q. Peng, Y.-J. Yan, S.-P. Gao, and J. Zhu, Synthesis of large-area silicon nanowire arrays via self-assembling nanoelectrochemistry, *Adv. Mater.* **14**(16), 1164–1167 (2002).
158. W. K. Hsu, S. Trasobares, H. Terrones, M. Terrones, N. Grobert, Y. Q. Zhu, W. Z. Li, R. Escudero, J. P. Hare, H. W. Kroto, and D. R. M. Walton, Electrolytic formation of carbon-sheathed mixed Sn-Pb nanowires, *Chem. Mater.* **11**(7), 1747–1751 (1999).
159. S. H. Yu, X. J. Cui, L. L. Li, K. Li, B. Yu, M. Antonietti, and H. Cölfen, From starch to metal/carbon hybrid nanostructures: Hydrothermal metal-catalyzed carbonization, *Adv. Mater.* **16**(18), 1636–1640 (2004).
160. A. Abdelouas, W. L. Gong, W. Lutze, J. A. Shelnut, R. Franco, and I. Moura, Using cytochrome  $c_3$  to make selenium nanowires, *Chem. Mater.* **12**(6), 1510–1512 (2000).
161. B. Gates, Y. D. Yin, and Y. N. Xia, A solution-phase approach to the synthesis of uniform nanowires of crystalline selenium with lateral dimensions in the range of 10–30 nm, *J. Am. Chem. Soc.* **122**(50), 12582–12583 (2000).
162. B. Gates, B. Mayers, B. Cattle, and Y. N. Xia, Synthesis and characterization of uniform nanowires of trigonal selenium, *Adv. Funct. Mater.* **12**(3), 219–227 (2002).
163. B. Mayers and Y. N. Xia, Formation of tellurium nanotubes through concentration depletion at the surfaces of seeds, *Adv. Mater.* **14**(4), 279–292 (2002).
164. M. S. Mo, J. H. Zeng, X. M. Liu, W. C. Yu, S. Y. Zhang, and Y. T. Qian, Controlled hydrothermal synthesis of thin single-crystal tellurium nanobelts and nanotubes, *Adv. Mater.* **14**(22), 1658–1662 (2002).
165. Y. Jiang, Y. Wu, S. Y. Zhang, C. Y. Xu, W. C. Yu, Y. Xie, and Y. T. Qian, A catalytic-assembly solvothermal route to multiwall carbon nanotubes at a moderate temperature, *J. Am. Chem. Soc.* **122**(49), 12,383–12,384 (2000).
166. Y. Xiong, Y. Xie, Z. Li, C. Wu, and R. Zhang, A novel approach to carbon hollow spheres and vessels from  $\text{CCl}_4$  at low temperatures, *Chem. Commun.* 904–905 (2003).
167. M. Cao, C. Hu, and E. Wang, The first fluoride one-dimensional nanostructures: Microemulsion-mediated hydrothermal synthesis of  $\text{BaF}_2$  whiskers, *J. Am. Chem. Soc.* **125**(37), 11,196–11,197 (2003).
168. Y.-H. Kim, Y.-W. Jun, B.-H. Jun, S.-M. Lee, and J. Cheon, Sterically induced shape and crystalline phase control of GaP nanocrystals, *J. Am. Chem. Soc.* **124**(46), 13,656–13,657 (2002).
169. C. Qian, F. Kim, L. Ma, F. Tsui, P. Yang, and J. Liu, Solution-phase synthesis of single-crystalline iron phosphide nanorods/nanowires, *J. Am. Chem. Soc.* **126**(4), 1195–1198 (2004).
170. S. D. Dingman, N. P. Rath, P. D. Markowitz, P. C. Gibbons, and W. E. Buhro, Low-temperature, catalyzed growth of indium nitride fibers from azido-indium precursors, *Angew. Chem. Int. Ed.* **39**(8), 1470–1472 (2000).
171. K. Tang, J. Hu, Q. Lu, Y. Xie, J. Zhu, and Y. Qian, A novel low-temperature synthetic route to crystalline  $\text{Si}_3\text{N}_4$ , *Adv. Mater.* **11**(8), 653–655 (1999).
172. Q. X. Guo, Y. Xie, X. J. Wang, S. Y. Zhang, T. Hou, and S. C. Lv, Synthesis of carbon nitride nanotubes with the  $\text{C}_3\text{N}_4$  stoichiometry via a benzene-thermal process at low temperatures, *Chem. Commun.* 26–27 (2004).

173. Q. Y. Lu, J. Q. Hu, K. B. Tang, Y. T. Qian, G. Zhou, X. M. Liu, and J. S. Zhu, Growth of SiC nanorods at low temperature, *Appl. Phys. Lett.* **75**(4), 507–509 (1999).
174. X. Wang, J. Lu, P. Gou, and Y. Xie, A “chemical-scissors-assemble” route to titanium carbide nanorods, *Chem. Lett.* **31**(8), 820–820 (2002).
175. J. H. Song, B. Messer, Y. Wu, H. Kind, and P. D. Yang,  $\text{MMo}_3\text{Se}_3$  ( $\text{M} = \text{Li}^+$ ,  $\text{Na}^+$ ,  $\text{Rb}^+$ ,  $\text{Cs}^+$ ,  $\text{NMe}^{4+}$ ) nanowire formation via cation exchange in organic solution, *J. Am. Chem. Soc.* **123**(39), 9714–9715 (2001).
176. D. S. Xu, Y. J. Xu, D. P. Chen, G. L. Guo, L. L. Gui, and Y. Q. Tang, Preparation and characterization of CdS nanowire arrays by dc electrodeposit in porous anodic aluminum oxide templates, *Chem. Phys. Lett.* **325**, 340–344 (2000).
177. S. H. Yu, Y. S. Wu, J. Yang, Z. H. Han, Y. Xie, Y. T. Qian, and X. M. Liu, A novel solventothermal synthetic route to nanocrystalline CdE ( $\text{E} = \text{S}, \text{Se}, \text{Te}$ ) and morphological control, *Chem. Mater.* **10**(9), 2309–2312 (1998).
178. Y. D. Li, H. W. Liao, Y. Ding, Y. T. Qian, L. Yang, and G. E. Zhou, Nonaqueous synthesis of CdS nanorod semiconductor, *Chem. Mater.* **10**(9), 2301–2303 (1998).
179. J. Yang, C. Xue, S. H. Yu, J. H. Zeng, and Y. T. Qian, General synthesis of semiconductor chalcogenide nanorods by using the monodentate ligand *n*-butylamine as a shape controller, *Angew. Chem. Ed. Int.* **41**(24), 4697–4700 (2002).
180. M. Chen, Y. Xie, J. Lu, Y. J. Xiong, S. Y. Zhang, Y. T. Qian, and X. M. Liu, Synthesis of rod-, twinrod-, and tetrapod-shaped CdS nanocrystals using a highly oriented solvothermal recrystallization technique, *J. Mater. Chem.* **12**(3), 748–753 (2002).
181. J. H. Zhan, X. G. Yang, D. W. Wang, S. D. Li, Y. Xie, Y. Xia, and Y. T. Qian, Polymer-controlled growth of CdS nanowires, *Adv. Mater.* **12**(18), 1348–1351 (2000).
182. N. Pinna, K. Weiss, J. Urban, and M. P. Pileni, Triangular CdS nanocrystals: Structural and optical studies, *Adv. Mater.* **13**(4), 261–264 (2001).
183. C.-C. Chen, C.-Y. Chao, and Z. H. Lang, Simple solution-phase synthesis of soluble CdS and CdSe nanorods, *Chem. Mater.* **12**(6), 1516–1518 (2000).
184. Y.-W. Jun, S.-M. Lee, N.-J. Kang, and J. Cheon, Controlled synthesis of multi-armed CdS nanorod architectures using monosurfactant system, *J. Am. Chem. Soc.* **123**(21), 5150–5151 (2001).
185. D. S. Xu, X. Shi, G. Guo, L. Gui, and Y. Q. Tang, Electrochemical preparation of CdSe nanowire arrays, *J. Phys. Chem. B* **104**(21), 5061–5063 (2000).
186. Z. A. Peng and X. G. Peng, Nearly monodisperse and shape-controlled CdSe nanocrystals via alternative routes: nucleation and growth, *J. Am. Chem. Soc.* **124**(13), 3343–3353 (2002).
187. Z. A. Peng and X. G. Peng, Formation of high-quality CdTe, CdSe, and CdS nanocrystals using CdO as precursor, *J. Am. Chem. Soc.* **123**(1), 183–184 (2001).
188. W. Z. Wang, Y. Geng, P. Yan, F. Y. Liu, Y. Xie, and Y. T. Qian, Synthesis and characterization of MSe ( $\text{M} = \text{Zn}, \text{Cd}$ ) nanorods by a new solvothermal method, *Inorg. Chem. Commun.* **2**(3), 83–85 (1999).
189. Q. Yang, K. Tang, C. Wang, Y. Qian, and S. Zhang, PVA-assisted synthesis, and characterization of CdSe and CdTe nanowires, *J. Phys. Chem. B* **106**(36), 9227–9230 (2002).
190. Q. Peng, Y. J. Dong, Z. X. Deng, and Y. D. Li, Selective synthesis and characterization of CdSe nanorods and fractal nanocrystals, *Inorg. Chem.* **41**(20), 5249–5254 (2002).
191. L. Manna, E. C. Scher, L.-S. Li, and A. P. Alivisatos, Epitaxial growth and photochemical annealing of graded CdS/ZnS shells on colloidal CdSe nanorods, *J. Am. Chem. Soc.* **124**(24), 7136–7145 (2002).



192. S. H. Yu, J. Yang, Z. H. Han, R. Y. Yang, Y. T. Qian, and Y. H. Zhang, Novel solvothermal fabrication of  $\text{CdS}_x\text{Se}_{1-x}$  nanowires, *J. Solid State Chem.* **147**(2), 637–640 (1999).
193. F. Gao, Q. Y. Lu, X. Y. Liu, Y. S. Yan, and D. Y. Zhao, Controlled synthesis of semiconductor PbS nanocrystals and nanowires inside mesoporous silica SBA-15 phase, *Nano Lett.* **1**(12), 743–748 (2001).
194. S. H. Wang and S. H. Yang, Preparation and characterization of oriented PbS crystalline nanorods in polymer films, *Langmuir* **16**(2), 389–397 (2000).
195. D. B. Yu, D. B. Wang, Z. Y. Meng, J. Lu, and Y. T. Qian, Synthesis of closed PbS nanowires with regular geometric morphologies, *J. Mater. Chem.* **12**(3), 403–405 (2002).
196. M. S. Mo, M. W. Shao, H. M. Hu, L. Yang, W. C. Yu, and Y. T. Qian, Growth of single-crystal PbS nanorods via a biphasic solvothermal interface reaction route, *J. Cryst. Growth.* **244**(3–4), 364–368 (2002).
197. W. Z. Wang, Y. Geng, Y. Qian, M. R. Ji, and X. M. Liu, A novel pathway to PbSe nanowires at room temperature, *Adv. Mater.* **10**(17), 1479–1481 (1998).
198. X. S. Peng, G. W. Meng, J. Zhang, X. F. Wang, C. Z. Wang, X. Liu, and L. D. Zhang, Strong quantum confinement in ordered PbSe nanowire arrays, *J. Mater. Res.* **17**(6), 1283–1286 (2002).
199. Y. Li, J. H. Wan, and Z. N. Gu, Synthesis of ZnS nanowires in liquid crystal systems, *Mol. Cryst. Liq. Cryst.* **337**, 193–196 (1999).
200. X. Jiang, Y. Xie, J. Lu, L. Y. Zhu, W. He, and Y. T. Qian, Simultaneous in situ formation of ZnS nanowires in a liquid crystal template by gamma-irradiation, *Chem. Mater.* **13**(4), 1213–1218 (2001).
201. Q. S. Wu, N. W. Zheng, Y. P. Ding, and Y. D. Li, Micelle-template inducing synthesis of winding ZnS nanowires, *Inorg. Chem. Commun.* **5**(9), 671–673 (2002).
202. S. H. Yu and M. Yoshimura, Shape and phase control of ZnS nanocrystals: template fabrication of wurtzite ZnS single-crystal nanosheets and ZnO flake-like dendrites from a lamellar molecular precursor  $\text{ZnS} \cdot (\text{NH}_2\text{CH}_2\text{CH}_2\text{NH}_2)_{0.5}$ , *Adv. Mater.* **14**(4), 296–300 (2002).
203. N. Kouklin, L. Menon, A. Z. Wong, D. W. Thompson, J. A. Woollam, P. F. Williams and S. Bandyopadhyay, Giant photoresistivity and optically controlled switching in self-assembled nanowires, *Appl. Phys. Lett.* **79**(26), 4423–4425 (2001).
204. Y. W. Jun, C. S. Choi, and J. Cheon, Size and shape controlled ZnTe nanocrystals with quantum confinement effect, *Chem. Commun.* 101–102 (2001).
205. Y. D. Li, Y. Ding, and Z. Y. Wang, A novel chemical route to ZnTe semiconductor nanorods, *Adv. Mater.* **11**(10), 847–850 (1999).
206. S. H. Yu, Y. T. Qian, L. Shu, Y. Xie, L. Yang, and C. S. Wang, Solvent thermal synthesis and characterization of ultrafine powder of bismuth sulfide, *Mater. Lett.* **35**(1–2), 116–119 (1998).
207. S. H. Yu, L. Shu, J. Yang, Z. H. Han, Y. T. Qian, and Y. H. Zhang, A solvothermal decomposition process for fabrication and particle sizes control of  $\text{Bi}_2\text{S}_3$  nanowires, *J. Mater. Res.* **14**(11), 4157–4162 (1999).
208. S. H. Yu, J. Yang, Y. S. Wu, Z. H. Han, Y. Xie, and Y. T. Qian, Hydrothermal preparation and characterization of rod-like ultrafine powders of bismuth sulfide, *Mater. Res. Bull.* **33**(11), 1661–1666 (1998).
209. X. S. Peng, G. W. Meng, J. Zhang, L. X. Zhao, X. F. Wang, Y. W. Wang, and L. D. Zhang, Electrochemical fabrication of ordered  $\text{Bi}_2\text{S}_3$  nanowire arrays, *J. Phys. D: Appl. Phys.* **34**(3), 3224–3232 (2001).

210. S. H. Yu, J. Yang, Y. S. Wu, Z. H. Han, J. Lu, Y. Xie, and Y. T. Qian, A new low temperature one-step route to metal chalcogenide semiconductors:  $\text{PbE}$ ,  $\text{Bi}_2\text{E}_3$  ( $\text{E} = \text{S}, \text{Se}, \text{Te}$ ), *J. Mater. Chem.* **8**(9), 1949–1951 (1998).
211. H. L. Su, Y. Xie, P. Gao, H. Lu, Y. J. Xiong, and Y. T. Qian, Synthesis and formation mechanism of  $\text{Bi}(\text{Se}, \text{S})$  nanowires via a solvothermal template process, *Chem. Lett.* **29**(7), 790–791 (2000).
212. M. S. Sander, A. L. Prieto, R. Gronsky, T. Sands, and A. M. Stacy, Fabrication of high-density, high aspect ratio, large-area bismuth telluride nanowire arrays by electrodeposition into porous anodic alumina templates, *Adv. Mater.* **14**(9), 665–667 (2002).
213. A. L. Prieto, M. S. Sander, M. S. Martin-Gonzalez, R. Gronsky, T. Sands, and A. M. Stacy, Electrodeposition of ordered  $\text{Bi}_2\text{Te}_3$  nanowire arrays, *J. Am. Chem. Soc.* **123**(29), 7161–7162 (2001).
214. Y. Zhang, G. H. Li, Y. C. Wu, B. Zhang, W. H. Song, and L. D. Zhang, Antimony nanowire arrays fabricated by pulsed electrodeposition in anodic alumina membranes, *Adv. Mater.* **14**(17), 1227–1230 (2002).
215. J. Yang, J. H. Zeng, S. H. Yu, L. Yang, Y. H. Zhang, and Y. T. Qian, Pressure-controlled fabrication of stibnite nanorods by the solvothermal decomposition of a simple single-source precursor, *Chem. Mater.* **12**(10), 2924–2929 (2000).
216. E. Roy, P. Fricoteaux, and K. Yu-Zhang, Electrochemical synthesis of antimony nanowires and analysis of diffusion layers, *J. Nanosci. Nanotechnol.* **1**(3), 323–329 (2001).
217. D. B. Wang, D. Yu, M. Shao, W. Yu, and Y. T. Qian, Solvothermal preparation of  $\text{Sb}_2\text{Se}_3$  nanowires, *Chem. Lett.* **31**(10), 1056–1057 (2002).
218. Q. Y. Lu, F. Gao, and D. Y. Zhao, Creation of a unique self-supported pattern of radially aligned semiconductor  $\text{Ag}_2\text{S}$  nanorods, *Angew. Chem. Int. Ed.* **41**(11), 1932–1934 (2002).
219. B. Gates, Y. Y. Wu, Y. D. Yin, P. D. Yang, and Y. N. Xia, Single-crystalline nanowires of  $\text{Ag}_2\text{Se}$  can be synthesized by templating against nanowires of trigonal Se, *J. Am. Chem. Soc.* **123**(46), 11,500–11,501 (2001).
220. B. Gates, B. Mayers, Y. Y. Wu, Y. G. Sun, B. Cattle, P. D. Yang, and Y. N. Xia, Synthesis and characterization of crystalline  $\text{Ag}_2\text{Se}$  nanowires through a template-engaged reaction at room temperature, *Adv. Funct. Mater.* **12**, 679–686 (2002).
221. S. H. Wang, S. H. Yang, Z. R. Dai, and Z. L. Wang, The crystal structure and growth direction of  $\text{Cu}_2\text{S}$  nanowire arrays fabricated on a copper surface, *Phys. Chem. Chem. Phys.* **3**(17), 3750–3753 (2001).
222. X. G. Wen and S. H. Yang,  $\text{Cu}_2\text{S}/\text{Au}$  core/sheath nanowires prepared by a simple redox deposition method, *Nano Lett.* **2**(5), 451–454 (2002).
223. Q. Y. Lu, F. Gao, and D. Y. Zhao, One-step synthesis and assembly of copper sulfide nanoparticles to nanowires, nanotubes, and nanovesicles by a simple organic amine-assisted hydrothermal process, *Nano. Lett.* **2**(7), 725–728 (2002).
224. Y.-W. Jun, Y.-Y. Jung, and J. Cheon, Architectural control of magnetic semiconductor nanocrystals, *J. Am. Chem. Soc.* **124**(4), 615–619 (2002).
225. H. Liao, Y. Wang, S. Zhang, and Y. Qian, A solution low-temperature route to  $\text{MoS}_2$  fiber, *Chem. Mater.* **13**(1), 6–8 (2001).
226. Q. Yang, K. B. Tang, C. R. Wang, D. Y. Zhang, and Y. T. Qian, The synthesis of  $\text{SnS}_2$  nanoflakes from tetrabutyltin precursor, *J. Solid State Chem.* **164**(1), 106–109 (2002).

227. J. Q. Hu, B. Deng, W. X. Zhang, K. B. Tang, and Y. T. Qian, Synthesis and characterization of  $\text{CdIn}_2\text{S}_4$  nanorods by converting CdS nanorods via the hydrothermal route, *Inorg. Chem.* **40**, 3130–3133 (2001).
228. Y. Cui, J. Ren, G. Chen, Y. Qian, and Y. Xie, A simple route to synthesize  $\text{MInS}_2$  ( $\text{M} = \text{Cu}, \text{Ag}$ ) nanorods from single-molecule precursors, *Chem. Lett.* **30**(3), 236–237 (2001).
229. B. Xie, S. W. Yuan, Y. Jiang, J. Lu, Q. Li, Y. Wu, W. C. Yu, H. B. Zhang, and Y. T. Qian, Molecular template preparation of  $\text{AgBiS}_2$  nanowhiskers, *Chem. Lett.* **31**(6), 612–613 (2002).
230. J. Q. Hu, B. Deng, W. X. Zhang, K. B. Tang, and Y. T. Qian, A convenient hydrothermal route to mineral  $\text{Ag}_3\text{CuS}_2$  nanorods, *Int. J. Inorg. Mater.* **3**(7), 639–642 (2001).
231. Y. J. Xiong, Y. Xie, G. Du, and H. Su, From 2D framework to quasi-1D nanomaterial: Preparation, characterization, and formation mechanism of  $\text{Cu}_3\text{SnS}_4$  nanorods, *Inorg. Chem.* **41**(11), 2953–2959 (2002).
232. C. R. Wang, K. B. Tang, Q. Yang, G. Z. Shen, B. Hai, C. H. An, J. Zuo, and Y. T. Qian, Characterization of  $\text{PbSnS}_3$  nanorods prepared via an iodine transport hydrothermal method, *J. Solid State Chem.* **160**(1), 50–53 (2001).
233. A. Rabenau, The role of hydrothermal synthesis in preparative chemistry, *Angew. Chem. Int. Ed. Engl.* **24**(12), 1026–1040 (1985).
234. K. Byrappa and M. Yoshimura (eds.), *Handbook of Hydrothermal Technology*, William Andrews, LLC/Noyes Publications, Park Ridge, NJ, 2000.
235. J. P. Corbett, Polyatomic zintl anions of the posttransition elements, *Chem. Rev.* **85**(5), 383–397 (1985).
236. H. Schafer, On the problem of polar intermetallic compounds: The simulation of zintl work for the modern chemistry of intermetallics, *Annu. Rev. Mater. Sci.* **15**, 1–41 (1985).
237. R. I. Walton, Subcritical solvothermal synthesis of condensed inorganic materials, *Chem. Soc. Rev.* **31**(4), 230–238 (2002).
238. S. S. Feng and R. R. Xu, New materials in hydrothermal synthesis, *Acc. Chem. Res.* **34**(3), 239–247 (2001).
239. W. S. Sheldrick and M. Wachhold, Solventothermal synthesis of solid-state chalcogenidometalates, *Angew. Chem., Int. Ed.* **36**(3), 206–224 (1997).
240. G. Demazeau, Solvothermal processes: a route to the stabilization of new materials, *J. Mater. Chem.* **9**(1), 15–18 (1999).
241. R. F. Morris and S. J. Weigel, The synthesis of molecular sieves from non-aqueous solvents, *Chem. Soc. Rev.* **26**(4), 309–317 (1997).
242. Y. Xie, Y. T. Qian, W. Z. Wang, S. Y. Zhang, and Y. H. Zhang, A benzene-thermal synthetic route to nanocrystalline GaN, *Science* **272**, 1926–1927 (1996).
243. J. Q. Hu, Q. Y. Lu, K. B. Tang, S. H. Yu, Y. T. Qian, G. E. Zhou, X. M. Liu, and J. X. Wu, Low-temperature synthesis of nanocrystalline titanium nitride via a benzene-thermal route, *J. Am. Ceram. Soc.* **83**(2), 430–432 (2000).
244. J. Q. Hu, Q. Y. Lu, K. B. Tang, S. H. Yu, Y. T. Qian, G. E. Zhou, X. M. Liu, and J. X. Wu, Synthesis and characterization of nanocrystalline boron nitride, *J. Solid State Chem.* **148**(2), 325–328 (1999).
245. M. Niederberger, H. J. Muhr, F. Krumeich, F. Bieri, D. Günther, and R. Nesper, Low-cost synthesis of vanadium oxide nanotubes via two novel non-alkoxide routes, *Chem. Mater.* **12**(7), 1995–2000 (2000).

246. H. J. Muhr, F. Krumeich, U. P. Schönholzer, F. Bieri, M. Niederberger, L. J. Gauckler, and R. Nesper, Vanadium oxide nanotubes: A new flexible vanadate nanophase, *Adv. Mater.* **12**(3), 231–234 (2000).
247. S. H. Yu, J. Yang, Z. H. Han, Y. Zhou, R. Y. Yang, Y. Xie, Y. T. Qian, and Y. H. Zhang, Controllable synthesis of nanocrystalline CdS with different morphologies and particle sizes by a novel solvothermal process, *J. Mater. Chem.* **9**(6), 1283–1287 (1999).
248. D. Arivuoli, F. D. Gnanam, and P. Ramasamy, Growth and micorhardenss studies of chalcogenides of arsenic, antimony and bismuth, *J. Mater. Sci. Lett.* **7**(7), 711–713 (1988).
249. C. Kaito, Y. Saito, and K. Fujita, Studies on the structure and morphology of ultrafine of metallic sulfides, *J. Cryst. Growth* **94**(4), 967–977 (1989).
250. B. F. Variano, D. M. Hwang, C. S. Sandroff, P. Wiltzius, T. W. Jing, and N. P. Ong, Quantum effects in anisotropic semiconductor clusters-colloidal suspensions of  $\text{Bi}_2\text{S}_3$  and  $\text{Sb}_2\text{S}_3$ , *J. Phys. Chem.* **91**(26), 6455–6458 (1987).
251. Z. P. Liu, S. Peng, Q. Xie, Z. Hu, Y. Yang, S. Zhang, and Y. T. Qian, Large-scale synthesis of ultralong  $\text{Bi}_2\text{S}_3$  nanoribbons via a solvothermal process, *Adv. Mater.* **15**(11), 936–940 (2003).
252. Y. Gogotsi, J. A. Libera, and M. Yoshimura, Hydrothermal synthesis of multiwall carbon nanotubes, *J. Mater. Res.* **15**(12), 2591–2594 (2000).
253. Y. Gogotsi, N. Naguib, A. Guvenc-Yazicioglu, and C. M. Megaridis, In situ multiphase fluid experiments in hydrothermal carbon nanotubes, *Appl. Phys. Lett.* **79**(7), 1021–1023 (2001).
254. Y. Gogotsi, N. Naguib, and J. Libera, In situ chemical experiments in carbon nanotubes, *Chem. Phys. Lett.* **365**(3–4), 354–360 (2002).
255. J. M. Calderon Moreno and M. Yoshimura, Hydrothermal processing of high-quality multiwall nanotubes from amorphous carbon, *J. Am. Chem. Soc.* **123**(4), 741–742 (2001).
256. Z. A. Peng and X. G. Peng, Mechanisms of the shape evolution of CdSe nanocrystals, *J. Am. Chem. Soc.* **123**(7), 1389–1395 (2001).
257. L. Manna, D. J. Milliron, A. Meisel, E. C. Scher, and A. P. Alivisatos, Controlled growth of tetrapod-branched inorganic nanocrystals, *Nature Mater.* **2**(6), 382–385 (2003).
258. D. L. Wang and C. M. Lieber, Inorganic materials: nanocrystals branch out, *Nature Mater.* **2**(6), 355–356 (2003).
259. B. A. Simmons, S. Li, V. T. John, G. L. McPherson, A. Bose, W. Zhou, and J. He, Morphology of CdS nanocrystals synthesized in a mixed surfactant system, *Nano Lett.* **2**(4), 263–268 (2002).
260. H. Cölfen, Double-hydrophilic block copolymers: Synthesis and application as novel surfactants and crystal growth modifiers, *Macromol. Rapid. Commun.* **22**(4), 219–252 (2001).
261. H. Cölfen and M. Antonietti, Crystal design of calcium carbonate microparticles using double-hydrophilic block copolymers, *Langmuir* **14**(3), 582–589 (1998).
262. S. H. Yu, H. Cölfen, J. Hartmann, and M. Antonietti, Biomimetic crystallization of calcium carbonate spherules with controlled surface structures and sizes by double-hydrophilic block copolymers, *Adv. Funct. Mater.* **12**(8), 541–545 (2002).
263. M. Antonietti, M. Breulmann, C. G. Goltner, H. Cölfen, K. K. W. Wong, D. Walsh, and S. Mann, Inorganic/organic mesostructures with complex architectures: Precipitation

- of calcium phosphate in the presence of double-hydrophilic block copolymers, *Chem. Eur. J.* **4**(12), 2491–2500 (1998).
264. L. M. Qi, H. Cölfen, and M. Antonietti, Crystal design of barium sulfate using double-hydrophilic block copolymers, *Angew. Chem. Int. Ed.* **39**(3), 604–607 (2000).
  265. M. Öner, J. Norwig, W. H. Meyer, and G. Wegner, Control of ZnO crystallization by a PEO-*b*-PMAA diblock copolymer, *Chem. Mater.* **10**(2), 460–463 (1998).
  266. A. Taubert, D. Palms, O. Weiss, M. T. Piccini, and D. N. Batchelder, Polymer-assisted control of particle morphology and particle size of zinc oxide precipitated from aqueous solution, *Chem. Mater.* **14**(6), 2594–2601 (2002).
  267. K. J. C. van Bommel, A. Friggeri, and S. Shinkai, Organic templates for the generation of inorganic materials, *Angew. Chem. Int. Ed.* **42**(9), 980–999 (2003).
  268. E. D. Sone, E. R. Zubarev, and S. I. Stupp, Semiconductor nanohelices templated by supramolecular ribbons, *Angew. Chem. Int. Ed.* **41**(10), 1705–1709 (2002).
  269. J. D. Hartgerink, E. Beniash, and S. I. Stupp, Self-assembly and mineralization of peptide-amphiphile nanofibers, *Science* **294**, 1684–1688 (2001).
  270. Y. Ono, K. Nakashima, M. Sano, Y. Kanekiyo, K. Inoue, J. Hojo, and S. Shinkai, Organic gels are useful as a template for the preparation of hollow fiber silica, *Chem. Commun.* 1477–1478 (1998).
  271. J. H. Jung, Y. Ono, and S. Shinkai, Novel preparation method for multi-layered, tubular silica using an azacrown-appended cholesterol as template and metal-deposition into the interlayer space, *J. Chem. Soc. Perkin Trans.* **2**(7), 1289–1291 (1999).
  272. Y. Ono, K. Nakashima, M. Sano, J. Hojo, and S. Shinkai, Template effect of cholesterol-based organogels on sol-gel polymerization creates novel silica with a helical structure, *Chem. Lett.* 1119–1120 (1999).
  273. J. H. Jung, Y. Ono, and S. Shinkai, Sol-gel polycondensation of tetraethoxysilane in a cholesterol-based organogel system results in chiral spiral silica, *Angew. Chem. Int. Ed.* **39**(10), 1862–1865 (2000).
  274. J. H. Jung, Y. Ono, and S. Shinkai, Sol-gel polycondensation in a cyclohexane-based organogel system in helical silica: creation of both right- and left-handed silica structures by helical organogel fibers, *Chem. Eur. J.* **6**(24), 4552–4557 (2000).
  275. J. H. Jung, Y. Ono, K. Hanabusa, and S. Shinkai, Creation of both right-handed and left-handed silica structures by sol-gel transcription of organogel fibers comprised of chiral diaminocyclohexane derivatives, *J. Am. Chem. Soc.* **122**(20), 5008–5009 (2000).
  276. Y. Ono, K. Nakashima, M. Sano, J. Hojo, and S. Shinkai, Organogels are useful as a template for the preparation of novel helical silica fibers, *J. Mater. Chem.* **11**(10), 2412–2419 (2001).
  277. S. Kobayashi, K. Hanabusa, N. Hamasaki, M. Kimura, H. Shirai, and S. Shinkai, Preparation of TiO<sub>2</sub> hollow-fibers using supramolecular assemblies, *Chem. Mater.* **12**(6), 1523–1525 (2000).
  278. S. Kobayashi, N. Hamasaki, M. Suzuki, M. Kimura, H. Shirai, and K. Hanabusa, Preparation of helical transition-metal oxide tubes using organogelators as structure-directing agents, *J. Am. Chem. Soc.* **124**(23), 6550–6551 (2002).
  279. J. H. Jung, H. Kobayashi, K. J. C. Bommel, S. Shinkai, and T. Shimizu, Creation of novel helical ribbon and double-layered nanotube TiO<sub>2</sub> structures using an organogel template, *Chem. Mater.* **14**(4), 1445–1447 (2002).
  280. B. C. Bunker, P. C. Rieke, B. J. Tarasevich, A. A. Campbell, G. E. Fryxell, G. L. Graff, L. Song, J. Liu, and J. W. Virden, Ceramic thin-film formation on functionalized interfaces through biomimetic processing, *Science* **264**, 48–55 (1994).

281. G. Falini, S. Albeck, S. Weiner, and L. Addadi, Control of aragonite or calcite polymorphism by mollusk shell macromolecules, *Science* **271**, 67–69 (1996).
282. A. M. Belcher, X. H. Wu, P. K. Christensen, P. K. Hansma, G. D. Stucky, and D. E. Morse, Control of crystal phase switching and orientation by soluble mollusc-shell proteins, *Nature* **381**, 56–58 (1996).
283. T. Sugimoto, Preparation of monodispersed colloidal particles, *Adv. Colloid. Interf. Sci.* **28**, 65–108 (1987).
284. A. P. Alivisatos, Perspectives: Biomineralization: Naturally aligned nanocrystals, *Science* **289**, 736–737 (2000).

# 4

## Assembly of Zeolites and Crystalline Molecular Sieves

JENNIFER L. ANTHONY AND MARK E. DAVIS

*California Institute of Technology, Chemical Engineering, Pasadena, CA 91125*

### 4.1. Introduction

Porous inorganic materials such as zeolites and zeolitelike crystalline molecular sieves are of great interest because of their range of commercial applications such as catalysis, adsorption/separation, and ion exchange. The term *zeolite* refers to the specific class of aluminosilicate molecular sieves, although the term is frequently used more loosely to describe compounds other than aluminosilicates that have frameworks similar to known zeolites.

Knowledge of the framework crystal chemistry of these materials is important in order to understand their physicochemical properties. Zeolites are constructed from  $\text{TO}_4$  tetrahedra, where T is a tetrahedral atom such as silicon or aluminum.<sup>1</sup> Each oxygen atom (O) is shared with an adjacent tetrahedral atom (T), resulting in a framework ratio of O/T equaling 2. Silicon has a +4 charge and oxygen has a -2 charge, thus giving in an overall charge of -4 for the individual group  $\text{SiO}_4$ . In a structured, tetrahedral framework, however, each oxygen atom is shared between two silicon atoms, so the overall charge for a pure-silica network is neutral. Replacing the T atoms with other elements result in different charges (e.g., aluminum gives -1 and zinc gives -2). These charges then have to be balanced with a cation, typically alkali metals (e.g.,  $\text{K}^+$  and  $\text{Na}^+$ ), alkaline earth metals (e.g.,  $\text{Ba}^{2+}$  and  $\text{Ca}^{2+}$ ), protons ( $\text{H}^+$ ), and combinations thereof. Figure 4.1 shows examples of these connectivities. Ratios of silicon to aluminum are not less than 1 (i.e., there are not two aluminum atoms bonded to the same oxygen atom), and this arrangement is rationalized by Loewenstein's rule that states that isolated negative charges ( $\text{Al}^- - \text{O} - \text{Si} - \text{O} - \text{Al}^- - \text{O} - \text{Si}$ ) will be more stable than adjacent negative charges ( $\text{Al}^- - \text{O} - \text{Al}^- - \text{O} - \text{Si} - \text{O} - \text{Si}$ ).<sup>2,3</sup> Silicon can also be replaced with compounds such as phosphorus, but never in a manner to give a positive framework charge.<sup>4</sup> Here, we will focus on the fully tetrahedral networks, particularly because the bulk of the literature on crystalline microporous materials involves them.

In this review, we address several important aspects in understanding the fundamental processes involved in the assembly of crystalline molecular sieves. First, we address the thermodynamics and kinetics of the synthesis processes. Second, we discuss several proposed mechanisms for zeolite assembly and the interactions

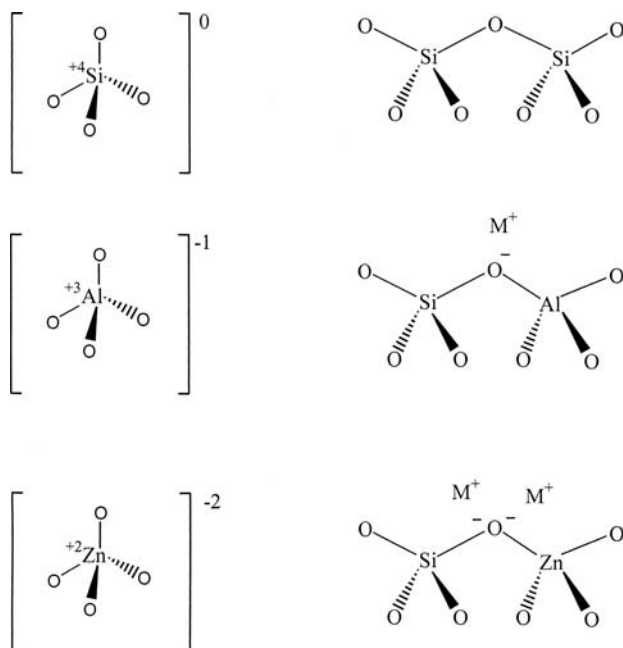


FIGURE 4.1. Structures, charges, and connectivities with  $\text{SiO}_2$  of  $\text{SiO}_2$ ,  $\text{AlO}_2^{-1}$ , and  $\text{ZnO}_2^{-2}$ .

among the components involved. Finally, we emphasize the importance of trying to understand the zeolite assembly process as it would apply to designing a molecular sieve, specifically a chiral molecular sieve.

## 4.2. Thermodynamics of Synthesis Processes

Attempts to understand the mechanism of molecular sieve assembly must include an understanding of the thermodynamics of the process. Petrovic et al. were the first to measure the enthalpy of formation of microporous, crystalline pure-silica molecular sieves.<sup>5</sup> They considered six high-silica zeolites and determined that all were only destabilized 7–14  $\text{kJ mol}^{-1}$  relative to quartz, the most stable form of silica. Piccione et al. extended this initial work and focused on a range of materials.<sup>6</sup> They measured the enthalpies for 11 different pure-silica molecular sieves with various framework densities. Like Petrovic et al., Piccione et al. found that the molecular sieves are metastable, but only differing 6–15  $\text{kJ mol}^{-1}$  with respect to quartz. This difference is similar to those seen with silica glasses and amorphous silica.<sup>6</sup> These results show a clear relationship that as the molar volume is increased (or the framework density is decreased), the enthalpy increases relative to quartz. Molar volume is defined as  $\text{cm}^3 \text{mol}^{-1} \text{SiO}_2$ , framework density (FD) is the number



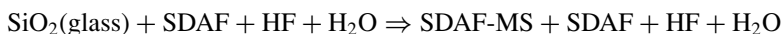
of T atoms per nm<sup>3</sup>, and the enthalpy is kJ mol<sup>-1</sup> SiO<sub>2</sub>.<sup>5,6</sup> The data of Petrovic et al. and Piccione et al. show that the transformation of amorphous silica to crystalline silica is not hindered significantly in terms of energetics. The entropies of formation for several pure-silica molecular sieves have also been calculated.<sup>7,8</sup> The entropies for each of the silicates investigated were relatively similar (44.7–45.7 J K<sup>-1</sup>mol<sup>-1</sup>), despite the samples having fairly diverse molar volumes (30–44 cm<sup>3</sup>mol<sup>-1</sup>). Entropies of dense silicates do vary with molar volume, but above 30 cm<sup>3</sup>mol<sup>-1</sup>, the entropy approaches a constant around 45 J K<sup>-1</sup>mol<sup>-1</sup>. All four samples had entropies only 3.2–4.2 J K<sup>-1</sup>mol<sup>-1</sup> higher than quartz.

The energetic trends observed from pure-silica materials are also obtained with aluminophosphates.<sup>9</sup> However, ordered mesoporous materials that are not crystalline show energy-independent behavior with increasing pore size (~15 kJ mol<sup>-1</sup> SiO<sub>2</sub> for pore sizes above 2 nm).<sup>10</sup> Because the less dense microporous crystalline materials have enthalpy values nearly the same as the ordered mesoporous materials, it is not clear whether thermodynamics place limits on the minimum FD that can be achievable with crystalline TO<sub>2</sub> frameworks. Recently, Moloy et al. showed that the average *internal* surface enthalpy of microporous crystalline silicas is 0.093 ± 0.009 J m<sup>-2</sup> and that this value is within experimental error of the value for the average *external* surface enthalpy of amorphous silica (0.100 ± 0.035 J m<sup>-2</sup>).<sup>11</sup> Thus, there appears to be no preference in surface energy between crystalline and amorphous silica at a fixed exposed area. This is somewhat surprising because crystalline silicas have very low silanol densities when compared to amorphous silicas, and the number of silanol groups should certainly affect the stability of the solids.

To compare the effect the T<sup>IV</sup> atom has on the framework stability, studies were conducted in which germanium rather than silicon was included in the structures. The enthalpies of formation with respect to a mixture of quartz polymorphs of germania and silica have been determined.<sup>12,13</sup> The Ge-containing zeolites were more metastable than the corresponding pure silica ones. All of the zeolite framework examined become energetically less stable with increasing Ge content, but the slope is different for each structure, and a possible crossover in framework stability with Ge content exists for structures that can compete in the synthesis. Changing the T<sup>IV</sup> composition can lead to a more thermodynamically stable structure that is less stable for another framework composition.

In addition to investigating the role of the framework composition in the stability, it is also important to evaluate the thermodynamics of the entire synthesis process, including the role of the structure directing agent (SDA). Helmkamp and Davis were the first to do this for the synthesis of pure-silica ZSM-5 using tetrapropylammonium fluoride as the SDA.<sup>3</sup> In a more recent work, Piccione et al. investigated the thermodynamic role of the SDA in the molecular sieve synthesis by carefully measuring the interaction energies between the silica frameworks and the enclathrated organic SDAs.<sup>14,15</sup> They studied various combinations using four different pure-silica molecular sieves and four organic SDAs. This synthesis process can be written as (using a F<sup>-</sup> mineralizer—see the later discussion on the

roles of the mineralizing agents)



where SDAF-MS represents the crystalline molecular sieve with enclathrated SDAF. No stoichiometric coefficients are given because they can be different for each synthesis (SDA framework) and the silica is assumed to be completely consumed (can be done experimentally in some syntheses). The thermodynamics of this process can be broken down into three steps: (1) transformation of silica glass to a silica molecular sieve, (2) the partitioning of the SDA from the aqueous solution into the open framework, and (3) the dilution of the remaining SDAF and HF in solution from the start to the end of the synthesis. These thermodynamic studies also show that the enthalpy and entropy contributions to the free energy of crystallization are similar in magnitude and that no single factor dominated the overall Gibbs free energies.<sup>14,15</sup> For example, with tetrapropylammonium (TPA) and tetraethylammonium (TEA) used to synthesize ZSM5 (MFI) and beta (\*BEA), respectively,  $\Delta H$  for TPA/MFI and TEA/\*BEA were both  $-3.2 \text{ kJ mol}^{-1} \text{ SiO}_2$ , whereas  $T\Delta S$  for TPA/MFI and TEA/\*BEA were 1.7 and 2.2  $\text{kJ mol}^{-1} \text{ SiO}_2$ , respectively. Thus, the self-assembly process depends on the delicate interplay between a large number of weak interactions (as is often observed in biological systems).

The energetic differences in the overall synthesis process between various SDA–molecular sieve combinations are sufficiently small (e.g., TEA/MFI =  $-4.9 \pm 2.8 \text{ kJ mol}^{-1} \text{ SiO}_2$ , TEA/\*BEA =  $-8.5 \pm 2.9 \text{ kJ mol}^{-1} \text{ SiO}_2$ .<sup>14,15</sup>) that energetic limitations are not likely to be the dominant factor in determining which molecular sieve is obtained from a synthesis. In fact, the small enthalpy and Gibbs free-energy changes seen during crystallizations using a SDA are consistent with the fact that most organocations are capable of directing the synthesis of multiple molecular sieve frameworks. Overall, these thermodynamic analyses suggest that kinetic factors are of major importance and, more specifically, the kinetics of nucleation are likely the critical process involved in determining the material obtained from a particular preparation.

These thermodynamic findings again emphasize some of the main differences in the process of synthesizing molecular sieves compared to traditional covalent synthesis. The significant differences between covalent and noncovalent syntheses were tabulated by Whitesides et al.<sup>16</sup> and modified specifically for zeolites later by Davis.<sup>17</sup> This table is replicated here as Table 4.1. Noncovalent syntheses result from a variety of different weak interactions and depend strongly on solvent effects, unlike traditional covalent syntheses, which are typically dominated by strong enthalpic interactions and strong bonds.

### 4.3. Kinetics of Synthesis Processes

Burkett and Davis showed by solid-state NMR methods that the first step in the assembly process of Si–ZSM-5 involved the organization of silicon-containing

TABLE 4.1. Comparison of covalent and noncovalent syntheses.

	Covalent	Noncovalent (zeolite)
Constituent bond types in the assembly process	Covalent	Ionic, hydrophobic, hydrogen (between organic and inorganic)
Bond strengths (kcal mol <sup>-1</sup> )	25–200	0.1–5 (between organic and inorganic)
Stability of bonds in product	Kinetically stable	Kinetically reversible (includes silica chemistry)
Number of interactions in the assembly steps	Few	Many
Contributions to $\Delta G$	Usually dominated by $\Delta H$	$\Delta H$ and $\Delta S$ can be comparable
Importance of solvent effects	Secondary	Primary
Other characteristics	—	Cooperative behavior important

Source: Modified from Ref. 16; reprinted from Ref. 17.

species around the organic SDAs.<sup>18</sup> These authors speculated that the driving forces for assembly were van der Waals contacts between organic groups and hydrophobic silicate species (enthalpic driving force) and the release of ordered water (hydrophobic hydration) around the organics and silicate species into the bulk water phase (entropic driving force).<sup>18</sup> It is this initial step in the organization where the geometric correspondence between the SDA and the final pore architecture likely originates. Organics that do not have a hydrophobic hydration sphere [e.g., tetraethanolammonium (same size as TPA but does not produce ZSM-5)] do not organize silica and do not nucleate the synthesis of molecular sieves.<sup>19</sup> The proposed driving forces for assembly are consistent with thermodynamics (see Section 4.2) and the initial assembled entities lead to nucleation centers, as will be discussed in Section 4.4. The kinetics of nucleation is typically slower than the kinetics of crystal growth in high- and/or pure-silica syntheses, based on experimental observation.

If nucleation is rate limiting, then the Ostwald ripening model would predict that increasing crystallization rates should be observed with increasing stability of the crystallization material.<sup>20</sup> Harris and Zones showed that there was a good correlation between the stabilization energy of various organic molecules in either the CHA or NON (three letter codes are set for each framework topology by the International Zeolite Structure Commission and can be found at [www.iza-structure.org/databases](http://www.iza-structure.org/databases)) structure types calculated via molecular modeling methods and the crystallization rates (the greater the stabilization, the faster the rate).<sup>21</sup> Because the crystallization rates are primarily determined by the rates of nucleation, these data are consistent with the Ostwald ripening model. The energy stabilizations mostly arise from van der Waals interactions. Direct evidence for the effects of multiple weak interactions working cooperatively to stabilize an organic SDA is provided by Behrens et al.<sup>22</sup> The single-crystal structure of [Cocp<sub>2</sub><sup>+</sup>F<sup>-</sup>]-NON showed that the cp rings were interacting via several weak C–H...O bonds to the NON structure.<sup>22</sup> These interactions as well as the steric confinement prevents any rotation of the cation.<sup>22</sup> This stabilization was shown to occur even at

synthesis temperatures. Thus, freely rotating cp rings of the  $\text{Cocp}_2$  cation, when located in the synthesis mixture, interact with the enclathrating structure in sufficient strength to stabilize the organometallic complex in a configuration absence of cp ring rotation.

It is clear that the kinetics of nucleation can be the rate-determining step in the assembly process and that the stabilization energy can affect the kinetics. Therefore, the organic–inorganic interactions can greatly influence the outcome of the synthesis.

#### 4.4. Assembly Processes

Crystalline molecular sieves are usually prepared using a hydrothermal synthesis method. For example, a typical zeolite synthesis would consist of a mixture of water, a source of the T atoms (for silica, these can be fumed silica, colloidal silica, and/or silicon alkoxides), a mineralizing agent (e.g.,  $\text{OH}^-$  or  $\text{F}^-$ ), and a SDA. The exact nature of the SDA can vary from organic species such as ammonium ions to alkali metal ions such as potassium and sodium. These reagents are all mixed and heated (typically less than  $200^\circ\text{C}$ ) and, over time, will self-assemble into the crystalline structure. Figure 4.2 shows a schematic of how the assembly of pure-silica MFI might occur starting from clear solutions (TPA is the SDA).<sup>23</sup>

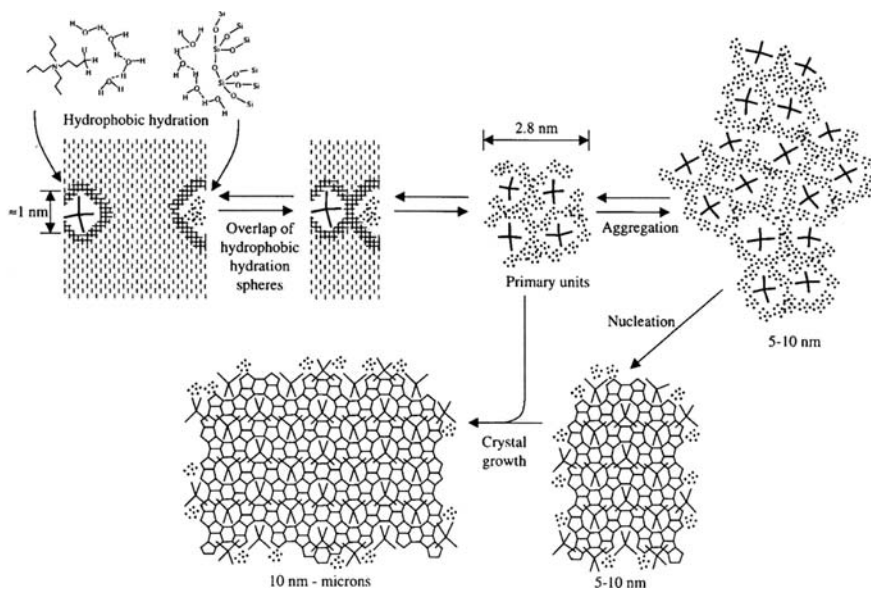


FIGURE 4.2. Scheme for the crystallization mechanism of Si-TPA-MFI. (Reproduced with permission from Ref. 23.)

#### 4.4.1. Proposed Mechanisms for Zeolite Assembly

Numerous groups have investigated the assembly processes of zeolite synthesis; yet the exact mechanism remains unknown. In the 1990s, Regev and co-workers,<sup>24</sup> Schoeman,<sup>25</sup> Thompson and co-workers,<sup>26</sup> and Iton and White and their co-workers<sup>27</sup> monitored zeolite syntheses by *in situ* methods. Conducting *in situ* measurements during synthesis is essential, as it is likely impossible to isolate the true intermediates of the synthesis process because the assembly is driven by cooperative weak interactions. These studies showed the existence of 3–5-nm entities that were composites of the organic SDAs and silicate species. Speculations on how these entities were involved in the synthesis process varied from author to author, and several of these points of view will be discussed in the following sections.

As pointed out in a recent review by Corma and Davis,<sup>28</sup> a significant breakthrough in the understanding of the assembly processes occurred with the work of van Santen and Beelen and their colleagues. This group developed techniques for the *in situ* monitoring of the assembly processes using simultaneous small-angle X-ray scattering (SAXS) and wide-angle X-ray scattering (WAXS) in combination with ultrasmall-angle X-ray scattering (USAXS) to probe length scales from 0.17 nm to 6  $\mu\text{m}$ .<sup>29,30</sup> These *in situ* techniques provide for dynamic observations of precursors and products and their interconversions. The imaging of the entire assembly process of the TPA-mediated synthesis was obtained and the proposed scheme for the crystallization is given in Fig. 4.2.<sup>23</sup> The initial assemblies of the organic and inorganic are around 3 nm in size. These particles contain silica and the SDA but do not have the final structure of ZSM-5. If these particles are the same as the ones trapped by Burkett and Davis,<sup>31</sup> then the TPA is not in the conformations observed either in solution or in the final ZSM-5; it is intermediate between these two states. These primary units aggregate in a pH-dependent manner to form entities in the 7–10-nm size range that are fractal in character. These larger entities give rise to nucleation centers, because the nucleation and number of nuclei correlate to the number of these larger entities.<sup>23</sup> Davis has proposed that these aggregated species give rise to nucleation centers for reasons discussed elsewhere.<sup>17</sup>

De Moor et al. speculated that crystal growth was via the primary building units (although no conclusive proof of this was provided).<sup>23,29</sup> Nikolakis et al.<sup>32</sup> combined experimental studies with the use of Derjaguin–Landau–Verwey–Overbeek (DLVO) theory to show that the growth of TPA–MFI seed crystals can proceed by a mechanism with the rate-limiting step being the addition of the 3-nm primary units identified by de Moor et al.<sup>23,29</sup> Thus, the schematic given in Fig. 4.2 is a reasonable representation of how TPA self-assembles with silica to produce the final organic–inorganic composite material. Although all molecular sieve assemblies are not likely to proceed through the same pathways, the assembly processes depicted in Fig. 4.2 provide a good working model for rationalizing and directing the design of high-silica, molecular sieve synthesis.

It should be noted that the solution-mediated mechanism (shown in Fig. 4.2) is typically associated with clear-solution synthesis. These syntheses are the most commonly studied syntheses for the simple fact that they are very reproducible

synthetic procedures that allow for a wider variety of analytical techniques to be used *in situ*. These features provide for a better understanding of the assembly mechanism. Other zeolite and molecular sieve syntheses go through a gel or solid phase. In these syntheses, it has been suggested that the zeolites are synthesized via a gel or solid transformation during which the amorphous solid particles convert to crystalline form. Tsapatsis et al. showed that zeolite L was most likely formed through a series of nucleation events within a gel network.<sup>33,34</sup> De Moor et al.<sup>23</sup> addressed the issue of precursor formation in the synthesis of zeolites via a gelling system or directly in the liquid phase; they concluded that there are nanometer-sized primary particles in both systems but differences in the assembly processes. Recently, Khatri et al.<sup>35</sup> also suggested that silicalite-1 also undergoes a gel transformation as determined by X-ray diffraction (XRD) and high-resolution transmission electron microscope (HRTEM). It is worthwhile to point out that de Moor et al. studied different synthesis procedures for making crystals with the MFI topology, one of which was a clear-solution procedure and the other involved a heterogeneous gel phase.<sup>23</sup> In both procedures, de Moor et al. detected the  $\sim 3$ -nm nanoparticles; they speculated that these nanoparticles are indeed important entities in the assembly process.<sup>23</sup>

Another proposed mechanism for nucleation and growth in zeolite synthesis involves the concept of building units comprised of small pieces of the crystal. An example of this approach was the proposed zeosil nanoparticles (also called nanoblocks or nanoslabs). In this proposed mechanism, the silica species initially forms into a series of small “building blocks” that has the same topology as the final crystal framework (ZSM-5 in this case). These building blocks then aggregate to form the final crystal structure. In a series of papers,<sup>36–40</sup> Martens and co-workers have discussed this concept of “nanoslabs,” claiming to have shown their existence in the synthesis of silicalite-1 (MFI-type zeolite). Through a variety of experimental techniques, including infrared (IR), <sup>29</sup>Si nuclear magnetic resonance (NMR), X-ray diffraction and scattering (XRD and XRS), and transmission electron microscopy (TEM), they claimed that nanoslabs with dimensions 4 nm  $\times$  4 nm  $\times$  1.3 nm exist in the clear-solution synthesis of silicalite-1, agglomerate into larger tablet-type particles, and then agglomerate into silicalite crystals.<sup>36–40</sup>

However, three recent articles by Knight and Kinrade,<sup>41</sup> Lobo and co-workers,<sup>42</sup> and Tsapatsis and co-workers<sup>43</sup> argued that there is no unambiguous proof of the existence of these nanoblocks. Knight and Kinrade pointed out that the concept of nanoblocks has been debated in the literature for over 40 years, and the concept is continually viewed with skepticism.<sup>41</sup> They explained that several of the experiments offered as “proof” of the nanoslabs by Martens and co-workers can also be explained by other phenomena frequently seen in the literature. For example, Martens and co-workers claimed that their <sup>29</sup>Si NMR experiments showed the existence of 10 different silicate species (denoted as trimer, three-ring, tricyclic, double three-ring, bicyclic pentamer, pentacyclic octomer, tetracyclic undecamer, 33-mer, capped double five ring, and double five ring) and these species organized around the SDA to form the nanoslabs.<sup>37</sup> Knight and Kinrade point out that 23 silicate structures have been found to exist in aqueous solutions.<sup>41</sup> Five

of the structures mentioned by Martens et al.<sup>37</sup> are among the 23 (e.g., trimer, three-ring, tricyclic, double three-ring, and bicyclic pentamer), whereas the other 5 structures discussed by Martens and co-workers have not been shown to exist in aqueous solutions. Knight and Kinrade argued that <sup>29</sup>Si NMR signals that Martens et al. attributed to the 5 unknown structures also could be explained by the existence of several of the remaining 18 known structures, which would be a much simpler explanation and consistent with the bulk literature.<sup>41</sup> Knight and Kinrade also observed that many of the structural attributes common among the 23 silicate species known to exist in aqueous solutions are not seen in microporous siliceous frameworks.<sup>41</sup> For example, almost half of the known silicate species contain three-membered rings, but three-membered rings have not been shown to exist in tectosilicate frameworks.<sup>41</sup> Certainly, if these silicate species were serving as “building blocks,” these features would exist in the final frameworks.

Lobo and co-workers<sup>42</sup> took great care to repeat the work by Martens and co-workers<sup>36</sup> of preparing, extracting, and analyzing the nanoparticles formed in the silicalite-1 synthesis. Lobo and co-workers also monitored the particle size in each step of the extraction using dynamic light scattering (DLS). They found that the particle sizes in the solution became stable following the hydrolysis of the tetraethoxysilane (TEOS), with most being less than 10 nm. However, the particles became unstable after the extraction process, aggregating to roughly 500 nm and continuing to grow over time. XRD patterns collected for these particles were similar to those for amorphous silica. Lobo and co-workers conceded that perhaps the crystalline structure was not appearing in the XRD pattern due to the small size of the nanoparticles. They also performed simulations of the particles, concluding that crystalline particles with dimensions of 2 nm × 2 nm × 1 nm should yield a recognizable XRD pattern. This obviously is smaller than the proposed 4 nm × 4 nm × 1.3 nm nanoslabs, suggesting that any crystalline pattern should have been detectable. Lobo and co-workers concluded that there is strong evidence indicating that the extracted nanoparticles in their work<sup>42</sup> and that of Martens and co-workers<sup>36</sup> are disordered like amorphous silica. Lobo and co-workers<sup>42</sup> also pointed out that the <sup>29</sup>Si NMR measured by Martens and co-workers for the extracted nanoparticles<sup>36</sup> were inconsistent with the later *in situ* measurements from the same group,<sup>44</sup> showing evidence of significant structural connectivity changes. Lobo and co-workers stated that it is not possible to draw conclusions about the *in situ* nanoparticles by analyzing the *ex situ* particles, as they likely will not have the same structure.

Tsapatsis and co-workers<sup>43</sup> addressed the TEM imaging of nanoslabs that have been presented in two articles.<sup>40,45</sup> Martens and co-workers<sup>40</sup> claimed to have images of the 4-nm × 4-nm × 1.3-nm and subsequent tablets formed as they begin to group together. However, when repeating the experiments, Tsapatsis and co-workers<sup>43</sup> concluded that the images reported by Martens and co-workers were likely due to residual sodium chloride contamination and that no evidence of nanoslabs was actually shown. Kremer et al. claimed to have created a mesoporous material by arranging, or tiling, nanoslabs<sup>45</sup> Tsapatsis and co-workers pointed out that the images shown by Kremer et al. were typical of mesoporous materials and

provide no evidence as to the existence of nanoslabs.<sup>43</sup> Overall, although certainly an appealing theory, there has been no concrete evidence to suggest that zeolites are actually formed from individual building blocks that are small pieces of the crystal.

#### 4.4.2. *Metal-Ion-Assisted Assembly Processes*

A study of the decomposition of silicon catecholate salts and subsequent silica oligomerization by Harrison and Loton provides some interesting insight on the mechanisms behind silica chemistry and can, perhaps, shed some additional light on the mechanism behind zeolite synthesis.<sup>46</sup> In their study, Harrison and Loton prepared aqueous solutions of silicon catecholate salts with the structure  $(M^+)_2H_2O$ , where  $M^+$  is  $Li^+$ ,  $Na^+$ ,  $K^+$ ,  $NH_4^+$ , or  $Et_3NH^+$ .<sup>46</sup> When the pH is dropped to neutral conditions, the salts decompose slightly to form orthosilicic acid. It is this form of silica that eventually oligomerizes into the larger particles. They noted that in the early reaction stages, no change in the orthosilicic acid concentration is observed, which indicates the conversion of monomer to dimer. In the second stage of the reaction, third-order kinetics are observed and suggest the formation of trimers. After a significant concentration of trimers has been formed, they observed a transition to first-order kinetics that indicates the monomers are interacting with the trimers or larger particles to form larger oligomers. In both cases, the reaction rate increases with decreasing metal cation size. The cations can interact with the silica thereby reducing the reaction rate. Smaller cations have the larger hydration spheres or a smaller charge per area, leading to weaker interactions with the silica (and therefore faster reaction rates). The presence of the metal cations not only slows down the reaction between silica monomers limiting individual particle formation, but they also tend to increase the formation of larger aggregates by allowing hydrogen-bonding between the silicic acid or silanol groups. The tetraalkylammonium cations interact differently with the silica due to their hydrophobic nature, but still exhibit comparable rates. As equilibrium with respect to orthosilicic acid loss is reached, the particles continue to grow and aggregate. The growth rate is dependent on the size distribution of the particles, as the smaller particles dissolve and the silica is deposited on the larger particles.

In another study of aqueous silicate systems at high pH, Kinrade and Pole found that small metal cations can increase the level of polymerization, enable the formation of siloxane bonds, and increase interactions between dissolved silicate anions by reducing their electrostatic repulsion.<sup>47</sup> Ion-paired cations can also stabilize specific oligomers by immobilizing appendages and large rings.<sup>47</sup>

These two studies are interesting when compared to a study on the effects that metal cations have on the synthesis of pure molecular sieves by Goepper et al.<sup>48</sup> Goepper et al. found that the presence of alkali metals (e.g.,  $K^+$  and  $Na^+$ ) catalyzes the synthesis of pure ZSM-12, affecting both the nucleation process and the crystal growth process. These findings are consistent with those by Harrison and Loton<sup>46</sup> and Kinrade and Pole,<sup>47</sup> in which the metal cation appeared to aid in particle



growth. The small amount of metal is most likely catalyzing the depolymerization of the silica source and then aiding in its “repolymerization” or crystallization. As was seen by Harrison and Loton<sup>46</sup> and by Goepper et al.,<sup>48</sup> nonmetallic cations (e.g., ammonium) do not exhibit the same behavior. In the case of ZSM-12, the crystallization is slower with ammonium cations than with alkali metal cations.<sup>48</sup>

Cambor et al. reported that the presence of metals such as  $\text{Zn}^{2+}$  also plays a significant role in the synthesis of VPI-8.<sup>49</sup> VPI-8 can be synthesized with a variety of techniques; Cambor et al. reported using seven different organic additives, two different alkali metals ( $\text{Na}^+$  and  $\text{Li}^+$ ), and various Si/Zn ratios. They found that unlike most molecular sieve syntheses, the organic compound do not appear to act as structure directing agents, but as space fillers. More interestingly, the presence of zinc is very important. In the absence of  $\text{Zn}^{2+}$ , other phases, such as ZSM-5 and ZSM-12, are formed in addition to some VPI-8. It appears that the presence of zinc inhibits the nucleation of the other phases, thus allowing for the sole formation of VPI-8.

## 4.5. Components of Synthesis

### 4.5.1. Organic Components

There is a long history of using of organic compounds to aid in the synthesis of molecular sieves. Frequently, these compounds are referred to as templating agents or structure directing agents. Davis and Lobo pointed out that these terms are not interchangeable and should only be used to describe specific scenarios.<sup>50</sup> A template suggests that there are significant guest–host interactions resulting in the host volume conforming to the geometry of the guest molecule. A SDA implies that the host volume is guided by the guest molecule but does not completely conform to the guest geometry. SDAs have weaker interactions with the inorganic framework and are typically able to rotate within the pore.

Early reviews by Lok et al.<sup>51</sup> and Liebau<sup>52</sup> and more recently by Davis and Lobo<sup>50</sup> and Lobo et al.<sup>53</sup> highlight several of the main issues that need to be considered when choosing a SDA. The organic compound should be sized so that it will fit with sufficient room in the pore or cage with as many van der Waals interactions as possible, but with minimal deformation. The molecule should obviously be soluble in the solvent (typically water), but should not tend to form strong complexes with the solvent. The organic should be somewhat rigid so that multiple configurations (with low-energy barriers for interconversion) are not possible under synthesis conditions. This criterion minimizes the likelihood of multiple products being formed from similar synthesis mixtures. Therefore, key issues in the design of the SDA are intermediate hydrophobicity (need hydrophobic hydration but not aggregation in aqueous media), size, and rigidity.

Much research has gone into the development of different SDAs to achieve different framework structures. Figure 4.3 shows just a few of the many possible SDAs. For example, a study by Wagner et. al. probed the effects that the structure

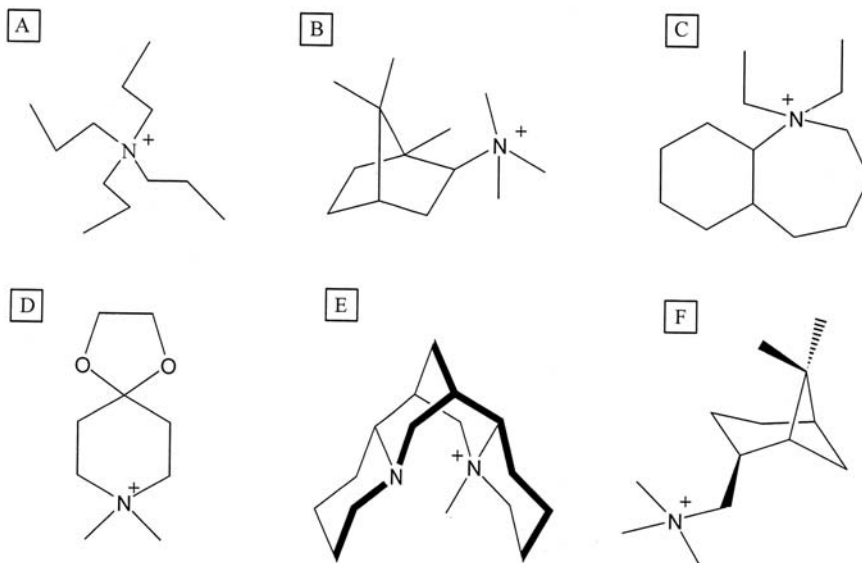


FIGURE 4.3. Examples of structure directing agents.

of the SDA had on the final molecular sieve structures formed by investigating the results of 37 different SDAs under various reaction conditions.<sup>54</sup>

One problem associated with the use of SDAs is the eventual removal from the molecular sieve framework. This removal is usually accomplished by high-temperature combustion to remove the organic compound. Recent work by Lee et al. has also focused on developing SDAs that can be disassembled and extracted from the framework without the need to thermally decompose the SDA.<sup>55</sup> This SDA is shown as compound D in Fig. 4.3.

## 4.5.2. Inorganic Components

### 4.5.2.1. Mineralizing Agents

The most common mineralizing agent is the hydroxide ion,  $\text{OH}^-$ . The mineralizing agent provides for the dissolution of silica (and/or other sources of T-atoms) and reversible T–O–T hydrolysis. This is important for the formation of crystalline structures. Without reversible linkage chemistry, fractal structures would be formed.

In the absence of atoms that provide charge to the framework structure (e.g.,  $\text{Al}^{3+}$  in silicates), the organic SDA cations are charge balanced by framework defects.<sup>56</sup> These defects can be thought of as  $\text{OH}^- + \text{H}_2\text{O}$  reacting with the neutral framework to give an  $\text{Si-O}^-$  (to balance the organic cation) and three  $\text{SiOH}$  groups.<sup>57</sup> These hydrogen-bonded clusters are observed in a variety of pure-silica

TABLE 4.2. Nonbonded radius ( $R$ ), bond length to oxygen in tetrahedral complexes ( $l$ ), and the ratio.

Atom	$R$ (Å)	$l$ (Å)	$R/l$
Be	1.35	1.65	0.82
Zn	1.65	1.98	0.83
B	1.26	1.49	0.85
Ge	1.58	1.77	0.89
Al	1.62	1.77	0.92
Si	1.53	1.64	0.93
P	1.65	1.55	0.94

Source: Reference 61.

structures.<sup>56</sup> Upon combustion of the SDA to open the pore space, the “defect” can anneal via the loss of  $2\text{H}_2\text{O}$  (one  $\text{H}^+$  from the organic).

In addition to  $\text{OH}^-$ ,  $\text{F}^-$  can also be used as a mineralizing agent. Flanigen and Patton were the first to show that the pure-silica materials could be prepared in  $\text{F}^-$ -containing syntheses.<sup>58</sup> Guth and co-workers<sup>59</sup> and Cambor and colleagues<sup>60</sup> have extended the discovery of Flanigen and Patton and have shown that numerous pure-silica structures can be prepared using  $\text{F}^-$  as a mineralizing agent. Of interest is the trend that less dense frameworks can be prepared at lower water concentrations using  $\text{F}^-$  but not with  $\text{OH}^-$ .<sup>60</sup> This point is discussed further below.

#### 4.5.2.2. T Atoms

In the scenario where two atoms (T) are connected by a single bridging atom, each of the two nonbridging atoms can be assigned a contact radius,  $R$ , where the distance between the two atoms is the sum of the radii, as shown in Eq. (4.1)<sup>61</sup>:

$$d(T \cdots T') = R(T) + R(T'). \quad (4.1)$$

These nonbonded radius values are tabulated for common T atoms in oxides in Table 4.2.

To determine what atoms can be substituted for another in various frameworks, it is not important that the nonbonded radii be similar, but, rather, the ratio of the nonbonded radius to the bond length to oxygen that is important.<sup>61</sup> This ratio is directly related to the T–O–T angle, which can be an important feature in determining the stability of the framework. For example, aluminum reveals a larger nonbonded radius ( $R$ ) than silicon and also a longer bond length ( $l$ ) to oxygen (see Table 4.2). However, the resulting  $R/l$  ratios are similar for aluminum and silicon, so they have a high likelihood of being interchangeable without introducing additional strain on the framework.

The T–O–T angles can be used to explain why certain frameworks are more favorable.<sup>61</sup> For example, the calculated Si–O–Si and Si–O–Al angles reveal that three-membered-ring (3-MR; only the T atoms are counted in denoting ring size)

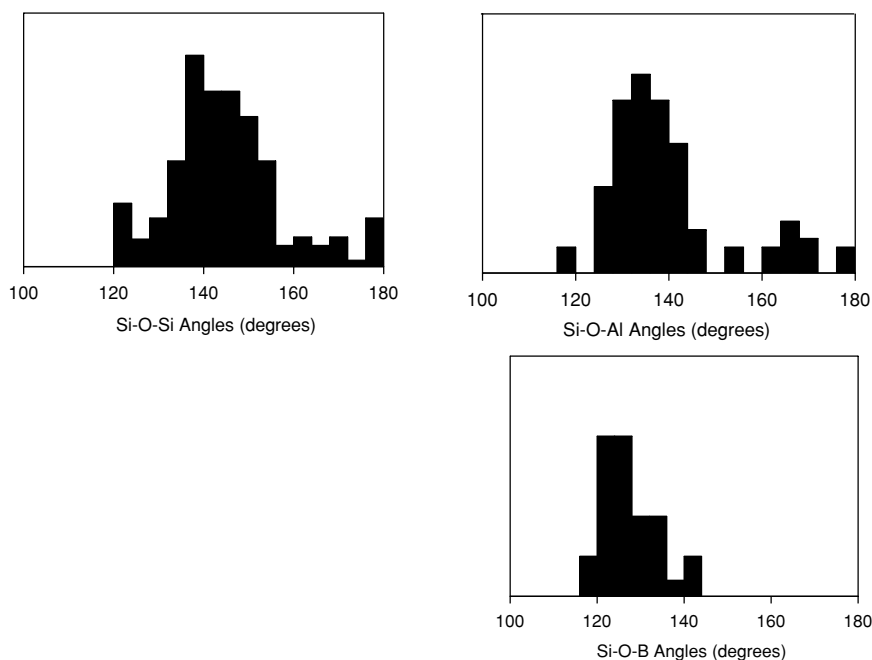


FIGURE 4.4. Histograms of T-O-T bonding angles for silicon, aluminum, and boron. (Adapted from Refs. 53 and 64.)

entities will have very strained angles, whereas 4-MR complexes will not.<sup>61</sup> Expanding on this concept suggests that atoms with smaller  $R/l$  values (e.g., Be and Zn) should be capable of forming 3-MR arrangements. This appears to be the case and is elaborated on further in the following paragraphs.

It is also interesting to compare the range of T-O-T angles that can be achieved with the various T atoms. Histograms in Fig. 4.4 show the frequency of T-O-T angles in silicates for Si-O-Si, Si-O-Al, and Si-O-B. The Si-O-Si angles have the broadest range of possible angles, implying a much more flexible angle. This flexibility suggests a reason for the variety of frameworks that can be formed from Si-O-Si combinations.<sup>53</sup> The variety of systems with other heteroatoms, such as boron, are limited, as suggested by the narrower range, or much stiffer angles. With Zn, the average T-O-T angle is 130 and the distribution of angles in known materials is centered around this small value. Thus, Zn tends to order in natural as well as synthetic<sup>62,63</sup> zinosilicates.

Understanding how to control the size of the rings in the frameworks is important, as it is directly related to the framework density. Brunner and Meier reported that there is a correlation between the minimum obtainable framework density and the size of the smallest ring in the structure.<sup>65</sup> In other words, frameworks with T atoms mostly bonded to multiple 3,4-MR will have to be prepared if molecular sieves with low framework densities are desired.

Piccione et al. showed that a linear correlation between enthalpy and framework density (FD) is observed for pure-silica materials, implying that the overall packing quality determines the relative enthalpies of zeolite frameworks.<sup>6</sup> Whereas FD is an important characteristic of molecular sieve structure, another issue worthy of discussion (especially for low-FD structures) is the number of three- and four-membered rings in the framework. Piccione et al. clearly showed that molecular sieves consisting mostly of zero or one 4-MR (e.g., AFI, MTW, MFI, MEL, FER and CFI structures) are the most stable structures, whereas those that contain mainly triple 4-MR such as CHA, ISV, FAU, and AST are the least stable structures.

One atomic arrangement that contains all T atoms in a triple 4-MR loop configuration is the double 4-MR structure (D4MR) (i.e., a cube). The number of molecular sieve structures that contain D4MR units is very small (zeolite A, octadecasil, ITW, and ISV). In agreement with the energetic features of these materials, molecular sieve structures containing D4MR will not be very favorable unless the D4MR units in the structure are stabilized by some other means. One method of stabilization can occur by carrying out the synthesis in  $F^-$  media, because  $F^-$  can be located inside the D4MR and stabilize this type of atomic arrangement.<sup>66</sup> Indeed, the presence of  $F^-$  within the D4MR of ISV (ITQ-7) and ITW (ITQ-12) is thought to play an important role in stabilizing the structure.<sup>67,68</sup> If entities constructed from  $T_8O_{20}$  units with T atoms at the vertices of a cube are  $Si^{4+}$  alone, then the T–O–T angles must be close to  $145^\circ$  for the tetrahedra to be regular. This condition can be relaxed if  $T^{IV}$  atoms other than  $Si^{4+}$  are considered. D4MR units exist in germinates<sup>69–71</sup> and gallium phosphates containing  $F^-$ .<sup>71–73</sup> The introduction of  $Ge^{4+}$  in a  $Si^{4+}$  D4MR should relax the structure and its corresponding stabilization. In one computational study, Zwijnenburg et al. explained that in all silica compounds, their energetic stability increases with increasing face size of the cages (i.e., small-faced cages like D4MR are energetically destabilized and do not form in all silica compounds).<sup>74</sup> However, they concluded that the presence of germanium decreases that destabilization energy, thus enabling the formation of D4MR.<sup>74</sup> In another work, these arrangements were investigated by the use of theoretical *ab initio* methods, and it was observed that the stability of a D4MR increases when  $Ge^{4+}$  was substituted for  $Si^{4+}$ , except when Ge–O–Ge bonds were formed (high  $Ge^+$  content).<sup>75</sup> These results agree well with experimental findings in which cubic octameric germanosilicate cages were studied; it was revealed that  $Ge^{4+}$  incorporation was site-selective to favor maximum separation between germanate tetrahedra.<sup>76</sup> Following this idea, the introduction of  $Ge^{4+}$  in the synthesis mixture that gives the ISV structure (a large-pore, pure-silica molecular sieve containing D4MR) gave  $Ge^{4+}$  incorporation, and the induction (nucleation) period for the crystallization was strongly reduced from 7 days to 12 h.<sup>77</sup> By means of  $^{19}F$  and  $^{29}Si$  MAS NMR, the position of  $Ge^{4+}$  was inferred, and it was found that  $Ge^{4+}$  selectively occupies D4MR positions with Ge–O–Ge bonding avoidance. It was deduced that  $Ge^{4+}$  can direct the formation of D4MR units in silicates and, as a consequence, may produce new structures that contain D4MR units. This concept was tested by carrying

out silicogermanates syntheses that gave rise to the pure polymorph C structure of Beta zeolite.<sup>78</sup> This polymorph, unlike the other two polymorphs A and B, contains D4MR units. It was shown that a series of organic SDAs all gave pure polymorph C when  $\text{Ge}^{4+}$  was introduced in the synthesis media, whereas many other pure-silica structures were formed in the absence of  $\text{Ge}^{4+}$ . Pure polymorph C was obtained even in the absence of  $\text{F}^-$  anions that stabilize the D4MR when  $\text{Ge}^{4+}$  was used.<sup>79</sup> A detailed XRD study showed unequivocally that  $\text{Ge}^{4+}$  selectively occupies the D4MR of polymorph C with Ge–O–Ge bonding avoidance.<sup>80</sup> This same concept was used to synthesize the polymorph C of the SSZ-33 family.<sup>81</sup> This family includes a series of disordered materials wherein the two end members, denoted as polymorphs A and B, are formed by the same periodic building unit, but with different stacking sequences. It was reported that a hypothetical structure denoted as polymorph C<sup>81,82</sup> would have a notorious difference with the other two polymorphs A and B, and this is that the structure of the former contains double four-membered rings as secondary building units. The synthesis of this elusive polymorph C has been a challenge that could be now achieved from the idea that Ge can direct the synthesis toward D4MR containing zeolites by the isomorphic incorporation of Ge atoms in the D4MR of siliceous zeolite frameworks.<sup>75,77–80</sup> Thus, a silicogermanate with the structure of the desired pure polymorph C has been recently synthesized and named ITQ-24.<sup>83</sup> The stabilizing effect of  $\text{Ge}^{4+}$  for D4MR has led to the synthesis of three new structures, ITQ-15,<sup>84</sup> ITQ-21<sup>81</sup> and ITQ-22,<sup>85</sup> all of them containing D4MRs. Even small  $\text{Ge}^{4+}$  contents ( $\text{Si}/\text{Ge} = 25$ ) can have a directing effect. A stable zeolite with the largest void volume ever reported (ITQ-21) was synthesized following this line of thought using methylsparteine as the SDA.<sup>86,87</sup> The absence of  $\text{Ge}^{4+}$  with this SDA gives the more dense CIT-5 that does not have D4MR units.<sup>88</sup> The structures of ITQ-21 and ITQ-22 are quite interesting and unique. The first one is formed by a tridimensional array of large pores with a 0.74-nm diameter that cross perpendicularly, leaving in the intersection a void volume of 1.2 nm. Zeolite ITQ-22, on the other hand, is the first reported zeolite containing fully interconnected 8-, 10- and 12-membered ring pores. Even more recently, two groups synthesized the first examples of “extra-large pore zeolites”: ITQ-15<sup>89</sup> and IM-12.<sup>90</sup> Both are germanium-containing molecular sieves with intersecting 14- and 12- ring channels.

It is clear that  $\text{Ge}^{4+}$  can direct toward the formation of D4MR and that structures containing these units have low FDs. To create even more open structures, 3-MRs will be necessary.<sup>91</sup> Although a synthetic aluminosilicate zeolite (ZSM-18) containing 3-MRs has been synthesized,<sup>92</sup> it appears that aluminosilicates will not be the most adequate compositions for producing 3-MR units. When introducing 3-MRs into four-connected frameworks, at least one tetrahedron of the 3-MR should have flexible d(T–O), large edge-length distortion, or flexible d(O–O).<sup>93–95</sup> Taking into account that the Ge–O–Ge angle ( $\sim 130^\circ$ ) in germanates is lower than the  $\sim 146^\circ$  found for unstrained Si–O–Si in microporous silicates, there is a possibility of synthesizing germanates that have 3-MR units.<sup>70</sup> Indeed, a gallium germanate

named UCSB-9 with framework composition ( $\text{Ga}_2\text{Ge}_3\text{O}_{10}$ ) has been synthesized and has a zeolitelike framework that contains 3-MR.<sup>96</sup> Unfortunately, the thermal stability of this structure is very limited.

With silicates, the introduction of  $\text{Be}^{2+}$ ,  $\text{Mg}^{2+}$ ,  $\text{Zn}^{2+}$ , and even  $\text{Li}^+$  in framework positions can provide the necessary flexibility in one of the  $[\text{TO}_4]$  tetrahedrons of the 3-MR to stabilize its accommodation in a four-connected framework. Indeed, the directing effect of  $\text{Be}^{2+}$  in the formation of structures containing 3-MRs is illustrated in the naturally occurring beryllosilicates such as phenakite, euclase, and lovdarite. However, these structures are relatively dense. Cheetham et al.<sup>97</sup> have reported the synthesis of beryllosilicates OSB-1 and OSB-2 ( $\text{K}_{48}[\text{Be}_{2.4}\text{Si}_{54}\text{O}_{152}] \cdot 96 \text{H}_2\text{O}$ ) that have tetrahedral topologies with framework densities of 13.3 and 12.7  $\text{T nm}^{-3}$ , respectively. The idealized unit-cell composition for OSB-1 is constructed from 3-MR units only, whereas in OSB-2, 18 out of 19 T atoms are in 3-MRs (the remaining T atom forms one 4-MR). The selectivity of  $\text{Be}^{2+}$  for the occupation of the 3-ring position is shown in the case of OSB-2. The T–O–T angles were confirmed to be around  $127^\circ$ , which is very close to those that can be achieved in Ge–O–Ge and in a 3-MR silicate structure with one  $\text{Si}^{4+}$  atom substituted by  $\text{Be}^{2+}$ ,  $\text{Zn}^{2+}$ ,  $\text{Mg}^{2+}$ , or  $\text{Li}^+$ . The OSB-1 material has a system of 14-MR parallel pores that are chiral and formed by a double helix chain composed of 3-MR. Structures such as these, where the walls are thin constructions of 3-MR bands, show relatively low thermal stability. It is interesting to notice that no organic SDA was used for the synthesis of these materials. Because beryllium is highly toxic, other ions that might direct/stabilize the formation of structures containing 3-MR units will be necessary in order to obtain commercially viable materials.  $\text{Zn}^{2+}$  is clearly the top candidate because it is nontoxic, it belongs to a group of flexible  $[\text{TO}_4]$  tetrahedral, and all of the beryllosilicate minerals containing 3-MRs have zincosilicate analogs. Over a decade ago, Annen et al.<sup>63</sup> reported that zinc could be a suitable substitute for beryllium in the formation of 3-MR-containing microporous solids. VPI-7 ( $\text{Na}_{26}\text{H}_6[\text{Zn}_{16}\text{Si}_{56}\text{O}_{144}] \cdot 44 \text{H}_2\text{O}$ ) was the first zincosilicate molecular sieve to contain 3-MRs. Another zincosilicate (RUB-17) containing building units similar to VPI-7 has been synthesized.<sup>98</sup> In VPI-7 and RUB-17, the alkali metal cations and water molecules play a decisive role in the stabilization of the structure. Unfortunately, the thermal stability of these structures is low. Davis and co-workers have synthesized a large number of zincosilicates and several of them contain 3-MR units.<sup>99</sup> Other divalent elements such as  $\text{Mg}^{2+}$  and  $\text{Ba}^{2+}$  can also form crystalline silicates and aluminosilicates that contain 3-MR units,<sup>100–102</sup> but all of them have high framework densities.

With the purpose of directing toward the formation of 3-MR units, it has been proposed that lithium could be used as a flexible framework cation because it is found in the framework of silicate minerals.<sup>103</sup> Recently, a porous lithiosilicate (RUB-23) has been synthesized, where the  $\text{Li}^+$  is in 3-MRs.<sup>103</sup> The framework density of RUB-23 is high (17.7) and the thermal stability is low. However, RUB-23 proves that structures containing 3-MRs can be prepared with  $\text{Li}^+$ .

#### 4.6. Chirality: Can a “Designer” Zeolite Be Synthesized?

The preceding sections showed that there are a wide range of structures for molecular sieves, and using various synthetic techniques, researchers are making progress in directing the framework material prepared through rational methodologies. However, molecular sieves and zeolites still cannot be “truly” designed yet. One example used in a previous work that emphasizes the desire to truly design zeolites and molecular sieves would be to design a chiral microporous solid.<sup>50</sup> A solid material that could be used in enantioselective separations and synthesis would be of great use in both industrial and pharmaceutical applications. Most successful enantioselective catalysts are soluble chiral organometallic complexes.<sup>104</sup>

As acknowledged in the review by Davis and Lobo,<sup>50</sup> the use of organic solids for chiral synthesis has been known for quite some time,<sup>105</sup> and many chiral inorganic solids are known.<sup>106–108</sup> Natural quartz is known to exist in the *d* and *l* forms, and these crystals can be separated for studying their enantioselective properties. Adsorption<sup>109</sup> and catalytic<sup>110</sup> studies have shown that quartz, as a chiral silica, is capable of an enantioselective performance; however, the enantiomeric excess (ee) in both cases was fairly small (approximately 10%). Because quartz is a dense material, it has a low overall surface area. If a chiral microporous solid could be designed, the large surface area would almost certainly lead to an increase in ee's in catalytic or absorption applications. Chiral microporous solids could also lead to shape-selectivity separations of the enantiomeric mixtures.

Despite the fact that a truly chiral zeolite does not exist yet, various studies have suggested that it should be possible. In their structural study of zeolite  $\beta$ , Treacy and Newsam found that zeolite  $\beta$  is an intergrowth of two distinct polymorphs: polymorph A and polymorph B.<sup>111,112</sup> The two structures are both formed from the same building units, which connect in either a right-handed (R) or left-handed (L) manner. The stacking pattern in polymorph A is homogeneous, either completely right-handed (RRRR...) or completely left-handed (LLLL...). Polymorph A also contains a helical pore along the *c* axis that can be either right- or left-handed. However, polymorph B does not exhibit any overall chirality, as the unit stacking pattern alternates (RLRL...). The probability of forming polymorph A or B is equally likely.

Davis and Lobo pointed out that the existence of chirality in crystal structures is not unique to zeolite  $\beta$ .<sup>50</sup> There are 11 enantiomorphous crystal classes (66 space groups) that lack inverse symmetry groups.<sup>50,113,114</sup> Therefore, theoretically, a variety of chiral frameworks should be possible. Davis and Lobo illustrated two such theoretical structures. One is an intergrowth similar to zeolite  $\beta$  with a chiral polymorph and is a nonchiral polymorph. The other example is generated using ZSM-5 building units. This structure, like quartz, forms the two enantiomeric crystals but does not form an intergrowth. However, it obviously is easier to develop theoretical chiral zeolites than to actually synthesize them.

Chiral crystalline frameworks and layered materials do exist. Harrison et. al. were the first to obtain a racemic mixture of a crystalline framework material that has a chiral topology with their open-framework sodium zincophosphate.<sup>115</sup>



Wilkinson and co-workers prepared a chiral-layered material using optically pure  $d$ -Co(en) $_3^{3+}$  (en: 1,2-diaminoethane).<sup>116</sup> These and other metal phosphates with chiral topologies have been reported over the past few years.<sup>117</sup> Examples of materials other than phosphates forming chiral frameworks have also been reported. Healey et al. described a chiral zincosilicate that is composed of linked tetrahedral frameworks of ZnO $_4$  and SiO $_3$ OH.<sup>118</sup> A recent study reports a new chiral germanium zeotype.<sup>119</sup> This is an open-framework material with interconnected, large-ring helical channels. However, this particular structure is orthorhombic, unlike the tetrahedral frameworks, which are the focus of this review.

In a recent work,<sup>104</sup> possible opportunities for making chiral molecular zeolites are overviewed. One approach would be to try to influence the synthesis of an intergrowth such as zeolite  $\beta$  so that one structure would be more favorable to form than the other. In their computational study of zeolite  $\beta$ , Tomlinson et al. calculated the lattice energies of the two polymorphs using lattice energy minimization calculations.<sup>120</sup> The energies of both polymorph A and polymorph B are virtually the same, which partially explains the random stacking found in zeolite  $\beta$ . There have been instances where spontaneous resolution of chiral systems have been achieved, as in works using sodium chlorate,<sup>121,122</sup> but that is unlikely to occur in the zeolite  $\beta$  scenario due to the apparent “short memory” in the stacking sequences.<sup>50</sup>

Another approach is to actually include chiral moieties into the framework of the zeolite. Typically, the chiral entities are chiral organic compounds or ligands on metal centers. Xiong et al. synthesized a material that is the sole example, to date, of a chiral material that is capable of performing separations typical of a molecular sieve.<sup>123</sup> They incorporated a functionalized chiral ligand into their inorganic framework. This compound was able to separate a racemic mixture of 2-butanol with an ee value of approximately 98.2%. However, applications of materials of this type are limited by the stability of the organic compounds used in the framework. These compounds may not be able to withstand typical reaction conditions. Nonetheless, the work by Xiong et al. certainly indicates that it should be possible to achieve enantiomorphous separations using chiral open frameworks.

Perhaps the most ideal situation would be to impart chirality directly into the inorganic framework through the use of a SDA. Potential directing molecules must be chiral, appropriately sized, and stable at the synthesis conditions (typically high pH and temperatures less than 125°C). In work referred to by Davis and Lobo, modifying the synthesis conditions of zeolite  $\beta$  and incorporating a chiral SDA does appear to enhance the growth of polymorph A relative to polymorph B.<sup>50</sup> However, many organic SDAs with chiral centers still yield achiral frameworks.<sup>104</sup> Two examples of such chiral SDAs are shown as structures E and F in Fig. 4.3. Davis speculated that this phenomenon is partly due to the mobility of the SDA in the pore of the crystal during synthesis.<sup>104</sup> However, because Behrens and co-workers were able to fix an organometallic SDA cation (with a fluoride anion) in their inorganic structure even at the high synthesis temperatures,<sup>124</sup> it should be possible to find a chiral molecule that would function in a similar manner. In another study, the ordering of fluoride counterions in a molecular sieve affected

the orientation of the cation in the pore such that a noncentrosymmetric topological symmetry resulted.<sup>125</sup> A combination of these techniques along with a chiral SDA could lead to the synthesis of a chiral molecular sieve.<sup>104,126</sup>

## 4.7. Summary

A comprehensive understanding of the complete assembly process for zeolites and zeolitelike crystalline molecular sieves is still elusive. This fact is highlighted by the variety of proposed synthetic mechanisms and the inability to truly design a specific zeolite or molecular sieve. Unlike traditional chemical synthesis for which scientists have developed techniques allowing the placement of specific atoms in desired positions, there are other factors in zeolite synthesis that prevent complete control of the assembly. For example, the tetrahedral configuration of zeolitelike materials poses additional constraints on the formation process. Studies of the individual aspects of assembly such as the thermodynamics, kinetics, and the apparent roles of the various components are continuing to provide further insights into molecular-level assembly processes of these materials. These understandings have allowed for improvements in “guided” synthesis techniques, such as larger SDAs yield larger pores. Yet, we will need to achieve a more thorough understanding of the chemistry behind the assembly of zeolite and zeolitelike molecular sieves before truly directed syntheses are possible.

## References

1. M. E. Davis, Zeolites and molecular-sieves: Not just ordinary catalysts, *Ind. Eng. Chem. Res.* **30**(8), 1675–1683 (1991).
2. W. Loewenstein, The distribution of aluminum in the tetrahedra of silicates and aluminates., *Am. Mineral.* **39**, 92–96 (1954).
3. M. M. Helmkamp and M. E. Davis, Synthesis of porous silicates, *Annu. Rev. Mater. Sci.* **25**, 161–192 (1995).
4. M. E. Davis, New vistas in zeolite and molecular-sieve catalysis, *Acc. Chem. Res.* **26**(3), 111–115 (1993).
5. I. Petrovic, A. Navrotsky, M. E. Davis, and S. I. Zones, Thermochemical study of the stability of frameworks in high-silica zeolites, *Chem. Mater.* **5**(12), 1805–1813 (1993).
6. P. M. Piccione, C. Laberty, S. Y. Yang, M. A. Camblor, A. Navrotsky, and M. E. Davis, Thermochemistry of pure-silica zeolites, *J. Phys. Chem. B* **104**(43), 10,001–10,011 (2000).
7. P. M. Piccione, B. F. Woodfield, J. Boerio-Goates, A. Navrotsky, and M. E. Davis, Entropy of pure-silica molecular sieves, *J. Phys. Chem. B* **105**(25), 6025–6030 (2001).
8. J. Boerio-Goates, R. Stevens, B. K. Hom, B. F. Woodfield, P. M. Piccione, M. E. Davis, and A. Navrotsky, Heat capacities, third-law entropies and thermodynamic functions of SiO<sub>2</sub> molecular sieves from  $T = 0$  K to 400 K, *J. Chem. Thermodyn.* **34**(2), 205–227 (2002).
9. Y. T. Hu, A. Navrotsky, C. Y. Chen, and M. E. Davis, Thermochemical study of the relative stability of dense and microporous aluminophosphate frameworks, *Chem. Mater.* **7**(10), 1816–1823 (1995).

10. A. Navrotsky, I. Petrovic, Y. T. Hu, C. Y. Chen, and M. E. Davis, Little energetic limitation to microporous and mesoporous materials, *Microporous Mater.* **4**(1), 95–98 (1995).
11. E. C. Moloy, L. P. Davila, J. F. Shackelford, and A. Navrotsky, High-silica zeolites: A relationship between energetics and internal surface areas, *Microporous Mesoporous Mater.* **54**(1–2), 1–13 (2002).
12. Q. H. Li, A. Navrotsky, F. Rey, and A. Corma, Thermochemistry of  $(\text{Ge}_x\text{Si}_{1-x})\text{O}_2$  zeolites, *Microporous Mesoporous Mater.* **64**(1–3), 127–133 (2003).
13. Q. H. Li, A. Navrotsky, F. Rey, and A. Corma, Thermochemistry of  $(\text{Ge}_x\text{Si}_{1-x})\text{O}_2$  zeolites (erratum), *Microporous Mesoporous Mater.* **66**(2–3), 365–365 (2003).
14. P. M. Piccione, S. Y. Yang, A. Navrotsky, and M. E. Davis, Thermodynamics of pure-silica molecular sieve synthesis, *J. Phys. Chem. B* **106**(14), 3629–3638 (2002).
15. P. M. Piccione, S. Y. Yang, A. Navrotsky, and M. E. Davis, Thermodynamics of pure-silica molecular sieve synthesis (erratum), *J. Phys. Chem. B* **106**(20), 5312–5312 (2002).
16. G. M. Whitesides, E. E. Simanek, J. P. Mathias, C. T. Seto, D. N. Chin, M. Mammen, and D. M. Gordon, Noncovalent synthesis: Using physical-organic chemistry to make aggregates, *Acc. Chem. Res.* **28**(1), 37–44 (1995).
17. M. E. Davis, Strategies for zeolite synthesis by design, *Studies Surf. Sci. Catal.* **97**, 35–43 (1995).
18. S. L. Burkett and M. E. Davis, Mechanism of structure direction in the synthesis of Si-ZSM-5: An investigation by intermolecular  $^1\text{H}$ - $^{29}\text{Si}$  CP MAS NMR, *J. Phys. Chem.* **98**(17), 4647–4653 (1994).
19. A. V. Goretzky, L. W. Beck, S. I. Zones, and M. E. Davis, Influence of the hydrophobic character of structure-directing agents for the synthesis of pure-silica zeolites, *Microporous Mesoporous Mater.* **28**(3), 387–393 (1999).
20. R. A. van Santen, J. Keijspar, G. Ooms, and A. G. T. G. Kortbeek, The role of interfacial energy in zeolite synthesis, *Studies Surf. Sci. Catal.* **28**, 169–175 (1986).
21. T. V. Harris and S. I. Zones, A study of guest/host energetics for the synthesis of cage structures NON and CHA, *Studies Surf. Sci. Catal.* **84**(Zeolites and Related Microporous Materials, Pt. A), 29–36 (1994).
22. G. van de Goor, C. C. Freyhardt, and P. Behrens, The cobalticinium cation  $\text{Co-III}(\text{ETA}(5)\text{-C}_5\text{H}_5)_2^+$ : A metal-organic complex as a novel template for the synthesis of clathrasils, *Z. Anorg. Allg. Chem.* **621**(2), 311–322 (1995).
23. P. de Moor, T. P. M. Beelen, B. U. Komanschek, L. W. Beck, P. Wagner, M. E. Davis, and R. A. van Santen, Imaging the assembly process of the organic-mediated synthesis of a zeolite, *Chem. Eur. J.* **5**(7), 2083–2088 (1999).
24. O. Regev, Y. Cohen, E. Kehat, and Y. Talmon, Precursors of the zeolite ZSM-5 imaged by Cryo-Tem and analyzed by SAXS, *Zeolites* **14**(5), 314–319 (1994).
25. B. J. Schoeman, A high temperature in situ laser light-scattering study of the initial stage in the crystallization of TPA-silicalite-1, *Zeolites* **18**(2–3), 97–105 (1997).
26. T. A. M. Twomey, M. Mackay, H. Kuipers, and R. W. Thompson, In-situ observation of silicalite nucleation and growth: A light-scattering study, *Zeolites* **14**(3), 162–168 (1994).
27. L. E. Iton, F. Trouw, T. O. Brun, J. E. Epperson, J. W. White, and S. J. Henderson, Small-angle neutron-scattering studies of the template-mediated crystallization of ZSM-5-type zeolite, *Langmuir* **8**(4), 1045–1048 (1992).
28. A. Corma and M. E. Davis, Issues in the synthesis of crystalline molecular sieves: Towards the crystallization of low framework-density structures, *Chem. Phys. Chem.* **5**, 304–313 (2004).

29. P. P. E. A. de Moor, T. P. M. Beelen, B. U. Komanschek, O. Diat, and R. A. van Santen, In situ investigation of Si-TPA-MFI crystallization using (ultra-) small- and wide-angle X-ray scattering, *J. Phys. Chem. B* **101**(51), 11,077–11,086 (1997).
30. W. H. Dokter, H. F. Vangarderen, T. P. M. Beelen, R. A. Vansanten, and W. Bras, Homogeneous versus heterogeneous zeolite nucleation, *Angew. Chem. Int. Ed. Engl.* **34**(1), 73–75 (1995).
31. S. L. Burkett and M. E. Davis, Mechanism of structure direction in the synthesis of pure-silica zeolites .1. Synthesis of TPA/Si-ZSM-5, *Chem. Mater.* **7**(5), 920–928 (1995).
32. V. Nikolakis, E. Kokkoli, M. Tirrell, M. Tsapatsis, and D. G. Vlachos, Zeolite growth by addition of subcolloidal particles: Modeling and experimental validation, *Chem. Mater.* **12**(3), 845–853 (2000).
33. M. Tsapatsis, M. Lovallo, and M. E. Davis, High-resolution electron microscopy study on the growth of zeolite L nanoclusters, *Microporous. Mater.* **5**(6), 381–388 (1996).
34. M. Tsapatsis, M. Lovallo, T. Okubo, M. E. Davis, and M. Sadakata, Characterization of zeolite-L nanoclusters, *Chem. Mater.* **7**(9), 1734–1741 (1995).
35. L. Khatri, M. Z. Hu, E. A. Payzant, L. F. Allard, Jr., and M. T. Harris, Nucleation and growth mechanism of silicalite-1 nanocrystal during molecularly templated hydrothermal synthesis, *Ceram. Trans.* **137**(Ceramic Nanomaterials and Nanotechnology), 3–21 (2003).
36. R. Ravishankar, C. E. A. Kirschhock, P.-P. Knops-Gerrits, E. J. P. Feijen, P. J. Grobet, P. Vanoppen, F. C. De Schryver, G. Mieke, H. Fuess, B. J. Schoeman, P. A. Jacobs, and J. A. Martens, Characterization of nanosized material extracted from clear suspensions for MFI zeolite synthesis, *J. Phys. Chem. B.* **103**(24), 4960–4964 (1999).
37. C. E. A. Kirschhock, R. Ravishankar, F. Verspeurt, P. J. Grobet, P. A. Jacobs, and J. A. Martens, Identification of precursor species in the formation of MFI zeolite in the TPAOH–TEOS–H<sub>2</sub>O system, *J. Phys. Chem. B.* **103**(24), 4965–4971 (1999).
38. C. E. A. Kirschhock, R. Ravishankar, L. van Looveren, P. A. Jacobs, and J. A. Martens, Mechanism of transformation of precursors into nanoslabs in the early stages of MFI and MEL zeolite formation from TPAOH–TEOS–H<sub>2</sub>O and TBAOH–TEOS–H<sub>2</sub>O mixtures, *J. Phys. Chem. B.* **103**(24), 4972–4978 (1999).
39. C. E. A. Kirschhock, R. Ravishankar, P. A. Jacobs, and J. A. Martens, Aggregation mechanism of nanoslabs with zeolite MFI-type structure, *J. Phys. Chem. B.* **103**(50), 11,021–11,027 (1999).
40. C. E. A. Kirschhock, V. Buschmann, S. Kremer, R. Ravishankar, C. J. Y. Houssin, B. L. Mojet, R. A. van Santen, P. J. Grobet, P. A. Jacobs, and J. A. Martens, Zeosil nanoslabs: Building blocks in *n*Pr<sub>4</sub>N<sup>+</sup>-mediated synthesis of MFI zeolite, *Angew. Chem., Int. Ed.* **40**(14), 2637–2640 (2001).
41. C. T. G. Knight and S. D. Kinrade, Comment on “Identification of precursor species in the formation of MFI zeolite in the TPAOH-TEOS-H<sub>2</sub>O system,” *J. Phys. Chem. B.* **106**(12), 3329–3332 (2002).
42. D. D. Kragten, J. M. Fedeyko, K. R. Sawant, J. D. Rimer, D. G. Vlachos, R. F. Lobo, and M. Tsapatsis, Structure of the silica phase extracted from silica/(TPA)OH solutions containing nanoparticles, *J. Phys. Chem. B* **107**(37), 10,006–10,016 (2003).
43. H. Ramanan, E. Kokkoli, and M. Tsapatsis, On the TEM and AFM evidence of zeosil nanoslabs present during the synthesis of silicalite-1, *Angew. Chem. Int. Ed.* **43**, 4558–4561 (2004).
44. C. E. A. Kirschhock, S. P. B. Kremer, P. J. Grobet, P. A. Jacobs, and J. A. Martens, New evidence for precursor species in the formation of MFI zeolite in the

- tetrapropylammonium hydroxide–tetraethyl orthosilicate–water system, *J. Phys. Chem. B* **106**(19), 4897–4900 (2002).
45. S. P. B. Kremer, C. E. A. Kirschhock, A. Aerts, K. Villani, J. A. Martens, O. I. Lebedev, and G. Van Tendeloo, Tiling silicalite-1 nanoslabs into 3D mosaics, *Adv. Mater.* **15**(20), 1705–1707 (2003).
  46. C. C. Harrison and N. Loton, Novel routes to designer silicas: Studies of the decomposition of  $(M^+)_2[Si(C_6H_4O_2)_3] \cdot xH_2O$ : Importance of  $M^+$  identity of the kinetics of oligomerization and the structural characteristics of the silicas produced, *J. Chem. Soc. Faraday Trans.* **91**(23), 4287–4297 (1995).
  47. S. D. Kinrade and D. L. Pole, Effect of alkali-metal cations on the chemistry of aqueous silicate solutions, *Inorg. Chem.* **31**(22), 4558–4563 (1992).
  48. M. Goepper, H. X. Li, and M. E. Davis, A possible role of alkali-metal ions in the synthesis of pure-silica molecular-sieves, *J. Chem. Soc. Chem. Commun.* 1665–1666 (1992).
  49. M. A. Camblor, M. Yoshikawa, S. I. Zones, and M. E. Davis, Synthesis of VPI-8: The first large pore zincosilicate, in: *Synthesis of Porous Materials: Zeolites, Clays, and Nanostructures*, edited by M. L. Occelli and H. Kessler, Marcel Dekker, New York, 1997, pp. 243–261.
  50. M. E. Davis and R. F. Lobo, Zeolite and molecular-sieve synthesis, *Chem. Mater.* **4**(4), 756–768 (1992).
  51. B. M. Lok, T. R. Cannan, and C. A. Messina, The role of organic-molecules in molecular-sieve synthesis, *Zeolites* **3**(4), 282–291 (1983).
  52. F. Liebau, *Structural Chemistry of Silicates*; Springer-Verlag, Berlin, 1985.
  53. R. F. Lobo, S. I. Zones, and M. E. Davis, Structure-direction in zeolite synthesis, *J. Incl. Phenom. Mol. Recogn. Chem.* **21**(1–4), 47–78 (1995).
  54. P. Wagner, Y. Nakagawa, G. S. Lee, M. E. Davis, S. Elomari, R. C. Medrud, and S. I. Zones, Guest/host relationships in the synthesis of the novel cage-based zeolites SSZ-35, SSZ-36, and SSZ-39, *J. Am. Chem. Soc.* **122**(2), 263–273 (2000).
  55. H. Lee, S. I. Zones, and M. E. Davis, A combustion-free methodology for synthesizing zeolites and zeolite-like materials, *Nature* **425**(6956), 385–388 (2003).
  56. H. Koller, R. F. Lobo, S. L. Burkett, and M. E. Davis,  $SiO^- \cdots HOSi$  hydrogen-bonds in as-synthesized high-silica zeolites, *J. Phys. Chem.* **99**(33), 12,588–12,596 (1995).
  57. D. F. Shantz, J. S. auf der Gunne, H. Koller, and R. F. Lobo, Multiple-quantum  $^1H$  MAS NMR studies of defect sites in as-made all-silica ZSM-12 zeolite, *J. Am. Chem. Soc.* **122**(28), 6659–6663 (2000).
  58. E. Flanigen and R. L. Patton, Silica polymorph and process for preparing same, US patent 4,073,685, 1978.
  59. J. L. Guth, H. Kessler, and R. Wey, New route to the pentasil-type zeolites using a non alkaline medium in the presence of fluoride ions, *Studies Surf. Sci. Catal.* **28**, 121–128 (1986).
  60. M. A. Camblor, L. A. Villaescusa, and M. J. Diaz-Cabanas, Synthesis of all-silica and high-silica molecular sieves in fluoride media, *Topics Catal.* **9**(1–2), 59–76 (1999).
  61. M. O’Keeffe and B. G. Hyde, The role of nonbonded forces in crystals, in: *Structure and Bonding in Crystals*, edited by M. O’Keeffe and A. Navrotsky, Academic Press, New York, 1981, pp. 227–254.
  62. L. B. McCusker, R. W. Grosse Kunstleve, C. Baerlocher, M. Yoshikawa, and M. E. Davis, Synthesis optimization and structure analysis of the zincosilicate molecular sieve VPI-9, *Microporous Mater.* **6**(5–6), 295–309 (1996).

63. M. J. Annen, M. E. Davis, J. B. Higgins, and J. L. Schlenker, VPI-7: The 1<sup>st</sup> zeolite molecular-sieve containing 3-membered T-atom rings, *J. Chem. Soc. Chem. Commun.* 1175–1176 (1991).
64. G. V. Gibbs, E. P. Meagher, M. D. Newton, and D. K. Swanson. A comparison of experimental and theoretical bond length and angle variations for minerals, inorganic solids, and molecules, in: *Structure and Bonding in Crystals*, edited by M. O'Keeffe and A. Navrotsky, Academic Press, New York, 1981, pp.195–225.
65. G. O. Brunner and W. M. Meier, Framework density distribution of zeolite-type tetrahedral nets, *Nature* **337**(6203), 146–147 (1989).
66. J. L. Guth, J. Hazm, J. M. Lamblin, and H. Gies, Synthesis, characterization and crystal structure of the new clathrasil phase octadecasil, *Eur. J. Solid State Inorg. Chem.* **28**(2), 345–361 (1991).
67. P. A. Barrett, T. Boix, M. Puche, D. H. Olson, E. Jordan, H. Koller, and M. A. Camblor, ITQ-12: A new microporous silica polymorph potentially useful for light hydrocarbon separations, *Chem. Commun.* **17**, 2114–2115 (2003).
68. L. A. Villaescusa, P. A. Barrett, and M. A. Camblor, ITQ-7: A new pure silica polymorph with a three-dimensional system of large pore channels, *Angew. Chem., Int. Ed.* **38**(13–14), 1997–2000 (1999).
69. H. L. Li and O. M. Yaghi, Transformation of germanium dioxide to microporous germanate 4- connected nets, *J. Am. Chem. Soc.* **120**(40), 10,569–10,570 (1998).
70. M. O'Keeffe and O. M. Yaghi, Germanate zeolites: Contrasting the behavior of germanate and silicate structures built from cubic T<sub>8</sub>O<sub>20</sub> units (T = Ge or Si), *Chem. Eur. J.* **5**(10), 2796–2801 (1999).
71. D. S. Wragg, A. M. Z. Slawin, and R. E. Morris, The synthesis of gallium phosphate frameworks with and without fluoride ions present: Attempts to direct the synthesis of double four-ring containing materials, *J. Mater. Chem.* **11**(7), 1850–1857 (2001).
72. P. Reinert, B. Marler, and J. Patarin, Synthesis and characterization of the new microporous fluorogallophosphate Mu-2 with a novel framework topology, *Chem. Commun.* 1769–1770 (1998).
73. P. Reinert, B. Marler, and J. Patarin, Structure analysis and general characterization of the fluorogallophosphate Mu-2: A new microporous material built from double-four-ring units hosting F<sup>−</sup> anions, *J. Mater. Sci.* **35**(12), 2965–2972 (2000).
74. M. A. Zwiijnenburg, S. T. Bromley, J. C. Jansen, and T. Maschmeyer, Computational insights into the role of Ge in stabilising double-four ring containing zeolites, *Microporous Mesoporous Mater.* **73**(3), 171–174 (2004).
75. T. Blasco, A. Corma, M. J. Diaz-Cabanas, F. Rey, J. A. Vidal-Moya, and C. M. Zicovich-Wilson, Preferential location of Ge in the double four-membered ring units of ITQ-7 zeolite, *J. Phys. Chem. B* **106**(10), 2634–2642 (2002).
76. C. T. G. Knight, R. J. Kirkpatrick, and E. Oldfield, Silicon-29 2D NMR evidence of 4 novel doubly germanium substituted silicate cages in a tetramethylammonium germanosilicate solution, *J. Am. Chem. Soc.* **109**(6), 1632–1635 (1987).
77. A. Corma, M. J. Diaz-Cabanas, and V. Fornes, Synthesis, characterization, and catalytic activity of a large-pore tridirectional zeolite, H-ITQ-7, *Angew. Chem., Int. Ed.* **39**, 2346–2349 (2000).
78. A. Corma, M. T. Navarro, F. Rey, J. Rius, and S. Valencia, Pure polymorph C of zeolite beta synthesized by using framework isomorphous substitution as a structure-directing mechanism, *Angew. Chem., Int. Ed.* **40**(12), 2277–2280 (2001).

79. A. Corma, M. T. Navarro, F. Rey, and S. Valencia, Synthesis of pure polymorph C of Beta zeolite in a fluoride-free system, *Chem. Commun.* 1486–1487 (2001).
80. G. Sastre, J. A. Vidal-Moya, T. Blasco, J. Rius, J. L. Jorda, M. T. Navarro, F. Rey, and A. Corma, Preferential location of Ge atoms in polymorph C of beta zeolite (ITQ-17) and their structure-directing effect: A computational, XRD, and NMR spectroscopic study, *Angew. Chem., Int. Ed.* **41**(24), 4722–4726 (2002).
81. R. F. Lobo, M. Pan, I. Chan, H. X. Li, R. C. Medrud, S. I. Zones, P. A. Crozier, and M. E. Davis, SSZ-26 and SSZ-33: 2 molecular-sieves with intersecting 10-ring and 12-ring pores, *Science* **262**(5139), 1543–1546 (1993).
82. R. F. Lobo, M. Pan, I. Chan, R. C. Medrud, S. I. Zones, P. A. Crozier, and M. E. Davis, Physicochemical characterization of zeolites SSZ-26 and SSZ-33, *J. Phys. Chem.* **98**(46), 12,040–12,052 (1994).
83. R. Castaneda, A. Corma, V. Fornes, F. Rey, and J. Rius, Synthesis of a new zeolite structure ITQ-24, with intersecting 10- and 12-membered ring pores, *J. Am. Chem. Soc.* **125**(26), 7820–7821 (2003).
84. A. Corma, M. J. Diaz-Cabanas, and F. Rey, Microporous crystalline material (ITQ-15), method for the preparation thereof and its use in processes for separating and transforming organic compounds, Patent WO 0230820, 2002.
85. A. Corma, F. Rey, S. Valencia, J. L. Jorda, and J. Rius, A zeolite with interconnected 8-, 10- and 12-ring pores and its unique catalytic selectivity, *Nat. Mater.* **2**, 493–497 (2003).
86. A. Corma, M. Diaz-Cabanas, and F. Rey, Synthesis of ITQ-21 in OH<sup>−</sup> media, *Chem. Commun.* 1050–1051 (2003).
87. A. Corma, M. Diaz-Cabanas, J. Martinez-Triguero, F. Rey, and J. Rius, A large-cavity zeolite with wide pore windows and potential as an oil refining catalyst, *Nature* **418**(6897), 514–517 (2002).
88. M. Yoshikawa, P. Wagner, M. Lovallo, K. Tsuji, T. Takewaki, C. Y. Chen, L. W. Beck, C. Jones, M. Tsapatsis, S. I. Zones, and M. E. Davis, Synthesis, characterization, and structure solution of CIT-5, a new, high-silica, extra-large-pore molecular sieve, *J. Phys. Chem. B* **102**(37), 7139–7147 (1998).
89. A. Corma, M. J. Diaz-Cabanas, F. Rey, S. Nicolopoulos, and B. Boulahya, ITQ-15: The first ultralarge pore zeolite with a bi-directional pore system formed by intersecting 14- and 12-ring channels, and its catalytic implications, *Chem. Comm.* **12**, 1356–1357 (2004).
90. J. L. Paillaud, B. Harbuzaru, J. Patarin, and N. Bats, Extra-large-pore zeolites with two-dimensional channels formed by 14 and 12 rings, *Science* **304**(5673), 990–992 (2004).
91. W. M. Meier, Zeolites and zeolite-like materials, *Studies Surf. Sci. Catal.* **28**, 13–22 (1986).
92. S. L. Lawton and W. J. Rohrbaugh, The framework topology of ZSM-18, a novel zeolite containing rings of three (Si,Al)-O species, *Science* **247**(4948), 1319–1322 (1990).
93. D. T. Griffen and P. H. Ribbe, Distortions in the tetrahedral oxyanions of crystalline substances, *Jahrb. Miner. Abh.* **137**(1), 54–73 (1979).
94. B. Renner and G. Lehmann, Correlation of angular and bond length distortions in TO<sub>4</sub> units in crystals, *Z. Kristallogr.* **175**(1–2), 43–59 (1986).
95. M. Wenger and T. Armbruster, Crystal chemistry of lithium: Oxygen coordination and bonding, *Eur. J. Miner.* **3**(2), 387–399 (1991).
96. X. H. Bu, P. Y. Feng, and G. D. Stucky, Novel germanate zeolite structures with 3-rings, *J. Am. Chem. Soc.* **120**(43), 11,204–11,205 (1998).

97. T. Cheetham, H. Fjellvag, T. E. Gier, K. O. Kongshaug, K. P. Lillerud, and G. D. Stucky, Very open microporous materials: from concept to reality, *Studies Surf. Sci. Catal. 135*(Zeolites and Mesoporous Materials at the Dawn of the 21st Century), 788–795 (2001).
98. C. Rohig and H. Gies, A new zincosilicate zeolite with nine-ring channels, *Angew. Chem. Int. Ed.* **34**, 63–65 (1995).
99. M. E. Davis, Evolution of extra large pore materials, *Studies Surf. Sci. Catal. 135*, 29–36 (2001).
100. R. M. Hazen, H. Yang, L. W. Finger, and B. A. Fursenko, Crystal chemistry of high-pressure  $\text{BaSi}_4\text{O}_9$  in the trigonal (P3) barium tetragermanate structure, *Am. Miner.* **84** (5-6), 987–989 (1999).
101. L. W. Finger, R. M. Hazen, and B. A. Fursenko, Refinement of the crystal structure of  $\text{BaSi}_4\text{O}_9$  in the benitoite form, *J. Phys. Chem. Solids* **56**, 1389–1393 (1995).
102. W. Gebert, Crystal structure of the barium aluminosilicate  $[\text{Ba}_{13}\text{Al}_{22}\text{Si}_{10}\text{O}_{66}]$ , *Kristallogr., Kristallgeom., Kristallphys., Kristallchem.* **135**(5–6), 437–452 (1972).
103. S. H. Park, P. Daniels, and H. Gies, RUB-23: A new microporous lithosilicate containing spiro-5 building units, *Microporous Mesoporous Mater.* **37**(1–2), 129–143 (2000).
104. M. E. Davis, Reflections on routes to enantioselective solid catalysts, *Topics Catal.* **25**(1–4), 3–7 (2003).
105. J. M. Thomas, Topography and topology in solid-state chemistry, *Phil. Trans. R. Soc. Lond. Ser. A: Math. Phys. Eng. Sci.* **277**(1268), 251 (1974).
106. R. D. Gillard, Stinking rich: Platinum polysulfides, *Chem. Br.* **20**(11), 1022–1024 (1984).
107. J. K. O’Loane, Optical-activity in small molecules, non-enantiomorphous crystals, and nematic liquid-crystals, *Chem. Rev.* **80**(1), 41–61 (1980).
108. A. M. Glazer and K. Stadnicka, On the origin of optical-activity in crystal-structures, *J. Appl. Crystallogr.* **19**, 108–122 (1986).
109. P. R. Kavasmanek and W. A. Bonner, Adsorption of amino-acid derivatives by *d*-quartz and *l*-quartz, *J. Am. Chem. Soc.* **99**(1), 44–50 (1977).
110. G. M. Schwab and L. Rudolph, Catalytic cleavage of racemates by *d*- and *l*-quartz, **20**, 363–364 (1932).
111. M. M. J. Treacy and J. M. Newsam, 2 new 3-dimensional 12-ring zeolite frameworks of which zeolite beta is a disordered intergrowth, *Nature* **332**(6161), 249–251 (1988).
112. J. M. Newsam, M. M. J. Treacy, W. T. Koetsier, and C. B. De Gruyter, Structural characterization of zeolite beta, *Proc. R. Soc. London A* **420**(1859), 375–405 (1988).
113. G. Burns and A. M. Glazer, *Space Groups for Solid State Scientists*; Academic Press, Boston, 1990.
114. J. Jacques, A. Collet, and S. H. Wilen, *Enantiomers, Racemates, and Resolutions*, Wiley, New York, 1981.
115. W. T. A. Harrison, T. E. Gier, G. D. Stucky, R. W. Broach, and R. A. Bedard,  $\text{NaZnPO}_4\cdot\text{H}_2\text{O}$ , an open-framework sodium zincophosphate with a new chiral tetrahedral framework topology, *Chem. Mater.* **8**(1), 145–151 (1996).
116. M. J. Gray, J. D. Jasper, A. P. Wilkinson, and J. C. Hanson, Synthesis and synchrotron microcrystal structure of an aluminophosphate with chiral layers containing Lambda tris(ethylenediamine)cobalt(III), *Chem. Mater.* **9**(4), 976–980 (1997).
117. J. H. Yu, Y. Wang, Z. Shi, and R. R. Xu, Hydrothermal synthesis and characterization of two new zinc phosphates assembled about a chiral metal complex:



- [CO<sup>II</sup>(en)<sub>3</sub>]<sub>2</sub>[Zn<sub>6</sub>P<sub>8</sub>O<sub>32</sub>H<sub>8</sub>] and [CO<sup>III</sup>(en)<sub>3</sub>][Zn<sub>8</sub>P<sub>6</sub>O<sub>24</sub>Cl]·2H<sub>2</sub>O, *Chem. Mater.* **13**(9), 2972–2978 (2001).
118. A. M. Healey, M. T. Weller, and A. R. Genge, Synthesis and structure of NaZnSiO<sub>3</sub>OH, a new chiral zincosilicate framework material, *Inorg. Chem.* **38**(3), 455–458 (1999).
119. M. E. Medina, M. Iglesias, N. Snejko, E. Gutierrez-Puebla, and M. A. Monge, Chiral germanium zeotype with interconnected 8-, 11-, and 11-ring channels. Catalytic properties, *Chem. Mater.* **16**(4), 594–599 (2004).
120. S. M. Tomlinson, R. A. Jackson, and C. R. A. Catlow, A computational study of zeolite beta, *J. Chem. Soc. Chem. Commun.* 813 (1990).
121. D. K. Kondepudi, R. J. Kaufman, and N. Singh, Chiral symmetry-breaking in sodium-chlorate crystallization, *Science* **250**(4983), 975–976 (1990).
122. J. M. McBride and R. L. Carter, Spontaneous resolution by stirred crystallization, *Angew. Chem. Int. Ed.* **30**(3), 293–295 (1991).
123. R. G. Xiong, X. Z. You, B. F. Abrahams, Z. L. Xue, and C. M. Che, Enantioseparation of racemic organic molecules by a zeolite analogue, *Angew. Chem. Int. Ed.* **40**(23), 4422–4425 (2001).
124. P. Behrens, G. van de Goor, and C. C. Freyhardt, Structure-determining C-H···O-Si hydrogen bonds in cobaltocenium fluoride nonasil, *Angew. Chem. Int. Ed.* **34**(23–24), 2680–2682 (1996).
125. I. Bull, L. A. Villaescusa, S. J. Teat, M. A. Camblor, P. A. Wright, P. Lightfoot, and R. E. Morris, Imposition of polarity on a centrosymmetric zeolite host: The effect of fluoride ions on template ordering in zeolite IFR, *J. Am. Chem. Soc.* **122**(29), 7128–7129 (2000).
126. M. E. Davis, Ordered porous materials for emerging applications, *Nature* **417**(6891), 813–821 (2002).

## 5

# Molecular Imprinting by the Surface Sol-Gel Process: Templated Nanoporous Metal Oxide Thin Films for Molecular Recognition

SEUNG-WOO LEE<sup>†</sup> AND TOYOKI KUNITAKE<sup>†,‡</sup>

<sup>†</sup>*Graduate School of Environmental Engineering, University of Kitakyushu, 1-1 Hibikino, Kitakyushu 808-0135, Japan* and <sup>‡</sup>*Frontier Research System (FRS), the Institute of Physical and Chemical Research (RIKEN), 2-1 Hirosawa, Wako, Saitama 351-0198, Japan*

### 5.1. Introduction

Molecular imprinting is a representative technique of template synthesis and has been recognized as a means to prepare specific binding sites for given molecules in appropriate matrices. In this approach, the shape and functionality of organic molecules as a template are transcribed onto microporous materials. The configuration of the functional groups in the template may be memorized within the matrix. The first example of molecular imprinting was probably presented by Dickey in 1949.<sup>1,2</sup> This study was inspired by the mechanism of antibody formation as proposed by Linus Pauling, in which antibody was assumed to be produced from antigen as a template. Based on this concept, Dickey prepared silica gel from silica sol in the presence of alkyl oranges and then demonstrated that adsorption of a given alkyl orange was enhanced for a silica gel that had been formed in the presence of the template alkyl orange. Since that time, a number of other related studies have been carried out using silica-based materials, showing enhancements in template readsorption relative to control samples.<sup>3–7</sup> Some features of the cavity in imprinted silica gel become apparent if we make a comparison with micropores in zeolites. Zeolites can be synthesized by using organic amines as a template and are often employed in the separation of small organic molecules. Their pores are made of highly symmetrical crystalline frameworks. Therefore, molecular recognition by zeolites is based on the inclusion of molecules in the pore. In contrast, the cavities of imprinted silica gel consist of amorphous matrices and can be a faithful replica of the shape of an organic template.

On the other hand, molecular imprinting in organic cross-linked polymers requires the introduction of discrete functionalities into polymeric matrices in order to improve molecular specificity of the resultant material. In the 1970s, Wulff et al. proposed the synthesis of polymers that were substrate-selective due to spatial

fixation of several functional groups that noncovalently interacted with the template molecules.<sup>8,9</sup> Similar studies have been extensively carried out to the present time, and their application to the separation of complicated organic compounds and biologically active substances is most important.<sup>10–23</sup> In this approach, a polymerizable functional monomer (i.e., methacrylic acid (MAA), vinylpyridine) that was chosen for its affinity for given print molecules, was combined with a large excess of the cross-linking agent (i.e., ethylene glycol dimethacrylate) and a free-radical initiator to form a rigid polymer. After the template was removed, complementary binding sites for the template were created. The molecular recognition properties of these synthetically designed binding sites are attractive and thus these materials have been routinely applied to the development of chromatographic stationary phases.

In spite of the earlier study of Dickey, inorganic matrices have rarely been employed for molecular imprinting, except for the following studies. Mosbach and co-workers allowed organic silanes to polymerize on the surface of porous silica particles in aqueous solution.<sup>24</sup> The resulting polysiloxane copolymers that were imprinted with dye molecules were found to be superior solid supports for separation in high-performance liquid chromatography. Morihara et al. developed the so-called footprint technique, where tailor-made catalysts for trans-acylation were designed by imprinting transition-state analogs onto aluminum ion-doped silica gel.<sup>25</sup> Heilmann and Maier similarly imprinted a transition-state analog for trans-esterification on amorphous silicon dioxide.<sup>26</sup> More recently, Pinel et al. examined the imprinting of silica gel and showed that regiospecificity for cresols was successfully imprinted by using *o*-cresol as a template.<sup>27</sup>

Molecular imprinting attracts practical interests especially in the form of ultrathin films, because separation capability can be enhanced by improvement of the adsorption rate.<sup>28,29</sup> In general, the conventional imprinting technique is associated with some drawbacks, such as low binding efficiency, slow binding process, and difficult fabrication, as the imprinted sites are embedded in bulk polymer matrices and ready access of guest molecules to imprinted binding sites is often suppressed. These drawbacks are relieved at least partially by the use of surfaces. Sagiv prepared mixed monolayers of trichloro-*n*-octadecylsilane (OTS) and a modified dye as a template on glass.<sup>30</sup> The dye molecules alone were removed because they were not covalently bound. The stable network of silane monolayer provides the imprinted site for the dye molecule. On the other hand, Kodakari et al. obtained a silica overlayer on tin oxide (SnO<sub>2</sub>) by chemical vapor deposition (CVD) using preadsorbed benzoate anion as a template.<sup>31</sup> The resulting silica overlayer acted as molecular sieve, due to the formation of an imprinted cavity. In these examples, the site of molecular imprinting has to be located at the surface and/or the crevice close to the surface, in order to secure efficient adsorption of guest molecules. This suggests that the positive use of ultrathin films should be advantageous. Organized molecular films such as Langmuir–Blodgett (LB) multilayers and surface-bound monolayers might appear to be good candidates for this purpose. However, they are not necessarily suitable, as the flexible structural modification that is required for

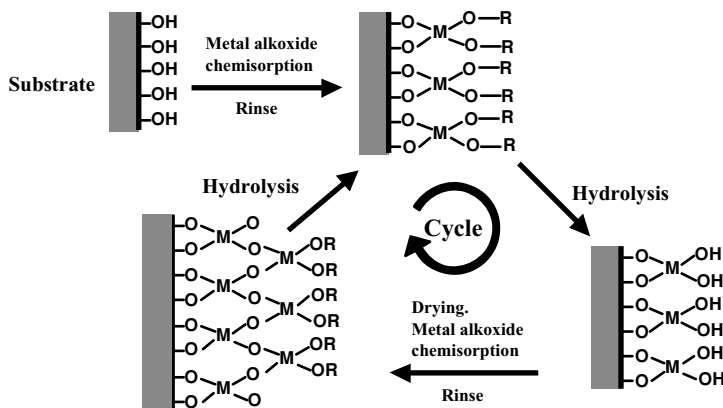


FIGURE 5.1. General scheme of the surface sol-gel process.

the imprinting process is, in principle, not compatible with the ordered molecular organization.

Over the last several years, we have studied the surface sol-gel process as a means for the preparation of ultrathin metal oxide films.<sup>32,33</sup> As illustrated in Fig. 5.1, a solid substrate with hydroxyl groups on its surface is allowed to react with metal alkoxides in solution to form covalently bound surface monolayers. The excessively adsorbed (physisorbed) alkoxide is washed out by rinsing with adequate organic solvents. The chemisorbed alkoxide monolayer is subjected to sol-gel reactions. This process forms an ultrathin metal oxide film with molecular thickness. Under carefully controlled conditions, the thickness of the metal oxide layer is close to 1 nm. This process can be repeated many times to give the desired multilayers. We named this process the “surface sol-gel process” because the sol-gel reaction proceeds only on the surface. The surface sol-gel process possesses the following distinctive features: (1) The thickness of the individual layers can be minimized to approximately 1 nm, (2) this process can be applied to any metal alkoxide that is reactive with surface hydroxyl groups, (3) the individual sol-gel procedure is independent of each other, and the multilayer organization is readily altered, (4) organic,<sup>34</sup> polymeric,<sup>34</sup> biological,<sup>35,36</sup> and metallic<sup>37,38</sup> materials are readily incorporated as second components and as unit layers, when they are reactive with the amorphous metal oxide layer. A variety of nanohybrid layers is thus created, and this feature has been used in the molecular imprinting experiment.<sup>39–41</sup>

In this chapter, we first discuss the characteristics of the surface sol-gel process, versus more conventional sol-gel procedures, and then various aspects of molecular imprinting in metal oxide matrices will be discussed. A comparison of this matrix with organic polymer matrices is important. Finally, the imprinting effect is discussed in relation to more general three-dimensional (3D) fabrication based on metal oxides.

## 5.2. Surface Sol-Gel Process

### 5.2.1. Preparation of Amorphous Metal Oxide Thin Films

The preparation of metal oxide thin films by means of stepwise adsorption of metal alkoxide has been carried out in the past for the activation of heterogeneous catalysts. For example, Asakura and colleagues prepared one atomic layer of niobium oxide by repeating chemisorption of  $\text{Nb}(\text{OEt})_5$  on silica beads. The catalyst obtained by immobilizing platinum particles on a niobium oxide layer showed improved reactivity for the hydrogenation of ethylene in comparison with platinum particles on bare silica beads.<sup>42,43</sup> Kleinfeld and Ferguson prepared an ultrathin  $\text{TiO}_2$  film by repeated adsorption of  $\text{Ti}(\text{O}^i\text{Bu})_4$  onto silicon wafers with an oxidized surface.<sup>44</sup> The substrate was dipped into the alkoxide solution (5 mM, 30 s) in a glove box filled with dry  $\text{N}_2$  gas, sufficiently rinsed with dry solvent and with pure water. Thickness growth of a  $\text{TiO}_2$  thin film estimated from ellipsometry measurement was 3–4 Å for the first adsorption cycle and about 1 Å for the following adsorption cycles. In this case, the amount of the chemisorbed  $\text{Ti}(\text{O}^i\text{Bu})_4$  was independent of adsorption time (30 s to 4 days) and was limited by the number of surface hydroxyl groups. Although the adsorbed thickness per cycle was smaller than the thickness of the  $\text{TiO}_2$  monolayer (3.4 Å), the film grew regularly in proportion to the number of adsorption cycles.

We examined stepwise adsorption of various metal alkoxides on the solid surface for the purpose of obtaining uniform oxide films.<sup>32,33</sup> Figure 5.2a shows an example where a gold-coated quartz crystal microbalance (QCM) was used as a substrate. The electrode modified by mercaptoethanol was immersed in a metal alkoxide solution and rinsed in an adequate organic solvent, and the alkoxide molecule chemisorbed on the surface was hydrolyzed by water or by moisture in the air. QCM frequency was measured after drying the electrode by flushing with nitrogen gas,

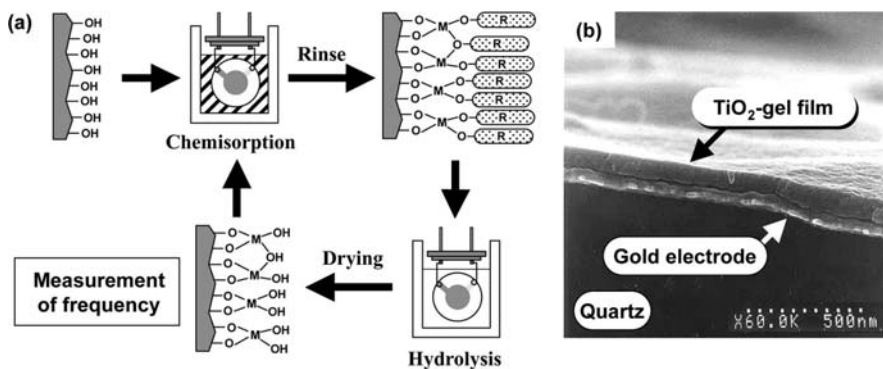


FIGURE 5.2. (a) Schematic illustration of stepwise adsorption of metal alkoxides using a QCM electrode. (b) Scanning electron micrograph of  $\text{TiO}_2$ -gel film on a gold-coated QCM resonator; total frequency shift: 5221 Hz.

and the adsorption, rinsing, and hydrolysis procedures were repeated. It is possible to carry out all of these operations in the ambient atmosphere. For example, the adsorption of  $\text{Ti}(\text{O}^n\text{Bu})_4$  was saturated within 1 min in toluene/ethanol = 1/1, and the frequency change was about 50 Hz. In our system with a 9-MHz resonator, the frequency decrease of 1 Hz corresponds to mass increase of about 0.9 ng and a frequency change of 50 Hz corresponds to thickness increase of 8 Å from Eq. (5.1), using the density of bulk  $\text{TiO}_2$ -gel ( $1.7 \text{ g cm}^{-3}$ ). This frequency shift varies with the concentration of alkoxide and the structure of the electrode surface. In the case of a gold-coated QCM resonator (USI System, Fukuoka) that was subjected to smoothing treatment of the electrode surface, a frequency change of about 30 Hz (thickness increase = 5 Å) was observed under the experimental conditions used. The QCM frequency shift ( $\Delta F$ ), the film density ( $\rho$ ), and the thickness ( $d$ ) of the film adsorbed on the one side of the resonator are related by Sauerbrey's equation<sup>45</sup> as follows;

$$2d(\text{\AA}) = -\Delta F(\text{Hz})/1.832\rho(\text{g/cm}^3). \quad (5.1)$$

Figure 5.2b shows a scanning electron micrograph of the cross section of the  $\text{TiO}_2$ -gel film ( $n = 2/3$ ) prepared on a gold-coated QCM resonator, where  $n$  is the mole ratio of water against  $\text{Ti}(\text{O}^n\text{Bu})_4$ . This thin film has a thickness of constant  $90 \pm 10 \text{ nm}$ , and the surface is smooth over a large area. The density is estimated to be  $1.6 \text{ g cm}^{-3}$ , by substituting the total frequency shift (5221 Hz) during film growth and the thickness (90 nm) in Eq. (5.1). Bulk  $\text{TiO}_2$ -gel, which was obtained by adding excessive water into titanium butoxide solution and sufficient drying the precipitates formed, gives a density of  $1.7 \text{ g cm}^{-3}$ . The density of an ultrathin film formed by the surface sol-gel process ( $1.6 \text{ g cm}^{-3}$ ) is very close to that of bulk  $\text{TiO}_2$ -gel and is about 40% of that of crystalline titania. The film is composed of a two-dimensionally extended dry gel (xerogel), hence is referred to as a "metal oxide-gel layer." The surface sol-gel process could also be applied to a variety of metal alkoxide precursors such as  $\text{Si}(\text{OMe})_4$ ,  $\text{Zr}(\text{O}^n\text{Pr})_4$ ,  $\text{Nb}(\text{O}^n\text{Bu})_5$ ,  $\text{Al}(\text{O}^n\text{Bu})_3$ ,  $\text{Sn}(\text{O}^i\text{Pr})_4$ ,  $\text{In}(\text{OCH}_2\text{CH}_2\text{OMe})_3$ ,  $\text{InSn}_3(\text{OR})_x$ ,  $\text{BaTi}(\text{OR})_x$ , and  $\text{VO}(\text{O}^i\text{Pr})_3$ . All of the compounds showed linear frequency shifts. Adsorption conditions such as concentration, temperature, and immersion time are dependent on the solubility, reactivity, and the ease of hydrolysis of alkoxides. These conditions might be varied as the structure of alkoxide units is changed.

### 5.2.2. Rich Variety of Organic Components in Nanohybrid Layers

The surface sol-gel process takes advantage of surface hydroxyl groups for adsorption of metal alkoxides. The surface hydroxyl groups need not be restricted to hydrolyzed metal oxide layers. We found that polyhydroxyl compounds, polymers, and small organic molecules are adsorbed readily onto the surface of the oxide layer formed by the surface sol-gel process.<sup>34</sup> The polyhydroxyl compounds on the surface provide free hydroxyl groups, and metal alkoxides are subsequently adsorbed.

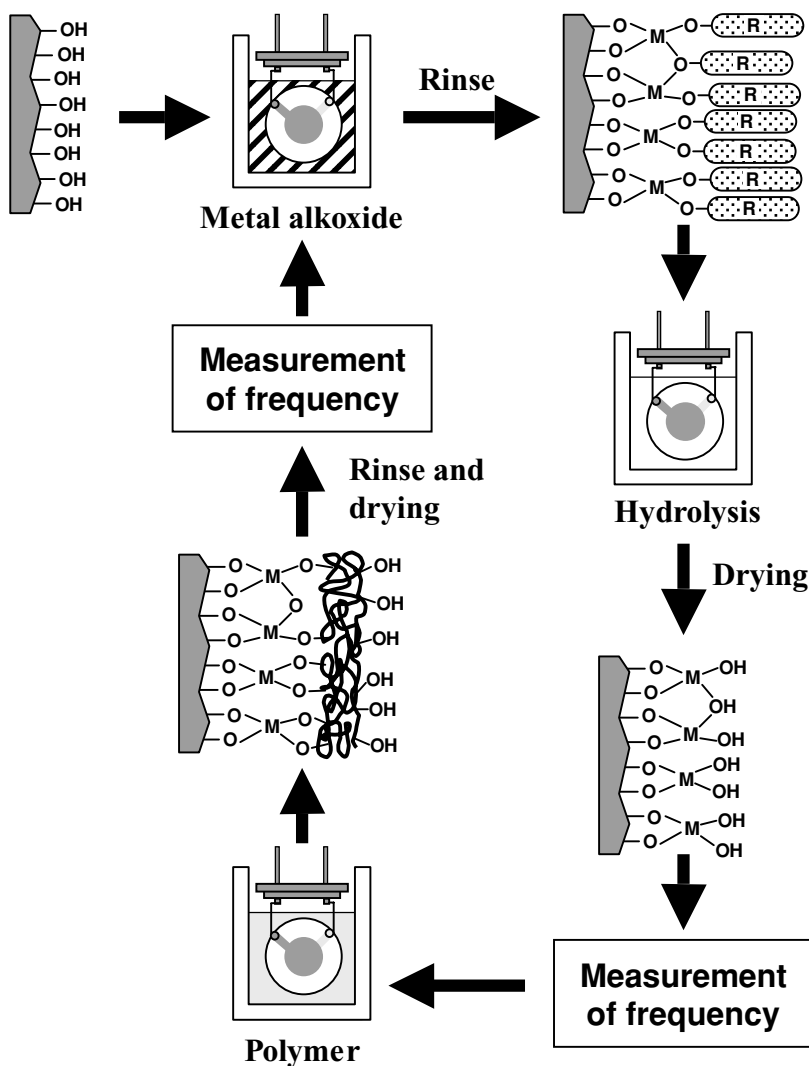


FIGURE 5.3. QCM measurement of the alternate adsorption process of metal alkoxide and organic hydroxyl polymer.

Thus, it is possible to extend the surface sol-gel process to alternate adsorption of polyhydroxyl organic compounds and metal alkoxides. A typical preparative operation is shown in Fig. 5.3. A QCM resonator is immersed into metal alkoxide solutions for given periods of time. Then it is washed in organic solvent, and intact chemisorbed alkoxides are hydrolyzed in water. The QCM frequency shift is measured after drying by flushing with nitrogen gas. Then the resonator is immersed in a solution of a polyhydroxyl compound and rinsed in water, and the frequency is measured after drying. By repeating these procedures, an alternately layered

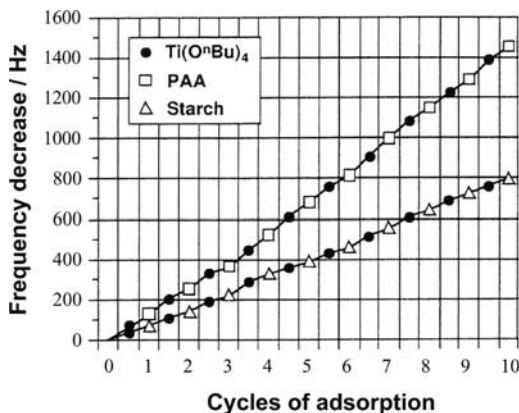


FIGURE 5.4. QCM frequency shift on alternate adsorption of  $\text{Ti}(\text{O}^n\text{Bu})_4$  and organic polymer:  $\text{Ti}(\text{O}^n\text{Bu})_4$  (100 mM in 1:1 v/v toluene/ethanol, 30 °C) (●); poly(acrylic acid) (10 mg mL<sup>-1</sup> in ethanol, 30 °C) (□); starch (1 mg mL<sup>-1</sup> in water, 40 °) (Δ).

film of organic and inorganic components is obtained. Figure 5.4 shows the QCM frequency change during the alternate adsorption of  $\text{Ti}(\text{O}^n\text{Bu})_4$  and poly(acrylic acid) (PAA). The linear frequency decrement indicates regular growth of  $\text{TiO}_2$ -gel/PAA multilayers on the electrode. In each step, the frequency change is  $68 \pm 34$  Hz for  $\text{Ti}(\text{O}^n\text{Bu})_4$  and  $87 \pm 26$  Hz for PAA, and the thicknesses of  $\text{TiO}_2$ -gel layer and PAA layer calculated from these frequencies are  $14 \pm 4$  Å and  $13 \pm 7$  Å, respectively. Frequency shifts for the alternate adsorption of  $\text{Ti}(\text{O}^n\text{Bu})_4$  and starch are also shown in Fig. 5.4.

Figure 5.5a shows a scanning electron micrograph of the cross section of a  $\text{TiO}_2$ -gel/PAA multilayer film. The film located on a gold electrode looks very uniform with a constant thickness of  $350 \pm 20$  Å. The density was estimated as  $1.9 \text{ g cm}^{-3}$  from the SEM thickness and the total QCM frequency change (2508 Hz) during film growth. Fourier transform infrared (FTIR) spectra of this film gave peaks at  $1560 \text{ cm}^{-1}$  (Ti-carboxylate complex) and  $1720 \text{ cm}^{-1}$  (free carboxylate acid) with

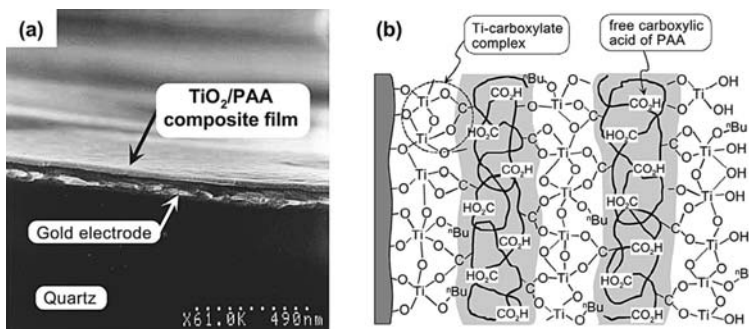


FIGURE 5.5. (a) Scanning electron micrograph of a  $\text{TiO}_2$ -gel/PAA film on a gold-coated resonator; total frequency shift: 2508 Hz. (b) Schematic illustration of a  $\text{TiO}_2$ -gel/PAA film.



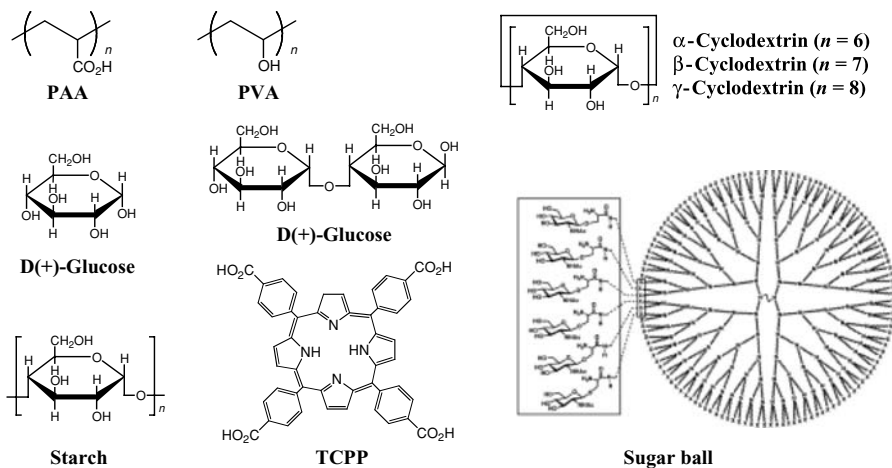


FIGURE 5.6. Compounds used as the organic component of inorganic/organic nonohybrid layers.

similar intensities. Therefore, it is presumed that half of the carboxylate group of PAA is coordinated to titanium atoms of the  $\text{TiO}_2$ -gel layer. We schematically illustrate the chemical structure of the alternate film in Fig. 5.5b. Both the  $\text{TiO}_2$ -gel and PAA layers are approximately 1 nm thick and are densely attached to each other. Compactness of the film is supported by the film density of  $1.9 \text{ g cm}^{-3}$ , which is larger than the densities of each component ( $\text{TiO}_2$ -gel:  $1.7 \text{ g cm}^{-3}$ ; PAA:  $1.4 \text{ g cm}^{-3}$ ).

The alternate adsorption can be applied to other hydroxyl molecules such as poly(vinyl alcohol) (PVA) and starch (Fig. 5.4), glucose, maltose, and porphyrin with carboxyl groups (TCPP), as given in Fig. 5.6. Uniform hybrid layers were obtained in the case of PVA and TCPP. On the other hand, combinations of  $\text{Ti}(\text{O}^i\text{Bu})_4$  and simple sugars did not always give composite films with smooth surfaces, although constant mass increases were observed from QCM measurements. Further examples of the alternate organic/inorganic adsorption include combinations with cyclodextrin, polyrotaxane, and dendrimer, which play important roles in host/guest chemistry.<sup>40</sup> For alternate adsorption of  $\text{Ti}(\text{O}^i\text{Bu})_4$  (100 mM in toluene/ethanol = 1/1) and  $\alpha$ -cyclodextrin (10 mM in water), regular adsorption with a frequency change of  $34 \pm 6 \text{ Hz}$  for  $\text{Ti}(\text{O}^i\text{Bu})_4$  and  $26 \pm 10 \text{ Hz}$  for  $\alpha$ -cyclodextrin was observed. A very similar adsorption behavior has been observed for  $\beta$ -cyclodextrin and  $\gamma$ -cyclodextrin. In the case of the fourth-generation dendrimer (sugar ball;  $0.2 \text{ mg mL}^{-1}$ ), which has 64 glucose units on the outer surface (see Fig. 5.6), regular film growth was achieved by repeating two adsorption cycles for  $\text{Ti}(\text{O}^i\text{Bu})_4$  against one adsorption of the sugar ball. Average frequency shifts are  $27 \pm 12 \text{ Hz}$  for  $\text{Ti}(\text{O}^i\text{Bu})_4$  and  $375 \pm 40 \text{ Hz}$  for the sugar ball. A greater frequency shift (about 650 Hz) was observed for the fifth-generation sugar ball. As describe earlier, smooth organic/inorganic multilayers are not necessarily formed

when sugar derivatives are used in combination with  $\text{TiO}_2$ -gel. In fact, spherical aggregates 10–100 nm in diameter are frequently seen on the film surface. It is possible that sugar molecules that are weakly bound with  $\text{TiO}_2$ -gel reassemble on the film surface to produce spherical aggregates.

Recently, two-dimensional alignment of metal nanoparticles was successfully conducted by using the  $\text{TiO}_2$ -gel surface.<sup>37</sup> A long-alkyl disulfide with two hydroxyl groups at both molecular termini [ $\text{HO}(\text{CH}_2)_{11}\text{SS}(\text{CH}_2)_{11}\text{OH}$ ] was used as a protective agent for small gold particles with an average diameter of 4.7 nm. When a solid substrate overlaid with a  $\text{TiO}_2$ -gel film was immersed in an aqueous dispersion of a gold nanoparticle ( $[\text{Au}] = 1.5 \times 10^{-3} \text{ mol L}^{-1}$ ), a densely packed monolayer of the nanoparticle was obtained. Saturation of the adsorption requires 10 h, in contrast to adsorption of polymeric PVA and starch, which requires only 10 min. Au nanoparticle/ $\text{TiO}_2$ -gel multilayers were obtainable by alternating formation of a  $\text{TiO}_2$ -gel layer for 15 cycles and adsorption of Au nanoparticles for 1 cycle. Unique catalytic and optical properties are expected for organized metal nanoparticles in oxide gel matrices.

The surface sol-gel process based on the stepwise adsorption from solution is applicable to any surface with hydroxyl groups, regardless of the size and shape of the substrate. This modification will be possible on the inner surface of tubes and porous materials and even the morphologically complex surface of natural materials. In practice, we applied this process to several curved surfaces such as those of latex particles, tobacco mosaic virus, cellulose fibers, and hydrophobic silk fibers to produce hollow spheres and tubular structures.<sup>46–48</sup> It is also possible to design various organic/inorganic multilayer films by the selection of adsorption cycle, sequence, and chemical structure of adsorbates. These points become an advantage that is not found in other thin-film techniques such as conventional dry process and the LB method. Superior optical and electronic properties might be expected because organic and inorganic components are molecularly hybridized with nanometer precision. Polymer/metal oxide composites will also give excellent mechanical properties. Among important chemical applications such as catalysis, separation, and molecular recognition, molecular imprinting is a most studied example, as described next.

### 5.3. Molecular Imprinting in Amorphous Metal Oxide Films

#### 5.3.1. Incorporation and Removal of Templates

The surface sol-gel process gives rise to oxide gel films of nanosize thickness and is capable of incorporating various organic molecules by sequential chemisorption and activation. We discovered that such ultrathin films are very useful as matrices of molecular imprinting, and we carried out extensive research.<sup>39–41</sup> The molecular imprinting can be performed using two different approaches: the complexation approach and the layer-by-layer approach. The complexation approach involves complexation of template molecules with metal alkoxides, and the complex is

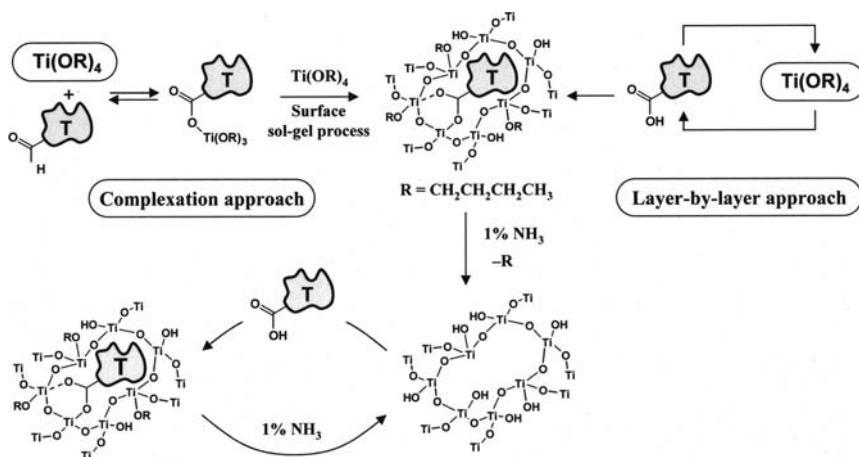


FIGURE 5.7. Two different approaches of molecular imprinting by the surface sol-gel process: the complexation approach (a) and the layer-by-layer approach (b).

solubilized in an organic solvent. This method is used for organic species that are not adsorbed by themselves. The layer-by-layer approach involves the alternate adsorption of template molecules and metal alkoxides, and it can be used for polar molecules (e.g., amino acids and peptides that are effectively adsorbed from aqueous solution). Figure 5.7 outlines the imprinting procedure of a template molecule, T, in TiO<sub>2</sub>-gel matrices. First, a given carboxylic acid template is assembled with Ti(OR)<sub>4</sub> on a solid substrate via the complexation or layer-by-layer approach. The carboxylic acid is incorporated in TiO<sub>2</sub>-gel matrices by the sol-gel polymerization of the mixture. Molecule-sized cavities that are imprinted with the structure of template molecules are created by removing organic components. As the first example of the complexation approach, we examined imprinting of aromatic carboxylic acids.<sup>39,49</sup>

Ti(O<sup>n</sup>Bu)<sub>4</sub> was mixed with a given carboxylic acid (C<sub>3</sub>AzoCO<sub>2</sub>H, 2-AnCO<sub>2</sub>H, or 9-AnCO<sub>2</sub>H, see Fig. 5.8 in toluene/ethanol (2:1, v/v). The resulting mixture, which included Ti(O<sup>n</sup>Bu)<sub>3</sub>-carboxylate complexes, was then stirred at room temperature for more than 12 h. Subsequently, ion-exchanged water was added with stirring, and the mixture was further stirred for 12 h. The composition of the mixed solution was 25 mM carboxylic acid, 100 mM Ti(O<sup>n</sup>Bu)<sub>4</sub>, and 275 mM water. This solution was diluted 20 times by toluene and used as a dipping solution. TiO<sub>2</sub>-gel thin films were prepared from these mixtures by the surface sol-gel process and it was confirmed that the template molecules were bound in the form of a complex with Ti in those films. In the case of C<sub>3</sub>AzoCO<sub>2</sub>H, the formation of the titanium-carboxylate complex could be confirmed by the presence of the carbonyl stretching bands at 1534 cm<sup>-1</sup> and 1416 cm<sup>-1</sup> in FTIR reflection spectra. The ν<sub>C=O</sub> peak (1685.5 cm<sup>-1</sup>) of free carboxylic acid was not found. It is clear that the

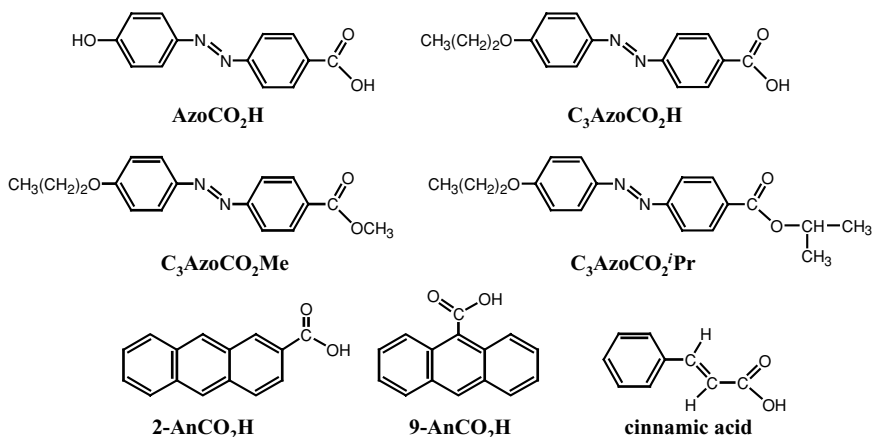


FIGURE 5.8. Chemical structures of template and guest molecules.

structure of the Ti complex in the solution ( $1547\text{ cm}^{-1}$ ,  $1410\text{ cm}^{-1}$ ) is maintained in the thin film.

Template-incorporated  $\text{TiO}_2$ -gel films were prepared on QCM electrodes. The QCM is a device that can detect a change in the mass adsorbed onto the electrode surface with accuracy on the order of nanograms. Figure 5.9 shows QCM frequency shifts due to adsorption of  $\text{Ti}(\text{O}^n\text{Bu})_4$  and a respective carboxylic acid existing in the form of  $\text{Ti}(\text{O}^n\text{Bu})_3$ -carboxylate. The QCM frequency uniformly decreased up to at least 10 cycles, indicating regular film growth in either case.

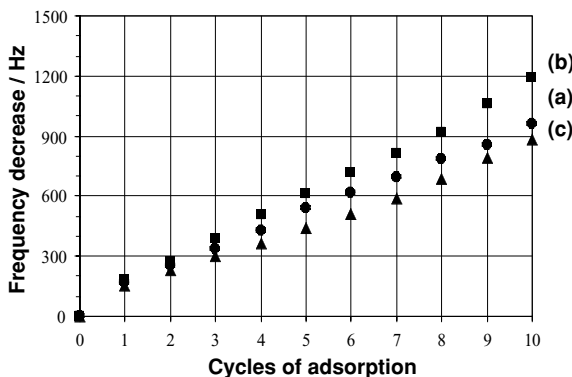


FIGURE 5.9. QCM frequency shifts due to adsorption of  $\text{Ti}(\text{O}^n\text{Bu})_4$  and carboxylic acids: (a)  $\text{C}_3\text{AzoCO}_2\text{H}$ , (b)  $2\text{-AnCO}_2\text{H}$ , and (c)  $9\text{-AnCO}_2\text{H}$ . Stock solutions were diluted 20 times by toluene [Stock solution:  $\text{Ti}(\text{O}^n\text{Bu})_4$ , 100 mM; carboxylic acid, 25 mM;  $\text{H}_2\text{O}$ , 275 mM in toluene/ethanol = 2 : 1]. Frequency shifts were measured after 1-min adsorption at room temperature, followed by washing for 1 min in toluene.

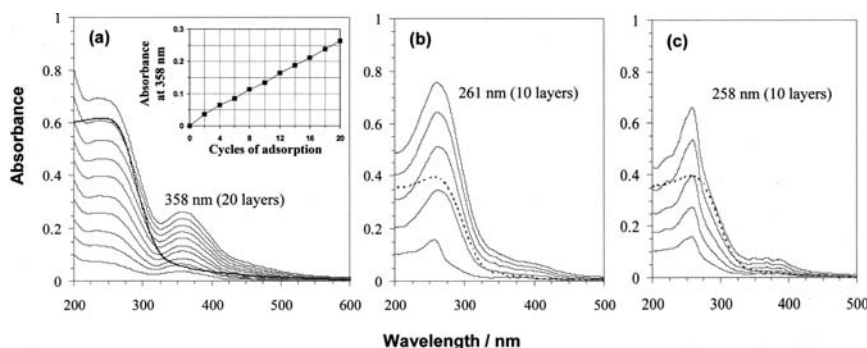


FIGURE 5.10. UV-vis absorption spectral changes due to adsorption of  $Ti(O^iBu)_4$  and carboxylic acids: (a)  $C_3AzoCO_2H$ , (b) 2-AnCO<sub>2</sub>H, and (c) 9-AnCO<sub>2</sub>H. The conditions are the same as those of Fig. 5.9. The dotted lines show the absorption of  $TiO_2$ -gel after template removal with ammonia solution.

The average frequency shifts were  $96 \pm 26$ ,  $119 \pm 24$ , and  $88 \pm 25$  Hz for  $C_3AzoCO_2H$ -, 2-AnCO<sub>2</sub>H-, and 9-AnCO<sub>2</sub>H-incorporated films, respectively. Incorporation of the template molecules and their removal can be confirmed by ultraviolet–visible (UV-vis) absorption spectroscopy for the aromatic moieties of azobenzene and anthracene. The  $Ti(IV)$ –carboxylate complexes condensed with  $Ti(O^iBu)_4$  were adsorbed onto activated quartz plates, and absorption spectra were measured at every two cycles. The absorbance increased in proportion to the adsorption cycle up to 20 cycles in the case of  $C_3AzoCO_2H$ , as shown in Fig. 5.10a. The 2-AnCO<sub>2</sub>H- and 9-AnCO<sub>2</sub>H-incorporated films were also regularly assembled up to 10 cycles (Figs. 5.10b and 5.10c). The incorporated carboxylates in the  $TiO_2$ -gel matrix were removed by treatment with ammonia solution. The UV absorbance of  $C_3AzoCO_2H$  at 358 nm became totally absent and the absorbances of 2-AnCO<sub>2</sub>H and 9-AnCO<sub>2</sub>H at 261 nm and 258 nm, respectively, were dramatically decreased. The imprinted films show only  $TiO_2$ -gel absorption in the near-UV and visible regions after template removal. Therefore, it is concluded that the template molecules were completely removed.

The amount of incorporated template molecules can be estimated from the absorbance difference before and after template removal. In the case of  $C_3AzoCO_2H$ , the amount of the template molecule introduced in one adsorption cycle onto one side of the plate is estimated to be  $1.76$  molecules/cycle·nm<sup>2</sup>. The film composition is also estimated from the QCM frequency shift. The total frequency shift of each film during 10 adsorption cycles is summarized in Table 5.1. The desorbed mass is estimated from the frequency increase upon  $NH_3$  treatment. Subsequently, the adsorption density in each case was calculated from the desorbed mass corrected for the molecular weights of the individual template molecules and the surface area of the electrode ( $0.159$  cm<sup>2</sup>). The desorption ratio against the total adsorbed mass is in the range 13–21%, and the films showed similar adsorption densities of  $1.08$ – $1.27$  molecules/cycle·nm<sup>2</sup> for the different template molecules. Film density

TABLE 5.1. Adsorbed and desorbed masses during the imprinting process and film densities.

Template	Total adsorbed mass/ corresponding frequency shift	Desorbed mass of template <sup>a</sup> /QCM desorption ratio <sup>b</sup>	Adsorption density <sup>c</sup> (molecule/cycle · nm <sup>2</sup> )	Film density ( $\rho$ , g cm <sup>-3</sup> )
C <sub>3</sub> AzoCO <sub>2</sub> H	907 ng/1008 Hz <sup>d</sup>	190 ng/21%	1.27	1.5 <sub>5</sub> <sup>e</sup>
2-AnCO <sub>2</sub> H	1074 ng/1193 Hz	135 ng/13%	1.15	1.6 <sub>1</sub>
9-AnCO <sub>2</sub> H	792 ng/880 Hz	127 ng/16%	1.08	1.5 <sub>9</sub>

<sup>a</sup>Estimated from frequency increase upon NH<sub>3</sub> treatment.<sup>b</sup>Estimated from frequency shift before and after desorption.<sup>c</sup>Calculated from molecular weights of template molecules and the surface area of the QCM (0.159 cm<sup>2</sup>).<sup>d</sup>Average frequency shift of four independent experiments.<sup>e</sup>(0.21 × 1.0 g cm<sup>-3</sup>) + (0.79 × 1.7 g cm<sup>-3</sup>).

before template removal can be easily calculated from the desorption ratio, when the densities of the template molecules and TiO<sub>2</sub>-gel are assumed to be ~1.0 and ~1.7 g cm<sup>-3</sup> (bulk density of TiO<sub>2</sub>-based gel), respectively. Therefore, the density of each film is estimated to be 1.5<sub>5</sub>–1.6<sub>1</sub>, and the film thickness for one cycle is estimated to be 1.5–2.0 nm using this film density.

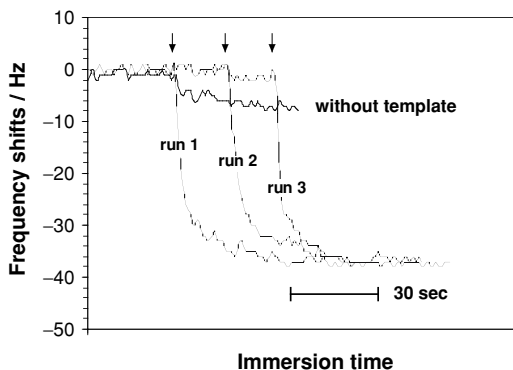
### 5.3.2. Stability and Selectivity of Imprinted Sites

Organic moieties incorporated in ultrathin metal oxide films can be removed readily by solvent washing or by degradative oxidation. Under proper conditions, nanosized cavities corresponding to the shape of the individual organic moiety are produced within the metal oxide network. The removal is particularly facile when small template molecules are used. For example, aromatic acids are removed from titania thin films by washing with dilute aqueous ammonia at room temperature.

Structural stability and guest selectivity of the imprinted films were examined by using a series of aromatic carboxylic acids. *In situ* QCM experiments of guest binding were repeated with an identical 10-adsorption-cycle film specimen (C<sub>3</sub>AzoCO<sub>2</sub>H-imprinted film) after complete removal of the template. Figure 5.11 illustrates that mass increase due to rebinding was complete within 40–60 s and that reproducible desorption–adsorption cycles were achieved at least three times. The frequency decrease was highly reproducible, giving a value of  $32 \pm 1$  Hz. In contrast, a similarly prepared TiO<sub>2</sub> film without the template showed a much smaller frequency decrease of only 2–3 Hz. It is clear that the imprinted cavity is maintained during repeated rebinding experiments under the conditions used.

Figure 5.12A describes *in situ* experiments of binding of several aromatic acids (see Fig. 5.8) toward this film. The adsorption process becomes essentially saturated in less than 1 min. The original template molecule, C<sub>3</sub>AzoCO<sub>2</sub>H, gave a greater frequency decrease than those of other related carboxylic acids. Imprinting

FIGURE 5.11. *In situ* QCM frequency decreases due to rebinding of  $C_3AzoCO_2H$ :  $5\ \mu L$  of  $50\ mM\ C_3AzoCO_2H$  in tetrahydrofuran (THF) was added into  $1\ mL$  of acetonitrile ( $CH_3CN$ ) at the time marked with an arrow to give a  $C_3AzoCO_2H$  concentration of  $0.25\ mM$ .



efficiency was defined as a molar ratio of bound guest and template molecules ( $\text{mol}_{\text{guest}}/\text{mol}_{\text{template}}$ ) and is summarized in Table 5.2. The relative binding efficiency in the  $C_3AzoCO_2H$ -imprinted film decreases in the order of  $AzoCO_2H$ , 2-An $CO_2H$ , cinnamic acid, benzoic acid, 9-An $CO_2H$ , and octanoic acid. The structurally closest acid,  $AzoCO_2H$ , was the second best substrate, and anthracene-9-carboxylic acid (9-An $CO_2H$ ) was least effective. Other aromatic carboxylic acids (benzoic acid, cinnamic acid, and octanoic acid) were bound even less efficiently, reflecting lessened structural similarities with the template. Anthracenecarboxylic acids show 30–60% binding efficiencies. The 2-isomer is a better substrate than the 9-isomer, as the former isomer appears structurally closer to the original template. Conversion of the carboxylic acid function to the corresponding ester depresses the binding efficiency (i.e.,  $C_3AzoCO_2Me$  and  $C_3AzoCO_2Pr$ ). Anthracene itself and 1-adamantanol showed frequency changes of only 1–2 Hz. Clearly, the presence of the carboxylic acid moiety is required for the recognition process, and other

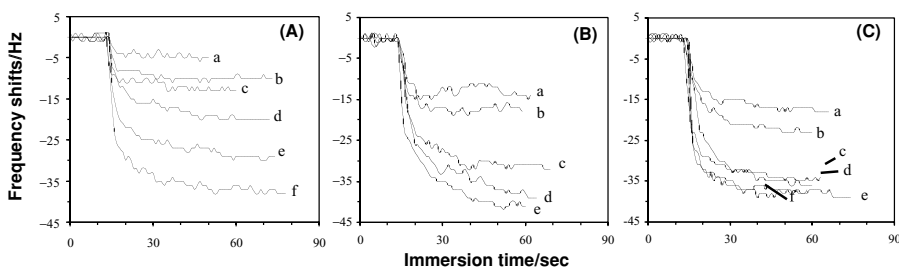


FIGURE 5.12. *In situ* QCM frequency shifts due to binding of a series of carboxylic acids. (A)  $C_3AzoCO_2H$ -imprinted film: (a) THF only, (b) benzoic acid, (c) 9-An $CO_2H$ , (d) 2-An $CO_2H$ , (e)  $AzoCO_2H$ , and (f)  $C_3AzoCO_2H$ ; (B) 2-An $CO_2H$ -imprinted film: (a) octanoic acid, (b) benzoic acid, (c) 9-An $CO_2H$ , (d)  $C_3AzoCO_2H$ , and (e) 2-An $CO_2H$ ; (C) 9-An $CO_2H$ -imprinted film: (a) benzoic acid, (b) cinnamic acid, (c)  $C_3AzoCO_2H$ , (d) 2-An $CO_2H$ , (e) 9-An $CO_2H$ , and (f)  $AzoCO_2H$ . Five microliters of  $50\ mM$  guest in THF was added to give a final guest concentration of  $0.25\ mM$ .

TABLE 5.2. Relative binding efficiency of imprinted TiO<sub>2</sub>-gel ultrathin films for various guest molecules.

Guest molecule MW	<i>In situ</i> frequency decrease <sup>a</sup> (Hz/pmol)			Relative binding efficiency <sup>b</sup>		
	IF <sub>C<sub>3</sub>Azo</sub> <sup>c</sup>	IF <sub>2-An</sub>	IF <sub>9-An</sub>	IF <sub>C<sub>3</sub>Azo</sub>	IF <sub>2-An</sub>	IF <sub>9-An</sub>
Benzoic acid (122.12)	5/37	12/88	12/88	0.36	0.61	0.64
Octanoic acid (144.21)	5/31	9/56	8/50	0.31	0.39	0.36
Cinnamic acid (148.16)	8/49	13/79	17/88	0.48	0.54	0.75
2-AnCO <sub>2</sub> H (222.24)	15/61	36/146	30/121	0.60	1.00	0.88
9-AnCO <sub>2</sub> H (222.24)	8/32	26/105	34/138	0.33	0.72	1.00
AzoCO <sub>2</sub> H (242.32)	24/88	30/111	33/123	0.88	0.76	0.89
C <sub>3</sub> AzoCO <sub>2</sub> H (284.31)	32/101	33/104	29/92	1.00	0.71	0.67

<sup>a</sup>All QCM data were corrected for molecular weights of bound species after subtraction of the frequency shift due to the solvent, THF (5 Hz).

<sup>b</sup>Molar ratio of bound species, mol<sub>guest</sub>/mol<sub>template</sub>.

<sup>c</sup>IF is an abbreviation for imprinted film.

molecular characteristics of the template are reflected in the nature of the imprinted cavity.

The binding efficiency for guest molecules was similarly examined by using the 2-AnCO<sub>2</sub>H- and 9-AnCO<sub>2</sub>H-imprinted films. Figures 5.12B and 5.12C show the frequency changes for the binding of carboxylic acid derivatives to the 2-AnCO<sub>2</sub>H- and 9-AnCO<sub>2</sub>H-imprinted sites. They respectively gave frequency decreases of 36 and 34 Hz for the original templates at the concentration of 0.25 mM. These mass increases are much larger than those (only 15 and 8 Hz for 2-AnCO<sub>2</sub>H and 9-AnCO<sub>2</sub>H, respectively) observed for the C<sub>3</sub>AzoCO<sub>2</sub>H-imprinted film. The rebinding reaches equilibrium within 1 min. The bound guest molecules are removed by treating with aqueous NH<sub>3</sub>, and the imprinted films are used for binding of other carboxylic acids. The addition of 9-AnCO<sub>2</sub>H to the 2-AnCO<sub>2</sub>H-imprinted film yields a rather large response (26 Hz), and the 9-AnCO<sub>2</sub>H-imprinted film also shows a similar binding characteristic for 2-AnCO<sub>2</sub>H (30 Hz). However, these imprinted films do not efficiently interact with octanoic acid, benzoic acid, and cinnamic acid. It is clear that the imprinted TiO<sub>2</sub> films accommodate the original template molecules much more efficiently than other guest molecules. The binding efficiencies of these two imprinted films for various guest molecules are summarized in Table 5.2 together with the results of the C<sub>3</sub>AzoCO<sub>2</sub>H-imprinted film. A graphical presentation of the relative binding efficiency is given in Fig. 5.13

### 5.3.3. Nature of Imprinted Sites for Guest Binding

In order to confirm the presence and absence of guest molecules bound in imprinted sites, FTIR measurements were conducted with the C<sub>3</sub>AzoCO<sub>2</sub>H-film (10 cycles). First, reflection FTIR spectra of the as-prepared film displayed azobenzene peaks at 1600 and 1500 cm<sup>-1</sup> together with peaks due to Ti-carboxylate complexes at



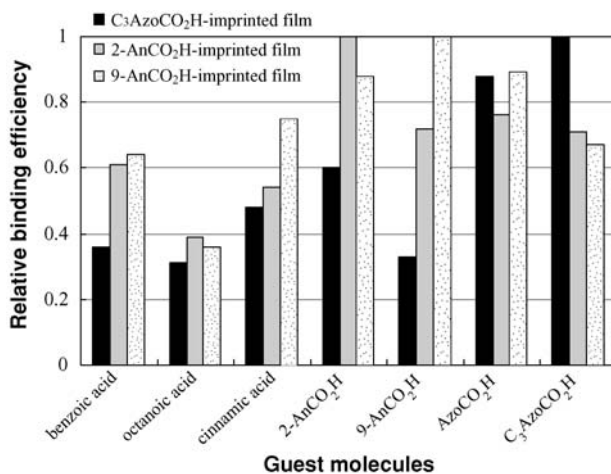


FIGURE 5.13. Relative binding efficiency for guest molecules in imprinted TiO<sub>2</sub>-gel ultrathin films. Templates are C<sub>3</sub>AzoCO<sub>2</sub>H, 2-AnCO<sub>2</sub>H, and 9-AnCO<sub>2</sub>H in each case. The data are the same as those listed in Table 5.2.

1534 (weak) and 1416 cm<sup>-1</sup> (strong), as shown in Fig. 5.14, curve a. This suggests that the template carboxylic acid is bound through covalent linking to TiO<sub>2</sub>-gel matrices. These peaks cannot be seen after the treatment with ammonia solution, indicating the disappearance of the Ti-carboxylate complex (Fig. 5.14, curve b). Incoming guest molecules might be bound to the imprinted site in a similar manner if they have a carboxylic acid function. This was confirmed by appearance of the peaks of the Ti-carboxylate complex upon rebinding of the carboxylic acid

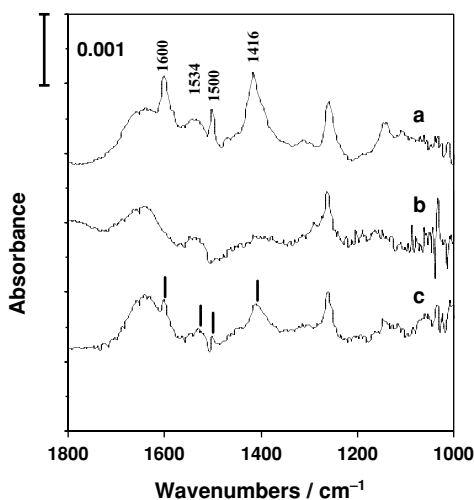


FIGURE 5.14. Reflection FTIR spectra: (a) TiO<sub>2</sub>-C<sub>3</sub>AzoCO<sub>2</sub>H hybrid film, (b) imprinted TiO<sub>2</sub> film, and (c) after rebinding of the template.

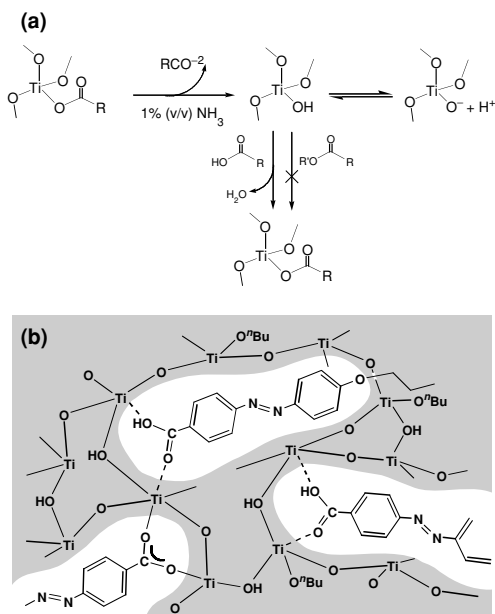


FIGURE 5.15. (a) Binding process of guest molecules to Ti(IV)-OH in an imprinted cavity. (b) Schematic illustration of a C<sub>3</sub>AzoCO<sub>2</sub>H imprinted film.

(Fig. 5.14, curve c), although the peak intensity is smaller than that of the original spectra before template removal.

We already discussed that the binding efficiency is much depressed by the conversion of carboxylic acid group to the corresponding ester group. This means that the presence of carboxylic acid moiety is indispensable for the recognition process because it is capable of forming a complex with the Ti(IV)-OH unit formed by bond cleavage of Ti(IV)-carboxylate, as shown in Fig. 5.15a. Carboxylic acid guests are probably incorporated through noncovalent bonding and hydrogen-bonding in addition to the covalent bonding, as illustrated in Fig. 5.15b. The hydrogen bonds might be easily broken by rinsing with polar solvents. An additional element of the molecular recognition is the shape and size of the aromatic moiety. The aromatic moiety in the guest would be surrounded by the hydrophobic domain of TiO<sub>2</sub>-gel that is composed of the titanium–oxygen network, Ti–O–Ti.

#### 5.3.4. Multifunctional Nature of Imprinted Cavity

The above-mentioned rebinding selectivity suggests that the imprinted cavity is composed of distinctive subcavity areas that are imprinted by the corresponding parts of a template molecule in terms of functionality and morphology. This hypothesis can be verified by using more complex (functionally as well as morphologically) template molecules. Derivatized amino acids are suitable for this

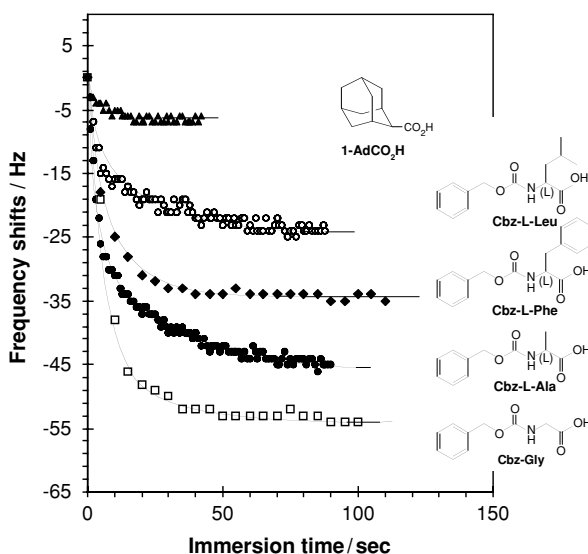


FIGURE 5.16. *In situ* QCM frequency decreases due to binding of a series of guest molecules in a  $\text{TiO}_2$ -gel film imprinted with Cbz-L-Ala.

purpose. As the first trial, we examined molecular imprinting of protected amino acids in a  $\text{TiO}_2$ -gel thin film.<sup>50</sup>

A mixed solution of  $\text{Ti}(\text{O}^n\text{Bu})_4$  and carbobenzyloxy-L-alanine (Cbz-L-Ala) was used to form a regular multilayer film, and the organic template was readily removed by immersion in dilute ammonia, as confirmed from the disappearance of characteristic peaks of the titanium-carboxylate complex and carbamate in reflection FTIR spectra. *In situ* QCM measurements were carried out for rebinding of the original template and other molecules in  $\text{CH}_3\text{CN}$ . Figure 5.16 shows selected examples of the guest binding experiment. The binding is rapid and saturated in 30–60 s. The relative binding efficiency of related guest molecules in acetonitrile increased in the order of Cbz-Gly < Cbz-L-Ala < Cbz-L-Phe < Cbz-L-Leu. Simpler carboxylic acids such as adamantane-1-carboxylic acid (1-AdCO<sub>2</sub>H), cinnamic acid, and benzoic acid revealed much less binding. It is clear that all of the protected amino acids are bound better than the latter more conventional carboxylic acids. The side-chain selectivity among the amino acid derivatives is obvious, although Cbz-Gly is bound better than the template itself. These binding data strongly suggest that the imprinting has produced specific receptor sites in the  $\text{TiO}_2$ -gel film. Therefore, the imprinted site must be constituted by carboxylate site, hydrogen-bonding site, and hydrophobic cavities corresponding to the Cbz unit and amino acid side chains, as shown in Fig. 5.17. These varied interaction sites act cooperatively to realize selective recognition of amino acid derivatives.

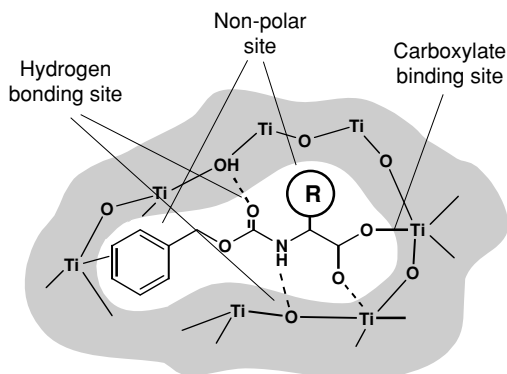


FIGURE 5.17. Schematic illustration of a Cbz-amino acid imprinted film. R denotes the side chain of Cbz-amino acid derivatives.

Even enantioselectivity is observed in this system.<sup>51</sup> Imprinted  $\text{TiO}_2$ -gel films were prepared in a similar way by using L- or D-amino acid derivatives (Cbz-Ala, Cbz-Leu, and Cbz-Phe) as templates. The QCM rebinding data for the L and D enantiomers in these imprinted films are shown in Table 5.3. Generally, the template molecules gave much larger frequency changes than their enantiomers. The enantiomeric difference in the frequency changes,  $\Delta\Delta F_{\text{enantiomer}} = \Delta F_t$  (template)  $-\Delta F_e$  (its enantiomer), becomes larger with increasing sizes of the side chain: Cbz-Ala < Cbz-Leu < Cbz-Phe. The selectivity of the imprinted films is directly represented by the frequency changes for the D and L-forms. Thus, chiral separation factor (as enantioselectivity) was defined as a ratio of frequency changes for template and its enantiomer ( $\Delta F_t/\Delta F_e$ , Hz/Hz). In the case of Cbz-Ala, the  $\Delta\Delta F_{\text{enantiomer}}$  values were less than 5 Hz, and the chiral separation factor was about 1.1 in either of the L- and D-imprinted films. In contrast, the template molecule was bound much better than its enantiomer in the Cbz-Leu or Cbz-Phe imprinted film. The  $\Delta\Delta F_{\text{enantiomer}}$  values for these optical isomers were 16–22 Hz, and the chiral separation factor amounted to 1.7–2.0.

TABLE 5.3. Rebinding data for L- and D-enantiomers in  $\text{TiO}_2$ -gel films imprinted with Cbz-amino acid derivatives.

Imprinted film	Guest (L-form)	Saturation- $\Delta F$ of binding (pmol/Hz)		
		Guest (D-form)	$\alpha^b$	
Cbz-Ala	L	173/43 <sup>a</sup> (65)	153/38 (60)	1.13
	D	157/39 (67)	177/44 (70)	1.13
Cbz-Leu	L	129/38 (74)	75/22 (58)	1.73
	D	81/24 (62)	139/41 (79)	1.71
Cbz-Phe	L	120/40 (69)	60/20 (49)	2.00
	D	96/32 (44)	162/54 (66)	1.68

<sup>a</sup>Frequency change except for surface adsorbed mass.

<sup>b</sup>Enantioselectivity factor ( $\alpha$ ) in each imprinted film is the ratio of the amounts of bound template molecule and its enantiomer ( $\text{mol}_{\text{template}}/\text{mol}_{\text{enantiomer}}$ ).

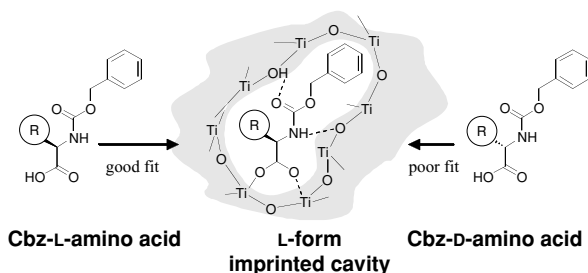


FIGURE 5.18. Schematic illustration of relative binding of enantiomers in a Cbz-L-amino acid imprinted  $\text{TiO}_2$ -gel film.

Chiral molecular imprinting in the previous studies has been mostly conducted by using organic polymers. Except for some special cases,<sup>13,52</sup> organic polymers imprinted with N-protected amino acids give small chiral separation factors: 1.84 for racemate resolution of Cbz-Phe in MAA–ethylene glycol dimethacrylate (EDMA) copolymer system<sup>53</sup> and 2.36 for enantiomeric resolution in acrylamide–EDMA copolymer system in acetonitrile.<sup>54</sup> These latter values are very close to what we found for Cbz-Phe. It is clear that the  $\text{TiO}_2$ -gel imprinted film is capable of chiral recognition of amino acid derivatives, comparable to those of functionalized cross-linked polymers. It is remarkable that a precursor as simple as titanium butoxide can produce specific binding cavities composed of such complex complementary areas. In comparison with cross-linked polymers, the amorphous network of metal oxides can, by itself, produce imprinting sites of varied functionalities: metal coordination, proton donor, proton acceptor, polar region, and apolar domain, as illustrated in Fig. 5.18. Spatial disposition of such individual domains is achieved in the cavity, making an enantioselective cavity. Such structural flexibility and functional diversity are the greatest advantages of the  $\text{TiO}_2$ -gel for molecular imprinting.

### 5.3.5. Varied Molecular Selectivity

From the preceding results, it is evident that the guest selectivity is closely associated with molecular structure (size and shape) and functionality. The nature of the imprinted cavity might be understood more clearly by comparing the relative binding efficiency for each guest in the three different  $\text{TiO}_2$ -gel imprinted films described in Section 5.3.2.

As seen from Fig. 5.13, benzoic acid, octanoic acid, and cinnamic acid give relatively low binding efficiencies of 0.3–0.6 in all cases. It means that the guest molecules smaller than the size of the imprinted cavity, even if they readily penetrate into the cavity, are not bound efficiently in spite of the existence of carboxylic function. In contrast,  $\text{C}_3\text{AzoCO}_2\text{H}$  and  $\text{AzoCO}_2\text{H}$  give high efficiencies of greater than 0.6 in either imprinted film. The isomeric structure of the two anthracenecarboxylic acids (2- and 9-isomers) is clearly discriminated by imprinting of the

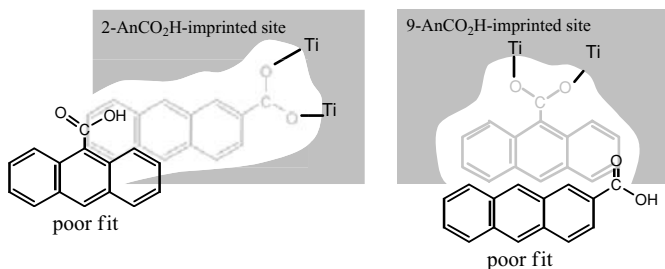


FIGURE 5.19. Schematic illustration of regioselective binding in imprinted  $\text{TiO}_2$ -gel ultra-thin films.

individual isomers, the template isomer being more efficiently bound than the other isomer. Interestingly, these isomers give different binding efficiencies for the  $\text{C}_3\text{AzoCO}_2\text{H}$ -imprinted film (i.e., 0.33 for 9-AnCO<sub>2</sub>H and 0.60 for 2-AnCO<sub>2</sub>H). This difference must reflect the molecular structures of the isomers, as illustrated in Fig. 5.19. It should be noted that the largest selectivity is found for 9-AnCO<sub>2</sub>H (see 9-AnCO<sub>2</sub>H in Fig. 5.13). The cavity that is created by imprinting of 9-AnCO<sub>2</sub>H is more discriminating than that by 2-AnCO<sub>2</sub>H, probably because the carboxylate site prepared with 9-AnCO<sub>2</sub>H is less exposed within the cavity.

The separation factor (regioselectivity) for the isomers can be expressed as a molar ratio of bound template and its isomer molecules ( $\text{mol}_{\text{template}}/\text{mol}_{\text{isomer}}$ ). The separation factor of the two anthracene isomers is estimated to be 1.1 and 1.4 in the 9-AnCO<sub>2</sub>H- and 2-AnCO<sub>2</sub>H-imprinted films, respectively. In general, the imprinting effect consists of different kinds of guest selectivity such as functional selectivity, structural selectivity, and enantioselectivity. For example, the structural selectivity is 1.7 for 2-AnCO<sub>2</sub>H (3.0 for 9-AnCO<sub>2</sub>H) in the  $\text{C}_3\text{AzoCO}_2\text{H}$ -imprinted film, and the chiral separation factor for Cbz-Leu (L and D) amounts to  $\sim 1.7$ . A comparison of the separation factors in  $\text{TiO}_2$ -gel films is given in Fig. 5.20. It is clear that  $\text{TiO}_2$ -gel imprinted films are capable of versatile molecular recognition.

## 5.4. Practical Potentials

### 5.4.1. Recognition of Biological Molecules

In the preceding examples, imprinting and rebinding experiments are conducted in organic solvents in order to ascertain film quality and reproducible mass changes. However, detection of most biological molecules would be more conveniently carried out in aqueous solution. For this purpose, ultrathin  $\text{TiO}_2$  films were imprinted with biomolecules such as saccharides and peptides. For example, an ultrathin  $\text{TiO}_2$ -gel film imprinted with glycytyrosine (Gly-Tyr) was prepared on a QCM electrode by the layer-by-layer approach.<sup>55</sup> The template was removed with

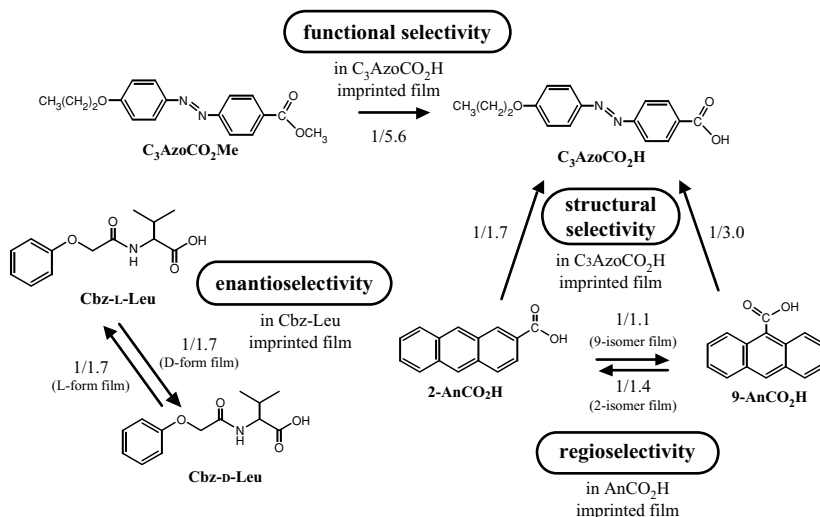


FIGURE 5.20. Comparison of separation factors of imprinted  $\text{TiO}_2$ -gel ultrathin films.

aqueous sodium hydroxide (10 mM), as dilute ammonia was not strong enough for the removal.

Figure 5.22a shows *in situ* frequency changes caused by the binding of dipeptides (see Fig. 5.21) on the Gly-Tyr imprinted film. After adding Gly-Tyr, the frequency change was essentially saturated within a few min at 17 Hz. In contrast, no frequency change was observed with glycylphenylalanine (Gly-Phe). The lack of Gly-Phe binding suggests that the Gly-Tyr-imprinted site contains a subsite that strongly interacts with the phenol hydroxyl group. In the case of glycylvaline (Gly-Val), the frequency began to change gradually a few minutes after the addition of the dipeptide. It is clear that the cavity formed in the  $\text{TiO}_2$ -gel retains the molecular shape of the Gly-Tyr template. In the same vein,  $\text{TiO}_2$ -gel films imprinted with peptides without functional side groups showed lower selectivities. In fact, a glycylglycine (Gly-Gly)-imprinted film gave frequency shifts of 2–3 Hz for both the Gly-Gly template and the Gly-Tyr guest. Selectivity of a glycylglycylglycine (Gly-Gly-Gly)-imprinted film was still worse. Undoubtedly, the functional side groups of peptides improve recognition efficiency in addition to their shapes and sizes. Figure 5.22b shows a schematic representation of a dipeptide molecule, glycylglutamic acid (Gly-Glu), included in  $\text{TiO}_2$ -gel matrices. The dipeptide in the cavity interacts with the surrounding gel by electrostatic attraction, coordination of the carboxyl group, and hydrogen-bonding. When the dipeptide template is removed, a cavity that mimics the shape of the dipeptide molecule is formed in the  $\text{TiO}_2$ -gel matrix and is capable of the selective adsorption of guest molecules. The concentration of the dipeptide solution in this system is only 10  $\mu\text{M}$ , indicating the very low detection limits of the dipeptides. It is surprising that the strong hydration of the dipeptide molecules does not interfere with molecular recognition even at such a low concentration.

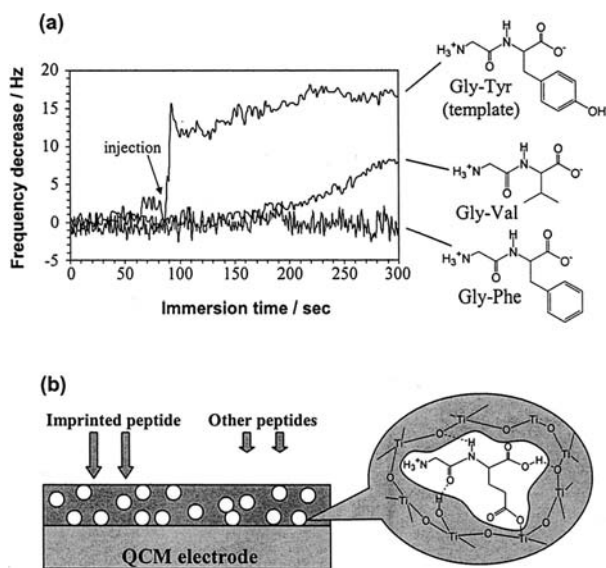


FIGURE 5.21. (a) *In situ* QCM frequency changes due to binding of dipeptides on a Gly-Tyr imprinted TiO<sub>2</sub>-gel film. Each guest molecule was injected at the point indicated by the arrow. (b) Schematic representation of a Gly-Glu imprinted TiO<sub>2</sub>-gel film on a QCM electrode.

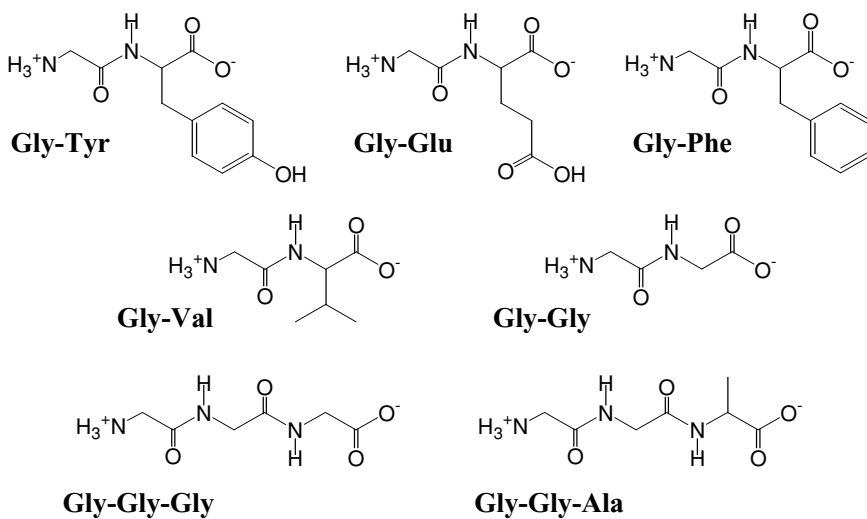


FIGURE 5.22. Chemical structures of di- and tri-peptides used as guest molecules.



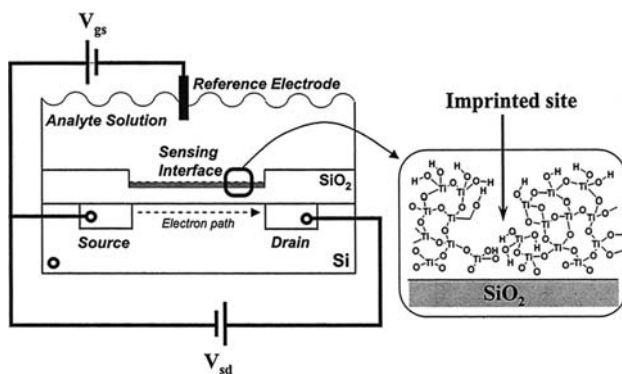


FIGURE 5.23. Schematic configuration of a molecular-imprinted ISFET device.

#### 5.4.2. Contrivance for High Sensitivity

Low sensitivity and inconvenience of QCM measurement in water will limit its use under physiological conditions. These problems might be relieved by detecting the binding process with electrochemical means and semiconductor sensors. For example, the use of ion-sensitive field-effect transistors (ISFETs) as electronic transducing elements of molecular recognition events can reveal important analytical advantages due to intrinsically high sensitivity, miniaturization capability, and cost-effectiveness. Recently, Lahav et al. conducted the successful detection of organic carboxylic acids by using an ISFET device that was modified with a TiO<sub>2</sub>-gel and imprinted with 4-chlorophenoxyacetic acid and 2,4-dichlorophenoxyacetic acid.<sup>56</sup> A schematic configuration of a molecular-imprinted FET device is illustrated in Fig. 5.23, where the molecular-imprinted site acts as the sensing interface on the ISFET gate. High selectivities were noted among the related guest molecules, and reasonable sensitivities in the concentration range of  $1 \times 10^{-6}$  to  $5 \times 10^{-4}$  M were observed in most cases. The detection limit would be much improved in the case of TiO<sub>2</sub>-gel films imprinted with more strongly binding biological molecules. More recently, they demonstrated that chiroselective<sup>57</sup> and stereoselective<sup>58</sup> imprinted TiO<sub>2</sub> films could be assembled on the ISFET devices for a variety of chiral carboxylic acids and for structural isomers of carboxylic acids.

In all of these systems, a TiO<sub>2</sub>-imprinted film that is associated with the gate surface of the ISFET is generated by the sol-gel deposition of the Ti(IV)-carboxylate complex on the gate interface. The subsequent elimination of the carboxylate yields the molecular contours of the carboxylate in the TiO<sub>2</sub> film and generates a Ti(IV)-OH site that undergoes dissociation that controls the gate potential. Thus, rebinding of the carboxylate to the imprinted sites can be electronically transduced by the functional ISFET device. Interestingly, these sensor systems were also applied to the detection of chemical pollutants such as phosphonic acid derivatives and mercaptans.<sup>59</sup> Imprinted TiO<sub>2</sub> matrices for other acidic organic compounds such as sulfonates or boronic acids can be fabricated in a similar way.

### 5.4.3. Recognition of Coordination Geometry

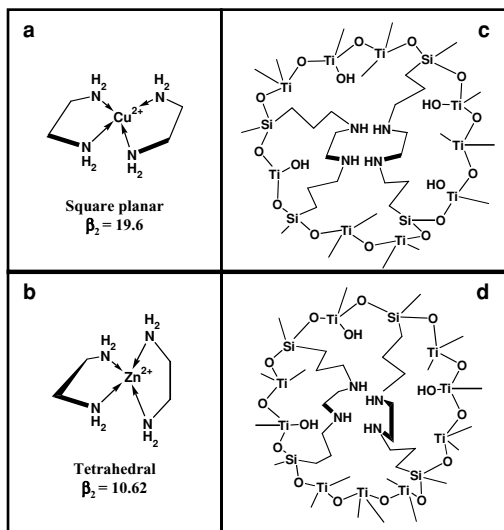
Metal ions are also important targets of imprinting, although they have received much less attention. From the viewpoint of binding efficiency, metal-ion imprinting has been focused on the use of surfaces (e.g., the surface of polymer particles and the inner wall of microporous silica). Ultrathin  $\text{TiO}_2$ -gel films were applied to imprinting of metal ions by incorporation of a carefully selected ligand, bis[3-(trimethoxysilyl)propyl]ethylenediamine (2SiEN).<sup>60</sup>  $\text{Cu}^{2+}$  and  $\text{Zn}^{2+}$  ions were selected as templates that have the same charges and almost the same ionic radii and were introduced in  $\text{TiO}_2$ -gel matrices with the two 2SiEN ligands. The metal ions were removed by acidifying the amine groups with aqueous HCl (pH 4), followed by neutralization with aqueous NaOH (pH 10).

The effect of imprinting was studied by QCM rebinding experiments. The  $\text{Cu}^{2+}$ -imprinted film showed greater binding to  $\text{Cu}^{2+}$  than to  $\text{Zn}^{2+}$  and the selectivity was estimated to be 10. On the other hand, the  $\text{Zn}^{2+}$ -imprinted film showed greater binding to  $\text{Zn}^{2+}$  than to  $\text{Cu}^{2+}$ . The selectivity was much lower, the average being 1.3. Competitive binding was tested by immersing the  $\text{Cu}^{2+}$ -imprinted film in a mixture of  $\text{Cu}^{2+}$  and  $\text{Zn}^{2+}$  in ethanol. The atomic ratio of bound  $\text{Cu}^{2+}$  and  $\text{Zn}^{2+}$ , as determined by X-ray photoelectron spectroscopy (XPS), was 8.2, in close agreement with the selectivity value (10) obtained from QCM studies.  $\text{Cu}^{2+}$  and  $\text{Zn}^{2+}$  ions assume square and tetrahedral configurations, respectively, with ethylenediamine chelates (Figs. 5.24a and 5.24b). The observed binding selectivity might arise from the configuration difference. Although the selectivity constant of  $[\text{Cu}(\text{en})_2]^{2+}$  ( $\beta_2 = 19.6$ ) is much larger than that of  $[\text{Zn}(\text{en})_2]^{2+}$  ( $\beta_2 = 10.62$ ), the  $\text{Zn}^{2+}$ -imprinted film shows stronger binding toward  $\text{Zn}^{2+}$ . During the imprinting process, the different configurations of the diamine ligand are apparently fixed in matrices, depending on the template metal ions. Therefore, the imprinted films can provide selective rebinding to its template rather than to the control, as illustrated in Figs. 5.24c and 5.24d. The double linkages of the ethylenediamine group to the  $\text{TiO}_2$ -gel network help to fix these configurations within ultrathin films, providing stable binding capacity.

### 5.4.4. Nanoporous Thin Films with Ion-Exchange Sites

The preceding results demonstrate that  $\text{Cu}^{2+}$  and  $\text{Zn}^{2+}$  ions were effective as template species with the help of the ethylenediamine ligand. On the other hand, the use of metal oxide gel itself as imprinting sites for metal ions would be more valuable if specific ligands are not required. It is conceivable that oxygen bridges and free hydroxyl groups act as ligands to metal ions. For this purpose, we developed a new ion-exchange approach for the incorporation of metal ions into metal oxide thin films (Fig. 5.25).<sup>61</sup>  $\text{Mg}(\text{OEt})_2$  was chosen as a source of the ion-exchange site, as it reacts with  $\text{Ti}(\text{O}^i\text{Bu})_4$  to form  $\text{Ti}-\text{O}-\text{M}$  linkages rather than separate  $\text{M}-\text{O}-\text{M}$  linkages during the sol-gel process. The  $\text{Mg}^{2+}$  moiety derived from the mixed-metal alkoxides is readily removed by treating with aqueous HCl, and ion-exchange sites are created within the thin film. These sites underwent

FIGURE 5.24. Configurations of  $[\text{Cu}(\text{en})_2]^{2+}$  (a) and  $[\text{Zn}(\text{en})_2]^{2+}$  (b), and schematic illustrations of the  $\text{Cu}^{2+}$  (c) and  $\text{Zn}^{2+}$  (d) imprinted sites (after template removal).



efficient ion exchange with a large variety of other metal ions such as alkaline, alkaline earth, transition metal, noble metal, and rare earth elements. The amount of metal ions introduced could be readily controlled by the amount of template and ion-exchange conditions. It should be noted that the ion-exchange site did not show significant ion selectivity.

An important feature of this approach is that incorporated metal ions could be quantitatively removed and reloaded under mild conditions for at least several

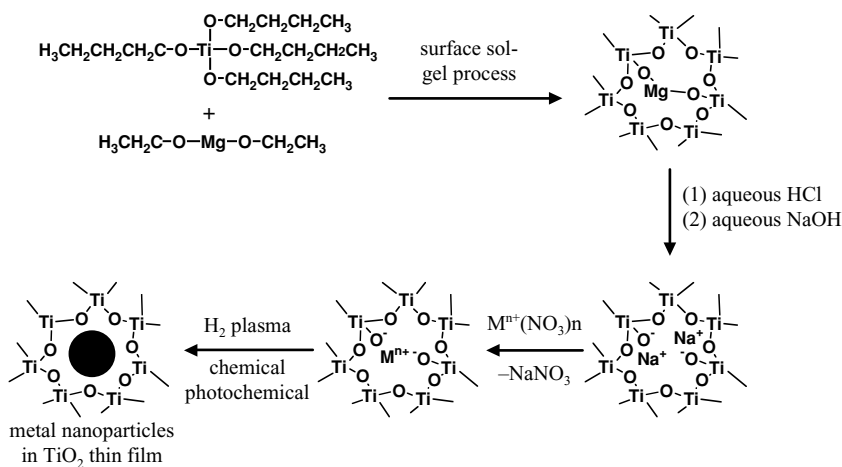


FIGURE 5.25. Ion-exchange and nanoparticle formation in  $\text{TiO}_2$  ultrathin films.

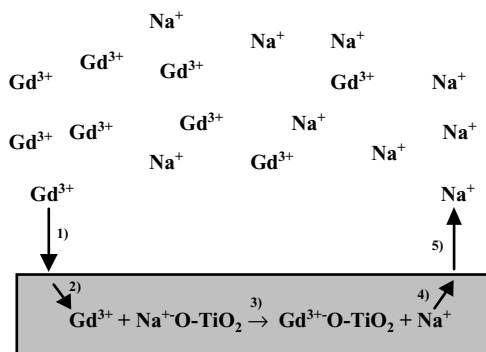


FIGURE 5.26. Schematic illustration of the ion-exchange process.

<sup>a</sup> Counterion  $\text{NO}_3^-$  not shown here simplicity.

cycles with limited deterioration of the ion-exchange capacity. This reversible process, on one hand, allows for many trial adsorptions to be executed on a single thin film, providing an efficient tool for examining the adsorption process. It is clear that both the film matrix and the ion-exchange site are stable and robust. From the kinetic results of  $\text{Gd}^{3+}$  incorporation, it was suggested that the ion-exchange process consists of five steps, as represented in Fig. 5.26: (1) diffusion of  $\text{Gd}^{3+}$  from the solution to the film surface, (2) diffusion of  $\text{Gd}^{3+}$  inside the film, (3) ion-exchange reaction ( $\text{Gd}^{3+} + \text{Na-O-TiO}_2 \rightarrow \text{Gd-O-TiO}_2 + \text{Na}^+$ ), (4) diffusion of  $\text{Na}^+$  to the film surface, and (5) diffusion of  $\text{Na}^+$  away from the film surface into the solution. The rate-determining step of the whole process was supposed to be Step 3. Step 1 would be rate determining at very low  $\text{Gd}^{3+}$  concentrations, but no longer so at high  $\text{Gd}^{3+}$  concentrations in a bulk solution. In this region, ion exchange proceeds according to zeroth-order kinetics, suggesting that the later steps (Steps 2–4) are rate determining. However, the diffusive migration of  $\text{Gd}^{3+}$  and  $\text{Na}^+$  ions within the film (Steps 2 and 4) cannot be rate determining if the ultrathin nature and loose gel structure of the film matrix are considered. Step 5 cannot be rate determining because the  $\text{Na}^+$  concentration in solution is extremely small. Thus, the ion-exchange step itself appears to be rate limiting, although further investigations are needed to clarify this point. Anyway, such a  $\text{TiO}_2$ -gel matrix itself might be used for the separation and recovery of metal ions for which the reversible process is essential. On the other hand, the ion-exchange method succeeded in the size-controlled preparation of monometallic and bimetallic nanoparticles of noble metal ions (see Fig. 5.25).<sup>62,63</sup> This approach would be useful in the preparation of novel materials of catalytic, electronic, photonic, and magnetic uses.

#### 5.4.5. Direct Observation of Imprinted Cavity–Physical Cavity Versus Topological Cavity

The outstanding features of the imprinted cavity in titania films are apparent from the preceding data. The cavity is robust enough for reproducible binding

experiments. It is composed of multifunctional areas complementary to the parts of a given template molecule. It can replicate complex morphologies of template molecules, including chiral structures. The adsorption and desorption processes are quite fast and selective, implying that the cavity maintains a certain level of flexibility. The titania network should be flexible at the atomic scale, as vibrational energies of metal oxygen bonds are smaller than those of carbon–carbon bonds. The thickness of the titania network around template molecules is estimated to be one to two layers from relative molar volumes of matrix and guest under the standard imprinting conditions. The morphology of the imprinted site surrounded by ultrathin titania networks is either physically or topologically kept intact.

Plasticity (or flexibility) and robustness of the titania wall was demonstrated by positive copying of latex nanoparticles.<sup>46</sup> A single layer of poly(styrene) latex particles with a diameter of 500 nm was formed on a substrate surface with most of the adsorbed particles forming domain structures. The titania layer of  $\sim 1$  nm thickness was then formed on the latex particle and was subjected to 30 min of the oxygen plasma treatment at room temperature. The particle diameter decreased to 200–250 nm, almost one-half of the original diameter, by the plasma treatment. At the same time, there appeared tubular structures with 10–20-nm widths that bridge adjacent particles, as seen in Fig. 5.27. It is noteworthy that the original particle morphology, although shrunk, is maintained with the titania shell of  $\sim 1$  nm thickness even after the inner particle is completely removed. This is an indication of robustness of the ultrathin titania layer. In addition, the formation of the connecting tube is evidence of the superior plasticity of the titania layer.

A direct proof was obtained for the formation of the imprinted site when nanopores arising from individual dendrimer molecules were recognized in electron microscopic observation of a plasma-treated titania film.<sup>64</sup> A single layer of hydroxyl-terminated fourth-generation poly(amidoamine) (PAMAM) dendrimers (G4-OHs) (see Fig. 5.28a) was sandwiched with titania layers and subjected to active oxygen treatment. The film formation process is schematically illustrated

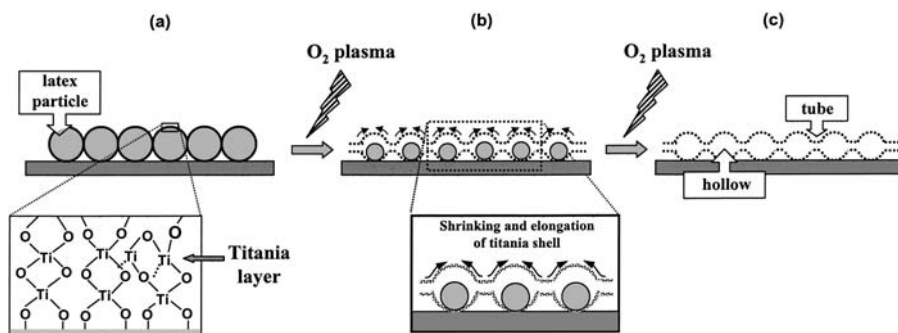


FIGURE 5.27. A scheme of generation of interconnected titania hollow structures.

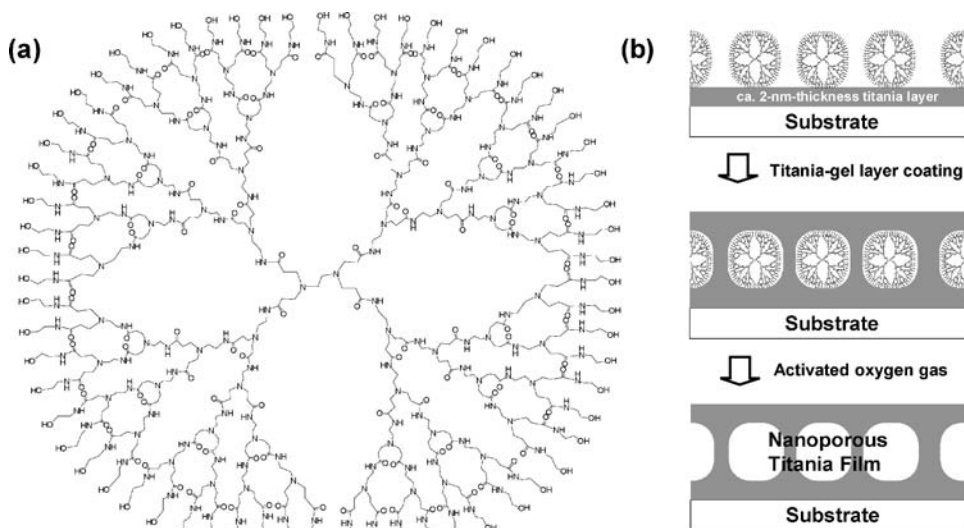


FIGURE 5.28. (a) Structure of PAMAM G4-OH dendrimer with 64 terminal hydroxyl units. (b) Schematic illustration of the formation process of a nanoporous titania film.

in Fig. 5.28b. In scanning electron microscopy, surfaces of the as-prepared and plasma-treated samples were smooth, uniform, and crack-free, indicating that the dendrimer layer and the corresponding cavity was totally buried in the titania matrix. Transmission electron microscopy (TEM) images, on the other hand, showed that the dendrimer molecules were embedded in the as-prepared film with a domain separation of around 5 nm, in close agreement with the size of the dendrimer molecule. After the template removal, ~50% of the film was occupied by nanopores 4–7 nm in size. The two-dimensional distribution of the nanopores is similar to that of the dendrimer templates. It is clear that the size and shape of nanopores reflect those of the organic template.

Similarly, amorphous metal oxide thin films with high nanoporosity could be prepared by low-temperature oxygen plasma treatment of  $\text{TiO}_2/\text{PAA}$  or  $(\text{ZrO}_2/\text{PAA})(\text{TiO}_2/\text{PAA})$  nanocomposite films.<sup>65,66</sup> The as-prepared sample showed a uniform and dense structure without any porosity. In contrast, numerous pores and channels were observed for the plasma-treated sample. The pores were estimated to have diameters of around 2 nm, which is similar to the pore size of surfactant-templated mesoporous silica films at the smallest.<sup>67,68</sup> More than 50% of the film was occupied by nanopores that were distributed randomly in the film without identifiable order or packing, as in the case with those of non-surfactant-templated mesoporous silica<sup>69</sup> and polymer-silica composites.<sup>70</sup> Control TEM observation was also carried out on an oxygen-plasma-treated titania film prepared without PAA. Porous structures were not observed in this case. The low-temperature  $\text{O}_2$  plasma treatment might be generally applicable to syntheses

of nanoporous films of various metal oxides. Also, the size and shape of the nanopore will be readily controlled according to the kinds of composite organic molecule.

## 5.5. Unsolved Problems and Future Prospects

The use of amorphous metal oxides has been attracting greater attention in recent years, as exemplified by transparent conductors and glass with nonlinear optical properties. Their unique features are more clearly seen in the form of ultrathin films and layers. In this respect, the surface sol-gel process that is based on stepwise adsorption of various metal alkoxides is advantageous. The network topology of metal/oxygen bonds makes it possible to produce varied three-dimensional structures with molecular precision. Successful molecular imprinting using a  $\text{TiO}_2$ -gel matrix is a typical example. We can conclude that imprinted  $\text{TiO}_2$ -gel films are capable of precisely recognizing the size of template molecules, the nature and position of functional groups, and molecular chirality. Particularly, the fact that monosaccharide isomers in which only the configuration of hydroxyl groups differs can be recognized sensitively indicates that the structure of imprinted  $\text{TiO}_2$ -gel is precisely controlled at the atomic level, although the data are not shown here.<sup>71</sup> A variety of molecular interactions such as coordination bond, hydrogen-bonding, electrostatic attraction, and hydrophobic interaction are involved in the cavities of the metal oxide network. However, there remain much to be done for the sol-gel imprinting technique to be useful in practical systems. A major problem is the long-term stability of the imprinted site. Our studies only indicated the fundamental effectiveness of this technique, and we are not yet sure that the current imprinting setup is satisfactory for practical use. Fortunately, it has been apparent that  $\text{TiO}_2$ -gel imprinted films are able to reveal reproducible responses under daily operation for at least several weeks.<sup>59</sup> In addition, metal oxide films other than titania have to be investigated as matrices of molecular imprinting. Second, sensitivity and selectivity of the imprinted site need to be improved much further. Sensitivity might be improved by adopting electrochemical and electronic detection, whereas selectivity must be improved by better design of template molecules and imprinting conditions.

Current imprinting investigations based on organic polymers have aimed at the construction of highly discriminating molecular recognition systems by three-dimensional arrangement of specific functional groups. However, the synthesis of such host compounds is not readily achieved because divinyl monomers cannot produce precisely structured cavities complementary to small guest molecules. The  $\text{TiO}_2$ -gel matrix obtained by the surface sol-gel process is totally different, as described earlier. Basic advantages of the metal oxide film as the imprinting matrix compared with cross-linked polymers are as follows: (1) thermal stability derived from metal oxide networks rather than organic networks, (2) formation of multifunctional sites from simple, single-component metal alkoxide precursors, and (3) simple operation of the imprinting process. These unique features must

be used in establishing high-performance, economical imprinting systems. Practical applications will be in the field of separation membranes, adsorbents, and chemical sensors. For example, the specialty chemicals industry and the pharmaceutical industry should be benefited by specific separation either by membrane or by adsorbent. The potential in the environmental technology would be enormous.

Finally, unique advantages of amorphous materials not available from crystalline materials should be noted. One is outstanding compatibility with other molecular materials. This property is indispensable for stabilizing the interface with other types of material in the preparation of hybrid materials. For example, it is possible to obtain novel isolated molecular species by forming an ultrathin metal oxide layer around individual template molecules in solution. We refer to this new category of template synthesis as “molecular wrapping”.<sup>72–75</sup> As shown in Fig. 5.29, individual fluorescein molecules are wrapped with a thin  $\text{TiO}_2$ -gel layer, and such isolated molecules do not lose their monomeric characteristics even if they undergo agglomeration. The advantages of molecular wrapping are not confined to functional isolation. Other physicochemical properties such as solubility, stability, reactivity, and association property might be altered by molecular wrapping. The high reactivity of amorphous metal oxide should contribute to the development of nanofabrication processes under mild conditions. We believe that amorphous metal oxides offer great potential for the creation of functional materials of nanometer dimensions.

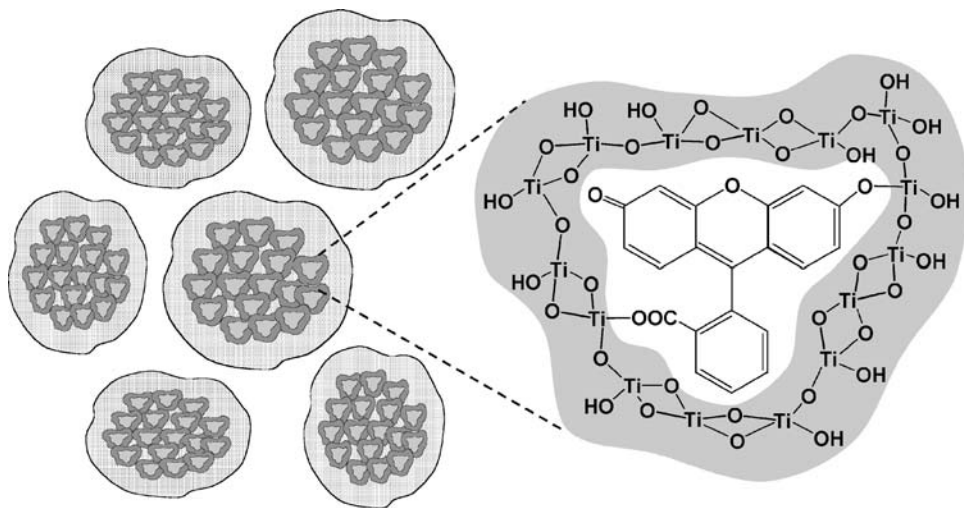


FIGURE 5.29. Schematic illustration of fluorescein/ $\text{TiO}_2$ -gel nanoparticles coated with capping reagents.



## References

1. F. H. Dickey, Preparation of specific adsorbents, *Proc. Natl. Acad. Sci. USA* **35**, 227–229 (1949).
2. F. H. Dickey, Specific adsorption, *J. Phys. Chem.* **59**, 695–707 (1955).
3. R. Curti and U. Colombo, Chromatography of stereoisomers with "tailor-made" compounds, *J. Am. Chem. Soc.* **74**, 3961 (1952).
4. A. H. Beckett and P. Anderson, A method for the determination of the configuration of organic molecules using stereo-selective adsorbents, *Nature* **179**, 1074–1075 (1957).
5. A. H. Beckett and P. Anderson, The determination of the relative configuration of morphine, levorphanol and laevophenazocine by stereoselective adsorbents, *J. Pharm. Pharmacol.* **12**, 228–236 (1960).
6. H. Erlenmeyer and H. Bartels, The problem of similarity in chemistry. Thin layer chromatography on silica gel of specific absorptivity, *Helv. Chim. Acta* **47**, 46–51 (1964).
7. H. Erlenmeyer and H. Bartels, The problem of similarity in chemistry. Specific adsorption on silica gels. II, *Helv. Chim. Acta* **47**, 1285–1288 (1964).
8. G. Wulff and A. Sarhan, Use of polymers with enzyme-analogous structures for the resolution of racemates, *Angew. Chem. Int. Ed. Engl.* **11**, 341 (1972).
9. G. Wulff, A. Sarhan, and K. Zabrocki, Enzyme-analog built polymers and their use for the resolution of racemates, *Tetrahedron Lett.* **44**, 4329–4332 (1973).
10. G. Vlatakis, L. I. Andersson, R. Müller, and K. Mosbach, Drug assay using antibody mimics made by molecular imprinting, *Nature* **361**, 645–647 (1993).
11. K. J. Shea, Molecular imprinting of synthetic network polymers: the *de novo* synthesis of macromolecular binding and catalytic sites, *Trends Polym. Sci.* **2**, 166–173 (1994).
12. G. Wulff, Molecular imprinting in cross-linked materials with the aid of molecular templates: A way towards artificial antibodies, *Angew. Chem. Int. Ed. Engl.* **34**, 1812–1832 (1995).
13. M. Kempe and K. Mosbach, Molecular imprinting used for chiral separations, *J. Chromatogr. A* **694**, 3–13 (1995).
14. K. Mosbach and O. Ramström, The emerging technique of molecular imprinting and its future impact on biotechnology, *Biotechnology* **14**, 163–170 (1996).
15. B. Sellergren, Noncovalent molecular imprinting: antibody-like molecular recognition in polymeric network materials, *Trends Anal. Chem.* **16**, 310–320 (1997).
16. A. G. Mayes and K. Mosbach, Molecularly imprinted polymers: useful materials for analytical chemistry? *Trends Anal. Chem.* **16**, 321–332 (1997).
17. D. Kriz, O. Ramström, and K. Mosbach, Molecular imprinting: new possibilities for sensor technology, *Anal. Chem.* **69**, 345–349 (1997).
18. O. Ramström and R. J. Ansell, Molecular imprinting technology: Challenges and prospects for the future, *Chirality* **10**, 195–209 (1998).
19. O. Ramström and K. Mosbach, Synthesis and catalysis by molecularly imprinted materials, *Curr. Opin. Chem. Biol.* **3**, 759–764 (1999).
20. B. Sellergren, Polymer- and template-related factors influencing the efficiency in molecularly imprinted solid-phase extractions, *Trends Anal. Chem.* **18**, 164–174 (1999).
21. K. Haupt and K. Mosbach, Molecularly imprinted polymers and their use in biomimetic sensors, *Chem. Rev.* **100**, 2495–2504 (2000).
22. M. J. Whitcombe and E. N. Vulfson, Imprinted polymers, *Adv. Mater.* **13**, 467–478 (2001).

23. B. Sellergren, *Molecularly Imprinted Polymers: Man-Made Mimics Of Antibodies And Their Applications in Analytical Chemistry*, Elsevier, Amsterdam, 2001.
24. M. Glad, O. Nörklow, B. Sellergren, N. Siegbahn, and K. Mosbach, Use of silane monomers for molecular imprinting and enzyme entrapment in polysiloxane-coated porous silica, *J. Chromatogr.* **347**, 11–23 (1985).
25. K. Morihara, S. Kurihara, and J. Suzuki, Footprint catalysis. I. A new method for designing tailor-made catalysts with substrate specificity: silica (alumina) catalysts for butanolysis of benzoic anhydride, *Bull. Chem. Soc. Jpn.* **61**, 3991–3998 (1988).
26. J. Heilmann and W. F. Maier, Selective catalysis with silicon dioxide imprinted with transition state analogs, *Angew. Chem. Int. Ed. Engl.* **33**, 471–473 (1994).
27. C. Pinel, P. Loisel, and P. Gallezot, Preparation and utilization of molecularly imprinted silicas, *Adv. Mater.* **9**, 582–585 (1997).
28. R. Makote and M. M. Collinson, Dopamine recognition in templated silicate films, *Chem. Commun.* **3**, 425–426 (1998).
29. R. Makote and M. M. Collinson, Template recognition in inorganic–organic hybrid films prepared by the sol–gel process, *Chem. Mater.* **10**, 2440–2445 (1998).
30. J. Sagiv, Organized monolayers by adsorption. III. Irreversible adsorption and memory effects in skeletonized silane monolayers, *Isr. J. Chem.* **18**, 346–353 (1979).
31. N. Kodakari, N. Katada, and M. Niwa, Molecular sieving silica overlayer on tin oxide prepared using an organic template, *J. Chem. Soc. Chem. Commun.* 623–624 (1995).
32. I. Ichinose, H. Senzu, and T. Kunitake, Stepwise adsorption of metal alkoxides on hydrolyzed surfaces: A surface sol–gel process, *Chem. Lett.* **25**, 831–832 (1996).
33. I. Ichinose, H. Senzu, and T. Kunitake, A surface sol–gel process of TiO<sub>2</sub> and other metal oxide films with molecular precision, *Chem. Mater.* **9**, 1296–1298 (1997).
34. I. Ichinose, T. Kawakami, and T. Kunitake, Alternate molecular layers of metal oxides and hydroxyl polymers prepared by the surface sol–gel process, *Adv. Mater.* **10**, 535–539 (1998).
35. I. Ichinose, R. Takaki, K. Kuroiwa, and T. Kunitake, Electrostatic adsorption of cytochrome *c* on ultrathin ZrO<sub>2</sub>-gel layers and preparation of alternate multilayers, *Langmuir* **19**, 3883–3888 (2003).
36. G. Acharya and T. Kunitake, A general method for fabrication of biocompatible surfaces by modification with titania layer, *Langmuir* **19**, 2260–2266 (2003).
37. T. Yonezawa, H. Matsune, and T. Kunitake, Layered nanocomposite of close-packed gold nanoparticles and TiO<sub>2</sub> gel layers, *Chem. Mater.* **11**, 33–35 (1999).
38. J. Sun, I. Ichinose, R. Takaki, A. Nakao, and T. Kunitake, Enhanced emission in composite multilayers of amorphous TiO<sub>2</sub>-gel and Eu<sup>3+</sup> ions, *Chem. Lett.* **31**, 742–743 (2002).
39. S.-W. Lee, I. Ichinose, and T. Kunitake, Molecular imprinting of azobenzene carboxylic acid on a TiO<sub>2</sub> ultrathin film by the surface sol-gel process, *Langmuir* **14**, 2857–2863 (1998).
40. I. Ichinose, S.-W. Lee, and T. Kunitake, in: *Supramolecular Organization and Materials Design*, edited by W. Jones and C. N. R. Rao, Cambridge University Press, Cambridge, 2002, pp. 172–213.
41. T. Kunitake and S.-W. Lee, Molecular imprinting in ultrathin titania gel films via surface sol-gel process, *Anal. Chim. Acta* **504**, 1–6 (2004).
42. A. Kase, K. Asakura, C. Egawa, and Y. Iwasawa, New “palladium/ultra-thin amorphous-oxide/ZSM-5” catalysts for selective formation of propane from carbon monoxide/hydrogen, *Chem. Lett.* **15**, 855–858 (1986).

43. K. Asakura and Y. Iwasawa, New reversible enhancement/depression phenomenon on catalysis of platinum supported on one-atomic layer niobium oxide for ethane hydrogenation, *Chem. Lett.* **17**, 633–636 (1988).
44. E. R. Kleinfeld and G. S. Ferguson, A molecular approach to ultrathin multilayered films of titanium dioxide, *Mater. Res. Soc. Symp. Proc.* **351**, 419–424 (1994).
45. G. Sauerbrey, The use of quartz oscillators for weighing thin layers and for microweighing, *Z. Phys.* **155**, 206–222 (1959).
46. S. Fujikawa and T. Kunitake, Surface fabrication of interconnected hollow spheres of nm-thick titania shell, *Chem. Lett.* **31**, 1134–1135 (2002).
47. J. Huang and T. Kunitake, Nano-precision replication of natural cellulosic substances by metal oxides, *J. Am. Chem. Soc.* **125**, 11,834–11,835 (2003).
48. J. He and T. Kunitake, Preparation and thermal stability of gold nanoparticles in silk-templated porous filaments of titania and zirconia, *Chem. Mater.* **16**, 2656–2661 (2004).
49. S.-W. Lee, D.-H. Yang, and T. Kunitake, Regioselective imprinting of anthracenecarboxylic acids onto TiO<sub>2</sub> gel ultrathin films: an approach to thin film sensor, *Sens. Actuators B*, **104**, 35–42 (2005).
50. S.-W. Lee, I. Ichinose, and T. Kunitake, Molecular imprinting of protected amino acids in ultrathin multilayers of TiO<sub>2</sub> gel, *Chem. Lett.* **27**, 1193–1194 (1998).
51. S.-W. Lee, I. Ichinose, and T. Kunitake, Enantioselective binding of amino acid derivatives onto imprinted TiO<sub>2</sub> ultrathin films, *Chem. Lett.* **31**, 678–679 (2002).
52. O. Ramst rm, I. A. Nichollos, and K. Mosbach, Synthetic peptide receptor mimics: highly stereoselective recognition in non-covalent molecularly imprinted polymers, *Tetrahedron: Asymmetry* **5**, 649–656 (1994).
53. M. Kemp and K. Mosbach, Separation of amino acids, peptides and proteins on molecularly imprinted stationary phases, *J. Chromatogr. A* **691**, 317–323 (1995).
54. C. Yu and K. Mosbach, Molecular imprinting utilizing an amide functional group for hydrogen bonding leading to highly efficient polymers, *J. Org. Chem.* **62**, 4057–4064 (1997).
55. I. Ichinose, T. Kikuchi, S.-W. Lee, and T. Kunitake, Imprinting and selective binding of di- and tri-peptides in ultrathin TiO<sub>2</sub>-gel films in aqueous solutions, *Chem. Lett.* **31**, 104–105 (2002).
56. M. Lahav, A. B. Kharitonov, O. Katz, T. Kunitake, and I. Willner, Tailored chemosensors for chloroaromatic acids using molecular imprinted TiO<sub>2</sub> thin films on ion-sensitive field-effect transistors, *Anal. Chem.* **73**, 720–723 (2001).
57. M. Lahav, A. B. Kharitonov, and I. Willner, Imprinting of chiral molecular recognition sites in thin TiO<sub>2</sub> films associated with field-effect transistors: Novel functionalized devices for chiroselective and chiro-specific analyses, *Chem. Eur. J.* **7**, 3992–3997 (2001).
58. M. Zayats, M. Lahav, A. B. Kharitonov, and I. Willner, Imprinting of specific molecular recognition sites in inorganic and organic thin layer membranes associated with ion-sensitive field-effect transistors, *Tetrahedron* **58**, 815–824 (2002).
59. S. P. Pogorelova, A. B. Kharitonov, I. Willner, C. N. Suenik, H. Pizem, and T. Bayer, Development of ion-sensitive field-effect transistor-based sensors for benzylphosphonic acids and thiophenols using molecularly imprinted TiO<sub>2</sub> films, *Anal. Chim. Acta* **504**, 113–122 (2004).
60. J. He, I. Ichinose, and T. Kunitake, Imprinting of coordination geometry in ultrathin films via the surface sol–gel process, *Chem. Lett.* **30**, 850–851 (2001).
61. J. He, I. Ichinose, S. Fujikawa, T. Kunitake, and A. Nakao, A general, efficient method of incorporation of metal ions into ultrathin TiO<sub>2</sub> films, *Chem. Mater.* **14**, 3493–3500 (2002).

62. J. He, I. Ichinose, T. Kunitake, and A. Nakao, In situ synthesis of noble metal nanoparticles in ultrathin TiO<sub>2</sub>-gel films by a combination of ion-exchange and reduction processes, *Langmuir* **18**, 10,005–10,010 (2002).
63. J. He, I. Ichinose, T. Kunitake, A. Nakao, Y. Shiraishi, and N. Toshima, Facile fabrication of Ag–Pd bimetallic nanoparticles in ultrathin TiO<sub>2</sub>-gel films: Nanoparticle morphology and catalytic activity, *J. Am. Chem. Soc.* **125**, 11,034–11,040 (2003).
64. J. Huang, I. Ichinose, and T. Kunitake, Replication of dendrimer monolayer as nanopores in titania ultrathin film, *J. Chem. Soc. Chem. Commun.* 2070–2071 (2002).
65. J. Huang, I. Ichinose, T. Kunitake, and A. Nakao, Zirconia-titania nanofilm with composition gradient, *Nano Lett.* **2**, 669–672 (2002).
66. J. Huang, I. Ichinose, T. Kunitake, and A. Nakao, Preparation of nanoporous titania films by surface sol-gel process accompanied by low-temperature oxygen plasma treatment, *Langmuir* **18**, 9048–9053 (2002).
67. H. Yang, N. Coombs, I. Sokolov, and G. A. Ozin, Free-standing and oriented mesoporous silica films grown at the air-water interface, *Nature* **381**, 589–592 (1996).
68. D. Zhao, Q. Huo, J. Feng, B. F. Chmelka, and G. D. Stucky, Tri-, tetra-, and octablock copolymer and nonionic surfactant syntheses of highly ordered, hydrothermally stable, mesoporous silica structures, *J. Am. Chem. Soc.* **120**, 6024–6036 (1998).
69. Y. Wei, D. L. Jin, T. Z. Ding, W. H. Shih, X. H. Liu, S. Z. D. Cheng, and Q. Fu, A non-surfactant templating route to mesoporous silica materials, *Adv. Mater.* **10**, 313–316 (1998).
70. Y. Wei, Q. Feng, J. Xu, H. Dong, K.-Y. Qiu, S. A. Jansen, R. Yin, and K. K. Ong, Polymethacrylate-silica hybrid nanoporous materials: A bridge between inorganic and polymeric molecular sieves, *Adv. Mater.* **12**, 1448–1450 (2000).
71. S.-W. Lee and T. Kunitake, Adsorption of TiO<sub>2</sub> nanoparticles imprinted with D-glucose on a gold surface, *Mol. Cryst. Liq. Cryst.* **371**, 111–114 (2001).
72. I. Ichinose and T. Kunitake, Molecular wrapping of a fluorescent dye with TiO<sub>2</sub>-gel and capping reagents, *Chem. Lett.* **30**, 626–627 (2001).
73. I. Ichinose and T. Kunitake, Wrapping individual chains of a viologen polymer with an ultrathin silicate sheath, *Adv. Mater.* **14**, 344–346 (2002).
74. I. Ichinose and T. Kunitake, Wrapping and inclusion of organic molecules with ultrathin, amorphous metal oxide films, *Chem. Rec.* **2**, 339–351 (2002).
75. I. Ichinose, Y. Hashimoto, and T. Kunitake, Wrapping of bio-macromolecules (dextran, amylopectin, and horse heart cytochrome *c*) with ultrathin silicate layer, *Chem. Lett.* **33**, 656–657 (2004).

# 6

## Fabrication, Characterization, and Applications of Template-Synthesized Nanotubes and Nanotube Membranes

PUNIT KOHLI<sup>†</sup> AND CHARLES R. MARTIN<sup>‡</sup>

<sup>†</sup>*Department of Chemistry and Biochemistry, Southern Illinois University, Carbondale, IL 62901, USA and* <sup>‡</sup>*Department of Chemistry and Center for Research at Bio/Nano Interface University of Florida, Gainesville, FL 32611, USA*

### 6.1. Introduction

Nanoscience is one of the most important research and development frontiers in modern science.<sup>1</sup> Nano is a Greek word meaning dwarf, and the nanometer (nm,  $10^{-9}$  m) defines the length scale that is used to measure systems being studied in nanoscience. In the most simplistic sense, nanoscience is the science of small particles of materials. Such small particles are of interest from a fundamental viewpoint because all properties of a material (e.g., melting point, electronic properties, optical properties) change when the size of the particles that makes up the material become nanoscopic. With new properties come new opportunities for technological and commercial development, and applications of nanoparticles have been demonstrated or proposed in areas as diverse as microelectronics, coatings and paints, and biotechnology.

For example, one application that is currently in the commercial marketplace entails using gold nanoparticles as visual indicators in over-the-counter medical diagnostic kits.<sup>2</sup> This application illustrates nicely how the unique properties of a nanoparticle can lead to technological opportunities. Macroscopic samples of pure gold have only one color—gold—but nanoparticles of gold can show essentially all of the colors of the rainbow, depending on the size and the shape of the nanoparticle.<sup>3</sup> Furthermore, the intensity of the optical absorption of gold nanoparticles is extraordinarily strong, which means that when suspended in a solution or deposited on a surface, the naked eye can detect a very small quantity of these particles. These properties make gold nanoparticles ideally suited as visual indicators.

Other applications of microparticles and nanoparticles in the biomedical sciences and biotechnology include use as vehicles for enzyme encapsulation,<sup>4</sup> DNA transfection,<sup>5–7</sup> biosensors,<sup>8–10</sup> and drug delivery.<sup>11–13</sup> For example, drugs can be incorporated into nanospheres composed of a biodegradable polymer, and this allows for timed release of the drug as the nanospheres degrade.<sup>11,12</sup> The circumstances that cause the particle to degrade can be adjusted by varying the nature of the chemical bonding within the particle. For example, when acid-labile bonds are used, the particles degrade in acidic microenvironments such as would be extant

in tumor cells or around a site of inflammation.<sup>13</sup> This allows for site-specific drug delivery. In another recent study, polymeric nanoparticles were labeled on their outer surfaces with a viral peptide sequence that promotes permeation of substances through cell membranes.<sup>14</sup> These peptide-derivatized nanoparticles passed through cell membranes and were incorporated into living cells, at much higher levels than nanoparticles without the surface-bound peptide.

Surface functionalized nanoparticles can also be used to deliver genetic material into living cells, a process called transfection. For example, silica nanospheres labeled on their outer surfaces with cationic ammonium groups were found to bind DNA (a polyanion) via electrostatic interactions.<sup>5</sup> These nanoparticles were then used to deliver the surface-bound DNA into cells. That transfection was successful was proven by showing that the cells produced the protein encoded by the DNA. There is also tremendous interest in using cationic lipid-based nanospheres—liposomes—as DNA transfection agents.<sup>6,7</sup> Finally, the gold nanoparticles introduced earlier have been used extensively in the development of new types of gene sensor.<sup>8–10</sup>

Spherical nanoparticles are typically used in such applications, but this only reflects the fact that spheres are easier to make than other shapes. Microtubes and nanotubes (structures that resemble tiny drinking straws) (Fig. 6.1) are alternatives to spherical nanoparticles. Examples include organosilicon polymer nanotubes,<sup>15</sup> self-assembling lipid microtubes,<sup>16–20</sup> fullerene carbon nanotubes,<sup>21–24</sup> template-synthesized nanotubes,<sup>25–31</sup> and peptide nanotubes.<sup>32–35</sup> Nanotubes offer some interesting advantages relative to spherical nanoparticles for biotechnological applications. For example, nanotubes have large inner volumes (relative to the

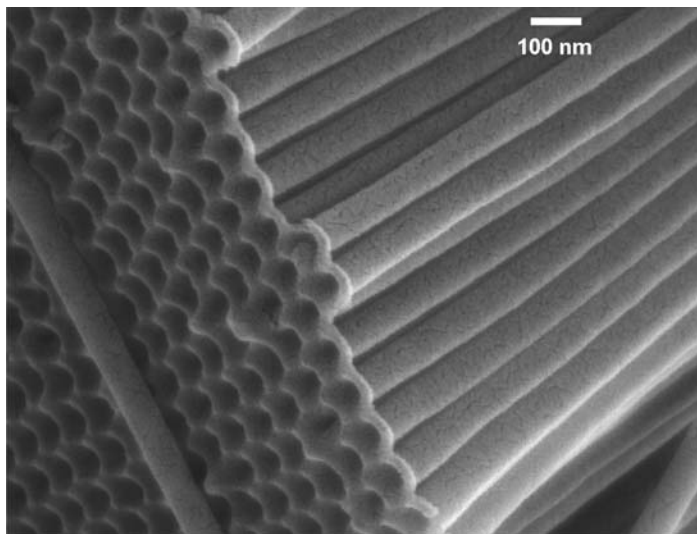


FIGURE 6.1. Scanning electron micrograph of an array of template-synthesized carbon nanotubes. These nanotubes are composed of disordered graphitic carbon.

dimensions of the tube), which can be filled with any desired chemical or biochemical species ranging in size from nucleic acids and proteins to small molecules. In addition, nanotubes have distinct inner and outer surfaces, which can be differentially chemically or biochemically functionalized.<sup>25</sup> This creates the possibility, for example, of loading the inside of a nanotube with a particular biochemical payload but imparting chemical features to the outer surface that render it biocompatible. Finally, nanotubes have open mouths, which make the inner surface accessible and incorporation of species within the tubes particularly easy.

Here, we report on the synthesis, characterization, and applications of nanotubes and nanotube membranes synthesized using template synthesis. We will briefly introduce the synthesis of nanotubes and nanotube membranes using the “template-synthesis” method. For more details on the template synthesis of nanoparticles, the readers are encouraged to refer to some excellent reviews available in the literature.<sup>3,30,31</sup> We discuss in detail the applications of nanotube and nanotube membranes in biosensing, bioseparation, and bioanalytical areas, including drug detoxification using functionalized nanotubes,<sup>36</sup> enzyme- and antibody-immobilized nanotubes for biocatalysis and bioextractions,<sup>25,26</sup> synthesis of nano test tubes,<sup>37</sup> DNA-functionalized nanotube membranes with single-nucleotide mismatch selectivity,<sup>27</sup> and the fabrication of an artificial ion channel using a single-conical nanotube membrane.<sup>38</sup>

## 6.2. Nomenclature

In the literature, the tubular structures of interest to this review are called by various names, including microtubules, microtubes, nanotubules, and nanotubes. This nomenclature can be simplified by noting that in this context, there is no difference between a tube and tubule; in this review, we use only the name tube. Nano versus micro is a more difficult issue because there is no universally accepted dimension scale above which a particle is micro and below which it is nano. In our research group, we have agreed that if a tube has at least one dimension that is 100 nm or less, it is called a nanotube.

## 6.3. Template Synthesis of Nanotubes

The template method is a general approach for preparing nanomaterials that entails synthesis or deposition of the desired material within the cylindrical and monodisperse pores of a nanopore membrane or other solid.<sup>3,30,31</sup> Cylindrical nanostructures with monodisperse diameters and lengths are obtained, and depending on the membrane and synthetic method used, these may be solid nanowires or hollow nanotubes. This method has been used to prepare nanowires and tubes composed of many different types of materials, including metals, polymers, semiconductors, and carbons.<sup>3,30,31</sup> In addition, the template method can be used to prepare composite nanostructures, both concentric tubular composites<sup>30,31</sup> and segmented composite nanowires.<sup>39</sup>

How one makes nanotubes within the pores of a template membrane can be illustrated by the carbon nanotubes shown in Fig. 6.1.<sup>40</sup> An alumina template (Fig. 6.2A) was heated to 670°C and ethylene gas was passed through the membrane. This causes the ethylene to decompose on the pore walls to yield graphitic carbon nanotubes within the pores. The alumina template membrane can then be dissolved away and the carbon nanotubes collected by filtration. These tubes have monodisperse outside diameters determined by the diameter of the pores in the template. The inside diameter is determined by the carbon deposition time. Other synthetic methods we have used include in-pore polymerization to make polymeric nanotubes, electroless deposition to make metal nanotubes, and sol-gel chemistry to make nanotubes composed of silica and other inorganic materials.<sup>3,30,31,40–44</sup> Templated silica nanotubes<sup>25,26</sup> are shown in Fig. 6.2B. These nanotubes are all the same length, which is determined by the thickness of the template membrane.

## 6.4. Silica Nanotubes

We have used these silica nanotubes as test vehicles to illustrate the power of the template method for preparing nanotubes for biomedical and biotechnological applications.<sup>25,26</sup> Silica nanotubes are ideal for such proof-of-concept experiments because they are easy to make, readily suspendable in aqueous solution and because silica surfaces can be derivatized with an enormous variety of different chemical functional groups using simple silane chemistry with commercially available reagents.<sup>25,26</sup>

### 6.4.1. Attaching Different Functional Groups to the Inside Versus Outside Surfaces<sup>25</sup>

As noted earlier, one of the most important attributes of a nanotube is that it has distinct inner and outer surfaces that can be differentially chemical and biochemically functionalized. The template method provides a particularly easy route to accomplish this differential functionalization. The details of nanotube modifications using differential silane chemistry on nanotubes are available elsewhere.<sup>25</sup> In the following paragraphs, we briefly describe the results of differential-functionalized nanotubes and their applications in highly selective chemical and biochemical extractions.<sup>25,36</sup>

To prove this concept, a set of nanotubes was prepared with the green fluorescent silane *N*-(triethoxysilylpropyl)dansylamide attached to their inner surfaces and the hydrophobic octadecyl silane (C<sub>18</sub>) attached to their outer surfaces. These nanotubes were added to a vial containing water and the immiscible organic solvent cyclohexane, which were mixed and allowed to separate. Because these nanotubes are hydrophobic on their outer surfaces, they partition into the (upper) cyclohexane phase (Fig. 6.3B). This may be contrasted to nanotubes that were labeled on their inner surfaces with the blue fluorescent silane triethoxysilylpropylquinineurethan,



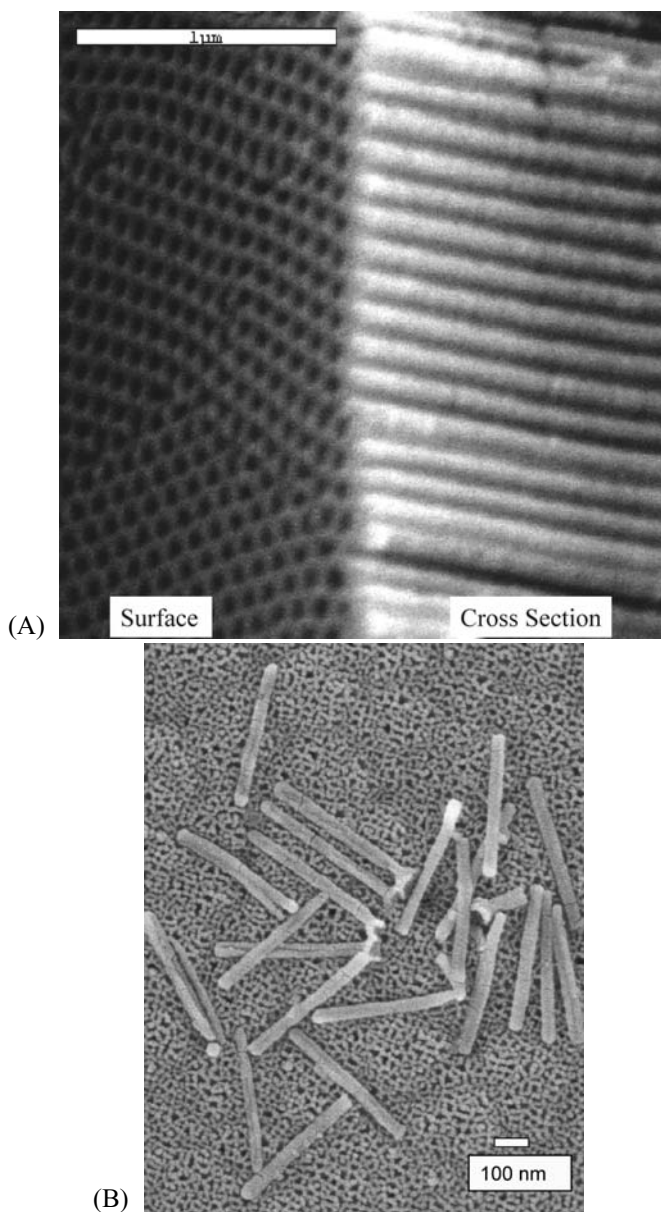


FIGURE 6.2. Scanning electron micrographs. (A) The surface and cross section of a typical nanopore alumina template membrane prepared in the authors' lab. Pores with monodisperse diameters that run like tunnels through the thickness of the membrane are obtained. (B) Silica nanotubes prepared by sol-gel template synthesis within the pores of a template like that shown in (A). After sol-gel synthesis of the nanotubes, the template was dissolved and the nanotubes were collected by filtration.

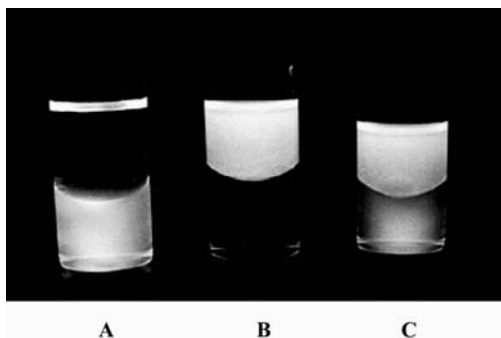


FIGURE 6.3. Photographs of vials containing nanotubes modified with different two different fluorophores in two different solvent media. (A) Cyclohexane (upper) and water (lower) under UV light excitation after the addition of 10 mg of nanotubes with dansylamide on inner and  $C_{18}$  on outer surfaces; (B) quinineurethan on inner and no silane on outer surfaces; (C) 10 mg of both A and B nanotubes (200-nm-diameter nanotubes were used).

but were not labeled with any silane on their outer surfaces. When the same experiment is done with these nanotubes, the quinineurethan fluorescence is seen only from the aqueous phase (Fig. 6.3A). When both sets of nanotubes are added to the solvent mixture in the same vial, the tubes with the  $C_{18}$  outer surface chemistry go to the cyclohexane and the tubes with the silica outer surface chemistry go to the aqueous phase (Fig. 6.3C).

#### 6.4.2. Nanotubes for Chemical and Bioextraction and Biocatalysis: Demonstration of Potential Drug Detoxification Using Nanotubes<sup>25,36</sup>

One application for such differentially functionalized nanotubes is as smart nanophase extractors to remove specific molecules from solution. Nanotubes with hydrophilic chemistry on their outer surfaces and hydrophobic chemistry on their inner surfaces are ideal for extracting lipophilic molecules from an aqueous solution. The hydrophobic molecule 7,8-benzoquinoline (BQ), which has an octanol/water partition coefficient of  $10^{3.8}$  was used as a model compound for such nanophase solvent extraction experiments. Figure 6.4A shows the UV-Vis (ultraviolet-visible) spectrum of control solution containing  $10^{-5}$  M aqueous BQ. Five milligrams of the silica-outer/ $C_{18}$ -inner nanotubes were suspended into 5 mL of  $1.0 \times 10^{-5}$  M aqueous BQ. The suspension was stirred for 5 min and then filtered to remove the nanotubes. UV spectroscopy showed that 82% of the BQ was removed from the solution (Fig. 6.4C). When a second 5-mg batch of these nanotubes was added to the filtrate, >90% of the original amount of BQ was removed from the solution (Fig. 6.4D). Control nanotubes that did not contain the hydrophobic  $C_{18}$  inner surface chemistry extracted less than 10% of the BQ (Fig. 6.4B). This proof of experiment clearly shows that nanotubes are possibly useful in applications involving drug detoxification and other chemical and biochemical extractions.

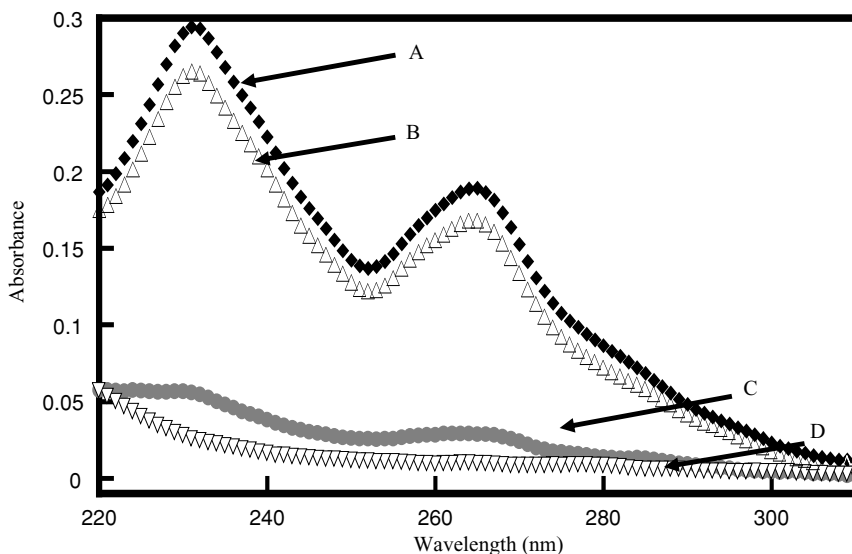


FIGURE 6.4. UV-Vis spectra showing the extraction of BQ from the aqueous solution by nanotubes with  $C_{18}$  silane on their inner surfaces. (A) UV-Vis spectrum of  $10^{-5} M$  aqueous BQ; (B) after extraction with  $SiO_2$  tubes (control experiments); (C) after first extraction with  $C_{18} SiO_2$  tubes; (D) after second extraction with  $C_{18} SiO_2$  tubes.

Nanotubes with the  $C_{18}$  inside will, in principle, extract any lipophilic molecule. This ability to sequester lipophilic molecules can be viewed as a generic type of extraction selectivity, which might be useful in some applications. However, nanotubes that have molecular-recognition capability and extract only one particular molecule from solution might also be useful. We have shown that antibody-functionalized nanotubes can provide the ultimate in extraction selectivity: the extraction of one enantiomer of a chiral drug molecule.

In collaboration with Hans Soderlund of VTT Biotechnology in Finland, we have been investigating an antibody that selectively binds one enantiomer of the drug 4-[3-(4-fluorophenyl)-2-hydroxy-1-[1,2,4]triazol-1-yl-propyl]-benzonitrile (FTB) (Fig. 6.5A), an inhibitor of aromatase enzyme activity.<sup>45</sup> This molecule has two chiral centers and thus four stereoisomers: RR, SS, SR, and RS. Soderlund supplied us with the  $F_{ab}$  fragment<sup>45</sup> of an antibody that selectively binds the RS relative to the SR enantiomer. The antibody was produced against the drug FTB (Fig. 6.5A). The antibody used selectively binds the RS enantiomer, and  $F_{ab}$  fragments of this antibody were immobilized to both the inner and outer surfaces of the silica nanotubes. This was accomplished by dissolving the template membrane, collecting the nanotubes, and then dispersing them into a solution of the aldehyde-terminated silane trimethoxysilylbutanal. The nanotubes were then dispersed into a solution of the  $F_{ab}$  fragments, which resulted in attachment of the  $F_{ab}$  to the nanotubes via Schiff base reaction between free amino groups on the protein and the surface-bound aldehyde.

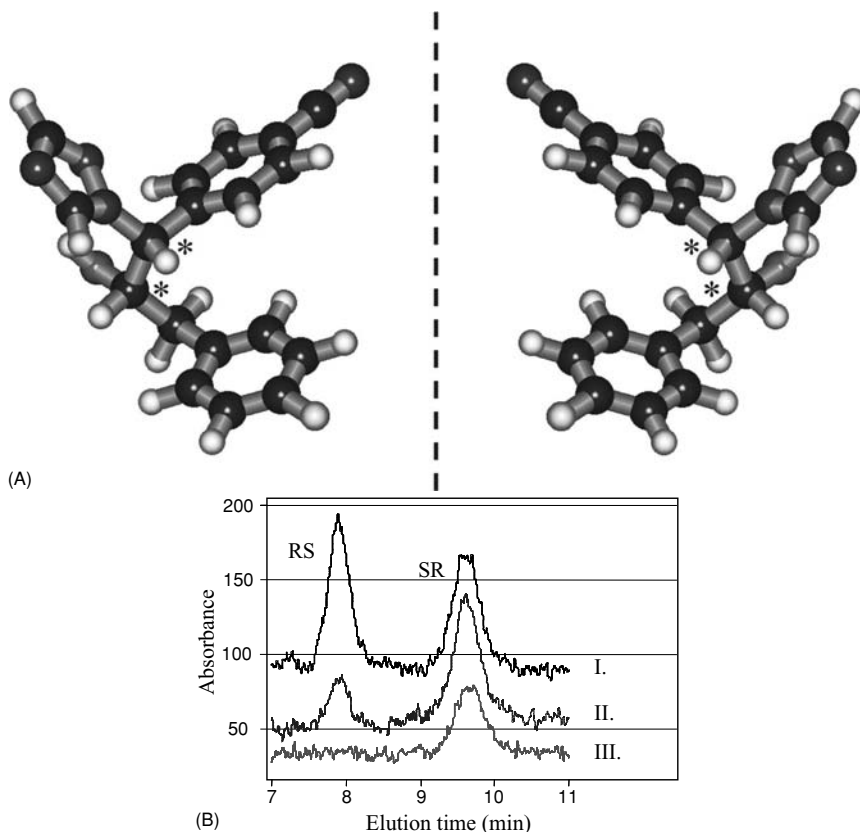


FIGURE 6.5. Enantioseparations. (A) Three-dimensional structures of the RS enantiomer (left) and the SR enantiomer (right) of the drug FTB. The black, white, blue, red, and yellow balls are carbon, hydrogen, nitrogen, oxygen, and fluorine, respectively, and the asterisks denote the chiral centers. The geometry optimization was done by *ab initio* calculation with minimal basis set in HyperChem 6.03. The drug is in clinical trials by Hormos Medical Corp., Turku, Finland. (B) Chiral HPLC chromatograms for racemic mixtures of FTB before (I) and after (II, III) extraction with 18 mg/mL of 200-nm  $F_{ab}$ -containing nanotubes. Solutions were 5% dimethylsulfoxide in sodium phosphate buffer, pH 8.5.

The  $F_{ab}$ -functionalized nanotubes were added to racemic mixtures of the SR and RS enantiomers of FTB. The tubes were then collected by filtration and the filtrate was assayed for the presence of the two enantiomers using a chiral high-performance liquid chromatography (HPLC) method (Fig. 6.5B). Chromatogram I is from a solution that was 20  $\mu M$  in both enantiomers, and chromatogram II was obtained for the same solution after exposure to the  $F_{ab}$ -functionalized nanotubes; 75% of the RS enantiomer and none of the SR enantiomer was removed by the nanotubes. When the concentration of the racemic

mixture was dropped to 10  $\mu M$ , all of the RS enantiomer was removed (chromatogram III). Nanotubes containing no  $F_{ab}$  did not extract measurable quantities of either enantiomer from the 20- $\mu M$  solution.

We have also developed a chemistry that allows us to attach the  $F_{ab}$  to only the inner surfaces of the nanotubes. While still within the pores of the template membrane, the inner surfaces were treated with aminopropyltrimethoxysilane. The template membrane was then dissolved and the amino sites on the inner surfaces were coupled to free amino groups on the  $F_{ab}$  fragment using the well-known glutaraldehyde coupling reaction.<sup>25</sup> When 18 mg of these interior-only  $F_{ab}$ -modified nanotubes were incubated with 1 mL of a 10- $\mu M$  racemic mixture of the drug, 80% of the RS (and none of the SR) enantiomer was extracted. This corresponds to 0.44 nmol RS enantiomer per milligram of tubes, whereas almost double that amount, 0.80 nmol  $mg^{-1}$ , was extracted by the nanotubes with  $F_{ab}$  on both their inner and outer surfaces.

We now briefly discuss the possible molecular interactions between the  $F_{ab}$  fragment and enantiomeric drug molecules. Our collaborators have produced  $F_{ab}$  fragments that bind only to the RS enantiomer of FTB drug molecules, but not to the SR enantiomer. The production of the  $F_{ab}$  fragment is reported elsewhere,<sup>45</sup> and it will not be discussed here. In general, numerous weak electrostatic, hydrogen-bond, and van der Waals interactions, reinforced by hydrophobic interactions, combine to give strong and specific binding between antibody and antigen.<sup>46</sup> Although we have not conducted detail studies to elucidate the interaction between  $F_{ab}$  and drug molecules at the molecular level, we believe that the  $F_{ab}$  fragment attached to silica nanotubes through Schiff base binds to the RS enantiomer through various molecular interactions such as hydrogen-bonding, van der Waals, and hydrophobic interactions.

Another example concerns the immobilization of a biocatalyst—the enzyme glucose oxidase (GOD)—to the silica nanotubes.<sup>25</sup> GOD was immobilized, on both the inside and outside surfaces, via the aldehyde silane route. These GOD nanotubes (60 nm indiameter) were dispersed into a solution that was 90 mM in glucose and also contained the components of the standard dianisidine-based assay for GOD activity. A GOD activity of  $0.5 \pm 0.2$  units  $mg^{-1}$  of nanotubes was obtained. These studies also showed that protein immobilized via the Schiff-base route is not leached from the nanotubes, in that all GOD activity ceased when the nanotubes were filtered from the solution.

## 6.5. Template Synthesis of Nano Test Tubes<sup>37</sup>

One application that we envision for nanotubes is as vehicles for the delivery of drugs, DNA, proteins, or other biomolecules.<sup>4,11</sup> Tubular structures are ideally suited for such applications because they are hollow, and with the template method, the inside and outside diameters of the tubes can be controlled at will.<sup>3,25,30,31</sup> However, a means for immobilizing the biomolecule within the interior of the nanotubes must be developed. In the past, we have covalently attached the biomolecule to the

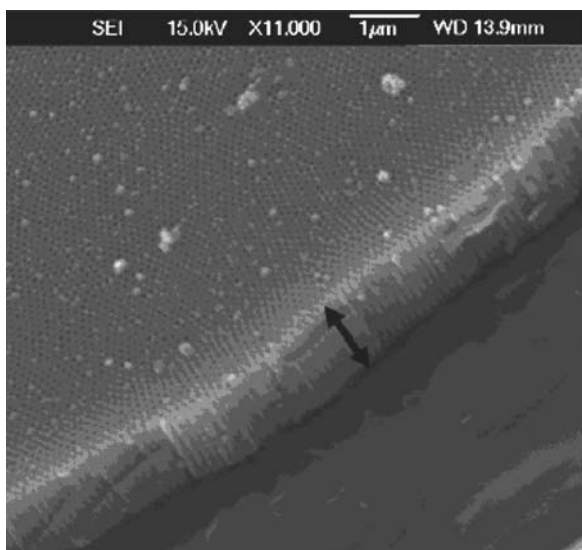


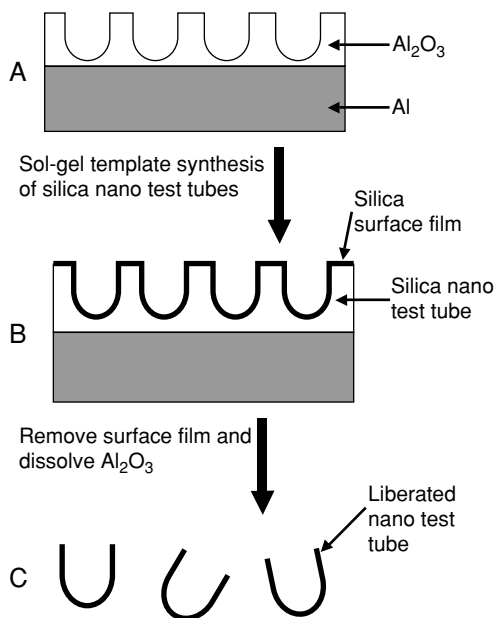
FIGURE 6.6. Field emission scanning electron micrograph (FESEM) of the nano test tube alumina membranes. FESEM of the surface and cross section of an alumina template membrane prepared using an anodization voltage of 50 V and an anodization prepared using an anodization time of 20 min. The cross section is denoted by the double arrow.

inside tube walls.<sup>3,25,26,27,30,31</sup> A much more convenient and general route would be to simply fill the nanotubes with the desired biomolecule and then cap the open ends of the tubes to keep the biomolecule “bottled up” inside. Immobilization by filling the nanotubes in this way would allow for a larger quantity of the desired biomolecule to be incorporated into the tube. Ideally, the chemistry holding the caps on would be labile, causing the caps to be released in the environment where the biomolecules are to be delivered.

Free-standing membranes were used as the templates in all of our previous investigations of template-synthesized nanotubes.<sup>3,25–27,30,31,47,48</sup> Because the pores in a free-standing membrane are open at both membrane faces, the nanotubes obtained were open on both ends, like pipes. It would be much more convenient to bottle a biomolecule within a nanotube if the tube was open on only one end, like test tubes. This would make it easier to fill the tube because the biomolecule could not simply flow out of the other open end of the tube during filling. Furthermore, this would make the capping process easier, as only one end of the tube would need to be capped.

Nanopore alumina membranes prepared by anodic oxidation of the surface of Al metal (Fig. 6.6)<sup>49,50</sup> are one of the workhorse materials for template synthesis of nanotubes.<sup>3,30,31</sup> It occurred to us that these templates might be ideally suited for preparing nano test tubes because, when still attached to the underlying Al surface, the pores in these membranes are closed at the Al/Al<sub>2</sub>O<sub>3</sub> interface (Fig. 6.7A).

FIGURE 6.7. Schematic of the template-synthesis method used to prepare the nano test tubes.



If the template-synthesis method used deposits the tube-forming material along these closed pore ends (as well as along the pore walls), then nano test tubes would be obtained (Fig. 6.7B). The resulting test tubes could then be liberated and collected by dissolution of the template membrane (Fig. 6.7C). The application of this approach to make silica nano test tubes is described below. We show that the outside diameter of these test tubes is determined by the pore diameter in the template membrane and that the length of the tube is determined by the thickness of the membrane.

The nanopore alumina template membranes were prepared in house by anodic oxidation of high-purity aluminum.<sup>50,51</sup> Two different anodization voltages were used to obtain membranes with pores that were either 70 nm or 170 nm in diameter (Table 6.1). The thickness of the template membrane was varied by varying the anodization time (Table 6.1). The silica nano test tubes were synthesized within the nanopores of these templates using sol-gel chemistry.<sup>3,25,26,30,31</sup>

Figure 6.8 shows a transmission electron microscope (TEM) image of a nano test tube prepared in a template that had 70-nm-diameter pores and was 0.6  $\mu\text{m}$  thick. Both the open end (top of image) and the closed end (bottom of image) of the

TABLE 6.1. Alumina template membranes used to prepare the nano test tubes.

Anodization voltage (V)	Anodization time (min)	Pore diameter (nm)	Membrane thickness ( $\mu\text{m}$ )
50	10	70	0.6
50	20	70	1.0
70	5	170	0.6

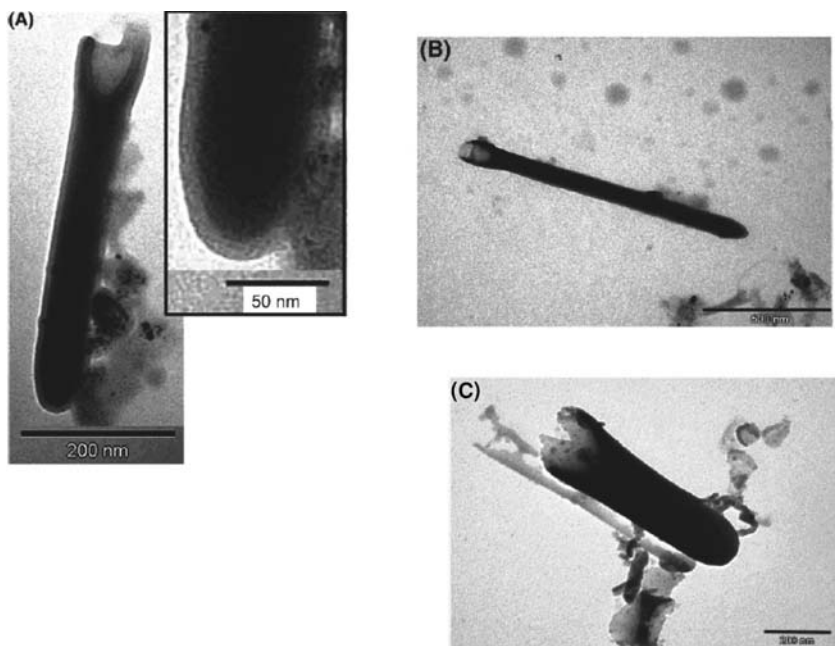


FIGURE 6.8. TEM of the prepared nano test tubes. (A) EM of a nano test tube prepared in the membrane described in row 1 of Table 6.1. The inset shows a close-up of the closed end of this nano test tube. (B) TEM of a nano test tube prepared in the membrane described in row 2 of Table 6.1. (C) TEM of a nano test tube prepared in the membrane described in row 3 of Table 6.1.

nano test tube are clearly seen. That the bottom is closed is shown more clearly by the inset in Fig. 6.8A, which is a higher magnification image of the bottom end of this nano test tube. In agreement with the membrane parameters (Table 6.1), these nano test tubes are  $70 \pm 14$  nm in diameter and  $\sim 600$  nm long. By controlling the anodization voltage, we can control the inner pore diameter of nano test tubes, whereas the thickness of the nanoporous membranes can be easily controlled by anodization time (Table 6.1).<sup>51</sup> We have control over the morphology of the alumina membrane containing nano test tubes by controlling the anodization conditions. For example, we have synthesized nano test tubes of inner pore diameter ranging from 30 nm to 120 nm by varying the anodization voltages between 30 V and 80 V, respectively.<sup>51</sup> Furthermore, nano test tube membranes with thicknesses ranging from 1  $\mu\text{m}$  to  $>60$   $\mu\text{m}$  are routinely prepared in our lab.<sup>51</sup> Figure 6.8B shows a TEM image of a nano test tube prepared in the membrane that was 1 mm thick and with a 70-nm pore diameter. Similarly, a TEM image of a nano test tube 0.6 mm thick and with a 170-nm pore diameter is shown in Fig. 6.8C.

The TEM images in Figure 6.8 do not allow us to unambiguously prove that these silica nano test tubes are hollow. As discussed earlier, one approach for proving this is to use these test tubes as templates to form nanotubes of a second material. If



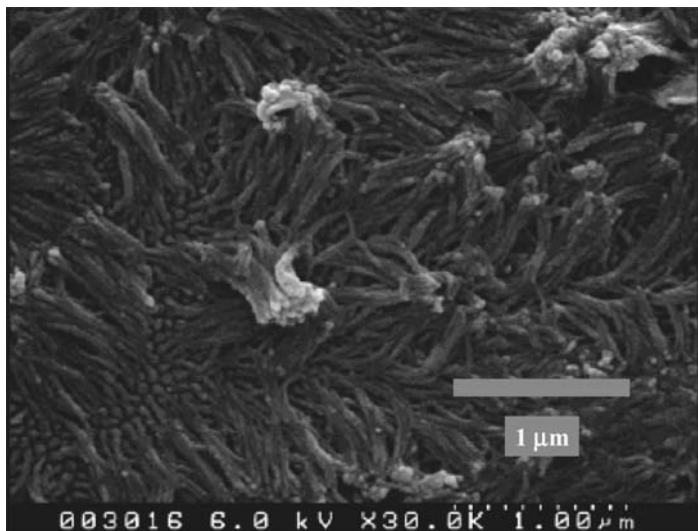


FIGURE 6.9. FESEM image of polystyrene nanotubes prepared within the silica nano test tubes.

the test tubes are hollow, then nanotubes of this second material will be obtained. If the test tubes are not hollow, they cannot act as templates, and nanotubes of the second material will not be obtained. To prove this, a 4% (w/w) polystyrene solution was prepared in 50:50 (v/v) toluene/dichloromethane. A drop of this solution was placed onto the surface of the silica nano test tube-containing membrane (i.e., Fig. 6.7B), and the solvent was allowed to evaporate. The template membrane was then dissolved in 1 *M* NaOH, yielding a film of polystyrene. The surface of this film was imaged with the field-emission scanning electron microscope (FESEM) to see if polystyrene nanotubes (formed in the hollow silica nano test tubes) protrude from this surface. If polystyrene nanotubes are observed, then the nano test tubes must be hollow.

Silica nano test tubes prepared in the membrane described in row 2 of Table 6.1 were used for these studies. Figure 6.9 shows an FESEM image of the polystyrene nanotubes synthesized within these silica nano test tubes. This image clearly shows that the silica nano test tubes are hollow. Furthermore, the outside diameter of these polystyrene nanotubes ( $\sim 35$  nm) provides an estimate for the inside diameter of the silica test tubes used. As is typically observed for template-synthesized nanostructures,<sup>41–43</sup> the polystyrene nanotubes aggregate into clumps after removal of the template membrane. This is undoubtedly due to the advent of capillary forces<sup>52</sup> between the nanotubes upon dissolution of the template membrane.

We have previously shown that the silica nanotubes can be chemically and biochemically functionalized using silane chemistry with commercially available reagents.<sup>2,3,30,31</sup> Furthermore, we have shown that different functional groups can be applied to the inner versus outer nanotube surfaces. We are currently using this approach to tag the outer surfaces of the silica nano test tubes with antibodies

that promote uptake by endothelial cells. The final challenge to be addressed, if these test tubes are to be used for biomolecule delivery, is to develop procedures for capping and uncapping the open mouth. We will report on this aspect of the research effort soon.

## 6.6. Nanotube Membranes for Bioseparations<sup>26,27</sup>

In all of the examples cited earlier, the template membrane was dissolved away and the liberated nanotubes were collected by filtration. The nanotubes may also be left embedded within the pores of the template to yield a free-standing nanotube-containing membrane. We have shown that the nanotubes can act as conduits for highly selective transport of molecules and ions between solutions present on either side of the membrane.<sup>26–29</sup> For example, membranes containing gold nanotubes with inside diameters of molecular dimensions (<1 nm) cleanly separate small molecules on the basis of molecular size.<sup>29</sup> Gold nanotubes with larger inside diameters (20–45 nm) can be used to separate proteins and, here again, rendering the nanotubes biocompatible is essential to prevent protein adsorption.<sup>47</sup> Generic chemical transport selectivity (lipophilic vs. hydrophilic) can also be imparted to these gold nanotube membranes.<sup>53</sup> We now present in detail “bio-tailored” nanotube membranes for the separation of enantiomeric drug molecules and nucleic acids.

### 6.6.1. *Antibody-Functionalized Nanotube Membranes for Selective Enantiomeric Separations*<sup>26</sup>

Recently, we have shown that membranes containing the silica nanotubes and the enantioselective FTB antibody  $F_{ab}$  fragment (Fig. 6.5A) discussed earlier can be used to make membranes for chiral separations.<sup>26</sup> In this case, the nanotube membrane separates a feed half-cell containing a racemic mixture of the RS and SR enantiomers of FTB and a permeate half-cell that initially contains only buffer solution. The time course of permeation of the two enantiomers across the membrane was determined by periodically assaying the permeate solution. Results for a membrane containing ~15-nm-diameter silica nanotubes are shown in Fig. 6.10 as plots of moles enantiomer transported versus permeation time. We see that the flux of the RS enantiomer, the one bound by the antibody, is five times higher than the flux of the SR enantiomer. Because, in principle, antibodies can be obtained that selectively bind to any desired molecule or enantiomer, this concept might provide a general approach for obtaining selectively permeable membranes for a host of enantioseparations and bioseparations.

Because it is the RS enantiomer that specifically binds to the immobilized anti-RS, these data suggest that this  $F_{ab}$  fragment facilitates the transport of the RS enantiomer. Further evidence that it is the  $F_{ab}$  fragment that is facilitating the transport of RS came from the feed concentration of drug versus flux curve, which showed a Langmuirian-type curve.

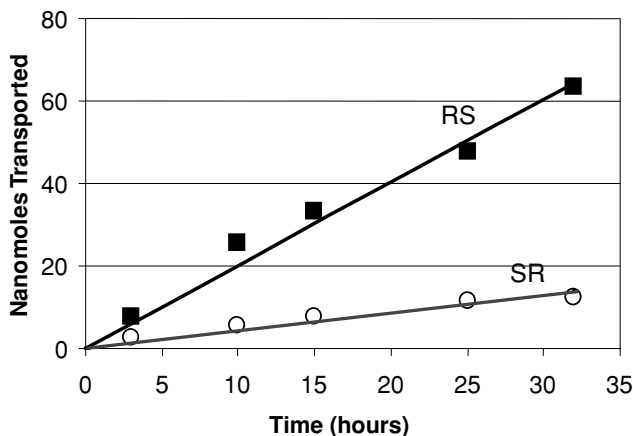


FIGURE 6.10. Enantioseparations using antibody-immobilized membranes. Plots of moles of each enantiomer transported versus time for a silica nanotube membrane containing the enantioselective antibody  $F_{ab}$  fragment. The inside diameter of the nanotubes was  $\sim 15$  nm.

We have not conducted detailed experiments to elucidate the effect of dimethyl sulfoxide (DMSO) concentration on the molecular interactions of binding of  $F_{ab}$  to the RS enantiomer drug molecule in phosphate-buffered saline (PBS).

The previous studies, however, have shown that the use of DMSO decreases the binding interactions between the drug molecule and  $F_{ab}$ -immobilized silica in chromatography experiments.<sup>45</sup> Qualitatively, our studies agrees with these results. We believe that there is an optimum binding affinity between drug and  $F_{ab}$  molecules that is expected to give the highest transport selectivity coefficient and that the addition of DMSO to the solution containing the antigen (FTB drug) decreases the binding constant between FTB and  $F_{ab}$  molecules immobilized on inner walls of silica nanotube membranes. In our studies, we have found that there is an optimum concentration of DMSO ( $\sim 15\%$ ) that maximizes the value of the selectivity coefficient.<sup>26</sup>

Another important factor that is important to consider is the orientation of the antibody immobilized on the surface. This factor is very important to maximize the antibody availability for antigen binding, because the binding between the antigen and antibody requires right orientation of the antibody for antigen binding. It is well known that histidine interacts strongly with copper and nickel ions. Therefore, one of the antibody immobilization methods to provide efficient, stable, and right orientation on surfaces for the antigen–antibody reaction utilizes histidine-tag antibodies onto copper- and nickel-containing surfaces.<sup>45</sup> The histidine modification of antibodies can be accomplished using conventional covalent bonding of the antibody with a reactive histidine or this can be also be accomplished using molecular biology (cloning) techniques. The modification of the antibody with histidine should be carried out only at the  $F_c$  fragment of the antibody but not on the  $F_{ab}$  fragment. In principle, the immobilization of histidine tagged at  $F_c$  of the antibody

should provide surfaces with favorable antibody orientation for antigen–antibody reaction, where antibody-binding fragments ( $F_{ab}$ ) are away from surfaces, and antigens can approach  $F_{ab}$  without significant steric hinderance.

### 6.6.2. Functionalized Nanotube Membranes with “Hairpin”-DNA Transporter with Single-Base Mismatch Selectivity<sup>27</sup>

There appears to be no previous examples of either biological or synthetic membranes where nucleic acid hybridization is used as the molecular recognition event to facilitate DNA/RNA transport through the membrane.<sup>54,55</sup> If such membranes could be developed, they might prove useful for DNA separations and sensors needed, for example, in genomic research.

We now describe synthetic membranes in which the molecular-recognition chemistry used to accomplish selective permeation is DNA hybridization. These membranes contain template-synthesized gold nanotubes with inside diameters of 12 nm, and a “transporter” DNA-hairpin molecule is attached to the inside walls of these nanotubes. These DNA-functionalized nanotube membranes selectively recognize and transport the DNA strand that is complementary to the transporter strand relative to DNA strands that are not complementary to the transporter. Under optimal conditions, single-base mismatch transport selectivity is obtained.

The gold nanotube membranes were prepared via the template synthesis<sup>76</sup> method by electrolessly depositing gold along the pore walls of a polycarbonate template membrane.<sup>3,29</sup> The template was a commercially available filter (Osmonics), 6  $\mu\text{m}$  thick, with cylindrical 30-nm-diameter pores and  $6 \times 10^8$  pores  $\text{cm}^{-2}$  of membrane surface area.

The hairpin-DNA transporter (Table 6.2) was 30 bases long (30-mer) and contained a thiol substituent at the 5' end that allowed it to be covalently attached to the inside walls of the Au nanotubes.<sup>27</sup> The first six bases at each end of this molecule

TABLE 6.2. DNA molecules used. For transporter DNAs, the 18 bases that bind to the permeating DNAs are in bold. For permeating DNAs, the mismatched bases are underlined. FAM is a fluorescein derivative (Applied Biosystems), and Cy5 is a cyanine dye (Amersham Biosciences).

---

#### Transporter DNAs

**Hairpin:** 5'HS-(CH<sub>2</sub>)<sub>6</sub>-CGCGAG **AAGTTACATGACCTGTAG** CTCGCG3'

**Linear:** 5'HS-(CH<sub>2</sub>)<sub>6</sub>-CGCGAG **AAGTTACATGACCTGTAG** ACGATC3'

#### Permeating DNAs

**Perfect complement (PC):** 3'TTCAATGTACTGGACATC5'

**Single base mismatch (3'end):** 3'CTCAATGTACTGGACATC5'

**Single base mismatch (middle):** 3'TTCAATGTA GTGGACATC5'

**7-mismatch:** 3'AAGTTACATGACCTAG5'

**FAM-labeled perfect complement:** 3'TTCAATGTACTGGACATC-(CH<sub>2</sub>)<sub>6</sub>-FAM 5'

**Cy5-labeled single-base mismatch:** 3'CTCAATGTACTGGACATC-(CH<sub>2</sub>)<sub>6</sub>-Cy5 5'

---

are complementary to each other and form the stem of the hairpin, and the middle 18 bases form the loop (Table 6.2). The permeating DNA molecules were 18-mers that are either perfectly complementary to the bases in the loop or contain one or more mismatches with the loop (Table 6.2). A second thiol-terminated DNA transporter was investigated (Table 6.2). This DNA transporter was also a 30-mer, and the 18 bases in the middle of the strand were identical to the 18 bases in the loop of the hairpin-DNA transporter. However, this second DNA transporter does not have the complementary stem-forming bases on either end and thus cannot form a hairpin. This linear-DNA transporter was used to test the hypothesis that the hairpin-DNA provides better transport selectivity because of its enhanced ability to discriminate the perfect complement permeating DNA from the permeating DNAs that contain mismatches.

The transport experiments were done in a U-tube permeation cell<sup>28</sup> where the Au nanotube membrane separates the feed half-cell containing one of the permeating DNA molecules (Table 6.2) dissolved in pH = 7.2 phosphate buffer (ionic strength  $\sim 0.2$  M) from the permeate half-cell that was initially only buffer. The rate of transport (flux) of the permeating DNA molecule from the feed half-cell through the Au nanotube membrane and into the permeate half-cell was determined by periodically measuring the UV absorbance of the permeate half-cell solution, at 260 nm, that arises from the permeating DNA molecule.

Transport plots (Figs. 6.11A and 6.12) show the number of nanomoles of the permeating DNA transported through the nanotube membrane versus permeation time. When the hairpin-DNA is not attached, a straight-line transport plot is obtained for the perfect-complement DNA (PC-DNA) (Fig. 6.11A), and the slope of this line provides the flux of the PC-DNA across the membrane (Table 6.3). The analogous transport plot for the membrane containing the hairpin-DNA transporter is not linear, but can be approximated by two straight-line segments: a lower-slope segment at short times followed by a higher-slope segment at times longer than a critical transition time. This transition is very reproducible; for example, for a feed concentration of  $9\text{ }\mu\text{M}$ , the critical transition time =  $110 \pm 15$  min (average of three membranes).

Figure 6.11A shows that the flux of the permeating PC-DNA in the membrane containing the hairpin-DNA transporter is at all times higher than the flux for an identical membrane without the transporter (Table 6.3). Hence, the hairpin-DNA is acting as a MR agent to facilitate the transport<sup>26,56–58</sup> of the PC-DNA. Additional evidence for this conclusion was obtained from studies of the effect of the concentration of the PC-DNA in the feed solution on the PC-DNA flux. If the hairpin-DNA is facilitating the transport of the PC-DNA, this plot should show a characteristic “Langmuirian” shape.<sup>26,56</sup> Figure 6.11B shows that this is, indeed, the case for transport data both before and after the critical transition time. The analogous plot for the identical membrane without the hairpin-DNA transporter is linear (Fig. 6.11B), showing that transport is not facilitated but rather described simply by Fick’s first law of diffusion. It is interesting to note that the transition to the higher-slope segment was not observed, during permeation experiments of total duration 300 min, for feed concentrations below  $9\text{ }\mu\text{M}$  (Fig. 6.11B).

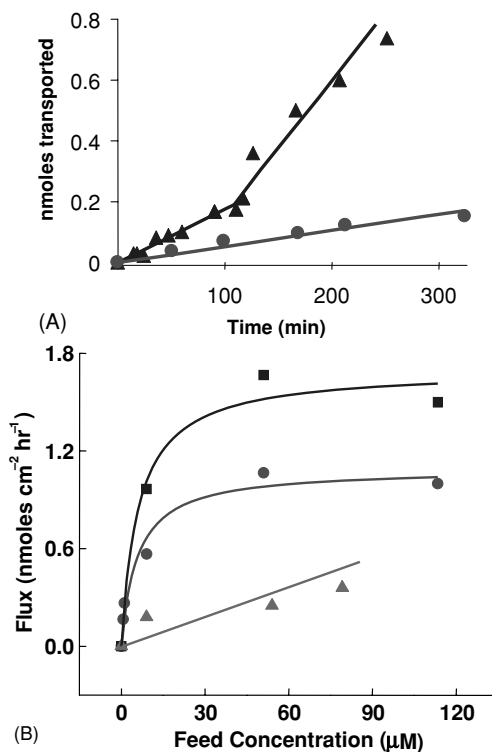


FIGURE 6.11. (A) Transport plots for PC-DNA through Au nanotube membranes with (▲) and without (●) the immobilized hairpin-DNA transporter. Concentration in feed solution =  $9\mu\text{M}$ . (B) Flux versus feed concentration for PC-DNA. The data in black and light gray were obtained for a Au nanotube membrane containing the hairpin-DNA transporter. At feed concentrations of  $9\mu\text{M}$  and above, the transport plot shows two linear regions. The data in black (■) were obtained from the high-slope region at longer times. The data in dark gray (●) were obtained from the low-slope region at shorter times. The data in light gray (▲) were obtained for an analogous nanotube membrane with no DNA transporter.

Analogous permeation data were obtained for the various mismatch-containing permeating DNA molecules (Table 6.2). The transport plots for these mismatch DNAs show only one straight-line segment (Fig. 6.12), and their fluxes are always lower than the flux for the PC-DNA obtained from the high-slope region of the PC-DNA transport plot (Table 6.3). Note in particular that the membrane containing the hairpin-DNA transporter shows a higher flux for PC-DNA than for the two permeating DNAs that contain only a single-base mismatch.

To illustrate this point more clearly, we define a selectivity coefficient  $\alpha_{\text{HP,PC/1MM}}$ , which is the flux for the PC-DNA divided by the flux for a single-base mismatch DNA in the membrane with the hairpin-DNA transporter. The data in Table 6.1 provide  $\alpha_{\text{HP,PC/1MM}} = 3$ . The analogous selectivity coefficient for the PC-DNA versus the DNA with seven mismatches is  $\alpha_{\text{HP,PC/7MM}} = 7$ . These selectivity coefficients show that nanotube membranes containing the hairpin-DNA

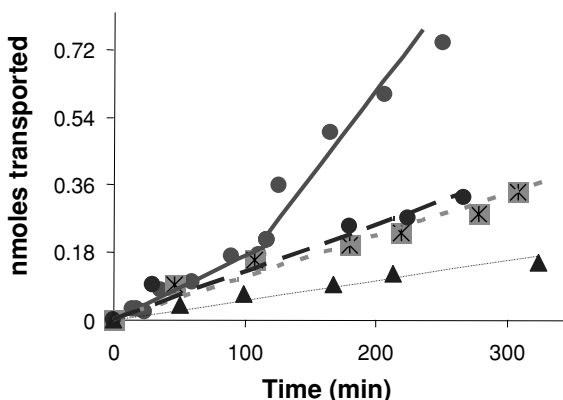


FIGURE 6.12. Transport plots for a Au nanotube membrane containing the hairpin-DNA transporter. The permeating DNA was as follows: (gray ●) PC DNA, (black ●) single mismatch (end), (▲) seven mismatches, (■) single mismatch (middle). The concentration in the feed solution was 9  $\mu\text{M}$ .

transporter selectively transport PC-DNA and that single-base mismatch transport selectivity can be obtained.

The importance of the hairpin structure to membrane selectivity is illustrated by analogous transport data for membranes containing the linear-DNA transporter (Table 6.2). With this transporter, all of the transport plots show only a single straight-line segment, and the fluxes for the single-mismatch DNAs are identical to the flux for the PC-DNA (Table 6.3); that is, the single-base mismatch selectivity coefficient for this linear (LN) DNA transporter is  $\alpha_{\text{LN,PC/1MM}} = 1$ . The linear-DNA transporter does, however, show some transport selectivity for the PC-DNA versus the seven-mismatch DNA,  $\alpha_{\text{LN,PC/7MM}} = 5$ .

We have also investigated the mechanism of transport in these membranes. In such MR-based facilitated-transport membranes, the permeating species is transported by sequential binding and unbinding events with the MR agent.<sup>26,56,57</sup> For these DNA-based membranes, the binding/unbinding events are sequential

TABLE 6.3. Fluxes for feed concentration of 9  $\mu\text{M}$ .

Transporter DNA	Permeating DNA	Flux (nmoles $\text{cm}^{-2} \text{h}^{-1}$ )
Hairpin	Perfect complement	0.57, 1.14 <sup>a</sup>
Linear	Perfect complement	0.94
None	Perfect complement	0.20
Hairpin	Single mismatch (middle)	0.37
Hairpin	Single mismatch (end)	0.44
Linear	Single mismatch (middle)	0.94
Hairpin	7 mismatch	0.17
Linear	7 mismatch	0.20

<sup>a</sup> Two fluxes are obtained because the transport plot shows two slopes (Fig. 11A).

hybridization/dehybridization reactions between the permeating DNA molecule and the DNA transporter attached to the nanotubes. To show that hybridization occurred in the membrane with the hairpin-DNA transporter, the membrane was exposed to PC-DNA, and then to a restriction enzyme (*SfcI*, New England Biolabs).<sup>27</sup> If hybridization between the PC-DNA and the hairpin transporter occurred, this enzyme will cut the resulting double-stranded DNA such that the last five bases of the binding loop and all of the stem-forming region at the 3' end of the hairpin are removed. This reaction will substantially damage the binding site, and based on our prior work,<sup>26</sup> we would predict that if this membrane is subsequently used in a permeation experiment, a lower PC-DNA flux should be obtained.<sup>27</sup>

After exposure to the restriction enzyme, the membrane was extensively rinsed to remove the enzyme and DNA fragments and then used for a transport experiment with PC-DNA as the permeating species. Unlike the data in Fig. 6.11A, the transport plot for this damaged-transporter membrane showed only one straight-line segment<sup>27</sup> corresponding to a flux of  $0.2 \text{ nmol cm}^{-2} \text{ h}^{-1}$ . This value is well below what we observe from membranes with an undamaged DNA-hairpin transporter (Table 6.3). The damaged DNA transporter was then removed from the nanotubes and fresh DNA-hairpin transporter applied. A subsequent transport experiment with PC-DNA showed a transport plot identical to that obtained before exposure to the restriction enzyme.<sup>27</sup> These data suggest that hybridization is, indeed, involved in the transport mechanism for the DNA-hairpin-containing membranes.

To show that dehybridization occurs on a reasonable timescale in these membranes, we exposed a hairpin-DNA membrane to a fluorescently labeled version of the PC-DNA (Table 6.2). The membrane was then rinsed with buffer solution and immersed into a solution of either pure buffer or buffer containing unlabeled PC-DNA. If the dehybridization reaction is facile, the fluorescently labeled PC-DNA should be released into the solution. We found that dehybridization does occur, but it is strongly accelerated when unlabeled PC-DNA is present in the solution (Fig. 6.13). Hence, dehybridization is much faster when it occurs by a cooperative process whereby one PC-DNA molecule displaces another from an extant duplex.<sup>59</sup>

We have also investigated transport selectivity for a feed solution containing fluorescently labeled versions (Table 6.2) of both the PC-DNA and the single-mismatch DNA. The fluorescent labels allow for quantification of both of these permeating DNAs simultaneously in the permeate solution. In analogy to the single-molecule permeation experiment, the flux of the PC-DNA was five times higher than the flux of the single-mismatch DNA.<sup>27</sup> To assess the practical utility of these membranes, transport studies with more realistic samples (such as cell lysates) will be needed.

Finally, we have not observed a spontaneous transition from a low-flux to a high-flux state (Fig. 6.11A) with our previous MR-based membranes.<sup>26,56</sup> Whether this transition is observed depends on the feed concentration suggests that the transition is a transport-related phenomenon. It is possible that this



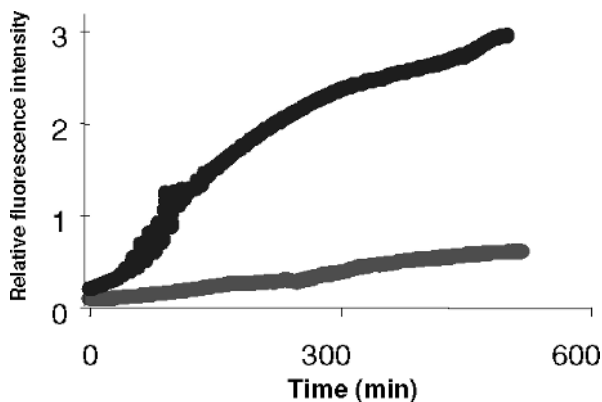


FIGURE 6.13. Release of fluorescently labeled PC-DNA from a membrane containing the hairpin-DNA transporter. The fluorescently labeled PC-DNA was released into a buffer solution containing no unlabeled PC-DNA (lower curve) or into a buffer containing  $9\ \mu\text{M}$  unlabeled PC-DNA (upper curve).

transition relates to the concept of cooperative (high flux) versus noncooperative (low flux) dehybridization (Fig. 6.13), but further studies, both experimental and modeling, will be required before a definitive mechanism for this transition can be proposed.

## 6.7. Conical Nanotubes: Mimicking Artificial Ion Channel<sup>38</sup>

There is considerable interest in developing chemical devices that mimic the function of biological ion channels.<sup>60–63</sup> We recently described such a device, which consisted of a single conically shaped gold nanotube embedded within a polymeric membrane.<sup>64</sup> This device mimicked one of the key functions of voltage-gated ion channels: the ability to strongly rectify the ionic current flowing through it. The data obtained were interpreted using a simple electrostatic model (*vide infra*).<sup>64</sup>

Although the details are still being debated,<sup>60–63,77,78</sup> it is clear that ion-current rectification in biological ion channels is more complicated and involves physical movement of an ionically charged portion of the channel in response to a change in the transmembrane potential.<sup>65</sup> We report here artificial ion channels that rectify the ion current flowing through them via this “electromechanical”<sup>66</sup> mechanism. These artificial channels are also based on conical gold nanotubes, but with the critical electromechanical response provided by single-stranded DNA molecules attached to the nanotube walls.

Single conically shaped nanopores were etched into  $0.07\text{-cm}^2$  samples of a  $12\text{-}\mu\text{m}$ -thick polycarbonate membrane.<sup>67</sup> For most of the studies reported here, the large-diameter opening of the pore was  $5\ \mu\text{m}$  (Fig. 6.14A) and the

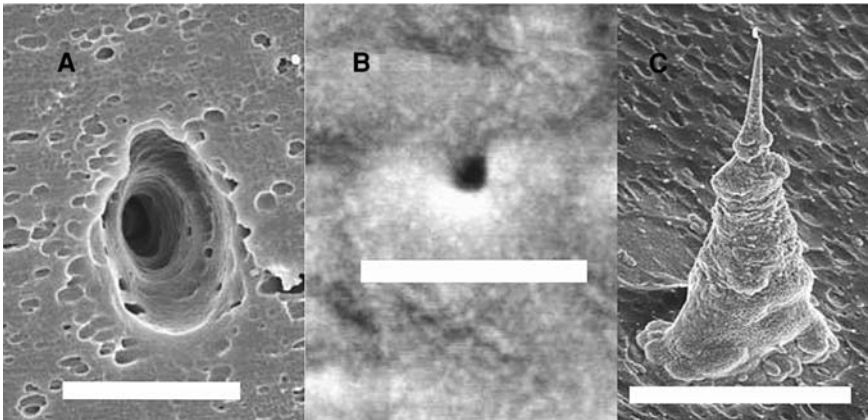


FIGURE 6.14. Electron micrographs showing (A) large-diameter (scale bar = 5.0  $\mu\text{m}$ ) and (B) small-diameter (scale bar = 333 nm) opening of a conical nanopore, and (C) a liberated conical Au nanotube (scale bar = 5.0  $\mu\text{m}$ ).

small-diameter opening was 60 nm (Fig. 6.14B). However, membranes having conical pores with large-diameter openings of 5  $\mu\text{m}$  and small-diameter openings of 150 and 100 nm were also used. An electroless plating method<sup>28</sup> was used to deposit a correspondingly conical gold nanotube within the pore. This entails coating the pore walls and membrane faces with a thin ( $\sim 10$  nm) layer of gold. Because this layer is so thin, the large-diameter opening of the conical gold nanotube remained 5  $\mu\text{m}$ . An approximate measure of the diameter of the small opening (hereafter called the “mouth”) of the conical nanotube was obtained using a simple electrochemical method<sup>67</sup> (Table 6.4).

In the final step, single-stranded DNA molecules were covalently immobilized to the gold surfaces. The following thiol-terminated DNAs were used in these studies:

TABLE 6.4. Nanotube mouth diameter ( $d$ ), DNA attached, current ratio ( $r_{\text{max}}$ ), radius of gyration ( $r_g$ ) and extended chain length ( $l$ ).

$d$ (nm)	DNA attached	$r_{\text{max}}$	$r_g$ (nm)	$l$ (nm) <sup>a</sup>
41	12-mer	1.5	1.4	5.7
46	15-mer	2.2	1.6	6.9
42	30-mer	3.9	2.9	12.9
38	45-mer	7.1	4.0	18.9
98	30-mer	1.1	2.9	12.9
59	30-mer	2.1	2.9	12.9
39	30-mer	3.9	2.9	12.9
27	30-mer	11.5	2.9	12.9
13	30-mer	4.7	2.9	12.9
39	hairpin	1.4	n/a	6.9

<sup>a</sup> Includes the  $(\text{CH}_2)_6$  spacer.

5'HS-(CH<sub>2</sub>)<sub>6</sub>-CGAGTCCATTCA3' (12-mer), 5'HS-(CH<sub>2</sub>)<sub>6</sub>-GACCGAGTCCATTCA3' (15-mer), 5'HS-(CH<sub>2</sub>)<sub>6</sub>-CGCGAGAAGTTACAT-GACCTGTAGACGATC3' (30-mer), 5'HS-(CH<sub>2</sub>)<sub>6</sub>-A<sub>45</sub>3' (45-mer), and 5'HS-(CH<sub>2</sub>)<sub>6</sub>-CGCGAGAAGTTACATGACCTG-TAGCTCGCG3' (30-mer hairpin).<sup>27,38</sup> In all of the experiments described here, the conically shaped gold nanotube was left embedded within the polycarbonate membrane. However, in order to prove that this nanotube is, indeed, conical, the membrane can be dissolved away and the liberated nanotube imaged via electron microscopy (Fig. 6.14C).

Current–voltage ( $I$ – $V$ ) curves for these artificial ion channels were obtained by mounting the membrane sample between the two halves of a U-tube conductivity cell.<sup>28</sup> Each half-cell was filled with ~5 mL of a 10 mM pH = 7 phosphate buffer that was also 100 mM in KCl. A Ag/AgCl reference electrode was inserted into each half-cell solution, and a Keithley Instruments 6487 picoammeter/voltage-source was used to apply the desired transmembrane potential and measure the resulting ionic current flowing through the gold nanotube.

In our prior work, the mouth diameter of the Au nanotubes was 10 nm and the rectification observed resulted from electrostatic interactions between cations traversing the nanotube and fixed surface charge (due, e.g., to adsorbed Cl<sup>−</sup>) at the nanotube mouth.<sup>64</sup> This mechanism only applies when the mouth diameter is comparable to the thickness of the electrical double layer associated with the fixed surface charge, and this is not the case for the larger-mouth-diameter nanotubes used here (Table 6.4). This is proven by the fact that without attached DNA molecules, these nanotubes do not rectify, even though there is adsorbed Cl<sup>−</sup> on the nanotube walls (Fig. 6.15A). In contrast, the DNA-containing nanotubes rectify the ion current; that is, they show an on-state at negative transmembrane potentials (anode facing the mouth of nanotube; Fig. 6.15B) and an off-state at positive potentials (Fig. 6.15C).

The extent of rectification may be quantified via the ratio  $r_{\max}$ , which is the absolute value of the current at −1 V (on-state) divided by the current at +1 V (off-state) (Table 6.4). The first four entries in Table 6.4 correspond to the nanotubes in Fig. 6.15A. As is evident from the figure,  $r_{\max}$  increases with the DNA chain length. The extent of rectification can also be controlled by holding the chain length constant and varying the diameter of the nanotube mouth (Table 6.4). With one exception (*vide infra*),  $r_{\max}$  increases with decreasing mouth diameter.

We propose that rectification in these nanotubes entails electrophoretic insertion of the DNA chains into (off-state; Fig. 6.15C) and out of (on-state; Fig. 6.15B) the nanotube mouth. The off-state is obtained because when inserted into the mouth, the chains partially occlude the pathway for ion transport, yielding a higher ionic resistance for the nanotube. There is ample evidence in the literature to support this hypothesis. First, because DNA chains are anionic, they can be driven electrophoretically through nanopores, and during translocation, occlusion of the nanopore by the DNA causes a transient increase in the pore's ionic resistance.<sup>68</sup> Furthermore, in complete analogy to our model, if one end of a DNA chain is immobilized in an electrophoresis experiment, the chain extends linearly in the

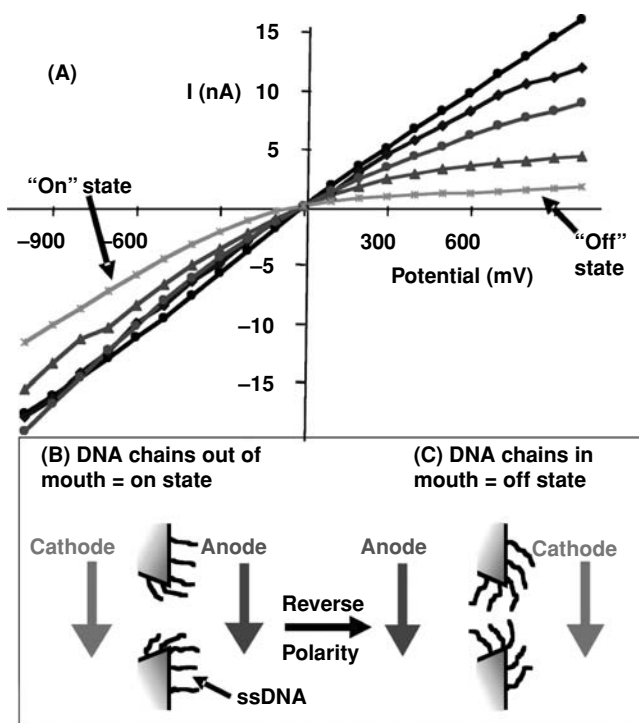


FIGURE 6.15. (A)  $I$ - $V$  curves for nanotubes with mouth diameters of 40 nm containing (from top to bottom) no DNA ( $\bullet$ ) and attached 12-mer ( $\blacklozenge$ ), 15-mer ( $\blacksquare$ ), 30-mer ( $\blacktriangle$ ), and 45-mer ( $\blacksquare$ ) DNAs. (B, C) Schematics showing electrode polarity and DNA chain positions for an on-state (B) and an off-state (C).

direction of the anode.<sup>69</sup> In addition, simulations of the electric field strength in conical nanopores, identical to those used here, show that the field in the electrolyte solution in the mouth of the nanopore is  $1 \times 10^6 \text{ V m}^{-1}$ , when the total voltage drop across the membrane is only 1 V.<sup>70</sup> This focusing of the electric field strength at the nanotube mouth means that there is ample field to extend the DNA chains toward the anode.

Further support for this model can be garnered from our experimental  $I$ - $V$  data. First, the magnitudes of the on-state currents in Fig. 6.15A decrease with increasing DNA chain length. This is because even in the on-state, the DNA chains partially occlude the mouth of the nanotube and increase the nanotube resistance. Second, although the general trend is that  $r_{\text{max}}$  increases with decreasing mouth diameter, one exception was noted: The nanotube with the  $\sim 13$ -nm mouth and the 30-base DNA rectifies less than the nanotube with the  $\sim 27$ -nm mouth and this same 30-base DNA (Table 6.4). These data suggest that the DNA chain can be too long, relative to the mouth diameter, to allow for efficient rectification. Table 6.4 lists two relevant lengths of the DNA chains: the length if the chain were completely

extended<sup>68</sup> and the radius of gyration<sup>71,72</sup> for the globular form. According to our model, in order to rectify, the chain must have the freedom to extend linearly toward the anode. The nanotube with the 13-nm mouth is the only case where the length of the extended DNA chain is equivalent to the mouth diameter. We suggest that this makes it sterically difficult for the chains to reorient and insert themselves into the mouth, and this is why poor rectification is observed.

Third, according to our model, the DNA chain must have the flexibility to extend in the direction of the anode. This issue was explored by comparing the extent of rectification for a nanotube containing the conventional 30-base DNA and an identical tube containing a hairpin 30-base DNA. The hairpin DNA<sup>73</sup> folds back on itself because the bases at one end of the chain are complementary to the bases at the other end, making the chain much less flexible. The nanotube containing this 30-base hairpin DNA is a very poor rectifier, much worse than the same nanotube with the conventional 30-base DNA (Table 6.4).

## 6.8. Conclusions

We believe that nanotubes offer some important advantages for biotechnological and biomedical applications of nanoparticles. Because of its tremendous versatility in terms of materials that can be used, sizes that can be obtained, and chemistry and biochemistry that can be applied, the template method might prove to be a particularly advantageous approach for preparing nanotubes for such applications. However, this field of nanotube biotechnology is in its infancy and there is much work to be done before products based on this technology are brought to the market place. For example, in our applications to date, we have incorporated the payload into the nanotubes by either covalent bonding or other chemical interactions. However, in some applications, it might be useful to simply fill the nanotube with a payload and then apply caps to the nanotube ends to keep the payload encapsulated. Furthermore, it might be useful to have these caps fall off, thus spilling the payload, when a particular chemical or biochemical signal is detected. We are currently exploring routes for preparing such capped nanotubes. The issues of cost of production and mass production of nanotubes must also be addressed.

Finally, the synthetic nanotubes discussed here can be thought of as mimics of naturally occurring nanotubes—protein channels<sup>38,74</sup>; indeed, the cyclic peptide nanotubes have been used as artificial ion channels.<sup>35</sup> Ion channels open and close in response to chemical and electrical stimuli. We are developing synthetic nanotubes with similar voltage<sup>28,38,64,75</sup> and chemical<sup>48</sup> gating characteristics. These nanotubes can be used in smart membranes whose transport properties change in response to an electrical stimulus<sup>28,75</sup> and in sensing devices where a chemical stimulus turns on a current that can be measured in an external circuit.<sup>48</sup> One of the major drawbacks of the membrane-based separation method is low transport flux of separating molecules. The use of conical nanotubes containing membranes can

possibly eliminate the low-transport-flux problem because conical pore-containing membranes are expected to have a much larger porosity. We have fabricated conical nanotube membranes; these membranes have the potential to greatly increase the transport flux without significantly losing the selectivity coefficients,<sup>38,64</sup> and we will report on the separation of biomolecules and biopolymers using conical-nanotube membranes.

*Acknowledgments.* This work was supported by the National Science Foundation (NIRT for Biomedical Nanotube Technology), DARPA, the Office of Naval Research, and the UF Engineering Research Center for Particle Science and Technology. We gratefully acknowledge our collaborator Professor Hans Soderlund for contributions to the antibody research projects.

## References

1. K. J. Klabunde, *Nanoscale Materials in Chemistry*, Wiley-Interscience, New York, 2001.
2. C. R. Martin and D. T. Mitchell, Nanomaterials in analytical chemistry, *Anal. Chem.* **70**, 322A–327A (1998).
3. C.R. Martin, Nanomaterials: A membrane-based synthetic approach, *Science* **266**, 1961–1966 (1994).
4. T. M. S. Chang and S. Prakash, Procedures for microencapsulation of enzymes, cells and genetically engineered microorganisms, *Mol. Biotech.* **17**, 249–260 (2001).
5. C. Kneuer, M. Sameti, U. Bakowsky, T. Schiestel, H. Schirra, H. Schmidt, and C. M. Lehr, A nonviral DNA delivery system based on surface modified silica-nanoparticles can efficiently transfect cells in vitro, *Bioconj. Chem.* **11**, 926–932 (2000).
6. J. Radler, I. Koltover, T. Salditt, and C. R. Safinya, Structure of DNA–cationic liposome complexes: DNA intercalation in multilamellar membranes in distinct interhelical packing regimes, *Science* **275**, 810–814 (1997).
7. I. Koltover, T. Salditt, J. O. Radler, and C. R. Safinya, An inverted hexagonal phase of cationic liposome–DNA complexes related to DNA release and delivery, *Science* **281**, 78–81 (1998).
8. Y. W. C. Cao, R. C. Jin, and C. A. Mirkin, Nanoparticles with Raman spectroscopic fingerprints for DNA and RNA detection, *Science* **297**, 1536–1540 (2002).
9. L. M. Demers, D. S. Ginger, S. J. Park, Z. Li, S. W. Chung, and C.A. Mirkin, Direct patterning of modified oligonucleotides on metals and insulators by dip-pen nanolithography, *Science* **296**, 1836–1838 (2002).
10. S. J. Park, T. A. Taton, and C. A. Mirkin, Array-based electrical detection with nanoparticles probes, *Science* **295**, 1503–1506 (2002).
11. K. E. Ulrich, S. M. Cannizzaro, R. S. Langer, and K. M. Shakeshelf, Polymeric systems for controlled drug release, *Chem. Rev.* **99**, 3181–3198 (1999).
12. K. E. Lee, B. K. Kim, and S. H. Yuk, Biodegradable polymeric nanospheres formed by temperature-induced phase transition in a mixture of poly(lactide-co-glycolide) and poly(ethylene oxide) –poly(propylene oxide) –poly(ethylene oxide) triblock copolymer, *Biomacromolecules* **3**, 1115–1119 (2002).

13. N. Murthy, Y. X. Thng, S. Schuck, M. C. Xu, and J. M. J. Frechet, A novel strategy for encapsulation and release of proteins: Hydrogels and microgels with acid-labile acetal cross-linkers, *J. Am. Chem. Soc.* **124**, 12,398–12,399 (2002).
14. M. Lewin, N. Carlesso, C. Tung, X.-W. Tang, D. Cory, D. T. Scadden, and R. Weissleder, Tat peptide-derivatized magnetic nanoparticles allow in vivo tracking and recovery of progenitor cells, *Nat. Biotech.* **18**, 410–414 (2000).
15. J. P. Linsky, T. R. Paul, and M. E. Kenny, Planar organosilicon polymers, *J. Polym. Sci. A-29*, 143–160 (1971).
16. P. Yager and P. Schoen, Formation of tubules by a polymerizable surfactant, *Mol. Crystal. Liq. Cryst.* **106**, 371–381 (1984).
17. J. M. Schnur, Lipid tubules: A paradigm for molecularly engineered structures, *Science* **262**, 1669–1676 (1993).
18. J. V. Selinger, M. S. Spector, and J. M. Schnur, Theory of self-assembled tubules and helical ribbons, *J. Phys. Chem. B* **105**, 7157–7169 (2001).
19. R. Price and M. Patchan, Controlled release from cylindrical macrostructures, *J. Microencapsul.* **8**, 301–306 (1991).
20. A. S. Goldstein, J. K. Amory, S. M. Martin, C. Vernon, A. Matsumoto, and P. Yager, Testosterone delivery using glutamide-based complex high axial ratio microstructures, *Bioorgan. Med. Chem.* **9**, 2819–2825 (2001).
21. S. Iijima, Helical microtubules of graphitic carbon, *Nature* **354**, 56–58 (1991).
22. P. M. Ajayan, Structure and morphology of carbon nanotubes, in: *Carbon Nanotubes: Preparation and Properties*, edited by T. Ebbesen, CRC Press, Cleveland, OH (1997).
23. P. M. Ajayan, Nanotubes from carbon, *Chem. Rev.* **99**, 1787–1800 (1999).
24. H. Dai, J. Kong, C. Zhou, N. Franklin, T. Tombler, A. Cassell, S. Fan, and M. Chapline, Controlled chemical routes to nanotube architectures, physics, and devices, *J. Phys. Chem. B* **103**, 11,246–11,255 (1999).
25. D. T. Mitchell, S. B. Lee, L. Trofin, N. Li, T. K. Nevanen, H. Söderlund, and C. R. Martin, Smart nanotubes for bioseparations and biocatalysis, *J. Am. Chem. Soc.* **124**, 11,864–11,865 (2002).
26. S. B. Lee, D. T. Mitchell, L. Trofin, N. Li, T. K. Nevanen, H. Söderlund, and C. R. Martin, Antibody-based bio/nanotube membranes for enantiomeric drug separations, *Science* **296**, 2198–2200 (2002).
27. P. Kohli, C. C. Harrell, Z. Cao, R. Gasparac, W. Tan, and C. R. Martin, DNA functionalized nanotube membranes with single-base mismatch selectivity, *Science* **305**, 984–986 (2004).
28. M. Nishizawa, V. P. Menon, and C. R. Martin, Metal nanotubule membranes with electrochemically switchable ion-transport selectivity, *Science* **268**, 700–702 (1995).
29. K. B. Jirage, J. C. Hulteen, and C. R. Martin, Nanotubule-based molecular-filtration membranes, *Science* **278**, 655–658 (1997).
30. C. R. Martin and P. Kohli, The emerging field of nanotube biotechnology, *Nat. Rev. Drug Discov.* **2**, 29–37 (2003).
31. J. C. Hulteen and C. R. Martin, A general template-based method for the preparation of nanomaterials, *J. Mater. Chem.* **7**, 1075–1087 (1997).
32. M. R. Ghadiri, J. R. Granja, R. A. Milligan, D. McRee, and N. Khazanovich, Self-assembled organic nanotubes based on a cyclic peptide, *Nature* **366**, 324–327 (1993).
33. N. Khazanovich, J. R. Granja, D. E. McRee, R. A. Milligan, and M. R. Ghadiri, Nanoscale tubular ensembles with specified internal diameters. Design of a

- self-assembled nanotube with a 13 angstrom pore, *J. Am. Chem. Soc.* **116**, 6011–6012 (1994).
34. S. Fernandez-Lopez, H. S. Kim, E. C. Choi, M. Delgado, J. R. Granja, A. Khasanov, K. Kraehenbuehl, G. Long, D. A. Weinberger, K. M. Wilcoxon, and M. R. Ghadiri, Antibacterial agents based on the cyclic D,L-alpha-peptide architecture, *Nature* **412**, 452–455 (2001).
  35. M. R. Ghadiri, J. R. Granja, and L. K. Buehler, Artificial transmembrane ion channels from self-assembling peptide nanotubes, *Nature* **369**, 301–304 (1994).
  36. S.B. Lee, D. T. Mitchell, L. Trofin, T. K. Nevanen, H. Soderlund, and C. R. Martin, Template-synthesized bionanotubes for separations and biocatalysis, in: *Carrier-Based Drug Delivery*, ACS Symposium No 879, American Chemical Society, Washington, DC, 2004, pp 98–117.
  37. R. Gasparac, P. Kohli, M. O. Mota, L. Trofin, and C. R. Martin, Template synthesis of nano test tubes, *Nano Lett.*, **4**, 513–516 (2004).
  38. C. C. Harrell, P. Kohli, Z. Siwy, and C. R. Martin, DNA-nanotube artificial ion channels, *J. Am. Chem. Soc.* **126**, 15,646–15,647 (2004).
  39. S. R. Nicewarner-Pena, F. R. Griffith, B. D. Reiss, L. He, D. J. Pena, I. D. Walton, R. Cromer, C. D. Keating, and M. J. Natan, Submicrometer metallic barcodes, *Science* **294**, 137–141 (2001).
  40. S. A. Miller, V. Y. Young, and C. R. Martin, Electroosmotic flow in template-prepared carbon nanotube membranes, *J. Am. Chem. Soc.* **123**, 12,335–12,342 (2001).
  41. V. M. Cepak and C. R. Martin, Preparation of polymeric micro- and nanostructures using a template-based deposition method, *Chem. Mater.* **11**, 1363–1367 (1999).
  42. N. Li and C. R. Martin, A high-rate, high-capacity, nanostructured Sn-based anode prepared using sol-gel template synthesis, *J. Electrochem. Soc.* **148**, A164–A170 (2001).
  43. V. P. Menon and C. R. Martin, Fabrication and evaluation of nanoelectrode ensembles, *Anal. Chem.* **67**, 1920–1928 (1995).
  44. V. M. Cepak, J. C. Hulteen, G. Che, K. B. Jirage, B. B. Lakshmi, E. R. Fisher, and C. R. Martin, Fabrication and characterization of concentric tubular composite micro- and nanostructures using the template synthesis method, *J. Mater. Res.* **13**, 3070–3080 (1998).
  45. T. K. Nevanen, L. Soderholm, K. Kukkonen, T. Suortti, T. Teerinen, M. Linder, H. Soderlund, and T. T. Teeri, Efficient enantioselective separation of drug enantiomers by immobilized antibody fragments, *J. Chromatogr. A* **925**, 89–97 (2001).
  46. L. Stryer, *Biochemistry*, W.H. Freeman, New York, 1995.
  47. S. Yu, S. B. Lee, M. Kang, and C. R. Martin, Size-based protein separations in poly(ethylene glycol)-derivatized gold nanotubule membranes, *Nano Lett.* **1**, 495–498 (2001).
  48. E. D. Steinle, D. T. Mitchell, M. Wirtz, S. B. Lee, V. Y. Young, and C. R. Martin, Ion channel mimetic micropore and nanotube membrane sensors, *Anal. Chem.* **74**, 2416–2422 (2002).
  49. G. L. Hornyak, C. J. Patrissi, and C. R. Martin, Fabrication, characterization, and optical properties of gold nanoparticle/porous alumina composites: The nonscattering Maxwell–Garnett limit, *J. Phys. Chem. B* **101**, 1548–1555 (1997).
  50. H. K. Masuda, F. Hasegawa, and S. Ono, Self-ordering of cell arrangement of anodic porous alumina formed in sulfuric acid solution, *J. Electrochem. Soc.* **144**, L127 (1997).
  51. L. Trofin, M. O. Miguel, and C. R. Martin, unpublished results.
  52. J. Israelachvili, *Intermolecular and Surface Forces*, 2nd ed., Academic Press, New York, 1991, pp 330–334.



53. K. B. Jirage, J. C. Hulteen, and C. R. Martin, Effect of thiol chemisorption on the transport properties of gold nanotubule membranes, *Anal. Chem.* **71**, 4913–4918 (1999).
54. S. Howorka, S. Cheley, and H. Bayley, Sequence-specific detection of individual DNA strands using engineered nanopores, *Nat. Biotech.* **19**, 636–639 (2001).
55. H. Fried and U. Kutay, Nucleocytoplasmic transport: taking an inventory, *Cell. Mol. Life Sci.* **60**, 1659–1688 (2003).
56. B. B. Lakshmi and C. R. Martin, Enantiomeric separation using apoenzymes in immobilized in a porous polymeric membrane, *Nature* **388**, 758–760 (1997).
57. M. Mulder, *Basic Principles of Membrane Technology*, Kluwer Academic, Boston, 1996, pp. 342–351.
58. Y. Osada, T. Nakagawa, Y. Osada, and T. Nakagawa (Eds.), *Membrane Science and Technology*, Marcel Dekker, New York, 1992, pp. 377–391.
59. M. C. Hall, H. Wang, D. A. Erie, and T. A. Kunkel, High affinity cooperative DNA binding by the yeast Mlh-1-Pms1 heterodimer, *J. Mol. Biol.* **312**, 637–647 (2001).
60. Z. Siwy and A. Fulinski, Fabrication of a synthetic nanopore ion pump. *Phys. Rev. Lett.* **89**, 198,103 (2002).
61. Z. Siwy and A. Fulinski, Synthetic ion channels, *Bioorg. Med. Chem.* **12**, 1265–1569 (2004).
62. T. M. Fyles, D. Loock, and X. Zhou, A voltage-gated ion channel based on a bis-macrocyclic bolaamphiphile, *J. Am. Chem. Soc.* **120**, 2997–3003 (1998).
63. Z. Wu, J. Tang, Z. Cheng, X. Yang, and E. Wang, Ion channel behavior of supported bilayer lipid membranes on a glassy carbon electrode, *Anal. Chem.* **72**, 6030–6033 (2000).
64. Z. Siwy, E. Heins, C. C. Harrell, P. Kohli, and C. R. Martin, Conical-nanotube ion-current rectifiers: The role of surface charge, *J. Am. Chem. Soc.* **126**, 10,850–10,851 (2004).
65. Y. Jiang, A. Lee, J. Chen, V. Ruta, M. Cadene, B. T. Chait, and R. MacKinnon, X-ray structure of a voltage-dependent  $K^+$  channel, *Nature*, **423**, 33–41 (2003).
66. Y. Jiang, A. Lee, J. Chen, M. Cadene, B. T. Chait, and R. MacKinnon, Crystal structure and mechanism of a calcium-gated potassium channel, *Nature* **417**, 515–522 (2002).
67. P. Apel, Y. E. Korchev, Z. Siwy, R. Spohr, and M. Yoshida, Diode-like single-ion track membrane prepared by electro-stopping, *Nucl. Instrum. Methods B* **184**, 337–346 (2001).
68. A. Meller, N. Lucas, and D. Branton, Voltage-driven DNA translocations through a nanopore, *Phys. Rev. Lett.* **86**, 3435–3438 (2001).
69. B. Maier, U. Seifert, and J. O. Raedler, Elastic response of DNA to external electric fields in two dimensions, *Europhys. Lett.* **60**, 622–628 (2002).
70. S. Lee, Y. Zhang, H. S. White, C. C. Harrell, and C. R. Martin, Electrophoretic capture and detection of nanoparticles at the opening of a membrane pore using scanning electrochemical microscopy, *Anal. Chem.* **76**, 6108–6115 (2004).
71. S. S. Sorlie and R. Pecora, A dynamic light scattering study of four DNA restriction fragments, *Macromolecules* **23**, 487–497 (1990).
72. M. C. Olmstead, C. F. Anderson, and M. T. Record, Importance of oligoelectrolyte end effects for the thermodynamics of conformational transitions of nucleic acid oligomers: A grand canonical Monte Carlo analysis, *Biopolymers* **31**, 1593–1604 (1991).
73. G. Bonnet, S. Tyagi, A. Libchaber, and F. R. Kramer, Thermodynamic basis of the enhanced specificity of structured DNA probes, *Proc. Natl. Acad. Sci. USA* **96**, 6171–6176 (1999).

74. B. Hille, *Ion Channels of Excitable Membranes*, Sinauer, Sunderland, MA, 2001.
75. M. Kang and C. R. Martin, Investigations of potential-dependent fluxes of ionic permeates in gold nanotubule membranes prepared via the template method, *Langmuir* **17**, 2753–2759 (2001).
76. C. R. Martin, M. Nishizawa, K. Jirage, and M. Kang, Investigations of the transport properties of gold nanotubule membranes, *J. Phys. Chem. B* **105**, 1925–1934 (2001).
77. R. O. Blaustein and C. Miller, Ion channels: Shake, rattle or roll? *Nature* **427**, 499–501 (2004).
78. K. J. Swartz, Opening the gate in potassium channels, *Nature Struct. Mol. Biol.* **11**, 499–500 (2004).

# 7

## Synthesis and Characterization of Core-Shell Structured Metals

TETSU YONEZAWA

*Department of Chemistry, Graduate School of Science, The University of Tokyo,  
Hongo, Bunkyo-ku, Tokyo, 113-0033 Japan*

### 7.1. Introduction

Many intensive studies on metal nanoparticles have been carried out from the point of view of a wide variety of scientific interests and practical properties.<sup>1–8</sup> These nanoparticles, with their diameters of 1–10 nm, consist of several tens or thousands of metal atoms in every one. Recently, these nanoparticles can be considered as a new class of materials in a presently hot nanotechnology. Examples include some specific properties: spectroscopic and magnetic properties of semiconductor nanoparticles, synthesis and catalysis of polymer-stabilized or ligand-coated metal nanoparticles, as well as nonlinear optical properties of metal nanoparticle-doped metal oxides. Thanks to the size limit of nanoparticles, they are expected to show novel properties that can be explained by the “nanoscopic effect,” “nanosize effect,” or “quantum size effect.” This effect has been theoretically established by Kubo.<sup>9</sup> This size limit introduces quite a high population of surface atoms rather than inner atoms. Therefore, the properties of nanoparticles are controlled by the corresponding surface atoms. Various preparative methods have been proposed to obtain perfectly uniform-size metal nanoparticles. Perfectly monodispersed metal nanoparticles are, of course, ideal, but special properties of nanoparticles are to be expected even if this ideal condition is not exactly realized. The synthesis of monodispersed nanoparticles is of key importance because their properties varied strongly based on their dimensions. Economical mass production of monodispersed metal nanoparticles is now becoming one of the very important issues for realizing these products as real materials.<sup>10</sup>

On the other hand, in order to improve the unique properties of metal nanoparticles, the addition of another element is one solution.<sup>11–13</sup> Especially, in the field of catalysis, the addition of second and third elements to the principal monometallic nanoparticles, which are known as good catalysts, is one of the commonest ways to improve catalytic properties.<sup>14,15</sup> Bimetalization can improve such catalytic properties of monometallic catalysts, sometimes drastically. Such effects have often been explained in terms of an ensemble and/or a ligand effect. Recently, optical properties of bimetallic nanoparticles composed of silver and/or gold are the subject of much interest. A comparison of the calculated and observed surface

plasmon spectra was employed in order to understand the detailed structures of such bimetallic nanoparticles.

In this chapter, “core-shell” structured bimetallic nanoparticles prepared by chemical processes will be treated. After surveying the preparation methods, the characterization of these novel nanosized materials will be discussed.

## 7.2. Preparation of Core-Shell Bimetallic Nanoparticles

### 7.2.1. Preparation Procedures

In this section, we concentrate on the liquid-phase preparation of core-shell bimetallic nanoparticles. The preparation procedures of core-shell-type bimetallic nanoparticles can be largely divided into three categories:

- Successive reduction of the corresponding two metal ions
- Simultaneous reduction of the corresponding two metal ions
- Other systems

Successive reduction of the corresponding metal ions is the easiest of the preparative procedures to understand to produce core-shell structured bimetallic nanoparticles. Depositing sequentially the metal element onto the metal nanoparticles of the previously reduced element is a very clear solution to obtain core-shell bimetallic nanoparticles. On the other hand, simultaneous reduction of the corresponding metal ions to prepare core-shell nanoparticles is often controlled by the redox potentials of the two metal ions. In this section, the preparative methods of core-shell metal nanoparticles are collected.

### 7.2.2. Successive Reduction of the Corresponding Two Metal Ions

As mentioned earlier, successive reduction of the corresponding two metal ions can be considered the smartest way to produce core-shell bimetallic nanoparticles. The deposition (or plating) thin layer of a metal element onto the preobtained metal nanoparticles of the other element can be considered a very effective method. For example, Turkevich et al. reported gold-shell palladium-core ( $\text{Au}_{\text{shell}}\text{Pd}_{\text{core}}$ ) type nanoparticles by successive reduction of the Au and Pd ions in solution.<sup>13</sup> Silver-shell gold-core ( $\text{Ag}_{\text{shell}}\text{Au}_{\text{core}}$ ) bimetallic nanoparticles and the inversion type gold-shell silver-core ( $\text{Au}_{\text{shell}}\text{Ag}_{\text{core}}$ ) bimetallic nanoparticles were successfully prepared by  $\gamma$ (gamma)-ray reduction procedures, which were reported by Henglein's group.<sup>16</sup> They also reported the formation of other bimetallic nanoparticles with various styles of core-shell. Remita's group in France also reported the formation of platinum-shell gold-core and gold-shell platinum-core bimetallic nanoparticles by  $\gamma$ (gamma)-ray irradiation.<sup>17</sup>

Schmid's group reported a series of work on the preparation of ligand-stabilized gold–palladium bimetallic nanoparticles. Their particles are large enough, with the

particle size several tens of nanometers (20–60 nm). The structure was controlled by successive reduction procedures. Solutions of a metal salt and hydroxylamine as the reducing reagent are simultaneously dropped into the dispersion of preformed metal nanoparticles. A very thick layer of gold (4–18 nm) could be deposited onto a palladium core of size  $\sim 20$  nm.<sup>18–20</sup>

Gold and silver bimetallic nanoparticles with core-shell structures are most widely studied from the viewpoint of their specific plasmon absorption in the visible-light region. Silver monometallic nanoparticles usually show a strong plasmon absorption peak at  $\sim 420$  nm, and gold monometallic nanoparticles also have a plasmon absorption peak in a visible-light region at  $\sim 520$  nm. This absorption color has already been used as paints, stained glasses, and so on. The gold/silver bimetallic nanoparticles show peak maxima different than the gold and silver monometallic nanoparticles, and the structure of the absorption peak can be varied by the detailed structures of the bimetallic nanoparticles.

Several preparative methods of Au-shell Ag-core ( $\text{Au}_{\text{shell}}\text{Ag}_{\text{core}}$ ) bimetallic nanoparticles were proposed by Vlčková et al.<sup>21</sup> Gold layers can be deposited onto a silver core by the reduction of  $\text{AuCl}_4^-$  by hydroxylamine ( $\text{NH}_2\text{OH}$ ) under various conditions. The thickness of the gold layer and the structure of the obtained “core-shell” particles can be controlled by the preparative conditions.

Light irradiation also reduces some noble metals. This system is very clean because no residues of the reducing reagents remained in the obtained nanoparticle dispersions. Toshima and Takahashi proposed this technique to prepare various noble metal nanoparticles.<sup>22</sup> Pal et al. proposed deposition of the silver shell onto the preformed gold core by the reduction of  $\text{Ag}^+$  by ultraviolet (UV) irradiation.<sup>23</sup> Preformed gold seeds were also prepared by the UV reduction process. In this case, the silver shell is not a smooth layer, but deposition of small silver clusters was observed in the transmission electron microscope (TEM) images.

Sequential impregnations of metal ions onto supports can also be used to generate core-shell nanoparticles on various supporting materials, such as metal oxides.<sup>24</sup>

Sometimes successive reduction of the corresponding metal ions fails to give core-shell structures. Toshima et al. tried to obtain Au-shell Pd-core ( $\text{Au}_{\text{shell}}\text{Pd}_{\text{core}}$ ) bimetallic nanoparticles by a successive alcohol reduction procedure.<sup>25</sup> In this case, the stabilizing reagent is poly(*N*-vinyl-2-pyrrolidone) (PVP) and the core palladium nanoparticles are very small (several nanometers). Pd monometallic nanoparticles were, of course, successfully obtained. However, after reduction of  $\text{AuCl}_4^-$  in the presence of PVP-stabilized Pd nanoparticles, no “core-shell”-type nanoparticles were obtained, but a “cluster-in-cluster” structure was observed. On the contrary, during reduction of Pd ions in the presence of PVP-stabilized Au nanoparticles, Pd-shell Au-core ( $\text{Pd}_{\text{shell}}\text{Au}_{\text{core}}$ ) type nanoparticles were observed. Such structures were revealed by the detailed extended X-ray absorption fine structure (EXAFS) analyses of the bimetallic nanoparticle dispersions by using synchrotron irradiation at Photon Factory in High Energy Accelerator Research Organization (KEK-PF, Tsukuba, Japan). This structural disorder was caused by the redox potentials of the two metal components. In this case, PVP-stabilized

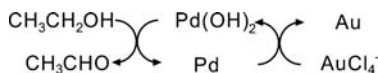


FIGURE 7.1. Gearcycle of the formation of gold and palladium nanoparticles. According to the difference of the redox potentials of the two corresponding metals, ethanol reduces palladium ions and palladium atoms reduce gold ions. By this metal–metal electron transfer, palladium atoms are oxidized to palladium ions and then reduced again by ethanol.

palladium nanoparticles were not large enough or crystallized and some palladium atoms were oxidized to palladium ions when gold ions were reduced, as shown in the gear cycle in Fig. 7.1; this step can be called as “transmetalation.” Palladium ions thus generated were reduced again by ethanol to deposit on the gold–palladium bimetallic nanoparticles. Therefore, no typical “core-shell” structure was obtained by this step, but “cluster-in-cluster” structures were observed (Fig. 7.2a).

On the contrary, for example, in Henglein’s system or Schmid’s system,  $\text{Au}_{\text{shell}}\text{Pd}_{\text{core}}$  nanoparticles were successfully obtained by successive reduction procedures. In their cases, the preformed palladium nanoparticles are relatively large, stable, and well crystallized. In such cases, palladium atoms on the particle surface are not readily oxidized. Then, the secondary added gold ions are reduced and deposited on the preformed palladium nanoparticles (Fig. 7.2b).

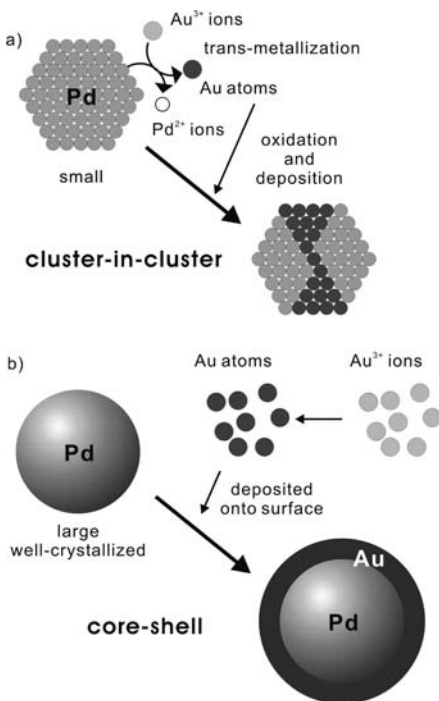
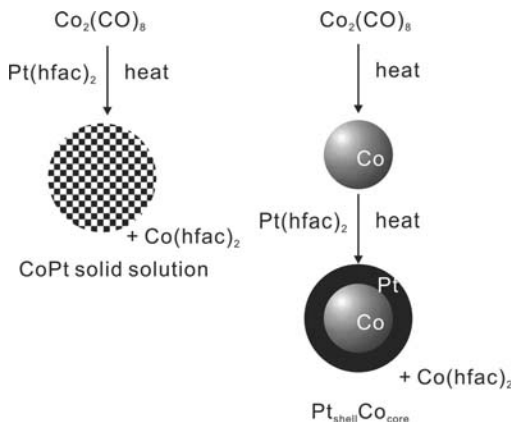


FIGURE 7.2. Illustration of the formation mechanisms of gold–palladium bimetallic nanoparticles. (a) Smaller preformed palladium nanoparticles. Palladium atoms on the surface of the palladium monometallic nanoparticles are oxidized during the reduction of Au ions. These formed palladium ions are again reduced and deposited onto the nanoparticles. This process results in “cluster-in-cluster” gold–palladium bimetallic nanoparticles. (b) Larger preformed palladium nanoparticles. The preformed palladium nanoparticles are stable and oxidation of palladium atoms of the preformed nanoparticles does not take place. This process results in “gold-shell palladium-core” ( $\text{Au}_{\text{shell}}\text{Pd}_{\text{core}}$ ) bimetallic nanoparticles.

FIGURE 7.3. Schematic illustration of synthetic routes of “solid-solution”-type and “core-shell”-type well-defined cobalt–platinum bimetallic nanoparticles. (Adapted from Ref. 26.)



From the same precursors, “solid solution-” type and “core-shell”-type well-defined bimetallic nanoparticles can be separately produced.<sup>26</sup> Pt-shell Co-core ( $\text{Pt}_{\text{shell}}\text{Co}_{\text{core}}$ ) bimetallic nanoparticles were obtained by reduction of  $\text{Pt}(\text{hfac})_2$  (hfac = hexafluoroacetylacetonate) in the presence of Co nanoparticles prepared from  $\text{Co}_2(\text{CO})_8$  by thermolysis. The stabilizer used here was dodecaneisocyanide. In this case, as a byproduct,  $\text{Co}(\text{hfac})_2$  generated by transmetalation was observed. The “solid-solution”-type Pt-Co nanoparticles were generated by heating  $\text{Co}_2(\text{CO})_8$  and  $\text{Pt}(\text{hfac})_2$  simultaneously (Fig. 7.3). These bimetallic nanoparticles are useful as magnetic material.

In order to form well-defined “core-shell”-type nanoparticles, the redox potentials of the corresponding metals should be considered carefully. It is possible to selectively grow certain metals on top of metallic nanoparticles, only where the redox potential is favorable between them, especially, in the case of smaller-core nanoparticles.

Gold shells are very useful for using thiol compounds as stabilizer molecules. Gold-shell copper-core ( $\text{Au}_{\text{shell}}\text{Cu}_{\text{core}}$ ) nanoparticles were synthesized by reducing  $\text{AuCl}_4^-$  by  $\text{NaBH}_4$  in the presence of citrate-stabilized copper preformed nanoparticles.<sup>27</sup> Copper preformed nanoparticles were obtained also by  $\text{NaBH}_4$  reduction of  $\text{CuSO}_4$ . The surface of this  $\text{Au}_{\text{shell}}\text{Cu}_{\text{core}}$  bimetallic nanoparticles were modified by alkanethiol-deviated oligonucleotides for biosensing.

Successive reduction of  $\text{FeSO}_4$  and  $\text{AuCl}_4^-$  in reverse micelle (cetyltrimethylammonium bromide) solution in octane generates magnetic bimetallic nanoparticles.<sup>28</sup> In ultraviolet–visible (UV-vis) spectra of these bimetallic nanoparticle dispersions, a specific plasmon absorption peak at  $\sim 520$  nm, which can be ascribed to the gold surface layer (i.e.,  $\text{Au}_{\text{shell}}\text{Fe}(\text{or } \text{FeO}_x)_{\text{core}}$ ), was observed. These magnetic particles can also be applied as biosensors, which can be separated by magnets. Cobalt-shell gold-core ( $\text{Co}_{\text{shell}}\text{Au}_{\text{core}}$ ) bimetallic nanoparticles could be obtained by polyol reduction of Co ions in the presence of gold preformed nanoparticles.<sup>29</sup>

### 7.2.3. Simultaneous Reduction of the Corresponding Two Metal Ions

Simultaneous reduction of the corresponding two metal precursor ions in one flask is the simplest procedure to produce bimetallic nanoparticles. In many reports, however, this system is used to generate “solid-solution”- or “alloy”-type nanoparticles but not to obtain well-defined “core-shell”-type nanoparticles. In even some cases, two separated monometallic nanoparticles are generated in one flask by this simple method.

Poly(*N*-vinyl-2-pyrrolidone) (PVP)-stabilized palladium–platinum bimetallic nanoparticles were prepared by refluxing an ethanol/water solution of  $\text{PdCl}_2$  and  $\text{H}_2\text{PtCl}_6$  in the presence of PVP.<sup>30</sup> The obtained bimetallic nanoparticles were considerably monodispersed and smaller than both of the corresponding monometallic nanoparticles. EXAFS studies of these bimetallic nanoparticles revealed that these nanoparticles had Pd-shell Pt-core ( $\text{Pd}_{\text{shell}}\text{Pt}_{\text{core}}$ ) structures.<sup>31</sup> Especially, Pd/Pt (4/1, mol/mol) bimetallic nanoparticles with an average particle size of 1.5 nm form a perfect one-layer covered structure, as shown in Fig. 7.4. UV-vis spectra, X-ray photospectroscopy (XPS) analyses, and X-ray diffractogram also strongly support this special “core-shell” structure formation.

The PVP-stabilized platinum–gold<sup>32</sup> and palladium–gold<sup>33</sup> nanoparticles are readily prepared by simultaneous reduction of the corresponding two metal ions,  $\text{PtCl}_6^{2-}/\text{AuCl}_4^-$  and  $\text{PdCl}_2/\text{AuCl}_4^-$ , respectively, by reflux of the ethanol/water mixed solutions. In Fig. 7.5, the UV-vis spectra of PVP-stabilized Pd/Au bimetallic nanoparticles and those of the physical mixtures of Pd and Au monometallic nanoparticles are collected. Because of the strong absorption peak in the red region of gold nanoparticles, it is clearly indicated that these bimetallic nanoparticles are not simple physical mixtures. As the absorption peak diminishes intensively with the increase of palladium content, we can assume that these particles have a Pd-shell Au-core ( $\text{Pd}_{\text{shell}}\text{Au}_{\text{core}}$ ) structure. Detailed analysis by XPS and EXAFS revealed that the simultaneous reduction of these two metal ions gave the well-arranged core-shell structures, although successive reduction of gold ions in the presence of palladium preformed nanoparticles gave “cluster-in-cluster” structures,<sup>25</sup> as described earlier.

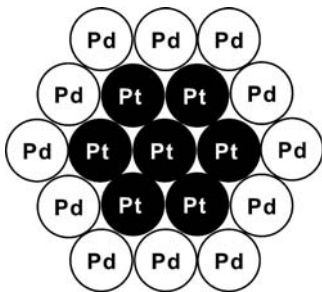


FIGURE 7.4. Cross section of PVP-stabilized Pd/Pt (4/1, mol/mol) bimetallic nanoparticles prepared by simultaneous ethanol reduction of the Pd and Pt metal salts. [Reprinted in part from Ref. 31 with permission, copyright (1991) American Chemical Society.]



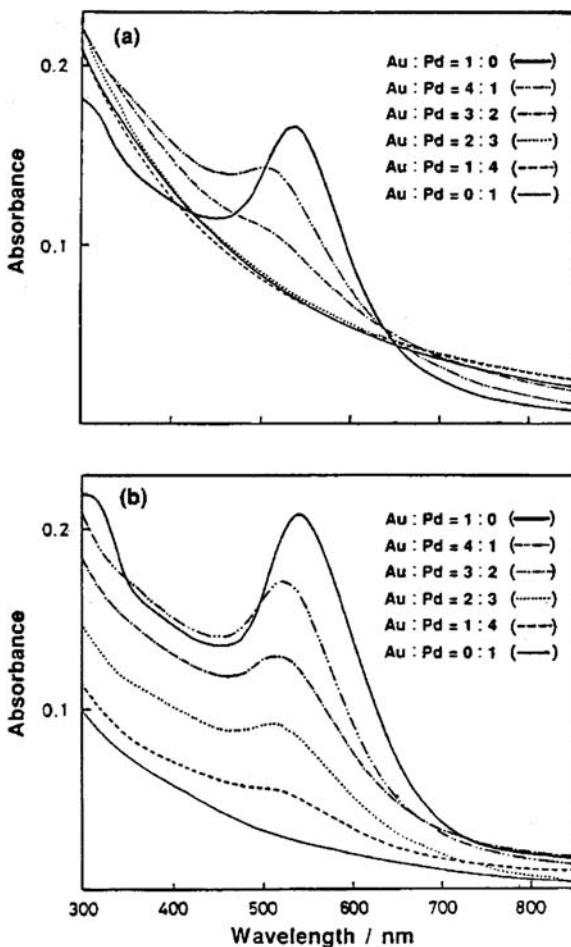


FIGURE 7.5. UV-vis spectra of (a) PVP-stabilized palladium-gold bimetallic nanoparticles prepared by simultaneous alcohol reduction of  $\text{PdCl}_2/\text{AuCl}_4^-$  and (b) simple physical mixtures of the dispersions of PVP-stabilized monometallic Pd and Au nanoparticles at various Pd : Au (mol/mol) ratios. [Reprinted from Ref. 33 with permission, copyright (1992) American Chemical Society.]

Simultaneous reduction of  $\text{AuCl}_4^-$  and  $\text{PdCl}_2$  by sonochemical reduction in the presence of SDS (sodium dodecyl sulfate) as the stabilizer molecules were also attempted.<sup>34</sup> As shown in Fig. 7.6, even by sonochemical reduction, gold ions are reduced first and palladium ions start to be reduced after the complete reduction of  $\text{Au}^{3+}$ . This phenomenon can be clearly explained by the geared cycles shown in Fig. 7.1. The products obtained by this reaction were  $\text{Pd}_{\text{shell}}\text{Au}_{\text{core}}$  bimetallic nanoparticles. The thickness of the palladium shell and the diameter of the gold core can be controlled by the Pd/Au ratio at preparation.<sup>35</sup>

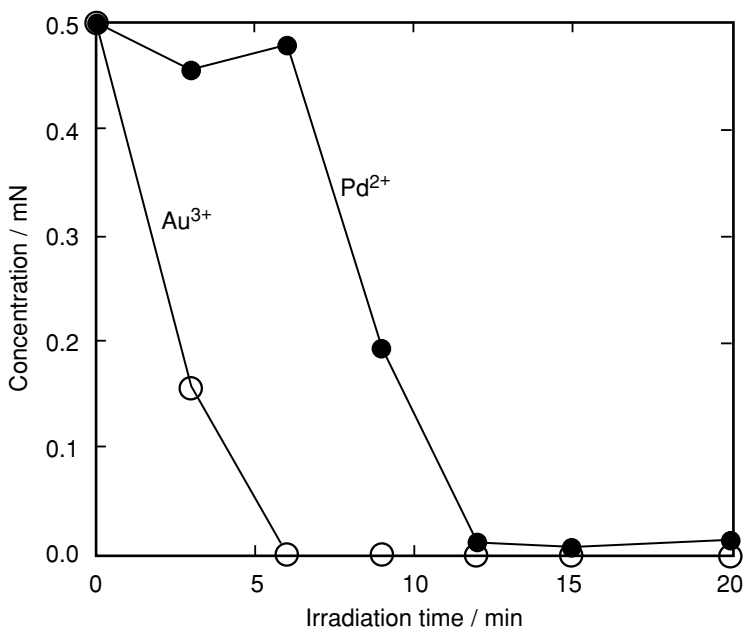


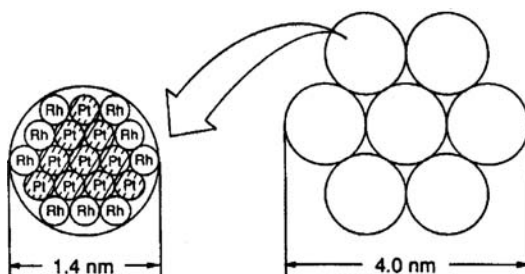
FIGURE 7.6. Time profile of the gold(III) ion and the palladium(II) ion with the duration of sonication of the mixed solution of 0.5 mM NaAuCl<sub>4</sub>, 0.5 mM PdCl<sub>2</sub>, and 8 mM SDS. [Reprinted from ref. 34 with permission, copyright (1997) American Chemical Society.]

Harpeness and Gedanken proposed a microwave-assisted polyol method to prepare Pd<sub>shell</sub>Au<sub>core</sub> bimetallic nanoparticles.<sup>36</sup> PdCl<sub>2</sub> and HAuCl<sub>4</sub> in ethylene glycol (EG) was placed in a 900-W, 2.45-GHz microwave oven for 1 h with on-off cycles of 21 s and 9 s. EDX and XPS analyses revealed that the obtained bimetallic nanoparticles had Pd<sub>shell</sub>Au<sub>core</sub> structures. From area-selective analysis by EDX, no gold was observed in shell area.

Simultaneous alcohol reduction of platinum and rhodium ions in the presence of PVP also gave ~4.0-nm nanoparticles with a specific assembly form. This size was determined by TEM observation.<sup>37</sup> However, detailed high-resolution TEM (HRTEM) and EXAFS analyses revealed this special aggregated structure. These 4.0-nm Pt/Rh bimetallic nanoparticles at a Pt/Rh ratio of 1/1 consisted of 13 × 1.4-nm Rh<sub>shell</sub>Pt<sub>core</sub> bimetallic subnanoparticles, as shown in Fig. 7.7. The structures of these bimetallic subnanoparticles were varied by the composition of these two elements (Fig. 7.8).

Simultaneous reduction of AuCl<sub>4</sub><sup>-</sup> and AgNO<sub>3</sub> by using Neem (*Azadirachta indica*) leaf broth was investigated by Sastry's group.<sup>38</sup> The flavonone and terpenoid constituents of the leaf broth are considered as the stabilizing reagent, and possibly the reducing sugars and/or terpenoids reduce metal ions to zerovalent metal atoms. With this simultaneous reduction, small Ag nanoparticles are deposited onto Au nanoparticles to form Ag<sub>shell</sub>Au<sub>core</sub> bimetallic nanoparticles.

FIGURE 7.7. Cross-sectional image of the assembly model of a PVP-stabilized Pt/Rh (1/1) bimetallic nanoparticles. The nanoparticles are assembled of  $13 \times 1.4$ -nm bimetallic subnanoparticles. [Reprinted from Ref 37 with permission, copyright (1994) American Chemical Society.]



Sastry et al. indicated that the reduction rate of Au ions during the preparation of Ag/Au bimetallic nanoparticles was higher than the Au monometallic preparation. This phenomenon can also be explained by geared cycles such as shown in Fig. 7.1.

#### 7.2.4. Other Systems

As described in the previous two subsections, the redox potentials of the component metals are very important for controlling the nanoscopic structures of bimetallic nanoparticles. To overcome this problem, Wang and Toshima proposed a sacrificial hydrogen system (Fig. 7.9) to prepare Pt-shell Pd-core ( $\text{Pt}_{\text{shell}}\text{Pd}_{\text{core}}$ ) bimetallic nanoparticles.<sup>39</sup> This system was designed based on the ability to adsorb hydrogen and form a metal-H bond on the metal surface. Also, hydrogen atoms adsorbed on noble metals have a very strong reducing ability. Reduction of noble metal ions with a higher redox potential, like  $\text{Pt}^{2+}$  or  $\text{Pt}^{4+}$  in this case, contact the hydrogen-adsorbed metal cores; like Pd nanoparticles, hydrogen atoms provide electrons to reduce metal ions ( $\text{Pt}^{4+}$ ) to deposit metal atoms ( $\text{Pt}(0)$ ) onto the metal core of the other metal core nanoparticles (Pd). With this system, Pt can be deposited onto very small Pd nanoparticles to form  $\text{Pt}_{\text{shell}}\text{Pd}_{\text{core}}$  bimetallic nanoparticles.

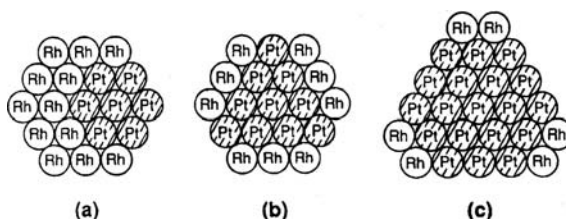


FIGURE 7.8. Cross-sectional images of the detailed models of bimetallic subnanoparticles: (a) Pt/Rh (1/4 (mol/mol)), (b) Pt/Rh (1/1), and (c) Pt/Rh (4/1) bimetallic subnanoparticles. [Reprinted from Ref. 37 with permission, copyright (1994) American Chemical Society.]

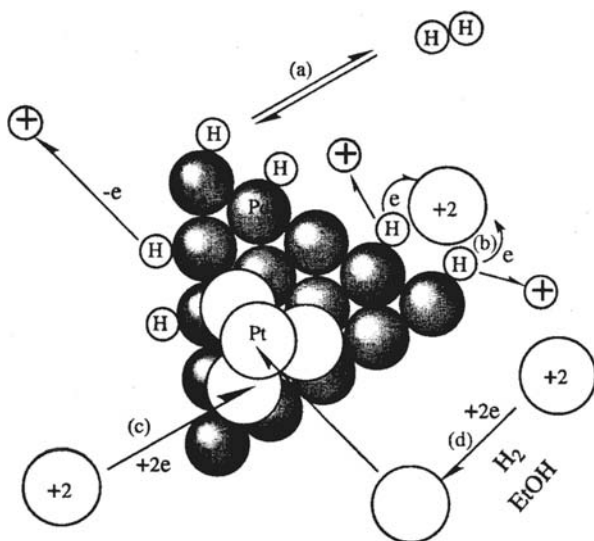


FIGURE 7.9. Sacrificial hydrogen system for the preparation of Pt<sub>shell</sub>/Pd<sub>core</sub> bimetallic nanoparticles by deposition of Pt atoms on Pd nanoparticles: (a) adsorption of hydrogen atoms on the Pd core, (b) reduction of Pt ions by the adsorbed hydrogen atoms, (c) deposition of Pt atoms onto Pd-core nanoparticles, and (d) reduction of Pt ions by hydrogen molecules in the solution or ethanol. [Reprinted from Ref. 39 with permission, copyright (1997) American Chemical Society.]

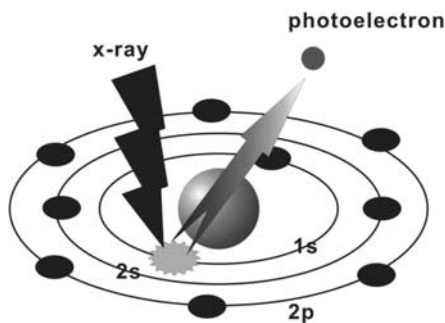
### 7.3. Characterization of Core-Shell Bimetallic Nanoparticles

Characterization procedures of bimetallic nanoparticles are widely divided into three categories: X-ray analysis, electron microscopic observation, and optical information. X-ray analysis methods are useful for understanding the crystallinity of the particles, the percentage of metal elements, and surface composition. Electron microscopic observation is the most important characterization method in order to know the particle structure and size. Optical information, such as UV-vis spectra of the particles or infrared (IR) spectra of surface chemical probe molecules, is also a very sensitive technique for understanding the surface structures of bimetallic nanoparticles. Especially, for bimetallic nanoparticles containing gold, silver, and/or copper as their component, UV-vis spectroscopy is the simplest and most effective technique for understanding their structures.

#### 7.3.1. X-ray Characterization

X-ray methods are quite powerful for analyzing bimetallic nanoparticles. Specific X-ray properties of metals are often used for the determination of metal composition and/or crystallinity of nanoparticles. Information of local composition or structure of bimetallic nanoparticles can be effectively obtained by using X-ray diffraction, X-ray photoelectron spectroscopy, and EXAFS (X-ray absorption).

FIGURE 7.10. Schematic illustration of the principal of the photoemission of XPS.



X-ray diffraction (XRD) is the most effective method for understand crystal structure and size of metal nanoparticles. Powder X-ray diffractograms of metal nanoparticles are easily obtained by simple dry of the nanoparticle dispersions, usually without any purification. For monometallic nanoparticles, the phase changes with their diameters can be investigated by detailed observation of X-ray diffractograms. Scherrer's equation can be used to find the size of crystal domain of the specimens.<sup>40</sup> In the case of single-crystal nanoparticles, the size of the crystal domain is the size of the nanoparticles themselves. Smaller nanoparticles show wider peaks in X-ray diffractograms. The simple physical mixture of the two independent monometallic nanoparticles gives the overlapping lines of the two corresponding diffractograms. The diffractogram of bimetallic nanoparticles is clearly different from those of the monometallic nanoparticles and the physical mixtures. Especially, "solid-solution"-type bimetallic nanoparticles or amorphous-type bimetallic nanoparticles usually show very broad peaks in XRD.

X-ray photospectroscopy (XPS) or ESCA (electron spectroscopy for chemical analysis) is very useful for elucidating the composition of the materials, especially for finding the surface composition. XPS provides not only an indication of the metal elements but also that of the oxidation states of the metals in nanoparticles by comparisons of their binding energies. This technique requires ultrahigh vacuum. XPS is a surface-sensitive method with a typical information depth of 1–5 nm (i.e., 4–20 atomic layers), which is determined by the mean free path of the electrons. The electronic states are characteristic for the elements emitting photoelectrons excited by X-ray radiation. Quantitative analysis can also be performed using elemental sensitivity factors (or comparing the standard specimens). A schematic illustration of the principle of XPS is presented in Fig. 7.10.

In the case of polymer- or surfactant-stabilized nanoparticles, usually prepared with excess amounts of such stabilizing molecules, XPS cannot work well if the samples are prepared by solvent evaporation of the nanoparticle dispersions, because the stabilizer molecules form very thick organic coating layers. Wang and Liu invented the "coordination capture" method to overcome this problem. They used capturing particles (i.e., thiol-modified silica supports) to adsorb nanoparticles without stabilizing the layer by thiols, leaving the polymers or surfactants in solution.<sup>41</sup>

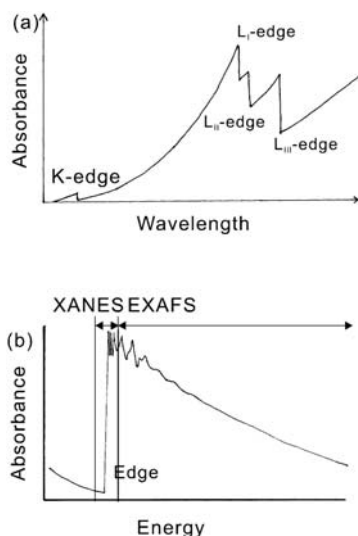


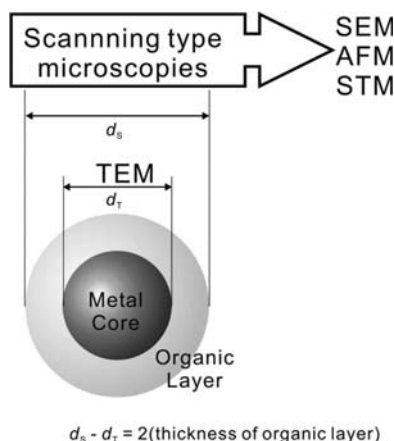
FIGURE 7.11. Typical illustration of EXAFS spectrum. (a) X-ray absorption spectra of metals in a large energy area. (b) The EXAFS spectrum can be observed at a higher-energy area just above the specific absorption edge.

Extended X-ray absorption fine structure is one of the most powerful characterization techniques for elucidating the detailed nanostructure of materials, especially of finite-sized ones. Large synchrotron radiation facilities, such as KEK in Tsukuba, SPring-8 in Hyogo (Japan), and ESRF in Grenoble (France) have made EXAFS a widely used tool for scientists and engineers in various fields to determine the detailed structure of complex materials.

Small oscillations observed over a range of several hundreds of electron volts just above the specific X-ray absorption edge (in many cases, the K-edge or L<sub>III</sub>-edge is used) involve the information on the environment of neighbors of the absorbing element. (Fig. 7.11) These small oscillations are generated by the backscattering of the emitted photoelectrons from the surrounding atoms. Using simulation programs, elements of neighbor atoms, the coordination numbers, and interatomic lengths can be obtained. In order to obtain such small oscillations effectively, a strong X-ray source is required. Synchrotron radiation factories have very much shortened the acquisition time to obtain good EXAFS spectra.

Energy disperse X-ray microanalysis (EDX, EDAX, or EDS) is similar to XPS analysis and is one of the most effective tool for microscale (or nanoscale) elemental analysis. EDX is usually attached to an electron microscope with high resolution. Bombarding a small sample with a beam of high-energy electrons, which is a focused electron beam of the attached electron microscope in a restricted area, the sample emits X-rays with characteristic energies. Detecting the strength and energy of this specific X-ray, quantitative elemental analysis can be conducted. Recently, an electron beam in a TEM can be focused on a single nanoparticle, and we can obtain elemental information from *individual* particles. For sufficiently large “core-shell”-type bimetallic nanoparticles, the electron beam can be spotted on the

FIGURE 7.12. Schematic illustration of the structural information obtained from TEM, SEM, and SPM (AFM, STM) images. From TEM images, the structural information of the metal core can be obtained. On the other hand, SEM or SPM images give the information on the whole particle including organic stabilizing layers.



surface area or the center area of *one* nanoparticle and show the nonuniformity in the composition.

### 7.3.2. Electron Microscopic Observations

Probably the most important question about metal nanoparticles to be revealed is concerned with aggregation state, size, and morphology. A direct and powerful technique used for this purpose is the direct observation by electron microscopies. The size, shape, and crystallinity of the metal core of nanoparticles can be revealed by transmission electron microscopies. The particle size distributions, which can be obtained by TEM observations, is another highly important factor, which introduces the uniformity of the nanoparticle. The uniformity can be one of the most important factors for their application to nanomaterials. With TEM observations, only metal cores can be observed, but organic stabilizing layers usually cannot show enough contrast in the images. TEM images are two dimensional; therefore, three-dimensional structures of the nanoparticles should be considered with the contrast and/or fringes (see below) observed in TEM images.

On the contrary, scanning electron microscopy (SEM) can be used in order to observe the entire structure of metal nanoparticles with organic coatings. Atomic force microscopy (AFM) and scanning tunneling microscopy (STM) can also be used for the same purpose. It should be noted that the diameter of the top of the cantilever should be considered when AFM and STM are applied, furthermore, the organic coating layer might be shrunk in a dry atmosphere or in vacuum. These microscopies can also give effective information on their three-dimensional structures (Fig. 7.12).

Lattice fringes on the nanoparticles observed by high resolution TEM (HRTEM) observation are another powerful message for understanding the crystallinity of the particles, especially for small nanoparticles or bimetallic nanoparticles. Even

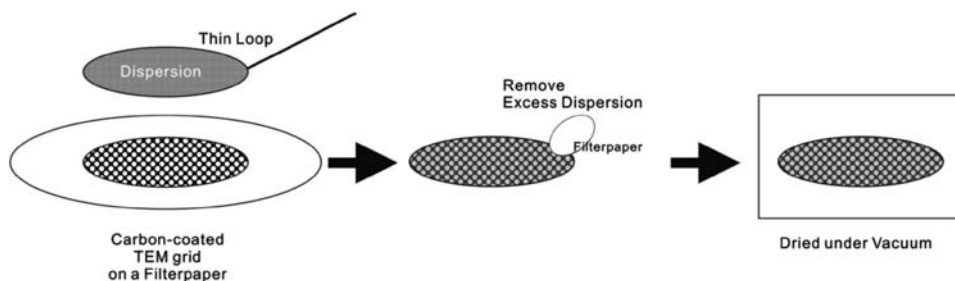


FIGURE 7.13. Schematic illustration of the preparation procedure of TEM samples.

for very small-sized nanoparticles (or clusters), lattice fringes can be found in the images. Lattice spacings are the characteristics of the elements and their states. In combination with the X-ray diffractogram, lattice fringes can provide detailed structural information of bimetallic nanoparticles.

For the preparation of TEM samples of metal nanoparticles, a carbon-coated TEM grid (usually 3 mm $\phi$ (phi *in italic*), copper) is used. Thinner carbon coats are required for high-resolution observation. As shown in Fig. 7.13, the preparation procedure is quite simple. A drop of the homogeneous dispersion of the metal nanoparticles is put onto a carbon-collosion-coated (or thin SiO-coated) copper (or other metal if elemental analysis of copper is applied) microgrids. Excess dispersion should be immediately removed by using filter papers in order to avoid aggregation of particles on the grid. Of course, the concentration of the dispersion of nanoparticles is highly important. Too much excess stabilizing reagent should be removed before the sample preparation, because such contamination could fade the contrast of the nanoparticles, especially in the case of light transition metals.

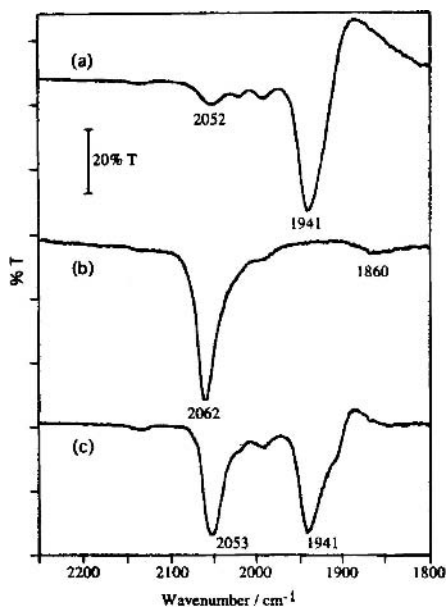
### 7.3.3. *UV-vis Spectroscopy*

UV-vis spectroscopy is effective for characterizing bimetallic nanoparticles, especially those containing gold, silver, and/or copper (group 1B). These three elements have a specific plasmon absorption in a visible-light region, which is varied with the size and the environment. Thus, for the bimetallic nanoparticles containing these metal elements, observation of their UV-vis spectra is very useful for characterizing the structure of metal nanoparticles.

As shown in Fig. 7.5, comparison of the UV-vis spectra of bimetallic nanoparticles with those of the physical mixtures of the corresponding two monometallic nanoparticles can strongly suggest a bimetallic structure of the particles; that is, each particle contains the two metal elements. Furthermore, formation processes of bimetallic nanoparticles can also be revealed by the observation of UV-vis spectral changes during the preparation of nanoparticles.<sup>42</sup>



FIGURE 7.14. FTIR spectra of carbon monoxide on PVP-stabilized (curve a) Pd and (curve b) Pt monometallic nanoparticles. Curve c represents the spectrum of the physical mixture of Pd(1) and Pt(1) monometallic nanoparticles. [Reprinted from Ref. 39 with permission, copyright (1997) American Chemical Society.]



#### 7.3.4. IR Spectroscopy of Chemical Probes

The most effective application of bimetallic nanoparticles is catalysis. As is well known, catalytic properties are affected most strongly by surface structures and surface compositions. Characterization of the surface composition of metal nanoparticles can be executed effectively by chemical probes, such as chemisorption of the hydrogen atom (H) or carbon monoxide (C=O). Particularly, IR) absorption spectroscopy of C=O adsorbed on a nanoparticle surface is a very good probe for determining the surface composition and condition of metals.

Infrared absorption bands of carbonyl (C=O) stretchings of carbon monoxide adsorbed onto a metal surface varied widely with the two adsorption states (i.e., bridging C=O and linear C=O). Figure 7.14 shows the FTIR spectra of CO adsorbed on PVP-stabilized palladium and platinum nanoparticles. On palladium nanoparticles, C=O adsorbed at a bridging site and the peak is observed at 1941  $\text{cm}^{-1}$ . On platinum nanoparticles, C=O adsorbed at linear structure and the peak is observed at 2062  $\text{cm}^{-1}$  (Fig. 7.14). In Fig. 7.15, FTIR spectra of CO adsorbed on PVP-stabilized  $\text{Pt}_{\text{shell}}\text{Pd}_{\text{core}}$  bimetallic nanoparticles prepared by the sacrificial hydrogen system are collected.<sup>39</sup> The peak is observed only at 2068  $\text{cm}^{-1}$  in the case of Pt/Pd mole ratios of 2/1 and 1/1, indicating that C=O is adsorbed at the linear structure. This result strongly suggests that these bimetallic nanoparticles have a  $\text{Pt}_{\text{shell}}$  structure.

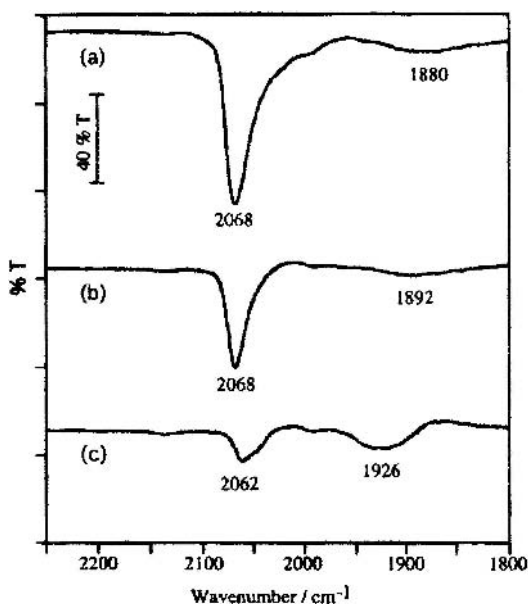


FIGURE 7.15. FTIR spectra of carbon monoxide on PVP-stabilized  $\text{Pt}_{\text{shell}}\text{Pd}_{\text{core}}$  (2/1) (curve a),  $\text{Pt}_{\text{shell}}\text{Pd}_{\text{core}}$  (1/1) (curve b), and  $\text{Pt}_{\text{shell}}\text{Pd}_{\text{core}}$  (1/4) bimetallic nanoparticles (curve c). [Reprinted from Ref. 39 with permission, copyright (1997) American Chemical Society.]

## 7.4. Summary

In this chapter, the preparation, characterization, and some specific properties of bimetallic nanoparticles with “core-shell”-type structures especially prepared in the liquid phase were surveyed. Many effective procedures have been developed in order to prepare “core-shell” structures.

Catalysis is the most highly developed application of metal nanoparticles, especially bimetallic nanoparticles. However, the specific property of metal nanoparticles is becoming a new hero in a number of areas of technological importance. In order to tune such a property, bimetallic formation can be a good solution. In fact, “core-shell”-type gold–silver nanoparticles show very unique properties in plasmon absorption.

Continuing progress of analytical technologies in nanofields will give us new ideas for creating novel applications of bimetallic and multimetallic (three or more) nanoparticles in the near future. The progress will again be the center of interest of nanofield researchers. Nanoparticles continue to be one of the key materials of nanotechnology in the 21st century.

*Acknowledgments.* The author expresses his thanks to Professor N. Toshima (Tokyo University of Science, Yamaguchi) for the encouragement of bimetallic nanoparticle studies and to Professor H. Nishihara (University of Tokyo) for his warm hospitality, allowing me to finish this manuscript.

## References

1. G. Schmid, Large clusters and colloids. Metals in the embryonic state, *Chem. Rev.* **92**, 1709 (1992).
2. H. Hirai and N. Toshima, *Tailored Metal Catalysts*, edited by Y. Iwasawa., D. Reidel, Dordrecht, 1986, pp. 87–140.
3. J. S. Bradley, *Clusters and Colloids*, edited by G. Schmid, Wiley–VCH, Weinheim, 1994, pp. 459–544.
4. J. S. Bradley, *Nanoparticles*, edited by G. Schmid, Wiley–VCH, Weinheim, 2004, pp. 186–238.
5. G. Schmid and L. F. Chi, Metal clusters and colloids, *Adv. Mater.* **10**, 515 (1998).
6. G. Schmid, M. Bäuml, M. Geerkens, I. Heim, C. Osemann, and T. Sawitowski, Current and future applications of nanoclusters, *Chem. Soc. Rev.* **28**, 179 (1999).
7. T. Sawitowski, S. Frantzka, N. Beyer, M. Levering, and G. Schmid, Nanostructured surfaces, *Adv. Funct. Mater.* **11**, 169 (2001).
8. M. Brust and C. J. Kiely, *Colloids and Colloid Assemblies*, edited by F. Caruso, Wiley–VCH, Weinheim, 2004, pp. 96–119.
9. R. Kubo, Electronic properties of metal fine particles I, *J. Phys. Soc. Jpn.* **17**, 975 (1962).
10. J. Park, K. An, Y. Hwang, J.-G. Park, H.-J. Noh, J.-Y. Kim, J.-H. Park, N.-M. Hwang, and T. Hyeon, Ultra-large-scale syntheses of monodisperse nanocrystals, *Nature Mater.* **3**, 891 (2004).
11. N. Toshima and T. Yonezawa, Bimetallic nanoparticles: Novel materials for chemical and physical applications, *New J. Chem.* **1998**, 1179 (1998).
12. T. Yonezawa, *Morphology Control of Materials and Nanoparticles*, edited by Y. Waseda and A. Muramatsu, Springer-Verlag, Berlin, 2003, pp. 85–112.
13. J. Turkevich and G. Kim, Palladium: Preparation and catalytic properties of particles of uniform size, *Science*, **169**, 873 (1970).
14. J. H. Sinfelt, Supported “bimetallic cluster” catalysts, *J. Catal.* **29**, 308 (1973).
15. J. H. Sinfelt, Structure of bimetallic clusters, *Acc. Chem. Res.* **20**, 134 (1987).
16. A. Henglein, Physicochemical properties of small metal particles in solution: “micro-electrode” reactions, chemisorption, composite metal particles, and the atom-to-metal transition, *J. Phys. Chem.* **97**, 5457 (1993).
17. S. Remita, G. Picq, J. Khatouri, and M. Mostafavi, Radiolytic formation of bilayered  $\text{Pt}_{\text{core}}/\text{Au}_{\text{shell}}$  and  $\text{Au}_{\text{core}}/\text{Pt}_{\text{shell}}$  clusters in aqueous solution, *Radiat. Phys. Chem.* **54**, 463 (1999).
18. G. Schmid, A. Lehnert, J. O. Halm, and J. O. Bovin, Ligand-stabilized bimetallic colloids indentified by HRTEM and EDX, *Angew. Chem. Int Ed. Engl.* **30**, 874 (1991).
19. A. F. Lee, C. J. Baddeley, C. Hardacre, R. M. Ormerod, R. M. Lambert, G. Schmid, and H. West, Structural and catalytic properties of novel Au/Pd bimetallic colloid particles: EXAFS, XRD, and acetylene coupling, *J. Phys. Chem.* **99**, 6096 (1995).
20. G. Schmid, H. West, J. O. Halm, J. O. Bovin, and C. Grenthe, Catalytic properties of layered gold–palladium colloids, *Chem. Eur. J.* **2**, 1099 (1996).
21. I. Smnová-Šloufová, B. Vlčková, Z. Bastl, and T. L. Hasslett, Bimetallic (Ag)Au nanoparticles prepared by the seed growth method: Two-dimensional assembling, characterization by energy dispersive X-ray analysis, X-ray photoelectron spectroscopy, and surface enhanced Raman spectroscopy, and proposed mechanism of growth, *Langmuir* **20**, 3407 (2004).

22. N. Toshima and T. Takahashi, Colloidal dispersions of platinum and palladium clusters embedded in the micelles. Preparation and application to the catalysis for hydrogenation of olefins, *Bull. Chem. Soc. Jpn.* **65**, 400 (1992).
23. K. Mallik, M. Mandal, N. Pradhan, and T. Pal, Seed mediated formation of bimetallic nanoparticles by UV irradiation: A photochemical approach for the preparation of "core-shell" type structures, *Nano Lett.* **1**, 319 (2001).
24. S. Giorgio and C. R. Henry, Core-shell bimetallic particles, prepared by sequential impregnations, *Eur. Phys. J. Appl. Phys.* **20**, 23 (2002).
25. M. Harada, K. Asakura, and N. Toshima, Catalytic activity and structural-analysis of polymer-protected Au/Pd bimetallic clusters prepared by the successive reduction of  $\text{HAuCl}_4$  and  $\text{PdCl}_2$ , *J. Phys. Chem.* **97**, 5103 (1993).
26. S. Gu, X. Yao, M. J. Hampden-Smith, and T. T. Kodas, Reactions of  $\text{Cu}(\text{hfac})_2$  and  $\text{Co}_2(\text{CO})_8$  during chemical vapor deposition of copper-cobalt films. *Chem. Mater.* **10**, 2145 (1998).
27. H. Cai, N. Zhu, Y. Jiang, P. He, and Y. Fang, Cu@Au alloy nanoparticle as oligonucleotides labels for electrochemical stripping detection of DNA hybridization, *Biosens. Bioelectron.* **18**, 1311 (2003).
28. T. Kinoshita, S. Seino, K. Okitsu, T. Nakayama, T. Nakagawa, and T. A. Yamamoto, Magnetic evaluation of nanostructure of gold-iron composite particles synthesized by a reverse micelle method, *J. Alloys Compounds* **359**, 46 (2003).
29. T. Yonezawa, K. Shibuya, and H. Nishihara, Synthesis of surfactant-stabilized Co/Au bimetallic nanoparticles with a core-shell structure, *Trans. Mater. Soc. Jpn.*, **30**, in press (2006).
30. N. Toshima, K. Kushihashi, T. Yonezawa, and H. Hirai, Colloidal dispersions of palladium-platinum bimetallic clusters by polymers. Preparation and application to catalysis, *Chem. Lett.*, 1769 (1989).
31. N. Toshima, M. Harada, T. Yonezawa, and K. Asakura, Structural analysis of polymer-protected palladium/platinum bimetallic clusters as dispersed catalysts by using extended X-ray absorption fine structure spectroscopy, *J. Phys. Chem.* **95**, 7448 (1991).
32. N. Toshima and T. Yonezawa, Preparation of polymer-protected gold/platinum bimetallic clusters and their application to visible light-induced hydrogen evolution, *Makromol. Chem. Macromol. Symp.* **59**, 281 (1992).
33. N. Toshima, M. Harada, Y. Yamazaki, and K. Asakura, Catalytic activity and structural analysis of polymer-protected gold-palladium bimetallic clusters prepared by the simultaneous reduction of hydrogen tetrachloroaurate and palladium dichloride, *J. Phys. Chem.* **96**, 9927 (1992).
34. Y. Mizukoshi, K. Okitsu, Y. Maeda, T. A. Yamamoto, R. Oshima, and Y. Nagata, Sonochemical preparation of bimetallic nanoparticles of gold/palladium in aqueous solution, *J. Phys. Chem. B* **101**, 7033 (1997).
35. Y. Mizukoshi, T. Fujimoto, Y. Nagata, R. Oshima, and Y. Maeda, Characterization and catalytic activity of core-shell structured gold/palladium bimetallic nanoparticles synthesized by the sonochemical method, *J. Phys. Chem. B* **104**, 6028 (2000).
36. R. Harpeness and A. Gedanken, Microwave synthesis of core-shell gold/palladium bimetallic nanoparticles, *Langmuir* **20**, 3431 (2004).
37. M. Harada, K. Asakura, and N. Toshima, Structural analysis of polymer-protected platinum/rhodium bimetallic clusters using extended X-ray absorption fine structure spectroscopy. Importance of microclusters for the formation of bimetallic clusters, *J. Phys. Chem.* **98**, 2653 (1994).

38. S. S. Shankar, A. Rai, A. Ahmad, and M. Sastry, Rapid synthesis of Au, Ag, and bimetallic Au core-Ag shell nanoparticles using Neem (*Azadirachta indica*) leaf broth, *J. Colloid Interf. Sci.* **275**, 496 (2004).
39. Y. Wang and N. Toshima, Preparation of Pd-Pt bimetallic colloids with controllable core/shell structures. *J. Phys. Chem. B* **101**, 5301 (1997).
40. J. W. Niemantsverdriet, *Spectroscopy in Catalysis*, VCH, Weinheim, 1995. p. 140.
41. Y. Wand and H. Liu, Preparation and immobilization of polymer-protected bimetallic colloids, *Polym. Bull.* **25**, 139 (1991).
42. T. Yonezawa and N. Toshima, Mechanistic consideration of formation of polymer-protected nanoscopic bimetallic nanoparticles, *J. Chem. Soc. Faraday Trans.* **91**, 4111 (1995).

# 8

## Cobalt Nanocrystals Organized in Mesoscopic Scale

MARIE-PAULE PILENI

*Laboratoire LM2N, UMR CNRS 7070, Université P. et M. Curie (Paris VI),  
75252 Paris cedex 05, France*

### 8.1. Introduction

The emergence of new methods and concepts for the organization of nanoparticles has rapidly induced great hopes in the world of magnetism. In fact, the organization of nanoscale ferromagnetic particles opens a new field of technologies through the controlled fabrication of mesoscopic materials with unique magnetic properties.<sup>1</sup> In particular, these ferromagnetic nanoparticles are potential candidates for magnetic storage,<sup>2</sup> where the idea is that each ferromagnetic particle corresponds to one bit of information.<sup>3</sup> Thin granular films of ferromagnetic particles formed by sputtering deposition are already the basis of conventional rigid magnetic storage media. However, there are several problems remaining to be solved before their application to the storage industry becomes feasible. Devices based on magnetic nanocrystals are limited by thermal fluctuations of the magnetization: Because of their reduced sizes, ferromagnetic nanocrystals become superparamagnetic at room temperature. The dipolar magnetic interaction between nanocrystals ordered in arrays is also an important limiting factor for their use in magnetic storage media. A detailed understanding of the magnetic properties of assemblies of nanocrystals is therefore essential to the development of magnetic recording technology.

Organized arrays of magnetic nanoparticles have been obtained for various metallic [Fe,<sup>4</sup> Co,<sup>5–12</sup> ferrite ( $\gamma$  Fe<sub>2</sub>O<sub>3</sub>,<sup>13,14</sup> Fe<sub>3</sub>O<sub>4</sub>,<sup>15,16</sup> and MFe<sub>2</sub>O<sub>4</sub> (M = Fe, Co, Mn)<sup>17,18</sup>] and alloy (AgCo,<sup>19,20</sup> CoPt,<sup>21–24</sup> and FePt<sup>25–30</sup>) nanomaterials. The most common organizations are the hexagonal network (two dimensional (2D))<sup>4–11,13–21,24–26,29,30</sup> and the face-centered-cubic (fcc) packing in three dimensions (3D).<sup>12,22,23,27,28</sup> These organizations are usually obtained by evaporation of a solution containing a low size distribution of magnetic nanocrystals on a substrate. Strong magnetic dipolar interactions between nanoparticles induce their organization in 2D chains and rings.<sup>31</sup> For weak dipolar interactions, one dimension (1D) chains, 3D cylinders, dots, and labyrinths are obtained by applying a magnetic field during the deposition process. Collective magnetic properties were reported.

## 8.2. Self-Organization of Cobalt Nanocrystals

Inorganic nanocrystals are able to self-assemble in compact hexagonal networks,<sup>32</sup> rings,<sup>33,34</sup> lines,<sup>35,36</sup> stripes,<sup>37</sup> tubes,<sup>38,39</sup> columns, labyrinths,<sup>40–42</sup> and large “supra” crystals characterized by an fcc structure.<sup>32,43–46</sup>

To produce well-defined 2D and 3D superlattices of nanocrystals, highly stable materials are needed. Usually, self-assemblies of nanocrystals are obtained by evaporation of the solution containing nanocrystals on a given substrate. The size distribution of nanocrystals is the major parameter in obtaining highly ordered “supra” crystals. When the nanocrystals are sufficiently uniform in size, they self-assemble in close-packed, ordered nanocrystal superlattices. This is well illustrated in Fig. 8.1, which shows transmission electron microscope (TEM) images of the various arrangements of cobalt nanocrystals characterized by various size distributions ( $\sigma$ ). [All of the depositions are made in the same way (i.e., by depositing the colloidal solution on an amorphous carbon grid<sup>11</sup>)]. The nanocrystals start to self-organize in a 2D hexagonal network when  $\sigma$  is equal to or lower than 13%. The Fourier transform (inset, Fig. 8.1E) made on a 200-nm  $\times$  200-nm array, displays three orders of reflections and thus confirms the long-range hexagonal network.

However, the long-range order of the organization depends on the particle–substrate interactions. The strength of the particle–substrate interaction depends on the Hamaker constant, which takes into account the nature of the nanocrystals, the solvent (oil), and the substrate (s). Hence, compact monolayers are produced on a large scale by deposition of cobalt nanocrystals<sup>12</sup> on the highly oriented pyrolytic graphite (HOPG) substrate (Fig. 8.2A). Conversely, with amorphous carbon as the substrate, the order is local and the monolayer shows defects (see arrows in Fig. 8.2B).

The capillary forces<sup>47</sup> arise when, during the evaporation process, the thickness of the film reaches the particle diameter. The speed of the solvent evaporation process plays a major role.

Furthermore, various forces have to be taken into account:

1. Van der Waals forces exhibit power-law distance dependence whose strength depends on the Hamaker constant and on a geometrical factor.<sup>48,49</sup>
2. The magnetic dipolar energy between spherical nanocrystals of equal size and with the same magnetic properties<sup>50</sup> is also a key parameter.
3. The electrostatic potential energy between charged particles exhibits an exponential distance dependence whose strength depends on the surface potential induced on the interacting colloidal particles and on the dielectric properties of the intervening medium.<sup>51</sup>
4. Steric stabilization forces provide an alternate route to controlling colloidal stability and can be used in aqueous and nonaqueous solutions.<sup>52</sup>
5. The stabilizing agent has to possess high affinity with the solvent in order to solvate the particles and form an extended layer for screening the attraction between particles.<sup>53</sup>

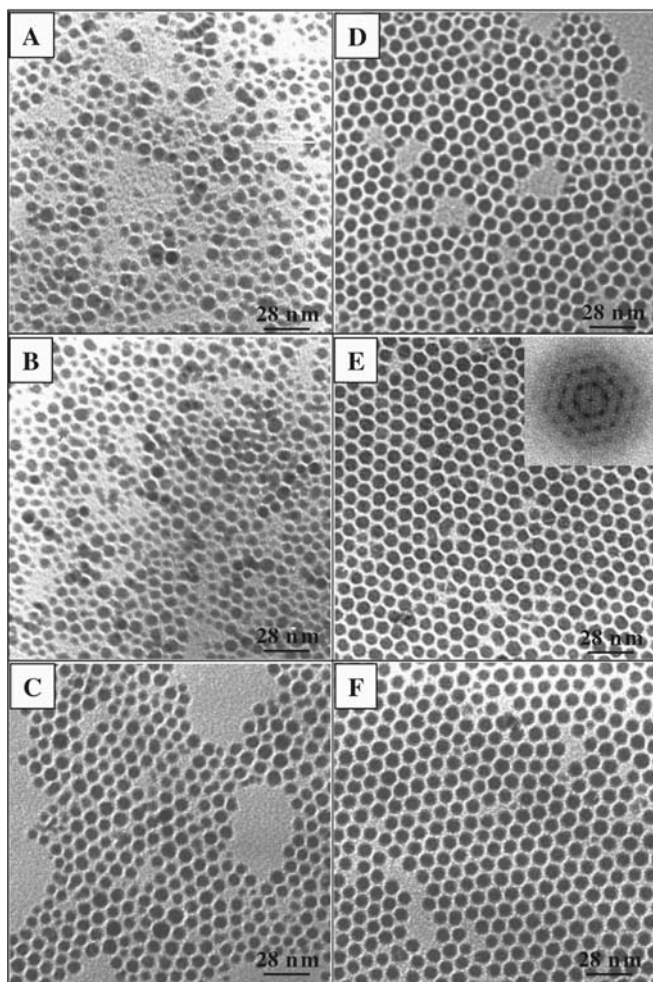


FIGURE 8.1. Transmission electron microscopy images of 7.2-nm cobalt nanocrystals obtained at various size distributions:  $\sigma = 30\%$  (A),  $\sigma = 18\%$  (B),  $\sigma = 13\%$  (C),  $\sigma = 12\%$  (D),  $\sigma = 12\%$  (E), and  $\sigma = 8\%$  (F). Inset of Fig. 8.1E: corresponding Fourier transform.

The 3D arrays are very inhomogeneous in size and shape. In order to obtain more regular 3D superlattices, also called “supra” crystals, control of the solvent evaporation rate is required. For this, the substrate is directly immersed in the colloidal solution and the solvent is allowed to evaporate. Both the substrate temperature and the solvent saturation degree of the surrounding atmosphere can control the solvent evaporation rate. By using this deposition process, “supra” crystals of cobalt<sup>12</sup> (Fig. 8.3A) nanocrystals are formed. They look like paving stones characterized by well-defined shapes and rims. The “supra” crystal thickness is about 5  $\mu\text{m}$ , which corresponds to the regular stacking of several hundred monolayers.



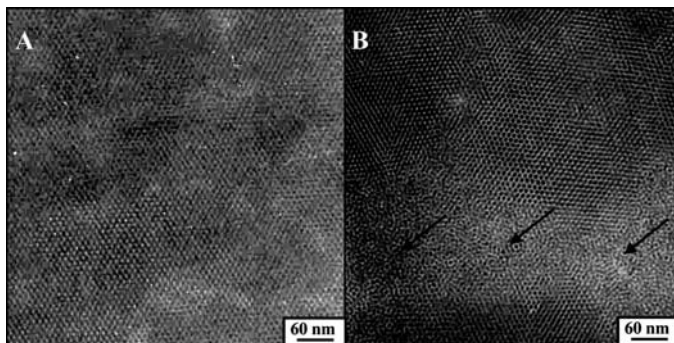


FIGURE 8.2. Transmission electron microscopy images of 2D self-assemblies of cobalt nanocrystals on (A) HOPG and (B) amorphous carbon substrates.

The optimal temperatures needed to reach the highest-ordered “supra” crystals are around 45°C. The ordering decreases with the decreasing substrate temperature, to reach, at 10°C, amorphous aggregates, highly polydispersed in size and shape and forming a nonhomogeneous film<sup>11</sup> (Fig. 8.3B) nanocrystals. Small-angle X-ray diffraction (XRD) measurements in a grazing incidence show “supra” crystals, an fcc packing. For cobalt “supra” crystals, nine spots are recorded (Fig. 8.4). Their coordinates, which are reciprocal distances, are in good agreement on conversion into  $d$ -spacing, with the calculated coordinates of diffraction spots assuming an fcc structure (Table 8.1). The XRD pattern of the amorphous aggregates described earlier shows a diffuse ring (insert in Fig. 8.5A).

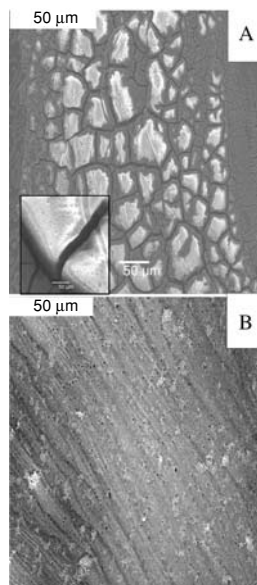


FIGURE 8.3. Scanning electron microscopy images of cobalt nanocrystals deposited on a HOPG substrate at 35°C and forming either “supra” crystals (A) or deposited amorphous carbon at 10°C and forming amorphous aggregates (B).

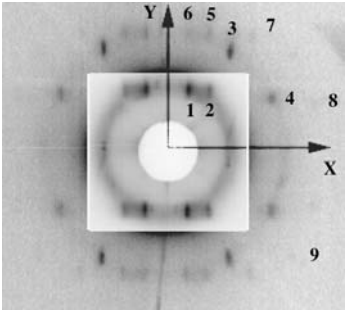


FIGURE 8.4. X-ray diffraction pattern obtained in a grazing incidence geometry of a “supra” crystal of Co nanocrystals. The intensity is reduced by a factor of 20 in the central inset.

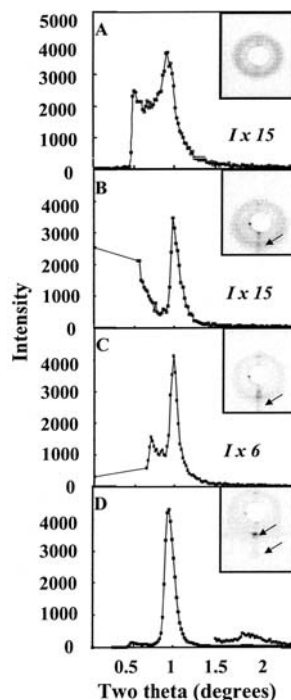
This is well demonstrated with cobalt nanocrystals, where the Bragg reflections, typical of the (111) lying planes, become more and more intense, whereas the diffuse ring intensity progressively decreases when the substrate temperature increases from 10°C to 45°C (Fig. 8.5 and Table 8.2). This behavior clearly indicates an increase in both size and out-of-plane ordering of the “supra” crystals. The average interparticle gap calculated from the stacking parameter and by assuming a core diameter of 7.2 nm is 3.55 nm when the nanocrystals are ordered and 4.55 nm for the disordered system. As expected, the packing of Co nanocrystals is less compact in the amorphous phase than in the “supra” crystal. Similar behavior with the substrate temperature was observed in the fabrication of “supra” crystals made of silver nanocrystals.<sup>43,44</sup> The second-order Bragg reflection is observed at 22°C and the interparticle distance is minimal at this temperature (3.6 nm). At substrate temperatures above 22°C, the “supra” crystal size increases.<sup>54</sup> On increasing the partial vapor pressure of the solvent during the evaporation

TABLE 8.1. Comparison of experimental and calculated coordinates of diffraction spots assuming an fcc structure.

Reflection label (see Fig. 8.4)	{ <i>h, k, l</i> } indices	<i>X</i> (measured) (nm)	<i>X</i> (calculated) (nm)	<i>Y</i> (measured) (nm)	<i>Y</i> (calculated) (nm)	<i>d<sub>hkl</sub></i> (measured) (nm)	<i>d<sub>hkl</sub></i> (calculated) (nm)
1	1, 1, -1	25.15	25.56	9.05	9.04	8.52	8.52
2	2, 0, 0	12.89	12.78	9.19	9.04	7.48	7.38
*	1, 1, 1	8.54	8.52	0	0	8.52	8.52
*	2, 2, 2	4.24	4.26	0	0	4.24	4.26
3	-1, 3, 1	8.53	8.52	5.24	5.22	4.46	4.45
4	1, 1, 3	5.12	5.11	9.51	9.04	4.51	4.45
5	2, 2, -2	13.22	12.78	4.52	4.52	4.28	4.26
6	1, 1, -3	26.09	25.56	4.47	4.52	4.41	4.45
7	4, 0, 0	6.38	6.39	4.55	4.52	3.70	3.69
8	3, 3, 1	3.67	3.65	10.10	9.04	3.45	3.39
9 +	4, 2, 0	4.31	4.26	5.44	5.22	3.38	3.30

*Note:* Coordinates are expressed as *d*-spacings. The asterisk corresponds to the various reflection in different orientations. The reflection is calculated (2, 0, 0) and compared to experiments whereas reflection 1, 1, 1 and 2, 2, 2 can be calculated but cannot be observed.

FIGURE 8.5. Diffractograms of cobalt films obtained from a HOPG substrate immersed in a highly concentrated cobalt colloidal solution. The different substrate temperatures are  $T = 10^\circ\text{C}$  (A),  $T = 25^\circ\text{C}$  (B),  $T = 35^\circ\text{C}$  (C),  $T = 45^\circ\text{C}$  (D). Insets: diffraction patterns.



process to close to 100% (i.e., by slowing down the solvent evaporation rate), crack-free homogeneous cobalt nanocrystal “supra” crystals with terraces are obtained (Fig. 8.6). XRD measurements confirm that they are highly crystallized and have the same structural characteristics as the fcc “supra” crystals described earlier. The change in the “supra” crystal morphology is related to the variation of the surface tension arising during the solvent evaporation. A similar behavior was previously observed with silver nanocrystals<sup>45</sup> with well-defined “supra” crystals in quasi-saturated vapor with a high degree of ordering, whereas a low extent of ordering and defects are found when the evaporation takes place in air.

TABLE 8.2. Various parameters extracted from the diffraction patterns and the corresponding diffractograms in Fig. 8.5.

Substrate temperature	12°C	25°C	35°C	45°C
Inner ring distance (nm)	9.60	8.80	8.80	8.70
$\delta q_{1/2}$ (nm <sup>-1</sup> )	0.19	0.050	0.035	0.034
$R_{\text{int}}: I_{\text{ref}}/I_{\text{halo}}$	1.6	11	87	674
$D_{\text{center-center}}$ (nm)	11.75	10.80	10.80	10.65
$D_{\text{interpart.}}$ (nm)	4.55	3.60	3.60	3.45

Note:  $\delta q_{1/2}$ : the half-width at half-maximum;  $R_{\text{int}}$ : the reflection intensity to the halo intensity ratio;  $D_{\text{center-center}}$ : center-to-center nanocrystal distance;  $D_{\text{interpart.}}$ : border-to-border nanocrystal distance;  $I_{\text{ref}}$ : the intensity of the reference;  $I_{\text{halo}}$ : the intensity of the halo.

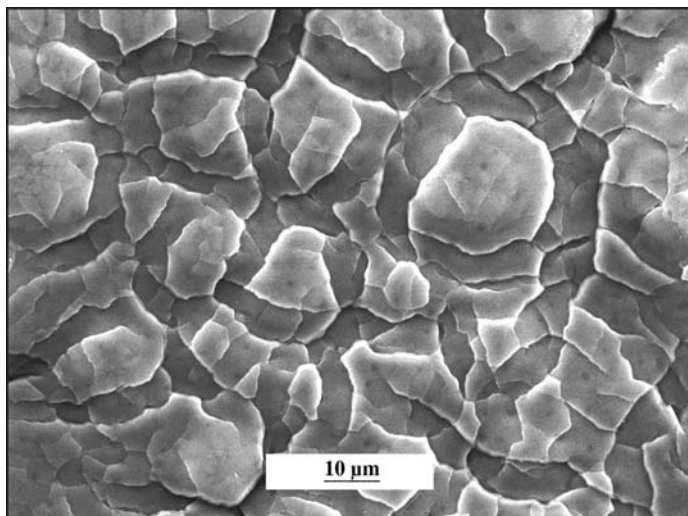


FIGURE 8.6. Scanning electron microscopy image of “supra” crystal of cobalt obtained from a HOPG substrate immersed in a highly concentrated cobalt colloidal solution. The solvent evaporation rate is very low.

The annealing of cobalt nanocrystals improves their crystallinity.<sup>55</sup> Native cobalt nanocrystals coated with dodecanoic acid, self-organized in 2D (Fig. 8.7A) or in 3D (Fig. 8.7D) superlattices are made of poorly crystallized fcc particles (Figs. 8.7B and 8.7C). The annealing at 300°C of these self-assemblies does not change

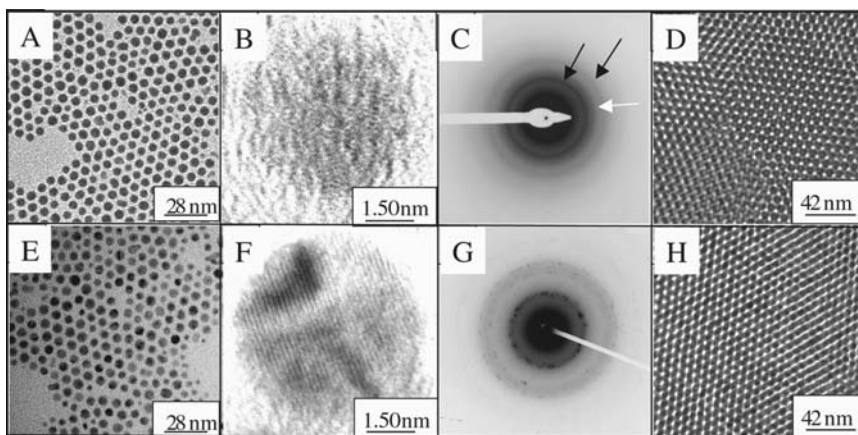


FIGURE 8.7. Transmission electron microscopy images of 7.2-nm cobalt nanocrystals coated with dodecanoic acid and ordered in a compact hexagonal network: not annealed (A) and annealed at 300°C (E). Corresponding high-resolution images (B, F) and electron diffraction patterns (C, G.). Multilayers of cobalt nanocrystals: not annealed (D) and annealed at 300°C (H).

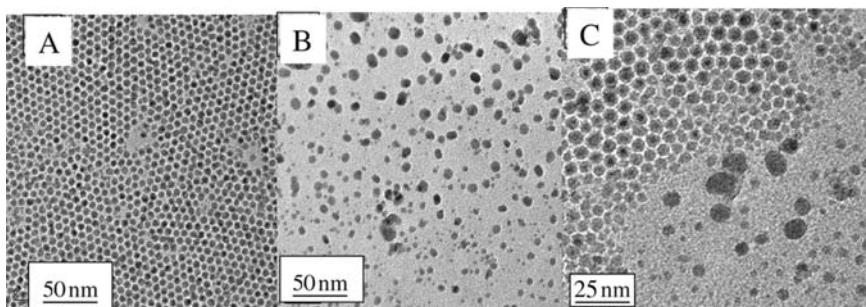


FIGURE 8.8. Transmission electron microscopy image of 7.2-nm cobalt nanocrystals after annealing at 300°C: a compact hexagonal network (A), isolated nanocrystals (B), and a monolayer with isolated nanocrystals in its surroundings (C).

(Figs. 8.7E and 8.7H) either the particle diameter (7.2 nm) or the average distance between their neighbors (3.55 nm). However, it improves the crystallinity of the particles with the formation of pure hexagonal compact packed (hcp) nanocrystals (Figs. 8.7F and 8.7G). Furthermore, by annealing cobalt nanocrystals in powder form at 275°C, it is possible to redisperse them in a nonpolar solvent and obtain the same organization as those formed before annealing. In addition, the crystallinity is improved with the formation of pure hcp nanoparticles.<sup>56</sup> It must be noted that the monolayers annealed at 300°C<sup>55</sup> are either oxidized in CoO or keep their hcp metal cobalt form. In both cases, the organization is not changed (Fig. 8.8A). For nanocrystals dispersed on a substrate, coalescence takes place (Fig. 8.8B). From this, it is concluded that self-organization of nanocrystals prevents coalescence. This claim is confirmed in Fig. 8.8C, where, obviously, the nanocrystals in the superlattice are protected from coalescence. This is one of the first intrinsic properties of the self-organization. This is explained in terms of collective entropy gained by nanocrystal ordering, which contributes a substantial amount of stabilization energy to the superlattice. Annealing “supra” crystals of cobalt nanocrystals does not change the ordering and keeps the fcc structure (Figs. 8.9A and 8.9B).<sup>55</sup> Furthermore, from the XRD patterns, the ordering of the “supra” crystals increases, with an increase in the Bragg peak of the (111) reflection—to-ring intensity ratio and a decrease in the Bragg peak width (Fig. 8.9E), compared to the native sample (Fig. 8.9D). Note that the interparticle gap decreases from 3.55 nm to 2.65 nm with increasing the temperature from 25°C to 300°C. Furthermore, cracks appear (Fig. 8.9B), favoring the decrease of the constraints existing in the native superlattice. The reduction of the interparticle gap is due to the coating agent compaction. From this, it is concluded that thermal treatment of “supra” crystals induces, as in the bulk phase, an increase in the nanocrystal order. A further increase in the annealing temperature to 350°C induces the formation of small domains (Fig. 8.9C) and breaks the “supra” crystal ordering with a shift of the Bragg peak toward a smaller angle in the XRD pattern (Fig. 8.9F). This indicates a dilatation of the (111) planes of about 0.8 nm compared to the “supra” crystal annealed at 300°C.

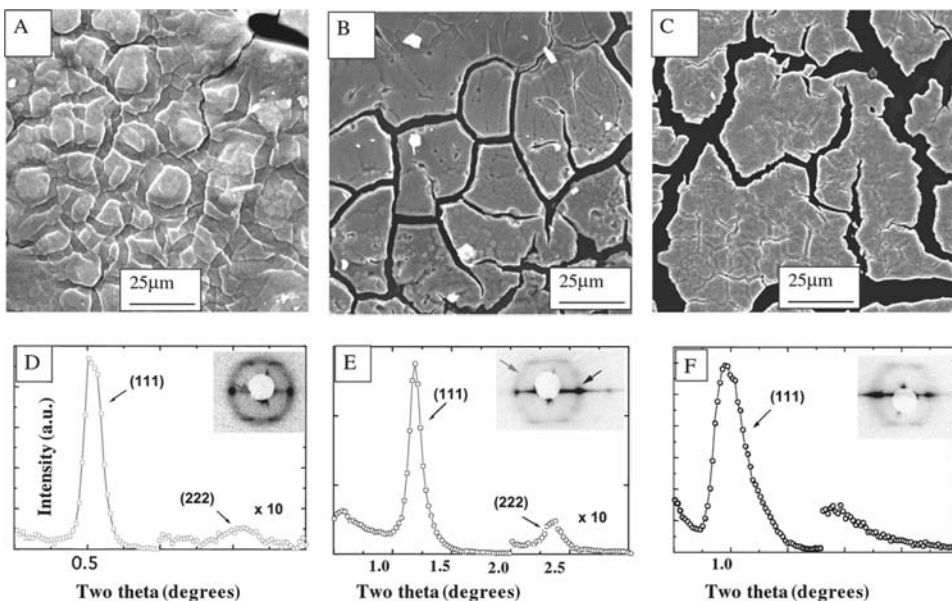


FIGURE 8.9. Scanning electron microscopy images of 7.2-nm cobalt nanocrystals ordered in “supra” crystals not annealed (A), annealed at 300°C (B), and annealed at 350°C (C). (D, E, F) Corresponding diffractograms obtained by imaging plate scanning and corresponding to the X-ray diffraction patterns obtained in a grazing incidence geometry (insets).

As already mentioned, 2D hexagonal networks of nanocrystals and 3D fcc superlattices are the most commonly observed organizations with low-size-distribution nanocrystals. However, it was shown that the use of external force as in the Langmuir–Blodgett technique can improve the 2D hexagonal nanocrystal organization.<sup>57–60</sup> Moreover, with this technique, the monolayer is transferred onto various substrates. Other external forces such as convection modes in the liquid phase<sup>33,34</sup> and application of a magnetic field induce the formation of new patterns. Magnetic nanocrystals with dominant dipolar attractions tend to organize in chainlike structures, for an applied field parallel to the substrate. This was well demonstrated with iron<sup>61</sup> and magnetite<sup>31</sup> nanocrystals. Similar organizations can be obtained with weakly dipolar nanocrystals by evaporation of the ferrofluid in a magnetic field applied parallel to the substrate. Such experiments were made with spherical cobalt ferrite,<sup>38</sup> maghemite,<sup>36,62,63</sup> and cobalt<sup>37</sup> and with acicular nickel<sup>64</sup> and maghemite<sup>65</sup> nanocrystals.

The organization in the absence and in presence of a magnetic field differs with the evaporation rate.<sup>37</sup> When evaporation takes place in air and in the absence of a magnetic field, a 3D film with high roughness is obtained (Fig. 8.10A). High magnification (insert in Fig. 8.10A) shows that cobalt nanocrystals tend to aggregate in 70-nm-diameter spherical shapes. The application of a magnetic field induces the formation of a linear structure (Fig. 8.10B), made of these 70-nm spherical

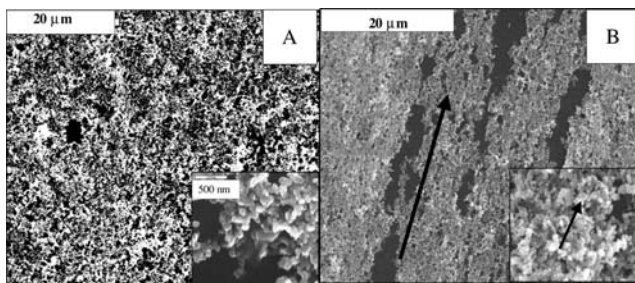
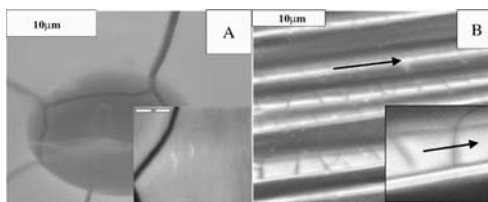


FIGURE 8.10. Scanning electron microscopy images of 3D films made of spherical cobalt nanocrystals, deposited in the absence (A) and in the presence (B) of an applied magnetic field ( $H = 0.78$  T) parallel to the substrate. The evaporation takes place in air in 45 min. The solvent is hexane.

aggregates (insert in Fig. 8.10B). Under hexane vapor, such aggregates are not observed and a homogeneous film, with cracks, is observed without an applied field (Fig. 8.11A), and, in its presence, long stripes corresponding to a highly compact film are seen (Fig. 8.11 B). Hence, these changes in morphologies are related to the evaporation rate and again to nanocrystal interactions. A rapid evaporation favors the close approach between nanocrystals and attractive van der Waals and dipolar interactions between nanocrystals increase, inducing spherical aggregation. In a slow evaporation, the nanocrystals freely diffuse in solution, leading to formation of homogeneous structures.

Recently in our laboratory, solid mesostructures such as columns or labyrinths of cobalt nanocrystals were produced by applying a magnetic field during the evaporation of the fluid containing magnetic nanocrystals dispersed in a nonpolar solvent. Columns and labyrinths are produced either simultaneously or separately. A theory was developed to understand the formation of these patterns. Taking into account the radius, the height of the cylinders, the magnetic phase to the total volume ratio, and the center-to-center distance between cylinders and by using the model developed in Ref. 41, the estimated interfacial tension, deduced by the minimization of the total free energy, is  $5 \times 10^{-5} \text{ N m}^{-1}$ . From this, it is concluded that the formation of structures takes place in a concentrated solution of nanocrystals induced by a liquid–gas phase transition and not via a Rosenweig instability.<sup>52</sup> This is confirmed by a video recorded during the evaporation process.

FIGURE 8.11. Scanning electron microscopy images of 3D films made of spherical cobalt nanocrystals, deposited in the absence (A) and in the presence (B) of an applied magnetic field ( $H = 0.78$  T). The evaporation takes place under a saturated hexane atmosphere in 12 h.



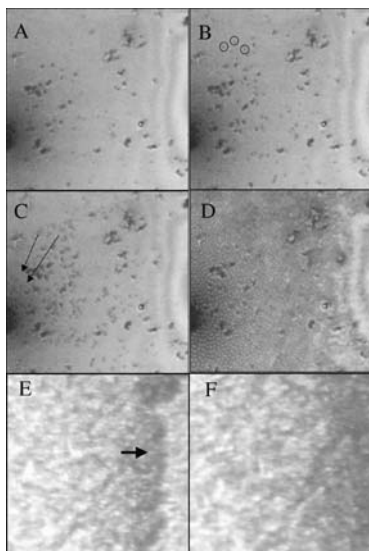


FIGURE 8.12. Video microscopy image obtained during the evaporation of a cobalt nanocrystal solution in a 0.25-T magnetic field at the instant when the columns appear. A silicon substrate is used. The ring in (B) encloses the columns, the arrows in (C) indicate the direction of column diffusion. (E, F) Images obtained at the end of the evaporation of a cobalt nanocrystal solution. The arrows indicate the direction of the wave created by the capillary forces.

Dots appear 7 h after the evaporation starts (Fig. 8.12A). Figure 8.12 shows that the number of dots increases progressively and then they migrate in the solution to form a hexagonal array (Fig. 8.12D). At the end of the evaporation, a wave due to capillary forces induces the collapse of the columns (Figs. 8.12E and 8.12F). This is confirmed by the scanning electron microscopy (SEM) image recorded at the end of the evaporation process (Fig. 8.13).



FIGURE 8.13. Scanning electron microscopy image obtained at the end of the evaporation process.



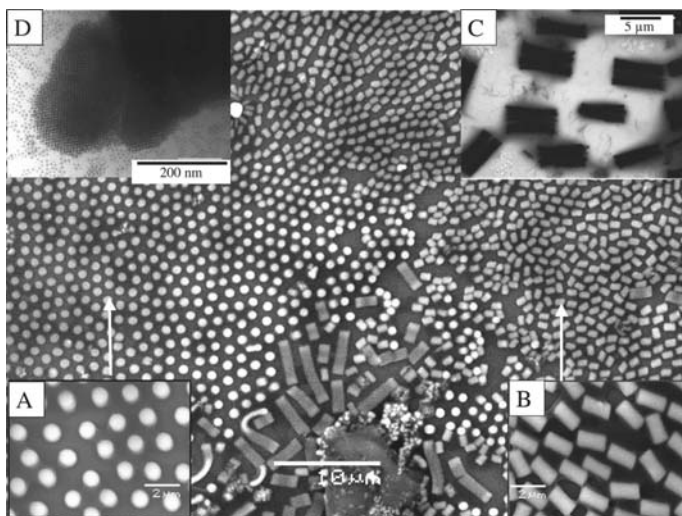


FIGURE 8.14. Scanning electron microscopy image of mesostructures made of 5.7-nm cobalt nanocrystals with 13% size distribution. The vertical magnetic field strength applied during the evaporation process is 0.25 T. Insets A and B are magnifications of the SEM image, insets C and D are TEM images at two different magnifications, obtained with the same experimental procedure.

At this point, a question arises: What process controls the formation of columns and/or labyrinths? To answer this, we have to take into account the size distribution of nanocrystals with mainly the same average nanocrystal size. The SEM image shown in Fig. 8.14 is produced with nanocrystals having a 5.7-nm average diameter and 13% size distribution. Well-defined structures are produced with formation of dots (inset A in Fig. 8.14), collapsed columns (inset B in Fig. 8.14) and very few labyrinths. On replacing HOPG by a TEM substrate, the columns are well defined, as shown in inset C of Fig. 8.14, and their ends are highly organized in fcc structures (inset D of Fig. 8.14).

By increasing the size distribution to 18% and keeping a similar average diameter (5.9 nm), the SEM pattern markedly differs, with the appearance of labyrinths and flowerlike patterns (Fig. 8.15). Insets A and B show that the flowerlike patterns are, in fact, the ends of fused columns and that they tend to form wormlike patterns and labyrinths, as shown in Fig. 8.15. By using the same procedure as that described earlier, the TEM image shows that the columns are not well defined (inset C in Fig. 8.15) and their extremities are totally disordered (inset D of Fig. 8.15). A careful examination of the labyrinthine structures shows that they are made of fused columns having more or less the same height (Fig. 8.16).

From these data and those reported in Refs. 42 and 66–68, we have quite good knowledge of the mechanism of the production of mesostructures when magnetic nanocrystals are subjected to a rather large vertical applied field. It can be concluded

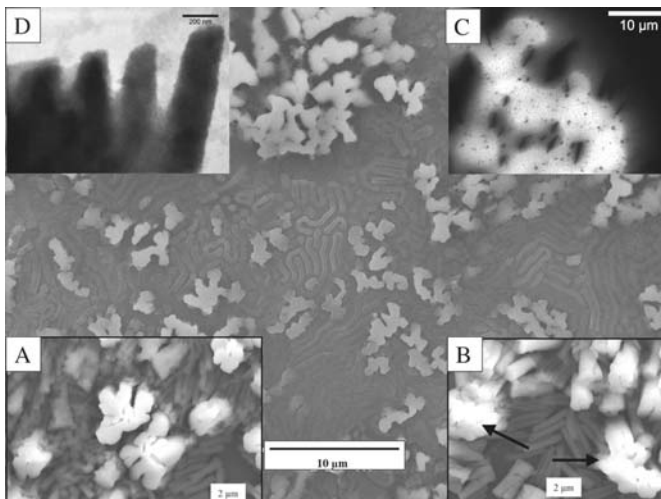


FIGURE 8.15. Scanning electron microscopy images of mesostructures made of 5.9-nm cobalt nanocrystals with 18% size distribution. The vertical magnetic field strength applied during the evaporation process is 0.25 T; silicon is used as the substrate. Insets A and B are magnifications of the structures in the SEM image. Insets C and D are TEM images at two different magnifications, obtained with the same experimental procedure.

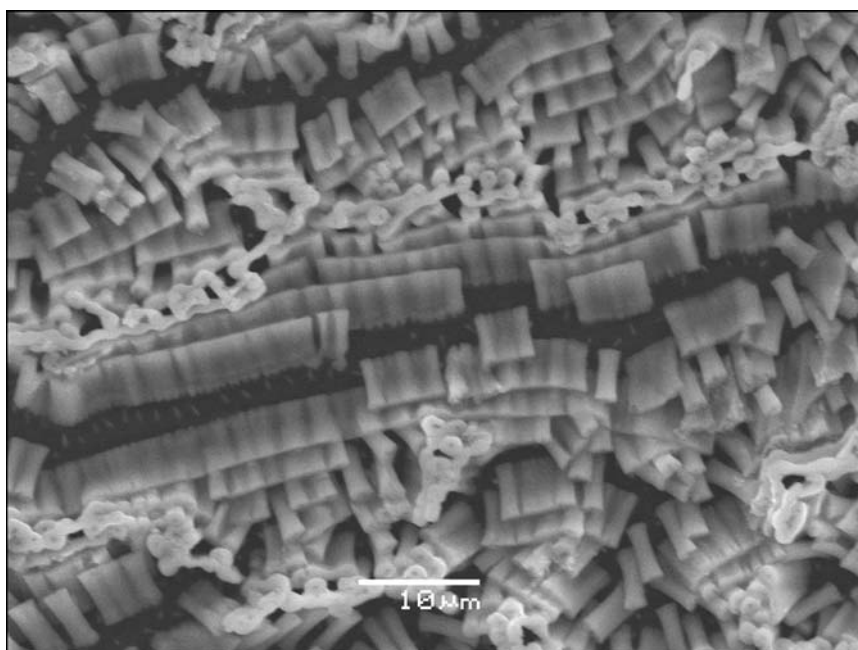


FIGURE 8.16. Scanning electron microscopy image of labyrinthine structures showing that they are made of fused columns.

that the column growth in the concentrated liquid phase of cobalt nanocrystals is induced by a phase transition. They migrate inside the solution to self-organize into a hexagonal network. Waves induced by capillary forces induce the collapse of most of these columns. Their rigidity is controlled by the ability of nanocrystals to self-organize into fcc structures. They retain their integrity. Conversely, the disorder inside and at the edges of the columns, mainly due to the large size distribution of the nanocrystals, induces their fusion. However, because the columns are formed in the solution, those having a similar size tend to attract each other by van der Waals interactions and to fuse. This makes it possible to produce rather homogenous wormlike structures or labyrinths. Furthermore, these mesostructures are independent of the strength of the applied field in the range 0–0.8 T because the experiments are carried out where there is nonlinear behavior of the magnetic field.

### 8.3. Collective Magnetic Properties of Mesostructures Made of Magnetic Nanocrystals

Beyond the experimental evidence of the influence of the dipolar interaction, we want to show how the various parameters influence the magnetic response. The mesostructures are obtained by evaporation of the ferrofluid on the HOPG substrate. During this process, a magnetic field is or is not applied parallel to the substrate plane.

At room temperature, due to their superparamagnetic behavior, the magnetization of the cobalt nanocrystals dispersed in solution shows no hysteresis. The blocking temperature, as determined by ZFC/FC experiments,\* increases with the nanocrystal size (Table 8.3). This corresponds to a decrease in the magnetic anisotropy energy (MAE), as it has been reported for magnetic nanocrystals.<sup>69</sup> For spherical nanocrystals, it is related to the increase in the surface anisotropy when the size decreases. Decreasing the temperature allows recovering classical ferromagnetic behavior, characterized by a nonzero value of the remanent magnetization,  $M_r$ , even when there is no applied field.

At 3 K, the thermal excitation vanishes and the magnetization curves of the cobalt nanocrystals dispersed in hexane show a classical hysteresis. For isolated nanocrystals, the saturation magnetization,  $M_s$ , is not reached and it is deduced

---

\* The zero-field-cooled/field-cooled experiment (ZFC/FC) is a typical experiment in the measurement of the magnetization of nanoparticles. The sample is initially cooled in a zero field to 3 K. A 75-Oe field is then applied and magnetization is recorded as the temperature is increased. This curve is called zero-field cooled. At a given temperature, called the blocking temperature,  $T_b$ , a maximum is the magnetization is observed. In the field cooled, (FC), far above  $T_b$ , the sample is progressively cooled and the magnetization is recorded. In a system without interactions, the magnetization increases continuously by decreasing the temperature. In a strongly interacting system, the FC curve shows a plateau below  $T_b$ , more or less pronounced, depending on the strength of the interactions.

TABLE 8.3. Magnetic properties of Co nanocrystals depending on their organization

Size (nm)	$M_s$ (emu/g)	0D			1D <sup>a</sup>			2D <sup>b</sup>		
		$H_c$ (T)	$M_r/M_s$	$T_b$	$H_c$ (T)	$M_r/M_s$	$T_b$	$H_c$ (T)	$M_r/M_s$	$T_b$
5.8	110 ± 5	0.12	0.25	60	0.13 (//) 0.10 (⊥)	0.31 (//) 0.19 (⊥)	—	0.12 (//) 0.12 (⊥)	0.29 (//) 0.21 (⊥)	65
8	120 ± 5	0.13	0.45	70	0.14 (//) 0.10 (⊥)	0.60 (//) 0.25 (⊥)	90	0.13 (//) 0.13 (⊥)	0.52 (//) 0.35 (⊥)	85

0D: isolated in solutions; 1D: linear chains; 2D: monolayers;  $T_b$ : blocking temperature.  
<sup>a</sup>(//) is for a field applied parallel to the chains and the substrates ( $x$  direction); (⊥) is for a field perpendicular to the chains but keeping the substrates parallel ( $y$  direction)  
<sup>b</sup>(//) is for a field applied parallel to the substrates ( $x,y$  planes); (⊥) is for a field perpendicular to the  $x,y$  plane ( $z$  direction).

from extrapolation (Table 8.3). The slight increase in  $M_s$  on increasing the size could be due to a relative decrease in the surface effect as the average size increases. Figure 8.17 shows the hysteresis loop of the cobalt nanocrystals having various average sizes (5.8 nm and 8 nm; Figs. 8.17A and 8.17B, respectively) either isolated in solution (Figs. 8.17C and 8.17D) or deposited as 2D monolayers on cleaved graphite (Figs. 8.17E and 8.17F). A typical monolayer of cobalt nanocrystals is shown in Fig. 8.18A. During the measurement at 3 K, the sample is kept parallel to the external applied field ( $x,y$  plane). For any size, the hysteresis loop is squarer than that for the same nanocrystals isolated in solution.<sup>70</sup> On the other hand, the reduced remanence increases (Table 8.3). This change is more pronounced for larger nanocrystals. Similarly, the blocking temperature increases when the nanocrystals are organized in 2D monolayers (Table 8.3). The hysteresis loop appears smoother when the sample is normal ( $z$  direction) compared to the

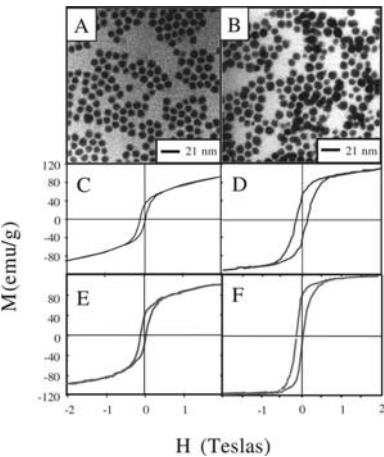
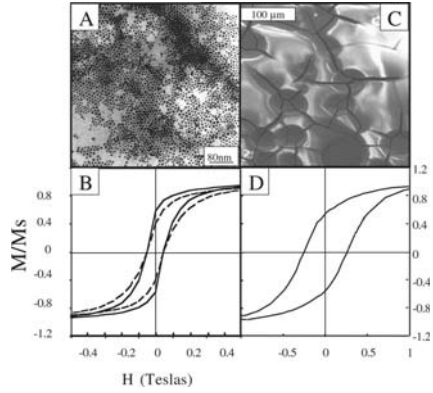


FIGURE 8.17. Transmission electron microscopy characterization (A and B) and corresponding hysteresis loop recorded at 3 K of cobalt nanocrystals either isolated in solution (C and D) or deposited as a monolayer on a HOPG substrate with the field applied parallel (E and F). (A, C, E) 5.8-nm diameter cobalt nanocrystals; (B, D, F) 8-nm diameter cobalt nanocrystals.

FIGURE 8.18. Transmission electron microscopy pictures: 2D showing organization (A) and 3D organization (C) of cobalt nanocrystals. The corresponding hysteresis loop at 3 K is reported for each mesostructure: (B) for 2D monolayers, solid line: the magnetic field is applied parallel to the substrate ( $x,y$  plane); dotted line: the magnetic field is applied perpendicular to the substrate ( $z$  direction); (D) for 3D film, the magnetic field is applied parallel to the substrate ( $x,y$  plane).



same sample kept parallel to the external field (Fig. 8.18B). As expected theoretically and shown in Fig. 8.19, this effect is attributed to the long-range dipolar interaction. This is quantified by the  $\gamma$  value, defined as the ratio of the reduced remanence in normal and parallel geometry [ $\gamma = (M_r/M_s)^\perp / (M_r/M_s)^\parallel$ ]. This experimental value is compared to the theoretical one knowing the value of the coupling constant  $\alpha_d$ . Hence, from a coupling constant,  $\alpha_d$ , of 0.05 calculated for 8-nm cobalt nanocrystals, the theoretical ratio,  $\gamma_{th} = 0.66$ , whereas it is 0.65

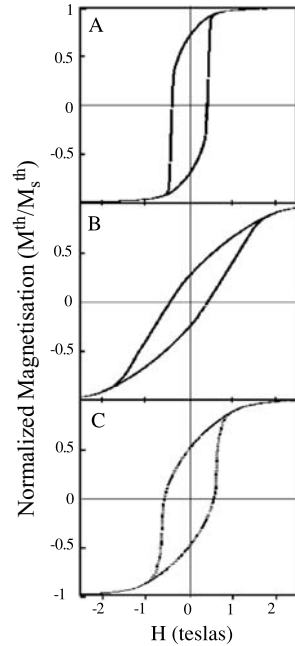


FIGURE 8.19. Calculated hysteresis curve for Stoner–Wohlfarth magnetic particles. The high value of  $\alpha_d$  is a limiting case for the 8-nm cobalt nanocrystals presented here. (A)  $\alpha_d = 0.1$ , the applied field is parallel to the surface  $x,y$  plane. (B)  $\alpha_d = 0.1$ , the applied field is perpendicular to the surface  $z$  direction. (C) Noninteracting particles ( $\alpha_d = 0$ ), this corresponds to isolated particles in solution.

from experiment.<sup>70</sup> Similar and less pronounced behavior is obtained for 5.8-nm cobalt nanocrystals (Table 8.3). Thus, the good agreement obtained between the experimental and theoretical values of  $\gamma$  confirms that the collective effects on the magnetic properties of the 2D monolayers made of cobalt nanocrystals are mainly due to the dipolar interaction between adjacent nanocrystals. Similar behavior also has been reported since then for  $\epsilon$ -cobalt nanocrystals in hexagonal ordered monolayers and, again, the collective properties were attributed to the dipolar interaction.<sup>8</sup>

The 3D thin films of cobalt nanocrystals can be obtained by slow evaporation (Fig. 18C).<sup>37</sup> The magnetic response, recorded in a parallel configuration, of these unorganized 3D films (Fig. 8.18D) is similar to that of the 2D monolayers; the reduced remanence,  $M_r/M_s$ , is 0.51 instead of 0.52. Conversely, the coercive field increases;  $H_c = 0.25$  T compared to that of isolated or 2D monolayers, 0.13 T. On the other hand, as for 2D organizations, the blocking temperature increases as a signature of the magnetic interaction. The change in the coercivity is attributed to small ferromagnetic domains made of several adjacent particles having the same orientation of their magnetic moment. Thus, in these unorganized 3D films of nanocrystals, dipolar interactions exist and induce changes in the magnetic response. However, the behavior is quite similar to those of granular films or to the observed increase in the dipolar interaction by increasing the volume fraction of nanoparticles in solution.<sup>71,72</sup>

The structural order does not seem to be a crucial parameter; as a matter of fact, the 2D monolayers described earlier (Fig. 8.18A) are rather highly disordered. This is confirmed by modeling. The hysteresis loop was calculated assuming two models: the real disordered model (Fig 8.20A) and a reference well-ordered model (Fig. 8.20B). For this, an effective coupling constant,  $\alpha_d^{\text{eff}}$ , is determined, which takes into account the mean density of nanocrystals in the disordered monolayers.<sup>73</sup> The surface occupation fraction,  $\Phi$ , is the ratio of the surface occupied by the nanocrystals,  $n_s \pi D^2/4$ , to that of the lattices,  $l^2$ . This determines the lattice spacing,  $d_0$ , which is the average distance between adjacent nanocrystals,  $d_0$ , and is related to the surface occupation fraction,  $\Phi$ , of the layer as follows:

$$(d_0/D) = (\pi/4\Phi)^{1/2}, \quad (8.1)$$

with  $\Phi = n_s \pi D^2/4l^2$ . Then, the effective coupling constant is

$$\alpha_d^{\text{eff}} = \frac{\pi M_s^2}{12K} \left( \frac{D}{d_0} \right)^3, \quad (8.2)$$

where  $\alpha_d^M = \pi M_s^2/12K$  is the maximum value of the coupling constant defined above.  $\alpha_d^{\text{eff}}$  is used to calculate the magnetization of the well-ordered reference model. Details of the calculation are given in Ref 73. Figure 8.20D shows no difference in the hysteresis loop for ordered and disordered monolayers. This is observed for the two orientations of the magnetic field. Hence, due to the long-range order of the dipolar interaction, the local structure of the monolayer is not important: A well-ordered reference model is suitable for calculating the hysteresis

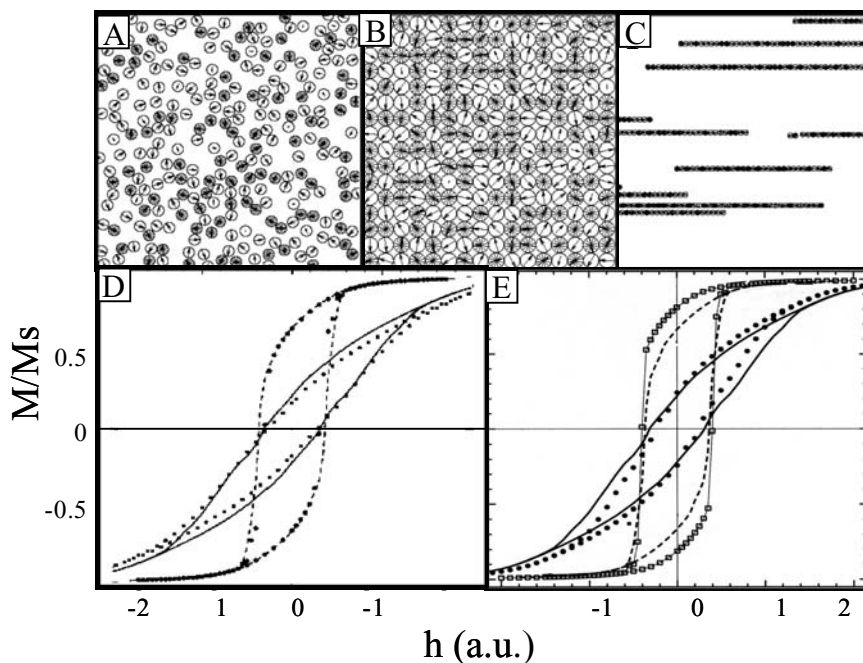


FIGURE 8.20. Calculated hysteresis curve for 2D (D) and 1D (E) mesostructures made of uncoalesced magnetic nanoparticles. The corresponding structures are, respectively, in A and C. Dotted line: applied field in the  $x$  direction assuming a perfect square lattice as reference model; (B) solid line; applied field in the  $z$  direction assuming a perfect square lattice with a similar density of nanoparticles. In each case, the exact calculations corresponding to the real structure correspond to the square ( $x$  directions) and to the circle ( $z$  direction). In the case of the linear chains, there is a large discrepancy if the magnetic field is applied in the  $x$  direction during the measurement. In PARTS A, B, and C, the length of the arrow corresponds to the projection of the magnetic moment in the  $x, y$  plane; there is no alignment of the magnetic moment due to the dipolar interactions.

curve of an isotropic disordered monolayer, for any orientation of the applied field relative to the substrate.

At this point, a question arises: Does ordering in 3D superlattices change the magnetic behavior? To answer this question, the magnetic properties of 3D films, either highly ordered in an fcc structure or disordered, are compared. Let us first describe the system used: 7.2-nm-diameter cobalt nanocrystals with a low size distribution (12 %) are produced.<sup>11</sup> As shown in Fig. 8.5, it is possible to obtain either “supra” crystals characterized by a long-range fcc ordering of the nanocrystals<sup>12</sup> or a disordered 3D film of uncoalesced cobalt nanocrystals.<sup>46</sup> The magnetization curves recorded at 3 K and with an applied magnetic field parallel to the substrate are shown in Fig. 8.21C. The hysteresis loop appears squarer when nanocrystals are ordered, compared to the disordered systems.<sup>46</sup> For “supra” crystals, the

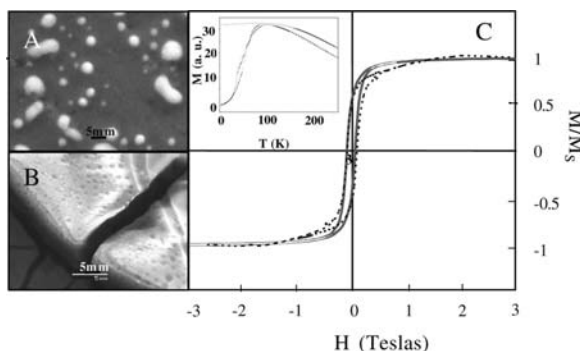


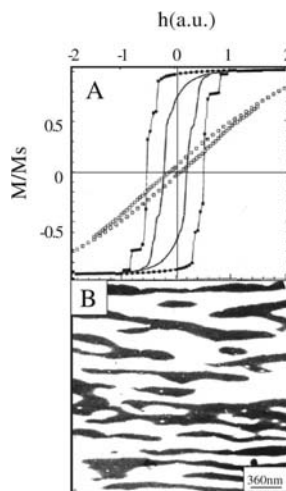
FIGURE 8.21. (A) Scanning electron microscopy image of disorganized 7.2-nm cobalt 3D film. (B) SEM image of superlattices made of 7.2-nm Co nanocrystals. (C) Corresponding hysteresis magnetization loops obtained at 3 K. In the inset are the ZFC/FC curves: Amorphous assembly (dotted line); “supra” crystal (solid line).

saturation magnetization is reached at 0.3 T, whereas with an amorphous aggregate, it is around 1.5 T. In both cases, the saturation magnetization is 120 emu/g and the coercivity is 0.07 T. Moreover, the zero-field-cooled and field-cooled (ZFC/FC) curves, recorded with a 75-Oe field (inset of Fig. 8.21C) show a lower blocking temperature for an amorphous film (95 K) compared to that obtained for fcc “supra” crystals (115 K). Such differences can be explained by taking into account the structural results described earlier. The decrease in the average distance between nanocrystals of 1 nm, when they are organized, induces an increase in the coupling constant,  $\alpha_d$ , from 0.025 in the disordered case to 0.030 in the fcc superlattices. This change in the blocking temperature and the squareness of the hysteresis loop correspond to an increase in the dipolar interaction. Hence, the internal order of 3D films plays a role in the collective magnetic properties via the increase in the coupling constant.

For magnetic nanocrystals in 1D chains (Fig. 8.20C), it is no longer possible to model the magnetic behavior of linear chains (open squares, Fig. 8.20E) made of uncoalesced nanocrystals by a well-ordered reference model (dotted line, Fig. 8.20E), when the magnetic field is applied parallel to the chains and the substrate. An exact calculation taking into account the position of each particle in the 1D organization is necessary to obtain the hysteresis loop of a network of linear chains.<sup>73</sup> To confirm such a claim, calculations have been made for a very high coupling constant ( $\alpha_d = 0.26$ ) with the same nanoparticle density. The hysteresis loop appears squarer than that observed for a monolayer of nanoparticles (Fig. 8.22A). Moreover, conversely to the isotropic monolayer, the magnetic response of the 1D chains changes drastically with the direction of the applied field parallel ( $x$  direction) or perpendicular ( $y$  direction) to the measured field, keeping the plane of the substrate parallel (Fig. 8.22A). In fact, due to the dipolar coupling, the linear chains behave roughly as homogeneous wires with an effective easy axis in the direction of the chains, although individual nanocrystals have randomly



FIGURE 8.22. (A) Magnetization for particles organized in chains;  $\alpha_d^{\text{eff}} = 0.26$ . Solid squares: linear chains parallel to the applied field ( $x$  direction); open squares: linear chains perpendicular to the applied field ( $y$  direction). Solid lines correspond to a perfect square lattice. (B) TEM pictures of 1D organization of 8-nm cobalt nanocrystals.



distributed easy axes. In this case, the strength of the structural effect is estimated theoretically by comparing the reduced remanence in the two geometries. As previously, a ratio  $\gamma'_{\text{th}} = (M_r/M_s)^\perp / (M_r/M_s)^\parallel$ , can be deduced for the linear chains oriented in the  $x$  direction from the two calculations corresponding to  $h = y$  and  $h = x$ , respectively.

In the experiments, cobalt nanocrystals (8 nm) dispersed in hexane are subjected to an applied field (1 T) during the evaporation process. This produces linear chains of uncoalesced nanocrystals (Fig. 8.22B). The average width is  $300 \pm 50$  nm and the interchain distance is around 600 nm. A closer view of the chains indicates that they are formed by uncoalesced cobalt nanocrystals in monolayers or bilayers, without any internal order.<sup>74</sup> Their magnetic properties differ markedly from those of the isotropic monolayers. When the measuring field is parallel to the chain and thus also to the substrate plane, the hysteresis curve appears to be squarer than that of the isotropic 2D monolayer measured with a field parallel to the substrate (Fig. 8.23A). The reduced remanence increases and the saturation is reached at a lower field. These changes increase with the coupling constant (i.e., with the size of the nanocrystals) (Table 8.3). On turning the chain by  $90^\circ$ , the field remains in the plane but perpendicular to the chains and induces a smoother loop with a decrease in the reduced remanence (Fig. 8.23B and Table 8.3). Similar and less pronounced behavior is observed for 5.8-nm cobalt nanocrystals (Table 8.3). For 8-nm cobalt nanocrystals, the coupling constant is 0.05. Figure 8.23C shows the theoretical change in the hysteresis loop with the orientation of the applied field with a ratio,  $\gamma'_{\text{th}} = (M_r/M_s)^\perp / (M_r/M_s)^\parallel$ , equal to 0.77. From the experimental data (Fig. 8.23B),  $\gamma'_{\text{exp}} = 0.42$ . Rather good agreement between experiments and calculated data is obtained. Obviously, the experimental samples do not have the perfect chainlike structure introduced in the model (compare Figs. 8.22B and 8.20C). This probably explains the difference in magnitude between experiment

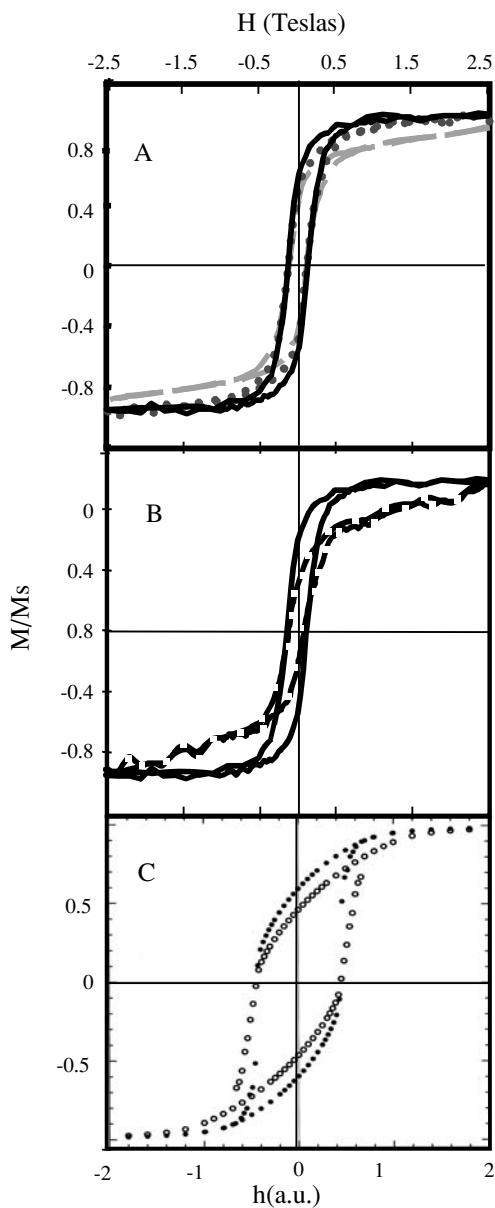


FIGURE 8.23. (A) The hysteresis loop at 3 K is reported for the 1D chains (solid line); the magnetic field is applied parallel to the substrate and to the chains ( $x$  direction). Comparison is made with the 2D monolayer (solid circle) and isolated in solution (dotted line). (B) Hysteresis loop, measured at 3 K, of aligned 8-nm cobalt nanocrystals. The applied field is either parallel (solid line) or normal (dotted line) to the directions of the chains, keeping the substrate parallel to the applied field. (C) Calculated hysteresis curve for linear chains made of 8-nm cobalt nanocrystals for  $\alpha_d^{\text{eff}} = 0.06$  with an applied field either parallel ( $\bullet$ ) or normal ( $\circ$ ) to the directions of the chains, keeping the substrate parallel to the applied field.

and theory. On the other hand, an effect of the alignment of the easy axes during the deposition in a field cannot be totally excluded and could also explain the discrepancy between theory and experiment. Indeed, the results reported above appear to be mainly a structural effect on the collective magnetic properties in the 1D chains made of uncoalesced cobalt nanocrystal, as predicted theoretically. Due to the dipolar interactions, the chains behave like wires with an effective easy axis in the direction of the wire.

## 8.4. Conclusion

The last few years have seen extremely rapid advances in the preparation of very narrow size distributions of various types of nanomaterial. These advances have enabled many groups to make 2D and 3D nanoparticle superlattices. In the same way, organizations of nanocrystals in mesoscopic patterns such as rings, chains, and ribbons have also been developed. Some of these patterns require the presence of external forces to be formed. These various systems constitute an open research field and many exciting phenomena remain to be discovered. Such new materials could have a significant impact on future electronic, optics, and magnetic storage devices. In fact, we demonstrated collective magnetic properties due to the self-organization of nanocrystals. For these mesostructures made of uncoalesced nanocrystals, the dipolar interactions are responsible for the collective behavior. The theoretical model presented here gives a general framework to explain, at least qualitatively, the magnetic collective properties. Furthermore, in spite of the long-range scale of the dipolar interaction, it has been shown that the structure of the organization of nanocrystals plays an important role in the magnetic response depending on whether they are in zero dimension (0D), 1D, 2D, or 3D. Beyond this, the internal order also changes the magnetic behavior and, indeed, these intrinsic properties can have an important role in the future.

## Acknowledgments

The data presented in this chapter are mainly produced by Dr. C. Petit, Dr. V. Russier, and Dr I. Lisiecki. I would like to thank them. Dr. G. Lebras and Dr. E. Vincent, who provided us the SQUID facility from CEA/DSM/DRECAM /SPEC have also to be thanked.

## References

1. X. Batlle and A. Labarta, Finite-size effects in fine particles: magnetic and transport properties, *J. Phys. D* **35**, R15–R42 (2002).
2. S. A. M. Tofail, I. Z. Rahman, and M. A. Rahman, Patterned nanostructured arrays for high-density magnetic recording, *App. Organometal. Chem.* **15**, 373–382 (2001).

3. D. N. Lambeth, E. M. T. Velu, G. H. Bellesis, L. L. Lee, and D. E. Laughlin, Impact of new magnetoresistive materials on magnetic recording heads, *J. Appl. Phys.* **79**, 4496–4501 (1996).
4. S. Yamamuro, D. F. Farrell, and S. A. Majetich, Direct imaging of self-assembled magnetic nanoparticle arrays: Phase stability and magnetic effects on morphology, *Phys. Rev. B* **65**, 22,4431 (2002).
5. C. Petit, A. Taleb, and M. P. Pileni, Self-organization of magnetic nanosized cobalt particles, *Adv. Mater.* **10**, 259–261 (1998).
6. C. Petit, A. Taleb, and M. P. Pileni, Cobalt nanosized particles organized in a 2D superlattice: Synthesis, characterization and magnetic properties, *J. Phys. Chem. B* **103**, 1805 (1999).
7. V. F. Puentes, K. Krishnan, and P. Alivisatos, Synthesis, self-assembly, and magnetic behavior of a two-dimensional superlattice of single-crystal e-Co nanoparticles, *Appl. Phys. Lett.* **78**, 2187–2189 (2001).
8. S. Sun and C. B. Murray, Synthesis of monodisperse cobalt nanocrystals and their assembly into magnetic superlattices, *J. Appl. Phys.* **85**, 4235 (1999).
9. U. Wiedwald, M. Spasova, M. Farle, M. Hilgendorff, and M. Giersig, Ferromagnetic resonance of monodisperse Co particles, *J. Vac. Sci. Technol. A* **19**, 1773–1776 (2001).
10. F. Luis, F. Petroff, J. M. Torres, L. M. Garcia, J. Bartolomé, J. Carrey, and A. Vaurés, Magnetic relaxation of interacting Co clusters: Crossover from two- to three-dimensional lattices, *Phys. Rev. Lett.* **88**, 217,205 (2002).
11. I. Lisiecki and M. P. Pileni, Synthesis of well-defined and low size distribution cobalt nanocrystals: The limited influence of reverse micelles, *Langmuir*, **19**, 9486–9489 (2003).
12. I. Lisiecki, P. A. Albouy, and M. P. Pileni, Face-centered-cubic “supracrystals” of cobalt nanocrystals, *Adv. Mater.* **15**, 712–716 (2003).
13. Q. Guo, X. Teng, S. Rahman, and H. Yanga, Patterned Langmuir–Blodgett films of monodisperse nanoparticles of iron oxide using soft lithography, *J. Am. Chem. Soc.* **125**, 630–631 (2003).
14. T. Hyeon, S. S. Lee, J. Park, Y. Chung, and H. Bin Na, Synthesis of highly crystalline and monodisperse maghemite nanocrystallites without a size-selection process, *J. Am. Chem. Soc.* **123**, 12,798–12,801 (2001).
15. M. D. Bentzon, J. van Wonerghem, S. Morup, A. Tholen, and C. J. W. Koch, Ordered aggregates of ultrafine iron oxide particles, *Phil. Mag. B* **60**, 169 (1989).
16. P. Poddar, T. Telem-Shafir, T. Fried, and G. Markovich, Dipolar interactions in two- and three-dimensional magnetic nanoparticle arrays, *Phys. Rev. B* **66**, 60403–60407 (2002).
17. S. Sun, H. Zeng, D. B. Robinson, S. Raoux, P. M. Rice, S. X. Wang, and G. Li, Monodisperse  $MFe_2O_4$  ( $M = Fe, Co, Mn$ ) nanoparticles, *J. Am. Chem. Soc.* **126**, 273–279 (2004).
18. H. Zeng, P. M. Rice, S. X. Wang, and S. Sun, Shape-controlled synthesis and shape-induced texture of  $MnFe_2O_4$  nanoparticles, *J. Am. Chem. Soc.* **126**, 11,458–11,459 (2004).
19. M. Angelakeris, O. Crisan, E. Papaioannou, N. Vouroutzisa, I. Tsiaoussisa, E. Pavlidou, A. D. Crisana, I. Kostic, N. Sobal, M. Giersig, and N. K. Flevaris, Fabrication of novel magnetic nanostructures by colloidal bimetallic nanocrystals and multilayers, *Mater. Sci. Eng. C* **23**, 873 (2003).
20. O. Crisan, M. Angelakeris, M. Nogues, Th. Kehagias, Ph. Komninou, N. Sobal, M. Giersig, and N. K. Flevaris, Observation of the domain structure in Fe–Au superlattices

- with perpendicular anisotropy, *J. Magn. Magn. Mater.* **272–276**, e1253–e1254 (2004).
21. J. I. Park and J. Cheon, Synthesis of “solid solution” and “core-shell” type cobalt–platinum magnetic nanoparticles via transmetalation reactions, *J. Am. Chem. Soc.* **123**, 5743–5746 (2001).
  22. E. Shevchenko, D. Talapin, A. Rogach, A. Kornowski, M. Haase, and H. Weller, Colloidal synthesis and self-assembly of CoPt<sub>3</sub> nanocrystals, *J. Am. Chem. Soc.* **124**, 11, 480–11,485 (2002).
  23. E. Shevchenko, D. Talapin, H. Schnablegger, A. Kornowski, O. Festin, P. Svedlindh, M. Haase, and H. Weller, Study of nucleation and growth in the organometallic synthesis of magnetic alloy nanocrystals: The role of nucleation rate in size control of CoPt<sub>3</sub> nanocrystals, *J. Am. Chem. Soc.* **125**, 9090–9101 (2003).
  24. C. Petit, S. Rusponi, and H. Brune, Magnetic properties of cobalt and cobalt–platinum nanocrystals investigated by magneto-optical Kerr effect, *J. Appl. Phys.* **95**, 4251–4260 (2004).
  25. E. Shevchenko, D. Talapin, A. Kornowski, F. Wiekhorst, J. Kötzler, M. Haase, A. Rogach, and H. Weller, Colloidal crystals of monodisperse FePt nanoparticles grown by a three-layer technique of controlled oversaturation, *Adv. Mater.* **14**, 287–290 (2002).
  26. S. Wang, S. S. Kang, D. E. Nikles, J. W. Harrell, and X. W. Wu, Magnetic properties of self-organized L1<sub>0</sub> FePtAg nanoparticle arrays, *J. Magn. Magn. Mater.* **266**, 49–56 (2003).
  27. H. Zeng, J. Li, J. P. Liu, Z. L. Wang, and S. Sun, Exchange-coupled nanocomposite magnets by nanoparticle self-assembly, *Nature* **420**, 395–398 (2002).
  28. S. Sun, C. B. Murray, D. Weller, L. Folk, and A. Moser, Monodisperse FePt nanoparticles and ferromagnetic FePt nanocrystal superlattices, *Science* **287**, 1989–1992 (2000).
  29. M. H. Lu, T. Song, T. J. Zhou, P. P. Wang, S. N. Piramanayagam, W. W. Ma, and H. Gong, FePt and Fe nanocomposite by annealing self-assembled FePt nanoparticles, *J. Appl. Phys.* **95**, 6735–6337 (2004).
  30. S. Kang, Z. Jia, D. E. Nikles, and J. W. Harrell, Synthesis and phase transition of self-assembled FePd and FePdPt nanoparticles, *J. Appl. Phys.* **95**, 6744–6746 (2004).
  31. A. Philipse and D. Maas, Magnetic colloids from magnetotactic bacteria: Chain formation and colloidal stability, *Langmuir* **18**, 9977–9984 (2002).
  32. L. Motte, F. Billoudet, and M. P. Pileni, Self-assembled monolayer of nanosized particles differing by their sizes, *J. Phys. Chem.* **99**, 16,425–16,429 (1995).
  33. M. Maillard, L. Motte, A. T. Ngo, and M. P. Pileni, Rings and hexagons made of nanocrystals: A Marangoni effect, *J. Phys. Chem. B* **104**, 11,871–11,877 (2000).
  34. M. Maillard, L. Motte, A. T. Ngo, and M. P. Pileni, Rings and hexagons made of nanocrystals, *Adv. Mater.* **13**, 200–204 (2001).
  35. J. Legrand, C. Petit, and M. P. Pileni, Domain shapes and superlattices made of 8 nm cobalt nanocrystals: Fabrication and magnetic properties, *J. Phys. Chem B* **105**, 5643–5646 (2001).
  36. Y. Lalatonne, J. Richardi, and M. P. Pileni, Van der Waals versus dipolar forces controlling mesoscopic organizations of magnetic nanocrystals, *Nature Mater.* **3**, 121–125 (2004).
  37. C. Petit, J. Legrand, V. Russier, and M. P. Pileni, Three dimensional arrays of cobalt nanocrystals: Fabrication and magnetic properties, *J. Appl. Phys.* **91**, 1502–1508 (2002).
  38. A. T. Ngo and M. P. Pileni, Nanoparticles of cobalt ferrite: Influence of the applied field on the organization of the nanocrystals on a substrate and on their magnetic properties, *Adv. Mater.* **12**, 276–279 (2000).

39. Y. Lalatonne, L. Motte, V. Russier, A. T. Ngo, P. Bonville, and M. P. Pileni, Mesoscopic structures of nanocrystals: Collective magnetic properties due to the alignment of nanocrystals, *J. Phys. Chem. B* **108**, 1848–1854 (2004).
40. J. Legrand, A. T. Ngo, C. Petit, and M. P. Pileni, Domain shapes and superlattices made of cobalt nanocrystals, *Adv. Mater.* **13**, 58–62 (2001).
41. V. Germain and M. P. Pileni, Mesostuctures of cobalt nanocrystals. 2. mechanism, *J. Phys. Chem. B* **109**, 5548–5553 (2005).
42. V. Germain and M. P. Pileni, Size distribution of cobalt nanocrystals: A key parameter in formation of columns and labyrinths in mesoscopic structures, *Advanced materials* **17**, 1424–1429, (2005).
43. L. Motte, F. Billoudet, E. Lacaze, and M. P. Pileni, Self-organization of size-selected, nanoparticles into three-dimensional superlattices, *Adv. Mater.* **8**, 1018–1020 (1996).
44. A. Courty, C. Fermon, and M. P. Pileni, “supra crystals” made of nanocrystals, *Adv. Mater.* **13**, 254–258 (2001).
45. A. Courty, O. Araspin, C. Fermon, and M. P. Pileni, “Supracrystals” made of nanocrystals. 2. Growth on HOPG substrate, *Langmuir*, **17**, 1372–1380 (2001).
46. I. Lisiecki, P. A. Albouy, and M. P. Pileni, “Supra” crystal: Control of the ordering of self-organization of cobalt nanocrystals at the mesoscopic scale, *J. Phys. Chem. B*, **108**, 20050–20055 (2004).
47. A. W. Adamson and A. P. Gast, *Physical Chemistry of Surface*, 6th ed., Wiley–Interscience, New York, 1997.
48. J. Mahanty and B. Ninham, *Dispersion Forces*, Academic Press, London, 1976.
49. J. Israelachvili, *Intermolecular and Surfaces Forces*, 2nd ed., Academic Press, New York, 1991.
50. H. Morimoto and T. Maekava, Dynamic Analysis of ferromagnetic colloidal systems, *Int. J. Mod. Phys. B* **13**, 2085 (1999).
51. J. A. Lewis, Colloidal processing of ceramics, *J. Am. Ceram. Soc.* **83**, 2341–2359 (2000).
52. R. E. Rosenweig, *Ferrohydrodynamics*, Cambridge University Press, Cambridge, 1985.
53. J. Israelachvili, Solvation forces and liquid structure, as probed by direct force measurements, *Acc. Chem. Res.* **20**(11), 415–421 (1987).
54. A. Courty, A. Mermé, P. A. Albouy, E. Duval, and M. P. Pileni, Vibrational coherence of self-organized silver nanocrystals in f.c.c. “supra” crystals, *Nature materials*, **4**, 395–398 (2005).
55. I. Lisiecki, P.A. Albouy, C. Andreazza, and M. P. Pileni, “Supra-crystals” of cobalt nanocrystals: Intrinsic properties via annealing processes, submitted for publication.
56. C. Petit, Z. L. Wang, and M. P. Pileni, Seven nanometer HCP cobalt nanocrystals for high temperature magnetic applications through a novel annealing process, *J. Phys. Chem. B*, in press.
57. B. O. Dabbousi, C. B. Murrau, M. F. Rubner, and M. G. Bawendi, Langmuir Blodgett manipulation of size selected CdSe nanocrystallites, *Chem. Mater.* **6**, 216 (1994).
58. J. R. Heath, C. M. Knobler, and D. Leff, Pressure–temperature phase diagram and superlattices of organically functionalized metal nanocrystals monolayers: The influence of particle, size distribution and surface passivation, *J. Phys. Chem. B* **101**, 189 (1997).
59. S. Huang, G. Tsutsui, H. Skaue, S. Shingubara, and T. Takahagi, Probing characteristics of proximity x ray lithography and comparison with optical lithography at 100 nm and 70 nm technology modes, *J. Vac. Sci. Technol. B* **19**, 115 (2001).
60. Q. Guo, X. Teng, S. Rahman, and H. Yang, Patterned Langmuir–Blodgett film of monodisperse nanoparticles of iron oxides using soft lithography, *J. Am. Chem. Soc.* **125**, 630 (2003).

61. L. Zhang and A. Manthiran, Experimental study of ferromagnetic chains composed of nanosize Fe spheres, *Phys. Rev. B* **54**, 3462 (1996).
62. Y. Lalatonne, L. Motte, J. Richardi, and M. P. Pileni, Mesoscopic structures of maghemite nanocrystals: Collective magnetic properties due to the alignment of nanocrystals, *Phys. Rev. E* **3**, 121 (2004).
63. Y. Sahoo, M. Cheon, S. Wang, H. Luo, E. P. Furlani, and P. N. Prasad, Field directed self assembly of magnetic nanoparticles, *J. Phys. Chem. B* **108**, 3380 (2004).
64. H. Niu, Q. Chen, M. Ning, Y. JiaY., and X. Wang, Synthesis of one dimensional self-assembly of acicular nickel nanocrystallites under magnetic fields, *J. Phys. Chem. B* **108**, 3996 (2004).
65. A. T. Ngo and M. P. Pileni, Organization and magnetic properties of cigar-shaped ferrite nanocrystals, *New J. Phys.* **4**, 87 (2002).
66. J. Richardi, D. Ingert, and M. P. Pileni, Labyrinthine instability in magnetic fluids revisited, *J. Phys. Chem.* **106**, 1521 (2002).
67. J. Richardi, D. Ingert, and M. P. Pileni, Theoretical study of the field-induced pattern formation in magnetic liquids, *Phys. Rev. E* **66**, 46,306 (2002).
68. J. Richardi and M. P. Pileni, Nonlinear theory of pattern formation in ferrofluid films at high field strengths, *Phys. Rev. E* **69**, 16,304 (2004).
69. J. P. Chen, C. M. Sorensen, K. J. Klabunde, and G. C. Hadjipanayis, Enhanced magnetization of nanoscale colloidal cobalt particles, *Phys. Rev. B* **51**, 11,527 (1995).
70. V. Russier, C. Petit, J. Legrand, and M. P. Pileni, Collective magnetic properties of cobalt nanocrystals self-assembled in a hexagonal network: Theoretical model supported by experiments, *Phys. Rev. B* **62**, 3910 (2000).
71. J. L. Dormann, D. Fiorani, and E. Tronc, Magnetic relaxation in fine particles systems, *Adv. Chem. Phys.* **98**, 283 (1997).
72. R. W. Chantrell, N. Wamsley, J. Gore, and M. Maylin, Calculations of the susceptibility of interacting superparamagnetic particles, *Phys. Rev. B* **63**, 024410 (2000).
73. V. Russier, C. Petit, and M. P. Pileni, Hysteresis curve of magnetic nanocrystals monolayers: Influence of the structure, *J. Appl. Phys.* **93**, 10,001–10,010 (2003).
74. C. Petit, V. Russier, and M. P. Pileni, Effect of the structure of cobalt nanocrystal organization on the collective magnetic properties, *J. Phys. Chem. B* **107**, 10,333–10,336 (2003).

# 9

## Synthesis and Applications of Highly Ordered Anodic Porous Alumina

HIDEKI MASUDA<sup>†,‡</sup> AND KAZUYUKI NISHIO<sup>†</sup>

<sup>†</sup>*Department of Applied Chemistry, Tokyo Metropolitan University, Minamiosawa, Hachioji, Tokyo 192-0397, Japan and* <sup>‡</sup>*Kanagawa Academy of Science and Technology (KAST), Nishihashimoto, Sagami-hara, Kanagawa, 229-1131 Japan*

### 9.1. Introduction

Anodic porous alumina, which is formed by the anodization of Al, is a typical self-organized material utilizable for the fabrication of several types of functional nanodevice. The geometrical structure of anodic porous alumina is described as a closed-packed array of uniform-sized cylindrical units called cells, each of which has central straight pores perpendicular to the surface.<sup>1</sup> Compared with other nanomaterials, one important advantage of anodic porous alumina is that the geometrical structure of anodic porous alumina (pore sizes, pore intervals, and pore depths) can be controlled easily based on the anodizing conditions.

Anodic porous alumina has been applied in a wide variety of fields for many years because of its unique geometrical nanostructures.<sup>2–5</sup> Here, the synthesis of highly ordered anodic porous alumina and its application to the preparation of functional nanodevices will be described.

### 9.2. Synthesis of Highly Ordered Anodic Porous Alumina

#### 9.2.1. *Growth of Anodic Porous Alumina on Al*

When Al is anodized in a neutral electrolyte (e.g., ammonium phosphate), a thin uniform oxide layer is formed on the surface of Al. The thickness of the oxide layer is in a good linear relationship with the applied voltages ( $\sim 1.2 \text{ nm V}^{-1}$ ), and the oxide layer cannot grow above this thickness. In contrast, when an acidic solution is used as the electrolyte for anodization, a thick porous oxide layer is formed on the surface (Fig. 9.1). In the case of the anodization of Al in acidic solution, the resulting oxide is etched partially due to the solvent power of the acid solution. Then, at the once-etched sites, the selective growth and etching of the oxide layer proceed. At the bottom of the oxide layer, called the barrier layer, an oxide grows at the barrier layer through the migration of  $\text{Al}^{3+}$  and  $\text{O}^{2-}$  ions under a strong electric field. The diameter of the obtained cell can be approximated as twice the thickness of the barrier layer, under the



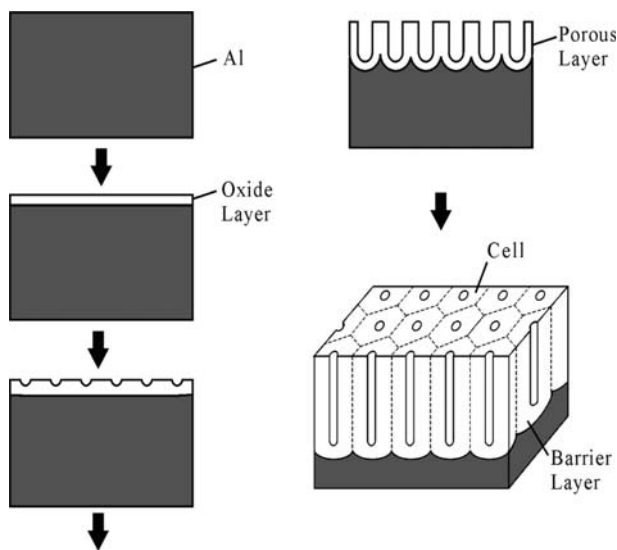


FIGURE 9.1. Scheme of the formation of anodic porous alumina.

condition that the ratio of occupation of the pores is neglected. This yields a simple relationship between the geometrical structures and applied voltage for anodic porous alumina. The hole interval, which is equivalent to the cell size, has a good linear relationship with the applied voltage ( $\sim 2.5 \text{ nm V}^{-1}$ ). The pore size is dependent on the concentration and temperature of the electrolyte, in addition to the applied voltage. However, it can also be controlled by the anodizing voltages. The pore diameter is, if needed, adjusted by postetching treatment in appropriate etching solutions. The depth of the pores is simply proportional to the anodizing time. Such controllability of the geometrical structures by the anodizing and the postanodizing conditions is an important aspect of anodic porous alumina.

### 9.2.2. *Synthesis of Highly Ordered Anodic Porous Alumina*

The ordering of the arrangement of the pores in anodic porous alumina is strongly dependent on the anodizing conditions. Under the appropriate anodizing conditions, long-range ordered anodic porous alumina with an ideally ordered pore arrangement in a large area can be obtained.<sup>6–10</sup> The most important parameter in anodizing conditions for obtaining long-range ordering is the applied voltage, which is specific for the electrolyte used for anodization. By selecting the appropriate electrolyte and applied voltage, anodic porous alumina with long-range ordering can be obtained with a wide variety of pore intervals. Figure 9.2 summarizes the examples of the anodic porous alumina with long-range ordered pore

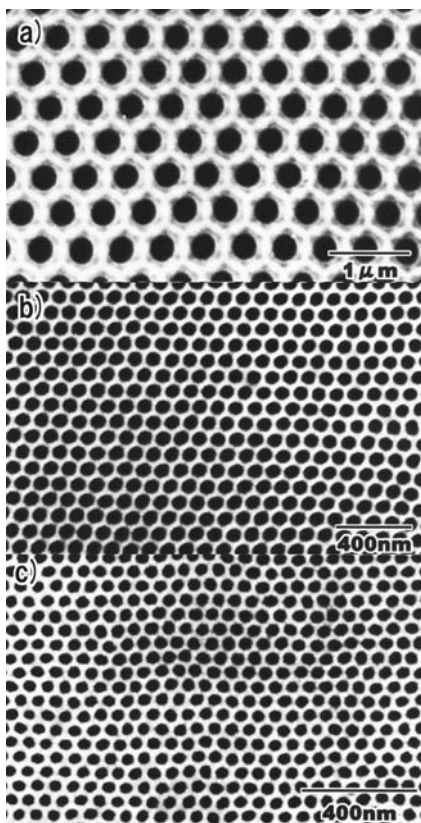


FIGURE 9.2. Long-range ordered pore arrangement in anodic porous alumina: (a) phosphoric acid,<sup>9</sup> (b) oxalic acid,<sup>6,7</sup> and (c) sulfuric acid.<sup>8</sup>

arrangement in anodic porous alumina prepared using several types of typical acidic solution.

The pore arrangement of anodic porous alumina in the initial stage of anodization is random and the degree of ordering is very low. The ordering of the anodic porous alumina proceeds with time under appropriate anodizing conditions. If the anodic porous alumina, at the surface of which the pore arrangement has long-range ordering, the special technique called two-step anodization can be applied effectively.<sup>7</sup> In this process, the porous layer is removed selectively in a mixed solution of chromium oxide and phosphoric acid after a long period of anodization under appropriate anodizing conditions. This results in the long-range ordering of the pore arrangement. During the second anodization, the long-range ordered pore arrangement can be obtained in the initial stage of anodization, because the ordered array of concaves obtained after the removal of the oxide layer formed at the first anodization can act as initiation sites for pore development and they guide the growth of straight pores. This process is effective for the preparation of anodic porous alumina with straight pores throughout the entire membrane.

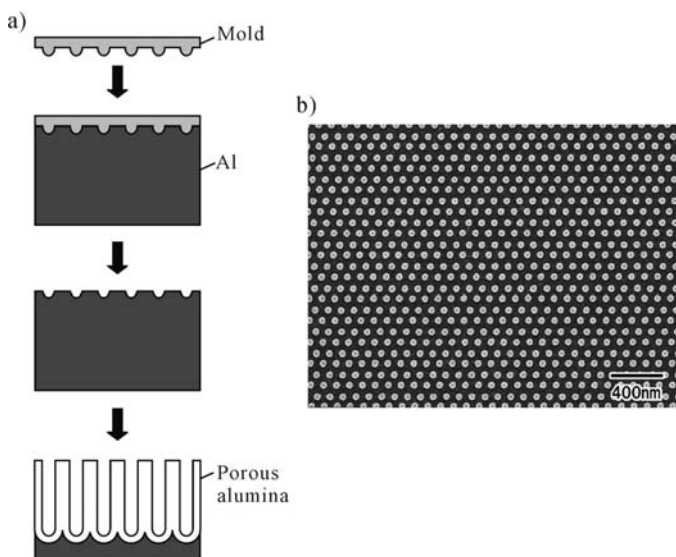


FIGURE 9.3. Formation of an ideally ordered pore arrangement: (a) imprinting process and (b) mold used for the imprinting.

### 9.2.3. Ideally Ordered Anodic Porous Alumina by the Pretexturing Process Using Molds

To form the ideally ordered pore arrangement over the entire sample in anodic porous alumina, the combined process of pretexturing of Al and subsequent anodization is applied.<sup>11–13</sup> In this process, the shallow concaves on Al formed by mechanical imprinting using a mold with ordered convexes introduce the ideally ordered hole development during anodization (Fig. 9.3). The mold for imprinting is prepared by electron-beam lithography using semiconductors<sup>11,12</sup> or metals.<sup>13</sup> In the subsequent anodization, the applied voltage must be adjusted to satisfy the linear relationship between the applied voltage and pore interval. Figure 9.4 shows the scanning electron microscopic (SEM) micrographs of an example of the obtained anodic porous alumina with an ideally ordered pore arrangement.<sup>11</sup> The highly ordered porous structures with an extremely high aspect ratio can be confirmed from the cross-sectional SEM image in Fig. 9.4.

Even in the case of anodization with the pretexturing process for the ideally ordered pore arrangement, the degree of ordering of the pore arrangement in the direction of the thickness is dependent on the anodizing conditions. The ideally ordered porous structure with a high aspect ratio cannot be obtained without the appropriate anodizing conditions. This implies that the self-organized mechanism in pore arrangement plays an important role in the growth of the ordered porous structures even in the case of anodization with the pretexturing process.

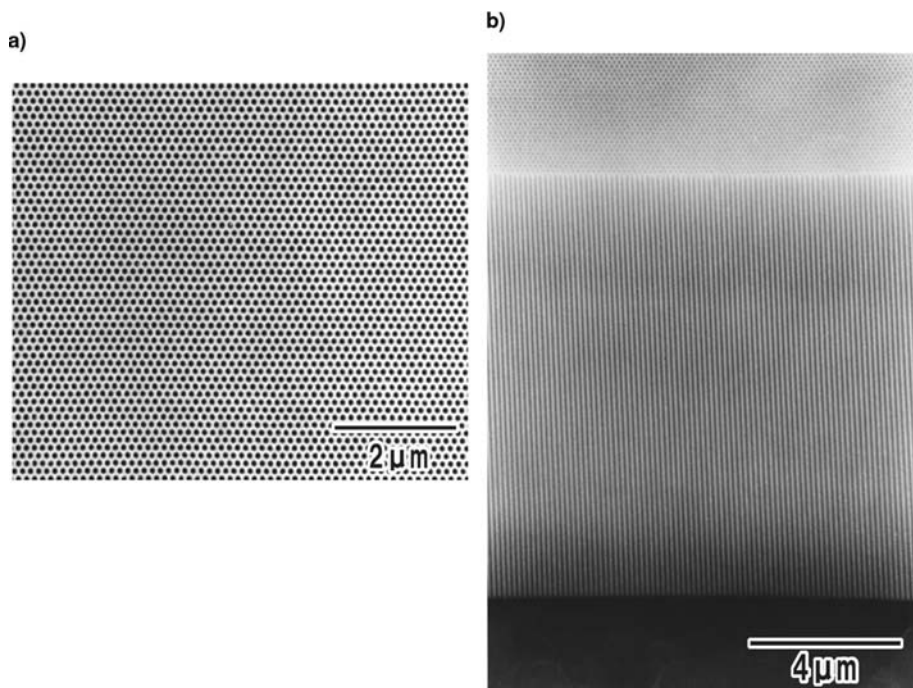


FIGURE 9.4. Fabricated ideally ordered porous alumina: (a) surface view and (b) cross-sectional view.

The fabrication of ideally ordered porous alumina by a similar process for the pretexturing using a focused ion beam (FIB) apparatus has been reported.<sup>14</sup>

For the preparation of textured Al, self-organized ordered structures can also be used as the starting structure. In Fig. 9.5, the processes for the pretexturing of Al using the self-organized array of polystyrene particles is described. This process generates the highly ordered pore arrangement in anodic porous alumina without the need for expensive apparatuses.<sup>15</sup>

### 9.3. Ordered Nanostructures Based on Highly Ordered Anodic Porous Alumina

#### 9.3.1. Nanocomposite Structures Using Highly Ordered Anodic Porous Alumina

Using anodic porous alumina as a template, several types of nanocomposite composed of nanocylinders or nanotubes in an alumina matrix can be prepared.<sup>2–5, 16–18</sup> Figure 9.6 shows a typical example of the ordered array of nanocylinders (Au) prepared using an anodic porous alumina template with an ideally ordered pore arrangement. For the preparation of nanocomposites, several techniques for

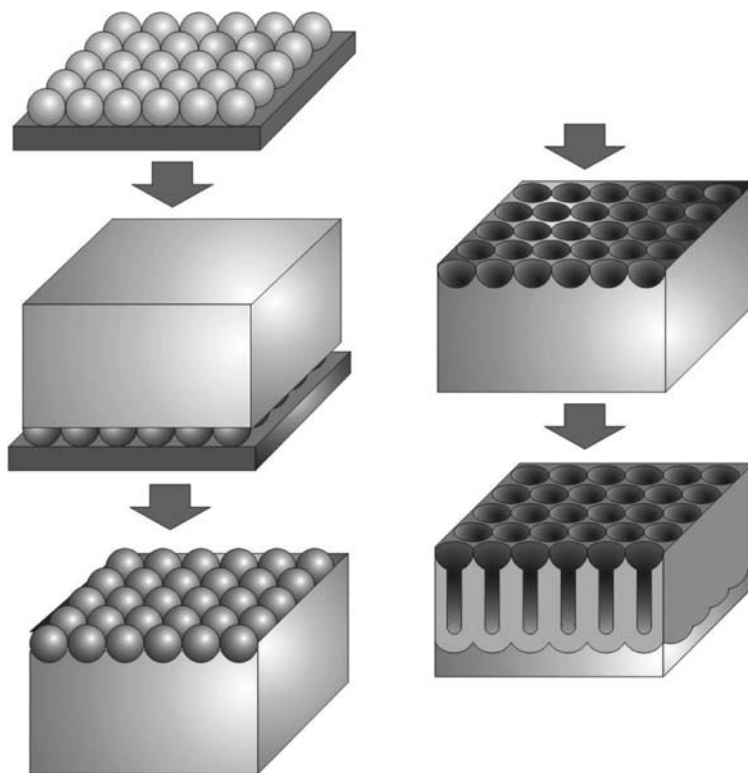


FIGURE 9.5. Processes of the pretexturing of Al using the self-organized array of polystyrene particles.<sup>15</sup>

depositing materials into the pores of the anodic porous alumina are available. One typical process for depositing materials into the pores of anodic porous alumina is electrochemical deposition of metal or semiconductors, which has the advantage of uniform filling of pores with high aspect ratios in anodic porous alumina.

By modifying the structure of anodic porous alumina and the process for the deposition of materials, nanocomposites with complex structures can be obtained.<sup>19</sup> Figure 9.7 shows the nanocomposites composed of two different kinds of guest material (Au and Ni) in the alumina matrix. This mosaic structure was prepared by the sequence of selective through-holing of the barrier layer and the subsequent deposition of materials based on the difference in the thickness of the barrier layer between imprinted and unimprinted sites in the pretexturing process using a mold with a graphite lattice. Such a structure will be used as the platform for the preparation of several nanopatterns composed of different kinds of functional molecule.

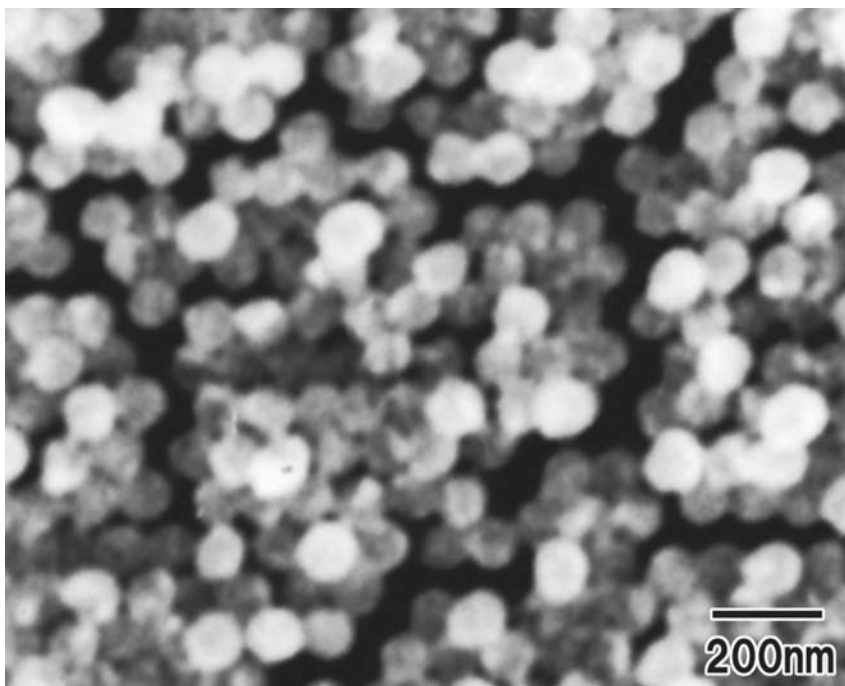


FIGURE 9.6. Ordered array of Au nanocylinders prepared using an anodic porous alumina template.

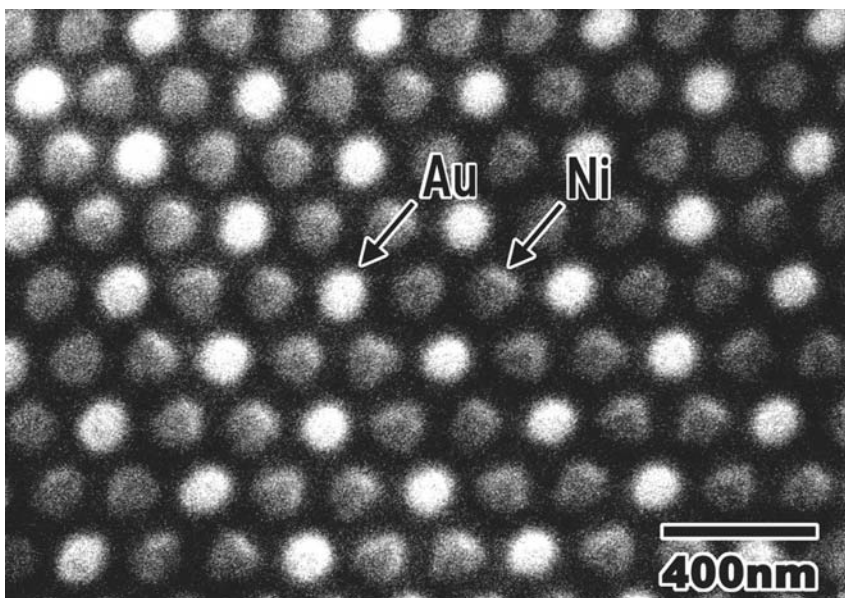


FIGURE 9.7. Nanocomposites composed of the two different kinds of guest material (Au and Ni).

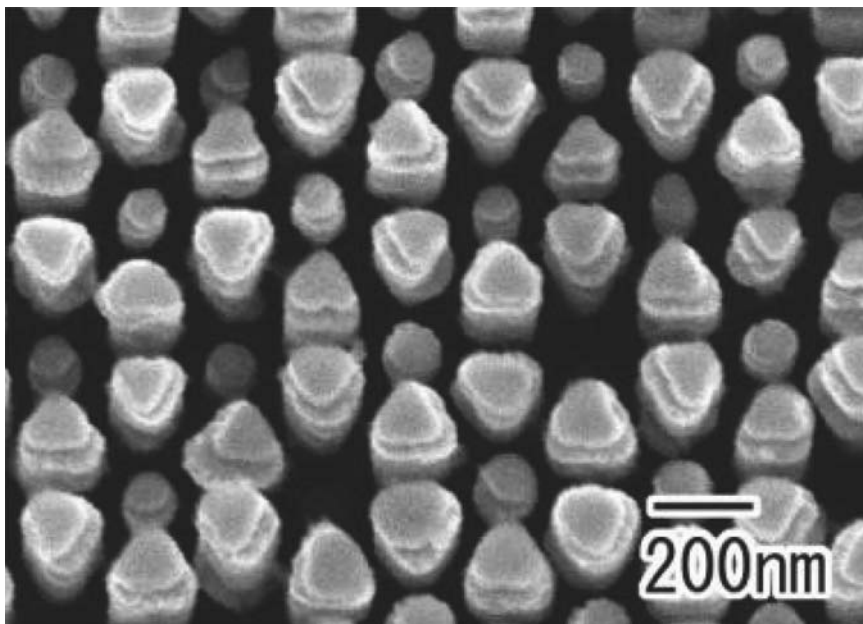


FIGURE 9.8. Ordered array of TiO<sub>2</sub> nanocylinders with triangular cross section.

Based on the pretexturing process of Al, in which the site of pore development can be determined artificially, the shape of the cells and, therefore, the shape of the pores can be modified. Square and triangular pores can be generated from the pore arrangement of the square and graphite lattices, respectively, in addition to hexagonal pores from the triangular lattice. Such shapes are generated by the tiling principle, called Volonui tessellation, which determines the boundary of the territory of influence of each pore in anodic porous alumina.

Once the geometrical structure of the anodic porous alumina template is modified, a wide variety of nanostructures with controlled shapes can be obtained. Figure 9.8 shows an example of shape-modified nanocylinders prepared by template synthesis. In this case, the ordered array of TiO<sub>2</sub> nanocylinders with triangular cross section was prepared by electrochemical deposition of TiO<sub>2</sub> using anodic porous alumina with triangular pores.<sup>20</sup>

Figure 9.9 shows the carbon nanotubes with triangular cross section formed by chemical vapor deposition (CVD) on porous alumina templates with triangular pores.<sup>21</sup> Template synthesis of carbon nanotubes using anodic porous alumina has been widely studied for the purpose of preparing an aligned array of uniform-sized carbon nanotubes applying the high thermal stability of the anodic porous alumina needed for the CVD process. The control of the shape of the carbon nanotubes will be used for the modification of the electronic properties of carbon nanotubes, which are used in a wide variety of applications.

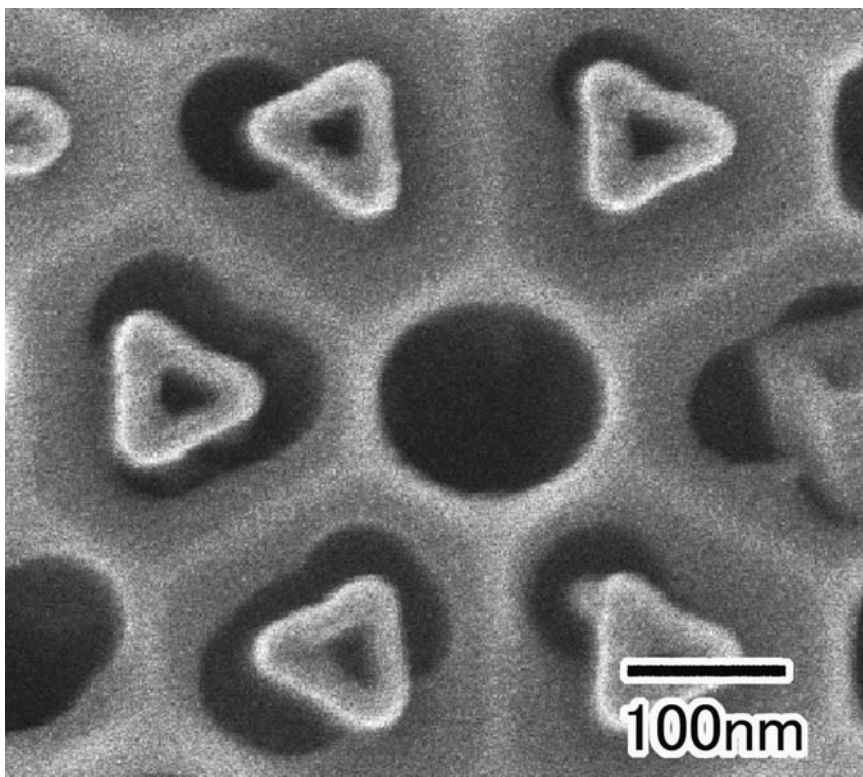


FIGURE 9.9. Carbon nanotubes with triangular cross section.

### 9.3.2. Nanofabrication Using Anodic Porous Alumina Masks

Anodic porous alumina membranes with through-holes are obtained by removing the barrier layer by wet etching in appropriate acidic solutions after removing the Al substrate in a saturated  $\text{HgCl}_2$  aqueous solution or a saturated  $\text{I}_2$  ethanol solution.

The anodic porous alumina membrane with through-holes can be applied to the fabrication of various nanostructures on the substrates (Fig. 9.10). Figure 9.10 shows the process of preparing a nanodot array using an anodic porous alumina mask.<sup>7</sup> For the mask preparation, the two-step anodization process was used because this process generates straight holes through the entire thickness of the membrane along which the vacuum-evaporated material can penetrate to be deposited on the substrate. Figure 9.10 also shows the SEM micrograph of the Au nanodot array formed on the Si substrate using an alumina mask prepared by the two-step anodization. Almost uniform-sized Au dots with ordered arrangement can be observed over the Si substrate. Similar mask processes have also been applied to molecular beam epitaxy (MBE) deposition of semiconductors on substrates.<sup>22</sup>



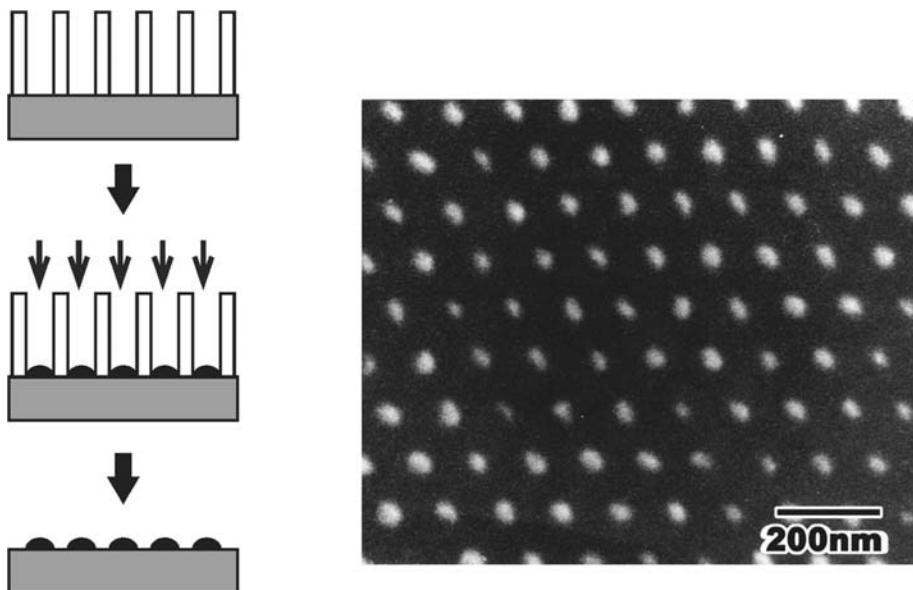


FIGURE 9.10. Process for the preparation of a nanodot array using an anodic porous alumina mask.

One of characteristic of the anodic porous alumina mask is its high aspect ratio. Making use of this property, a ordered arrays of multiple dots composed of two different kinds of metal were formed on a Si substrate (Fig. 9.11).<sup>23</sup> Metals were deposited on the substrate through the alumina mask by varying the incident angles of the metal beam. Shadowed evaporation of metals results in the spatially resolved deposition of metals at the bottom of the aperture of the mask and produces the multiple dots composed of two or three kinds of metal. This ordered array of composite nanodots are promising for the preparation of various functional ordered arrays of composite on substrates utilizable for model catalysts or sensors with high selectivity or sensitivity.

Another advantage of the anodic porous alumina mask is the high resistance to the plasma etching used for dry etching of substrates. The high resistance of the alumina mask to plasma etching contributes to enabling the nanofabrication of high-aspect-ratio features in semiconductor substrates such as InP or GaAs.

To improve the reproducibility and uniformity of the alumina masks prepared, another mask process is applicable in which a thin Al layer formed by vacuum evaporation or sputtering on a substrate is anodized to form a porous alumina mask on the substrate. Figure 9.12 shows a typical example of the anodic porous alumina mask prepared on Si using vacuum-deposited Al.<sup>24</sup> In this case, the texturing of vacuum-evaporated Al was carried out to generate the anodic porous alumina mask with an ideally ordered pore arrangement.

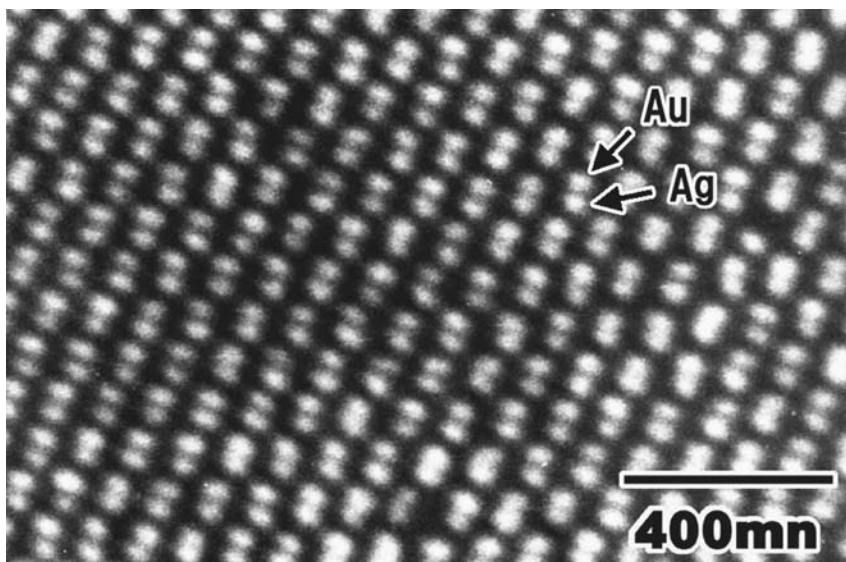


FIGURE 9.11. Ordered arrays of nanodots composed of two different kinds of metal (Au and Ag).

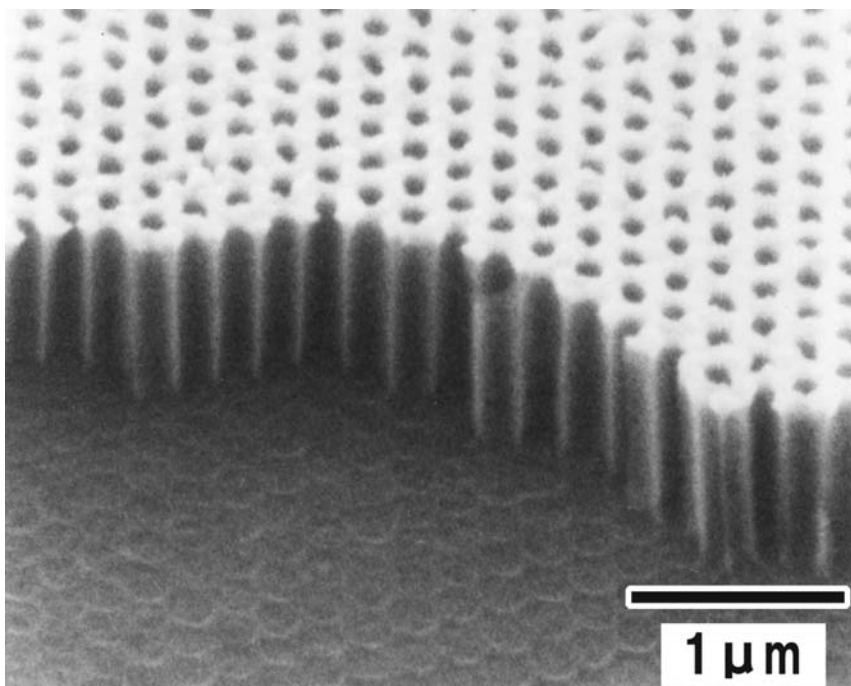


FIGURE 9.12. Anodic porous alumina mask prepared on Si.

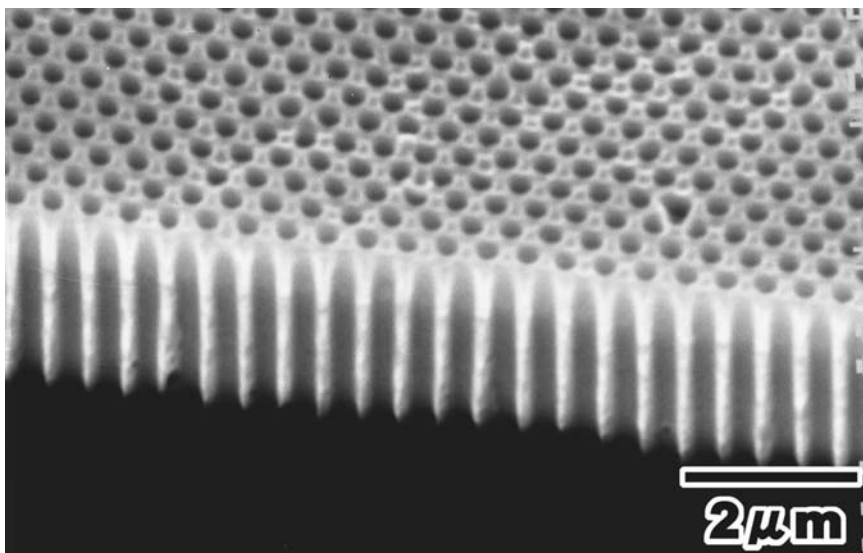


FIGURE 9.13. Metal (Ni) hole array prepared by the two-step replication process using the ideally ordered anodic porous alumina.

### 9.3.3. Two-Step Replication Process for Functional Nanohole Arrays

Full replication of the geometrical nanostructures of the anodic porous alumina contributes to the expansion of the applicability of anodic porous alumina. The two-step replication process is used for the formation of the replicated negative of the anodic porous alumina and the subsequent formation of the replicated positive. It results in a hole array of metals or semiconductors that has a geometrical structure identical to that of the starting porous alumina.<sup>25–29</sup> Figure 9.13 shows an example of the metal hole array prepared by the two-step replication process using the ideally ordered anodic porous alumina.<sup>25</sup>

Such ordered metal hole arrays show the unique optical properties arising from their geometrical structures. The metal hole arrays transmit the incident light selectively, depending on their pore sizes (Fig. 9.14). Such unique transmission properties will be used for the preparation of several types of functional optical device.

Figure 9.15 shows an example of the hole array structure made of semiconductors.  $\text{WO}_3$ , which is a typical electrochromic material, was deposited on the negative type to form the  $\text{WO}_3$  porous structures.<sup>28</sup> The electrochromic property of the porous  $\text{WO}_3$  obtained was enhanced corresponding to the porosity of the membrane during polarization (Fig. 9.16). Such an increase of coloring and bleaching is due to the enhancement of ion ( $\text{Li}^+$ ) migration during electrolysis, according to the geometrical structures of  $\text{WO}_3$ .

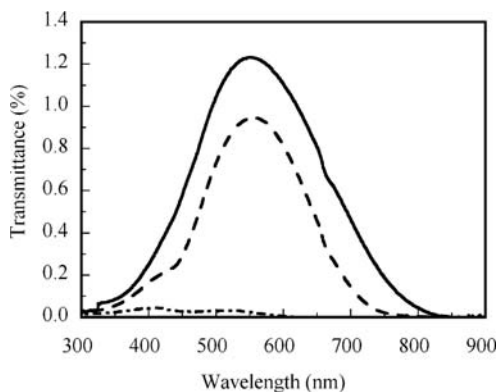


FIGURE 9.14. Transmission spectra of Ni hole array membranes with different hole sizes: 390 nm (—), 370 nm (---), and 220 nm (- · -).

#### 9.3.4. Ordered Array of Biomolecules Using Highly Ordered Anodic Porous Alumina

The fabrication of ordered arrays of functional biomolecules, such as proteins, DNA, and enzymes, is important because of its potential for application to several kinds of biomolecular nanodevice. The use of highly ordered anodic porous alumina results in the efficient formation of ordered arrays of biological molecules. Figure 9.17 shows the SEM micrograph of the ferritin molecules, which have ferric oxide cores of 13 nm, formed on the Au disk array in the anodic porous alumina.<sup>30</sup> A Au disk array was prepared by depositing Au into the pores of the anodic porous alumina substrate. From Fig. 9.17, it is confirmed that the ferritin molecules are adsorbed selectively on the Au disk to form the distinct array on anodic porous alumina.

Figure 9.18 shows the ordered pattern of DNA using the Au disk array.<sup>31</sup> Fluorescent-dye-labeled, thiolated DNA was fixed on the Au disks in the anodic porous alumina substrates. Under the fluorescence microscope, ordered

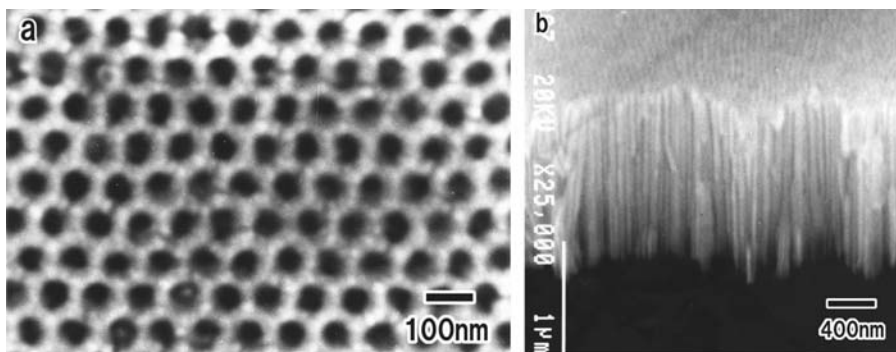


FIGURE 9.15.  $\text{WO}_3$  hole array membrane: (a) surface view and (b) cross-sectional view.

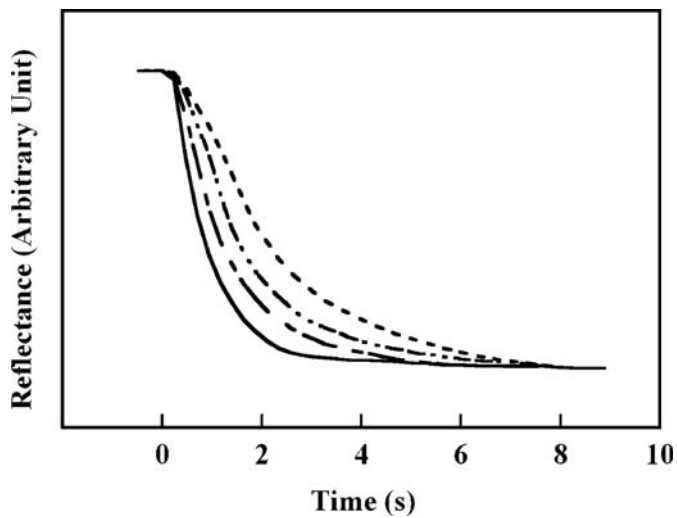


FIGURE 9.16. Electrochromic property of the porous  $\text{WO}_3$  membrane with different pore sizes: 65 nm (—), 53 nm (---), 38 nm (- · - · -), and flat membrane (· · ·).

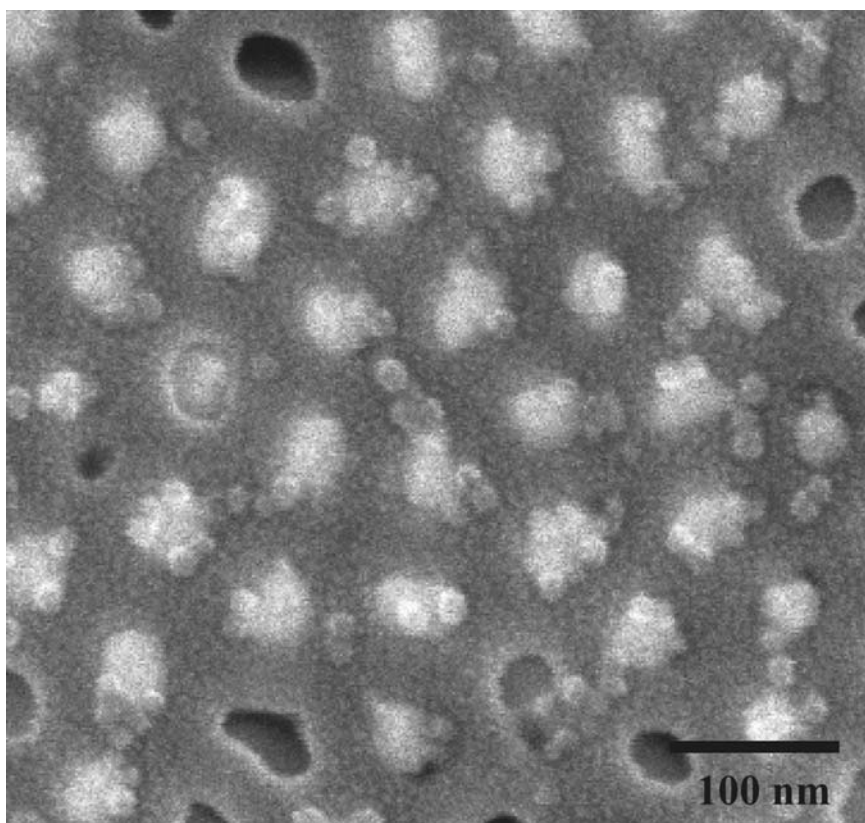


FIGURE 9.17. SEM micrograph of the ferritin molecules formed on the Au disk array in the anodic porous alumina.

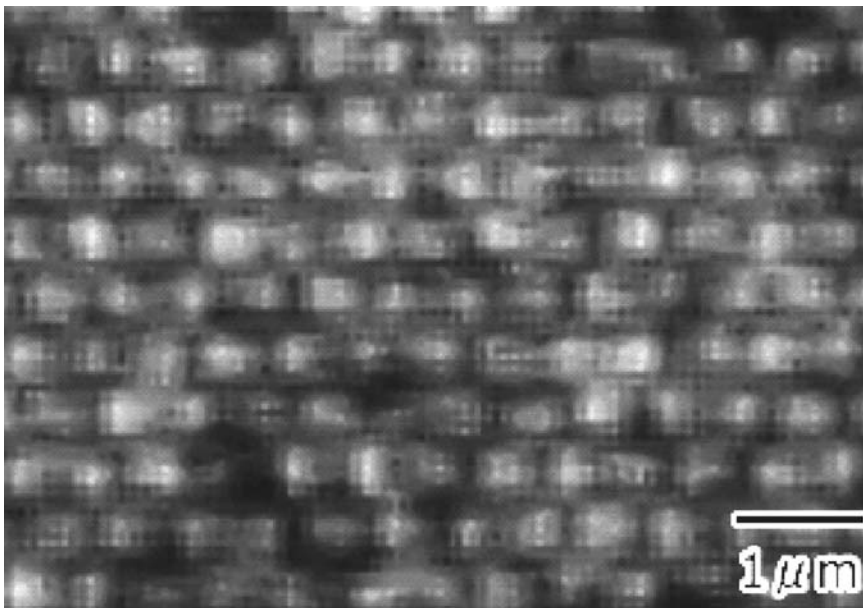


FIGURE 9.18. Ordered pattern of dye-labeled, thiolated DNA using the Au disk array in the anodic porous alumina.

fluorescence spots coincident with the Au disk array in anodic porous alumina could be observed. The ordered array of DNA on Au disks maintained the ability to recognize the target DNA and could be applied to hybridization with the target DNA in sample solutions.

The present process is also applicable to the preparation of ordered arrays of proteins, antibodies, and enzymes, with control of the size and intervals. Further reduction of the sizes and intervals of the patterns will be effective for the preparation of ordered arrays of individual functional biomolecules applicable in functional molecular devices.

## 9.4. Conclusions

In this chapter, the synthesis and applications of highly ordered anodic porous alumina have been described. Highly ordered anodic porous alumina was prepared based on the naturally occurring self-ordering and pretexturing processes of Al. The obtained anodic porous alumina with highly ordered pore arrangement could be applied, for example, to the fabrication of several types of ordered metal and semiconductor nanostructures, nanocomposite, nanodots array, and nanohole array.

The highly ordered anodic porous alumina will be applicable to the preparation of a wide variety of functional nanodevices because of its unique fine geometrical structures that are easily controlled by adjusting the anodizing conditions.

## References

1. F. Keller, M. Hunter, and D. L. Robinson, Structural features of oxide coating on aluminum, *J. Electrochem. Soc.* **100**, 411 (1953).
2. S. Kawai and R. Ueda, Magnetic properties of anodic oxide coatings on aluminum containing electrodeposited cobalt and cobalt-nickel, *J. Electrochem. Soc.* **122**, 32 (1975).
3. D. G. W. Goad and M. Moskovits, Colloidal metal in aluminum oxide, *J. Appl. Phys.* **49**, 2929 (1978).
4. M. J. Tierney and C. R. Martin, Transparent metal microstructures, *J. Phys. Chem.* **93**, 2878–2880 (1989).
5. C. A. Huber, T. E. Huber, M. Sadoqi, J. A. Lubin, S. Manalis, and C. B. Prater, Nanowire array composites, *Science*, **263**, 800–802 (1994).
6. H. Masuda and K. Fukuda, Ordered metal nanohole arrays made by a two-step replication of honeycomb structures of anodic alumina, *Science* **268**, 1466–1468 (1995).
7. H. Masuda and M. Satoh, Fabrication of gold nanodot array using anodic porous alumina as an evaporation mask, *Jpn. J. Appl. Phys.* **35**, L126–L129 (1996).
8. H. Masuda, F. Hasegawa, and S. Ono, Self-ordering of cell arrangement of anodic porous alumina formed in sulfuric acid solution, *J. Electrochem. Soc.* **144**, L127–L130 (1997).
9. H. Masuda, K. Yada, and A. Osaka, Self-ordering of cell configuration of anodic porous alumina with large-size pores in phosphoric acid solution, *Jpn. J. Appl. Phys.* **37**, L1340–L1342 (1998).
10. P. Li, F. Muller, A. Brirner, K. Nielsh, and U. Gosele, Hexagonal pore arrays with a 50–420 nm interpore distance formed by self-organization in anodic alumina, *J. Appl. Phys.* **84**, 6023–6026 (1998).
11. H. Masuda, H. Yamada, M. Satoh, H. Asoh, M. Nakao, and T. Tamamura, Highly ordered nanochannel-array architecture in anodic alumina, *Appl. Phys. Lett.* **71**, 2770–2772 (1997).
12. H. Asoh, K. Nishio, M. Nakao, A. Yokoo, T. Tamamura, and H. Masuda, Fabrication of ideally ordered anodic porous alumina with 63 nm hole periodicity using sulfuric acid, *J. Vac. Sci. Technol. B* **19**, 569–572 (2001).
13. H. Masuda, M. Yotsuya, M. Asano, K. Nishio, M. Nakao, A. Yokoo, and T. Tamamura, Self-repair of ordered pattern of nanometer dimensions based on self-compensation properties of anodic porous alumina, *Appl. Phys. Lett.* **78**, 826–828 (2001).
14. C. Y. Liu, A. Datta, and Y. L. Wang, Ordered anodic alumina nanochannels on focused-ion-beam-prepatterned aluminum surfaces, *Appl. Phys. Lett.* **78**, 120–122 (2001).
15. H. Masuda, Y. Matsui, M. Yotsuya, F. Matsumoto, and K. Nishio, Fabrication of highly ordered anodic porous alumina using self-organized polystyrene particle array, *Chem. Lett.* **33**, 584–585 (2004); Y. Matsui, K. Nishio, and H. Masuda, Highly Ordered Anodic Porous Alumina by Imprinting Using Ni Molds Prepared from Ordered Array of Polystyrene Particles, *Jpn. J. Appl. Phys.*, **44**, 7726–7728 (2005).
16. S. G. Yang, H. Zhu, G. Ni, D. L. Yu, S. L. Tang, and Y. W. Du, A study of cobalt nanowire arrays, *J. Phys. D* **33**, 2388–2390 (2000).
17. T. Kyotani, L. Tsai, and A. Tomita, Preparation of ultrafine carbon tubes in nanochannels of an anodic aluminum oxide film, *Chem. Mater.* **8**, 2109–2113 (1996).
18. T. Iwasaki, T. Motoi, and T. Den, Multiwalled carbon nanotubes growth in anodic alumina nanoholes, *Appl. Phys. Lett.* **75**, 2044–2046 (1999).
19. H. Masuda, A. Abe, M. Nakao, A. Yokoo, T. Tamamura, and K. Nishio, Ordered mosaic nanocomposites in anodic porous alumina, *Adv. Mater.* **15**, 161–164 (2003).

20. T. Yanagishita, M. Sasaki, K. Nishio, and H. Masuda, Fabrication of TiO<sub>2</sub> nanoparticles with triangular cross section by template process, *J. Surf. Fin. Soc. Jpn.* **55**, 1 (2004).
21. T. Yanagishita, M. Sasaki, K. Nishio, and H. Masuda, Carbon nanotubes with a triangular cross-section, fabricated using anodic porous alumina as the template, *Adv. Mater.* **16**, 429–432 (2004).
22. X. Mei, D. Kim, H. E. Ruda, and Q. X. Guo, Molecular-beam epitaxial growth of GaAs and InGaAs/GaAs nanodot arrays using anodic Al<sub>2</sub>O<sub>3</sub> nanohole array template masks, *Appl. Phys. Lett.* **81**, 361–363 (2002).
23. H. Masuda, K. Yasui, and K. Nishio, Fabrication of ordered arrays of multiple nanodots using anodic porous alumina as an evaporation mask, *Adv. Mater.* **12**, 1031–1033 (2000).
24. H. Masuda, K. Yasui, Y. Sakamoto, M. Nakao, T. Tamamura, and K. Nishio, Ideally ordered anodic porous alumina mask prepared by imprinting of vacuum-evaporated Al on Si, *Jpn. J. Appl. Phys.* **40**, L1267–L1269 (2001).
25. K. Nishio, M. Nakao, A. Yokoo, and H. Masuda, Ideally ordered metal hole arrays with high aspect ratios prepared from anodic porous alumina, *Jpn. J. Appl. Phys.* **42**, L83 (2003).
26. H. Masuda, K. Nishio, and N. Baba, Fabrication of porous TiO<sub>2</sub> films using two-step replication of microstructure of anodic porous alumina, *Jpn. J. Appl. Phys.* **31**, L1775 (1992).
27. H. Masuda, T. Mizuno, N. Baba, and T. Ohmori, Fabrication of Pt microporous electrodes from anodic porous alumina and immobilization of GOD into their micropores, *J. Electroanal. Chem.* **368**, 333–336 (1994).
28. K. Nishio, K. Iwata, and H. Masuda, Fabrication of nanoporous WO<sub>3</sub> membranes and their electrochromic properties, *Electrochem. Solid-State Lett.* **6**, H21–H23 (2003).
29. T. Ohmori, T. Kimura, and H. Masuda, Impedance measurement of platinum cylindrical porous electrode replicated from anodic porous alumina *J. Electrochem. Soc.* **144**, 1286 (1997).
30. H. Masuda, H. Hogi, K. Nishio, and F. Matsumoto, Arrangement of ferritin molecules on a gold disk array fabricated on highly ordered anodic porous alumina substrate, *Chem. Lett.* **33**, 812–813 (2004).
31. F. Matsumoto, K. Nishio, T. Miyasaka, and H. Masuda, Ideally Ordered, High-Density Patterning of DNA on Au Disk Array Fabricated Using Anodic Porous Alumina, *Jpn. J. Appl. Phys.* **43**, L640 (2004).



# Index

## A

- ACA-TIPT mole ratio, effect of, 77
- aluminum contact rings, 40
- amorphous metal oxide thin films
  - molecular imprinting in
    - incorporation and removal of templates, 194–198
    - multifunctionality of imprinted sites, 202–205
    - nature of the imprinted sites, 200–202
    - stability and selectivity of imprinted sites, 198–200
    - varied molecular selectivity, 205–206
- preparation of, 189–190
- anodic porous alumina
  - application of
    - nanocomposite structures, preparation of, 300–304
    - in nanofabrication, 304–306
    - ordered array of biomolecules, formation of, 308–310
    - in two step replication process, 307
  - growth on Al, 296–297
  - ideally ordered, 299–300
  - synthesis of highly ordered, 297–299
- anthracenecarboxylic acids, 199
- antibody immobilization methods, 235
- Asaro-Tiller-Grinfeld instability, 9
- atomic force microscope (AFM), 5, 263
- Au disk array, 308

## B

- BET (Brunauer–Emmett–Teller)-specific surface area, 91
- bimetallization, 251
- bio-inspired approach
  - polymer controlled crystallization, 134–136

- small molecular organic species-mediated crystallization, 139–140
- supramolecular self-assembly, 137–139

## C

- C<sub>3</sub>AzoCO<sub>2</sub>H-imprinted film, 198, 206
- capacitance–voltage spectroscopy, 50
- capping agents/surfactants assisted synthesis
  - self assembly under hot conditions, 126–131
  - self assembly under natural/mild conditions, 132–134
- carbon pretreatment effects, on Ge dots, 44–45
- carrier generation efficiency, 46–47
- CdSe nanocrystallites, 126
- chiral microporous solids, 176–178
- chiral separation factor, 204
- Co<sub>3</sub>O<sub>4</sub>, 72
- coaxed nanobelt-within-nanotube structure, 122
- cobalt nanocrystals, self-organization of
  - annealing effects, 276–277
  - evaporation effects, 278
  - influential forces, 271
  - Langmuir–Blodgett technique, effect of, 278
  - solvent evaporation process, role of, 271
  - surface tension, role of, 275
  - temperature, role of, 273–274
- CoFe<sub>2</sub>O<sub>4</sub> nanocrystals, 72
- conducting glass
  - fluorine-doped tin oxide (FTO), 88
  - indium–tin oxide (ITO), 88
- conical nanotubes, 241–245
- core-shell bimetallic nanoparticles
  - characterization

core-shell bimetallic nanoparticles (*cont.*)  
 electron microscopic observations,  
 263–264  
 IR spectroscopy of chemical probes, 265  
 UV-visible spectroscopy, 264  
 X-ray, 260–262  
 preparation procedures  
 other systems, 259  
 successive reduction of metal ions,  
 252–255  
 simultaneous reduction of metal ions,  
 256–259  
 critical minimum wavelength  $\lambda_c$ , for stable  
 undulations, 9  
 crystalline molecular sieve synthesis process  
 assembly processes  
 metal-ion assisted, 168–169  
 proposed mechanisms for zeolite assembly,  
 165–168  
 components of  
 mineralizing agents, 170–171  
 organic, 169–170  
 T atoms, 171–175  
 kinetics of, 162–164  
 thermodynamics of, 160  
 steps in, 162

## D

1D-growth stage, 126  
 Debye–Sherrer rings, 75, 77, 86  
 defect-free growth, 2  
 dendrimer molecules, 213–214  
 dendron rodcoils (DRC), 138  
 Derjaguin–Landau–Verwey–Overbeek (DLVO)  
 theory, 165  
 dot engineering, significance of, 41  
 double 4-MR structure (D4MR), 173  
 double-hydrophilic block copolymers (DHBCs),  
 134  
 dye-sensitized solar cells, making of, 88–89

## E

EL quantum efficiency (QE), 41  
 exciton diffusion effects, 32  
 extrinsic surface morphology, 43–44

## F

4-[3-(4-fluorophenyl)-2-hydroxy-1-  
 [1,2,4]triazol-1-yl-propyl]-benzonitrile  
 (FTB), 227  
 field-emission scanning electron microscope  
 (FESEM), 233  
 footprint technique, 187

Frank–van der Merwe growth mode, 2  
 free energy, 2

## G

Gallium phosphide semiconductor nanocrystals,  
 128  
 GaP–HDA complexes, 130  
 Ge concentrations, 47, 49, 161  
 gradient, 7, 36  
 Ge dome islands, 8, 26, 50  
 Ge-rich platelets, 26  
 Gibbs free energies, 162  
 Gibbs–Thompson law, 126  
 glucose oxidase (GOD) immobilization, 229  
 Gly–Phe binding, lack of, 207  
 gold nanoparticles, use of, 221  
 gold nanotubes, 234, 236  
 gold shells, 255  
 gold-coated quartz crystal microbalance (QCM),  
 189  
 green fluorescent silane  
*N*-(triethoxysilylpropyl)dansylamide,  
 224

## H

hairpin-DNA transporter, 236, 238–240  
 highly oriented pyrolytic graphite (HOPG)  
 substrate, 271  
 hut clusters, 4, 26  
 hydrothermal/solvothermal process  
 hydrothermal usage effects, 110  
 solvothermal process advantages, 111  
 syntheses of low-dimensional oxide  
 nanostructures  
 lanthanide hydroxide nanowires,  
 nanotubes, nanorods, 113  
 lanthanide orthophosphate nanowires, 115  
 $\text{MoO}_3 \cdot \text{H}_2\text{O}/\text{MoO}_3$  nanorods, 112  
 tungstate/molybdate nanowires, nanotubes,  
 nanorods, 113–114  
 $\text{VO}_x$  nanotubes, 112  
 syntheses of low-dimensional nonoxide  
 nanocrystals  
 Bi nanotubes, 122  
 carbon nanostructures, 123  
 CoPt alloy nanowires, 122  
 II–VI group, 116–119  
 tellurium nanobelts, nanotubes,  
 nanohelices, 122  
 ternary metal chalcogenide nanorods,  
 121–122  
 V–VI group, 120  
 hysteresis loop, 286, 288

**I**

intrinsic surface morphology, 42–43  
ion-sensitive field-effect transistors (ISFETs), 209

**J**

Joint Committee on Powder Diffraction Standards (JCPDS), 77

**L**

Leybold Sirius deposition system, 10  
linear elastic theory, 8  
Loewenstein's rule, 159  
low dimensional nanocrystals, synthetic  
    strategies  
    assisted synthesis  
        hydrothermal/solvothermal process, *see*  
        hydrothermal/solvothermal process  
        oriented attachment growth mechanism,  
        140–142  
        solution–liquid–solid (SLS) mechanism,  
        125–126  
hard approaches, 102  
    oxide-assisted nanowires growth route, 103  
    template-directed growth method, 102  
    vapor–liquid–solid (VLS) mechanism, 102  
    vapor–solid (VS) mechanism, 102  
soft approaches, 103–108  
    bio-inspired approach, *see* bio-inspired  
    approach  
    capping agents/surfactants assisted  
    synthesis, *see* capping agents/surfactants  
low-pressure chemical vapour deposition  
    (LPCVD) growth, 46

**M**

magnetic storage media, 270  
mask processes, 304  
mesostructures of magnetic nanocrystals,  
    magnetic properties of  
        depending on organization, 284  
        magnetic anisotropy energy (MAE), 283  
        structural order, 286  
        temperature effects, 283  
microparticles, application of, 221  
minimization of surface energy, effects of, 2–3  
misfit dislocations, 42  
MnO<sub>2</sub>, 72  
molecular imprinting, 186  
    drawbacks of, 187  
    future prospects of, 215–216  
    practical potential of  
        biological molecule recognition, 206–208  
        contrivance for high sensitivity, 209

    coordination geometry recognition, 210  
    direct observation of imprinted sites,  
        212–215  
        new ion exchange process, 210–212  
    significance of, 187  
molecular wrapping, 216  
monodispersed metal nanoparticles, 251  
monomer concentration, effect of, 71–72

**N**

nano nomenclature, 223  
nano test tubes, template synthesis of, 229–234  
nanoparticles, application of, 221  
    spherical nanoparticles, 222  
    surface functionalized nanoparticles, 222  
nanopore alumina membranes, 230  
    for bioseparations  
        for selective enantiomeric separations,  
        234–236  
        for single-base mismatch transport  
        selectivity, 236–241  
nanosize materials, morphological control of,  
    71  
nanotubes, attributes of  
    for biocatalysis, 226–229  
    for chemical and bioextraction, 226–229  
    differential functionalization attachment,  
    224  
natural quartz, 176

**O**

optical phonon frequency shift, 20  
Ostwald ripening model, 7, 163

**P**

“pearl necklace” agglomerates, 72  
photocurrent spectra, modeling of, 49  
polyhol process, 131  
powder X-ray diffractograms, 261  
pretexturing process, 299  
PSS/PAH polyelectrolyte capsule, 136  
PVP-stabilized nanoparticles  
    palladium–gold, 252, 256  
    platinum–gold, 252, 256

**R**

Raman spectroscopy, 16  
    errors of, 21  
    FLA modes, of spectra, 23  
Rigaku goniometer, 80  
ripple formation, 9  
rocking scans, 15  
RUB-23, 175

**S**

SAED patterns, 75, 77  
 Sauerbrey's equation, 190  
 scanning electron microscopy (SEM), 263  
 scanning transmission electron microscopy (STEM), 72  
 scanning tunneling microscopy (STM), 263  
 Schimmel etch, 29, 40  
 $\text{Si}_{1-x}\text{Ge}_x$  interdiffusion phenomena, 7  
 $\text{Si}_{1-x}\text{Ge}_x$  islands  
   applications of  
     other, 50–51  
     photodetectors, 46–50  
   engineering, 41  
     influence of adsorbed species, 42–44  
     influence of surface morphology, 44–46  
   growth, 2  
     composition and strain distribution, 7–8  
     modes in heteroepitaxy, 2–4  
     and shape evolution, 4–7  
   intermixing in Ge islands, 7  
   stacked, 8  
     development of morphological instabilities in heteroepitaxy, 9  
     grown by UHV-CVD, 12  
     optical properties, *see*  $\text{Si}_{1-x}\text{Ge}_x$  islands, optical properties of  
     satellite peaks, 13–15  
     structure, 10  
     vertical correlation of, 11  
     vibrational properties, *see*  $\text{Si}_{1-x}\text{Ge}_x$  islands, vibrational properties of  
 $\text{Si}_{1-x}\text{Ge}_x$  islands, optical properties of  
   electroluminescence, 40–41  
   photoluminescence, 25–38  
     2D–3D growth transition with accumulated strain, 28–29  
     carrier localization, 31–32, 34  
     dot-related broad PL features, 34  
     dot stability, 29–31  
     PL of isolated quantum dots, 33  
     PL of self-organized quantum dots, 34–39  
 $\text{Si}_{1-x}\text{Ge}_x$  islands, vibrational properties of  
   annealing studies, 23–24  
   Si/Ge/C dots growth characteristics, 24  
 $\text{Si}_{1-x}\text{Ge}_x$  dots, composition and strain  
   phonon confinement, effect of, 20  
   Si–Si mode frequency in, 21  
   three mode frequencies, 19  
 $\text{Si}_{1-x}\text{Ge}_x/\text{Si}$  superlattices, interfaces of, 22–23

folded longitudinal acoustic (FLA) modes, 22

silica nanotubes, 224  
 solvent-mediated controlling mechanism, 119  
 solvothermal decomposition process (SDP), 120–121  
 sonochemical reduction, 257  
 SSZ-33 family, 174  
 standard lithographic techniques, 43  
 step-bunching bunching, 9  
 strain concentration, role of, 8  
 strained-layer epitaxy, development of, 3  
 strain-energy density, 29  
 Stranski–Krastanow growth mode, 2, 4, 49  
 super quantum interface device (SQUID) analysis, 72  
 “supra” crystals, 271, 287, *see also* cobalt nanocrystals, self-organization of  
 surface pits, 42  
 surface sol-gel process, 188  
   organic compounds in nanohybrid layer, 190–194  
   preparation of amorphous metal oxide thin films, 189–190

**T**

teflon-lined stainless-steel autoclave, 110  
 template-synthesis method, 223–224  
 tetrabutylammonium hydroxide (TBAOH), 87  
 tetraethyl orthosilicate (TEOS) solutions, 139  
 tetraisopropylorthotitanate (TIPT), 74  
 $\text{TiO}_2$  single-crystal anatase nanowires, 73  
   application of, for dye-sensitized solar cells, 87–94  
   by oriented attachment mechanism, 73–79  
     formation of, 74  
     synthesis process of, 74  
   using dodecanediamine as surfactant, 79–87  
     formation of, 80–84  
     molecular nanosheet formation of lepidocrocite phase, 85–87  
     synthesis process of, 80  
 $\text{TiO}_2$ -gel/PAA multilayer film, 192  
 Titania nanocrystals, formation of, *see*  $\text{TiO}_2$  single-crystal anatase nanowires  
 transfection process, 222  
 transmetalation, 254  
 transmission electron microscopy (TEM), 72  
 triton 100-X, 134  
 two-dimensional wetting layer (WL), 4

**U**

UHV-CVD  $\text{Si}_{0.5}\text{Ge}_{0.5}/\text{Si}$  superlattices, 10

**V**

Volmer–Weber growth mode, 2

Volonui tessellation, 303

VPI-8, 169

**W**

waveguide metal–semiconductor–metal (MSM)

photodetector, 47

WO<sub>3</sub>, 72

**X**

X-ray diffraction, 72

**Z**

zeolites, construction of, 159, *see also* crystalline  
molecular sieve synthesis process

zinc salts, solvothermal reaction of, 117

ZnO, 73

ZSM-18, 174